MODELING AND MONITORING THE LONG-TERM BEHAVIOR OF POST-TENSIONED CONCRETE BRIDGES

A DISSERTATION
SUBMITTED TO THE FACULTY OF THE GRADUATE SCHOOL
OF THE UNIVERSITY OF MINNESOTA
BY

Brock D. Hedegaard

IN PARTIAL FULFILLMENT OF THE REQUIREMENTS
FOR THE DEGREE OF
DOCTOR OF PHILOSOPHY

Catherine E.W. French
Carol K. Shield

June 2014

Acknowledgements

I would like to acknowledge the support of the Minnesota Department of Transportation. Numerical computations were performed using resources provided by the University of Minnesota Supercomputing Institute.

Table of Contents

List of Tables

List of Figures

Chapter 1: Introduction

1.1 Problem Statement

In situ post-tensioned concrete structures are subject to ever-changing conditions, including live loading, environmental changes in temperature and humidity, and deformations due to the time-dependent behavior of concrete. Better understanding and sound predictions of the behavior of concrete structures under operational conditions are critical towards the development and implementation of long-term maintenance strategies for these systems.

The field of structural health monitoring is concerned with identifying problematic or damage-related behavior in a structure, with the ultimate goal of providing tools for aiding in structural maintenance and decision making. Predictive modeling of expected bridge behavior is an important component for applications of structural monitoring. Detecting damage that occurs suddenly and causes abrupt and large changes in readings is relatively simple if the damage-related changes in behavior are larger than those of, or strongly orthogonal to, the structure's natural behavior under varying environmental conditions. The process is complicated if environmental factors cause considerably larger changes in measurements than those expected by damage. Furthermore, deterioration of a system is usually a time-dependent process, meaning that the degradation of a structure will not necessarily produce abrupt changes in behavior. Consequently, the undamaged response must be predicted over the course of several months or years so that the structural damage or deterioration can be reliably diagnosed. Accurate predictions of long-term behavior can inform infrastructure maintenance engineers of the possible need and timing for restorative efforts to counteract unwanted behaviors such as excessive deflections or tensile stresses.

Recent studies by Bažant et al. (2009, 2010) regarding the collapse of the Koror-Babeldaob Bridge have highlighted a need for more thorough investigations of time-dependent

(creep and shrinkage) models applied towards post-tensioned concrete bridges. Furthermore, as identified by Sohn (2007), the complexities introduced by the effects that environmental, non-damage related factors have on measurements pose a challenge to monitoring applications that has yet to be definitively overcome.

The research conducted for this project has focused on characterizing the long-term behavior of the St. Anthony Falls Bridge (also known as the I-35W Bridge) so that environmental and time-dependent behavior of post-tensioned concrete bridges might be better understood and implemented into structural monitoring applications. Specifically, this investigation focuses on comparisons between the measured data and time-dependent finite element analysis with regards to the long-term behavior of the structure (e.g., prestress losses, stresses within the cross section, deflections), and techniques for predictive data analysis to be applied towards structural monitoring applications.

1.2 Research Approach and Outline

The time-dependent behavior of post-tensioned concrete bridges was explored through the case study of the St. Anthony Falls Bridge, a post-tensioned concrete box girder structure crossing the Mississippi River in Minneapolis, Minnesota. The behavior of this structure was measured by multiple sensor systems providing information to support the construction process and investigate the long-term performance. Of particular interest were the time-dependent phenomena of creep (continued deformation under sustained load) and shrinkage (reduction in volume due to moisture loss), and how these behaviors would manifest in an in-service structure. Better understanding of these phenomena can facilitate the development of structural monitoring systems that can identify anomalous behavior from in situ readings.

The investigation of time-dependent behavior was divided into four components. The first consisted of laboratory measurements of concrete aging (strength gain), creep, and shrinkage, and comparing these results to various time-dependent provisions from the literature.

The second component was an investigation of the in situ behavior of the St. Anthony Falls Bridge. Time-dependent deformations were extracted from the installed instrumentation, and examined for long-term trends and interactions with temperature. The in situ investigation was closely supported by the third facet of this study, time-dependent finite element modeling of the St. Anthony Falls Bridge. Different time-dependent provisions from the literature were integrated into the finite element analysis to observe how these predictions varied, and to see how each prediction compared to the in situ behavior. The finite element model was also used to explore uncertainty in creep and shrinkage predictions and (using a separate simplified model) the effects of cyclic temperatures on long-term time-dependent behavior. The final component was the development of prediction protocols that would form the basis of an anomaly detection routine tracking the long-term time-dependent performance of the bridge.

The report is organized as follows: the remainder of Chapter 1 consists of a description of the investigated St. Anthony Falls Bridge; Chapter 2 contains a description of the instrumentation types, gage locations, and data collection for the sensors relevant to monitoring the time-dependent behavior of the bridge; Chapter 3 contains material testing procedures and results necessary for the definition of the numerical models presented in this report; Chapter 4 includes a discussion of time-dependent properties of concrete, including provisions for the six investigated literature models; Chapter 5 presents the validation of the time-dependent concrete provisions from the previous chapter with laboratory results; Chapter 6 covers the details of the St. Anthony Falls Bridge finite element model, including the procedures used for viscoelastic computations necessary for the investigation of time-dependent behavior; Chapter 7 shows how time-dependent behavior can be extracted from measured data under varying environmental conditions, including corrections for the dependency of time-dependent deformation rates on concrete temperature; Chapter 8 presents a comparison between the measured time-dependent data and results from finite element analysis of the St. Anthony Falls Bridge; Chapter 9 examines the effects that cyclic

temperature fluctuations, common to field structures, can have on time-dependent behavior; Chapter 10 presents an application of a data prediction and anomaly detection routine to the longitudinal bridge movement for purposes of long-term monitoring; and Chapter 11 summarizes the conclusions from the investigation.

1.3 Bridge Description

The St. Anthony Falls Bridge was constructed as two separate post-tensioned concrete box girder bridges built adjacent to each other: the northbound bridge (Br. 27410) and the southbound bridge (Br. 27409). Each bridge consisted of four spans numbered in ascending order from south to north. An elevation view with span lengths and labels is shown in Figure 1.1. Spans 1 through 3 were continuous, and Span 4 was separated from the rest of the structure by an expansion joint at Pier 4. The three-span continuous structure was supported by sliding bearings with an expansion joint at Abutment 1 (south end of Span 1), pinned connections at Piers 2 and 3, and sliding bearings with an expansion joint at Pier 4 (north end of Span 3). Span 4 was pinned to Pier 4 at the south end and built integrally with Abutment 5 at the north end. Span 2 was constructed using precast segmental construction while the other spans were constructed with cast-in-place concrete.

Each bridge was 90 ft-4 in. (27.5 m) wide and carried five 12-ft (3.7-m) lanes of traffic, a 13-ft (4.0-m) wide shoulder on the exterior side of the bridge, and a 14-ft (4.3-m) wide shoulder on the interior side of the bridge. The bridge was designed to accommodate future contingency dead and live loads, such as light-rail transit along the interior shoulder and a pedestrian bridge hanging beneath the superstructure.

Spans 1 through 3 of each bridge consisted of two single-cell boxes with depth varying from approximately 25 ft (7.6 m) deep near the pier to approximately 11 ft (3.4 m) deep at midspan of Span 2. The dimension between the inner surfaces of the webs at the top of the boxes was 21 ft-2 in. (6.5 m). The thinnest portion of the top flange across the width of the section had a

nominal thickness of 11.5 in. (0.29 m) and remained constant along the entire length of Spans 1 through 3. The bottom flange was 9 in. (0.23 m) thick at midspan of Span 2 and increased to 4 ft-10 in. (1.5 m) thick near each pier in Span 2. The bottom flange of Span 1 and Span 3 varied similarly. The webs were 1 ft-4 in. (0.41 m) thick in Spans 1 and 2, and 2 ft (0.61 m) thick in Span 3. Each precast box was 43 ft-2 in. (13 m) wide, tip-to-tip. The boxes were transversely post-tensioned together with a 4-ft (1.2 m) transverse closure pour between them, such that the total section width from the tip of one box to the opposing tip of the other box was 90 ft-4 in. (27.5 m). Figure 1.2 shows a cross section of the southbound bridge exterior box at midspan of Span 2 (the other box being symmetric across the transverse closure pour). Figure 1.3 shows a cross section of Span 2 near Pier 2. The thickened diaphragm section shown in Figure 1.3 extended 5 ft (1.5 m) on either side of the centerline of the piers.

The northbound and southbound bridge designs had similar cross sections for Spans 1 and 2, but differed in Span 3 where the north end of northbound Span 3 widened to allow for exiting traffic onto University Avenue. The widening of Span 3 was gradually introduced starting near midspan, such that the total section width was equal to 95 ft-4 in. (29.1 m) at Pier 4. The widening of the bridge was accomplished by symmetrically increasing the width of the two boxes while keeping the distance between the boxes constant.

Span 4 consisted of two multi-celled boxes for each bridge. The northbound bridge contained three cells per box while the southbound bridge contained two cells per box. Northbound Span 4 continued to widen from Pier 4 to Abutment 5, where the total width of the section was 104 ft-11 in. (32.0 m).

Major construction of the bridge started in early November 2007. The cast-in-place (CIP) spans were shored on falsework during most of construction. Table 1.1 shows casting dates of the CIP spans and dates that the tendons in these spans were stressed. The first precast segment was cast on February 14, 2008, and the first segment was erected on May 25, 2008. After the first

segment was put into place for each cantilever, a 1.5-ft (0.46 m) closure pour was cast connecting the segment to the CIP span. The final precast segment was erected on July 5, 2008. Table 1.2 shows the date that each precast segment was cast and the date on which each was erected.

After all segments were erected, the two halves of the northbound and southbound bridges were each jacked apart with a total force of approximately 1,120 kips (5,000 kN). This jacking force was held by Piers 2 and 3 on either side of the river span, causing these piers to deflect away from midspan. An approximately 7-ft (2.1-m) long closure pour was then cast between the cantilevered half-spans. The jacks were subsequently released, which put the closure pour in compression. The outward deflection built into Piers 2 and 3 was intended to allow for continued creep and shrinkage of the superstructure, such that the piers would bend back towards a vertical orientation as time-dependent deformations took place. Table 1.3 shows significant events, other than erection of precast segments, during construction that induced loads on the bridge. The bridge opened to traffic on September 18, 2008 with just minor work left to be done.

Chapter 2: Instrumentation

2.1 Overview

Over 500 sensors were installed in the I-35W St. Anthony Falls Bridge to investigate the structural behavior. The types of sensors included: vibrating wire strain gages (VWSGs), thermistors, fiber optic (SOFO) sensors, resistance strain gages, accelerometers, linear potentiometers (LPs), and corrosion monitoring sensors. The VWSGs and thermistors were wired to a slow-rate data acquisition system, henceforth referred to as the "static" system. Resistance strain gages, accelerometers, and the linear potentiometers were wired to a system capable of high data acquisition rates, henceforth termed the "dynamic" system. The SOFO sensors were delivered with a slow-rate data acquisition system; however, these same gages could be attached to a data processing system capable of dynamic rates.

Table 2.1 denotes the general location and quantity of each type of gage in the bridge. For the reader's convenience, the following sections summarize the particular instrumentation referenced in this investigation of time-dependent behavior. This includes the superstructure VWSGs and thermistors attached to the static system (Section 2.2), and the linear potentiometers connected to the dynamic system (Section 2.3). The pier and caisson instrumentation, the SOFO fiber optic system, and the corrosion monitoring system are not presented. For detailed discussion of all the instrumentation systems installed within the bridge, see French et al. (2012).

2.2 Static System: VWSGs and Thermistors

The static system contained the 147 VWSGs and 48 thermistors located in the superstructures of the northbound and southbound bridges, and also the 50 VWSGs located in the piers and caissons (i.e., drilled shafts) of Pier 2 of the southbound bridge. Each VWSG had an integral thermistor to measure the temperature at the location where the strain was read. These gages were used to monitor strain in the concrete which could be used to compute changes in

curvatures and estimate mechanically induced changes in stresses in the bridge. In this investigation of time-dependent behavior, only the superstructure VWSGs and thermistors were analyzed from the static system.

2.2.1 Superstructure VWSGs

2.2.1.1 Naming Scheme

Numbers were assigned to each of the locations instrumented with VWSGs. The numbers increased going from south to north, and were similar for both northbound and southbound structures. Location 3 was near the midspan of Span 1. Location 4 was just to the south of Pier 2, Location 5 was 10.5 ft (3.2 m) north of the centerline of Pier 2, and Location 6 was 20 ft (6.1 m) north of the centerline of Pier 2. Location 7 was near the midspan of Span 2, Location 8 was just south of Pier 3, and Location 9 was near the midspan of Span 3. Location 14 was near the midspan of Span 4 and Location 15 was just to the south of Abutment 5. Figures 2.1 through 2.5 show these locations and their corresponding station numbers on the elevation view of the bridge.

The VWSG labels consisted of eight characters. The first character denoted whether the strain (V) or temperature (T) of the gage was being measured. In other words, each VWSG gage had two labels, one for strain and one for temperature. The second character in the label denoted whether the gage was located in the northbound (N) bridge or southbound (S) bridge. The third and fourth characters denoted the location of the gage along the length of the bridge. The possible locations corresponded to those shown in Figure 2.1 (i.e., 03, 04, 05, 06, 07, 08, 09, 14, or 15). The fifth character in the label specified whether the gage was located in the interior (I) box or the exterior (E) box. The sixth character specified whether the gage was located within the top flange (T), the bottom flange (B), the east web (E) (i.e., on the interior side for the southbound bridge and exterior side for the northbound bridge), the west web (W) (i.e., on the exterior side for the southbound bridge and interior side for the northbound bridge), or the middle web (M) (i.e., in the case of Span 4) of the box. The seventh character denoted whether the orientation of the gage was

longitudinal (L), transverse (T), vertical (V), or at 45° (A). Finally, the eighth character was a number assigned to the gage to separate it from the other gages with the same first seven characters in their label. The eighth character typically increased from exterior to interior and from the top of the section down. For example, the gage labeled "VS07EEA1" represented the vibrating wire strain gage located near midspan of Span 2 of the southbound bridge (i.e., Location 7), in the exterior (west) box, in the east (interior) web, oriented at 45° in the rosette. If a sensor's first seven digits were unique to that sensor, the eighth digit was "1" by default.

The assigned data collection labels are given in Table 2.2 along with associated locations of the gages within the bridge. Listed X and Y gage locations are coordinates in inches relative to the nominal top deck surface at the centerline of the box in which the gage was installed. For both structures, X-coordinates are positive to the east and negative to the west, and Y-coordinates are positive up and negative down.

One source of uncertainty that affected the exact X- and Y-coordinates of the VWSGs and their expected measurement was the thickness of the deck. The coordinates of gages given in Table 2.2 were taken from the nominal top of deck as specified in the as-built drawings. This, however, was not necessarily equivalent to the final top of deck elevation as constructed. The deck thickness had a tolerance of 0.375 in. (9.5 mm) for the precast segments (i.e., Span 2), and the cast-in-place sections had a higher deck thickness tolerance. The goal was to achieve 4 in. (100 mm) of cover to the top mat of rebar though, prior to planing, the actual pours may have provided up to 5.5 in. (140 mm) of cover (from email correspondence with Dustin Thomas, MnDOT, July 30, 2009). After casting, the deck of the bridge was planed to achieve the desired ride quality. This required the deck to be planed by varying amounts along the length of the bridge, and typically 0.25 to 0.5 in. (6 to 13 mm) of concrete was removed. Using ground penetrating radar after planing, the majority of the scanned length had top mat cover in the range of 4 to 5 in. (100 to 130 mm) with the most likely cover at any particular location being

approximately 4.25 in. (110 mm). Due to the tolerance in deck thickness and the planing operation, the final thickness of the deck varied throughout the bridge, resulting in actual vertical dimensions of the gages from the top of deck different than those given in Table 2.2. Ultrasonic tomography performed on April 14, 2011 (31 months after bridge opening) at midspan of Span 2 (Location 7) in the southbound bridge revealed that the thickness of the deck at the centerline of the box was, to an accuracy of ±0.25 in. (±6 mm), 10.6 in. (270 mm), which was 0.9 in. (23 mm) thinner than specified.

2.2.1.2 Gage Models

Two types of VWSGs were used in the bridge superstructure. Most of the VWSGs were Roctest EM-5 gages cast within the concrete. The second type of VWSG used was the Roctest SM-5A. These gages were installed externally on the interior face of the exterior box at southbound Location 6. The segment to which they were attached was cast before determining the final gage locations, so the external SM-5As were used in lieu of the EM-5s to instrument this section. Roctest SM-5A gages were also installed externally as replacements for malfunctioning embedded Roctest EM-5 strain gages as described in Section 2.2.6.1 in the report by French et al. (2012).

The Roctest EM-5 VWSGs had a specified range of 3,000 με. The resolution of these gages was a minimum of 1 με, and their specified operating temperatures were −4°F (−20°C) to 176°F (80°C). The Roctest EM-5 VWSGs contained a 3 kΩ thermistor with a range of −58°F (−50°C) to 302°F (150°C) and a resolution of 0.18°F (0.1°C). Based on the temperature range of the cable, the effective range of the thermistor was limited to −4°F (−20°C) to 176°F (80°C). The Roctest SM-5A VWSGs and thermistors had the same ranges and resolutions as those associated with the Roctest EM-5 VWSGs. Both the Roctest EM-5 and Roctest SM-5A VWSGs were approximately 6.75 in. (0.17 m) in length.

2.2.1.3 Summary of Gage Locations

VWSGs were placed in at least the top and bottom flanges at southbound structure Locations 3, 4, 5, 6, 7, 8, 9, 14 and 15 and northbound structure Locations 3, 5, 7, 8, 9, 14, and 15. Most of the VWSGs were oriented longitudinally within the bridges. To provide redundancy for the longitudinal curvature measurements, gages were oriented longitudinally above, below, and in the webs of the section.

The majority of the instrumentation was located within the exterior box of the southbound bridge. The heavily instrumented sections included Location 3 (near midspan of Span 1), Location 4 (negative moment region just to the south of the Pier 2 diaphragm section), Location 5 (negative moment region just to the north of the Pier 2 diaphragm section), and Location 7 (near midspan of Span 2 within the precast segment adjacent to the closure pour). The majority of the VWSGs were placed near the midspan of the river span section because this was where the largest deformations were anticipated. Both boxes of the southbound bridge were instrumented at Location 7 to capture more information on the behavior across the section.

Detailed discussion regarding the rationale for the chosen gage locations and the sources of uncertainty in the installed gages is presented in French et al. (2012).

2.2.2 Superstructure Thermistors

2.2.2.1 Naming Scheme

The labels assigned to the thermistors had eight characters. The first character denoted that the thermistor measured temperature (T). The second character in the label specified whether the thermistor was in the northbound (N) bridge or southbound (S) bridge. The third character denoted whether the thermistor was in the interior (I) box or exterior (E) box. The fourth character specified whether the thermistor was located within the top flange (T), the bottom flange (B), the east web (E), or the west web (W) of the box. The fifth character in the label specified to which set of thermistors the gage belonged (i.e., to differentiate between sets with the

same first four characters). A set of gages consisted of thermistors measuring a gradient through a thickness (e.g., top flange, bottom flange, etc.) in the section. Sets consisted of one to six thermistors. The thermistors used to measure thermal gradient through the depth of the web (i.e., gradient from the top flange to the bottom flange through the depth of the web) were not labeled as a single set of gages, and instead consisted of gages from multiple sets. The sixth, seventh, and eighth characters denoted the location of the thermistor within the set with the numbering starting at one and increasing from the exterior surface of the box to the interior surface or from the top of the deck to the bottom of the deck in the case where the thermistor was in the deck. Although only one digit was required to number the gages, three digits were used to keep the entire label eight digits in length. This was consistent with the VWSG labels and was required for data collection purposes because the thermistors and VWSGs were connected to the same datalogger. Thermistor names, channels and positions are summarized in Table 2.2 in the same manner as was done for the VWSG sensors in Section 2.2.1.1.

2.2.2.2 Gage Model

All thermistors installed independently from the VWSGs were Roctest Model TH-T. These were 3 kΩ thermistors with an operating temperature range of −4°F (−20°C) to 176°F (80°C) as limited by the cable.

2.2.2.3 Summary of Gage Locations

Of the 48 total individual thermistors installed in both structures, 42 were located at midspan of Span 2 (Location 7 as shown in Figure 2.1) of the southbound bridge. The remaining six thermistors were located in the exterior box at midspan of Span 2 (Location 7) of the northbound bridge. These thermistors were used in conjunction with the VWSG thermistors to provide information on the thermal gradient through the section.

Cross sections of Location 7 showing the layout of the thermistors in the southbound and northbound bridges are shown in Figures 2.6 and 2.7, respectively. For all thermistor sets within

the top flange, including the three-gage installation just below the roadway crown, the topmost thermistor was nominally (i.e., according to the as-built construction documents (Minnesota Department of Transportation, 2008)) located 1.75 in. (44 mm) below the top surface of the deck, the lowest thermistor was nominally 9.75 in. (250 mm) below the top surface of the deck, and the remaining thermistors were spaced evenly between the two. Figure 2.8 shows a typical installation of six thermistors through the depth of the top flange.

Measurements of the thermistor positions after installation were not in agreement with the nominal thermistor positions for the top flange. For this investigation, the measured thermistor positions as presented in Table 2.2 were always used. On average, the topmost thermistor was measured to be approximately 2 in. (51 mm) below the nominal top surface of the deck instead of 1.75 in. (44 mm). Furthermore, the uncertainty in deck thickness as discussed in Section 2.2.1.1 resulted in expected bounds for the vertical positions of the thermistors within ±1 in. (±25 mm).

Recorded locations for the thermistors in the three-thermistor set below the roadway crown in the southbound bridge (gage numbers TSITA001 through TSITA003) and above the east web of the interior box of the southbound bridge (gage numbers TSITC001 through TSITC006) were not consistent with their nominal positions. Assuming the measured locations were correct, plotting the temperatures through the depth of the deck for these two thermistor sets resulted in unrealistic temperature distributions. It was concluded that the measured locations could not be correct for these two gage sets, meaning either the gages were mislabeled or the records contained typographical errors. Because no other position measurements were available, these two thermistor sets were excluded from all further investigation.

For three-thermistor installations in the webs, the exterior and interior thermistors were installed with 2.25 in. (57 mm) of cover, with the center thermistor placed at the midpoint between the two. For single thermistors in the web, the sensor was placed at the center of the

web. Location measurements confirmed that the positions of the web gages were consistent with the nominal locations, with the exception of the innermost thermistor in the set of three gages in the east web of the southbound interior box (gage number TSIEB003). This gage provided temperature readings approximately equal to those from the topmost deck gages, which was deemed impossible given that this gage, if in its specified location, would be subject to no heating from solar radiation. It was suspected that this gage may have been mislabeled in connection to the multiplexer, and thus this gage was not used in this investigation.

Installation of the thermistors in the bottom flanges were spaced such that the local VWSGs at the same sections were effectively added to the set. For the three-thermistor installations in the bottom flange, the topmost thermistor was nominally 1.75 in. (44 mm) below the top of the bottom flange, with the second thermistor 2.75 in. (70 mm) below the first, then the VWSG located 2.75 in. (70 mm) below the previous thermistor, and the bottommost thermistor located 2.75 in. (70 mm) below that (nominally 1.75 in. (44 mm) above the bottom of the bottom flange). For the two-thermistor installation, the topmost and bottommost thermistors were located as described above, with the VWSG at the midpoint between the two thermistors. Location measurements confirmed that the positions of the bottom flange thermistors were consistent with the nominal locations.

2.2.3 Data Collection for the Static System

2.2.3.1 Construction

During construction of the St. Anthony Falls Bridge, data was collected from only a portion of the static gages. For the VWSGs located in the superstructure, strain readings were taken at the time of installation to ensure that the gages were reading near the middle of their range. The day after the concrete was cast around a given gage, a “24 hour” strain reading was recorded. Temperature readings from the “24 hour” reading were not obtained, thus strain measurements can only provide relative strains; without the temperature readings, absolute strain

measurements were not possible, and only relative strain measurements between any two readings were possible. Individual thermistors (i.e., those not integrated into the VWSGs) were also recorded with a "24 hour" reading.

In addition to the initial readings, some of the VWSGs in the southbound bridge exterior box were recorded for a brief period of time during the construction process. Selected gages were read using three Campbell Scientific CR10 dataloggers connected at midspan of Span 2, midspan of Span 1, and near Pier 2 in Span 1. The CR10 data collection times and sensors are summarized in Table 2.3. A maximum of 16 channels were available for each CR10, and gages were chosen for collection such that the wires connecting to the dataloggers would not cross the walking paths or work areas within the bridge (due to safety concerns). The entire construction process could not be recorded using the CR10 dataloggers because the contractor had to remove the wires in order to connect them to the permanent multiplexers in the bridge.

2.2.3.2 Long-Term Monitoring Setup

In the permanent data acquisition setup, the server to which the dataloggers were connected was used to command and download the data from the dataloggers. The system was set up to be accessed remotely by authorized users who could copy data files to their local computers for further analysis. The sampling rate and other factors could be adjusted remotely.

The long-term monitoring setup for the static system was instituted on the southbound bridge beginning on September 1, 2008. Prior to September 14, 2008, a single sample was collected from each VWSG in the southbound superstructure every hour. Truck tests were performed on September 14 and 17, 2008 (French et al., 2012), during which data were collected from the northbound and southbound superstructures only when prompted by the system. The northbound superstructure was integrated into the long-term monitoring setup after September 17, 2008.

Following the truck tests, data was sampled once every six hours (at midnight, 6:00 AM, noon, and 6:00 pm) from both superstructures until noon on March 26, 2009. At that time, in order to better quantify average strains and to be able to detect anomalous or spurious readings, five readings were taken from every static system gage every six hours. For the vast majority of measurements, all five readings were similar, and spurious readings were rare in most gages. All five readings for one given set of measurements were taken within 15 minutes of initiating the reading routine.

Beginning at 2:00 PM on September 17, 2009, the routine was changed such that five readings would be taken every hour instead of every six hours. This was done to better quantify daily thermal changes given that maximum temperature or thermal gradients would not necessarily occur at the six-hour interval.

On October 28, 2010, the power supply that converted AC power to 12V DC for the fiber optic converters (B&B Electronic Media Converter) inside the control shed failed. This failure cut off connection between the server and dataloggers located inside the bridge. The dataloggers continued to run and collect data without continuous connection to the server. The power supply was replaced on January 4, 2011. It was found that the northbound bridge datalogger did not lose any data; the onboard hard disk had enough storage space such that none of the data collected during the outage was overwritten. The datalogger in the southbound bridge, which collected data from more sensors but had the same size of hard disk as the northbound datalogger, overwrote data from November 8, 2010 to December 15, 2010. This data was not recoverable.

No other outages interrupted the collection of data from the static system. A summary of all the repairs conducted for the static system instrumentation through May 1, 2012, is provided in French et al. (2012).

2.3 Dynamic System: Linear Potentiometers

The dynamic system contained all accelerometers, linear potentiometers, and resistive strain gages installed in the bridge. The system was provided by Dataq, and Minnesota Measurements was in charge of the installation and service of the system. Of the sensors connected to the dynamic system, only the 12 linear potentiometers were used for this investigation of time dependent behavior. Details regarding the accelerometers and resistive strain gages are documented in French et al. (2012).

2.3.1 Linear Potentiometers

2.3.1.1 Naming Scheme

Linear potentiometers were named according to the box, expansion joint, and superstructure region to which they were attached. Names were in the form of (A)(B)(C), where (A) was either NB or SB denoting to which structure the sensor was attached, (B) was SP 1 (LP was attached to Span 1 at the Abutment 1 expansion joint), SP 3 (LP was attached to Span 3 at the Pier 4 expansion joint), or SP 4 (LP was attached to Span 4 at the Pier 4 expansion joint), and (C) was either Ext or Int denoting whether the LP was attached to the exterior or interior box, respectively. Linear potentiometer names and positions are summarized in Table 2.4.

2.3.1.2 Gage Model

The overall longitudinal movement of the bridge at the expansion joints was measured by a total of 12 Unimeasure HX-P420 Series linear potentiometers, which had a measurement range of 20 in. (0.51 m) and an operating temperature range of −40°F (−40°C) to 203°F (95°C).

2.3.1.3 Gage Locations

The linear potentiometers were located in both boxes of the northbound and southbound bridges attached to the south end of Span 1 at Abutment 1, the north end of Span 3 at Pier 4, and the south end of Span 4 to Pier 4. Figure 2.9 shows a cross section depicting the locations of these instruments at the south end of Span 1 and north end of Span 3. Figure 2.10 shows the cross

section depicting the location of the instruments at the south end of Span 4 for the southbound bridge, and Figure 2.11 shows the location of the instruments at the south end of Span 4 for the northbound bridge.

The linear potentiometers were installed similarly at all locations. Each was attached to the inside surface of the box and connected to a horizontal extension tube, as shown in Figure 2.12. At Abutment 1, this tube was attached directly to the abutment wall, and at Pier 4, the horizontal extension tube was attached to a vertical extension tube connecting down to the top of the pier.

Linear potentiometers attached at the south end of Span 1 measured the expansion joint movement at Abutment 1. Linear potentiometers attached to Span 3 and Pier 4 measured the relative displacement between the superstructure at Span 3 and the top of Pier 4. Because the superstructure of Span 4 was pinned to the top of Span 4, the expansion and contraction of Span 4 due to thermal changes would deflect the top of Pier 4. The linear potentiometers attached to Span 4 and Pier 4 were expected to measure virtually no relative movement between Span 4 and Pier 4 because of this pinned connection. The absolute deflection of Pier 4 was not able to be measured, and could only be assumed. Because of the vertical positions of the LPs, rotations of the superstructure would alter the measured expansion joint movements. Also, for LPs attached to Span 3 and Span 4, rotation of the top of Pier 4 would move the extension tubes and further alter the expansion joint measurements. Because the length of the tubes and gages were small compared to the length of the structures being measured, thermal expansion and contraction of the gages and tubes were assumed to be negligible compared to total measured bridge movements.

2.3.2 Data Collection for the Dynamic System

Data collection for the dynamic system began on October 31, 2008. All dynamic system data was read continuously at 1,000 Hz, though collection was interrupted each night around 1:00 AM Central Standard Time to allow for data file management.

The dynamic system setup consisted of eight dynamic junction boxes (i.e., nodes). Of the eight junction boxes, three were located in the northbound bridge, and five were located in the southbound bridge. The junction boxes were named "Node X", where X was a number ascending from 1 for the first node in the series (northbound bridge Span 3) up to 8 for the final node in the series (southbound bridge Span 3). Table 2.4 shows the channel and node to which each linear potentiometer was connected. Linear potentiometer connections are summarized as follows:

- Node 1 = Pier 4 (Span 3 and Span 4) expansion joint in the northbound bridge
- Node 3 = Abutment 1 (Span 1) expansion joint in the northbound bridge
- Node 4 = Abutment 1 (Span 1) expansion joint in the southbound bridge
- Node 8 = Pier 4 (Span 3 and Span 4) expansion joint in the southbound bridge

The collection sample rate of all instruments attached to the dynamic system was set to 1,000 Hz, with analog filtering (anti-aliasing) done by a resistance-capacitance low-pass filter with cutoff frequency of 159 Hz. The digitized data was then low-pass filtered using a Kaiser window with cutoff frequency of 23 Hz. Following the Kaiser window filtering, the data was decimated. At first, all data was decimated by a factor of 5 to 200 Hz. Beginning on September 1, 2009, the decimation was increased to a factor of 10, reducing the effective sample rate to 100 Hz. On February 1, 2010, the decimation was again increased so that the linear potentiometer data was reduced to a sample rate of 4 Hz.

To streamline the daily collection of the linear potentiometer data, a routine was developed that extracted hourly readings from the continuously collected data. Each hourly

readings was equal to the average over 100 points, regardless of the sample rate. For a sample rate of 4 Hz, this was equivalent to averaging over 25 seconds.

2.3.2.1 Dynamic System Outages

The dynamic system, either in part or in whole, was shut down on multiple separate occasions. The timing for these outages appeared to coincide with electrical storms in the area. Repairs for this system have typically involved replacement of the datalogger boards or repeater nodes (which connect datalogger nodes together), but have occasionally necessitated replacement of linear potentiometers as noted in Section 2.3.2.2. For a detailed presentation of all the repairs conducted on the dynamic system through May 1, 2012, refer to French et al. (2012).

The first complete system outage occurred on August 15, 2009, and persisted until the replacement of several nodes on September 28, 2009 (1.5 months of data loss).

A second complete system outage occurred on June 25, 2010. Nodes 1 through 5 were brought online on August 28, 2010 (about 2 months downtime). Nodes 6, 7 and 8 were brought online on September 19, 2010 (3 months downtime).

On June 25, 2011, difficulties were encountered when attempting to collect data from Nodes 5–8 simultaneously with Nodes 1–4. Collecting Nodes 5–8 without Nodes 1–4 worked, as did collecting Nodes 1–4 without 5–8, but collecting both sets at the same time was not possible. The problem was discovered to be a poor synchronization signal between Nodes 4 and 5. On September 13, 2011, Node 5 was replaced and the issue was resolved. Nodes 5–8 were not collected for approximately 3 months.

The third complete system outage occurred on May 27, 2012. Node 1 was brought online on August 23, 2012 (3 months of downtime), and the full system was brought online on January 9, 2013 (8 months of downtime).

Following a lightning storm on June 21, 2013, only Nodes 1, 2 and 3 continued to collect. The remainder of the nodes were brought back online on July 8, 2013 (less than one month

downtime) without the replacement of any nodes. However, it was later discovered that while the Node 4 board was still operating, the data from that node was corrupt, thus indicating the need for replacement. Node 4 was replaced on August 6, 2013, resolving the issue.

Communication to Nodes 4 though 8 was lost on April 26, 2014, though Nodes 1, 2 and 3 still continued to collect data. As of June 13, 2014, repairs for these nodes have not been completed.

2.3.2.2 Linear Potentiometer Repairs

The four LPs attached to the southbound bridge at Pier 4 (Node 8) were not collecting data at bridge opening. It was found that the LPs were operational, but were not powered properly. This issue was resolved on September 28, 2009, and approximately one full year of data was lost since bridge opening.

It was discovered that the LP braces extending down to the top of Pier 4 from the interior box of southbound bridge Span 3 were colliding with the vermin guard across the expansion joint. This caused erroneous LP readings during the winter of 2009–2010. On June 18, 2010, the vermin guard was sufficiently trimmed back for all LP braces extending down to Pier 4.

After the second dynamic system outage on August 28, 2009, it was found that four of the linear potentiometers had failed during the outage. The two LPs attached to the northbound bridge at Abutment 1 were replaced September 21, 2010, and the two LPs attached to Span 4 of the southbound bridge at Pier 4 were replaced September 30, 2010. For these replacements, the new LPs were mounted on the same concrete embedded bolts as were used to mount the original LPs.

After the system outage on May 27, 2012, eight of the linear potentiometers were not collecting data after the system was brought back online on January 9, 2013, including:

- Northbound Span 1 Interior
- Northbound Span 1 Exterior

- Northbound Span 4 Interior
- Southbound Span 1 Exterior
- Southbound Span 1 Interior
- Southbound Span 3 Exterior
- Southbound Span 3 Interior
- Southbound Span 4 Interior

Each of these was replaced on February 5, 2013. Again, the new LPs were mounted on the same concrete embedded bolts as were used to mount the original LPs. It was discovered at this same time that some of the multiplexer channels to which the LPs were originally connected were no longer functioning. Therefore, the LPs connected to Nodes 1, 3, and 4 were moved to new channels. The channel swap required that the Node 1 LPs be moved from collection channels 1 through 4 to channels 3 through 6 as noted in Table 2.4. All other LPs kept the same collection channels as before. In the process of changing channels, the data from Node 4 (Southbound Span 1) were significantly altered; the data jumped substantially with respect to the previous readings on May 27, 2012. Because no evidence of substantial bridge movement was seen in any other data, it was believed that this jump was nonphysical. Channel switches on Nodes 1 and 3 did not appear to cause any notable jumps. On April 8, 2013, the LP connections at Node 4 were moved which mostly reversed the jump in readings. Following this channel swap, LP readings from Node 4 were only approximately 0.2 in. (5 mm) off from expected values from the previous year. Therefore, it was concluded that this jump in data was caused by damaged signal board channels.

After the partial outage on June 21, 2013, the linear potentiometer at Southbound Span 1 interior box was damaged. This sensor was replaced on July 25, 2013 in the same manner as described above.

A summary of the linear potentiometer replacements is as follows:

- Northbound Span 1 Interior (replaced on September 21, 2010, and again on February 5, 2013)
- Northbound Span 1 Exterior (replaced on September 21, 2010, and again on February 5, 2013)
- Northbound Span 4 Interior (replaced on February 5, 2013)
- Southbound Span 1 Exterior (replaced on February 5, 2013)
- Southbound Span 1 Interior (replaced on February 5, 2013, and again on July 25, 2013)
- Southbound Span 3 Exterior (replaced on February 5, 2013)
- Southbound Span 3 Interior (replaced on February 5, 2013)
- Southbound Span 4 Exterior (replaced on September 30, 2010)
- Southbound Span 4 Interior (replaced on September 30, 2010 and again on February 5, 2013)

Each time these sensors were replaced, a variety of errors may have been introduced into the readings. First, although the same mounting bolts and holes were used for reinstallation, small positional errors may have been introduced in the readings by moving and reattaching the sensors and strings. Second, after sensor replacement, the calibration of the new sensor may not have been exactly equivalent to the old sensor, thereby erroneously indicating different measured elongations. Finally, and most importantly, the replacement of these gages and particularly changing the channels as done on February 5, 2013 may have introduced additional resistance into the circuit, thereby changing the measured current. Though the first two errors were expected to be small and generally undetectable, resistance changes from channel swaps could potentially introduce large errors. This was clearly evident from the jump in the Southbound Span 1 LPs, though it is possible that other sensors suffered from smaller and less noticeable jumps. Because the magnitude of these errors was unknown, LP data were analyzed either assuming that pre- and

post-replacement data were comparable, or correcting the measured data using Heaviside functions in the regression process described in Section 7.1.

2.3.2.3 Summary of Data Loss in Linear Potentiometer Data

The following is a summary of the collected data for the Northbound Span 3 (Node 1), Northbound Span 1 (Node 3), Southbound Span 1, (Node 4) and Southbound Span 3 (Node 8) linear potentiometers. Linear potentiometers attached to Span 4 – Pier 4 were not investigated in this report, and thus not summarized below, as these sensors only collected the motion between the Span 4 superstructure and Pier 4 to which the Span 4 superstructure was pinned.

Collection of Node 1 – Northbound Span 3 LPs began on November 31, 2008. As of June 13, 2014, readings were collected continually except for the following breaks:

- August 15, 2009 to September 28, 2009 (first system outage)
- June 25, 2010 to August 28, 2010 (second system outage)
- May 27, 2012 to August 23, 2012 (third system outage)

Collection of Node 3 – Northbound Span 1 LPs began on November 31, 2008. As of June 13, 2014, readings were collected continually except for the following breaks:

- August 15, 2009 to September 28, 2009 (first system outage)
- June 25, 2010 to August 28, 2010 (second system outage)
- May 27, 2012 to February 5, 2013 (third system outage, LPs replaced)

Collection of Node 4 – Southbound Span 1 LPs began on November 31, 2008. As of June 13, 2014, readings were collected continually except for the following breaks:

- August 15, 2009 to September 28, 2009 (first system outage)
- June 25, 2010 to August 28, 2010 (second system outage)
- May 27, 2012 to April 8, 2013 (third system outage, LPs replaced, channels reassigned)
- June 21, 2013 to July 8, 2013 (partial outage of Nodes 4–8)
- April 26, 2014 to present (partial outage of Nodes 4–8)

Collection of Node 8 – Southbound Span 3 LPs began on September 28, 2009. As of June 13, 2014, readings were collected continually except for the following breaks:

- June 25, 2010 to August 28, 2010 (second system outage)
- June 25, 2011 to September 13, 2011 (partial outage of Nodes 5–8)
- May 27, 2012 to February 5, 2013 (third system outage, LPs replaced)
- June 21, 2013 to July 8, 2013 (partial outage of Nodes 4–8)
- April 26, 2014 to present (partial outage of Nodes 4–8)

Chapter 3: Concrete Material Testing

To develop an accurate finite element model of the bridge, it was necessary to determine the material properties to be included in the model. The properties and behaviors of interest included the concrete compressive strength, tensile strength, elastic modulus, creep and shrinkage, coefficient of thermal expansion, and unit weight.

Bridge casting took place over the course of eleven months during a variety of environmental conditions with extreme temperature ranges. Consequently, a variety of mix designs were used for purposes of workability. The different mix designs used in the construction of the St. Anthony Falls Bridge were separated into two categories based on their specified nominal strengths. The superstructure of the bridge was built using various concrete mixes all with nominal strength equal to 6.5 ksi (45 MPa). Likewise, the mixes used for the piers, concrete barrier rails, and various nonstructural components all had nominal strength of 4.0 ksi (28 MPa). For modeling purposes (Chapter 6), all concrete mixes with identical nominal strength were assumed to have identical material properties after hardening.

Sample preparation, instrumentation, testing procedures, and other commentary on the material testing conducted at the University of Minnesota has been documented in French et al. (2012). The chapter presents a summary of the material testing results, starting with the compressive strength and modulus of elasticity in Section 3.1, followed by tensile strength in Section 3.2, creep and shrinkage in Section 3.3, coefficient of thermal expansion of the concrete in Section 3.4, and unit weight in Section 3.5.

3.1 Compressive Strength and Modulus of Elasticity

Concrete compressive properties for the St. Anthony Falls Bridge were tested independently by the Minnesota Department of Transportation (MnDOT), University of Minnesota (UMN), and Cemstone (the concrete supplier).

The specified 28-day compressive strength of concrete, f_c', for the superstructure was 6.5 ksi (45 MPa). The superstructure mix design was primarily controlled by permeability and serviceability concerns rather than compressive strength (from personal communication with Kevin MacDonald, representing Cemstone, July 10, 2013), and therefore it was expected that the measured compressive strength and modulus might be significantly higher than the nominal strength and modulus.

The specified 28-day compressive strength for the pier and barrier rail concrete was 4.0 ksi (28 MPa). No testing data was available for this concrete.

3.1.1 MnDOT Testing

The Minnesota Department of Transportation (MnDOT) conducted compressive strength tests on the superstructure concrete. Samples were collected from Span 4 deck pours of both the northbound and southbound bridges between July 28 and August 9, 2008. A total of 75 samples from the northbound bridge and 67 from the southbound bridge were tested. All samples were 4 x 8 in. (100 x 200 mm) cylinders. Tests were performed at concrete ages equal to 7 days, 28 days, and 56 days. Measured data from pier or barrier rail concrete were not available.

A summary of the superstructure concrete test results provided by MnDOT is presented in Table 3.1. Box plots showing the minimum, maximum, first quartile, median, and third quartile of the MnDOT strength data are given in Figure 3.1. The mean strengths at 7 days, 28 days, and 56 days for both the northbound and southbound bridge samples were 5.64 ksi (38.9 MPa), 7.45 ksi (51.4 MPa), and 7.37 ksi (50.8 MPa), respectively. Although concrete compressive strengths should increase with age, this was not observed in the results collected after 28 days. One possible explanation for the unexpected results was the number of samples tested at each age. The 7-day and 28-day MnDOT test results each consisted of 60 or more test specimens between both structures, while the 56-day results consisted of only 7 samples.

The 7-day and 28-day mean strength results between both northbound and southbound bridge were directly used for input into the finite element analysis, as discussed in Section 4.2.

3.1.2 UMN Testing

The University of Minnesota (UMN) conducted concrete strength and modulus tests on samples collected from the superstructure concrete. The sampling method, storage, instrumentation, and testing procedures are documented in French et al. (2012). Testing was conducted in two stages. For the first stage, nine samples from Span 4 of the southbound bridge were tested. All samples were 4 x 8 in. (100 x 200 mm) cylinders. Tests were conducted 56, 93, and 130 days after casting. At each testing day, a single cylinder was loaded to failure, followed by two cylinders for which the modulus was measured before loading to failure. For the second stage of testing, a total of eight samples provided by the Minnesota Department of Transportation from Span 4 (either northbound or southbound bridge) were tested. All samples were 4 x 8 in. (100 x 200 mm) cylinders, and these tests were all conducted approximately 2,116 days (5.8 years) after casting. For this testing stage, a single cylinder was loaded to failure, followed by seven cylinders for which the modulus was measured prior to loading to failure.

Results from the UMN cylinder testing are summarized in Table 3.2. The average measured 56-day, 93-day, 130-day, and 2,116-day compressive strengths were 7.1 ksi, 6.7 ksi, 6.2 ksi, and 8.0 ksi (49 MPa, 46 MPa, 43 MPa, and 55 MPa), respectively. The average measured moduli at 56, 93, 130, and 2,116 days were 4,400 ksi, 4,700 ksi, 4,200 ksi, and 5,200 ksi (30 GPa, 32 GPa, 29 GPa, and 36 GPa), respectively. Contrary to expectations, the mean measured concrete strength and modulus decreased from 56 days to 130 days. This was believed to be due, at least in part, to the low sample size.

Testing conducted by the UMN was not directly used in specifying input parameters for the finite element analysis as discussed in Section 4.2. Instead, these results were used for

verification of the aging properties assumed for the time-dependent models. This verification is presented in Chapter 5.

3.1.3 Cemstone Testing

During construction of the bridge, the concrete supplier (Cemstone) contracted testing services to Stork Materials Technology and American Engineering Testing, Inc. Strength results from 32 cylinders cast from the superstructure concrete were provided. All samples were 4 x 8 in. (100 x 200 mm) cylinders. Strength tests were conducted at ages of 1, 3, 7, 20, 28, 56, and 90 days. Modulus and Poisson's ratio results from 26 superstructure cylinders, each tested twice, were provided. Modulus tests were conducted at 3, 7, 20, 28, and 90 days.

A summary of the results provided by Cemstone is given in Table 3.3. Unlike the test results from MnDOT and UMN, the mean concrete strength consistently increased with age as expected. The average measured Poisson's ratio was equal to 0.21 with a coefficient of variation of 17.5%.

Results for strength and elastic modulus from Cemstone was used only to validate the aging properties used in the finite element modeling, and were not used to determine the input parameters for the models. Validation of time-dependent material properties is presented in Chapter 5.

3.2 Tensile Strength

Concrete split cylinder tensile testing was conducted by the University of Minnesota. Five superstructure samples were tested, with two samples from the deck pour of Span 4 of the northbound bridge and three samples from the deck pour of Span 4 of the southbound bridge. All samples were 6 x 12 in. (150 x 300 mm) cylinders. The storage and testing procedures are documented in French et al. (2012). No samples from the pier and barrier rail concrete were tested. No tensile strength results were provided by MnDOT or Cemstone.

The results of the split cylinder tensile strength tests of the concrete specimens at 58 and 59 days old are given in Table 3.4. For the specimens from the southbound bridge, the overall average tensile strength was 395 psi (2.7 MPa) with a maximum tensile strength of 469 psi (3.2 MPa) and a minimum tensile strength of 328 psi (2.3 MPa). The average tensile strength of the northbound bridge samples was 410 psi (2.8 MPa).

For concrete with specified compressive strength of 6,500 psi (45 MPa), the average splitting tensile strength can be estimated from section R8.6.1 of ACI 318-08 (2008) as

$$f_{ct} = 6.7\sqrt{f_c'} = 540 \text{ psi } (3.7 \text{ MPa}) \quad (3\text{-}1)$$

All the measured split cylinder tensile strengths were less than the predicted value from ACI 318 (2008). This was believed to be due, at least in part, to the small sample size.

3.3 Creep and Shrinkage

Creep and shrinkage of the superstructure concrete were measured by the University of Minnesota. The samples were taken from two pours during construction. The first set of samples (three shrinkage cylinders) came from concrete used in Span 4 of the northbound bridge and was collected on August 8, 2008. The second set of samples (six shrinkage cylinders and eight creep cylinders) came from concrete used in Span 4 of the southbound bridge collected on August 9, 2008. All samples were 4 x 11.5 in. (100 x 280 mm) cylinders with three sets of DEMEC (demountable mechanical strain gage) points along the axis of the cylinder. Sample preparation, storage, instrumentation, and testing are discussed in French et al. (2012).

All creep and shrinkage samples were kept in an environmental chamber nominally held at 73.4°F (23°C) and 40% relative humidity as per the ACI-209 (1992) standard for measuring creep and shrinkage. The temperature of the room varied from 70.3 to 79.0°F (21.3 to 26.1°C), with an average temperature of 73.0°F (22.8°C). The relative humidity varied from 30.2% to 40.1% and the average was equal to 37.5%.

Shrinkage measurements began immediately after the specimens were removed from their molds. These results are presented in Chapter 5, where they are compared to the shrinkage models discussed in Chapter 4.

Creep samples were loaded into four frames constructed using steel plates, steel threaded rods, and disk springs. Each frame contained two creep samples in series, such that each cylinder held equal load. Loading and unloading procedures for the four frames are summarized in Table 3.5. Creep strains were computed by subtracting the measured shrinkage strains from the total measured strains. Measured results were recorded for: Frame 1 loaded to 1.90 ksi (13.1 MPa) at an age of 130 days; Frame 2 loaded to 2.92 ksi (20.1 MPa) at an age of 57 days; Frame 3 loaded to 1.90 ksi (13.1 MPa) at an age of 130 days; and Frame 4 loaded to 1.90 ksi (13.1 MPa) at an age of 93 days. These creep strains are presented in Chapter 5, where they are compared to the creep models discussed in Chapter 4.

3.4 Coefficient of Thermal Expansion

The coefficient of thermal expansion (CTE) of the concrete was important for both modeling purposes and data reduction. The CTE was measured from samples collected and tested by the University of Minnesota, as well as from investigation of the monitoring system data from the in situ bridge.

3.4.1 UMN Laboratory Testing

The CTE of the superstructure concrete and the pier and barrier rail concrete were measured by the University of Minnesota. Six samples were collected from the superstructure concrete at various locations along the bridge. Two samples of pier and barrier rail concrete were collected from Pier 2 of the southbound bridge. Sample preparation, storage, instrumentation, and testing are discussed in French et al. (2012).

Table 3.6 summarizes the measured coefficients of thermal expansion (CTE) for each laboratory specimen over the entire measured temperature range. The superstructure average CTE

computed from the laboratory specimens was 5.72 με/°F (10.3 με/°C). The average CTE from the pier specimens was equal to 4.85 με/°F (8.73 με/°C).

To determine whether the coefficient of thermal expansion varied by temperature, the incremental CTE values were calculated for each 9°F (5°C) temperature increment. The incremental CTE was estimated to be equal to the slope of the least-squares fit line using only the data points from one temperature increment and the following increment. These CTE values are plotted for the superstructure laboratory specimens against the average temperature between the two increments in Figure 3.2. In general, the CTE values appeared to be invariant with temperature. However, when the temperature stopped increasing and began decreasing, the CTE appeared to spike up to a considerably higher value. This effect seemed to be related to the reversal of the direction of the strain, and occurred regardless of the temperature at which this reversal occurred. Thus, it was assumed that this disturbance was mechanical in nature, and it followed that the CTE remained relatively invariant with temperature. This finding was inconsistent with in situ results as discussed in Section 3.4.2.

3.4.2 In Situ Testing

The CTE of the superstructure concrete was computed using data from the vibrating wire strain gages (VWSG) and linear potentiometers (LP) installed on the St. Anthony Falls Bridge. Instrumentation is documented in Chapter 2. The in situ testing procedure documented in French et al. (2012) was changed for the current investigation, and thus the new procedure is documented below.

3.4.2.1 In Situ Testing Procedure

Using the VWSG data, the total measured change in strain was assumed to be equal to

$$\Delta\varepsilon_{total} = \Delta\varepsilon_{temp} + \Delta\varepsilon_{constraint} + \Delta\varepsilon_{time} + \Delta\varepsilon_{mech} \quad (3\text{-}2)$$

where $\Delta\varepsilon_{temp}$, $\Delta\varepsilon_{constraint}$, $\Delta\varepsilon_{time}$, and $\Delta\varepsilon_{mech}$ are the changes in strain due to temperature, boundary condition constraints to expansion, time-dependent effects, and external loading, respectively. The temperature-dependent change in strain can be defined as

$$\Delta\varepsilon_{temp} = \frac{\alpha}{A}\int b(y)\Delta T dy + \frac{y_{gage}\alpha}{I_x}\int b(y)\Delta T y dy \tag{3-3}$$

where α is the CTE, A is the cross-sectional area, $b(y)$ is the width of the cross section at height y from the neutral axis of the section, y_{gage} is the distance of the measurement point (i.e., strain gage) from the neutral axis, I_x is the section moment of inertia, and ΔT is the temperature change.

To simplify the computation of α, particular conditions were imposed on the data used for this calculation. First, only measurements with low thermal gradient were considered, meaning the data was limited to times with approximately constant temperature throughout the entire section. The thermal gradient T_{grad} was estimated by computing the first moment of the temperature profile through the section as follows:

$$T_{grad} = \frac{1}{A}\int y\left(T - T_{avg}\right)dA \tag{3-4}$$

where y is the vertical distance from the neutral axis of the section, T is the temperature, T_{avg} is the average temperature in the section, computed by

$$T_{avg} = \frac{1}{A}\int T dA \tag{3-5}$$

and A is the cross-sectional area. The resulting gradient had units of temperature-length. The only section with sufficient instrumentation to accurately compute the first moment of the temperature profile was Location 7 of the southbound bridge. To perform the integrals in Eqn. (3-4) and (3-5), all operational thermistors within Location 7 were used. The temperatures among all thermistors at a given depth from the top surface were averaged together, and these average temperatures were integrated through the total depth of the section using the trapezoidal rule. Top deck (or

bottom fiber) surface temperatures were approximated by extrapolating a line up (or down) from the two topmost (or two bottommost) average temperatures to the surface.

The thermal gradients computed using Eqn. (3-4) varied from −140°F-in. to 455°F-in. (−1.97°C-m to 6.43°C-m). For purposes of determining the coefficient of thermal expansion, a small gradient was classified as having T_{grad} less than 4.0°F-in. (0.056°C-m). Filtering the gradient in this manner reduced the total number of readings considered by approximately 95%. This method of filtering differed from the original method documented in French et al. (2012), where only the difference between two thermistors was used to determine the magnitude of the gradient.

Readings with low thermal gradients tended to cluster, meaning if one reading had a low gradient, it was likely that readings around the same time also had low gradient. This would typically occur during cloudy days with low solar radiation. Clustered low-gradient readings tended to have similar temperatures, meaning that a high concentration of clustered points could adversely bias linear regression used to compute the coefficient of thermal expansion. To alleviate this issue, the low-gradient readings were filtered again such that all readings were at least 24 hours apart. This filtering reduced the low-gradient readings by 60% again, such that only about 2% of the total readings were used for computing the coefficient of thermal expansion. This second filter was new to the present method, and had no analogue in the results from French et al. (2012).

To reduce the impact of the boundary condition constraints, only gages at the midspans of Spans 1, 2 and 3 were used for computation of the CTE. The expansion joints at Abutment 1 and Pier 4 were assumed to remove any axial restraint felt within Spans 1 and 3, and Piers 2 and 3 were assumed to be sufficiently flexible such that axial restraint on Span 2 was minimal. Bending restraint was still present due to the continuity of the structure, but this was factored out by considering strains either at the neutral axis, or from gages oriented vertically or transversely.

Time-dependent strains over the course of the linear regression analysis were minimized either by considering sufficiently small time frames, or by only using data taken at least two years after bridge opening. Mechanical strains due to external traffic loading were assumed to be negligible.

Assuming that the temperature was constant throughout the section and that constraint, traffic, time-dependent effects were negligible, then Eqn. (3-2) simplifies to

$$\Delta\varepsilon_{total} = \alpha\Delta T \tag{3-6}$$

meaning the coefficient of thermal expansion could be estimated by

$$\alpha = \frac{\Delta\varepsilon_{total}}{\Delta T} \tag{3-7}$$

The procedure for estimating the coefficient of thermal expansion from the VWSG data was as follows:

1. Gather temperature and strain readings for the time period of interest.
2. Find the change in total strain from the readings, as given by

$$\Delta\varepsilon_{total} = (R - R_0) + \alpha_{gage}(T - T_0) \tag{3-8}$$

   where R and T were the current gage reading and temperature, respectively, R_0 and T_0 were the reference reading and temperature, respectively, and α_{gage} was the coefficient of thermal expansion of the vibrating wire strain gage, given as 6.39 με/°F (11.5 με/°C) per Roctest Instrumentation Manual (2006) for embedded strain gage model EM-5.
3. Consider only the measurements where T_{grad} is less than 4.0°F-in. (0.056°C-m).
4. Remove excess data points such that measurements are separated by at least 24 hours.
5. Plot the change in total strain (y-axis) versus temperature (x-axis). The temperature is taken from the thermistor integral with the vibrating wire strain gage.
6. Perform a least-squared linear fit on the change in total strain versus temperature plot.
7. For gages that were oriented longitudinally at the neutral axis, or vertically or transversely anywhere in the section, the slope of this line was assumed to be equal to the

coefficient of thermal expansion. For longitudinal gages not located on the neutral axis, the gage also measured the curvature of the box (due to the bending restraint provided by the adjacent continuous spans). To remove the curvature, corresponding top and bottom gages were used to interpolate the coefficient of thermal expansion to the location of the neutral axis.

The coefficient of thermal expansion was also estimated using the linear potentiometers (LPs) located at the expansion joints at Abutment 1 and Pier 4 of both the northbound and southbound structures.

The LP data were filtered in a method identical to that used for the VWSG data, keeping only measurements with minimal gradients and spaced at least 24 hours from any other reading.

The movement measured by the LPs attached to Span 1 at Abutment 1 represented the distance between the centerline of the bearing pad and the abutment backwall. The movement measured by the LPs attached to Span 3 at Pier 4 represented the differential movement between the centerline of the Span 3 bearing pad and the top of Pier 4. Span 4 was pinned to the top of Pier 4 and integral at Abutment 5; therefore, the thermal movement in Span 4 caused deflections at the top of Pier 4 or Abutment 5. Because the top of Pier 4 deflected under thermal loading, the Span 3 LPs measured the elongation of the three-span structure plus the movement of Pier 4.

There was no method for measuring the absolute deflection of the top of Pier 4. It was assumed that the integral abutment did not deflect, and that all the thermal movement of Span 4 was transferred to Pier 4. Finite element analysis indicated that Pier 4 was highly flexible and did not sufficiently restrain longitudinal deformation of the superstructure, and thus it was assumed that the top of Pier 4 deflected according to

$$\Delta L_{Pier\,4} = \alpha \Delta T L_4 \tag{3-9}$$

where L_4 was the length of Span 4, equal to 1,743 in. (44.3 m) for both southbound and northbound structures, and ΔT was the mean change in temperature estimated from the

thermistors installed at Location 7 of the southbound bridge using Eqn. (3-5). This change in length was subtracted from the measured change in length from the Span 3 LPs to represent the elongation of the three-span continuous portion of the superstructure.

Because the LP data measured the expansion of the total superstructure, the average bridge temperature computed using Eqn. (3-5) was used to compute the superstructure CTE. Least-squares linear fits was performed on the change in length measured at Span 1 and the measured change in length from Span 3 minus the assumed Pier 4 deflection from Eqn. (3-9), both plotted with respect to mean temperature, and the slope of each line was calculated. Axial restraint of Span 2 applied by Piers 2 and 3 was assumed to be minimal. Furthermore, rotation of the superstructure and pier during temperature changes were assumed to only minimally affect LP readings. Therefore, the above values were taken to be equal to the total elongation of all three spans. The coefficient of thermal expansion was calculated by the following equation:

$$\alpha = \frac{m_1 + m_3}{L} \tag{3-10}$$

where m_1 was the slope of the least-squares linear fit line for the LP attached to Abutment 1, m_3 was the slope of the least-squares linear fit line for the LP attached to Span 3 minus the longitudinal deflection of Pier 4, and L was the length of bridge measured between the two LPs. For the southbound bridge L was taken to be 12,780 in. (324.6 m), and for the northbound bridge L was taken to be 12,870 in. (326.9 m).

The solution procedure followed an iterative approach. First, the coefficient of thermal expansion for Span 4 was assumed. Slopes m_1 and m_3 were computed, noting that slope m_3 was dependent on the assumed value of α. The coefficient of thermal expansion was then calculated using Eqn. (3-10) and compared to the assumed value. The elongation of Span 4 was recalculated from Eqn. (3-9) using the computed α, and the process was repeated until the computed α converged with the assumed Span 4 CTE.

3.4.2.2 In Situ Results

The coefficient of thermal expansion was calculated using a linear fit to all of the filtered VWSG and LP data from January 1, 2011 until June 30, 2011. This data was assumed to have little creep or shrinkage, as the bridge was opened in September of 2008.

VWSGs were selected at the midspans of each span (i.e., Location 3 for Span 1, Location 7 for Span 2, and Location 9 for Span 3). The coefficient of thermal expansion was calculated individually for each gage. The top flange gages across the width of the section were averaged together for each location, as were the bottom flange gages.

An example of the data used for this calculation from gage VS03ETL2 is presented in Figure 3.3 (other gages provided similar results). The linear fit was found to be robust, indicating that time-dependent strains and thermal gradients were not significant over the examined duration. The resulting CTE values computed from the vertical gages (for which no correction was necessary) and the longitudinal gages interpolated to the neutral axis were averaged at each location. These averaged CTE values per instrumented location for the southbound and northbound bridges are presented in Table 3.7. At any given location, the standard deviation among all averaged gages was never greater than 0.45 με/°F (0.80 με/°C).

The CTE values computed at each instrumented location were found to be consistent along the length of the structures, with minimum and maximum estimates being 5.40 με/°F (9.72 με/°C) and 5.54 με/°F (9.97 με/°C), respectively, representative of a 2.6% relative difference. The overall average CTE using the in situ VWSG method from the three investigated sections on both the southbound and northbound structures was equal to 5.47 με/°F (9.85 με/°C).

An example of the LP data from the exterior box of the southbound structure at Abutment 1 plotted with respect to the average structure temperature and used to calculate the coefficient of thermal expansion is shown in Figure 3.4 (other LPs exhibited similar results).

The slopes measured at each end of the bridge were averaged between the two boxes. Slopes measured from each individual box at either end of the bridge (that is, before any averaging) were noted to be different by no more than 0.1 με/°F (0.2 με/°C), or approximately 2% relative difference, and therefore the average was believed to be representative for both boxes. Eqns. (3-9) and (3-10) were then applied in the iterative procedure as described in Section 3.4.2.1 until the CTE converged. The results are summarized in Table 3.8. The average CTE from both structures as calculated from the linear potentiometer data was equal to 5.25 με/°F (9.45 με/°C).

3.4.2.3 Variation of CTE with Temperature

The strain readings given in Figure 3.3 showed a subtle nonlinearity, whereby the slope of the change in strain plotted with respect to temperature increased as temperature increased. The consistency of the coefficient of thermal expansion with respect to temperature was therefore investigated using the vibrating wire strain gage data. The VWSG data were investigated from September 1, 2008 until February 19, 2013. To minimize time-dependent behavior, only the vertically oriented gages located at Location 3 and Location 7 of the southbound bridge were considered. This included three gages in the east web of the exterior box of Location 3 (VS03EEV1, VS03EEV2, VS03EEV3) and three gages in the east web of the exterior box of Location 7 (VS07EEV1, VS07EEV2, VS07EEV3). It was assumed that these gages measured only unrestrained thermal strains and shrinkage. Longitudinal gages were excluded from this exercise because they were believed to have significant early age time-dependent behavior due to creep. The VWSG data were first filtered in the same manner as described in Section 3.4.2.1.

Linear regression was performed on each set of 30 consecutive points, starting with point 1 to 30, point 2 to 31, point 3 to 32, and so on. The window size of 30 points was chosen because it allowed for sufficient variation in the temperature to accurately perform linear regression, while still minimizing the impact of time-dependent behavior. Because the window size was always 30

data points, the temperature range and total time during each set of measurements was consequently allowed to vary. Typically, temperature ranges within each 30-point set were on the order of 54–72°F (30–40°C) during the first year of readings, and around 36°F (20°C) for all future windows. The total time passing within each 30-point window was typically 100–200 days during the first year, and 50–100 days for future readings. This discrepancy between the first year and future years was because VWSG data was only collected every 6 hours until September 17, 2009, whereas readings were collected hourly afterwards. Consequently, readings with nearly zero gradient were more rare during the first year than later years. Regardless of the year, the typical temperature ranges observed during the 30-point datasets were large enough such that a reliable CTE measurement could be computed by linear regression.

Linear regression was performed on the change in total strain readings and the temperature reading from the gage under inspection. The CTE values were computed individually for each gage, and the resulting values were averaged together separately for each instrumented location; the results are shown in Figure 3.5. The plotted average temperature is the mean temperature (taken from all three gages investigated at each location) of the data set over which the regression was computed. The CTE value clearly trended linearly with temperature, increasing as the temperature increased. Arrows on the plot show the trend with time to track any particular hysteretic behavior, which appeared to be quite mild except for readings from very early ages (for example, the dip in the CTE plots around 50°F (10°C) and some of the looping at the high temperature end). The CTE varied from 4.7 με/°F to 6.4 με/°F (8.5 με/°C to 11.5 με/°C). The average CTE was 5.5 με/°F (10.0 με/°C), which was comparable to the estimates using the laboratory data in Section 3.4.1 and the in situ data from Section 3.4.2.2.

Linear regression was performed on the resulting CTE values from Figure 3.5 to determine the relationship between temperature and CTE, which was found to be

$$\alpha(T) = 4.30 + 0.0269 \cdot T \tag{3-11}$$

where α is the coefficient of thermal expansion as a function of temperature specified in microstrain per degrees Fahrenheit, and the temperature *T* is in degrees Fahrenheit. This amounted to a 30% variation of the CTE over the course of a year.

This large seasonal trend in the coefficient of thermal expansion was not seen in the laboratory results as presented in Section 3.4.1. The cause for this discrepancy was uncertain, though was possibly due to differences in humidity between the ambient VWSG data and the laboratory tests, or because only one full temperature cycle was used in the laboratory tests. A summary by Emanuel and Hulsey (1977) has shown that the coefficient of thermal expansion of concrete depends on relative humidity, with the maximum CTE occurring at approximately 65% relative humidity and lower values of CTE for dry (0% relative humidity) and saturated (100% relative humidity) concrete. For the laboratory specimens, the humidity was held constant. However, for the field readings, the ambient humidity was always highest during the winter and lowest during the summer. Because of this correlation between ambient relative humidity and ambient temperature, an apparent dependence of the CTE on temperature may, in fact, be due to changes in humidity.

This temperature-humidity relation is further complicated because the concrete CTE is affected by the internal (concrete pore) relative humidity and not the external (ambient) relative humidity, though the internal humidity is dependent on the ambient humidity. Internal humidity changes due to the processes of hydration, shrinkage, and drying creep. Furthermore, temperature also impacts the internal humidity, as illustrated by Figure 3.6 (Grasley and Lange, 2007). As the concrete heats and expands, the adsorbed water inside the concrete pores is stretched. This expansion in turn increases the radius of the meniscus. The surface tension of the pore water is greater when the menisci radius is small. An increased surface tension means that it takes more energy to evaporate the adsorbed water into the voids, while a decreased surface tension allows for water to evaporate more readily. Therefore, cold concrete (low menisci radius and high

surface tension) will have less evaporation and therefore lower internal humidity than warm concrete (high menisci radius and low surface tension). This trend is the opposite of the ambient external humidity, whereby colder temperatures are related to higher external relative humidity. Both the in situ concrete and the laboratory samples are subject to this phenomenon, in spite of the different environments.

The internal humidity at any given time is expected to be primarily driven by the adsorbed water and the temperature change, and less dependent on the processes of hydration, shrinkage, and drying creep. This is because the internal humidity adjusts quickly to changes in temperature; the evaporation of the adsorbed water into the concrete pores is expected to be orders of magnitude faster than the rate of the hydration reaction and diffusion of the water out of the bulk concrete. Therefore, although the mechanism for the variation of the CTE might be due to changes in internal humidity, the strong correlation between internal humidity and temperature means that the CTE in an uncontrolled environment will appear to be temperature dependent.

3.4.3 Results Summary

The superstructure average CTE computed from the laboratory specimens was 5.72 με/°F (10.3 με/°C). The overall average CTE using the in situ VWSG method from the three investigated sections on both the southbound and northbound structures was equal to 5.47 με/°F (9.85 με/°C). From the superstructure VWSGs, it was found that the CTE was constant along the length of the bridge, with maximum relative difference between any two investigated locations being 2.6%. Using the linear potentiometer data, the average CTE from both structures was equal to 5.25 με/°F (9.45 με/°C). Considering each method with equal weight, the recommended thermal expansion value for modeling purposes was an overall average superstructure CTE of 5.48 με/°F (9.87 με/°C). For the piers, only laboratory specimens were used to estimate the CTE; this result gave an average pier CTE equal to 4.85 με/°F (8.73 με/°C). Results are summarized in Table 3.9.

Results measured from the in situ VWSG data indicated that the coefficient of thermal expansion was temperature dependent, with variations up to 30% over the course of a year. This variation appeared to be roughly linear, and was hypothesized to be primarily caused by the thermal expansion and evaporation of the adsorbed water inside the concrete pores.

3.5 Unit Weight

Measurement of the unit weight of the superstructure concrete was conducted by the University of Minnesota. These tests were not performed prior to the report by French et al. (2012), and thus the testing procedure is documented below.

3.5.1 Sample Preparation

The unit weight of the superstructure concrete was measured using standard 4 x 8 in. (100 x 200 mm) cylinders provided by the Minnesota Department of Transportation. These cylinders were not stored in environmental chambers, but were instead kept on pallets located in the UMN Structures Laboratory or in storage rooms in the UMN Civil Engineering Building. A total of 25 cylinders were tested from the northbound and southbound bridge superstructure concrete. No samples from the pier or barrier rail concrete were tested. Cylinders were tested on April 25, 2013, over four years after completion of the bridge. Consequently, the measured unit weight likely accounted for the vast majority of the water loss due to shrinkage, and therefore was expected to be less than the unit weight at time of casting. Data for the unit weight of the fresh cast concrete were not available.

3.5.2 Testing Procedure

To compute the unit weight of the cylinders, the weight and apparent submerged weight were measured. These were performed using an Ohaus Explorer Pro Model EP12001 digital scale. A wire bucket was hung from underneath the scale into a tub of tap water. The samples were first weighed outside the water to compute their total weight. Then, each sample was placed in the hanging wire bucket, and the apparent submerged weight of the cylinder was recorded.

Because the buoyant force on the cylinder is the difference between the total weight and the apparent submerged weight, and because the buoyant force is equal to the weight of the displaced water, then the volume of the cylinder V can be computed by

$$V = \frac{\left(W_{total} - W_{submerged}\right)}{\gamma_{water}} \tag{3-12}$$

where W_{total} is the total weight, $W_{submerged}$ is the apparent submerged weight, and γ_{water} is the unit weight of water equal to 62.3 lbs/ft^3 (9.79 kN/m^3) at 70°F (21°C). The unit weight of the concrete is then equal to W_{total}/V.

When measuring the submerged weight of the cylinders, the concrete was not soaked in the water for any extended period of time either prior to or during the readings. The weight was measured immediately upon submersion to avoid diffusion of water into the concrete pores.

3.5.3 Results

A histogram of the 25 concrete unit weights is shown in Figure 3.7. Though all samples were from the superstructure concrete, the distribution of the unit weight had two clear peaks around 142.0 and 146.5 lbs/ft^3 (2,270 and 2,350 kg/m^3). The cause for the bimodal distribution was uncertain, but it was possible that different batches of the superstructure concrete may have had different aggregate sources or mix parameters, and thus differing unit weights. It was unknown how much of the placed concrete in the constructed bridge fell under each of these two unit weights, or if other batches had weights different from any of the tested samples. For lack of better information, it was necessary to simply assume that the superstructure concrete had a mean unit weight equal to the mean of all the measured samples. Thus, the average superstructure unit weight was equal to 143 lbs/ft^3 (2,290 kg/m^3). The unit weight for pier and barrier rail concrete mixes was untested, but was assumed to be similar to the measured superstructure concrete unit weight.

Chapter 4: Time-Dependent Behavior of Concrete

The time-dependent phenomena of creep and shrinkage of concrete are discussed in a wide range of literature and design documents, with widely ranging recommended relationships. This chapter describes the processes of time-dependent creep and shrinkage, the material properties required to define typical time-dependent models, and an overview of the time-dependent models investigated in this study.

Section 4.1 presents a brief overview of the phenomena of concrete creep and shrinkage, and provides a summary of other studies on the measured time-dependent behavior of existing structures. Section 4.2 presents the material properties from the St. Anthony Falls Bridge necessary for the definition of the presented creep and shrinkage models. Sections 4.3 through 4.8 individually document each considered time-dependent model, including the ACI Committee 209 model (1992), the B3 model from Bažant and Baweja (1995a), the CEB/FIP Model Codes (1978, 1990), the GL2000 model by Gardner and Lockman (2001), and a model based on the AASHTO LRFD Bridge Design Specifications (2010). Each section contains discussions of the respective creep model, shrinkage model, original calibration of the time-dependent model, and finally the assumed material properties that were specific to that particular time-dependent model and not covered in Section 4.2.

4.1 Phenomena of Creep and Shrinkage

4.1.1 Concrete Creep

Creep is the continued deformation (strain) under a constant applied stress. Creep strains are caused by some combination of crystalline flow in the aggregates and hardened cement paste, plastic flow in the cement paste, closing of internal voids, and flow of water out of the cement gel due to external load and drying (Wang et al., 2007). Deformations caused by viscoelastic properties of the material are called basic creep, while the deformation due to load-induced water

movement is called drying creep. The amount of creep that a specimen undergoes is affected by a large number of parameters including the constituent materials (aggregates, cement, etc.), water-cement ratio, curing temperature and humidity, relative humidity during loading, age at loading, duration of loading, magnitude of stress, volume-to-surface ratio of member, and the mix slump (Wang et al., 2007).

Creep is commonly described as either a creep coefficient $\varphi(t,t_0)$ or as a compliance function $J(t,t_0)$. The creep coefficient is the ratio of the time-dependent creep strain to the instantaneous elastic strain. The compliance function is the total strain as a function of time due to the application of a unit stress. The relationship between the creep coefficient and the compliance function is equal to

$$J\left(t,t_0\right)=\frac{1+\varphi\left(t,t_0\right)}{\left(E_c\right)_{t0}} \tag{4-1}$$

where $(E_c)_{t0}$ is the elastic modulus at the time of loading t_0. Because the elastic modulus $(E_c)_{t0}$ changes as the concrete ages, the definition of the creep coefficient can be inconvenient. For purposes of consistency, this report presents all creep models as compliance functions.

Divorcing the compliance function from the creep coefficient means that the modulus in the denominator of Eqn. (4-1) need not change with time. The compliance function must return the proper total elastic and creep strain, whereas the modulus expression, whether aging or not, is only a parameter in the strain predictions. Consequently, most compliance functions are not defined in terms of a creep coefficient, but rather as

$$J\left(t,t_0\right)=\frac{1}{\left(E_c\right)_{t0}}+\frac{\psi\left(t,t_0\right)}{\left(E_c\right)_{28}} \tag{4-2}$$

where the term $1/(E_c)_{t0}$ describes the instantaneous elastic deformation due to a unit stress applied at time t_0, $\psi(t,t_0)$ is a dimensionless function describing the time-dependent creep strains, and $(E_c)_{28}$ is the elastic modulus at 28 days required for dimensional consistency. This form of the

compliance function is valid because only the total time-dependent strain (and not the creep coefficient per se) is relevant to structural behavior, and the dimensionless function $\psi(t,t_0)$ can be defined to return the appropriate strains. Definition of $\psi(t,t_0)$ is often more convenient than using Eqn. (4-1) because all the effects of concrete age on creep strains are subsumed into the $\psi(t,t_0)$ term, while all the effects of concrete age on instantaneous elastic deformation are considered independently in the elastic modulus $(E_c)_{t0}$. This differs from the expression in Eqn. (4-1) in which the effects of age on creep strains must be taken into account using both the creep coefficient $\varphi(t,t_0)$ and the elastic modulus $(E_c)_{t0}$.

Though it is possible to formulate the compliance function such that a non-aging elastic modulus is substituted for the aging elastic modulus $(E_c)_{t0}$ in the denominator of the instantaneous strain term, this is typically not done. The exception to this is the B3 model (Bažant and Baweja, 1995a), which accomplishes this by including creep strains that occur over extremely short time scales (i.e., less than 10 milliseconds). The apparent increase in the elastic modulus is modeled by decreasing the magnitude of these short-time creep strains as the concrete ages. This special case for the B3 model is discussed more in Section 4.4.

Creep strain predictions using any given time-dependent model must use the definition of the concrete modulus as used for the derivation of that particular creep model. Mixing the dimensionless function $\psi(t,t_0)$ from one source with the strength-to-modulus conversion from a separate source will return incorrect strains.

Using the compliance function, the total strain (elastic plus creep strain) for a constant stress σ_0 applied at time t_0 is equal to

$$\varepsilon(t) = \sigma_0 J(t,t_0) \tag{4-3}$$

Under the conditions of changing stress, assuming that the material behaves linearly, the Boltzmann superposition principle can be applied:

$$\varepsilon(t) = \int_0^t J(t,\tau)\frac{\partial\sigma(\tau)}{\partial\tau}\partial\tau \tag{4-4}$$

Concrete is assumed to follow linear viscoelasticity for compressive stresses up until approximately 45% of the maximum compressive strength. For this report, nonlinear viscoelastic behavior is never considered, and the Boltzmann superposition principle is assumed to always hold true.

Creep models specified in the literature can be roughly divided into two categories: asymptotic models and logarithmic models. Most creep models presented in design codes, recommendations, and standards predict long-term ultimate creep strains that are approached asymptotically with time, and are thus termed asymptotic models. This category includes the AASHTO LRFD (2010), CEB/FIP Model Codes (1978, 1990), and ACI-209 (1992). On the other hand, logarithmic models do not predict an ultimate creep strain. Instead, the long-term creep strains trend linearly with the logarithm of time. This includes several creep models in the literature, the most notable being the B3 model (Bažant and Baweja, 1995a). Though the mathematical form of the GL2000 creep model (Gardner and Lockman, 2001) implies an asymptotic creep strain, for load duration less than thousands of years the asymptotic behavior is never observed. For normal structural life spans up to 150 years, the GL2000 creep model behaves much like a logarithmic creep model. Consequently, in this report the GL2000 model is classified as logarithmic.

4.1.2 Concrete Shrinkage

Shrinkage is the volume change of concrete unrelated to load application. Shrinkage is divided into two mechanisms: autogenous shrinkage and drying shrinkage. Autogenous shrinkage is the loss of water and subsequent reduction in volume due to the chemical processes of the hydration reaction, and is typically relatively small (Neville, 1996). Drying shrinkage is the diffusion-driven process of volume change due to water movement into and out of the concrete.

In typical applications, drying shrinkage strains imply a reduction in volume as water leaves the concrete; however, the volume can increase (i.e., swell) if the concrete is submerged in water. Though the mechanism for drying shrinkage is similar to that of drying creep, shrinkage strains are specifically those that are independent of external load. The parameters that affect shrinkage are largely the same as those that impact creep, as discussed in Section 4.1.1.

Because shrinkage occurs independently of load, there is no need to define any type of compliance function as is done for creep strains. Instead, shrinkage is simply specified as a volumetric strain change with time, $\varepsilon_{sh}(t)$.

Unlike creep, all shrinkage models progress asymptotically to an ultimate shrinkage strain. Physically, this is true because the mechanisms that induce shrinkage are limited by the movement or chemical processes of water. Once the system has reached an equilibrium state, shrinkage will cease.

4.1.3 Review of Time-Dependent Studies on Existing Structures

A study by Goel, Kumar and Paul (2007) compared creep and shrinkage models from ACI-209 (1982), CEB/FIP Model Code (1990), B3 (Bažant and Baweja, 1995a), Müller et al. (1999), and GL2000 (Gardner and Lockman, 2001). The models were compared to time-dependent measurements of Water Tower Place (Russell and Larson, 1989), from which the authors concluded that the GL2000 model was the best at predicting shrinkage. No creep models were found to be accurate for all load durations and types of concrete from the Water Tower Place data, but the authors concluded that GL2000 was the best at predicting creep strains under most circumstances. The creep and shrinkage models were further compared to data from the RILEM database, a compilation of concrete creep and shrinkage data from a wide variety of specimen shapes and properties. The database contained 518 creep and 426 shrinkage tests, including over 180 creep specimens with load duration greater than 500 days so that long-term creep properties might be investigated. Both the B3 and GL2000 models were found to best

match creep and shrinkage estimates from the database. Because these two models were calibrated to RILEM database results as discussed in Sections 4.4 and 4.7, this was not an unexpected result. The authors concluded that GL2000 model was the best practical model for prediction of time-dependent behavior of concrete, because it was simple, effective, and relied only on a small set of parameters known to the designers.

Robertson (2005) measured the deflections for the North Halawa Valley Viaduct, a post-tensioned concrete box girder bridge in Hawaii. Eight years after bridge erection, the design time-dependent deflection estimates were found to be both higher and lower (varying by span) than measured deflections. As a "final" model, the B3 short-form creep model (Bažant and Baweja, 1996) and the Gardner and Zhao (1993) shrinkage model were chosen to best fit the measured data. Design envelopes using upper and lower bounds for variable model input parameters were constructed for the time-dependent deflections of the structure.

Investigation by Bažant et al. (2009, 2010) of the collapse of the Koror-Babeldaob (KB) Bridge in Palau indicated the need for continued efforts toward better prediction of concrete creep and shrinkage over the design life of prestressed concrete structures. The authors reported that the ACI-209, B3, 1990 CEB/FIP Model Code, GL2000 and the JSCE Japanese Code models all underestimated the deflection of the KB Bridge. However, the authors further noted that only the B3 creep model (Bažant and Baweja, 1995a) could be scaled by linear regression to fit the measured deflections. This was primarily due to the summative form of the B3 creep model (as opposed to a multiplicative form common to most design creep provisions), and the use of numerous fitting parameters in the model.

4.2 Material Parameters for Time-Dependent Models

Time-dependent models require many material and environmental conditions to be defined. Parameters common to all of these models are presented here, and the derived properties assumed for each time-dependent model are discussed in their respective section.

The values presented in this section are specific to the material, environmental, and geometric properties of the I-35 St. Anthony Falls Bridge. Material properties and environmental conditions used for the laboratory tests and other finite element test cases may vary from the values presented here, particularly the volume-to-surface ratios and the environmental humidity.

Concrete compressive strength was a parameter common among all considered time-dependent models. For the superstructure concrete strength with a nominal design strength of 6.5 ksi (45 MPa), the 28-day strength was specified in the model according to material tests performed by MnDOT as presented in Section 3.1.1. The average 28-day compressive strength among the samples tested by MnDOT, denoted by $(f_c)_{28}$, was equal to 7.45 ksi (51.4 MPa) and was used for all time-dependent models. The average experimental 7-day strength among the specimens tested by MnDOT was equal to 5.64 ksi (38.9 MPa). The 7-day strength was not used as a direct input into the models, but was instead used to derive the cement type and concrete aging model. Laboratory measurements were not available for the compressive strength of the pier and barrier rail concrete with nominal design strength of 4.0 ksi (28 MPa). The 28-day mean strength of the pier and barrier rail concrete was assumed to be 23.5% larger than the nominal strength as determined according to a statistical study on ordinary ready-mix concrete strengths by Nowak and Szerszen (2003). Thus the mean strength of the pier and barrier rail concrete was taken as 4.94 ksi (34.1 MPa).

The ACI-209 (1992) and B3 (Bažant and Baweja, 1995a) models required the specification of the concrete mix proportions. The mix designs for the superstructure concrete (mix number ITF 6136) and pier concrete (mix number ITF 4136) were provided by Dustin Thomas from MnDOT (email correspondence on December 7, 2012), and are given in Table 4.1.

Air content and slump values for the concrete batches were provided by MnDOT. For the superstructure mix, average air content and slump values were 6.9% and 7.3 in. (185 mm), respectively, as measured for 39 samples from the cast-in-place concrete from Span 4. No

specimens were provided with the mix properties given for the pier concrete (ITF 4136). However, air content and slump results were provided by MnDOT for 24 specimens from the barrier rail and other non-structural elements, but with different cementitious content (for example, no slag) and mix parameters than specified for the pier concrete. These samples were presumed to have similar strength to the specified pier concrete mix, and so average air content and slump values were computed using these 24 samples. Thus, the pier mix was assumed to have average air content and slump values equal to 6.4% and 1.8 in. (46 mm), respectively.

The specified mix design used for the concrete barrier rails was not consistently listed in the bridge documentation. The as-built construction documents did not prescribe a concrete mix, but did specify that the nominal strength of barrier rail concrete was 4.0 ksi (28 MPa) like the pier concrete. According to the samples provided by MnDOT, the rails consisted of at least three different mixes, none of which were ITF 4136 as specified for the pier or ITF 6136 as specified for the superstructure. No concrete strength data was available for any of these barrier rail samples. According to documentation from Cemstone (personal correspondence with Kevin MacDonald), the barriers were intended to be cast from the superstructure mix (ITF 6136) though, as noted above, none of the MnDOT samples collected of mix ITF 6136 were from the barrier rails. Despite the uncertainty, the modeled results were computed assuming that the concrete used for the barrier rail was identical to the pier concrete, and that the slump and air content characteristics of the MnDOT barrier rail samples were indicative of both the pier and barrier rail mixes. Ultimately, this assumption was not expected to significantly alter the time-dependent analysis for the St. Anthony Falls Bridge, as the behavior of the superstructure was of the most interest and was unlikely to be strongly affected by minor changes in the piers and barriers.

The concrete elastic modulus was estimated from the measured strength data provided by MnDOT. It was assumed that each time-dependent model was originally derived and calibrated

using different expressions for the strength-to-modulus conversion. Per the discussion regarding compliance functions in Section 4.1.1, each model was consequently assigned a different modulus as described in their respective sections. This approach was considered valid because computing the total time-dependent strains according to each model was of more value than precisely calculating elastic behavior. The chosen strength-modulus conversions are presented in Sections 4.3 through 4.8 for the investigated time-dependent models. A validation of the chosen elastic moduli with measured modulus values from UMN and Cemstone (see Sections 3.1.2 and 3.1.3) is presented in Chapter 5.

Poisson's ratio was common among all considered time-dependent models, and was always assumed to be equal to a typical value of 0.20. The average measured Poisson's ratio as provided by Cemstone (Section 3.1.3) was equal to 0.21.

Some of the strength-to-modulus conversions required the unit weight of the plain concrete. Samples of the superstructure concrete were weighed four years after casting as discussed in Section 3.5, and the average unit weight was found to be 143 lbs/ft^3 (2,290 kg/m^3). No data were available for the pier and barrier rail concrete, so the unit weight for this concrete was assumed to be identical to that of the superstructure mix. These unit weights were not directly used as inputs to the gravity loading in the finite element model, as the dead load was based on the weight of the reinforced concrete, and not the plain concrete as specified here.

The cement type (i.e., Type I, Type II, Type III, or different specifications for European models) was derived individually for each model. According to Dustin Thomas of MnDOT (email correspondence on April 18, 2013), Type I cement was specified for all mix designs. However, concrete providers are allowed to use either Type I or Type III cement in the mix if Type I is specified. Therefore, it was uncertain what type of cement was used during construction, or if this type varied for different concrete batches.

In all time-dependent models, the cement type primarily impacts the concrete aging model. For each time-dependent model, the superstructure cement type was determined by choosing the aging curve that best fit the MnDOT measured strength values of the superstructure concrete at 7 and 28 days. Because each time-dependent model assumes a different form for the concrete aging behavior, the cement type was allowed to vary among the considered time-dependent models. Some shrinkage curves are specified with factors and coefficients dependent on the cement type. In these cases, the cement type was still assumed to be the same as derived from fitting the aging model to the measured strengths. The measured 7-day and 28-day strengths were unknown for the pier and railing concrete, so the pier and barrier rail cement was assumed to be Type I as specified.

Relative humidity was common among all time-dependent models. Daily average relative humidity was taken between September 1, 2008 and September 1, 2011 from weather station KMNMINNE17 located on the University of Minnesota campus approximately one mile from the St. Anthony Falls Bridge. The data included only full years of readings to avoid bias introduced by seasonal variations in humidity. The minimum and maximum daily average relative humidity taken during this time were 23% and 93%, respectively. However, because the process of water diffusion out of concrete is slow, the daily humidity variations were not believed to significantly impact the time-dependent behavior of the bridge. Therefore, time-dependent analyses used a constant relative humidity equal to 64.1%, taken as the average of all the daily average relative humidity readings between September 1, 2008 and September 1, 2011.

Curing conditions varied by the location on the superstructure and also by surface for any given section. According to email correspondence with Dustin Thomas from MnDOT (April 18, 2013), the precast segments were cured in the following fashion:

- Deck surfaces were sprayed with a curing compound immediately after placement, then wet cured with blankets for 4 days.

- Concrete surfaces abutting the core form and bulkhead forms (i.e., interior walls of the box section and the end regions of each segment) were form cured for approximately 1 to 2 days. Afterwards, a curing compound was sprayed on the surface.
- Concrete surfaces abutting the outside formwork (i.e., exterior walls of the box section and the underside of the deck wingtips) were form cured for weeks, dependent on the casting and erection dates of the segment.

Cast-in-place concrete was cured as follows:

- Deck surfaces were sprayed with a curing compound immediately after placement, then wet cured with burlap and soaker hoses for 7 days.
- Concrete surfaces abutting the core form (i.e., interior walls of the box section) were form cured for 7 to 14 days.
- Concrete surfaces abutting the outside formwork (i.e., exterior walls of the box section and the underside of the deck away from the boxes) were form cured for weeks, dependent on the casting dates and when the shoring was removed.

Emulating the different curing conditions on each surface would require conducting diffusion analysis, which was beyond the scope of this investigation. This process could also be approximated by changing the volume-to-surface ratio as curing surfaces were opened to the atmosphere. However, this level of detail was presumed to be unwarranted due to the uncertainties inherent in the accurate prediction of creep and shrinkage, and because it was unclear exactly how much accuracy would be gained from this still rough approximation. Instead, this process was simplified such that each element in the computational analyses was individually assigned a single curing duration without regard to the changing curing conditions. All cast-in-place concrete was assumed to have a curing duration of 7 days, equal to the wet cure duration of the top deck and within the bounds for interior form curing. All precast segments were assumed to have a curing duration of 4 days, equal to the wet cure duration of the top deck.

Bridge geometry included factors for volume-to-surface ratios and reinforcement ratios, which were identical for all time-dependent models. These parameters varied along the length and through the cross sections. Sets of elements comprising the deck, the webs, and the bottom flange were assigned volume-to-surface and reinforcement ratios that were averaged from the bridge geometry within that region. Regions were typically 15 ft (4.6 m) in length along the longitudinal axis of the bridge, but were larger in areas where the bridge geometry was constant (such as the southern end of Span 1 and the northern end of Span 3) and smaller in regions where the geometry changed quickly (such as near Piers 2 and 3). These ratios were also designated for the concrete barrier rail, the diaphragms above the piers and abutments, and the piers. Reinforcement ratios were defined separately for longitudinal, transverse, and vertical mild steel. Tables 4.2 through 4.5 define the volume-to-surface ratios and reinforcement ratios for each element set in the model.

Each element was assigned a casting date so that the loading age of the concrete could be computed. Casting dates for the cast-in-place concrete and the precast segments are summarized in Tables 1.1 and 1.2, respectively. Erection dates were captured by the construction staging sequence programmed into the finite element analyses as discussed in Section 6.1.3.

4.3 ACI Committee 209

4.3.1 Creep

ACI Committee 209 (1992) defines the creep coefficient $\varphi(t,t_0)$, that is the ratio of the creep strain to the elastic strain due to a stress σ imposed at time t_0 and specified in ACI 209R-92 Eqn. (2-8), to be equal to

$$\varphi\left(t,t_0\right)=\frac{\left(t-t_0\right)^{0.6}}{10+\left(t-t_0\right)^{0.6}}v_u \tag{4-5}$$

where t is the total age of the concrete in days, v_u is the ultimate creep coefficient, and t_0 is the age of the concrete at loading in days. The ultimate creep coefficient is dependent upon loading age, relative humidity, volume-to-surface ratios, temperature, and concrete composition:

$$v_u = 2.35\prod_i \gamma_i \tag{4-6}$$

where Π represents the product operator over all i, and γ_i are the correction factors as follows:

Correction for loading age γ_{la} from Eqns. (2-11) and (2-12) of ACI 209R-92:

$$\gamma_{la} = \begin{cases} 1.25(t_0)^{-0.118} & \text{moist-cured concrete} \\ 1.13(t_0)^{-0.094} & \text{steam-cured concrete} \end{cases} \tag{4-7}$$

Correction for relative humidity γ_H from Eqn. (2-14) of ACI 209R-92:

$$\gamma_H = 1.27 - 0.67H \tag{4-8}$$

where H is the greater of either the ambient relative humidity in decimal form or 0.40.

Correction for volume-to-surface ratio γ_{vs} from Eqn. (2-21) of ACI 209R-92:

$$\gamma_{vs} = \frac{2}{3}\left(1 + 1.13e^{-0.54V/S}\right) \tag{4-9}$$

where V/S is the volume-to-surface ratio in inches.

Correction factors accounting for the concrete composition, including factors for slump γ_{slump} from Eqn. (2-23) of ACI 209R-92, fine aggregate content γ_{fine} from Eqn. (2-25) of ACI 209R-92, and air content γ_{air} from Eqn. (2-29) of ACI 209R-92:

$$\gamma_{slump} = 0.82 + 0.067s \tag{4-10}$$

$$\gamma_{fine} = 0.88 + 0.0024\kappa \tag{4-11}$$

$$\gamma_{air} = 0.46 + 0.09\alpha \geq 1.0 \tag{4-12}$$

where s is the slump measured in inches, κ is the ratio in percent of fine aggregates to total aggregates by weight, and α is the air content in percent. No correction factors accounting for cement content are given for creep.

Guidelines are provided for corrections due to high temperatures. However, because sustained high temperatures were not considered in any of the time-dependent analyses for this study, temperature corrections were ignored. Furthermore, the specifications provide no specifics on the temperature dependence, and simply provide rough guidelines for changes in the creep strain magnitude for high temperatures (ACI Committee 209, 1992). For example, Section 2.5.6 of ACI 209R-92 states that the creep strain at 122°F (50°C) is approximately 2 to 3 times that at 68–75°F (19–24°C). Effects of temperature on concrete creep are presented in more detail in Section 7.2.

Provisions for concrete strength gain with time were taken from Eqn. (2-1) of ACI 209R-92:

$$(f_c)_t = \frac{t}{a + \beta t}(f_c)_{28} \tag{4-13}$$

where $(f_c)_t$ is the strength at time t after casting, $(f_c)_{28}$ is the concrete strength 28 days after casting, and a and β, documented in Table 4.6, are constants dependent on the cement type and curing conditions of the concrete.

The time-dependent modulus of elasticity was calculated using the time-dependent strength and Eqn. (2-5) of ACI 209R-92:

$$(E_c)_t = 33 w_c^{1.5} \sqrt{(f_c)_t} \tag{4-14}$$

where w_c is the unit weight of the concrete in lbs/ft^3, and $(E_c)_t$ and $(f_c)_t$ are the elastic modulus and strength, respectively, at time t after casting and specified in psi. Assuming a concrete unit weight equal to 0.143 kips/ft^3 as measured from samples of the superstructure concrete and recorded in Section 3.5, substituting Eqn. (4-13) into Eqn. (4-14) provides the specification for the time-dependent modulus $(E_c)_t$:

$$(E_c)_t = 56400 \sqrt{\frac{t}{a + \beta t}(f_c)_{28}} \tag{4-15}$$

where $(E_c)_t$ and $(f_c)_{28}$ have units of psi, t is days since casting, and values for a and β are documented in Table 4.6.

The creep strain predicted by the ACI 209 creep coefficient was equal to

$$\varepsilon_{cr} = \frac{\sigma}{(E_c)_{t0}} \varphi(t, t_0) \tag{4-16}$$

where $(E_c)_{t0}$ is the concrete elastic modulus at time t_0. Therefore, the creep compliance function, defined as the total creep plus elastic strain with time due to an imposed unit stress, was equal to

$$J(t, t_0) = \frac{\varepsilon_{el} + \varepsilon_{cr}}{\sigma} = \frac{1 + \varphi(t, t_0)}{(E_c)_{t0}} \tag{4-17}$$

4.3.2 Shrinkage

ACI Committee 209 (1992) defines the shrinkage strain ε_{sh} in Eqns. (2-9) and (2-10) of ACI 209R-92:

$$\varepsilon_{sh} = \frac{(t - t_c)}{f + (t - t_c)} \varepsilon_{shu} \tag{4-18}$$

where ε_{shu} is the ultimate shrinkage strain, t is the time in days since casting, t_c is the duration of curing in days, and f is the time coefficient equal to 35 days for moist-cured concrete and 55 days for steam-cured concrete. The ultimate shrinkage is dependent on the duration of curing, relative humidity, volume-to-surface ratio, temperature, and concrete composition:

$$\varepsilon_{shu} = -780 \times 10^{-6} \prod_i \gamma_i \tag{4-19}$$

where γ_i are the correction factors as follows:

Correction for duration of curing, γ_{cp}, is listed in Table 4.7.

Correction for relative humidity γ_H from Eqns. (2-15) and (2-16) of ACI 209R-92:

$$\gamma_H = \begin{cases} 1.4 - H & \text{for} \quad 0.4 \le H \le 0.8 \\ 3.0 - 3H & \text{for} \quad 0.8 < H \le 1 \end{cases} \tag{4-20}$$

where H is the ambient relative humidity in decimal form. At 100% relative humidity, this equation specifies that no shrinkage will occur. Consequently, these provisions cannot account for swelling of concrete at 100% relative humidity.

Correction for volume-to-surface ratio γ_{vs} from Eqn. (2-22) of ACI 209R-92:

$$\gamma_{vs} = 1.2e^{-0.12V/S} \geq 0.2 \tag{4-21}$$

where V/S is the volume-to-surface ratio in inches.

Correction factors accounting for the concrete composition, including factors for slump γ_{slump} from Eqn. (2-24) of ACI 209R-92, fine aggregate content γ_{fine} from Eqns. (2-26) and (2-27) of ACI 209R-92, cement content γ_{cement} from Eqn. (2-28) of ACI 209R-92, and air content γ_{air} from Eqn. (2-30) of ACI 209R-92:

$$\gamma_{slump} = 0.89 + 0.041s \tag{4-22}$$

$$\gamma_{fine} = \begin{cases} 0.3 + 0.014\kappa & \text{for} \quad \kappa \leq 50 \\ 0.9 + 0.002\kappa & \text{for} \quad \kappa > 50 \end{cases} \tag{4-23}$$

$$\gamma_{cement} = 0.75 + 0.00036c \tag{4-24}$$

$$\gamma_{air} = 0.95 + 0.008\alpha \tag{4-25}$$

where s is the slump measured in inches, κ is the ratio in percent of fine aggregates to total aggregates by weight, c is the cement content in lbs/yd^3, and α is the air content in percent.

Rough guidelines are provided for corrections due to high temperatures. However, because sustained high temperatures were not considered in any of the time-dependent analyses for this study, temperature corrections were ignored.

4.3.3 Comments on Original Calibration of the ACI-209 Time-Dependent Model

The ACI 209R-92 time-dependent model was originally calibrated using 120 creep and 95 shrinkage specimens as discussed in Branson and Christiason (1971). Of the total sample set, 75 creep and 56 shrinkage specimens had a testing duration of 20 years, and the rest had shorter

durations. The time-dependent behavior was selected to follow a modification of the Ross (1937) hyperbolic function. Each individual creep and shrinkage curve was fitted by an equation of the form

$$y(t) = y_u \frac{t^c}{d + t^c} \tag{4-26}$$

where $y(t)$ is the total creep or shrinkage with time, y_u is the ultimate creep or shrinkage, t is the time since loading for creep or the time since end of curing for shrinkage, and c and d are fitting constants. The best fit values of the y_u, c, and d constants from each individual creep and shrinkage test were averaged together separately for the normal-weight, sand light-weight, and all light-weight concrete samples. These three averages were again averaged together to arrive at the coefficients presented in Eqn. (4-5) for creep and Eqn. (4-18) for shrinkage.

To compute the correction factors based on loading age or curing time, humidity, *V*/*S* ratio, and concrete composition, subsets of the data were examined in a parametric study (Branson and Christiason, 1971). Of particular note, the variations for humidity only used data from a single source (Keeton, 1965), for which ambient relative humidity was varied from 20% to 100% for samples of normal-weight concrete with Type III cement and moist curing conditions. Likewise for the variations on *V*/*S*, only one data source was used (Hansen and Mattock, 1966), for which the volume-to-surface ratio was varied from 1.0 to 6.0 in. (25 to 152 mm) on two different mix designs both using Type III cement.

The form and derivation of the ACI-209 creep and shrinkage models have some features that might negatively affect accurate time-dependent predictions. First, because all creep and shrinkage curves were fitted individually and then all the coefficients were averaged, the calibration did not have any overarching weighting system whereby some data were trusted more strongly than others. Because all samples have measurements at low durations of loading while only a subset of the data had readings up to 20 years after loading or curing, the net effect of not

performing any weighting would be to bias the fit more towards time-dependent behavior at young ages. Furthermore, estimation of the ultimate strain coefficient y_u is an ill-posed problem for any short duration sample that has not yet reached its asymptotic value.

The method used by the ACI-209 time-dependent model to account for volume-to-surface is not strongly supported. Much of the St. Anthony Falls Bridge has a *V*/*S* ratio around 8.0 in. (203 mm) or higher, while the maximum ratio for calibration of the ACI-209 model was 6.0 in. (152 mm). Furthermore, because drying creep and shrinkage are driven by diffusion of water in the concrete, the rate at which the asymptotic creep and shrinkage are reached should depend on the *V*/*S* ratio. This means that the *d* coefficient in Eqn. (4-26) should be greater for specimens with larger *V*/*S*. The ACI Committee 209 (1992) recognized this effect in their remarks on creep and shrinkage of special structures as presented in Sections 2.4 and 2.8 of the ACI 209R-92, where the recommended creep function for structures with large *V*/*S* takes the form of a double power curve instead of the Ross hyperbola. Only the general recommendations as presented in the previous sections of this chapter are considered in this report.

4.3.4 Derived Material Properties for FEM Input

As discussed in Section 4.2, the average 28-day compressive strength among all superstructure concrete samples tested by MnDOT was equal to 7.45 ksi (51.4 MPa), and this number was adopted for the value of $(f_c)_{28}$. To determine the cement type, the 7-day concrete strength estimated using the *a* and β parameters from Table 4.6 was compared to the MnDOT measured 7-day strength equal to 5.64 ksi (38.9 MPa). The best fit was provided by assuming Type III moist-cured concrete ($a = 2.3$ and $\beta = 0.92$) for which the estimated 7-day strength was 5.96 ksi according to Eqn. (4-13). The relative error between the estimated strength and measured strength at 7-days was 5.7%. The 28-day modulus of elasticity was computed using Eqn. (4-15) assuming Type III moist-cured concrete and was equal to 4,860 ksi (32.3 GPa). Strength data was not available for the pier and barrier rail concrete, so Type I moist-cured concrete (parameters *a* =

4.0 and $\beta = 0.85$ from Table 4.6) was assumed. The 28-day modulus of the pier and barrier rail concrete was equal to 3,980 ksi (27.4 GPa) according to Eqn. (4-15).

Mix design properties as listed in Table 4.1 were required for derivation of the fine aggregate ratio and the total cement content. The fine aggregate ratio was equal to 42.3% for the superstructure concrete and 44.2% for the pier and rail concrete. The total cement content was taken as the sum of all cementitious materials (Portland cement, fly ash, silica fume, and slag) in the mix, and was equal to 743 lbs/yd^3 (441 kg/m^3) and 545 lbs/yd^3 (323 kg/m^3) for the superstructure and pier concretes, respectively.

For a summary of the material properties used in the superstructure concrete and pier and barrier rail concrete, refer to Tables 4.8 and 4.9, respectively.

4.4 B3

4.4.1 Creep

The B3 time-dependent model for concrete, developed by Bažant and Baweja (1995a), differs significantly from the majority of models in the literature. The B3 model is derived from solidification theory (Bažant and Prasannan, 1989a, 1989b) which models the aging process of concrete. Solidification theory is based on the notion that the apparent time-dependent properties of a system are never due to aging of individual components, but rather due to changes in composition or concentrations of the various substances in a system. In other words, the aging properties of concrete are assumed to be due to the progressive hydration and solidification of the cement, but the properties of the already solidified cement are nonaging.

The B3 creep model consists of five terms that additively contribute to the total compliance:

$$J(t,t_0) = q_1 + q_2 Q(t,t_0) + q_3 \ln\left(1 + (t-t_0)^n\right) + q_4 \ln\left(\frac{t}{t_0}\right) + q_5 C_d(t,t_0,t_c) \qquad (4\text{-}27)$$

where t is the total age in days since casting, t_0 is the age in days at loading, and t_c is the age in days when drying and shrinkage begin, typically assumed to be at the end of the moist or steam curing period. Constants q_1 through q_5 all have units of inverse stress (psi^{-1}). The term q_1 refers to the nonaging instantaneous modulus of the concrete and is assumed to be constant with time. The B3 model accounts for the apparent increase of the modulus of elasticity with time by reducing the short-term (i.e., time-scales ranging from less than 10 milliseconds to 15 minutes) creep as the material ages and solidifies. Terms for q_2 and q_3 are derived from the viscoelastic behavior of the concrete, whereby the q_3 is solely due to the nonaging viscoelastic behavior of the material, and the q_2 term comes from the convolution between the nonaging viscoelastic behavior and a concrete aging term. The exponent n in the nonaging viscoelastic term is equal to 0.1 for all concrete regardless of mix parameters (Bažant and Prasannan, 1989a). The q_4 term is due to the viscous flow of the material assuming that the viscosity increases linearly with time. The q_5 term is due to the drying creep, i.e., the stress-dependent deformation due to loss of water in the concrete.

The equation for $Q(t,t_0)$ describing the aging viscoelastic behavior cannot be expressed analytically, and must instead be defined by the integral equation:

$$Q(t,t_0) = \int_{t_0}^{t} \left(\frac{\lambda_0}{\tau} \right)^m \frac{n(\tau - t_0)^{n-1}}{\lambda_0^n + (\tau - t_0)^n} d\tau \tag{4-28}$$

where τ is the variable of integration, n is the nonaging exponent equal to 0.1, m is the aging exponent equal to 0.5, and λ_0 is the aging time factor equal to 1 day (Bažant and Prasannan, 1989a). An approximate form of this equation as presented by Bažant and Baweja (1995a) can be written as

$$Q(t,t_0) \approx Q_f(t_0) \left[1 + \left(\frac{Q_f(t_0)}{Z(t,t_0)} \right)^{r(t_0)} \right]^{-1/r(t_0)} \tag{4-29}$$

where

$$r(t_0) = 1.7(t_0)^{0.12} + 8 \tag{4-30}$$

$$Z(t,t_0) = (t_0)^{-m} \ln\left(1 + (t - t_0)^n\right) \tag{4-31}$$

$$Q_f(t_0) = \left[0.086(t_0)^{2/9} + 1.21(t_0)^{4/9}\right]^{-1} \tag{4-32}$$

Using the constants n = 0.1 and m = 0.5, this approximation is within 1% of the exact formula for $t - t_0$ up to 10,000 days and t_0 from 1 to 10,000 days (Bažant and Baweja, 1995a, and Bažant and Prasannan, 1989a).

The equation for drying creep $C_d(t,t_0,t_c)$ is expressed as

$$C_d(t,t_0,t_c) = \sqrt{e^{-8G(t)} - e^{-8G(t_0)}} \tag{4-33}$$

in which

$$G(t) = 1 - (1 - H)\tanh\left(\sqrt{\frac{t - t_c}{\tau_{sh}}}\right) \tag{4-34}$$

where H is the relative humidity expressed as a decimal, and τ_{sh} is the shape factor in days given by

$$\tau_{sh} = k_t\left(\frac{2k_s V}{S}\right)^2 \tag{4-35}$$

for which V/S is the volume-to-surface ratio in inches, k_s is the shape coefficient, and k_t is the age factor expressed as

$$k_t = 190.8(t_c)^{-0.08}\left((f_c)_{28}\right)^{-0.25} \tag{4-36}$$

where $(f_c)_{28}$ is the 28-day mean concrete strength in psi, and t_c is the curing time in days. The k_s shape coefficient, which ranges from 1.0 for infinite slabs up to 1.55 for cubes, does not significantly impact the total time-dependent behavior, and Bažant and Baweja (1995a) suggest that this value be set equal to 1.0 for most simplified analyses. For analysis of the St. Anthony

Falls Bridge, infinite slabs reasonably approximate most elements in the box girders, and therefore $k_s = 1.0$ was adopted for the entire model.

Constants q_1 through q_5 (specified in psi^{-1}) are dependent upon the composition of the concrete:

$$q_1 = \frac{0.6}{(E_c)_{28}} = \frac{0.6}{57000\sqrt{(f_c)_{28}}} \tag{4-37}$$

$$q_2 = 4.511\times10^{-4} c^{0.5} \left((f_c)_{28}\right)^{-0.9} \tag{4-38}$$

$$q_3 = 0.29(w/c)^4 q_2 \tag{4-39}$$

$$q_4 = 1.4\times10^{-7} (a/c)^{-0.7} \tag{4-40}$$

$$q_5 = 1.90\times10^{-4} \left((f_c)_{28}\right)^{-1} (\varepsilon_{shu})^{-0.6} \tag{4-41}$$

where $(f_c)_{28}$ is the 28-day mean concrete strength in psi, c is the cement content of the concrete in lbs/ft^3, w/c is the water to cement weight ratio, a/c is the aggregate (coarse and fine) to cement weight ratio, and ε_{shu} is the ultimate shrinkage strain. The 28-day elastic modulus $(E_c)_{28}$ used in the B3 model and specified in Eqn. (4-37) is a simplified version of the concrete modulus from ACI-209 (1992), as described in Section 4.3.1.

The ultimate shrinkage strain, required for the computation of the drying creep term, is defined by

$$\varepsilon_{shu} = \alpha_1\alpha_2 \left[2.6\times10^{-5} w^{2.1} \left((f_c)_{28}\right)^{-0.28} + 2.7\times10^{-4} \right] \frac{(E_c)_{607}}{(E_c)_{tc+\tau sh}} \tag{4-42}$$

where α_1 is the correction for cement type, equal to 1.0 for Type I, 0.85 for Type II, and 1.1 for Type III, α_2 is the correction for curing conditions, equal to 0.75 for steam cured, 1.0 for water or moist cured, and 1.2 for sealed concrete, w is the water content of the concrete in lbs/ft^3, the ratio of $(E_c)_{607}$ to $(E_c)_{tc+\tau sh}$ (i.e., the ratio between the elastic moduli calculated at 607 days after casting and $t_c+\tau_{sh}$ days after casting) is an empirical expression used to correct for the aging of the

concrete, and τ_{sh} is the shape factor defined in Eqn. (4-35). As suggested by Bažant and Baweja (1995a), the concrete elastic modulus at time t after casting $(E_c)_t$ may be computed using the form of the ACI-209 strength gain equation:

$$\left(E_c\right)_t = \frac{t}{a+\beta t}\left(E_c\right)_{28} \tag{4-43}$$

where the 28-day modulus $(E_c)_{28}$ is equal to

$$\left(E_c\right)_{28} = 57000\sqrt{\left(f_c\right)_{28}} \tag{4-44}$$

and parameters a and β are identical to those from ACI-209 (1992) and specified in Table 4.6. The modulus provisions in the B3 model do not account for the variation of concrete unit weight, but are otherwise identical to the ACI-209 specifications. This aging modulus expression is only used for correction of the ultimate shrinkage strain; the instantaneous strains are modeled by q_1 as given in Eqn. (4-37), with short-term creep strains subsumed into the basic creep terms.

4.4.2 Shrinkage

The B3 model estimates shrinkage strains using the following equation:

$$\varepsilon_{sh}\left(t,t_c\right) = -\varepsilon_{shu} k_h \tanh\left(\sqrt{\frac{t-t_c}{\tau_{sh}}}\right) \tag{4-45}$$

where ε_{shu} is the ultimate shrinkage strain defined in Eqn. (4-42), τ_{sh} is the shape factor defined in Eqn. (4-35), k_h is the humidity correction factor equal to

$$k_h = \begin{cases} 1-H^3 & \text{for} \quad 0 \le H < 0.98 \\ 12.94\left(1-H\right)-0.2 & \text{for} \quad 0.98 \le H \le 1.0 \end{cases} \tag{4-46}$$

where H is the relative humidity expressed as a decimal.

4.4.3 Comments on Original Calibration of the B3 Time-Dependent Model

The B3 time-dependent model was originally calibrated using the RILEM database of creep and shrinkage measurements (Bažant and Baweja, 1995b). At the time of the calibration of the B3 model, the RILEM database contained 518 creep and 426 shrinkage tests. The database

has grown since the development of the B3 and, in 2008, was renamed the NU-ITI database with a total of 621 creep and 490 shrinkage tests (Bažant and Li, 2008a).

Because the database contained far more data points for creep and shrinkage at early ages after loading or curing, and comparatively few readings at later times, using all the data without applying some form of weighting would introduce bias towards the early age time-dependent behavior. This is generally undesirable as designers are primarily interested in the long-term implications of creep and shrinkage, and not the short-term deformations. To circumvent this problem, Bažant and Baweja (1995b) applied weighting to data points in each logarithmic decade after loading or curing (i.e., points from 0–10 days after loading/curing in one decade, 10–100 days in the second decade, and so on) in inverse proportion to the number of points within that decade. Thus, the individual readings from decades with more data were weighted less heavily than individual readings from decades with sparse data. In this way, each logarithmic decade had equal weight in the calibration.

Though the B3 model was calibrated with far more data than was used for the ACI-209 model as discussed in Section 4.3.3, results for concrete specimens with large volume-to-surface ratios were still rare. In fact, within the RILEM database, only 9 samples had *V*/*S* ratios greater than or equal to 3.0 in. (76 mm), with the maximum ratio of any sample equal to 6.0 in. (152 mm). The majority of these samples were from a single study (Hansen and Mattock, 1966). Thus, with regards the volume-to-surface ratio, the RILEM database did not have any significant advantage over the data used to calibrate the ACI-209 model. In comparison between the ACI-209 and B3 models, the B3 model only includes effects due to *V*/*S* into the rates of drying creep and shrinkage, as opposed to correcting the total asymptotic strain as done for ACI-209.

4.4.4 Derived Material Properties for FEM Input

Because, per Bažant and Baweja (1995a), the concrete strength gain relation with age for the B3 model can be assumed to be identical to that from the ACI-209 model, the cement type

parameters were taken to be identical to those specified in Section 4.3.4. Thus, the superstructure mix was assumed to be Type III moist-cured concrete, and the pier and barrier rail mix was assumed to be Type I moist-cured concrete. The 28-day elastic modulus, computed using Eqn. (4-44), was equal to 4,920 ksi (33.9 GPa) for the superstructure concrete and 4,020 ksi (27.7 GPa) for the pier and rail concrete. For computing the ultimate shrinkage values in Eqn. (4-45), coefficients α_1 and α_2 were equal to 1.1 and 1.0, respectively, for the Type III moist-cured superstructure concrete, and both coefficients were equal to 1.0 for the Type I moist-cured pier and barrier rail concrete. Using the superstructure mix design parameters as listed in Table 4.1, relevant parameters for the B3 model included the total cementitious material content equal to 27.5 lbs/ft^3 (743 lbs/yd^3, 441 kg/m^3), the water to cement ratio equal to 9.63/27.5 = 0.35, and the aggregate to cement ratio equal to 105.8/27.5 = 3.85. Relevant parameters for the pier and rail concrete included the total cement content totaling 20.2 lbs/ft^3 (545 lbs/yd^3, 323 kg/m^3), the water to cement ratio equal to 9.07/20.2 = 0.45, and the aggregate to cement ratio equal to 114.9/20.2 = 5.70.

Inputs required to implement the B3 time-dependent specifications into the St. Anthony Falls Bridge finite element model are summarized in Tables 4.8 and 4.9 for the superstructure concrete and pier and barrier rail concrete, respectively.

4.5 CEB/FIP Model Code 1978

4.5.1 Creep

During the design of the I-35W St. Anthony Falls Bridge, time-dependent behavior was investigated using the 1978 CEB/FIP Model Code (Minnesota Department of Transportation, 2008). Concrete creep behavior as presented here is documented in Appendix B, Annex E of the 1978 CEB/FIP Model Code.

The creep compliance function, defined as the elastic strain plus the creep strain with time due to an imposed unit stress at time t_0, was equal to

$$J(t,t_0)=\frac{\varepsilon_{el}+\varepsilon_{cr}}{\sigma}=\frac{1}{(E_c)_{t0}}+\frac{\psi(t,t_0)}{(E_c)_{28}} \tag{4-47}$$

where $(E_c)_{28}$ is the modulus of elasticity of the concrete at 28 days, $(E_c)_{t0}$ is the modulus at the time of loading t_0, and $\psi(t,t_0)$ is the dimensionless function describing the creep strains at time t. The current time t and the loading time t_0 are specified in days after casting. The creep coefficient is a function of a series of parameters including ambient humidity, dimensions, concrete rate of hardening, and concrete composition. Specifically, the 1978 CEB/FIP Model Code defines the creep strain function as

$$\psi(t,t_0)=\beta_a(t_0)+\varphi_d\beta_d(t-t_0)+\varphi_{f1}\varphi_{f2}\left[\beta_f(t)-\beta_f(t_0)\right] \tag{4-48}$$

The first term, $\beta_a(t_0)$, represents partially irreversible rapid deformation during the first day of loading. The second term, $\varphi_d\beta_d(t-t_0)$, represents the recoverable portion of the long-term deformation. The final term, $\varphi_{f1}\varphi_{f2}[\beta_f(t)-\beta_f(t_0)]$, is the irreversible "flow" long-term deformation.

With the exception of the $\varphi_d\beta_d(t-t_0)$ term, all times should be corrected based on the ambient mean temperature and the type of concrete according to

$$t_{corrected}=\frac{q}{30}\sum_{0}^{t_m}(T+10)\Delta t_m \tag{4-49}$$

for which t_m is the total uncorrected time, T is the mean ambient temperature in degrees Celsius, Δt_m is the time increment over which the ambient temperature is averaged, and q is a factor accounting for the type of cement. The Model Code specifies that q should be equal to 1 for normally or slowly hardening cements, 2 for rapid-hardening cements, and 3 for rapid-hardening high-strength cements. The $\varphi_d\beta_d(t-t_0)$ term is excluded from this time correction because it is defined as completely recoverable, and thus independent of concrete age and degree of hydration.

This temperature correction was not adopted in the finite element model for two reasons. First, to simplify the computational analysis of the St. Anthony Falls Bridge, temperature correction for creep rates was taken into consideration by adjusting the time scale for the

measured data to allow comparison with the FEM results, as discussed in Section 7.3.2. Second, according to this equation, the change in corrected time for temperatures less than −10°C (14°F) would be negative, implying that during very cold temperatures creep deformations would progress in the opposite direction of the applied stress. Such a result is clearly non-physical. Therefore Eqn. (4-49) was only used to adjust the times according to the cement type factor q while the temperature T was always held constant at 20°C (68°F).

The partially irreversible rapid deformation, $\beta_a(t_0)$, is specified as

$$\beta_a(t_0) = 0.8\left[1 - \frac{(f_c)_{t0}}{(f_c)_\infty}\right] \tag{4-50}$$

where $(f_c)_{t0}$ is the mean concrete compressive strength at t_0, and $(f_c)_\infty$ is the concrete strength at infinite time (i.e., the maximum attainable concrete strength). The strain associated with $\beta_a(t_0)$, being independent of the duration of loading, effectively occurs immediately upon the application of load, and as such, functions much like a time-dependent modification to the elastic modulus.

The maximum attainable concrete strength $(f_c)_\infty$ is computed using the provisions for time-dependent strength gain, adopted from Figure e-1 of the 1978 CEB/FIP Model Code and presented in Figure 4.1. The value for the time of loading t_0 used to compute the strength should be adjusted by the cement type and temperature according to Eqn. (4-49). The shape of the aging curve does not change based on concrete composition, and the effects of cement type on strength gain are completely modeled by the change in the corrected age of loading. Knowing the strength and corrected age at any one concrete age (typically 28 days), the maximum attainable strength can be extrapolated from the plot.

The 1978 CEB/FIP Model Code employs graphical-based approaches to calculating the long term recoverable and irrecoverable deformations. For the recoverable deformation, φ_d represents the coefficient of delayed elasticity, and is always taken as 0.4. The recoverable deformation coefficient $\beta_d(t - t_0)$, shown in Figure 4.2, is given in graphical format as a function

of the time after initial loading. This definition of recoverable deformation does not vary by section shape; the coefficient of delayed elasticity is assumed constant, and the recoverable deformation coefficient only depends on the uncorrected duration of loading.

The irrecoverable long-term deformation is dependent on the corrected total time and time of loading, the ambient humidity, and the shape of the specimen. The creep flow coefficient φ_{f1} is a function of the ambient humidity and is documented in Table 4.10. The creep flow coefficient φ_{f2} depends of the shape of the specimen characterized by the effective thickness *h*, specified in millimeters and defined by

$$h = \frac{2\lambda V}{S} \tag{4-51}$$

where λ is a humidity dependent parameter as specified in Table 4.10, and *V*/*S* is the volume-to-surface ratio in millimeters (1 in. = 25.4 mm). The plot for coefficient φ_{f2} as a function of *h* is shown in Figure 4.3. The Model Code plot provided for flow coefficient β_f is given in Figure 4.4.

The concrete modulus of elasticity can be determined as a function of concrete strength using Eqn. (2.4) of the 1978 CEB/FIP Model Code, converted to units of psi, such that

$$E_c(t) = 262000\left(f_c(t)\right)^{1/3} \tag{4-52}$$

where $f_c(t)$ is the strength at time *t* in days after casting. According to the commentary in Section e-1.3 of the 1978 CEB/FIP Model Code, the elastic modulus $(E_c)_{t0}$ that accounts for the instantaneous deformation of the concrete in Eqn. (4-47) should be increased by 25% over the predicted modulus from Eqn. (4-52). The creep modulus $(E_c)_{28}$ in Eqn. (4-47) is not adjusted in this fashion.

4.5.2 Shrinkage

Concrete shrinkage behavior as presented here is documented in Appendix B, Annex E of the 1978 CEB/FIP Model Code.

The shrinkage strain ε_s for concrete at time *t* is assumed to follow:

$$\varepsilon_s = \varepsilon_{s1}\varepsilon_{s2}\beta_s\left(t - t_c\right) \tag{4-53}$$

where ε_{s1} and ε_{s2} are the shrinkage constants dependent on humidity and shape, respectively, β_s is the shrinkage curve as a function of time and shape, and t_c is the time when shrinkage begins at the end of steam or moist curing. The humidity dependence of constant ε_{s1} is listed in Table 4.10. The positive value for ε_{s1} for concrete in water indicates that the specimen will swell instead of shrink. Shape dependency is quantified in terms of the effective thickness *h*, specified in millimeters and defined in Eqn. (4-51).

Times *t* and t_0 are corrected by the correction procedure for temperature as specified in Eqn. (4-49), except that the *q* parameter is always set equal to 1 for shrinkage computations regardless of cement type. This implies that the temperature dependence of the shrinkage according to the Model Code is independent of the cement type. As mentioned in Section 4.5.1, temperature variations were not considered in the computational analysis of the St. Anthony Falls Bridge.

The 1978 CEB/FIP time-dependent procedure is primarily graphical; Model Code plots for shape-dependent constant ε_{s2} and shrinkage function β_s are presented in Figures 4.5 and 4.6, respectively.

4.5.3 Comments on Original Calibration of the 1978 CEB/FIP Time-Dependent Model

The 1978 CEB/FIP Model Code provisions for creep and shrinkage were based on the Rüsch-Jungwirth method (Rüsch, Jungwirth, and Hilsdorf, 1983). This method assumed that the total creep is the summation of reversible delayed elastic strains, irreversible flow strains (which includes a portion of basic creep plus all the drying creep), and short-term strains.

The reversible delayed elastic strains were derived assuming that the creep recovery curve was identical to the delayed elastic component of creep (Rüsch, Jungwirth, and Hilsdorf, 1983). The authors acknowledged that this assumption had not been verified due to an absence of

sufficient experimental data. The delayed elastic strain was assumed to be constant for all concrete compositions, and furthermore independent of specimen shape, age, and environment. The shape of this behavior was derived from the nonaging Kelvin-Voigt model (Mola and Pellegrini, 2012).

For the irreversible flow creep, both the basic and drying creep phenomenon were assumed to approach limiting values with time. Rüsch, Jungwirth, and Hilsdorf (1983) justified this by stating that continued viscous deformation will redistribute internal stresses away from the cement paste and towards the stiffer aggregates, and that continued stiffening and polymerization of the cement gel will reduce the rate of viscous deformation with time. The shape of flow creep was derived from the aging Dischinger model (Mola and Pellegrini, 2012).

The short-term creep strains were assumed to occur effectively instantaneously upon loading in relation to the compressive strength of the concrete (Rüsch, Jungwirth, and Hilsdorf, 1983).

The shrinkage curve of the Rüsch-Jungwirth method was derived from a study by Hilsdorf (1967). The effects of the volume-to-surface ratio on the rate of shrinkage were based on the results from Hansen and Mattock (1966).

Statistical optimization of the 1978 Model Code method was performed using results from 112 shrinkage samples and 150 creep samples (Hilsdorf, Müller, and Oppermann, 1983). With few exceptions, the samples were limited to tests performed after 1950, though some earlier results were used for evaluating the long-term development of creep and shrinkage with time. No concretes with admixtures were permitted. Similar to the ACI-209 model, results for specimens with large *V/S* were limited to the study by Hansen and Mattock (1966).

4.5.4 Derived Material Properties for FEM Input

The cement type was determined by comparing the measured strength values to the time-dependent strength relationship from Figure 4.1. The strength at infinite time was unknown, so

instead the ratio between the MnDOT measured 28-day and 7-day strengths was compared to the ratio between the 28- and 7-days strengths estimated from Figure 4.1 using different cement types. For lookup in the strength-gain figure, the concrete age was corrected using Eqn. (4-49) assuming constant temperature equal to 20°C (68°F). The best fit to the strength ratio of the superstructure concrete was achieved by assuming q = 2.4, which lies between the 1978 CEB/FIP Model Code specifications for rapid-hardening and high-strength cements. Extrapolating the concrete strength out to infinite time gave a maximum superstructure concrete strength of 9.26 ksi (63.8 MPa). Using Eqn. (4-52), the 28-day modulus of the superstructure concrete was equal to 5,120 ksi (35.3 GPa).

For pier and barrier rail concrete with nominal strength equal to 4.0 ksi (28 MPa), the 28-day strength was assumed to be equal to 4.94 ksi (34.1 MPa) as discussed in Section 4.2. Cement type was assumed to be normal-hardening cement with q = 1.0. Extrapolating the concrete strength out to infinite time gave a maximum pier and rail concrete strength of 7.18 ksi (49.5 MPa). Using Eqn. (4-52), the 28-day modulus of the pier and barrier rail concrete was equal to 4,460 ksi (30.8 GPa).

Inputs required to implement the 1978 CEB/FIP Model Code time-dependent specifications into the St. Anthony Falls Bridge model are summarized in Tables 4.8 and 4.9 for the superstructure concrete and pier and barrier rail concrete, respectively.

4.6 CEB/FIP Model Code 1990

Compared to the 1978 CEB/FIP Model Code, the 1990 CEB/FIP Model Code eschews the graphical method in favor of equations. Both methods specify asymptotic creep and shrinkage curves where the rate at which the asymptote is approached is dependent on the volume-to-surface ratio. The 1990 Model Code creep curve is not divided into recoverable and irrecoverable terms, and is instead given as a single total creep curve.

4.6.1 Creep

Concrete creep behavior as presented here is documented in Section 2.1.6 of the 1990 CEB/FIP Model Code.

The total stress-dependent strain is expressed in Eqn. (2.1-62) of the 1990 CEB/FIP Model Code as:

$$\varepsilon_{total} = \sigma(t_0)\, J(t,t_0) = \sigma(t_0)\left[\frac{1}{(E_c)_{t0}} + \frac{\psi(t,t_0)}{(E_c)_{28}}\right] \tag{4-54}$$

where $\sigma(t_0)$ is the stress applied at time t_0, $J(t,t_0)$ is the creep compliance function, $(E_c)_{t0}$ is the modulus at time t_0 and $(E_c)_{28}$ is the modulus at 28 days, and $\psi(t,t_0)$ is the dimensional creep function.

The creep function is computed using Eqns. (2.1-64) through (2.1-70) of the 1990 CEB/FIP Model Code, the combination of which provides:

$$\begin{aligned}\psi(t,t_0) = &\left[1 + \frac{1-H}{0.46\left(0.508V/S\right)^{1/3}}\right]\left[\frac{5.3}{\sqrt{6.895\times10^{-4}\left(f_c\right)_{28}}}\right] \\ &*\left[\frac{1}{0.1+\left(t_0\right)^{0.2}}\right]\left[\frac{\left(t-t_0\right)^{0.3}}{\left(\beta_H + t - t_0\right)^{0.3}}\right]\end{aligned} \tag{4-55}$$

where H is the relative humidity in decimal form, V/S is the volume-to-surface ratio defined in inches, $(f_c)_{28}$ is the mean concrete strength at 28 days in psi, and β_H is a humidity and shape dependent parameter with units of days and defined by

$$\beta_H = 150\left(1+\left(1.2H\right)^{18}\right)\left(0.508V/S\right) + 250 \le 1500 \tag{4-56}$$

The 1990 CEB/FIP Model Code includes adjustments to the time of loading t_0 based on the cement type and temperature:

$$\left(t_0\right)_{adj} = t_{0T}\left(\frac{9}{2+\left(t_{0T}\right)^{1.2}} + 1\right)^{\tau} \ge 0.5 \text{ days} \tag{4-57}$$

where t_{0T} is the time of initial loading dependent on the temperature history prior to loading, and τ is a factor accounting for the cement type. Using the cement classifications in Appendix D of the 1990 CEB/FIP Model Code, $\tau = 1$ for rapid-hardening high-strength cements RS, $\tau = 0$ for normal and rapid-hardening cements N and R, and $\tau = -1$ for slowly hardening cements SL. The temperature adjusted time t_{0T} is taken from Eqn. (2.1-87) of the 1990 CEB/FIP Model Code:

$$t_{0T} = \sum_{i=1}^{n} \Delta t_i e^{\left(13.65 - \frac{4000}{273 + T(\Delta t_i)}\right)} \tag{4-58}$$

where Δt_i is the time increment over which the ambient temperature is averaged, $T(\Delta t_i)$ is the mean ambient temperature in degrees Celsius over time increment Δt_i, and the sum of all Δt_i must equal the total unadjusted time t_0. This equation reflects the change in the hydration and aging rate of the concrete as a function of temperature. Consequently, the adjusted value $(t_0)_{adj}$ only affects the value of t_0 in the third term of Eqn. (4-55); all instances of $t - t_0$ which represent the duration of creep and not the rate of hydration are unaffected by this adjustment.

The majority of long-term stresses in the bridge were imparted during the erection procedure, which occurred from May 25, 2008 until August 5, 2008. During this time, the average air temperature was approximately 72°F (22°C) according to weather station KMNMINNE17 located on the University of Minnesota campus approximately one mile from the St. Anthony Falls Bridge. Applying this temperature to Eqn. (4-58) returns a correction factor of approximately unity. Therefore, the temperature correction for concrete age was neglected for loads applied during the erection procedure. For changes in loading occurring later in the life of the bridge, such as those due to post-tensioning losses, the temperature correction factor was again neglected because the changes in load after erection were assumed to be substantially less than the sustained loads applied during the erection procedure. Thus, the temperature correction to concrete age was effectively ignored for finite element analysis and t_{0T} was always equal to t_0, though the age correction from Eqn. (4-57) for the cement type was still applied.

Provisions for the temperature-dependence of creep and shrinkage other than the hydration rate as described above are provided in Section 2.1.8.7 of the 1990 CEB/FIP Model Code. These provisions only apply to concrete subject to constant temperatures other than 20°C (68°F). The temperature dependence of creep and shrinkage was ignored for the finite element analysis, as the bridge temperature was not constant, and corrections for temperature were expected to take place only within the measured data according to the procedure discussed in Chapter 7.

The adjustment from Eqn. (2.1-73) of the 1990 CEB/FIP Model Code accounting for high-stress conditions above 40% of $(f_c)_{28}$ was ignored, as stresses were expected to always stay within the elastic range.

Provisions for time-dependent strength are from Section 2.1.6.1 of the 1990 CEB/FIP Model Code:

$$f_c(t) = e^{\left[p\left(1-\sqrt{\frac{28}{t_T}}\right)\right]}(f_c)_{28} \tag{4-59}$$

where $f_c(t)$ is the strength at adjusted time t in days after casting, $(f_c)_{28}$ is the mean concrete strength at 28 days, and p is a coefficient dependent on the cement type. Time t_T is the adjusted time according to the temperature correction in Eqn. (4-58), but for the same reasons as listed above, t_T was always assumed to be equal to t. Using the cement classifications in Appendix D of the 1990 CEB/FIP Model Code, $p = 0.20$ for rapid-hardening high-strength cements RS, $p = 0.25$ for normal and rapid-hardening cements N and R, and $p = 0.38$ for slowly hardening cements SL. Provisions from Section 2.1.6.2 of the 1990 CEB/FIP Model Code for the modification of the concrete strength with time due to sustained large compressive forces were ignored, as the long-term stresses in the structure were all assumed to be within the elastic range of the concrete (i.e., less than 45% of $(f_c)_{28}$).

The modulus of elasticity used in the creep compliance function can be computed using the provisions from Eqn. (2.1-16) of the 1990 CEB/FIP Model Code, converted to units of psi, such that

$$\left(E_c\right)_{28} = 593500\left(\left(f_c\right)_{28} / 10\right)^{1/3} \tag{4-60}$$

where $(f_c)_{28}$ is the mean concrete strength at 28 days specified in psi. The time-dependent modulus, as documented in Section 2.1.6.3 of the 1990 CEB/FIP Model Code is equal to

$$E_c\left(t\right) = \left(E_c\right)_{28} \sqrt{e^{\left[p\left(1-\sqrt{\frac{28}{t_T}}\right)\right]}} \tag{4-61}$$

where $E_c(t)$ is the strength at adjusted time t_T in days after casting, $(E_c)_{28}$ is the concrete modulus as defined in Eqn. (4-60), and p is a coefficient dependent on the cement type as specified above. Again, time t_T is the adjusted time according to the temperature correction in Eqn. (4-58), but was always assumed to be equal to t. The relationship in Eqn. (4-61) is not the same as if the time-dependent strength gain in Eqn. (4-59) were simply substituted into Eqn. (4-60). The 1990 CEB/FIP Model Code assumes that the modulus develops more quickly than the compressive strength, as a large component of the total modulus is dependent on the aggregate stiffness which is independent of age (Hilsdorf and Müller, 1999).

4.6.2 Shrinkage

Concrete shrinkage behavior as presented here is documented in Section 2.1.6.4.4 of the 1990 CEB/FIP Model Code.

The shrinkage strain ε_s can be computed as

$$\begin{aligned}\varepsilon_s\left(t,t_c\right) = &\left[160 + 10\beta_{sc}\left(9 - 6.895\times10^{-4}\left(f_c\right)_{28}\right)\right] \\ &*\left(\beta_{RH}\times10^{-6}\right)\sqrt{\frac{t-t_c}{350\left(0.508V/S\right)^2 + t - t_c}}\end{aligned} \tag{4-62}$$

where t_c is the age at end of curing in days, $(f_c)_{28}$ is the mean concrete strength at 28 days specified in psi, V/S is the volume-to-surface ratio specified in inches, β_{sc} is a factor dependent on

cement type, and β_{RH} is a factor dependent on the relative humidity. The cement classifications in Appendix D of the 1990 CEB/FIP Model Code give $\beta_{sc} = 8$ for rapid-hardening high-strength cements RS, $\beta_{sc} = 5$ for normal and rapid-hardening cements N and R, and $\beta_{sc} = 4$ for slowly hardening cements SL. The humidity dependent factor is equal to

$$\beta_{RH} = -1.55\left(1 - H^3\right) \tag{4-63}$$

where H is the relative humidity in decimal form and varies from 0.4 to 0.99. If H is greater than 0.99, then $\beta_{RH} = +0.25$ to model swelling.

4.6.3 Comments on Original Calibration of the 1990 CEB/FIP Time-Dependent Model

The time-dependent provisions of the 1990 CEB/FIP Model Code were developed by the CEB General Task Group 9 to address deficiencies in the 1978 CEB/FIP Model Code provisions (Müller and Hilsdorf, 1990). As opposed to the 1978 Model Code provisions which adopted a summation type model, the General Task Group 9 chose a product model similar to the ACI-209 recommendations, with the rationale primarily based on ease of use for designers.

The 1990 CEB/FIP Model Code provisions were calibrated using 134 creep samples and 103 shrinkage samples which was largely similar to the database used to develop the ACI-209 model. Because the creep model was not separated into basic and drying creep terms, Müller and Hilsdorf (1990) expected that the provisions would overestimate the creep of specimens subject to large amounts of drying, such as thin sections, samples exposed to low ambient relative humidity, or specimens loaded at late ages. For concrete dominated by basic creep, such as specimens with large *V*/*S* or samples subject to high ambient relative humidity, the predictions of the 1990 Model Code were expected to perform marginally better.

One notable deficiency of the 1990 Model Code creep model is the development of negative stresses under relaxation (i.e., constant strain conditions). This implies a strain rate reversal upon total unloading, meaning that for creep recovery the strains will decrease for a

period of time and then, without any change in load, will again begin to increase. Müller and Hilsdorf (1990) state that this is usually only problematic when analyzing creep recovery for concrete loaded at a very young age, or for samples with large *V*/*S* ratio or high relative humidity. This problem is not unique to the 1990 Model Code and can be shown to occur for nearly all creep models except the B3 model, which was designed specifically to avoid this concern.

4.6.4 Derived Material Properties for FEM Input

To determine the type of cement of the superstructure concrete, the mean 7-day strength equal to 5.64 ksi (38.9 MPa) as measured by MnDOT (Section 3.1.1) was compared to the estimated 7-day strength according to Eqn. (4-59). It was found that $p = 0.25$ provided the best estimate of the strength at 7 days, with the estimate within 5% of the measured mean. Therefore, it was assumed that all superstructure concrete consisted of normal and rapid-hardening cements N and R (equivalently Type I cement), such that τ as required for Eqn. (4-57) was equal to 0 and β_{sc} as required by Eqn. (4-62) was equal to 5. The 28-day elastic modulus as calculated from Eqn. (4-60) was equal to 5,380 ksi (37.1 GPa).

The cement type for the pier and rail concrete was assumed to be normal and rapid-hardening cements N and R (Type I), meaning that variables p, τ, and β_{sc} were equal to 0.25, 0 and 5, respectively. Using Eqn. (4-60), the 28-day modulus of the pier and barrier rail concrete was equal to 4,690 ksi (32.3 GPa).

Inputs required to implement the 1990 CEB/FIP Model Code time-dependent specifications into the St. Anthony Falls Bridge finite element model are summarized in Tables 4.8 and 4.9 for the superstructure concrete and pier and barrier rail concrete, respectively.

4.7 GL2000

4.7.1 Creep

The GL2000 time-dependent model was developed by Gardner and Lockman (2001) as a simple design-office procedure requiring relatively few input parameters. Similar to the B3 model

(Bažant and Baweja, 1995a), the GL2000 model was calibrated using the RILEM database of creep and shrinkage measurements.

The compliance function $J(t,t_0)$ for the GL2000 model is given as

$$J\left(t,t_0\right)=\frac{1}{\left(E_c\right)_{t0}}+\frac{\psi}{\left(E_c\right)_{28}} \tag{4-64}$$

where $(E_c)_{t0}$ is the concrete modulus at the time of loading t_0, $(E_c)_{28}$ is the concrete modulus at 28 days, and ψ is the creep function equal to

$$\psi=\Phi\left(t_0,t_c\right)\left[2\left(\frac{\left(t-t_0\right)^{0.3}}{14+\left(t-t_0\right)^{0.3}}\right)+\left(\frac{7}{t_0}\right)^{0.5}\left(\frac{t-t_0}{t-t_0+7}\right)^{0.5}+2.5\left(1-1.086H^2\right)\left(\frac{t-t_0}{t-t_0+97\left(V/S\right)^2}\right)^{0.5}\right] \tag{4-65}$$

where $t-t_0$ is the time in days since loading, H is the relative humidity in decimal form, and V/S is the volume-to-surface ratio in inches. The term $\Phi(t_0,t_c)$ is the correction factor accounting for drying of the concrete prior to loading and is equal to

$$\Phi\left(t_0,t_c\right)=\left[1-\left(\frac{t_0-t_c}{t_0-t_c+97\left(V/S\right)^2}\right)^{0.5}\right]^{0.5} \tag{4-66}$$

If loads are applied prior to the end of moist-curing, meaning that t_0 is less than t_c, then the predrying factor is equal to 1.

The strength and modulus properties used in the GL2000 model are specified by Gardner and Lockman (2001). The mean concrete strength can be converted to the elastic modulus E_c using

$$E_c\left(t\right)=500000+52000\sqrt{f_c\left(t\right)} \tag{4-67}$$

where E_c and f_c are specified in psi. The concrete is assumed to age by application of the following time-dependent mean concrete strength function:

$$f_c(t) = (f_c)_{28} \frac{t^{3/4}}{a + bt^{3/4}} \tag{4-68}$$

where $f_c(t)$ is the mean concrete strength at time t in days after casting, $(f_c)_{28}$ is the 28-day mean concrete strength, and a and b are parameters dependent on the cement type. For Type I cement, a = 2.8 and b = 0.77, for Type II cement, a = 3.4 and b = 0.72, and for Type III cement, a = 1.0 and b = 0.92. Therefore by combining Eqns. (4-67) and (4-68), the time-dependent elastic modulus is equal to

$$E_c(t) = 500000 + 52000\sqrt{(f_c)_{28} \frac{t^{3/4}}{a + bt^{3/4}}} \tag{4-69}$$

In calibrating the GL2000 model with the RILEM database, if both concrete strength and modulus were provided, Gardner and Lockman used the average of the measured 28-day mean strength and the 28-day mean strength back-calculated from the measured 28-day modulus using the strength-modulus relation from Eqn. (4-67). The effective modulus for calibration was then determined from Eqn. (4-67) using this averaged strength. Therefore, to remain consistent with the derivation of the GL2000 model, material properties should be defined in the following way:

- If only the 28-day mean strength is given, compute the 28-day modulus using Eqn. (4-67).
- If only the 28-day modulus is given, back calculate the 28-day mean strength using Eqn. (4-67).
- If both the 28-day mean strength $(f_c)_{28}$ and 28-day modulus $(E_c)_{28}$ are given, first back calculate the 28-day mean strength $f_{c\text{-}bc}$ using the given 28-day modulus $(E_c)_{28}$ and Eqn. (4-67). Then average the measured 28-day mean strength $(f_c)_{28}$ and the back-calculated 28-day mean strength $f_{c\text{-}bc}$ to get the effective 28-day strength $(f_{ce})_{28}$. Use Eqn. (4-67) again to convert the effective 28-day strength $(f_{ce})_{28}$ into the effective 28-day modulus

$(E_{ce})_{28}$. For input into the GL2000 model, use the effective material properties $(f_{ce})_{28}$ and $(E_{ce})_{28}$.

4.7.2 Shrinkage

The GL2000 model computes shrinkage strain ε_{sh} as follows:

$$\varepsilon_{sh} = \varepsilon_{shu}\left(1-1.18H^4\right)\left(\frac{t-t_c}{t-t_c+97\left(V/S\right)^2}\right) \tag{4-70}$$

where H is the relative humidity in decimal form, V/S is the volume-to-surface ratio in inches, t_c is the time in days when shrinkage begins at the end of moist or steam curing, and ε_{shu} is the ultimate shrinkage strain given by

$$\varepsilon_{shu} = -0.001K\left(\frac{4350}{\left(f_c\right)_{28}}\right)^{0.5} \tag{4-71}$$

where $(f_c)_{28}$ is the 28-day mean concrete strength in psi, and K is a parameter dependent on the cement type equal to 1.0, 0.7 and 1.15 for Type I, Type II and Type III cement, respectively.

4.7.3 Comments on Original Calibration of the GL2000 Time-Dependent Model

The GL2000 model was originally calibrated using 167 creep and 108 shrinkage tests listed in the RILEM database (Lockman, 2000). Tests in the RILEM database with durations less than 500 days, and those with parameters outside of the intended applicability of the GL2000 model were excluded. By considering only long-duration tests, the bias towards early-age creep and shrinkage that would normally impact studies using the entire RILEM database was minimized.

The forms of the GL2000 creep and shrinkage equations were influenced by a previous model developed by Gardner and Zhao (1993), which was in turn a modification of the 1990 CEB/FIP Model Code. The form of the GL2000 was intended to correct the problems of negative relaxation, unrealistic creep recovery, and unbounded shrinkage present in the Gardner and Zhao (1993) model (Lockman, 2000). Humidity dependence of the GL2000 creep and shrinkage curves

was derived assuming hygral equilibrium (i.e., no shrinking or swelling) at 96% relative humidity (Gardner, 2000), and was verified with respect to data from Keeton (1965), and Troxell et al. (1958). Much like for the calibration of the B3 model presented in Section 4.4.3, the dependence on volume-to-surface ratio was again derived from a pool of samples which contained only a few with large *V*/*S* ratios, most of which were from a single study (Hansen and Mattock, 1966).

4.7.4 Derived Material Properties for FEM Input

Because only the concrete compressive strength was available from the provided MnDOT data, no averaging between the measured and back-calculated strength as discussed in Section 4.7.1 was conducted. Rather, the mean superstructure concrete strength $(f_c)_{28}$ used in the GL2000 time-dependent behavior was taken equal to 7.45 ksi (51.4 MPa) as computed from material tests conducted by MnDOT (Section 3.1.1). To determine the type of cement, the mean 7-day strength equal to 5.64 ksi (38.9 MPa) as measured by MnDOT was compared to the estimated 7-day strength according to Eqn. (4-68). It was found that Type I cement with parameters $a = 2.8$ and $b = 0.77$ provided the best estimate of the strength at 7 days, with the estimate within 7% of the measured mean. Therefore, it was assumed that all superstructure concrete was Type I cement, and thus K as required for Eqn. (4-71) was equal to 1. The 28-day elastic modulus as calculated using Eqn. (4-67) was equal to 4,980 ksi (34.3 GPa).

The 28-day mean strength was not known for the pier and barrier rail concrete, and the 28-day strength was assumed to be 4.94 ksi (34.1 MPa) as discussed in Section 4.2. Cement type for the pier and rail concrete was assumed to be Type I, and the 28-day modulus was equal to 4,150 ksi (28.6 GPa) according to Eqn. (4-67).

Inputs required to implement the GL2000 time-dependent specifications into the St. Anthony Falls Bridge finite element model are summarized in Tables 4.8 and 4.9 for the superstructure concrete and pier and barrier rail concrete, respectively.

4.8 AASHTO LRFD Bridge Design Specifications

In contrast with the other creep and shrinkage models presented in this chapter, the AASHTO LRFD Bridge Design Specifications (2010) do not present a complete time-dependent model, but instead just include guidelines. Critically, no mention of a concrete aging law is included in the AASHTO LRFD specifications, though the concrete strength at various times, including at the beginning of loading and at 28 days, is required in the provisions. Though the AASHTO LRFD provisions are denoted as a "time-dependent model" throughout this investigation, the reader should recognize that said provisions were not intended to be used as a standalone prediction of creep and shrinkage.

The AASHTO LRFD (2010) method was based on a report by Tadros et al. (2003) regarding the estimation of prestress losses in pretensioned high-strength concrete girders. The study excluded post-tensioning applications, and was primarily focused on estimating the total long-term losses as opposed to accurately capturing early age creep and shrinkage behavior. Because of the exclusive focus on pretensioning, the methodology proposed by Tadros et al. (2003) ignored the development of concrete strength with time, and instead utilized only the strength at transfer and the service strength. For non-prestressed members or for prestressed members for which no strength at transfer was available, it was recommended that 80% of the service strength be used regardless of the age at transfer.

For typical prestressing applications, the designer will be given or will need to assume strength values at transfer (first loading) and at service, thus fulfilling the needs of the equations provided in the AASHTO specifications. However, for post-tensioned segmental construction, each segment of concrete has multiple times for application of post-tensioning as opposed to a single time of transfer. Furthermore, the implementation of the finite element procedure as discussed in Chapter 6 required some form of aging law to be specified. Assuming 80% of the service strength for the strength at transfer as recommended by Tadros et al. (2003) was not

appropriate for this type of analysis. Therefore, the ACI-209 aging law presented in Section 4.3.1 was adopted for the AASHTO LRFD provisions. Assuming an aging law, and by extension altering the computation of the elastic modulus, violates the principle discussed in Section 4.1.1 that the elastic modulus must be chosen in accordance with what was used to derive the time-dependent model. However, this violation was deemed acceptable in this case because without this assumption, the AASHTO LRFD provisions could not have been explored in the same manner as was done for all other time-dependent models.

4.8.1 Creep

Creep strain predictions are provided in Section 5.4.2.3.2 in the AASHTO LRFD Bridge Design Specifications 5th Edition (2010). AASHTO uses the following parameters for calculating creep:

H = relative humidity in decimal form

k_s = factor for the effect of the volume-to-surface ratio

k_{hc} = humidity factor for creep

k_f = factor for the effect of concrete strength

k_{td} = time development factor

t = maturity of the concrete in days since casting

t_0 = age (in days) of the concrete when loaded

V/S = volume-to-surface ratio in inches

$(f_c)_{t0}$ = strength of the concrete at the time of loading, specified in ksi

Parameters can be determined from AASHTO Eqns. (5.4.2.3.2-2) through (5.4.2.3.2-5):

$$k_s = 1.45 - 0.13(V/S) \geq 1.0 \tag{4-72}$$

$$k_{hc} = 1.56 - 0.8H \tag{4-73}$$

$$k_f = \frac{5}{1 + (f_c)_{t0}} \tag{4-74}$$

$$k_{td} = \frac{(t - t_0)}{61 - 4(f_c)_{t0} + (t - t_0)} \tag{4-75}$$

The creep coefficient, defined as the ratio between the time-dependent creep strain and the elastic deformation due to an imposed stress σ at time t_0, can be calculated using AASHTO Eqn. (5.4.2.3.2-1):

$$\phi(t, t_0) = 1.9 k_s k_{hc} k_f k_{td} t_0^{-0.118} \tag{4-76}$$

The AASHTO-predicted creep strain is then computed as

$$\varepsilon_{cr} = \frac{\sigma}{(E_c)_{t0}} \phi(t, t_0) \tag{4-77}$$

where $(E_c)_{t0}$ is the concrete elastic modulus at time t_0. Therefore, the creep compliance function, defined as the total creep plus elastic strain with time due to an imposed unit stress, is equal to

$$J(t, t_0) = \frac{\varepsilon_{el} + \varepsilon_{cr}}{\sigma} = \frac{1 + \phi(t, t_0)}{(E_c)_{t0}} \tag{4-78}$$

The AASHTO LRFD specifications do not include provisions for the increase in concrete strength and modulus with time. Therefore, provisions for time-dependent strength were adopted from Eqn. (2-1) of the ACI 209R-92 (1992):

$$(f_c)_t = \frac{t}{a + \beta t} (f_c)_{28} \tag{4-79}$$

where $(f_c)_t$ is the strength at time t after casting, $(f_c)_{28}$ is the concrete strength 28 days after casting, and a and β, documented in Table 4.6, are constants dependent on the cement type and curing conditions of the concrete. As explained earlier, use of this concrete aging model and the resultant change in the derived concrete modulus was necessary but technically invalid because time-dependent models should use the elastic modulus applied to derive that model.

The modulus of elasticity used in the creep compliance function can be computed using the provisions from Eqn. (5.4.2.4-1) of the AASHTO LRFD (2010) specifications, such that

$$E_c = 33000 K_1 w_c^{1.5} \sqrt{f_c} \tag{4-80}$$

where K_1 is equal to 1.0 unless otherwise determined by physical test, and w_c is the unit weight of the concrete in kips/ft^3, and E_c and f_c are specified in ksi. Assuming K_1 is equal to 1.0 and a unit weight equal to 0.143 kips/ft^3 as measured from samples of the superstructure concrete and recorded in Section 3.5, then substituting Eqn. (4-79) into Eqn. (4-80) and converting to units of psi, the time dependent modulus $(E_c)_t$ is equal to

$$(E_c)_t = 56400 \sqrt{\frac{t}{a + \beta t} (f_c)_{28}} \tag{4-81}$$

where $(E_c)_t$ and $(f_c')_{28}$ have units of psi, t is days since casting, and values for a and β are documented in Table 4.6.

4.8.2 Shrinkage

Estimated shrinkage strains in concrete are provided in Section 5.4.2.3.3 of the AASHTO LRFD Bridge Design Specifications 5th Edition (2010). AASHTO uses the following parameters for calculating shrinkage:

H = relative humidity in percentage (%)

k_s = factor for the effect of the volume-to-surface ratio

k_f = factor for the effect of concrete strength

k_{hs} = humidity factor for shrinkage

k_{td} = time development factor

t = maturity of the concrete in days since casting

t_c = age of concrete at end of curing, assumed to always be equal to 1 day

V/S = volume-to-surface ratio in inches

Coefficients k_f and k_{td} are identical to those defined for the creep model, and require knowledge of the initial concrete compressive strength $(f_c)_{t0}$ in ksi. The use of the initial concrete compressive strength at transfer was due to the particular derivation by Tadros et al. (2003)

whereby only pretensioning applications were considered. Under this specific set of circumstances, the curing time was assumed to be identical to the time to transfer. However, in the case of post-tensioned structures for which the curing time and time to transfer are generally not identical, this value should be assumed to be equal to the concrete strength at end of curing, $(f_c)_{tc}$. The AASHTO LRFD (2010) Eqns. (5.4.2.3.2-2), (5.4.2.3.2-4), (5.4.3.2-5) and (5.4.3.3-2) define the aforementioned parameters:

$$k_s = 1.45 - 0.13(V/S) \geq 1.0 \tag{4-82}$$

$$k_f = \frac{5}{1 + (f_c)_{tc}} \tag{4-83}$$

$$k_{hs} = 2.0 - 1.4H \tag{4-84}$$

$$k_{td} = \frac{(t - t_c)}{61 - 4(f_c)_{tc} + (t - t_c)} \tag{4-85}$$

The code-predicted shrinkage strain is calculated by AASHTO Eqn. (5.4.2.3.3-1):

$$\varepsilon_{sh} = -k_s k_{hs} k_f k_{td} \cdot 0.48 \times 10^{-3} \tag{4-86}$$

The AASHTO LRFD (2010) equations do not provide any means for concrete swelling if the relative humidity is at 100%. Therefore, the strain predicted by Eqn. (4-86) will always be negative (shrinking).

If the concrete is allowed to dry before five days of curing, shrinkage estimates from Eqn. (4-86) should be increased by 20%.

The ACI 209R-92 (1992) concrete aging provisions as discussed in Section 4.3.1 were used for computation of the strength at the end of curing, $(f_c)_{tc}$.

4.8.3 Comments on Original Calibration of AASHTO Time-Dependent Provisions

Original calibration of the AASHTO LRFD (2010) time-dependent provisions was performed by Tadros et al. (2003). The proposed time-dependent behavior was a modification of provisions from the AASHTO LRFD Bridge Design Specifications (1998) and ACI-209 (1992).

Calibration of the creep curve used a total of 48 specimens. All specimens were prisms with square cross sections of 4 in. by 4 in. (100 mm by 100 mm) and length of 24 in. (610 mm), such that *V/S* was equal to 1.0 in. (25 mm). Samples were collected from four different states (Nebraska, New Hampshire, Texas, and Washington) with three different mix designs per state. Four samples were collected from each mix, with three of the samples being loaded at an age of 1 day and the fourth sample loaded at 56 days. The different mixes contained a variety of cementitious materials, water reducers, air content, and aggregate content, and are covered in detail in Tables 3 through 6 in Tadros et al. (2003). The total creep testing duration was typically around 1 year.

Calibration of the shrinkage curve used a total of 48 specimens identical in shape to the creep samples described above. The same four states provided the samples, but with four different mix designs per state (the same three mixes as noted above plus one mix typical of cast-in-place decks). Three samples were cast of each mix. The total testing duration for shrinkage was the same as for the corresponding creep samples.

A number of variables were not varied over the design space of the collected creep and shrinkage samples, including volume-to-surface ratio and ambient humidity. The proposed correction factors to account for these variables were instead derived as simplifications of the ACI-209 (1992) and AASHTO LRFD (1998) recommendations. Furthermore, the proposed loading age correction factor for creep, shown in Eqn. (4-76), was identical to the factor previously used in the AASHTO LRFD (1992) provisions.

To validate the creep and shrinkage predictions, the resulting long-term prestressing losses from seven instrumented girders were estimated by Tadros et al. (2003) using the proposed creep and shrinkage methodologies. All girders had volume-to-surface ratios around 3.0 in. (76 mm) and nominal service concrete strengths ranging from 8,000 to 10,000 psi (55 to 69 MPa). Losses were estimated by measuring the strain in the concrete directly adjacent to the post-

tensioning strands using embedded vibrating wire strain gages and, approximately 1 to 2 years after casting, were found to correspond closely to the estimations using the proposed creep and shrinkage provisions.

The AASHTO LRFD (2010) provisions have a number of features which make application of this time-dependent model problematic, particularly for post-tensioning applications and structures with large *V*/*S*. First, the volume-to-surface ratios used in the calibration were limited in scope, and the model was primarily intended for smaller members with *V*/*S* less than 5.0 in. (127 mm). Many sections in the St. Anthony Falls Bridge have *V*/*S* ratios around 8.0 in. (203 mm), and near the piers this ratio is even larger. Furthermore, according to the AASHTO provisions, the *V*/*S* ratio only has a multiplicative effect on the total creep and shrinkage strains, and has no impact on the rate at which the asymptotic strain values are approached. For drying creep and shrinkage, which are both assumed to be driven by diffusion of water in the concrete, the volume-to-surface ratio should theoretically impact how quickly the asymptote is approached.

The AASHTO LRFD (2010) provisions were not developed with the accurate prediction of short-term creep and shrinkage strains in mind, and thus application of this model towards segmental construction is undesirable. By extension, using this model to extrapolate out early age strains to predict long-term total time-dependent strains is not reliable and should not be performed. Finally, because the test data used to calibrate the curve was exclusively from short-term data with duration less than 1,000 days, the asymptotic shrinkage and creep strains (if even reached) are likely underestimated.

4.8.4 Derived Material Properties for FEM Input

As discussed in Section 4.2, the average 28-day compressive strength among all MnDOT-tested superstructure concrete samples was equal to 7.45 ksi (51.4 MPa), and this number was adopted for the value of $(f_c)_{28}$. To determine the cement type, the 7-day concrete

strength estimated using the a and β parameters from Table 4.6 was compared to the MnDOT-measured 7-day strength equal to 5.64 ksi (38.9 MPa). The best fit was provided by assuming Type III moist-cured concrete (a = 2.3 and β = 0.92) for which the estimated 7-day strength was 5.96 ksi (41.1 MPa) according to Eqn. (4-79). The relative error between the estimated strength and measured strength at 7-days was 5.7%. The 28-day modulus of elasticity was computed using Eqn. (4-81) assuming Type III moist-cured concrete and was equal to 4,860 ksi (33.5 GPa).

Strength data was not available for the pier and barrier rail concrete, so Type I moist-cured concrete (parameters a = 4.0 and β = 0.85 from Table 4.5) was assumed. The 28-day modulus of the pier and barrier rail concrete was equal to 3,980 ksi (27.4 GPa) according to Eqn. (4-81).

Because the precast segments were wet-cured for only 4 days as assumed in Section 4.2, the shrinkage strains for all precast concrete elements were increased by 20% as discussed in Section 4.8.2.

Inputs required to implement the AASHTO LRFD time-dependent specifications into the St. Anthony Falls Bridge finite element model are summarized in Tables 4.8 and 4.9 for the superstructure concrete and pier and barrier rail concrete, respectively.

4.9 Summary

The primary mechanisms of time-dependent behavior of concrete can be classified as creep and shrinkage. Creep is the continued deformation of the concrete under constant load, and is typically divided into basic creep (deformation in the absence of moisture movement) and drying creep (additional stress related deformations when moisture movement is allowed). Shrinkage is the volumetric strain change of concrete with time. Shrinkage is independent of the applied stress and is divided into autogenous shrinkage (volume reduction due to the chemical processes of the hydration reaction) and drying shrinkage (volume change due to movement of water into or out of the concrete).

There exist a wide variety of models and prediction methods for estimating the time-dependent behavior of concrete. Creep models largely fall into two categories: logarithmic and asymptotic. Logarithmic models, including the B3 model (Bažant and Baweja, 1995a) and, for practical durations of structural life, the GL2000 model (Gardner and Lockman, 2001), predict that the long-term creep strains approach a line in log-time space, meaning that no maximum creep strain exists. Asymptotic models, including ACI-209 (1992), 1978 and 1990 CEB/FIP Model Codes, and AASHTO LRFD (2010), all approach an ultimate creep within the expected lifetime of the structure. All shrinkage models are asymptotic, as both autogenous and drying shrinkage must stop when no more water is available.

The provisions from the time-dependent models considered in this investigation are compared and contrasted below. The predictions from each of these models are compared to measured laboratory data in Chapter 5.

4.9.1 Discussion of Basic and Drying Creep

Many time-dependent models lump basic and drying creep together in a single, total creep formulation. For example, the ACI-209, AASHTO LRFD, and 1990 CEB/FIP Model Code provisions all present a multiplicative form for the creep predictions, meaning that the total creep is defined by a single time function modified by a set of multiplicative coefficients.

The 1978 CEB/FIP Model Code creep formulation includes a summation of multiple time functions, though the creep strains are not specifically divided into basic and drying components. According to Rüsch, Jungwirth, and Hilsdorf (1983), the reversible delayed elastic strains incorporate a portion of the basic creep, while the irreversible flow strains include all the drying creep plus another portion of the basic creep. The remainder of the basic creep is assumed to occur very rapidly, and is captured by the partially irreversible rapid deformations.

The GL2000 and B3 creep formulations directly separate the total creep into basic and drying creep. For the GL2000, the first two time functions in Eqn. (4-65) describe the basic creep

while the final term, being the only one modified by humidity and the volume-to-surface ratio, represents the drying creep (Lockman, 2000). Similarly, the q_2, q_3, and q_4 terms in the B3 model all describe basic creep, whereas the q_5 term is the drying creep. The logarithmic nature of the B3 model is due entirely to the basic creep terms.

Though separating the total creep into basic and drying components is more accurate in describing the physics of concrete viscoelasticity, it does not guarantee that the predictions of total creep will necessarily be more accurate for a given concrete structure. For purposes of generalizing the models, however, dividing the total creep into the distinct mechanisms can inform researchers how different parameters (particularly humidity and *V*/*S* ratio) affect creep deformations.

4.9.2 Discussion of Shrinkage

The investigated shrinkage models exhibit a degree of uniformity not observed among the investigated creep models. As expected, all shrinkage models are asymptotic, implying that once the diffusion process is complete no more shrinkage can occur. Furthermore, none of the shrinkage models represent the summation of autogenous and drying shrinkage terms, and rather present only the total expected shrinkage strains. Because autogenous shrinkage strains are typically small compared to drying shrinkage, this approximation is commonly accepted.

All examined shrinkage models respond to ambient relative humidity similarly, with the exception of the AASHTO LRFD provisions. The ultimate shrinkage for both the 1990 CEB/FIP Model Code and B3 models are dependent on the third power of relative humidity. The ACI-209 and 1978 CEB/FIP Model Code rely on linear approximations of the cubic function. The GL2000 ultimate shrinkage is dependent on the fourth power of humidity, but in practice the relation is similar to the third power curve from the previous models. The AASHTO LRFD provisions, on the other hand, use a linear function that does not appear to correlate with the other five models. All models allow for swelling of the concrete at 100% relative humidity, except for the ACI-209

and AASHTO LRFD provisions. The ACI-209 model allows no shrinkage or swelling at 100% relative humidity. The AASHTO LRFD provisions allow significant shrinkage at 100% relative humidity, predicting only a 40% reduction from strains computed at 70% relative humidity.

The ultimate shrinkage predictions from the 1978 CEB/FIP Model Code are completely independent of concrete composition. The ACI-209 shrinkage provisions are only dependent on secondary factors, such as cement content, fine to coarse aggregate ratio, slump, and air entrainment, but are independent of concrete strength. For all other considered models, higher strength concrete is predicted to exhibit less total shrinkage.

4.9.3 Discussion of Volume-to-Surface Ratio and Predrying

The volume-to-surface ratio impacts each of the considered time-dependent models in different ways. The ACI-209 and AASHTO LRFD models are unique in that, per standard recommendations, the *V*/*S* ratio of the concrete specimen only influences the ultimate creep and shrinkage strains as opposed to the rate of these strains with time. This is at odds with the nature of diffusion of water through concrete, whereby drying creep and shrinkage should progress more slowly towards similar ultimate values for larger *V*/*S* as compared to smaller values.

For the 1978 CEB/FIP Model Code, the ultimate strains and the strain rates for both creep and shrinkage are reduced by increases in the specimen *V*/*S* ratio. The 1990 CEB/FIP Model Code incorporates reduced ultimate creep and creep rate due to increases in *V*/*S*, but for shrinkage only the strain rate (and not the ultimate shrinkage) is affected.

Due to the presence of the predrying factor, the behavior of the GL2000 model with respect to changes in volume-to-surface ratio is counterintuitive. The predrying factor is a multiplicative coefficient to the creep formulation which reduces the long-term creep if the concrete is dried before loading. Because a reduced *V*/*S* indicates faster drying, specimens with smaller *V*/*S* will have a lower predrying factor than those with larger *V*/*S*. Unrelated to predrying, increases in *V*/*S* will reduce the rate of both creep and shrinkage strains as expected from

diffusion. The combination of the predrying and diffusion effects is that, for increasing *V*/*S*, the predicted creep rate will decrease while the total long-term creep will increase. Because the GL2000 emulates a logarithmic creep model, these two effects are difficult to separate. However it is possible that, using the GL2000 provisions with all other parameters being equal, a sample with large *V*/*S* may experience more creep after 150 years than one with smaller *V*/*S*. The shrinkage rate for the GL2000 model is reduced by increasing *V*/*S*, but the ultimate shrinkage is unaffected.

Because the B3 model considers a summative formulation for basic and drying creep, it can incorporate the effects of volume-to-surface ratio in a more consistent manner. Because basic creep does not involve the movement of water, it is assumed that basic creep is independent of *V*/*S*. The B3 model defines a shape factor that impacts the shrinkage and drying creep rates. Although this model does not include any multiplicative factors for adjusting the ultimate drying creep or shrinkage based on *V*/*S*, the form of the drying creep expression guarantees that concrete dried prior to loading will not experience drying creep. Thus, predrying is incorporated into the B3 model, but only as an adjustment to the ultimate drying creep instead of the total creep as proposed in the GL2000 model. Similar to the GL2000 and 1990 CEB/FIP Model Code models, the shrinkage rate for the B3 model is reduced by increasing volume-to-surface ratio while the ultimate shrinkage is unaffected.

Aside from the GL2000 and B3 models as described above, none of the other investigated creep provisions included corrections for predrying.

While each model varies in the particulars of the data selected for model calibration, all models have similar sample sets for the estimation of the effects of *V*/*S* on creep and shrinkage. The impacts of the *V*/*S* ratio on time-dependent behavior were examined in only one study (Hansen and Mattock, 1966), and all considered time-dependent models rely on this data exclusively for calibration with respect to volume-to-surface ratio. Furthermore, that study was

limited to specimens with a *V*/*S* ratio no larger than 6.0 in. (152 mm), whereas the majority of the St. Anthony Falls Bridge has *V*/*S* ratios of 8.0 in. (203 mm) and up. Therefore, all models must rely on extrapolation to allow for prediction of the behavior of structures with large *V*/*S* .

4.9.4 Applicability and Usability of Models

The different models differ in their applicability towards particular design problems. The AASHTO LRFD provisions are not intended to estimate short-term creep or shrinkage. This makes application towards segmental construction problematic. Furthermore, the AASHTO LRFD does not contain a concrete aging model which is necessary for the complete definition of time-dependent strains. For this investigation, the ACI-209 strength gain law was adopted for use in the AASHTO recommendations.

All other considered models are assumed to be generally applicable to post-tensioned construction, but the diverging complexity of the models means that some are more convenient than others. For example, the B3 model is complex and not ideal for design office use due to the inclusion of many parameters that are likely unknown by the designer, whereas the GL2000 model was developed with designers in mind by including only a small quantity of commonly known variables. Though the B3 model depends on many material parameters, these parameters are often correlated to concrete strength (i.e., aggregate to cement ratio, water to cement ratio, etc.), and as such it is unclear how much benefit is gained by such a complex formulation. The 1978 CEB/FIP Model Code provides a graphical method which, while convenient for simple hand calculations, is not ideal for computer simulation.

Chapter 5: Validation of Time-Dependent Properties

The time-dependent concrete properties presented in Chapter 4 were validated with respect to measured data. The aging compressive strength, aging elastic modulus, and creep and shrinkage strains for each model were compared to experiments performed by the University of Minnesota and Cemstone, independent of the measured concrete strengths provided by MnDOT which were used to determine the time-dependent properties. Some of the MnDOT data are also included in the figures for comparison.

5.1 Aging Compressive Strength

As described in Section 4.2, the superstructure cement type for each of the considered time-dependent models was chosen using the measured 7- and 28-day compressive strengths provided by MnDOT (Section 3.1.1). To validate the varied choices for the cement type, the compressive strength aging curves from each of the time-dependent models were compared to measured strength values from the UMN and Cemstone, as documented in Sections 3.1.2 and 3.1.3. Data from these sources were not used in the selection of the FEM material parameters, and consequently served as an independent check on the chosen properties. Figure 5.1 shows the comparison. The MnDOT data are also included in the plot, including data measured at 56 days; only the MnDOT data at 7 and 28 days were used in the selection of the FEM material parameters. Curves for AASHTO LRFD and the B3 model are not explicitly included in the figure. Per the discussion in Section 4.8, the ACI-209 strength curve was adopted for use in the AASHTO LRFD time-dependent recommendations. Due to its specific form, the B3 model does not include strength gain with time except in the correction factor for the ultimate shrinkage in Eqn. (4-42), which uses the same expression as from ACI-209 except without adjustment for unit weight.

The results show the strength gain prior to 28 days was predicted well by all the chosen strength gain curves. After 28 days, the UMN measured samples unexpectedly exhibited a decrease in strength up until 130 days. However, at 2,116 days (5.8 years) the UMN measured samples increased in strength, and were best predicted, on average, by the ACI-209 aging strength curve. The 1978 and 1990 CEB/FIP Model Code and GL2000 aging curves overestimated the UMN measured strength at 2,116 days.

Compared to the Cemstone samples, the ACI-209 strength gain curve tended to underestimate the strength at 100 days. The 1978 and 1990 CEB/FIP Model Code and GL2000 aging provisions all provided good fits for the post 28-day strengths as measured by Cemstone. The MnDOT measured concrete strengths at 56 days were best matched by the ACI-209 aging curve.

The ACI-209 aging curve approached a lower asymptotic value than all the other chosen curves. The difference between the ACI-209 aging curve and the other investigated aging laws was primarily because a Type III cement was found to best fit the MnDOT measured 7- and 28-day strength values for the ACI-209 aging curve. On the other hand, Type I cement was chosen for the 1990 CEB/FIP Model Code and GL2000 time-dependent models, while for the 1978 CEB/FIP Model Code an aging coefficient between rapid-hardening and high-strength cement was used. If Type I cement was instead used for the ACI-209 model, the resulting aging strength curve would be similar to those from the CEB/FIP Model Codes and GL2000.

In comparison to all the available data, the ACI-209 aging curve appeared to provide the best estimate of concrete strength throughout the entire investigated timeframe. Among the investigated time-dependent models, only the AASHTO LRFD and 1978 CEB/FIP Model Code provisions directly incorporate the aging strength curve into predictions of creep and shrinkage. The ACI-209, 1990 CEB/FIP Model Code, and GL2000 models all use the aging elastic modulus, presented in the next section, but do not require the concrete strength at any age other than 28

days. The B3 model does not directly incorporate any form of aging strength or modulus curve in the predictions, except in a single correction factor for shrinkage. All models indirectly use the concrete aging curve in correction factors related to the cement type. Although the aging strength curves for the 1978 and 1990 CEB/FIP Model Codes and GL2000 models overestimated the measured strengths at late ages, this was not expected to significantly impact predictions of time-dependent behavior.

5.2 Aging Elastic Modulus

The aging elastic moduli for each considered time-dependent model were computed using the strength-to-modulus relations listed in the appropriate sections in Chapter 4. The specified elastic moduli were compared to measured modulus values from the UMN and Cemstone, as documented in Sections 3.1.2 and 3.1.3.

The superstructure elastic moduli with time from each of the considered time-dependent models are compared to measured results in Figure 5.2. The AASHTO LRFD modulus was assumed to be identical to the plotted ACI-209 curve. The B3 model does not use the typical definition of elastic modulus, and is therefore not included in the plot.

The scatter of the measured modulus values was higher at all ages than the scatter observed in the measured strength data. Furthermore, the scatter among the different modeled modulus curves was larger than the scatter among the modeled strength aging curves. The modulus from the 1990 CEB/FIP Model Code slightly overestimated the measured moduli, while the ACI-209 curve slightly underestimated the moduli at late ages. The 1978 CEB/FIP Model Code and GL2000 aging modulus curves provided the best estimates over the entire investigated timeframe.

In all the time-dependent models except for B3, the aging elastic modulus was used to compute the instantaneous elastic deformation given a change in loading. The creep provisions for the 1978 and 1990 CEB/FIP Model Codes and the GL2000 depend only on the 28-day elastic

modulus, and thus the aging modulus curve has no impact on the time-dependent deformations. However, the ACI-209 and AASHTO creep provisions are defined as a magnification of the instantaneous deformation, and hence are dependent on the concrete elastic modulus at the age of loading. This means that the aging elastic modulus curve directly impacts both the elastic and creep strains in the ACI-209 and AASHTO creep provisions, while for all other models only the instantaneous elastic strains are affected by the aging elastic modulus. The ACI-209 modulus (adopted for both ACI-209 and AASHTO provisions) tended to be lower than indicated by the other models, and therefore the ACI-209 and AASHTO creep provisions would approach a higher asymptotic ultimate strain than had another aging modulus curve been chosen. With the exception of the B3 model (see Eqn. (4-42)), shrinkage provisions are not dependent on the aging modulus.

5.3 Shrinkage

Shrinkage measurements were taken for up to 1,365 days (3.75 years) after casting by the University of Minnesota as discussed in Section 3.3. The shrinkage models presented in Sections 4.3 through 4.8 are plotted in Figure 5.3 relative to the overall average shrinkage strains measured for both the southbound and northbound bridge samples. The shrinkage models were calculated assuming superstructure material parameters as described in Section 4.2 and the respective sections (i.e., Sections 4.3 through 4.8) for each individual shrinkage model, except that the curing duration was set to 4.0 days (equal to the average between the southbound and northbound specimens), the volume-to-surface ratio was 1.0 in. (25 mm), the reinforcement ratio was equal to zero, and the humidity was equal to 37.5% (equal to the average relative humidity in the environmental chamber for all shrinkage readings). Two samples (cylinders S4SB4 and S4NB2) were removed from their respective averages due to the anomalous readings as noted in French et al. (2012).

The experimental results for the samples from the southbound and northbound bridge were comparable, which was expected as they were both taken from the deck concrete poured on

consecutive days. The similarity between the northbound and southbound bridge shrinkage samples was in spite of the fact that the northbound samples had been left uncovered at the bridge for a day after casting before being transported to the laboratory.

At early ages (less than approximately 100 days old), the measured results were larger than the predicted strains from the AASHTO, 1990 CEB/FIP Model Code, and the B3 model, but the other models appeared to capture the early age behavior. For long-term shrinkage strain estimates, the GL2000 model slightly overestimated the measured strains, while the ACI-209 model greatly overestimated the shrinkage. The 1990 CEB/FIP Model Code and the B3 models both slightly underestimated the long-term shrinkage strains. All shrinkage strain estimates were within ±20% of the measured averages except for the 1990 CEB/FIP Model Code and the ACI-209 model, which were 22% less and 50% greater, respectively, than the measured average shrinkage strain at 1,365 days after casting. The AASHTO and 1978 CEB/FIP Model Code long-term estimates were the best of all examined models, with both estimates within 5% of the measured average strain at 1,365 days after casting. The 1978 CEB/FIP Model Code shrinkage model provided the best approximation (i.e., lowest unweighted sum of squared residuals) of the measured shrinkage curve over the entire duration of testing.

5.4 Creep

Creep measurements of the superstructure concrete were performed by the University of Minnesota as discussed in Section 3.3. To obtain the experimental creep strain, the average southbound bridge experimental shrinkage strains, excluding sample S4SB4 which was determined to be anomalous as discussed in French et al. (2012), were subtracted from the total strain measured in the creep specimens. The average southbound bridge shrinkage strains were used because they came from the same batch of concrete as the creep specimens.

As the samples remained in the creep frames, the applied load was reduced by the continued deformation of the cylinders. This reduced load caused a reduction in the elastic strain

of the cylinders by an amount equal to the difference between the initial and current stress divided by the modulus of elasticity of the concrete. Furthermore, the reduction in load allowed some of the creep to recover according to the Boltzmann superposition principle. To correct for the reduced elastic strain, all creep readings were corrected by adding back the "lost" elastic deformation assuming a nominal concrete modulus equal to the 28-day modulus predicted by the ACI-209 (1992) strength-to-modulus relation from Eqn. (4-14) and a 28-day concrete strength equal to 7.45 ksi (51.4 MPa). The effects of concrete aging were not factored into this correction procedure, though including aging would not have noticeably altered the measured results as the magnitudes of the reduced loads were typically small. This correction had the effect of smoothing the presented creep curves at the times of reloading. No corrections were performed to account for the creep recovery that occurred due to the temporarily reduced load, though this reduction in the total creep strain was expected to be minor.

Figures 5.4 through 5.7 show the experimental creep strains obtained for each of the four creep frames compared to predictions using the creep models discussed in Sections 4.3 through 4.8. Creep predictions from the literature assumed material properties typical of the superstructure concrete as discussed in Section 4.2 and in the respective sections for each time-dependent model, except that the curing duration was set to 4.0 days (equal to the average between the southbound and northbound specimens), the volume-to-surface ratio was 1.0 in. (25 mm), the reinforcement ratio was equal to zero, and the relative humidity was taken equal to 37.5%. Because each creep model used a different definition of the instantaneous elastic strains (see discussion in Section 4.2), the predicted creep strains were computed as the total strain computed from the compliance function minus the total strain computed at 0.01 days. The duration of 0.01 days was chosen because, according to the specification of the B3 model (Bažant and Baweja, 1995a), the total compliance of the B3 creep formulation after 0.01 days is approximately equal to the traditional definition of elastic modulus used for the other considered time-dependent models. Thus, the

early-age creep specified in the B3 model was removed so that it could be reasonably compared to the other literature models. The reduction of applied stress and subsequent reloading of the cylinders during the creep measurements was not considered in the computation of the creep predictions using the literature models, for which the applied stress was assumed to be constant.

Figure 5.4 shows the plots of experimental and predicted creep strains for the samples loaded in Frame 2 at an age of 57 days to 2.92 ksi (20.1 MPa). The applied stress was equal to 45% of the design 28-day strength of 6.5 ksi (44.8 MPa), and the age of loading was approximately equal to the earliest age at which any precast segment was first erected for the St. Anthony Falls Bridge. Creep was measured until an age of 528 days after casting, or equivalently 471 days of loading. The measured creep strains represent the average of the creep strains obtained for the two specimens in the frame, where the creep strains were determined for the respective cylinders from the average strains using only two of the three pairs of DEMEC points as explained below.

The experimental procedure used for collection of data from Frame #2 contained a number of discrepancies that may have contributed to errors in the measured data. For the first two weeks of creep measurements, only two of the three sides (Sides "A" and "B") of the samples in Frame 2 were measured because one of the four rods in the creep frame was obstructing Side "C" such that the DEMEC points could not be accessed for measurement. Because the elastic compression and early-age creep of cylinders was unknown, further measurements along Side "C" were of little value for computing the total creep strain. Furthermore, it was suspected that the sulfur caps placed on the ends of the Frame 2 samples were not perpendicular to the axis of the cylinder, which may have introduced bending into the specimens. Because only two of the three sides were measured, this could not be verified. Upon reloading the cylinders on January 19, 2010 (528 days after casting), the specimens cracked and spalled, causing a steep rise in the measured strain. Strain readings were discontinued for these specimens thereafter. The cracking

either indicated that more load had been applied to the cylinders than was recorded by the strain gage readouts, or that the specimens were under significant bending stresses.

In comparison with the creep strain predictions from the literature, the measured strains from Frame 2 appeared to be best approximated by the 1978 CEB/FIP Model Code procedure. The AASHTO LRFD model appeared to provide good predictions for the first 30 days after loading, but severely underestimated the total creep strain at 471 days after loading. The GL2000 model overestimated the creep strains prior to 100 days after loading, but the estimates from 100 days onwards were reasonable. The 1990 CEB/FIP Model slightly overpredicted the creep strains throughout the entire test duration. The ACI-209 model overestimated the creep strains for the full test duration, with estimates near the end of loading about 50% larger than measured strains. Estimates from the B3 model were nearly double the measured strains over the full test duration.

The plots of the experimental and predicted creep strains for the samples loaded in Frame 4 at an age of 93 days to 1.90 ksi (13.1 MPa) are shown in Figure 5.5. The applied stress was chosen to approximate the applied concrete stresses in the St. Anthony Falls Bridge at end of construction, and the age of loading was approximately equal to the median age of the precast segments at erection. The specimens were measured until the concrete was 1,364 days (3.75 years) old, equivalent to 1,271 days of loading. The experimental creep strains represent the average strains taken between the two samples using all pairs of DEMEC points. The caps on these specimens were oriented more orthogonally to the length of the specimens than the caps of the specimens in Frame 2, which helped to eliminate the effects of bending.

The creep strains prior to 100 days after loading were best predicted by the AASHTO LRFD model, while after 100 days the 1978 CEB/FIP Model Code provided the best estimates. All other models overestimated the total creep strain throughout the entire test duration. At the end of the measurements at 1,271 days (3.5 years) of loading, the GL2000 model prediction was approximately 10% greater than the measured creep strains, whereas the 1990 CEB/FIP Model

Code was nearly 50% over, the ACI-209 prediction was nearly 75% over, and the B3 prediction was 100% over.

Figures 5.6 and 5.7 present the predictions and experimental results of creep strains for the samples in Frame 3 and Frame 1, respectively, each of which represent the averages between two samples with all DEMEC points measured. Both frames were loaded with 1.90 ksi (13.1 MPa) at an age of 130 days. The applied stress was again chosen to approximate the applied concrete stresses in the St. Anthony Falls Bridge at end of construction, and the age of loading was approximately equal to the maximum age of any precast segment at erection. Specimens in Frame 3 was loaded until the concrete was 598 days old (468 days of loading), while the Frame 1 samples were measured until the concrete was 1,364 days (3.75 years) old (1,234 days of loading).

The samples in Frame 1 had previously been loaded and unloaded at an earlier age as shown in Table 3.5. Results of the Frame 1 specimens for the initial loading at an age of 56 days and during creep recovery after unloading at an age of 83 days are not presented. Results from the first loading suffered from significant bending of the cylinders and were recorded for only two sides of DEMEC points. The elastic response to unloading was unknown because, although all three sides of DEMEC points were measured after the cylinders were removed from the frame, only two sides were measured before the load was removed. The impact that continued creep recovery, irreversible creep strains, or other effects associated with the first loading and unloading process had on the presented data for the reloaded Frame 1 was unknown, and thus no effort was made to correct for the loading and unloading procedure.

Comparisons between the measured strains from Frames 1 and 3 and predicted strains were similar to those from Frame 4. The 1978 CEB/FIP Model Code and AASHTO LRFD appeared to provide the best predictions, though the AASHTO LRFD model approached its asymptotic limit sooner than indicated by the measured results from Frame 1 after 1,234 days.

For both frames, the GL2000, 1990 CEB/FIP Model Code, ACI-209, and B3 models all overpredicted the creep strains throughout the entire duration of testing. At the end of measurement (468 days after loading for Frame 3 and 1,234 days after loading for Frame 1), estimates from GL2000, 1990 CEB/FIP Model Code, ACI-209, and B3 models were greater than the measured creep strains by 10%, 50%, 80%, and over 100%, respectively.

Judging from all four creep frames, it was concluded that the 1978 CEB/FIP Model Code creep strain was consistently the best predictor of the measured creep strains. The AASHTO LRFD (2010) procedure provided good estimates prior to 100 days after loading, but typically underestimated the long-term creep strains. All other time-dependent models overestimated the creep over the entire testing duration. The GL2000 always overestimated the strains by a small margin. The B3 consistently predicted creep strains nearly double of what was measured.

5.5 Summary and Conclusions

Comparison of the aging strength and modulus curves from the ACI-209, 1978 and 1990 CEB/FIP Model Codes, and GL2000 provisions with the measured results provided by UMN and Cemstone showed that the assumed material properties for the time-dependent computational analysis were valid. The ACI-209 aging strength curve best fit the measured cylinder strengths, while the 1978 CEB/FIP Model Code and GL2000 aging modulus curves best estimated measured modulus values. Although the late-age strengths from the 1978 and 1990 CEB/FIP Model Codes and the GL2000 model overestimated the UMN measured strengths at 5.8 years, this was not expected to negatively impact the creep and shrinkage predictions from these models in any significant way.

Prediction of shrinkage strains using the models from the literature was, in general, much more reliable than prediction of the creep strains. The only model which greatly overestimated the shrinkage strains was the ACI-209, with all other models returning reasonable predictions.

The creep strains were consistently overpredicted by all models except for the 1978 CEB/FIP Model Code, which was the most reliable, and the AASHTO LRFD, which provided accurate estimates up to 100 days after loading but underestimated the strains at later times. The creep strains predicted by the B3 model were consistently twice the measured strains. The magnitudes of the differences among the predictions offered by the various time-dependent models are significant, such that the creep or shrinkage predictions between any two models might vary by a factor of 2.

For the tested samples, the maximum duration of sustained loading was 1,271 days for Frame 4, followed by 1,234 days for Frame 1. Within this time period, there was no definitive evidence that the creep strains had reached an asymptotic value. By 1,271 days, the ACI-209, CEB/FIP 1978 Model Code, and CEB 1990 Model Code asymptotic creep models predicted that at least 90% of the total expected creep strain had occurred. The AASHTO predictions were the quickest to approach the asymptotic strain, such that nearly 98% of the total strain was predicted to have occurred over the testing duration. In comparison, the logarithmic models B3 and GL2000 had only undergone 79% and 83% of their expected 150-year creep strains, respectively, after this duration of loading. For Frames 2 and 3 which were only measured for a total of 471 and 468 days, respectively, no meaningful conclusions could be drawn regarding the asymptotic or logarithmic nature of the creep phenomenon. Overall, there was no definitive evidence regarding whether or not the creep samples reached an ultimate strain, and thus these tests cannot be used to validate or invalidate either the asymptotic or logarithmic form of creep models.

Chapter 6: Time-Dependent Finite Element Modeling

Time-dependent finite element modeling was used to predict the long-term behavior of the I-35W St. Anthony Falls Bridge. The adopted methodology accounted for phenomena such as concrete creep, shrinkage, and steel relaxation to compute long-term deformations and stresses. This chapter presents the construction of the time-dependent finite element model of the St. Anthony Falls Bridge and the specific methodology adopted to compute the viscoelastic behavior.

An overview of the time-dependent finite element model of the St. Anthony Falls Bridge is presented in Section 6.1. This includes the geometry of the bridge, the finite element mesh, the material properties, the construction staging sequence, and the loads applied to the structure. Though the creep and shrinkage provisions were varied, the presented geometry and loads were used for all time-dependent analyses of the I-35W St. Anthony Falls Bridge. The construction staging sequence was employed for all analyses except in the particular case for which the impact of modeling a simplified construction sequence was examined; this exception is discussed in Appendix C. The investigation of how cycled temperatures might impact time-dependent behavior was examined using a different model with simplified geometry and no construction staging sequence, and is presented in Section 9.3.

Analysis of the time-dependent behavior of concrete using the finite element method required a particular formulation for the constitutive relationships. The chosen formulation was the Kelvin Chain model for plain concrete by Bažant and Prasannan (1989a, 1989b), Bažant and Xi (1995), and Bažant et al. (2010), the synthesis of which is presented in Section 6.2 for the reader's benefit. To account for the reduction in creep and shrinkage due to the presence of compression reinforcement, a novel modification extending the Kelvin Chain model to composite materials was developed as part of this research. The composite Kelvin Chain model is presented in Section 6.3. Summaries of the Kelvin Chain model for homogenous materials (plain concrete)

and the composite (reinforced concrete) Kelvin Chain model are presented in Sections 6.2.6 and 6.3.3, respectively.

6.1 Time-Dependent Finite Element Model Overview

6.1.1 Geometry and Mesh

The presented geometry and mesh for the finite element model of the St. Anthony Falls Bridge were used to generate all the numerical results presented in Chapter 8 for comparison with the measured creep and shrinkage deformations, regardless of the choice of time-dependent model. The investigation of the interactions between cyclic temperatures and time-dependent phenomena used a simplified geometry, as discussed in Section 9.3.

The three-dimensional finite element model, created using Abaqus (Dassault Systèmes, 2010a), was used to represent Spans 1 through 3 of the southbound bridge, as shown in Figure 6.1. This choice was made because Span 4 was separated from the end of Span 3 by an expansion joint, and was thus assumed to act independently; the southbound bridge was modeled because most of the instrumentation was concentrated in the southbound superstructure and piers. Piers 2 and 3 supporting the river span were modeled and assumed to be fixed at the base.

The concrete was modeled using 20-node three-dimensional quadratic continuum elements with reduced integration (element type C3D20R). The characteristic element size was approximately 42 in. (1,070 mm), such that the structure consisted of approximately 300 elements along the length of the three spans, ranging from 8 to 11 elements through the depth.

To simplify the meshing of the superstructure, the bridge was divided into portions where the bridge geometry changed substantially. The portions were as follows:

1. The expansion joint and diaphragm in Span 1 above Abutment 1.
2. The main body of Span 1.
3. The 10-ft (3.0-m) diaphragm above Pier 2.
4. The cast-in-place transition from the Pier 2 diaphragm to the precast construction.

5. The main body (precast segments) of Span 2.
6. The cast-in-place transition from the precast construction to the Pier 3 diaphragm.
7. The 10-ft (3.0-m) diaphragm above Pier 3.
8. The main body of Span 3.
9. The expansion joint and diaphragm in Span 3 above Pier 4.

The mesh for each portion was constructed independently using automatic mesh generation in Abaqus, specifically relying upon the sweep technique with the advancing front algorithm (i.e., element generation advancing along the longitudinal axis of the bridge) using only hexahedral elements. The webs were thin sections meshed with a single element through the thickness, which was not found to cause any issues due to the choice of quadratic elements with reduced integration. The top flange was partitioned such that two elements were generated through the depth. For the main bodies of Spans 1 through 3, the bottom flange was meshed with a single element through the depth. In the cast-in-place transitions between the pier diaphragms and precast construction, two elements were generated through the depth of the bottom flange. Diaphragms were meshed with multiple elements through the thickness of the webs and depths of the flanges in keeping with the characteristic element size of 42 in. (1,070 mm).

After meshing, each portion was tied together using surface-to-surface constraints. Although each portion was meshed with identical characteristic element size, the sudden changes in geometry meant that the meshes did not match at the interfaces between two portions. It was observed, however, that the mesh discontinuities had negligible effect on the overall model. This was due to the choice of C3D20R elements to define the concrete geometry, and also because the breaks in geometry were always normal to the longitudinal axis of the bridge, and thus typically remained planar throughout the analysis.

Transverse post-tensioning tendons embedded within the deck of the concrete box were smeared and approximated as 4-node linear membrane elements (element type M3D4) with

characteristic element lengths of 42 in. (1,070 mm). The embedment mimicked the behavior of grouted (bonded) tendons. Membrane elements have no bending stiffness or out-of-plane shear stiffness, and only carry load in the plane of the element. The membrane thickness was equal to the average area of the transverse post-tensioning steel per unit length along the longitudinal direction of the bridge. The material constitutive law was adjusted as discussed in Section 6.2.5 to remove the in-plane shear stiffness and longitudinal axial stiffness of the membrane, leaving only transverse axial stiffness associated with the orientation of the tendons. The constitutive law included relaxation of the transverse tendons. Post-tensioning was applied to the transverse tendons by specifying initial stresses in the membrane elements.

Longitudinal post-tensioning was modeled using 2-node linear truss elements (element type T3D2), with element lengths of approximately 42 in. (1070 mm). Typically, the truss elements were embedded within the concrete elements to model the behavior of the bonded tendons. However, the portion of the longitudinal tendons crossing the midspan closure pour was not bonded to the concrete in the finite element model. During construction of the physical bridge, the midspan closure-pour concrete was first loaded 0.25 days after casting and consequently had a very low concrete strength at initial loading. In the finite element model, bonding the tendons to the low-strength closure-pour concrete caused unrealistic concentrations of stress in the concrete around the tendon. This induced large deformations in the closure pour that were not expected to be indicative of the deformations of the physical bridge, for which the tendons were not bonded until much later. As a consequence, unbonded tendons were used in the model over the 7-ft (2.1-m) closure pour region plus 8.25 ft (2.5 m) to either side of the closure pour. This assumption allowed the applied stress to be distributed more evenly over the closure-pour cross section, and thus alleviated the concerns for unrealistic deformations. The unbonded tendons in the finite element model were never rebonded to the closure pour concrete, as was the case for the physical bridge after the tendons were grouted. This was believed to cause only

minimal differences in the overall bridge response. Post-tensioning was applied to the longitudinal tendons by specifying initial stresses in the truss elements. Relaxation of the longitudinal tendons was computed using the procedure documented in Section 6.2.5.

External draped tendons were modeled using 2-node linear truss elements. In the physical bridge, the draped tendons were unbonded along their length and only attached to the structure at deviators. In the model, only a single truss element was used between any two tie-down points. Unlike the behavior from the physical bridge, the modeled formulation did not allow slipping of the draped tendons through the deviators. However, the accuracy gained from a more physically representative formulation was believed to be negligible, certainly less than the expected errors between any prescribed time-dependent model and the behavior of the physical structure.

Mild steel was not explicitly modeled. Instead, reinforcement ratios were specified as internal variables at each integration point of the continuum concrete elements. Separate ratios were specified for steel aligned in the longitudinal, transverse, and vertical directions. The presence of the steel reinforcement was taken into account in the composite time-dependent procedure as presented in Section 6.3. Reinforcement ratios applied to the model are documented in Tables 4.2 through 4.5 for Span 1, Span 2, Span 3, and the pier and barrier rail, respectively.

Boundary conditions were chosen to approximate the physical constraints on the bridge, as determined from the as-built documents (Minnesota Department of Transportation, 2008) and the bearing manufacturer's shop drawings (R.J. Watson, Inc., 2008). At Abutment 1 and Pier 4, the ends were supported by a combination of multidirectional and guided bearings. This meant that the bridge was constrained to have only longitudinal deflection at Abutment 1 and Pier 4. Modeling the as-built bearing assemblies in the three-dimensional model was found to be computationally taxing, so simplifying approximations were made regarding the bearing pad geometries. To account for the dimensions and locations of the pads, boundary conditions were specified along one-element wide patches across the bottom of the boxes (about 26 in. (0.66 m)

wide), with the center of the patches at about 40 in. (1.0 m) from the ends of the bridge. These dimensions were chosen as convenient approximations to those found in the as-built drawings, where Abutment 1 bearing pads had diameter equal to 24.5 in. (0.62 m) centered about 48 in. (1.24 m) from the face of the stemwall, and Pier 4 bearing pads had diameter equal to 21.25 in. (0.55 m) centered 28 in. (0.71 m) from the centerline of Pier 4 (Minnesota Department of Transportation, 2008). Transverse and vertical deflections were specified as zero along these locations. Any frictional restraint due to longitudinal deflection was neglected, but some restraining moment was induced by the width of the boundary condition region. The physical geometries of Abutment 1 and Pier 4 were considered unnecessary for computations, and were consequently not modeled.

At Piers 2 and 3, the superstructure was tied to the piers by nodal constraints. Initially, surface-to-surface constraints were used to tie the superstructure to the top of the pier over the dimension of the bearing pads, similar to the procedure described above for the Abutment 1 and Pier 4 boundary conditions. However, preliminary results using the surface-to-surface constraints were not meaningfully different from nodal constraints emulating pin connections between Piers 2 and 3 and the superstructure. Consequently, the nodal (pin) constraints were adopted for computational simplicity. The nodal constraints were applied in a line across the entire width of the bottom flanges of both boxes, thus restraining all relative translational deflection between the superstructure and the piers, but allowing rotation about the axis of the line of nodes (i.e., rotation that would be expected under longitudinal bending). The bottoms of the piers were fixed at ground level, meaning that all displacements and rotations were specified as zero. Any soil-structure interaction was assumed negligible with respect to the overall structural response.

The geometry of the undeformed model was assumed to follow the profile grade line at the end of construction as documented in the as-built documents (Minnesota Department of Transportation, 2008). Consequently, the deformed shape of the bridge after the completion of the

construction staging sequence (refer to Section 6.1.3) would not be equivalent to the as-built profile grade line. In the ideal case, the undeformed state would have been chosen such that at bridge opening, the modeled deflection would be equivalent to the as-built profile grade line. This would have required inverse analysis for each time-dependent model. Ultimately, the behavior of the model would be nearly unaffected by the subtle change in the initial shape of the structure, so this inverse problem was not solved. Consequently, deflections of the model could not be directly compared to the absolute elevations of the bridge, but changes in elevation could be investigated.

6.1.2 Material Properties

Material properties for the concrete were specified for each time-dependent model. Concrete material properties common to all time-dependent models are documented in Section 4.2. Specific material properties necessary for the definition of the specific time-dependent models are covered in their respective sections in Chapter 4.

The modulus of elasticity for the post-tensioning steel was assumed to be equal to 28,500 ksi (196 GPa), as presented in the Saint Anthony Falls Bridge Erection Manual (Figg, 2008). The post-tensioning steel was specified as Grade 270 low-relaxation tendons with a yield stress of 243 ksi (1.68 GPa). The relaxation of the post-tensioning steel was calculated according to the procedure in Section 6.2.5. Mild steel reinforcement was assumed to have an elastic modulus of 29,000 ksi (200 GPa). The mild steel was assumed to not undergo any relaxation. Poisson's ratio was equal to 0.3 for all steel. All materials were assumed to remain in the linear-elastic range (i.e., uncracked concrete with compressive stresses below 45% of f_c' and steel below yield stress). This assumption was found to be valid for all conducted finite element analyses, as shown by the results given in Chapter 8.

As specified in Section 4.2, the plain concrete unit weight was equal to 143 lbs/ft^3 (2,290 kg/m^3). For purposes of applying gravity loading, however, the unit weight of the reinforced concrete was required. This was assumed to be equal to 148 lbs/ft^3 (2,370 kg/m^3), which was

5 lbs/ft^3 (80 kg/m^3) greater than the plain concrete as suggested by commentary C3.5.1 in the AASHTO LRFD Bridge Design Specifications (2010).

According to Appendix C of the St. Anthony Falls Bridge Erection Manual (Figg, 2008), the weight of the 0.6-in. (15-mm) diameter post-tensioning steel strands was 0.74 lbs/ft (1.1 kg/m), and the strand cross-sectional area was equal to 0.223 in.^{2} (144 mm^2). This corresponded to a unit weight of 478 lbs/ft^3 (7,700 kg/m^3).

6.1.3 Construction Staging Sequence

6.1.3.1 Modeling Procedures

The construction staging sequence was modeled to accurately represent the stress state of the bridge at the end of construction. All numerical results presented in Chapter 8 for comparison with the measured time-dependent deformations included the presented construction staging sequence. The simplified model for investigating the effects of cyclic temperature on time-dependent behavior, discussed in Section 9.3, did not include any construction sequence. Modeling of the St. Anthony Falls Bridge using a simplified construction sequence is presented in Appendix C.

Modeling the erection procedure was facilitated by an interaction within Abaqus known as "Model Change," which allowed the user to activate or deactivate regions of the model during analysis. Using this procedure, much of the structure, including the segmental portion of the bridge and all post-tensioning, was deactivated at the start of the analysis prior to any equilibrium calculations. Segments and tendons were then progressively activated according to the as-built construction schedule.

The initial state of activation was controlled by two options. The first option was to define initial stress conditions, and was used for the post-tensioning tendons. For elements deactivated at the start of the analysis, the specified initial state of stress was enforced at the beginning of the time step when those elements were first activated in the model (Dassault

Systèmes, 2010b). During the time step of activation, the initial stresses in the post-tensioning steel were transferred to the concrete. The compressive strains in the modeled concrete during this time step would normally correspond to immediate elastic shortening losses in the steel. However, loss of steel stress due to elastic shortening are typically ignored for post-tensioning processes, as the reaction forces from the tensioning jack compress the concrete before the tendons are anchored. In order to apply the correct as-built stresses to the model, the initial stresses in the modeled steel were held constant over the first time step after initial activation. The initial applied stresses were modified to account for immediate friction and anchorage losses, computed as described in Section 6.1.4.

The second feature used to control the initial state of activation was called strain-free activation, which set the activated elements to a state of zero stress while still keeping the deformed state at their activation. In other words, the deformed state was specified as the state of zero stress/strain, and any subsequent stresses were caused by a deviation from this newly assigned zero-strain state. This method is useful for modeling cast-in-place concrete, and was specifically applied to the closure pour at the midspan of the river span. After erection of the two cantilevers but prior to placing the closure pour, the cantilevers were in a deformed state different from the condition at which they were first deactivated at the start of the analysis. Thus the elements which comprised the closure pour connecting the two deformed cantilevers, when activated, were also necessarily deformed relative to the time at which they were deactivated (i.e., start of analysis). However, because the cast-in-place concrete hardens into a zero-stress state, the strain-free activation option was required for the closure pour. Addition of the precast segments did not require strain-free activation, as the concrete had already hardened prior to erection.

One particular difficulty with strain-free activation occurs when finite deflections are introduced to the system. When the deformed state of an element is entirely divorced from its stress state, the deformed state cannot be computed uniquely using the finite element method.

Therefore, absent other constraints, the nodes added during a strain-free activation would keep the same locations that they occupied when first deactivated, thus introducing discontinuous deflections between the cantilever ends and the closure pour. This was remedied by defining dummy elements which tracked the position of the deflected cantilever ends. The dummy elements were defined to have exactly the same undeformed element geometry as the closure pour, but had modulus of elasticity and Poisson's ratio nearly zero (as exactly zero modulus can cause computational difficulties), and density equal to zero. Before adding the closure pour elements, the dummy elements were added to the analysis using a nonzero-strain activation. Because the modulus of the dummy elements was effectively zero, the activated elements were still at nearly zero stress, and thus the rest of the model was unaffected for purposes of equilibrium. Unlike strain-free activation, however, it was possible to compute the locations of the nodes of the dummy elements using the nonzero-strain activation. The closure pour was then constrained to follow the deformed shape of the dummy elements during the strain-free activation, ensuring that the deflections of the cantilever tips and closure pour were aligned.

6.1.3.2 Modeled Construction Sequence

The modeled bridge was erected using a series of alternating loading and time-dependent analysis steps. During loading steps, a portion of the bridge was erected and the elastic deformation from that addition to the structure was computed. During time-dependent steps, the structure was allowed to creep and shrink for the duration until the next segment or load was added. Due to the particular methodology employed for modeling time-dependent behavior (as discussed in Section 6.2 for plain concrete and Section 6.3 for reinforced concrete), both loading and time-dependent steps were considered as general static steps in Abaqus. Loading steps were treated the same as time-dependent steps but with very short duration (0.001 days) over which negligible time-dependent behavior could occur.

The time steps used in modeling the construction procedure are detailed in Table 6.1. In the initial preparatory step, the entire model was deactivated except for the cast-in-place concrete comprising Span 1 and Pier 2. This initial step corresponded to an analysis start date of May 25, 2008, when post-tensioning was first applied to Span 1. Prior to this time, the cast-in-place concrete was held on shoring and assumed to be unstressed. Deformation due to shrinkage prior to this date was not computed as it would not affect the post-tensioning stresses. However, the cast date and curing duration of the concrete were specified as inputs to the model so that the shrinkage would be properly computed during the analysis time steps. Span 3 and Pier 3 were not included in the model until all cast-in-place pours had been completed in June 12, 2008.

Shoring for Span 1 and Span 3 was provided by modeling a set of compression-only truss elements connecting the superstructure to the ground. The stiffness of the shoring provided during the construction of the physical bridge was unknown, so the modeled shoring was given arbitrarily high stiffness properties to prevent any downward vertical deflection of the superstructure. Because the trusses were not allowed to carry tensile loads, the modeled superstructure was allowed to lift off the shoring during upward vertical deflections. The trusses were pinned to both the ground and superstructure, and therefore provided no restraint to horizontal motion.

Segmental sections were added according to the erection schedule of the as-built bridge. These segments were named SB{A}-{B}, where "SB" stood for the southbound bridge, {A} was a number corresponding to the pier from which the cantilever originated (either Pier 2 or Pier 3), and {B} was the segment number varying from 1 to 15, with 1 being the segments nearest the piers. This naming procedure was used to remain consistent with the I-35W Erection Manual (Figg, 2008). Tendons in the top flange were named as {D}-C{E}, where {D} was a number corresponding to the pier from which the cantilever originated (either Pier 2 or Pier 3), "C" meant that the tendons were added as part of the cantilevering construction procedure, and {E} was a

number corresponding to the order of stressing. Tendons in the bottom flange and draped tendons were named as {F}-{G}{H}, where {F} was the span in which the tendon was installed (Span1, 2, or 3), {G} was either "B" for bottom flange tendons or "D" for draped tendons, and {H} was a number corresponding to the order of stressing. Post-tensioning tendon names were chosen to remain consistent with names presented in the I-35W Erection Manual (Figg, 2008).

When adding precast segments, the concrete was added using a nonzero-strain activation, as discussed in Section 6.1.3.1. This was because the concrete had hardened prior to erection. To compute the proper shrinkage strains during each analysis time step, the cast dates and curing durations for each segment were specified as inputs in the model. During construction of the physical bridge, precast segments were cast individually for each box and then tied together by a 4-ft (1.2-m) transverse deck closure pour. To simplify the addition of the segments to the model, both boxes and the transverse closure pour for a given cantilever segment were assumed to be added simultaneously, and the cast and erection dates of the entire cross section were assumed to be equal to the average cast and erection dates between the two boxes. For the two boxes of any given cross section, the cast dates were rarely more than a few days apart, and the precast segments were typically erected months after casting, and so this averaging of cast dates was not assumed to significantly impact time-dependent estimations. Erection of both boxes for any given section always took place within a single day, so averaging of erection dates would have negligible impact on results. The cast-in-place transverse deck closure pour between the two boxes was only 4 ft (1.2 m) out of the total 90-ft (27-m) width of the bridge. Furthermore, the tendon jacking sites (located above the webs of the precast boxes) were far from the transverse closure pour. Therefore, the inaccuracies of equating the transverse closure pour cast date with the average cast date of the precast boxes were assumed to be of minimal consequence for the overall model behavior. The transverse post-tensioning for each given segment was added to the model when the next segment was erected, in accordance with the construction procedure.

One major difference between the as-built construction procedure and the modeled erection procedure was the process of correcting segment elevation during construction. Per discussion with Chris Burgess of Figg Bridge Engineers (via teleconference on May 10, 2012), as the segments of the physical bridge were erected, the elevation was corrected to better match the expected final elevations by adjusting the joints between the previously erected and newly erected segments. Information about how each segment was specifically adjusted during erection was not provided, and so this correction procedure was not considered during modeling. Furthermore, as noted in Section 6.1.1, the undeformed shape of the modeled bridge followed the end-of-construction profile grade line specified in the as-built documents. Consequently, it was not expected that the modeled procedure would replicate the absolute elevations of the structure at bridge completion. However, because the stresses in the structure were only indirectly changed by this adjustment (i.e., changed only by second-order effects), the modeled stresses at bridge completion were expected to be comparable to those obtained during construction. As a corollary, the relative time-dependent changes in stress and deflection after completion of the bridge, being functions of the stress state of the bridge, were not expected to be significantly impacted by this difference in procedure.

The midspan closure pour procedure was conducted in a series of steps to replicate the effective stresses that this procedure applied to the cast-in-place closure and the precast cantilevers. First, the cantilever ends were aligned using strongback beams, then jacks were used to push the cantilever tips apart, and finally the concrete closure pour was placed. This procedure was intended to deflect the piers at either end of Span 2 away from midspan, thus compensating for the expected deflections of the piers towards midspan due to creep and shrinkage of the superstructure.

The following is a description of the alignment procedure used during construction of the physical bridge. This procedure is shown schematically in Figure 6.2. After both cantilevers of

the bridge were erected, the cantilever tips were aligned using strongback beams placed across the closure gap. Four strongback beams were used, one positioned above each of the webs. Each beam was comprised of two 34.3-ft (10.5-m) long W24x162 steel girders welded together along the top and bottom flanges to create a flanged box shape. The strongbacks were first pinned to the higher cantilever at two locations: one point near midspan of the strongback and another point at the far end of the strongback. This configuration left half the strongback spanning over the closure region, such that the free end of the strongback was located above the lower precast cantilever. Post-tensioning bars were strung vertically between the free end of the strongbacks and the deck of the lower cantilever. The bars were then tensioned, pulling the higher and lower cantilevers into alignment. Once aligned, the strongback beams were effectively supported by two pin connections on one cantilever end and a single point connection on the opposite cantilever end. Due to the nature of connection of the strongback beams to the deck, the beams were not expected to carry any axial load across the closure pour region.

The modeled alignment procedure differed from the alignment of the physical bridge. In the model, the process of using vertical post-tensioning was not necessary for alignment of the cantilever ends, and instead the beam was added to the model in the final three-point support configuration. When the strongback beams were added using a nonzero-strain activation, the bending stiffness of the beams aligned the cantilevers in a manner equivalent to the vertical post-tensioning procedure used during construction of the physical bridge.

When modeling the connections of the strongback beams to the cantilever ends, it was necessary to specify the position of each pin connection between the beams and the deck before the beginning of the analysis. However, after the cantilevers had been added through the construction staging sequence, the distance between the two cantilever ends was different from when the cantilevers were first deactivated at the start of the analysis. Consequently, the strongback beams would have built-in axial stresses which would not have been present had the

vertical post-tensioning alignment procedure been followed in the model. These axial stresses would have effectively jacked apart the cantilever ends. Built-in axial stresses were removed by setting the beam cross-sectional area to zero while keeping the beam bending stiffness consistent with the flanged box shape.

Setting the cross-sectional area to zero had two impacts on the modeling procedure. First, any axial restraint provided by the strongback beams during construction of the physical structure after the beams had been secured to both cantilever ends was neglected, which was consistent with the assumptions regarding the behavior of the as-built alignment procedure. Second, a Timoshenko beam bending formulation, the default beam formulation used by Abaqus which captures shear deformations as well as bending deformations, was invalid as Timoshenko beam bending contains a $1/A$ term for shear deformations, where A is the area of the beam. Therefore, Bernoulli beam theory using quadratic beam elements was required for the strongback beams. This was not believed to meaningfully alter the effects of the alignment procedure.

Gravity loads were not applied to the strongback beams in the model, and instead the self-weight of the beams was applied to the cantilever ends as discussed in Section 6.1.4.

After alignment of the cantilevers, jacking forces were applied to the cantilever tips. Jacking forces were applied to each of the webs, with 45 kips (200 kN) per jack just above the bottom flange and 235 kips (1,050 kN) per jack just below the top flange, for a total of 1,120 kips (4,980 kN). Jacking loads were modeled by two-node truss elements spanning the closure pour. The truss elements were specified with axial stresses as initial conditions, such that the line of action of the jacking forces was along the axis of the jacks. The jack struts were assumed to have a cross-sectional area of 30 in.^{2} (190 cm^2) and modulus of elasticity of 29,000 ksi (200 GPa) for purposes of computing the losses in the jack after it was locked off. Similar to the tensioning of the post-tensioning tendons, jacking stresses were held constant over the first time step after activation so that the model would not compute any immediate elastic shortening losses.

Immediately following the jacking procedure in the model, zero-stiffness dummy elements used for tracking the position of the closure pour were added with a nonzero-strain activation as explained prior. The jacking forces were held for one day, then the cast-in-place closure pour was added using a strain-free activation constrained to the position of the dummy elements as described in Section 6.1.3.1. The closure pour was allowed to harden for 0.25 days before releasing the jacks and compressing the cast-in-place concrete. Finally, the bottom flange and draped post-tensioning for Span 2 were applied, and the strongback beams used for alignment were removed.

6.1.4 Loading

Loading was applied progressively as the construction staging sequence was modeled. All numerical results presented in Chapter 8 employed the following loads.

Gravity was incorporated into the model by specifying the material densities as described in Section 6.1.2. The acceleration due to gravity was set to 386.4 in./sec^2 (9.81 m/sec^2).

Post-tensioning was applied as initial stress conditions in the post-tensioning tendons. Stress values specified in the model were taken as the average jacking stresses recorded in the St. Anthony Falls Bridge Erection Manual (Figg, 2008) minus the immediate friction and seating losses. Friction losses along the length of the tendons were estimated using a wobble coefficient of 0.0002 ft^{-1} (0.00066 m^{-1}), a friction coefficient of 0.25 rad^{-1}, and an anchor seating length of 0.375 in. (9.5 mm) as specified in the as-built construction documents (Minnesota Department of Transportation, 2008). Friction losses were averaged over the lengths of the tendons such that each tendon had uniform stresses along the entire length after anchorage. The estimated difference between the maximum and minimum stresses along the length of the tendons just after immediate losses was typically around 6 ksi (41 MPa), or about 3% of the total jacking stresses, and thus averaging the losses along the length of the strands was deemed to be acceptable. A summary of the post-tensioning stresses applied to the model are given in Table 6.2.

Due to the strain compatibility enforced between the embedded tendons and the concrete, post-tensioning losses due to stressing sequence, creep, and shrinkage were automatically factored into the applied loads. As the concrete deformed with time, the strains in the steel were reduced, resulting in a reduction in post-tensioning for computation of future time steps. As mentioned in Section 6.1.3, the initial applied stress was held constant for the first time step after activation of the tendon to prevent the model from computing elastic shortening losses. Elastic shortening losses caused by the sequential jacking of the strands at the addition of each precast segment were ignored.

Temporary loads on the bridge during the construction procedure were not modeled unless the application of the load coincided with the timing of the midspan closure pour. In general, the temporary loads would not impact the long-term behavior of the bridge, as the creep induced by such loading would eventually recover after the load was removed. However, temporary loads present on the bridge during the closure pour procedure and then later removed locked permanent stresses into the structure. According to Chris Burgess of Figg Bridge Engineers (personal correspondence via email on June 26, 2013), transient loads that might contribute to locked in stresses included cranes and trucks located near the closure pour region, self-weight of the strongback alignment beams, and the closure pour formwork. These loads were estimated to be approximately 135 kips (600 kN) on the southern cantilever tip (i.e., from Pier 2) and 5 kips (22 kN) on the northern tip (i.e., from Pier 3). In the model, these loads were distributed evenly over the entire surface of the final precast segment of the respective cantilevers, were added simultaneously with the addition of precast segment 3-C15 (the final segment to be erected), and were removed when the Span 2 bottom and draped tendons were stressed after the closure pour procedure.

Additional long-term loads were applied to the model as specified in the as-built construction documents (Minnesota Department of Transportation, 2008). The load from the steel

exterior rail, which was not modeled, was applied as a line load of 440 lbs/ft (6.4 kN/m) along the exterior edge of the bridge. A utility allowance of 100 lbs/ft (1.4 kN/m) was applied as a distributed downward pressure across the entire width of the bridge, amounting to a pressure of 1.1 lbs/ft^2 (52.7 kN/m^2) over the entire deck. In the modeled construction sequence, both of these loads were applied at the same time as when the interior concrete barrier rail was placed on August 5, 2008 (Step 62 in Table 6.1). Design dead loading for the light rail and the suspended pedestrian bridge were not applied in the model, as it was unknown when or if these loads would be applied.

6.2 Modeling Time-Dependent Behavior of Viscoelastic Materials

The procedure employed for creep modeling was the rate-type model developed for the solidification theory of concrete creep by Bažant and Prasannan (1989a, 1989b). This procedure was further documented by Bažant and Xi (1995), and an implementation example for the Koror-Babeldaob Bridge was later provided by Bažant et al. (2009, 2010).

Creep models, which are typically presented in the form of compliance functions, were converted to rate-type models based on the Kelvin Chain model. The premise of a rate-type model is that the load history does not need to be known, and instead only the rate of creep during the current time-step is needed. The rate-type formulation greatly simplifies the computation of creep under changing stresses, which normally requires convolution integrals between the stress history and the creep compliance function. This is not only more efficient with respect to computation time, but also memory allocation, as the entire load histories do not need to be saved at each integration point.

The use of the Kelvin Chain model facilitates the conversion from the compliance function to the rate-type formulation. The Kelvin Chain model is a viscoelastic model with the form of a series of exponential functions. Because the exponential functions always approach some asymptotic value at a set rate, only the remaining creep needs to be saved after each time

step. Assuming that the viscoelastic (spring and dashpot) constants are known, the amount of creep strain over a time step for the Kelvin Chain model can be computed exactly using only the change in stress over the current time step, the duration of the time step, and the remaining creep in each of the exponential terms. Knowledge of the entire load history is unnecessary, and thus the benefits of the rate-type formulation are realized.

This section first presents an overview of the Kelvin Chain viscoelastic model in Section 6.2.1. The viscoelastic constants of the Kelvin Chain model must be estimated from the creep compliance function. This is done using the Post-Widder theorem as presented in Section 6.2.2. Having the viscoelastic constants, the rate-type equations needed for implementing the Kelvin Chain model into the finite element analysis are presented in Section 6.2.3. The proof for these equations is given in Appendix A. The procedures for incorporating concrete shrinkage strains and steel relaxation into the finite element analysis are given in Sections 6.2.4 and 6.2.5, respectively. A summary of the Abaqus implementation of all the time-dependent processes is presented in Section 6.2.6. The B3 and 1978 CEB/FIP Model Code creep models had forms that required slight modifications, documented in Section 6.2.7, to the presented Kelvin Chain procedure. The methodology was validated with respect to a series of simple test cases in Section 6.2.8, and was found to provide results nearly identical to those from hand calculations.

6.2.1 Kelvin Chain Model for Viscoelastic Materials

The Kelvin model, shown in Figure 6.3, is a simple mechanical model for viscoelastic behavior, represented by a linear spring and dashpot connected in parallel. The stress-strain relationships of the spring and dashpot are, respectively

$$\sigma_{spring} = K\varepsilon \tag{6-1}$$

$$\sigma_{dashpot} = C\dot{\varepsilon} \tag{6-2}$$

where K is the spring stiffness, C is the damping value of the dashpot, σ_{spring} and $\sigma_{dashpot}$ are the stresses applied to the spring and dashpot, respectively, ε is the total strain, and $\dot{\varepsilon}$ is the strain rate. Because the spring and dashpot are connected in parallel, both elements have equal strain and strain rate, and the total stress applied to the system is the sum

$$\sigma = \sigma_{spring} + \sigma_{dashpot} = K\varepsilon + C\dot{\varepsilon} \tag{6-3}$$

The solution to this differential equation under a constant total stress σ_0 applied at time $t_0 = 0$ is given by

$$\varepsilon = \frac{\sigma_0}{K}\left(1 - e^{-Kt/C}\right) \tag{6-4}$$

This curve, along with the similar unloading curve, is presented in Figure 6.4. The Kelvin model does not allow for instantaneous elastic strain during the application or removal of the stress. The strain will asymptotically approach a maximum of σ_0/K, representing that at infinite time the total stress is held only by the spring element. The constant C/K, with units of time, is known as the retardation time of the system, t_r. Approximately 63% of the asymptotic strain will have occurred between the time of loading and the retardation time.

If a constant unit stress $\sigma_0 = 1$ is applied at time t_0, then Eqn. (6-4) describes the compliance function $J(t,t_0)$ of the Kelvin model, such that under constant stress,

$$\varepsilon = \sigma_0 J(t,t_0) = \sigma_0\left[\frac{1}{K}\left(1 - e^{-K(t-t_0)/C}\right)\right] \tag{6-5}$$

If the applied stress is not constant, and assuming the Boltzmann superposition principle holds, the convolution between the changing stress rate $\partial\sigma(\tau)/\partial\tau$ and the compliance function $J(t,\tau)$ must be considered:

$$\varepsilon(t) = \int_0^t J(t,\tau)\frac{\partial\sigma(\tau)}{\partial\tau}d\tau \tag{6-6}$$

The Kelvin Chain model for viscoelastic behavior represents a set of Kelvin models in series, as shown in Figure 6.5. Each Kelvin element in the series is subject to the same total stress, and the total strain is given as a summation of the strains from each individual Kelvin element, such that for constant stress σ_0 applied at t_0, the total strain is equal to

$$\varepsilon(t) = \sigma_0 J(t, t_0) = \sigma_0 \sum_{i=1}^{N} A_i \left(1 - e^{-(t-t_0)/t_{ri}}\right) \tag{6-7}$$

where $A_i = 1/K_i$ is the compliance of element i, and t_{ri} is the retardation time for element i given by C_i/K_i. In the general case where it is useful to model instantaneous elastic strain due to changes in stress, the retardation time for a single Kelvin element can be specified as zero, meaning that the dashpot for that element is non-existent and all that remains is an elastic spring. Similarly, linear viscous flow can be modeled by setting the retardation time of one element to infinity, meaning that the element's spring stiffness is zero and all that remains is a linear dashpot.

The Kelvin Chain model can be used to describe many real viscoelastic materials. First a set of Kelvin elements with a range of retardation times can be specified. Then, the spring stiffness for each element can be calculated to best fit the compliance function of the material. Identification of these stiffness values is an ill-posed problem because different retardation times can give equally good fits of the compliance. This difficulty was overcome by Bažant and Xi (1995) by defining and then discretizing a complete compliance spectrum using the Post-Widder theorem (Cohen, 2007).

6.2.2 Post-Widder Theorem and Curve Fitting the Compliance Function

The presented methodology for fitting a creep compliance function with the Kelvin Chain model is from Bažant and Xi (1995), and is presented as background for the reader's benefit.

First, it is convenient to remove the instantaneous elastic deformation from the compliance function (because setting $t_{ri} = 0$ can be computationally problematic), to yield the creep function

$$C_c(t-t_0) = J(t-t_0) - \frac{1}{E_0} \tag{6-8}$$

where E_0 is the linear modulus of elasticity at the time of loading. In this example for which only the Kelvin Chain model is considered, the variables t and t_0 only appear as the difference $t - t_0$, and so Eqn. (6-8) reflects this change of variables. Extending the form of the compliance function presented in Eqn. (6-7) to an infinite number of Kelvin elements with positive, non-zero relaxation times, the creep function for the Kelvin Chain model can be represented in integral form:

$$C_c(\xi) = \int_{0+}^{\infty} \varphi(t_r)\left(1 - e^{-\xi/t_r}\right) dt_r \tag{6-9}$$

where the variable ξ has replaced $t - t_0$, and $\varphi(t_r)$ represents the compliance spectrum with units of inverse stiffness per time (psi^{-1}/day). Given a known arbitrary creep function $C_c(\xi)$, the compliance spectrum $\varphi(t_r)$ for the Kelvin Chain model that best fits the creep function is unknown.

Let $\Phi(t_r) = \varphi(t_r)t_r$, a quantity with units of inverse stiffness, and $t_r = 1/\zeta$. Performing this substitution on Eqn. (6-9) results in

$$C_c(\xi) = \int_{0+}^{\infty} \Phi(\zeta^{-1})\left(1 - e^{-\xi\zeta}\right)\zeta^{-1} d\zeta = \int_{0+}^{\infty} \Phi(\zeta^{-1})\zeta^{-1} d\zeta - \int_{0+}^{\infty} \Phi(\zeta^{-1}) e^{-\xi\zeta}\zeta^{-1} d\zeta \tag{6-10}$$

The Laplace transform of $\Phi(\zeta^{-1})\ \zeta^{-1}$ is equal to $L(\xi)$:

$$L(\xi) = \int_{0+}^{\infty} \Phi(\zeta^{-1}) e^{-\xi\zeta}\zeta^{-1} d\zeta \tag{6-11}$$

Therefore, it can be concluded that the creep function is equal to

$$C_c(\xi) = L(0) - L(\xi) \tag{6-12}$$

The task for curve fitting involves calculation of the compliance spectrum for the continuous system, then discretizing the spectrum down to the compliance of each individual

element in the Kelvin Chain model. From the above discussion, the computation of the compliance spectrum requires the use of an inverse Laplace transform, which can be approximated using the Post-Widder theorem (Cohen, 2007). The Post-Widder theorem states that if $F(s)$ is the Laplace transform of $f(t)$, meaning

$$F(s) = \int_0^\infty f(t) e^{-st} dt \tag{6-13}$$

then the inverse Laplace transform of $F(s)$ is given by

$$f(t) = \lim_{k\to\infty} \frac{(-1)^k}{k!} \left(\frac{k}{t}\right)^{k+1} F^{(k)}\left(\frac{k}{t}\right) \tag{6-14}$$

where $F^{(k)}(k/t)$ represents the k-th derivative with respect to s evaluated at k/t. Application of the Post-Widder theorem to Eqns. (6-11) and (6-12) produces the following result:

$$\Phi(\zeta^{-1})\zeta^{-1} = -\lim_{k\to\infty} \frac{(-1)^k}{k!} \left(\frac{k}{\zeta}\right)^{k+1} \left[C_c\left(\frac{k}{\zeta}\right) - L(0) \right]^{(k)} \tag{6-15}$$

The term $L(0)$ is a constant, for which the derivative will necessarily be zero, and therefore can be excluded from Eqn. (6-15). Substituting $t_r = 1/\zeta$ and simplifying the result produces (Bažant and Xi, 1995)

$$\Phi(t_c) = -\lim_{k\to\infty} \frac{(-kt_r)^k}{(k-1)!} C_c{}^{(k)}(kt_r) \tag{6-16}$$

where $C_c{}^{(k)}(kt_r)$ is the k-th derivative of the creep function with respect to $\xi = t - t_0$ and evaluated at kt_r. For practical applications, a good approximation of typical creep functions can be obtained using values of k equal to 3 or greater (Bažant et al., 2009).

For computational analysis, it is convenient to convert the compliance spectrum into a finite set of discrete compliance values A_i as shown in Eqn. (6-7). One simple discretization assumes a set of Kelvin elements with retardation times equal to β^i, with integer i varying from m to n. For example, a set of retardation times can be chosen to vary by powers of 10 from 10^{-3} to

10^6, or by powers of 2 from 2^{-10} to 2^{20}. A smaller β will result in a finer discretization at the cost of computational speed, whereas a larger β may not accurately approximate the creep function at all times.

Theoretically, the limits of *m* and *n* should be infinite to include the entire compliance spectrum in the discretization process. For practical purposes this is not feasible, so upper and lower bounds for *m* and *n* must be chosen. Because only the creep function $C_c(\xi)$ and not the total compliance function $J(\xi)$ has been used in the Post-Widder theorem, the instantaneous elastic behavior has been removed from the Kelvin Chain model approximation, and has instead been included in the analysis as the typical elastic modulus. Therefore, for retardation times approaching zero, the compliance spectrum of the creep function will also approach zero. Consequently, the lower limit of *m* can be chosen such that the smallest retardation time has a compliance value of effectively zero, as all smaller retardation times will have no response in the model. The value of *m* will vary depending on the choice of viscoelastic model used to define the concrete.

As long as $A_i(t_r)$ is bounded as t_r approaches infinity, the total strain of a given Kelvin Chain element over the entire analysis duration (assumed to be finite) will limit to zero as the retardation time of that element approaches infinity. Effectively, a Kelvin Chain element with very large retardation time deforms too slowly and has no effect on an analysis of comparatively short duration. Consequently, the upper limit of *n* should be specified such that the maximum retardation time is at least an order of magnitude greater than the total analysis duration. The upper limit is independent of the chosen viscoelastic model, and varies only by total analysis duration.

To aid in the discretization of the compliance spectrum, the integral from Eqn. (6-10) can be rewritten as

$$C_c(\xi) = \int_0^{\infty} \Phi(\zeta^{-1})\left(1 - e^{-\xi\zeta}\right)\zeta^{-1} d\zeta = \int_{-\infty}^{\infty} \Phi(t_r)\left(1 - e^{-\xi/t_r}\right) d\left(\ln t_r\right) \tag{6-17}$$

noting that $t_r = 1/\zeta$ and $d(\ln t_r) = dt_r/t_r$. The integral in Eqn. (6-17) can be approximated as a summation:

$$C_c(\xi) \approx \sum_i^N \Phi(t_{ri})\left(1 - e^{-\xi/t_r}\right)\Delta\left(\ln t_r\right) \tag{6-18}$$

which assumes constant $\Phi(t_{ri})$ over a step of $\Delta(\ln t_r)$. The summation from Eqn. (6-18) has the same form as the discrete Kelvin Chain model from Eqn. (6-7), for which the creep function is

$$C_c(\xi) = \sum_i^N A_i\left(1 - e^{-\xi/t_r}\right) \tag{6-19}$$

Therefore, by equating Eqns. (6-18) and (6-19), the compliance of the *i*-th Kelvin element in the Kelvin Chain model can be approximated by

$$A_i = \Phi(t_{ri})\Delta\left(\ln t_r\right) = \Phi(t_{ri})\ln\beta \tag{6-20}$$

where β is the base for the Kelvin Chain discretization as described above.

6.2.3 Rate-Type Creep Model in Elastic Finite Element Analysis

To avoid the use of convolution integrals in the finite element implementation of creep, compliance equations must be converted to rate-based creep models. The approximation of the creep function by the Kelvin Chain model as previously described makes this conversion possible. The rate-type formulation of the Kelvin Chain model is from Bažant and Prasannan (1989a, 1989b), and is presented below as background for the reader's convenience. A proof showing the derivation of the rate-type creep model is given in Appendix A.

The changes in strain were computed over time step $\Delta t = t_e - t_b$, where t_e is the time at the end of the time step and t_b is the time at the beginning of the time step. Any applied load was assumed to change linearly over the time step. For aging viscoelastic materials such as concrete, the center of the time step was defined as the geometric mean $t_{nh} = [(t_e)(t_b)]^{1/2}$. Over a small time

step, it is reasonable to assume that the material is effectively nonaging. Thus, the aging material properties were assumed to be constant over the time step and calculated at the time t_{nh}. The geometric mean of the time step was used so that the material properties were weighted closer to the beginning of the time step rather than the end, as according to the Kelvin Chain model more creep will occur in the first half of the time step as compared to the second half. For short time steps, accuracy was not significantly impacted by computing aging properties at the beginning or algebraic mean of the time step instead of the geometric mean.

For each integration point in the finite element model, vectors $\boldsymbol{\gamma}_{\mathbf{ci}}^{(n)}$ representing the remaining inelastic creep strain in the i-th Kelvin element with retardation time t_{ri} at time step n were defined. Each integration point had N such vectors ($i = 1, 2, \ldots, N$), where N is the number of Kelvin elements in the Kelvin Chain model. At the beginning of the analysis, these variables were set equal to zero (assuming no stress was acting on the system before analysis begins). The total remaining creep in each Kelvin element was known because the deformation in the Kelvin element always progresses asymptotically to $A_i\boldsymbol{\sigma}$ according to the exponential function from Eqn. (6-7). These variables were updated for each integration point in the model by use of

$$\boldsymbol{\gamma}_{\mathbf{ci}}^{(n)} = \frac{A_i \mathbf{D}^{-1} \Delta\boldsymbol{\sigma}}{\Delta t}\left(t_{ri} - t_{ri} e^{-\Delta t/t_{ri}}\right) + \boldsymbol{\gamma}_{\mathbf{ci}}^{(n-1)} e^{-\Delta t/t_{ri}} \tag{6-21}$$

where $\mathbf{D}^{-1}$ is the inverse of the 6 x 6 isotropic material matrix with Poisson's ratio ν,

$$\mathbf{D} = \begin{bmatrix} D_{11} & D_{12} & D_{12} & & & \\ D_{12} & D_{11} & D_{12} & & 0 & \\ D_{12} & D_{12} & D_{11} & & & \\ & & & D_{44} & 0 & 0 \\ & 0 & & 0 & D_{44} & 0 \\ & & & 0 & 0 & D_{44} \end{bmatrix} \quad \text{where} \quad \begin{aligned} D_{11} &= \frac{1-\nu}{(1+\nu)(1-2\nu)} \\ D_{12} &= \frac{\nu}{(1+\nu)(1-2\nu)} \\ D_{44} &= \frac{1}{2(1+\nu)} \end{aligned} \tag{6-22}$$

$$\mathbf{D}^{-1} = \begin{bmatrix} 1 & -\nu & -\nu & & & \\ -\nu & 1 & -\nu & & \mathbf{0} & \\ -\nu & -\nu & 1 & & & \\ & & & 2(\nu+1) & 0 & 0 \\ & \mathbf{0} & & 0 & 2(\nu+1) & 0 \\ & & & 0 & 0 & 2(\nu+1) \end{bmatrix} \tag{6-23}$$

and $\Delta\boldsymbol{\sigma}$ is the change in stress vector over the time increment from step $n-1$ to n. As described in Section 6.2.1, the compliance value A_i was the inverse of the spring stiffness of the i-th Kelvin element, so the elastic modulus (not seen in Eqns. (6-22) and (6-23)) was already accounted for in the formulation of $\boldsymbol{\gamma}_{\mathbf{ci}}^{(n)}$.

To update the stress state from one time step to the next, the incremental modulus $E''(t_{nh})$ for the time step was calculated as (Bažant and Prasannan, 1989b)

$$E''(t_{nh}) = \left[\frac{1}{E_0} + \sum_{i=1}^{N} A_i \left(1 - \frac{t_{ri}}{\Delta t} + \frac{t_{ri}}{\Delta t} e^{-\Delta t/t_{ri}} \right) \right]^{-1} \tag{6-24}$$

The incremental modulus is always less than, but for increasingly small time step Δt will converge to, the instantaneous modulus E_0. The incremental modulus was required for the constitutive equation

$$\Delta\boldsymbol{\sigma} = E''(t_{nh})\mathbf{D}\left(\Delta\boldsymbol{\varepsilon} - \Delta\boldsymbol{\varepsilon}''\right) \tag{6-25}$$

where $\mathbf{D}$ is the isotropic material matrix as defined in Eqn. (6-22), $\Delta\boldsymbol{\varepsilon}$ is the total strain change vector over the increment, and $\Delta\boldsymbol{\varepsilon}''$ is the inelastic (i.e., stress independent) strains over the increment defined by

$$\Delta\boldsymbol{\varepsilon}'' = \sum_{i=1}^{N} \boldsymbol{\gamma}_{\mathbf{ci}}^{(n-1)} \left(1 - e^{-\Delta t/t_{ri}} \right) + \Delta\boldsymbol{\varepsilon}_{\mathbf{sh}} + \Delta\boldsymbol{\varepsilon}_{\mathbf{T}} \tag{6-26}$$

which represents the summation of the exponential decrements of the remaining creep strain $\boldsymbol{\gamma}_{\mathbf{ci}}^{(n-1)}$ in each Kelvin Chain element over the time step Δt, plus the changes in strain over the time step due to shrinkage $\Delta\boldsymbol{\varepsilon}_{\mathbf{sh}}$ and temperature changes $\Delta\boldsymbol{\varepsilon}_{\mathbf{T}}$.

The finite element analysis program provided the total change in strain $\Delta\boldsymbol{\varepsilon}$ over the time step Δt, and Eqn. (6-25) served as the constitutive relation to convert this change in strain to a change in stress. To converge to the correct solution, the finite element analysis required the Jacobian matrix with components j_{ik} defined as

$$j_{ik} = \frac{\partial \Delta\sigma_i}{\partial \Delta\varepsilon_k} \tag{6-27}$$

where i and k are the indices from 1 to 6 for the changes in stress and strain tensors, respectively. For nonlinear stress-strain relationships, the finite element analysis must perform equilibrium iterations, over which the Jacobian is applied via Newton's method to converge to the equilibrium state (Dassault Systèmes, 2010c). For linear elastic formulations, the Jacobian does not depend on the current stress or strain in the material, and the finite element analysis will consequently converge in a single equilibrium iteration. By observation of Eqn. (6-25), the Jacobian for the rate-type creep model presented herein was equal to

$$j_{ik} = E''(t_{nh})D_{ik} \tag{6-28}$$

As shown in Eqn. (6-24), the incremental modulus was a constant dependent upon the time step duration, but not dependent on the current stress or strain, and thus the analysis was guaranteed to converge in a single equilibrium iteration.

6.2.4 Implementation of Shrinkage Strains

Computation of shrinkage strains does not require the use of hereditary integrals, as shrinkage is not a function of the stress state. Therefore, equations for shrinkage were coded directly into the analysis as functions of time without need of any special procedure. Because shrinkage strains are not associated with changes in stress, the method for applying shrinkage to the model was equivalent to the procedure for applying strains due to temperature changes.

6.2.5 Relaxation of Post-Tensioning Steel

To compute the total losses in the post-tensioning steel, relaxation of the steel was implemented in the finite element methodology. Relaxation was assumed to follow the equation formulated by Magura et al. (1964), which was used as the basis for AASHTO (2010), ACI Committee 209 (1992), and the PCI Design Handbook (2004) relaxation estimates. For steel held at constant strain, the loss in stress due to relaxation $\Delta\sigma_{RE}$ is given by

$$\Delta\sigma_{RE} = \frac{\sigma_i}{R}\left(\frac{\sigma_i}{\sigma_y} - 0.55\right)\log_{10}\left(24t + 1\right) \tag{6-29}$$

where σ_i is the initial stress when the constant strain was first applied, R is the relaxation coefficient of the steel and equals 10 for stress-relieved strands and 45 for low-relaxation strands, σ_y is the yield stress of the strand, and t is the time in days measured since the application of the constant strain. A constant of 1 hour has been added inside the logarithm term to prevent singularity at time $t = 0$. If the stress ratio σ_i/σ_y is less than 0.55, no relaxation occurs.

Because the function is not linear with respect to stress and because no relaxation occurs for small stresses, the Boltzmann superposition principle does not apply to this formulation of steel relaxation. This makes computation of the total relaxation difficult when considering changing strain states as are observed in concrete post-tensioning applications. As an approximation, the relaxation loss over the time step from times t_b to t_e in days was specified as

$$\Delta\sigma_{RE} = \frac{\sigma_j}{R}\left(\frac{\sigma_j}{\sigma_y} - 0.55\right)\log_{10}\left(\frac{24t_e + 1}{24t_b + 1}\right) \tag{6-30}$$

where σ_j is the stress at the beginning of the time step. Times t_b to t_e are times with respect to the initial post-tensioning of the tendon.

For the constant strain case, Eqn. (6-30) provided slightly lower losses than predicted by Eqn. (6-29). For low-relaxation strands stressed to 80% of σ_y and held at constant strain, Eqn. (6-30) predicted losses after 1,000 days that were 0.25 ksi (1.7 MPa) lower (i.e., approximately

5% lower losses) than those predicted by Eqn. (6-29). For lower values of initial post-tensioning, the absolute and relative differences between the two equations would be less than those given for 80% of the yield stress. Because total relaxation losses were expected to be at most approximately 5.0 ksi (34 MPa), and combined losses due to creep and shrinkage were expected to be much higher than the relaxation losses, the accuracy of Eqn. (6-30) was deemed sufficient for analysis.

The stress at the beginning of the time step input into Eqn. (6-30) already included creep and shrinkage losses from previous time steps. However, changes in the steel stress due to creep or shrinkage during the analysis time step were ignored for purposes of computing relaxation during the same time step. This approximation tended to overestimate the amount of relaxation losses during the time step, and slightly offset the underestimation of the losses by Eqn. (6-30) with respect to Eqn. (6-29).

Accounting for the elastic behavior of the tendons, the change in steel stress over the time step was therefore approximated as

$$\Delta\sigma = E_s \Delta\varepsilon - \frac{\sigma_j}{R}\left(\frac{\sigma_j}{\sigma_y} - 0.55\right)\log_{10}\left(\frac{24t_e + 1}{24t_b + 1}\right) \tag{6-31}$$

where E_s is the modulus of the steel and $\Delta\varepsilon$ is the change in strain over the time step. The Jacobian for the steel as required by the finite element routine was equal to E_s.

The above procedure was applied to both the truss and membrane post-tensioning steel elements. For the truss elements, the provided one-dimensional formulation was used as shown. For the membrane elements, the desired behavior was still one-dimensional (i.e., axial stiffness only in the direction of the transverse post-tensioning) although the stress and strain output were two-dimensional. Therefore, the modulus of elasticity for the membrane was set equal to that of steel in the transverse direction (i.e., the direction of the tendons), and set to nearly zero for the shear and longitudinal axial stiffnesses.

6.2.6 Summary of Kelvin Chain Approximation in Finite Element Implementation

The time-dependent algorithm was implemented in Abaqus using user-defined subroutines *uexpan* and *umat*. All subroutines were written in FORTRAN, and were compiled into the finite element code upon job initialization. The *uexpan* subroutine, normally used for defining custom thermal expansion behavior, was used to apply shrinkage strains. Like thermal strains, shrinkage strains cause no change in stress except for those enforced by geometric boundary conditions, and therefore the *uexpan* subroutine can be applied in both scenarios. The *umat* subroutine was used for defining custom constitutive equations for elastic and creep properties of the concrete, and also for computing the relaxation of the post-tensioning steel.

Assigning material properties for the concrete and post-tensioning steel in Abaqus required the use of the "User Material" definition in the model, which took an arbitrary number of predefined constants and passed them to the *umat* subroutine. For this analysis, the instantaneous modulus E_0 at 28 days and Poisson's ratio were defined for the concrete, and the instantaneous modulus E_s, the yield strength σ_y, and the relaxation factor R (see Eqn. (6-31)) were defined for the steel. Shrinkage was computed by enforcing that the concrete "Expansion" property, typically used for thermal expansion, run the subroutine *uexpan* containing the shrinkage time functions. No other constants were defined for the "Expansion" property. The materials also required a set of solution-dependent state variables, which were specified by the "Depvar" parameter. The minimum number of custom state variables for the concrete creep procedure was $6N+1$, where N was the number of Kelvin elements defining the Kelvin Chain model: these state variables were reserved for the $\boldsymbol{\gamma}_{\mathbf{ci}}^{(n)}$ remaining-creep vectors for each Kelvin Chain element, plus 1 additional variable to define the value of N. Additional parameters such as humidity, day of concrete casting, day of first loading, volume-to-surface ratios, 28-day strength, or any other relevant data that could vary by time or position were also specified as custom state variables for the concrete. For the relaxation of post-tensioning steel, no state variables were needed other than one for the

time at which the tendons were first post-tensioned. "User Material" constants could not be called into the *uexpan* routine, whereas the custom state variables could be called by both *umat* and *uexpan*. Therefore for any constant that was applicable to both creep and shrinkage of concrete, a custom state variable was used for storage.

By default, custom state variables always start with an initial condition of zero, which was correct for the remaining-creep vectors (assuming that the structure was unloaded until analysis began), but was problematic for many other predefined parameters such as volume-to-surface ratio and humidity. Initial values for custom state variables were set for each integration point in the model using the "Initial Conditions" keyword with the "type=solution" option in the input file.

When building the model and applying loading, all analysis steps were static with the total step duration specified in days. An analysis step in Abaqus is defined as a time unit over which the inputs are consistent (though not necessarily constant). For example, one static analysis step would need to be defined for the erection and post-tensioning of each segment, plus an additional step would be defined for the creep and shrinkage time between erection of segments. Each static analysis step was subdivided into a number of time increments summing to the total duration of the analysis step. Time increments were specified such that the assumption that stress changed linearly over any given time increment was approximately valid.

The use of static analysis steps differed from built-in Abaqus creep analysis, by which creep occurs only during a viscoelastic step. The constitutive relations defined in Eqns. (6-21) through (6-26) for concrete creep and Eqn. (6-31) for relaxation account for the inelastic behavior over the step duration as though it were extra static deformation (i.e., by defining the incremental modulus for each step less than the instantaneous modulus), and so the viscoelastic step procedure was not required. The described methodology will always converge in a single

equilibrium iteration regardless of the duration of the time increment, though as explained above, time increments must be small enough such that stress changes approximately linearly with time.

The algorithm used for finite element modeling implementation is presented below:

1. Specify the initial conditions for any pertinent custom state variables at each integration point in the model. Specify material properties for instantaneous modulus E_0 and Poisson's ratio ν.
2. Specify the discrete retardation times t_{ri} used for each of the Kelvin Chain elements (recommendations for t_{ri} provided below). At each integration point, initialize remaining-creep internal vector $\boldsymbol{\gamma}_{\mathbf{ci}}^{(0)}$ for all Kelvin Chain elements.
3. Loop over all time increments:
    a. Loop over all integration points in the model:
        i. Calculate the shrinkage strain vector $\Delta\boldsymbol{\varepsilon}_{\mathbf{sh}}$ and change in thermal strain $\Delta\boldsymbol{\varepsilon}_{\mathbf{T}}$ using shrinkage model and thermal expansion coefficient implemented in user subroutine *uexpan*.
        ii. Begin elastic and creep behavior using user subroutine *umat*:
            1. Define time increment $\Delta t = t_e - t_b$ and $t_{nh} = [(t_e)(t_b)]^{1/2}$, unless $t_b = 0$, in which case let $t_{nh} = t_e/2$. Variables t_b and t_e are the age of the concrete at the beginning and end of the time step, respectively.
            2. The total strain, $\Delta\boldsymbol{\varepsilon}$, is supplied as an input to *umat* by Abaqus, so there is no need to define it.
            3. Apply the Post-Widder theorem from Eqn. (6-16) for each Kelvin Chain element. The k-th derivative of the creep function was directly defined in the code. When computing the derivative of the creep function, any instances of the t_0 variable (for example, in factors that adjust the creep depending on the concrete age at loading) should take the value of t_{nh}.

4. Discretize the compliance spectrum according to Eqn. (6-20).
5. Compute the incremental modulus from Eqn. (6-24).
6. Compute the inelastic strain from Eqn. (6-26). Due to the built-in method of how Abaqus interfaces between the *umat* and *uexpan* subroutines, the changes in shrinkage $\Delta\boldsymbol{\varepsilon}_{\mathbf{sh}}$ and thermal strains $\Delta\boldsymbol{\varepsilon}_{\mathbf{T}}$ in Eqn. (6-26) should be set equal to zero in the *umat* routine. Abaqus automatically subtracts the strain changes computed by *uexpan* from the input total strain change $\Delta\boldsymbol{\varepsilon}$, and thus setting the shrinkage and thermal strains to values other than zero in the *umat* subroutine will double-count their contributions.
7. Compute the change in stress vector from Eqn. (6-25).
8. Update the remaining-creep internal vector from Eqn. (6-21) for each Kelvin Chain element.
9. Compute the Jacobian from Eqn. (6-28).

iii. Simultaneously with creep behavior, begin steel relaxation using subroutine *umat*:

1. Compute the change in tendon stress using Eqn. (6-31).

iv. End user subroutine *umat*.

b. End loop over integration points.

4. End loop over time steps. Analysis is complete.

As discussed in Section 6.2.2, selection of discrete retardation times was required for implementation of the Kelvin Chain approximation. For all models except for the B3 model, retardation times were chosen as 2^{i-21} days, where i represents the integers from 1 to 41. Therefore, the minimum retardation time was $2^{-20} = 9.54\text{x}10^{-7}$ days (approximately 0.08 seconds) and the maximum retardation time was $2^{20} = 1.05\text{x}10^{6}$ days (approximately 2,875 years). All

creep models except the B3 model had reached effectively zero compliance by 2^{-20} days. The total duration of analysis was 150 years, so a maximum retardation time of nearly 2,875 years was deemed sufficient. Exceptions for the Kelvin Chain discretization of the B3 model are presented in Section 6.2.7.1.

For the approximation of the compliance spectrum using the Post-Widder theorem, the *k*-th derivative of the creep function was required as discussed in Section 6.2.2. Typically, the third derivative is adequate for an accurate approximation (Bažant et al., 2009), though higher derivatives tend to produce a better approximation of the creep behavior. For all the considered creep models, the third derivative was found to be sufficiently accurate, as evinced by the validation presented in Section 6.2.8.

6.2.7 Exceptions to Kelvin Chain Model Methodology

Most of the time-dependent models as discussed in Chapter 4 were implemented into the Kelvin Chain methodology from Section 6.2.6 without exceptions. However, implementation of the B3 and CEB/FIP 1978 Model Code time-dependent models required specific alterations to the described method.

6.2.7.1 Alterations to Kelvin Chain Methodology for the B3 Model

All terms in the B3 creep model, described in Eqn. (4-27) in Section 4.4, were discretized into the Kelvin Chain approximation, with the exception of the logarithmic q_4 term for viscous flow. Though the logarithmic function can be approximated as a series of exponentials, application of this deformation directly and explicitly in the analysis is more convenient and accurate.

Considering only the viscous flow term from Eqn. (4-27), the compliance function is

$$J(t,t_0) = q_4 \ln\left(\frac{t}{t_0}\right) \tag{6-32}$$

For use in the finite element analysis, the change in strain $\Delta\varepsilon$ over the time step Δt must be computed for the increment of stress $\Delta\sigma$. Assuming a linear changing stress through the time step, the total change in strain is the sum of the change in strain due to a constant stress σ_0 at the beginning of the time step plus the change in strain due to the linear change in stress $\Delta\sigma$ over the time step with duration Δt. Using the compliance function in Eqn. (6-32), the change in strain between start time t_b and end time t_e due to a constant stress applied at time t_0 is equal to

$$\Delta\varepsilon_{time} = q_4\sigma_0 \ln\left(\frac{t_e}{t_0}\right) - q_4\sigma_0 \ln\left(\frac{t_b}{t_0}\right) = q_4\sigma_0 \ln\left(\frac{t_e}{t_b}\right) \tag{6-33}$$

This change in strain is independent of the initial time at which the constant stress was applied. Therefore the stress history does not need to be saved for this term; for application in the finite element method, the constant stress σ_0 is simply the stress at the beginning of the time step, regardless of the history of how that stress was developed. Over the duration of the time step, the change in strain due to linear change in stress can be computed by the superposition principle:

$$\Delta\varepsilon_{stress} = \int_{t_b}^{t_e} J\left(t_e, t_0\right)\frac{\partial\sigma}{\partial t_0}dt_0 - \int_{t_b}^{t_b} J\left(t_b, t_0\right)\frac{\partial\sigma}{\partial t_0}dt_0 = \int_{t_b}^{t_e} q_4 \ln\left(\frac{t_e}{t_0}\right)\frac{\Delta\sigma}{\Delta t}dt_0 \tag{6-34}$$

Integrating this expression gives

$$\Delta\varepsilon_{stress} = q_4\Delta\sigma\left[1 - \frac{t_b}{\Delta t}\ln\left(\frac{t_e}{t_b}\right)\right] \tag{6-35}$$

All other terms in the B3 creep model, being modeled using the Kelvin Chain approximation, were treated in the manner described in Section 6.2.6. The equations for incremental modulus and inelastic strain unrelated to changes in stress (converted to three-dimensions) were modified by Eqns. (6-33) and (6-35) as follows:

$$E'' = \left[q_1 + q_4\left[1 - \frac{t_b}{\Delta t}\ln\left(\frac{t_e}{t_b}\right)\right] + \sum_{i=1}^{N} A_i\left(1 - \frac{t_{ri}}{\Delta t} + \frac{t_{ri}}{\Delta t}e^{-\Delta t/t_{ri}}\right)\right]^{-1} \tag{6-36}$$

$$\Delta\boldsymbol{\varepsilon}'' = q_4\mathbf{D}^{-1}\boldsymbol{\sigma}_\mathbf{0}\ln\left(\frac{t_e}{t_b}\right) + \sum_{i=1}^{N}\boldsymbol{\gamma}_{\mathbf{ci}}{}^{(n-1)}\left(1-e^{-\Delta t/t_{ri}}\right) + \Delta\boldsymbol{\varepsilon}_{\mathbf{sh}} + \Delta\boldsymbol{\varepsilon}_{\mathbf{T}} \quad (6\text{-}37)$$

where the values for A_i reflect the discretized compliance spectrum of the basic and drying creep terms (q_2, q_3, and q_5). The procedure in Section 6.2.6 was followed as before, except that Eqn. (6-36) replaced Eqn. (6-24) in Step 3.a.ii.5, and Eqn. (6-37) replaced Eqn. (6-26) in Step 3.a.ii.6.

According to Bažant (1982), Poisson's ratio of the concrete strains associated with drying creep (i.e., the q_5 term of the B3 creep model) is approximately equal to zero. Furthermore, in an implementation of the Kelvin Chain methodology (Bažant et al., 2009), the Poisson's ratio for the drying creep term was set equal to zero while the basic creep term used a Poisson's ratio of 0.21. For the implementation in this report, Poisson's ratio for both drying creep and basic creep was set equal to 0.20 as specified in Section 4.2. Because the stresses in the bridge were primarily in the longitudinal direction, and because the total drying creep was typically only a fraction of the basic creep, it was believed that specifying the Poisson's ratio in this manner would not significantly alter the results of the analysis.

Unlike basic creep, drying creep requires the movement of water into and out of the concrete, and much like shrinkage can only start once the moist curing stage has completed. Using the Kelvin Chain methodology, this caused difficulties if load was applied before the end of moist curing. For a physical creep specimen loaded during moist curing, the basic creep would be expected to begin immediately, but the drying creep would be delayed until moist curing had ended. Once moist curing has completed, the specimen will undergo drying creep according to the present stress state at the end of moist curing. The difficulty arose because the Kelvin Chain approximation only uses the change in stress over the time increment, and in general ignores the present stress state.

As an example, a stress $\Delta\sigma$ is applied to a concrete cylinder prior to the end of moist curing, and this stress is held constant. Because no drying creep is expected prior to the end of

moist curing, the Kelvin Chain compliance values A_i associated with the drying creep term will all be equal to zero. Once curing has ended, it would be expected that the cylinder would begin to creep at a rate due to the basic creep plus the drying creep. However, because the drying creep compliance values A_i were all zero when the load was applied, the cylinder will not undergo any drying creep at all. The Kelvin Chain model recalls load history through the use of the internal variables $\boldsymbol{\gamma}_{\mathbf{ci}}^{(n)}$. From inspection of Eqn. (6-26), these variables for the drying creep term will all be equal to zero at end of curing. Thus, the Kelvin Chain model as presented will predict no drying creep for any load applied before curing ends.

A correction for drying creep due to loads applied prior to curing can be performed in two ways. The first method is to check the stress state in the concrete immediately at the end of curing. This stress state should then be applied to update the internal variables $\boldsymbol{\gamma}_{\mathbf{ci}}^{(n)}$ associated with the drying creep term. The other method is to ignore that drying creep does not occur prior to the end of moist curing, and instead specify that any load applied before curing ends is, for purposes of computing the drying creep, applied at end of moist curing. This second method is simpler to introduce into the Kelvin Chain model because it does not require knowledge of the stress history or even the current stress state. The drying creep is computed as normal except that if the geometric mean of the time increment t_{nh} is less than the curing time t_c, then t_{nh} is set equal to t_c only for the drying creep term. Because the drying creep term for the B3 model is asymptotic, the total drying creep at the end of the structure service life will be nearly identical for both methods. For early age behavior, the drying creep behavior is time shifted by the number of days equal to the difference between the application of the load and the curing time, which should have a negligible impact on the behaviors of interest.

For implementation of the B3 drying creep in the finite element model, this second method was used such that drying creep could occur before moist curing had ended. Typically, loads were always applied after curing was complete, except for the case of the midspan closure

pour which was first stressed at an age of 0.25 days despite having a moist curing duration of approximately one week.

This method of computing the B3 drying creep term was consistent with the method implicitly assumed for all other investigated creep models. For each these models, the apparent drying creep was lumped into the total creep strain predictions. This meant that all models except for the B3 implicitly allowed drying creep to occur prior to the end of moist curing, while the modifications introduced in this section for the B3 model explicitly allowed drying creep during moist curing.

As mentioned in Section 6.2.6, the Kelvin Chain discretization of the B3 model was different than that for all other models. From inspection of Eqn. (4-37), the instantaneous strain of the B3 model represented by the q_1 term was only 60% of the expected instantaneous elastic strain assuming the 28-day modulus defined according to ACI-209 (1992). The other 40% of the "instantaneous" deformation observed in typical modulus tests with a finite duration (on the order of 0.01 days, equivalently 15 minutes) was attributed to short-term creep deformation. To capture the short-term creep, the Kelvin Chain discrete retardation times for the B3 model were chosen such that they accounted for times much smaller than what was used for other creep models. Therefore, discrete retardation times for the B3 model were chosen as 4^{i-31} days, where i represents the integers from 1 to 41. The minimum retardation time was $4^{-30} = 8.67\text{x}10^{-19}$ days ($7.5\text{x}10^{-14}$ seconds) and the maximum retardation time was $4^{10} = 1.05\text{x}10^{6}$ days (approximately 2,875 years). Discretization by base 4 was chosen instead of base 2 to increase the range between the maximum and minimum relaxation times while keeping the number of Kelvin Chain elements the same as used for the other models. Tests using a base 10 discretization gave differences between the B3 design equation and the Kelvin Chain approximation up to 10%, which was deemed to be an unacceptable fit. Using base 4 discretization did not sacrifice much accuracy when compared to the base 2 discretization.

For creep models composed of a summation of various terms, such as the B3 model, the Kelvin Chain discretization can be performed separately for each term in the sum. The compliance values for each term can then be summed afterwards to arrive at the total creep compliance. This is a particularly useful technique for separating the drying creep q_5 term from the basic creep terms in the B3 model. The drying creep, unlike the basic creep, is asymptotic. Also, the short-term creep from the B3 model is accounted for solely by the basic creep, and virtually no drying creep occurs for times less than one second (10^{-5} days). Therefore, to simplify computations of the drying creep discretization, Kelvin Chain elements with very short relaxation times (less than $4^{-10} = 9.54\text{x}10^{-7}$ days) were specified with zero drying creep compliance. For large relaxation times, floating point errors due to the particular form of the B3 drying creep term become problematic. For Kelvin Chain elements with $(kt_r + t_0 - t_c)/\tau_{sh} \geq 1.18\text{x}10^5$, where k is the number of derivatives used in the Post-Widder theorem and t_r is the relaxation time of the Kelvin Chain element, a hyperbolic cosine term in the denominator was greater than allowed by double precision and caused an illegal floating point operation. Therefore, for all such relaxation times, the drying creep compliance for the Kelvin Chain element was set equal to zero. The above floating point errors were only encountered with the B3 model, and compliance values for all other models were computed for all specified relaxation times.

6.2.7.2 Alterations to Kelvin Chain Methodology for the CEB/FIP 1978 Model Code

The creep model from the 1978 CEB/FIP Model Code is presented in Section 4.5. Some modifications to the procedure were necessary to account for the instantaneous partially irreversible deformation from the $\beta_a(t_0)$ term. Furthermore, the graphical method needed to be numerically approximated to interface with the computational method.

The instantaneous deformation associated with the $\beta_a(t_0)$ term as given in Eqn. (4-50) was not approximated by a Kelvin Chain model, and was instead directly specified as a change in the incremental modulus:

$$E'' = \left[\frac{1}{1.25\left(E_c\right)_{t0}} + \frac{\beta_a\left(t_0\right)}{\left(E_c\right)_{28}} + \sum_{i=1}^{N} A_i \left(1 - \frac{t_{ri}}{\Delta t} + \frac{t_{ri}}{\Delta t} e^{-\Delta t / t_{ri}} \right) \right]^{-1} \tag{6-38}$$

The Kelvin Chain compliance values A_i were derived from only the long-term recoverable $\varphi_d\beta_d(t-t_0)$ and irrecoverable $\varphi_{f1}\varphi_{f2}[\beta_f(t)-\beta_f(t_0)]$ terms present in Eqn. (4-48). The factor of 1.25 modifying the elastic modulus at time t_0 was applied in accordance with the commentary in Section e-1.3 of the 1978 CEB/FIP Model Code, as discussed in Section 4.5.1. For the 1978 CEB/FIP Model Code analysis, Eqn. (6-38) replaced Eqn. (6-24) in Step 3.a.ii.5 of the procedure discussed in Section 6.2.6.

Each of the plots in Figures 4.2 through 4.6 was approximated numerically for input into the finite element model. The $\beta_d(t-t_0)$ recoverable deformation in Figure 4.2 was approximated using an equation of the following form:

$$\beta_d\left(t-t_0\right) = \sum_{i=1}^{3} C_i \frac{\left(t-t_0\right)^{n_i}}{\left(t-t_0+m\right)^{n_i}} \tag{6-39}$$

where C_i and m were constants that were fit to the given curve, and n_1, n_2 and n_3 were chosen as 0.1, 1, and 10, respectively. Constants C_i were constrained such that $\Sigma C_i = 1$ so that the asymptotic strain approached at infinite time by the approximate curve and Model Code curve were identical. The form of the approximation equation was chosen due to its similarity to the prescribed creep and shrinkage equations from the 1990 CEB/FIP Model Code as discussed in Section 4.6. Constants C_i and m were computed iteratively to minimize the sum of the squared errors between the provided and approximate curves. This method did not guarantee the best possible fit to the provided curve, as the problem was ill-conditioned and could stabilize about local minima depending on the initial assumptions for C_i and m. For the chosen coefficients given in Table 6.3, the relative error between the provided and approximated curves was always less than 3%, so the fit was assumed to be adequate.

The flow shape factor φ_{f2} shown in Figure 4.3 was linear with the logarithm of the effective thickness h (related to the volume-to-surface ratio as defined in Eqn. (4-51)) specified in millimeters. Therefore, this factor was approximated as

$$\varphi_{f2} = a + b \ln h \tag{6-40}$$

where a and b were coefficients computed by linear regression to be equal to 2.677 and −0.212, respectively. Relative errors between the provided values and the approximate curve for φ_{f2} were all less than 1%.

Each provided line for the $\beta_f(t)$ flow deformation in Figure 4.4 was approximated by the form

$$\beta_f(t) = \sum_{i=1}^{3} C_i \frac{(t)^{n_i}}{(t+m)^{n_i}} \tag{6-41}$$

where C_i and m were constants that were fit to the given curve, and n_1, n_2 and n_3 were chosen as 0.1, 1, and 10, respectively. Constants C_i were constrained such that $\Sigma C_i = 1$ so that the asymptotic strain approached at infinite time by the approximate and Model Code curves were identical. Constants C_i and m were computed independently for each of the six curves (h = 50, 100, 200, 400, 800, and 1,600 mm) using the same iterative procedure as used for approximating $\beta_d(t - t_0)$. These approximations were again not guaranteed to converge to the best possible fit, but were found to provide relative errors below 3%. The chosen coefficients are summarized in Table 6.3. For values of h between those specified in Table 6.3, these coefficients were computed by linear interpolation on $\ln(h)$.

The shrinkage shape factor ε_{s2} in Figure 4.5 was approximated by an equation of the form

$$\varepsilon_{s2} = \frac{a}{(h+b)^n} + c \tag{6-42}$$

where a, b, c, and n were constants chosen to be equal to 4.037, 1.621, 0.569, and 0.468, respectively, in order to minimize the sum of squared errors between the approximate and

provided curves. The relative error between the approximate and specified values was always less than 2%.

The shrinkage function $\beta_s(t)$ in Figure 4.6 was approximated by

$$\beta_s(t) = \frac{t^n}{(t+m)^n} \tag{6-43}$$

where *m* and *n* were iteratively computed to minimize the sum of squared errors between the provided and approximate curves. These values were computed independently for each specified effective thickness (h = 50, 100, 200, 400, 800, and 1,600 mm) and are listed in Table 6.4. For thicknesses between the specified values, *m* and *n* were computed using linear interpolation on ln(h). Relative errors for thickness less than 200 mm (7.9 in.) were small, typically less than 1%. However, for large effective thicknesses of 800 mm (31.5 in.) and 1,600 mm (63.0 in.), the approximation function from Eqn. (6-43) did not provide a good fit for times around 4,000 to 10,000 days (11.0 to 27.4 years), with relative errors up to nearly 10%.

For the St. Anthony Falls Bridge, most typical *V*/*S* ratios were around 200 mm (8.0 in.), which translated to an effective thickness h of approximately 600 mm (23.6 in.). The effective thickness was even larger in the bottom flange near the piers, the large pier diaphragms, and the piers. Thus, the adopted approximation function was expected to have discrepancies with the graphical plots in the Model Code. However, this was considered acceptable. The nature of the poor fit was because, at late concrete ages over 4,000 days (11 years) for high values of effective thickness, the graphical method in the 1978 CEB/FIP Model Code reached the asymptote faster than the approximation function. However, both the approximate and graphical methods would limit to the same value, and would thus eventually converge to the same ultimate shrinkage strain for a sufficiently long analysis duration (e.g., longer than 100 years). Furthermore, the nearly 10% error in shrinkage estimates at over 4,000 days (11.0 years) would have only a minor impact on post-tensioning losses and creep strains, as these behaviors would have nearly reached the

asymptotic strain values by this time. Therefore, it was presumed that for sufficiently long analysis periods, the differences in the ultimate long-term structural behavior would not be significantly affected by the error in the shrinkage approximation.

Variables from Table 4.10 were computed using linear interpolation on humidity. The concrete strength with time was computed from Figure 4.1 by linear interpolation on ln(t) after correcting for temperature and cement type.

6.2.8 Validation of Kelvin Chain Approximation

6.2.8.1 Discretization of Kelvin Chain

Each creep model presented in Chapter 4 was approximated as an equivalent Kelvin Chain model using the discretization process and the Post-Widder theorem discussed in Section 6.2.6 with exceptions to specific methodologies presented in Section 6.2.7.

The discretized compliance values A_i for the Kelvin Chain elements computed by the Post-Widder theorem are shown in Figures 6.6 through 6.11. Different loading times of 10 and 100 days are plotted to show the effects of concrete age on the compliance values. Material and environmental properties for each plot were identical to those for the superstructure concrete as described in Chapter 4, with the exceptions that the volume-to-surface ratio was always set to 8.0 in. (203 mm) to reflect an average V/S from the superstructure, all reinforcement ratios were zero, and the curing duration was set equal to 1 day.

The AASHTO (2010) compliance spectrum is shown in Figure 6.6. This compliance spectrum was a single peak centered about 28 days. For low retardation times, the compliance spectrum limited to zero, as expected. Compliance values also limited to zero for very high retardation times due to the asymptotic behavior of the AASHTO creep provisions. The entire range of retardation times from 2^{-20} to 2^{20} days was clearly unnecessary for capturing the complete behavior of this creep model, but the full spectrum was kept for computational consistency among the models.

The compliance spectrum for the ACI-209 (1992) creep model is shown in Figure 6.7. The ACI and AASHTO spectrums were similar, though the ACI single peak was much wider and centered about 64 days. Both high and low retardation times limited to zero compliance as expected for asymptotic models.

The basic creep, drying creep, and total creep spectra of the B3 creep model are shown in Figure 6.8. The basic creep values did not include the q_4 logarithmic term, as this was not discretized using the Post-Widder theorem but was instead entered into the model explicitly as documented in Section 6.2.7.1. The peak for the basic creep compliance was much lower than the peaks of either the AASHTO or ACI-209 models, but this was likely because the B3 basic creep compliance spectrum was so wide. Even for retardation times as short as 10^{-7} days (less than 0.01 seconds), the compliance value was significant. At high retardation times, the compliance spectrum asymptotically approached a value greater than zero (approximately $4.5\text{x}10^{-10}$ psi^{-1} ($6.5\text{x}10^{-8}$ MPa^{-1})), though the scale of this plot masks this fact. Combined with the q_4 logarithmic term, it was apparent that the B3 basic creep would continue forever. The B3 drying creep spectrum was entirely different from the B3 basic creep, in that the drying creep spectrum was asymptotic to zero for very high retardation times and did not capture short-term creep behavior. The drying creep term peaked quickly; if the discretization interval were too large (for example, discretization by base 10 instead of base 2 or 4), the peak would likely be inadequately captured, leading to inaccurate calculation of the drying creep. Unlike the basic creep, the drying creep showed only slight dependence on the loading age. The total creep spectrum was the sum of the basic and drying creep spectrums.

The creep compliance spectrum of the 1978 CEB/FIP Model Code is shown in Figure 6.9. For early ages of loading, the spectrum appeared to be the summation of two bell-shaped peaks. At later ages of loading, the spectrum appeared as a single peak, much like the AASHTO and ACI-209 models. The peak compliance values of the 1978 Model Code creep model reached

levels similar to those shown for the B3 drying creep. The spectrum limited to zero for both very high and low retardation times, as expected for asymptotic models.

The CEB/FIP 1990 Model Code compliance spectrum is plotted in Figure 6.10. This creep spectrum more closely resembled the AASHTO and ACI-209 spectrums than it did the 1978 Model Code spectrum. The 1990 Model Code spectrum contained a single peak that scaled with the loading age. As expected, the spectrum limited to zero for high and low retardation times.

The GL2000 compliance spectrum is shown in Figure 6.11. The spectrum was clearly composed of two distinct bell-shaped curves. Only the first peak appeared to be significantly dependent on the loading age, which was analogous to the loading age dependence of the B3 model whereby only the basic creep compliance changed with age. At low retardation times, the spectrum limited to zero as expected. For high retardation times, the spectrum had not yet limited to zero. The form of the GL2000 creep model guarantees the existence of an asymptotic creep strain, and therefore for infinitely large retardation times, the compliance will limit to zero. However, the creep function will not reach 95% of the asymptotic strain value until after nearly 10^7 days of loading, or over 27,000 years. For practical structural lives less than 10^5 days, the GL2000 model appears to behave linearly with log time, much like the B3 model.

6.2.8.2 Comparison between Creep Provisions and Kelvin Chain Approximations

The total creep compliance curve for concrete loaded at 10 days was computed for each discussed creep model using both the Kelvin Chain model approximation and the explicit formulas as defined in Chapter 4. Comparisons between the specified formulas and their Kelvin Chain approximations are shown in Figure 6.12. Values for material and environmental properties for each creep model were identical to those used to derive the compliance spectrums in Section 6.2.8.1. Maximum relative errors between the Kelvin Chain approximation and the literature creep equations were as follows:

- AASHTO = 3.9% error at approximately 12 days after loading
- ACI-209 = 3.2% error at approximately 7 days after loading
- B3 = 1.0% immediately upon loading
- 1978 CEB/FIP Model Code = 3.0% at approximately 30 days after loading
- 1990 CEB/FIP Model Code = 2.6% at approximately 50 days after loading
- GL2000 = 2.5% at approximately 1 day after loading

For long-term predictions, the relative error at 55,000 days (approximately 150 years) between each Kelvin Chain approximation and its respective creep equation was always less than 1%. Therefore, it was concluded that the Kelvin Chain approximation accurately modeled the creep behavior for all the considered creep models.

6.2.8.3 Validation of Total Time-Dependent Strains and Boltzmann Superposition Principle

To ensure that the total time-dependent strains including both shrinkage and creep were properly computed by the finite element analysis, and furthermore that the Kelvin Chain approximation properly incorporated the Boltzmann superposition principle, a sample finite element model was defined. The model consisted of a plain concrete cylinder with length of 11 in. (280 mm) and diameter of 4 in. (102 mm) subject to uniaxial stress. Compression equal to 1,900 psi (13 MPa) was applied to the cylinder at an age of 10 days and held constant until an age of 100 days, at which time the stress was increased to 2,900 psi (20 MPa) and held for the remainder of the analysis. Material properties of the cylinder were typical for that from the superstructure concrete as discussed in Chapter 4, except that the volume-to-surface ratio of the cylinder was set to 1.0 in. (25 mm), the reinforcement ratios were equal to zero, and the curing duration was 1 day. The analysis was conducted until an age of 55,010 days (equivalently 150 years of loading). Shrinkage strains were computed as relative strains since the beginning of the analysis at 10 days.

Total longitudinal strains were computed from the Kelvin Chain approximation implemented in the finite element model and compared with hand-calculated estimates using the superposition principle and the time-dependent models from the literature. The total strains computed using these two methods are compared in Figure 6.13. The Kelvin Chain approximation as implemented in the finite element model returned nearly identical total strains to the hand calculations, meaning that the Kelvin Chain model implemented in the finite element analysis correctly accounted for shrinkage and the Boltzmann superposition principle.

6.3 Modeling Time-Dependent Behavior of Composite Materials

For analyzing the time-dependent behavior of large and complex post-tensioned concrete structures such as the St. Anthony Falls Bridge, explicitly modeling both the steel and concrete materials is undesirable. For purposes of finite element modeling, defining elements for each individual steel rebar increases the time to construct the model and the time to analyze the results. However, the presence of reinforcement impacts the time-dependent behavior of the steel-concrete composite, and consequently cannot be ignored. As the concrete deforms due to creep and shrinkage, stress is redistributed to the steel, reducing the overall long-term deformation of the structure. Modeling the concrete and reinforcement together as a composite material simplifies the analysis.

The behavior of composite materials has been covered extensively. The elastic moduli for unidirectional fiber composite materials was derived by Hill (1964) and also Hashin and Rosen (1964). For the viscoelastic behavior of composite materials, stress analysis using Laplace transforms and the correspondence principle was covered by Schapery (1967), while the derivation of the complex moduli for fiber composites was derived by Hashin (1970). A review of elasticity, thermal expansion, shrinkage/swelling, and viscoelasticity of composites was later provided by Hashin (1983).

The viscoelastic behavior for fiber composites reinforced in multiple directions is more complicated than the unidirectional cases considered in the aforementioned literature, but can be simplified greatly by a series of discerning assumptions. The purpose of this section is to develop an approximate method for analyzing the viscoelastic behavior of multidirectional reinforced concrete.

First, the effects of mild steel on the total strains and stresses in the composite material will be discussed to show that it is necessary to account for the different materials. Then, the rate-type creep methodology for plain concrete by Bažant and Prasannan (1989a, 1989b) will be expanded to include the effects of the concrete-steel composite. Finally, several test cases will be presented to verify the accuracy of the composite finite element models.

6.3.1 Effects of Mild Steel on Concrete Time-Dependent Behavior

Accounting for mild steel by means of a transformed (composite) elastic modulus was deemed to be unacceptable for modeling creep behavior. As the concrete continues to deform due to time-dependent behavior, the mild steel must also deform due to strain compatibility. However, unlike the concrete strains which occur without a change in stress, the strains in the steel (assuming no relaxation or thermal strains) are always accompanied by a change in steel stress. This force in the steel must be balanced out by an equal and opposite force in the concrete matrix. To illustrate this, consider a composite section of concrete and steel that is loaded instantaneously with some force. Both materials deform elastically in the manner that would be expected for composite materials. However, the concrete continues to deform after initial loading, and this deformation increases the stress in the steel. The stress in the concrete must be reduced to maintain equilibrium, and the end result is that the applied stress is gradually transferred from the concrete to the steel.

For simple finite element models, including the mild steel explicitly may be feasible. However, for a model with the scope of the St. Anthony Falls Bridge, explicitly modeling

individual reinforcing bars was not feasible. First it was investigated if the effects of the mild steel were worth considering in the modeling process, that is, if their impact would be larger than the inherent inaccuracies of the time-dependent prediction process.

The uniaxial behavior of the concrete-steel composite was investigated using finite element models of the cylinder shown in Figure 6.14 with different reinforcement ratios. The modeled 4-in. (100-mm) diameter by 11-in. (280-mm) length cylinder was axially loaded with 2,000 psi (13.8 MPa) at 28 days. The load was held constant for the entire duration of the analysis equal to 150 years. Eight mild steel reinforcement bars were placed axially in a circumferential pattern with 1.0 in. (25 mm) from the exterior surface of the cylinder to the center of the bars. The area of the mild steel reinforcement was adjusted to achieve reinforcement ratios ρ of 0, 0.003, and 0.01 in the axial direction, chosen to roughly bound the longitudinal mild steel reinforcement ratios present in the St. Anthony Falls Bridge as shown in Tables 4.2 through 4.5. Creep and shrinkage were computed using the GL2000 time-dependent model; other models were assumed to provide similar findings. Relevant material and environmental parameters included:

- 28-day concrete strength of 6.5 ksi (44.8 MPa)
- GL2000 aging curve with Type I cement
- Mild steel elastic modulus of 29,000 ksi (200 GPa)
- Ambient temperature equal to 20°C (68°F)
- 60% relative humidity
- Volume-to-surface ratio of 1.0 in. (25 mm)
- Moist curing duration of 1 day

Figure 6.15 shows the total strain in each of the reinforced cylinders. Figure 6.16 shows the stress in the concrete for each of the cylinders, keeping in mind that the applied stress for each model was a constant 2,000 psi (13.8 MPa). Figure 6.17 shows the stress in the mild steel.

The inclusion of the mild steel had a significant impact on the time-dependent behavior of the cylinder. Furthermore, the reduction in total strains was not simply equal to the ratio of the unreinforced cylinder elastic modulus and the composite elastic modulus. In fact, the ratio of the strains in the 1% reinforced cylinder to the strains in the unreinforced cylinder was 94.2% immediately upon loading, whereas the same ratio decreased to 85.2% after 55,000 days of loading. Not only did the reinforcement increase the transformed elastic modulus of the cylinder, but it also progressively decreased the stress in the concrete as shown in Figure 6.16. Furthermore, the development of stress in the reinforcement over time was significant, nearly reaching 40 ksi (276 MPa) by 55,000 days as shown in Figure 6.17. Greater reinforcement ratios would result in lower steel stresses due to the reduced creep and shrinkage.

6.3.2 Adjustment of Kelvin Chain Creep Methodology for Composites

To account for the effects of mild steel reinforcement on the time-dependent behavior of the concrete-steel composite, a novel modification of the Kelvin Chain model was proposed. Assumptions used in the development of the model included the following: (1) stress changes over a given time step are linear with time; (2) creep compliance functions are known for all viscoelastic materials in the composite; (3) the steel reinforcement carries only axial stress and has much higher elastic modulus than the concrete matrix; (4) all viscoelastic materials follow linear viscoelasticity and the Boltzmann superposition principle; and (5) no damage or yielding is present in either the steel or concrete.

The derived methodology was approximate, not only in the fitting of the creep compliance function with the Kelvin Chain model, but also in the composite formulation. The reinforcement was treated specifically as a one-dimensional entity, meaning that it could only carry axial stress. Any effects of differing Poisson's ratio between the concrete and the reinforcement and any contribution of the reinforcement to composite shear stiffness were neglected. Such effects are discussed by Hill (1964) and Hashin and Rosen (1964).

For the following derivation, the steel and concrete are labeled with subscripts *s* and *c*, respectively. A single differential element of material over which the steel was uniformly distributed through the volume was considered. Modeling of reinforced concrete as representative volume elements (RVEs) incorporating both the mild reinforcement bars and the concrete greatly simplifies finite element analysis. The benefits of this method primarily manifest in simplifying the model construction, in that individual elements do not need to be defined for reinforcing steel. This also positively impacts computational efficiency by reducing the degrees of freedom in the analysis.

Though this derivation assumes a single differential element of material over which the reinforcement is uniformly distributed, in the general case the reinforced ratio can be set on an element-by-element basis. The presented derivation begins with the one-dimensional case, followed by generalization to three-dimensions.

The force balance equation for equilibrium is

$$F_c + F_s = F_{ext} \tag{6-44}$$

where F_c is the force held by the concrete, F_s is the force held by the steel, and F_{ext} is the external force. Converting the force balance to stresses gives

$$\sigma_c A_c + \sigma_s A_s = \sigma_{ext} A_g \tag{6-45}$$

where σ_c, σ_s, and σ_{ext} are the concrete stress, steel stress, and external traction, respectively, and A_c, A_s, and A_g are the concrete, steel, and gross areas, respectively. The gross area is the sum of the concrete and steel areas, assuming no voids or other materials. The reinforcement ratio ρ is defined as

$$\rho = A_s / A_g \tag{6-46}$$

Substituting the reinforcement ratio into Eqn. (6-45) and solving for the concrete stress gives

$$\sigma_c (1-\rho) + \sigma_s \rho = \sigma_{ext} \tag{6-47}$$

$$\sigma_c = \frac{\sigma_{ext} - \sigma_s \rho}{(1-\rho)} \tag{6-48}$$

This equation can be used to compute stresses in the concrete given the stresses in the steel and the external loads.

Only the concrete stress, and not the total external stress, is applied to compute the strains using the compliance function $J(t,t_0)$ of the viscoelastic concrete. As in Section 6.2, the time-dependent behavior of the concrete follows the Kelvin Chain model, such that

$$\varepsilon(\xi) = \sigma_c \left(\frac{1}{E_0} + \sum_{i=1}^{N} A_i \left(1 - e^{-\xi/t_{ri}}\right) \right) + \varepsilon_{sh} + \varepsilon_T \tag{6-49}$$

The strain $\varepsilon(\xi)$ is the strain for the full composite material (due to strain compatibility), but the stress σ_c represents only the stress in the concrete which is dependent upon the steel stress and external traction as described in Eqn. (6-48). Shrinkage strains are represented by ε_{sh} and concrete thermal strains are ε_T; both are computed assuming that the concrete is unrestrained by geometry or the presence of mild steel (i.e., computed for the non-composite concrete). Though computed independently of the stress state, these strains may cause internal stresses in the concrete and steel due to strain compatibility. This occurs when, for instance, the steel and concrete do not undergo equivalent thermal expansion or shrinkage.

Similar to the development of the non-composite stress-strain relationship, the total strain change over a time step is the sum of the change in strain due to change in stress, and the change in strain due to time. Following an identical derivation to the one documented in Appendix A, the change in strain is equal to

$$\begin{aligned} \Delta\varepsilon = \Delta\sigma_c \left[\frac{1}{E_0} + \sum_{i=1}^{N} A_i \left(1 - \frac{t_{ri}}{\Delta t} + \frac{t_{ri}}{\Delta t} e^{-\Delta t/t_{ri}} \right) \right] \\ + \sum_{i=1}^{N} \gamma_{ci}{}^{(n-1)} \left(1 - e^{-\Delta t/t_{ri}}\right) + \Delta\varepsilon_{sh} + \Delta\varepsilon_T \end{aligned} \tag{6-50}$$

The finite element model does not record the concrete or steel stresses. The stresses on each element represent the external traction. Therefore, the change in concrete stress must be converted to an equivalent change in external traction using Eqn. (6-48):

$$\Delta\varepsilon = \left[\frac{\Delta\sigma_{ext} - \Delta\sigma_s\rho}{(1-\rho)}\right]\left[\frac{1}{E_0} + \sum_{i=1}^{N} A_i\left(1 - \frac{t_{ri}}{\Delta t} + \frac{t_{ri}}{\Delta t}e^{-\Delta t/t_{ri}}\right)\right] + \sum_{i=1}^{N}\gamma_{ci}{}^{(n-1)}\left(1 - e^{-\Delta t/t_{ri}}\right) + \Delta\varepsilon_{sh} + \Delta\varepsilon_T \tag{6-51}$$

Because the steel is assumed to be perfectly elastic, the change in steel stress is

$$\Delta\sigma_s = E_s\left(\Delta\varepsilon - \Delta\varepsilon_{st}\right) \tag{6-52}$$

where E_s is the modulus of elasticity of steel, and $\Delta\varepsilon_{st}$ is the change in stress-independent strain of the steel (e.g., unrestrained thermal strains). Substituting Eqn. (6-52) into Eqn. (6-51) gives:

$$\Delta\varepsilon = \left[\frac{\Delta\sigma_{ext} - E_s\rho(\Delta\varepsilon - \Delta\varepsilon_{st})}{(1-\rho)}\right]\left[\frac{1}{E_0} + \sum_{i=1}^{N} A_i\left(1 - \frac{t_{ri}}{\Delta t} + \frac{t_{ri}}{\Delta t}e^{-\Delta t/t_{ri}}\right)\right] + \sum_{i=1}^{N}\gamma_{ci}{}^{(n-1)}\left(1 - e^{-\Delta t/t_{ri}}\right) + \Delta\varepsilon_{sh} + \Delta\varepsilon_T \tag{6-53}$$

For input into the finite element model, the stress tensor σ_{ext} must be computed from the change in strain. This is facilitated by defining the incremental modulus E'' of the composite material, which can be derived by rearranging Eqn. (6-53). To simplify the algebra, some terms are redefined as follows:

$$E_c'' = \left[\frac{1}{E_0} + \sum_{i=1}^{N} A_i\left(1 - \frac{t_{ri}}{\Delta t} + \frac{t_{ri}}{\Delta t}e^{-\Delta t/t_{ri}}\right)\right]^{-1} \tag{6-54}$$

$$\Delta\varepsilon_c'' = \sum_{i=1}^{N}\gamma_{ci}{}^{(n-1)}\left(1 - e^{-\Delta t/t_{ri}}\right) + \Delta\varepsilon_{sh} + \Delta\varepsilon_T \tag{6-55}$$

where E_c'' is the incremental modulus of the non-composite concrete, and $\Delta\varepsilon_c''$ is the inelastic strain of the non-composite concrete. Substituting these terms in Eqn. (6-53) provides

$$\Delta\varepsilon = \frac{1}{E_c''}\left[\frac{\Delta\sigma_{ext} - E_s\rho\left(\Delta\varepsilon - \Delta\varepsilon_{st}\right)}{\left(1-\rho\right)}\right] + \Delta\varepsilon_c'' \tag{6-56}$$

Solving Eqn. (6-56) for the change in stress $\Delta\sigma_{ext}$:

$$\Delta\sigma_{ext} = \left(E_c''\left(1-\rho\right) + E_s\rho\right)\Delta\varepsilon - E_c''\left(1-\rho\right)\Delta\varepsilon_c'' - E_s\rho\Delta\varepsilon_{st} \tag{6-57}$$

The composite incremental modulus can thus be defined as

$$E'' = E_c''\left(1-\rho\right) + E_s\rho \tag{6-58}$$

which, due to the nature of the adopted rate-type formulation for viscoelastic behavior, conveniently shares an identical form to the so-called law of mixtures which describes the elastic behavior of composite materials assuming equal Poisson's ratio between the matrix and the fiber (Hashin and Rosen, 1964). In the general case where fiber and matrix Poisson's ratios are not equal and the three-dimensional behavior of the fibers is considered, the total composite modulus is larger than the modulus specified by the law of mixtures as presented in Eqn. (6-58) (Hill, 1964). For typical fiber composites in which the reinforcement is much stiffer than the matrix, as is the case for reinforced concrete, this increase in the composite modulus is negligible (Hashin, 1983).

Generalizing the composite equations to three dimensions can be performed in the same manner as was done for the concrete-only material model. Thus, the equations required for input into the finite element model include:

$$E_c'' = \left[\frac{1}{E_0} + \sum_{i=1}^{N} A_i\left(1 - \frac{t_{ri}}{\Delta t} + \frac{t_{ri}}{\Delta t}e^{-\Delta t/t_{ri}}\right)\right]^{-1} \tag{6-59}$$

$$\boldsymbol{\gamma}_{\mathbf{ci}}{}^{(n)} = \boldsymbol{\gamma}_{\mathbf{ci}}{}^{(n-1)}e^{-\Delta t/t_{ri}} + \frac{A_i\mathbf{D}_\mathbf{c}^{-1}\Delta\boldsymbol{\sigma}_\mathbf{c}}{\Delta t}\left(t_{ri} - t_{ri}e^{-\Delta t/t_{ri}}\right) \tag{6-60}$$

$$\Delta\boldsymbol{\varepsilon}_\mathbf{c}'' = \sum_{i=1}^{N}\boldsymbol{\gamma}_{\mathbf{ci}}{}^{(n-1)}\left(1 - e^{-\Delta t/t_{ri}}\right) + \Delta\boldsymbol{\varepsilon}_\mathbf{sh} + \Delta\boldsymbol{\varepsilon}_\mathbf{T} \tag{6-61}$$

$$\Delta\boldsymbol{\sigma}_\mathbf{ext} = E_c''\left(\mathbf{I} - \boldsymbol{\rho}\right)\mathbf{D}_\mathbf{c}\left(\Delta\boldsymbol{\varepsilon} - \Delta\boldsymbol{\varepsilon}_\mathbf{c}''\right) + E_s\boldsymbol{\rho}\mathbf{D}_\mathbf{s}\left(\Delta\boldsymbol{\varepsilon} - \Delta\boldsymbol{\varepsilon}_\mathbf{st}\right) \tag{6-62}$$

where $\mathbf{D_c}$ and $\mathbf{D_s}$ are the constitutive material matrices for concrete and steel, respectively, $\mathbf{I}$ is the 6x6 identity matrix, and $\boldsymbol{\rho}$ is a 6x6 diagonal matrix containing the different reinforcement ratios for each direction. The reinforcement ratios for the shear directions (indices 4, 5, and 6) should always be set equal to zero. The concrete material matrix is assumed to be isotropic as given in Eqn. (6-22). Assuming that the steel only provides axial stiffness, $\mathbf{D_s}$ is equal to

$$\mathbf{D_s} = \begin{bmatrix} 1 & & & & & \\ & 1 & & & 0 & \\ & & 1 & & & \\ & & & 0 & & \\ & 0 & & & 0 & \\ & & & & & 0 \end{bmatrix} \tag{6-63}$$

Similar to the plain concrete case, the incremental modulus for the concrete can be defined as a function of time t_{nh} at the geometric mean of the current time step. The Jacobian for the composite formulation is equal to

$$\mathbf{j} = \frac{\partial \Delta \boldsymbol{\sigma}}{\partial \Delta \boldsymbol{\varepsilon}} = E_c''\left(\mathbf{I} - \boldsymbol{\rho}\right)\mathbf{D_c} + E_s \boldsymbol{\rho} \mathbf{D_s} \tag{6-64}$$

which is independent of stress and strain, meaning that the finite element analysis will still always converge in a single equilibrium iteration.

6.3.3 Summary of Kelvin Chain Approximation for Composite Materials

To account for the behavior of the composite material, the finite element implementation of the Kelvin Chain model for plain concrete was altered. First, all material behaviors, including shrinkage, thermal strains, elastic deformation, and creep, were implemented using the FORTRAN subroutine *umat*. This was necessary because the stresses in the concrete were no longer independent of shrinkage and thermal strains.

Most of the procedures followed for the plain concrete Kelvin Chain method were unchanged, including the need to define internal variables for remaining creep, the use of static time step analysis, and the need to keep time increments small enough such that stresses changed

approximately linearly with time. Twelve extra internal variables were required to specify the concrete and steel stresses at each integration point, as by default the finite element analysis only computed the composite stresses.

The methodology for the Kelvin Chain model as modified for composite materials was as follows:

1. Specify the initial conditions for any pertinent custom state variables at each integration point in the model. Typically, this will include variables that may change with time, such as humidity and temperature, as well as relevant constants needed for the creep and shrinkage models, such as volume-to-surface ratios and concrete composition and strength. Specify material properties for instantaneous concrete modulus E_0, concrete Poisson's ratio ν, and steel modulus E_s. At each integration point, specify the reinforcement ratios in each direction.
2. Specify the discrete retardation times used for each of the Kelvin Chain elements. Initialize remaining-creep internal vector $\boldsymbol{\gamma}_{\mathbf{ci}}^{(0)}$ for all Kelvin Chain elements. Also initialize internal variables σ_{ci} and σ_{si} for the six components of both the concrete and steel stresses at each integration point.
3. Loop over all time increments:
    a. Loop over all integration points in the model:
        i. Calculate the unrestrained shrinkage strain vector $\Delta\boldsymbol{\varepsilon}_{\mathbf{sh}}$ and unrestrained concrete thermal strain vector $\Delta\boldsymbol{\varepsilon}_{\mathbf{T}}$ in user subroutine *umat*.
        ii. Begin elastic and creep behavior using user subroutine *umat*:
            1. Define time increment $\Delta t = t_e - t_b$ and $t_{nh} = [(t_e)(t_b)]^{1/2}$, unless $t_b = 0$, in which case let $t_{nh} = t_e/2$. Variables t_b and t_e are the age of the concrete at the beginning and end of the time step, respectively.
            2. Apply the Post-Widder theorem from Eqn. (6-16) for each Kelvin Chain element. The *k*-th derivative of the creep function was directly

defined in the code. When computing the derivative of the creep function, any instances of the t_0 variable (for example, in factors that adjust the creep depending on the age of the concrete at loading) should take the value of t_{nh}.

3. Discretize the compliance spectrum according to Eqn. (6-20).
4. Compute the incremental concrete modulus from Eqn. (6-59).
5. Compute the total inelastic strain from Eqn. (6-61).
6. Compute the change in the external (composite) stress vector from Eqn. (6-62).
7. Compute the change in steel stress from Eqn. (6-52).
8. Use the changes in the external (composite) stress and the steel stress to compute the change in concrete stress from Eqn. (6-48).
9. Using the change in concrete stress, update the remaining-creep internal vector from Eqn. (6-60) for each Kelvin Chain element.
10. Compute the Jacobian from Eqn. (6-64).

iii. Simultaneously with creep behavior, begin steel relaxation using subroutine *umat*:

1. Compute the change in tendon stress using Eqn. (6-31).

iv. End user subroutine *umat*.

b. End loop over integration points.

4. End loop over time steps. Analysis is complete.

The definition and discretization of the Kelvin Chain compliance values were identical to the procedures for plain concrete, and the incremental concrete modulus from the composite procedure was identical to the total incremental modulus of the non-composite material. Otherwise, the definitions of the concrete viscoelastic deformation used the concrete stress. Mild

steel was always assumed to have only axial stiffness, and used the material matrix $\mathbf{D}_s$ as defined in Eqn. (6-63).

6.3.4 Validation of Time-Dependent Modeling of Composite Materials

To validate the methodology for modeling composite materials, a number of test scenarios were devised. Models using the plain concrete Kelvin Chain procedure as summarized in Section 6.2.6 and containing truss elements to model the reinforcement were called explicit models. Results from these explicit models were compared to analyses following the procedure in Section 6.3.3 accounting for the composite behavior of the steel and concrete. Because the explicit method used one-dimensional truss elements for the rebar, the volume of the voids in the concrete filled by the embedded rebar were not taken into account (i.e., the volume was double-counted for steel and concrete). The composite methodology automatically accounted for the voids, as the gross volume of the reinforced concrete was correctly defined as the volume of the continuum (C3D20R) finite elements. Thus, the explicit model was expected to undergo smaller deformations than the composite model. For reinforcement ratios less than 0.01, this was assumed to be adequate for validation purposes.

Results from the composite Kelvin Chain method were compared to the finite element model results for the explicitly modeled reinforced concrete cylinder as described in Section 6.3.1 and shown in Figure 6.14. The method was tested for the AASHTO, ACI-209, B3, 1978 and 1990 CEB/FIP Model Codes, and GL2000 concrete creep and shrinkage models. The typical element size for both explicit and composite methodologies was 1.0 in. (25 mm). The explicit model contained 4,407 degrees of freedom (DOFs), whereas the reinforced composite model required only 4,119 DOFs, approximately a 6.5% reduction. Total strain results for each creep and shrinkage model are shown in Figure 6.18. For all cases, the composite FEM method overestimated the total strains as compared to the explicitly modeled cylinder, though relative errors were always less than 1%. Comparisons between the concrete stresses calculated using the

two FEM methods are not shown, but were similar to the strain comparisons and always within 1% relative error.

To test the composite methodology for multiaxial behavior, a simple reinforced cube was constructed. The cube had 10-in. (254-mm) sides and was loaded axially on all sides, such that the applied stresses were 2,000 psi (13.8 MPa), 1,000 psi (6.9 MPa), and 500 psi (3.4 MPa) in compression in the 1-, 2-, and 3-directions, respectively. The load was applied at a concrete age of 28 days and was held constant for the entire 150-year duration of the analysis. Each direction was reinforced differently, such that the reinforcement ratios were 0.005, 0.013, and 0.003 for the 1-, 2-, and 3-directions, respectively. For the explicitly modeled case, eight mild steel reinforcement bars were placed in each axial direction. To achieve the specified reinforcement ratios, bar areas were equal to 0.063 $in.^2$ (41 mm^2) in the 1-direction, 0.164 $in.^2$ (106 mm^2) in the 2-direction, and 0.038 $in.^2$ (24 mm^2) in the 3-direction. For the composite method, the reinforcement ratios for each direction were specified as internal variables at each integration point. The typical element size for both cube models was 1.0 in. (25 mm). The explicit model contained 15,675 DOFs, whereas the composite model had 14,883 DOFs, approximately a 5% reduction. Concrete creep and shrinkage were computed using the GL2000 time-dependent model. Material and environmental parameters included:

- 28-day concrete strength of 6.5 ksi (44.8 MPa)
- GL2000 aging curve with Type I cement
- Mild steel elastic modulus of 29,000 ksi (200 GPa)
- 60% relative humidity
- Volume-to-surface ratio of 1.67 in. (42 mm)

Strain and concrete stress were computed at the centroid of the cube for both the explicit and composite test cases. Figure 6.19 shows a comparison between the two methods. Both

methods returned nearly identical results, with strains always within 6.5 με and stresses within 12 psi (82 kPa), less than 1.5% relative errors for both variables at the end of analysis.

As a final check, the composite method was applied to beam bending. A schematic of the beam model is shown in Figure 6.20. The beam had a 10-in. by 10-in. (254-mm by 254-mm) square cross section, a length of 100 in. (2540 mm), and was fixed at both ends. Reinforcement steel was placed longitudinally near the top and bottom of the beam. The two layers of steel were centered 1 in. (25 mm) below the top surface of the beam and 1 in. (25 mm) above the bottom surface of the beam. Each layer consisted of 5 bars each with area of 0.20 in^2 (130 mm^2), for a total of 1.0 in^2 (650 mm^2) of steel in each layer. To capture the reinforcing steel in the composite model, the bars were effectively smeared throughout the top or bottom 2 in. (51 mm) of the beam. Thus, each layer of steel was smeared over an area of 20 in^2 (12,900 mm^2). For the composite model, the integration points in the top and bottom 2 in. (51 mm) of the beam were therefore assigned a longitudinal reinforcement ratio of 0.048, while all other integration points were assigned no reinforcement. Loading was applied as a distributed load along the top surface of the beam equal to 10 psi (69 kPa), or equivalently 100 lbs/in. (17.5 N/mm). Self weight of the beam was ignored. The load was applied at a concrete age of 28 days and was held constant for the remainder of the 150-year analysis. The typical element size for the beam models was 2.0 in. (50.8 mm). The explicit model contained 21,618 DOFs, while the composite model had 20,088 DOFs, approximately a 7% reduction. Concrete creep and shrinkage behavior was checked using the GL2000 model. Relaxation for steel was ignored. Concrete was assumed to behave identically in tension as in compression (i.e., no cracking), as would be the case assuming the computed deformation was superimposed with axial compression from sufficient prestressing. Material and environmental parameters included:

- 28-day concrete strength of 6.5 ksi (44.8 MPa)
- GL2000 aging curve with Type I cement

- Mild steel elastic modulus of 29,000 ksi (200 GPa)
- 60% relative humidity
- Volume-to-surface ratio of 2.5 in. (64 mm)

The downward deflection (for the entire loading history) and the strain profile (computed after 150 years of creep and shrinkage) at the midspan of the fixed-fixed beam were computed for the explicitly reinforced and composite models. Results from an unreinforced beam were also computed for comparison. In this case, the concrete was still assumed to behave the same in tension and compression as though it were sufficiently prestressed. Figure 6.21 shows the comparison of the midspan deflections (downward positive) and strain profiles (compression positive) for each of the modeled cases. Estimations of downward deflection between the explicitly reinforced and composite model cases were nearly identical, with less than 3% relative errors. Similarly for the midspan strain profile, the composite model predicted strains within 3% of the explicitly modeled case.

The unreinforced test case showed that the presence of reinforcement had a significant impact on the beam behavior, and is plotted in Figure 6.21 to illustrate the potential errors of excluding the mild steel from the viscoelastic analysis. Considering only the instantaneous elastic behavior, the unreinforced concrete beam had only 20% greater midspan deflection than the reinforced concrete beam. However, after 150 years of creep and shrinkage, the unreinforced concrete beam had 56% greater deflection than the reinforced concrete beam. As the concrete continued to deform, the applied stress was gradually transferred away from the concrete and to the steel, and consequently the reinforcement had proportionally more impact on the long-term behavior than the elastic results.

These tests ensured that modeling the concrete as a composite material using the methods described in Section 6.3.3 was functionally equivalent to modeling the reinforcement explicitly, and that inclusion of the composite behavior due to mild steel would have a measurable

difference from results excluding mild steel entirely. Thus for modeling of the I-35W St. Anthony Falls Bridge, the composite Kelvin Chain methodology was adopted.

For the examined implementations, the composite model typically had 5 to 7% fewer degrees of freedom than the models with explicitly modeled steel. However, these cases did not have reinforcing bars embedded within each concrete element. For reinforced structures with three mild steel elements (one per Cartesian direction) embedded in each concrete element, using the proposed composite methodology can reduce the computed degrees of freedom by 25% or more depending on the model geometry and element designation. For example, computation of the viscoelastic behavior of the I-35W St. Anthony Falls Bridge, utilizing a mesh discretization described in Section 6.1.1, would result in at least three mild steel elements per concrete element. In this case, the composite method would require nearly 30% fewer degrees of freedom compared to the explicit method.

6.3.5 Summary and Conclusions

A methodology for analyzing the time-dependent behavior of reinforced concrete as a composite material was developed. This method was intended to account for the composite behavior between the viscoelastic concrete and linear elastic reinforcement, as the presence of steel reinforcement can have a significant impact on reducing the long-term time-dependent behavior of concrete structures. The presented methodology for analyzing the viscoelastic behavior of uncracked reinforced concrete was based on a rate-type formulation of the Kelvin Chain model developed by Bažant and Prasannan (1989b) for plain concrete.

Bažant et al. (2009) showed that the rate-type Kelvin Chain formulation offers a number of computational advantages for time-dependent analysis of homogeneous unreinforced concrete, and the proposed composite methodology has been designed to leverage these benefits. First, the use of the Kelvin Chain model means that this formulation is general for any linear viscoelastic material model as long as a creep compliance function is available and can be approximated as a

summation of exponential functions. Second, the rate-type formulation removes the need to perform the hereditary integral when considering the superposition of loading, which is a significant benefit for problems with complex load histories. Finally, the constitutive equations in the finite element formulation are posed using an incremental modulus which is only dependent on the duration of the time step and not on the current stress or strain. This means that the viscoelastic calculations are handled in an identical manner to linear elastic static analysis. All of these benefits are preserved when extending the Kelvin Chain methodology to the concrete-steel composite by using the law of mixtures to combine the concrete incremental modulus with the steel elastic modulus.

The composite methodology provides distinct advantages to the user. For complex reinforced concrete structures, a significant amount of modeling effort may be saved by replacing explicitly modeled reinforcement with a simple specification of the reinforcement ratio. This in turn reduces the quantity of elements required to accurately model the structure, saving in computational time as well. For reinforced structures with multiple mild steel elements per solid concrete element, this can reduce the necessary degrees of freedom by 25% or more depending on model geometry. Computational stability and mesh dependency are not concerns with the proposed composite method because, much like the method with explicitly modeled reinforcement, it is computationally identical to linear elastic analysis with an incremental modulus.

The presented methodology for analyzing the behavior of reinforced concrete has been shown to be equally as accurate as explicitly modeling the separate materials of the composite. In uniaxial, multiaxial, and bending behavior, the composite methodology results are within 3% of the explicitly modeled case. Furthermore, a comparison between an unreinforced and reinforced concrete beam shows that, even for structures with relatively small amounts of reinforcement, failure to account for the change in viscoelastic behavior caused by the elastic reinforcement can

result in significantly larger deformations. The presence of reinforcement has proportionally more impact on the total time-dependent behavior as compared to the elastic behavior, because an increasing proportion of the external load is transferred to the steel as the concrete continues to deform.

Chapter 7: Examining Measured Data for Time-Dependent Behaviors

One particular challenge of using field measurements for investigating time-dependent behavior is that the environmental and loading conditions of the structure are not controlled, as would typically be the case for laboratory testing. The structure exists in an environment with changing temperature, humidity, and loading. This chapter presents the methodology used to separate the time-dependent behavior from other factors impacting the measured data. This methodology is exclusively for use with static monitoring data, but could also be used with results derived from dynamic systems (e.g., modal behavior from accelerometer data).

The methodology adopted for extracting the time-dependent behavior from measured data containing both time- and temperature-related deformations is presented in Section 7.1. Because the rates of time-dependent deformations are temperature-dependent, an overview of the interactions between temperature and hydration, creep, and shrinkage is given in Section 7.2. Measured time-dependent data from the St. Anthony Falls Bridge illustrating the impacts of temperature on creep and shrinkage are shown in Section 7.3.

7.1 Extraction of Time-Dependent Behavior using Linear Regression

The most straightforward method of separating the time-dependent behavior from the measured readings is to perform linear regression on the data series. This is done by fitting the data with a linear function of the form

$$y = \sum_i \alpha_i \theta_i(x) + \delta \tag{7-1}$$

where y is the measured data, α_i are the coefficients used to fit functions $\theta_i(x)$ to the data, x are the input parameters to the model, and δ is the error or residual between the linear prediction and the measured data. The problem involves first deciding what functions should be used to approximate

the measured data, and then computing the appropriate coefficients that best fit the measurements.

For analysis of the static system data from the I-35W St. Anthony Falls Bridge, the primary input parameters to the measured behavior were temperature and time. Because no information was available on traffic loading at any given point in time, effects of live loading on the static readings, though assumed to be minor, were necessarily considered as part of the residual term. Ambient humidity as measured by the weather station KMNMINNE17 located on the University of Minnesota campus approximately one mile from the bridge was not considered as a direct input parameter. Because the diffusion process of water through concrete is slow, the humidity at any given time was assumed to be unrelated to the measured strains and displacements of the structure at that same time.

To account for temperature in the measured data, three distinct functions were applied. The first function θ_1 was taken as the average bridge temperature:

$$\theta_1 = \frac{\int T dV}{V} \tag{7-2}$$

where T is the temperature at any point in the structure and V is the volume of the structure. Due to the particular instrumentation setup, the temperature was only well known at one cross section, that being Location 7 of the southbound bridge as shown in Figure 2.1. Therefore, the function θ_1 was approximated as

$$\theta_1 \approx \frac{\int T dA}{A} \tag{7-3}$$

where T is now the temperature measured at the cross section of Location 7, and A is the cross-sectional area of Location 7. To perform this integral, all operational thermistors within Location 7 were used. The temperatures among all thermistors at a given depth from the top surface were averaged together, and these average temperatures were integrated through the total depth of the

section using the trapezoidal rule. Top deck (or bottom fiber) surface temperatures were estimated by extrapolating a line up (or down) from the two topmost (or two bottommost) average temperatures to the surface.

Because Location 7 was nearly the smallest cross section in the entire bridge, thermal gradients (temperature differences through the depth of the cross section) had a larger impact on the average section temperatures here than on any other cross section. At locations with a deeper cross section, the thermal gradient in the deck would affect a smaller proportion of the cross section as compared to the same gradient applied at Location 7. Consequently, this temperature function overestimated the average bridge temperature, and thus overcompensated for the influence of thermal gradients on axial movement. Regardless, no other data were available, so the Location 7 average was assumed to be an acceptable approximation for the average superstructure temperature.

The average temperature of the bridge was intended to capture strains or deflections associated with axial elongation of the structure. However, as shown in Section 3.4.2.3, the coefficient of thermal expansion for the in situ measurements showed a clear linear variation with temperature. Assuming that the CTE varies linearly with temperature, then the uniform axial strain is equal to

$$\varepsilon_{axial} \approx \frac{\int (\alpha_1 + \alpha_2 T) T dA}{A} = \alpha_1 \frac{\int T dA}{A} + \alpha_2 \frac{\int T^2 dA}{A} \tag{7-4}$$

where $\alpha_1 + \alpha_2 T$ captures the linearly changing coefficient of thermal expansion. From this equation, it was clear that two functions should be used to describe the uniform axial elongation of the structure, namely θ_1 from Eqn. (7-3) and

$$\theta_2 \approx \frac{\int T^2 dA}{A} \tag{7-5}$$

Bending behavior due to thermal effects was assumed to be captured by the first moment of the temperature profile through the cross section:

$$\phi \approx \frac{\int z\left(\alpha_1 + \alpha_2 T\right) T dA}{I_x} = \alpha_1 \frac{\int zTdA}{I_x} + \alpha_2 \frac{\int zT^2 dA}{I_x} \tag{7-6}$$

where ϕ is the curvature, z is the vertical distance from the centroid of the cross section, and I_x is the moment of inertia of the cross section about the x-axis (transverse axis, relating to longitudinal bending). The strain and deflection readings were assumed to be linearly related to the curvature. Therefore, the third and fourth fitting functions were defined as

$$\theta_3 \approx \frac{\int zTdA}{I_x} \tag{7-7}$$

$$\theta_4 \approx \frac{\int zT^2 dA}{I_x} \tag{7-8}$$

In practice, the measured data was not strongly dependent on the quadratic term of the first moment of the temperature profile, and an almost equivalent fit was attained after dropping the θ_4 function. For the remainder of this investigation, the temperature dependence of the data was modeled exclusively with fitting functions θ_1, θ_2, and θ_3 as shown in Eqns. (7-3), (7-5), and (7-7).

A single fitting function θ_5 was used to describe all time-dependent behavior, regardless of the source. As described in Section 7.2, the rates of time-dependent deformations were found to also depend on temperature. The form of the θ_5 fitting function is described in Section 7.3.1.

The fitting function of $\theta_6 = 1$ was used to best fit the constant offset of the measured data. Because all measured data only captured relative motion, computation of this coefficient by linear regression was necessary for fitting the data, but the specific value did not confer any physical insight.

As discussed in Section 2.3.2.2, replacement or rewiring of sensors could introduce offsets in the data. The data offset was assumed to occur instantaneously, and thus the behavior of

the data was assumed to follow the Heaviside function $H(t,b)$ equal to 0 for all values of t less than b and equal to 1 for all t greater than or equal to b. Thus, fitting functions $\theta_j = H(t,t_j)$ were added to the linear regression analysis on a case-by-case basis where t_j was the time of a jump in the data.

The addition of the Heaviside step functions can come into conflict with accurate estimation of the time-dependent behavior. For example, suppose that a given sensor fails and does not return any data. The sensor is then replaced one year later, at which point a corresponding jump in the data is expected. However, the time-dependent deformation is not known over the course of the year when no data was collected, and instead must be assumed to follow the fitting function θ_5. In such circumstances, the regression coefficients α_j for Heaviside functions θ_j are strongly dependent on the form of the time-dependent fitting function.

Furthermore, the addition of the Heaviside fitting function means that the time-dependent behavior before and after the break are effectively fitted separately. Again consider the case of the replaced sensor, such that two years of data are collected, one year is lost, then another two years are collected after the repairs and resultant jump in the readings. The addition of the Heaviside function means that the regression will minimize the errors before the break independently of minimizing the errors after the break. If the assumed time-dependent equation does not accurately capture the shape of the measured time-dependent deformation (for instance, the assumed curve reaches an asymptotic value long before the measured data), then the estimate for the magnitude of the data jump will continuously be updated as new data is added. In this way, the value of the regression coefficients α_j for functions θ_j are not only dependent on the creep and shrinkage predictions over the break in data, but also upon systemic inaccuracies of the future time-dependent predictions.

To alleviate the above concern, the Heaviside fitting function was only computed via linear regression for the first month after the data jump. After this time, the regression coefficient

was never recalculated, and was instead held equal to the value computed at the end of the one-month period. Also, the quantity of Heaviside fitting functions was kept to a minimum; even in the event of sensor replacement, the Heaviside function was not applied unless a noticeable jump in the data was observed.

Therefore, the final form of the linear regression used to capture the temperature and time-dependent behavior of the measured data was

$$y = \alpha_1 \frac{\int TdA}{A} + \alpha_2 \frac{\int T^2 dA}{A} + \alpha_3 \frac{\int zTdA}{I_x} + \alpha_5\theta_5 + \alpha_6 + \sum_j \alpha_j H\left(t, t_j\right) + \delta \tag{7-9}$$

where the α-coefficients are computed through linear regression and δ represents the residual between the prediction and the measured data *y*. Because all time-dependent behavior was captured by the θ_5 term, the temperature-dependent and time-dependent deformations were separated by

$$\alpha_5\theta_5 + \delta = y - \alpha_1 \frac{\int TdA}{A} - \alpha_2 \frac{\int T^2 dA}{A} - \alpha_3 \frac{\int zTdA}{I_x} - \alpha_6 - \sum_j \alpha_j H\left(t, t_j\right) \tag{7-10}$$

Thus, if coefficients α_1, α_2, α_3, α_6, and α_j are computed, then the time-dependent behavior can be extracted from the data (within some error denoted by δ) regardless of the form of the θ_5 equation. Accurate computation of the coefficients for thermal behavior required that some form be assumed for θ_5, if only to ensure that the data being fitted was stationary in time.

7.2 Temperature Dependence of Time-Dependent Phenomena

In addition to instantaneous concrete dilation in accordance with the coefficient of thermal expansion (Section 3.4), ambient temperatures also impact the time-dependent strains and the concrete aging rate. This has ramifications for how the measured data can be processed using the linear regression model described in Section 7.1. This section presents an overview of the temperature-dependence of the typical time-dependent processes of concrete.

7.2.1 Temperature Dependence of Concrete Aging

The process of concrete hydration and aging is a function of both time and temperature (Neville, 1996). Because hydration of cement is a chemical process, the hydration reaction rate and, by extension, the rate at which the concrete strength increases are commonly assumed to be dependent on temperature in accordance with the Arrhenius equation. Higher temperatures increase the rate of the reaction, while lower temperatures slow the aging process. This can be modeled by calculating an adjusted concrete age based on the temperature history:

$$\left(t_0\right)_{adj} = \int_0^{t_0} e^{\left[\frac{U_h}{R}\left(\frac{1}{T_0} - \frac{1}{T(t')}\right)\right]} dt' \tag{7-11}$$

where $(t_0)_{adj}$ is the temperature corrected concrete age in days, t_0 is the unadjusted concrete age in days since casting, U_h/R is an activation energy constant with units of absolute temperature (Kelvin), T_0 is the reference absolute temperature equal to 293 K (20°C), $T(t')$ is the absolute temperature history, and time t' is specified in days. The adjusted concrete age is analogous to the equivalent age of the concrete assuming that the temperature was held constant at the reference temperature T_0. In general, strength gain and aging of concrete are due to more processes than just the hydration reaction (Thomas and Jennings, 2006). For typical analytical purposes, however, the temperature-dependence of all aging-related phenomena can be assumed to be inseparable from that of hydration.

The value of the activation energy term U_h/R varies throughout the literature. From inspection of Eqn. 2.1-87 in the CEB/FIP 1990 Model Code, U_h/R is equal to 4,000 K. Bažant and Kim (1992) use the same value for U_h/R, as justified by data from Maréchal (1969). In a study of thermal effects on concrete creep, Hauggaard et al. (1999) also use U_h/R equal to 4,000 K. In describing the B3 time-dependent model, Bažant and Baweja (1995a) specify that U_h/R is equal to 5,000 K. Bažant, Cusatis, and Cedolin (2004) consider the effects of both internal pore humidity and temperature on the rate of hydration, and specify a temperature activation energy

constant U_h/R of 2,700 K. Accounting for the facts that internal pore humidity will increase as temperature increases (Grasley and Lange, 2007, and Grasley et al., 2006) and that increases in humidity increase the rate of hydration, temperature changes will tend to have a more pronounced impact on the hydration rate than suggested by Bažant, Cusatis, and Cedolin (2004). This means that for studies considering only temperature changes, U_h/R will likely be greater than 2,700 K. According to a recent study by Pang et al. (2013), U_h/R is approximately equal to 6,300 K for API Class A cement (similar to ASTM Type I) and 5,900 K for API Class C cement (similar to ASTM Type III).

From the above literature search, the most common consensus on the constant U_h/R was approximately equal to 4,000 K. Unless the concrete is loaded at a very young age, significant accuracy for this term is not necessary, as the rate of aging is greatly slowed after the initial curing period. Even in the case of concrete loaded at an early age, uncertainty in the shape of the concrete aging law itself will add to the complications of predicting early age behavior. For concrete that has mostly hardened by the time it is loaded, the concrete age correction makes little difference in predictions of the concrete strength. The effects that this adjusted age of loading will have on the total time-dependent strains depends on the particular assumed time-dependent model.

7.2.2 Temperature Dependence of Basic Creep

Basic creep, that is the concrete creep in the absence of moisture movement, is primarily caused by dislocation and movement of particles within the cement gel (Wittmann, 1982). The rate of basic creep is commonly assumed to depend on the Arrhenius equation in a similar fashion as the rate of concrete aging. For basic creep independent of moisture loss, the change in creep rate is taken into account by computing an adjusted duration of loading, such that

$$\left(t-t_0\right)_{adj}=\int_{t_0}^{t} e^{\left[\frac{U_c}{R}\left(\frac{1}{T_0}-\frac{1}{T(t')}\right)\right]}dt' \tag{7-12}$$

where $(t-t_0)_{adj}$ is the temperature corrected duration of loading in days, t_0 is the unadjusted concrete age at which the load was applied, t is the current unadjusted concrete age in days, U_c/R is an activation energy constant with units of absolute temperature describing the dependence of concrete creep rate on temperature, T_0 is the reference temperature equal to 293 K (20°C), $T(t')$ is the temperature history specified in Kelvin, and time t' is specified in days. The Arrhenius-adjusted duration of loading is analogous to an equivalent loading duration of the concrete assuming that the temperature was held constant at T_0. If $T(t')$ is a constant less or greater than T_0, then the Arrhenius-adjusted duration of loading is correspondingly less or greater than the total duration.

Again, the literature does not appear to have a consensus of the value of U_c/R. In specification of the B3 model, Bažant and Baweja (1995a) included both an increase to the creep rate and the total creep due to increases in temperature. The increase to the creep rate assumed an empirical activation energy factor equal to

$$\frac{U_c}{R} = 110\left(w\right)^{-0.27}\left(\left(f_c\right)_{28}\right)^{0.54} \tag{7-13}$$

where w is the water content in pounds per cubic foot of concrete and $(f_c)_{28}$ is the mean 28-day concrete strength specified in psi. Using the mix parameters from the superstructure mix as given in Section 4.2, the activation energy constant U_c/R was equal to 7,360 K. The basic creep at any given time t was multiplied by an empirical factor R_T equal to (Bažant and Baweja, 1995a)

$$R_T\left(t\right) = e^{\left[0.18\frac{U_c}{R}\left(\frac{1}{T_0}-\frac{1}{T(t)}\right)\right]} \tag{7-14}$$

Applying this to the B3 basic creep from Eqn. (4-27) in Section 4.4.1 gave

$$C_0\left(t,t_0\right) = R_T\left[q_2 Q\left(t,t_0\right) + q_3 \ln\left(1+\left(t-t_0\right)^n\right) + q_4 \ln\left(\frac{t}{t_0}\right)\right] \tag{7-15}$$

where $C_0(t,t_0)$ is the basic creep compliance extracted from the B3 model and times t and t_0 are corrected according to Arrhenius equation. Instances of t_0 were corrected using the aging law

correction from Eqn. (7-11), and instances of $t - t_0$ were corrected using Eqn. (7-12). The total time t from the q_4 term was computed as $(t - t_0) + t_0$ wherein $t - t_0$ and t_0 were corrected as explained.

Bažant, Cusatis, and Cedolin (2004) considered temperature and humidity effects together for basic creep. The temperature factor U_c/R was set equal to 5,000 K and an additional humidity factor was included as follows:

$$\left(t - t_0\right)_{adj} = \int_{t_0}^{t} \left(0.1 + 0.9H^2\right) e^{\left[\frac{U_c}{R}\left(\frac{1}{T_0} - \frac{1}{T(t')}\right)\right]} dt' \tag{7-16}$$

where H is the internal pore humidity in decimal form. Because the internal pore humidity increases as the temperature increases (Grasley and Lange, 2007, and Grasley et al., 2006), and because according to this formula increasing temperature and humidity both raise the basic creep rate, then by supplanting the combined temperature and humidity expressions with a single temperature expression, the equivalent U_c/R constant would be greater than the specified 5,000 K.

In defining the BP model (the precursor to the B3 model and not presented in this report), Bažant and Kim (1992) assumed that U_c/R was not constant with time. Instead, the following empirical expression was used:

$$\frac{U_c}{R} = \frac{U_0}{R} + \frac{U_1}{R} \ln\left(1 + t - t_0\right) \tag{7-17}$$

where

$$\frac{U_0}{R} = 130c^{-0.80}\left(w/c\right)^{-0.70}\left(\left(f_c\right)_{28}\right)^{0.70} \tag{7-18}$$

$$\frac{U_1}{R} = 0.2\frac{U_0}{R} \tag{7-19}$$

and c is the total cement content in pounds per cubic foot, w/c is the water to cement ratio, $(f_c)_{28}$ is the mean 28-day concrete strength in psi, and both U_0/R and U_1/R are specified in Kelvin. This increase in activation energy with loading duration was consistent with results from Day and

Gamble (1983), whereby the creep activation energy was assumed to be a function of the state of the concrete microstructure and that any two concrete specimens from the same mix with equivalent load histories, but regardless of their temperature histories, have identical microstructure if they have both undergone an equal amount of creep strain. Using these assumptions, Day and Gamble (1983) computed higher activation energy constants than expected from the provisions from Bažant and Baweja (1995a) and Bažant, Cusatis, and Cedolin (2004). By extension, the magnitude of the activation energy from the method by Bažant and Kim (1992), with U_0/R equal to 9,820 K for the superstructure mix, was considerably higher than the activation energy constants from the other discussed methods.

Transitional thermal creep, defined by a transient increase in the creep rate immediately after an increase or decrease in temperature (Bažant, Cusatis, and Cedolin, 2004), was not considered in this investigation.

Section 2.1.8.7 of the CEB/FIP 1990 Model Code included specifications on how to incorporate temperatures other than 68°F (20°C) into creep predictions. This included adjustments to the total creep strains, the time-development of these strains by adjusting the β_H term presented in Eqn. (4-56), and addition of a transitional creep term. The form of this adjustment was not conducive for investigating measured data under variable temperature conditions, as a simple adjusted time could not be computed as could be done using Arrhenius equation adjustments. The ACI-209 committee (1992) noted that increased temperatures increase the amount of creep, but provided no direct guidance on how to incorporate this into analysis.

7.2.3 Temperature Dependence of Shrinkage and Drying Creep

Available relations for the temperature dependence of shrinkage and drying creep are rare. For the BP model, Bažant, Kim, and Panula (1991) specified that the shrinkage and drying creep depend on the Arrhenius equation with a form similar to that from Eqn. (7-12), except that the shrinkage or drying creep duration is used instead of the basic creep duration, and the

activation energy constant is specified as U_s/R. According to Bažant, Kim, and Panula (1991), this U_s/R constant was equal to 5,000 K.

Section 2.1.8.7 of the CEB/FIP 1990 Model Code included provisions for adjustment of shrinkage at constant temperatures differing from 68°F (20°C). This included adjustments to the total shrinkage and the rate of shrinkage. Again, this form of temperature correction was not conducive to the understanding of measured data, unlike the Arrhenius equation time adjustment presented in the next section.

7.3 Time-Dependent Behavior in Measured Data

7.3.1 Evidence Showing Temperature Dependence of Time-Dependent Behavior

To illustrate the impacts of temperature on the rate of the time-dependent behavior, the linear regression procedure presented in Section 7.1 was applied to linear potentiometer and vibrating wire strain gage data from the I-35W St. Anthony Falls Bridge. Refer to French et al. (2012) for samples of the changes in displacement and strain measured by the linear potentiometers and vibrating wire strain gages, respectively, prior to extraction of the time-dependent behavior.

Five time-dependent fit functions θ_5 were chosen for the linear regression. The objective was to observe whether the choice of the time-dependent fitting function had a significant impact on the extraction of the temperature-dependent behavior. For each time-dependent model, the time at loading t_0 was assumed to be equal to a constant 50 days, which was near the average age at which any given concrete in the bridge (precast or cast-in-place) was first stressed per Tables 1.1 and 1.2. The V/S ratio was set equal to 8.0 in. (200 mm), which was a typical value for much of the superstructure. The relative humidity H was 64.1%, identical to the average value used for the finite element results as discussed in Section 4.2. For computing the duration of loading $t - t_0$, the initial date t_0 was chosen as July 25, 2008, which was when the midspan closure pour was placed and the final stresses were locked into the bridge. Any other parameters, such as material

constants, were taken from the superstructure concrete properties as given in Section 4.2. Though many of the θ_5 equations share the forms of the time-dependent models presented in Chapter 4, multiplicative factors have been removed from the investigated θ_5 functions because the process of linear regression negates the need for such coefficients. The five investigated functions for θ_5 are presented below.

1. GL2000 – An equation in the form of the GL2000 (Gardner and Lockman, 2001) creep model,

$$\theta_5 = \left[2\left(\frac{(t-t_0)^{0.3}}{14+(t-t_0)^{0.3}} \right) + \left(\frac{7}{t_0} \right)^{0.5} \left(\frac{t-t_0}{t-t_0+7} \right)^{0.5} + 2.5\left(1-1.086H^2\right)\left(\frac{t-t_0}{t-t_0+97(V/S)^2} \right)^{0.5} \right] \tag{7-20}$$

   which is similar in form to Eqn. (4-65) without the predrying coefficient.

2. CEB1990 – An equation with a form similar to that from the 1990 CEB/FIP Model Code,

$$\theta_5 = \left[\frac{t-t_0}{\beta_H + t - t_0} \right]^{0.3} \tag{7-21}$$

   where the time constant β_H is defined in Eqn. (4-56) and is equal to 865 days using the parameters stated above. This equation has a similar form to Eqn. (4-55).

3. AASHTO – An equation with the form of the AASHTO LRFD (2010) hyperbola,

$$\theta_5 = \frac{t-t_0}{61-4(f_c)_{t0}+t-t_0} \tag{7-22}$$

   where $(f_c)_{t0}$ is the concrete strength in ksi at age t_0, and is equal to 7.71 ksi (53.1 MPa) at t_0 = 50 days using the aging law from ACI-209 (1992) as justified in Section 4.8. This equation has a similar form to Eqn. (4-75).

4. ACI – An equation with the form of the ACI-209 (1992) hyperbola,

$$\theta_5 = \frac{\left(t - t_0\right)^{0.6}}{10 + \left(t - t_0\right)^{0.6}} \tag{7-23}$$

which has a similar form to Eqn. (4-5).

5. Log Power – The log power equation approximates a simplified version of the B3 model (Bažant and Xi, 1995),

$$\theta_5 = \ln\left[1 + \left(t - t_0\right)^{0.1}\right] \tag{7-24}$$

For long-term creep, this equation follows the logarithmic trends observed in the GL2000 and B3 creep models.

Linear regression as described in Section 7.1 using the above time-dependent curves for θ_5 was conducted on the linear potentiometer data from October 31, 2008, until June 5, 2013. The temperature-dependence of the time-dependent strains was at first ignored, meaning that the loading duration $t - t_0$ was not adjusted in any way using the Arrhenius equation and the procedures discussed in Section 7.2. The goodness of fit, as determined by the sum of the squared residuals and the standard deviation of the residual, and the fitting coefficients α_1, α_2, and α_3 for the temperature dependent behavior are given in Tables 7.1 through 7.4 for LP data from northbound Span 1, northbound Span 3, southbound Span 1, and southbound Span 3, respectively. One instance of the Heaviside fitting function as discussed in Section 7.1 was applied to the southbound Span 1 data with the time of the jump t_j equal to April 8, 2013, following a sensor outage of approximately 10.5 months. In spite of the replacement of other linear potentiometers, no other Heaviside functions were deemed necessary for regression. For purposes of the regression analysis, the relative movements measured by the two linear potentiometers installed at each location were averaged together. Regression analysis was not conducted for the LPs attached to Span 4 at Pier 4 because the pinned connection between the

pier and Span 4 superstructure at this location meant that these sensors could not capture temperature- and time-dependent behavior.

Regardless of the chosen time-dependent equation θ_5, the linear regression coefficients for the temperature dependent behavior remained largely unchanged. The coefficient for average bridge temperature α_1 at each given location rarely varied by more than 1% of the mean coefficient for any tested model at that same location. Coefficients for the squared temperature α_2 and the thermal gradient α_3 at each of the given locations varied more strongly, up to 25% of the mean coefficient among all models at each given location. The AASHTO and ACI-209 models consistently performed the worst among the tested forms of θ_5; these two models approached their asymptotic values much sooner than witnessed for any of the data sets, which resulted in difficulties for the linear regression. Though the choice of the time-dependent equation θ_5 does not have a strong impact on the estimation of the coefficients for the temperature fit, models which best match the data such as the GL2000, CEB1990, or the Log Power curves are likely to provide better overall results.

The θ_5 equation similar to the GL2000 creep model and provided in Eqn. (7-20) consistently performed among the best of the tested models. Therefore, extraction of the time-dependent component of the LP data via Eqn. (7-10) was performed using the coefficients derived from the GL2000 curve. The resulting estimated time-dependent deflections from each LP location are given in Figure 7.1. Despite removing the temperature-dependent behavior, the data still showed seasonal trends that were particularly pronounced during the first two years after bridge opening. The time-dependent strains slowed during the winters and sped up during the summers, similar to what would be expected from the discussion concerning the Arrhenius equation in Section 7.2.

The linear regression procedure as presented in Section 7.1 was also used to extract time-dependent strains from the data collected by the vibrating wire strain gages. The time-dependent

function θ_5 was assumed to be the GL2000 curve as given in Eqn. (7-20). The linear regression was performed on the change in total strain readings from September 1, 2008, until July 19, 2013. The use of Heaviside functions in the regression was not necessary for the plotted VWSG data, as no data jumps were present. The resulting estimated time-dependent strains from a selection of longitudinal gages in the southbound bridge are plotted with respect to the unadjusted time in Figure 7.2.

With the exception of the bottom flange strain gage installed at Location 5, all time-dependent strain estimates appeared to follow seasonal trends much like the linear potentiometer data. With respect to the data from the bottom flange of Location 5 located near Pier 2, it was likely that the aggregated temperature values taken exclusively from Location 7 in the southbound bridge did not accurately capture the behavior at this cross section. This may have been caused by the vastly different cross-sectional shape at Location 5 compared to Location 7, or was possibly due to the proximity of the gage to the boundary condition imposed by the bearing assemblies. As shown in Hedegaard et al. (2013), during times of peak gradients, the measured temperatures in the bottom flanges near the piers differed from the temperatures in the bottom flanges near midspan by approximately 9°F (5°C). Bottom flange strains from Locations 4, 6, and 8, not plotted, showed similar issues. For the strain gage data well-predicted by the linear regression procedure, the seasonal dependence of the time-dependent strain rates was clear.

7.3.2 Temperature Correction of Time-Dependent Behavior in Measured Data

The estimated time-dependent data from the strain gages and linear potentiometers contained a combination of basic creep, drying creep, shrinkage, and aging. Rather than accounting for an adjusted age for each individual phenomena, a simplified and aggregated time adjustment procedure was adopted when investigating the measured data. Measurement times were adjusted according to

$$t_{adj} = \int_{t_{cl}}^{t} e^{\left[\frac{Q}{R}\left(\frac{1}{T_0} - \frac{1}{T(t')}\right)\right]} dt' \tag{7-25}$$

where t_{adj} is the temperature corrected duration of loading in days, the start time for the integration t_{cl} is July 25, 2008 when the closure pour was placed, t is the current unadjusted time in days, Q/R is an activation energy constant with units of absolute temperature (Kelvin) describing the dependence of all time-dependent strain rates on temperature, T_0 is the reference temperature equal to 293 K (20°C), $T(t')$ is the temperature history specified in Kelvin, and time t' is specified in days. Ideally, the start time of integration should represent the build-up of stresses and time-dependent strains during the erection procedure. For simplicity, however, this value was specified as the time when the closure pour was placed and the long-term stresses were effectively locked into the superstructure. Though this simplification may have affected early age readings (i.e., during the first year after completion), it was not expected to negatively impact long-term results. The temperature history $T(t')$ used to compute the adjusted time was taken as the average temperature through the Location 7 cross section in the southbound bridge, as computed using Eqn. (7-3).

From the discussion of the temperature dependence of basic creep in Section 7.2.2, the activation energy value specified for the B3 model (Bažant and Baweja, 1995a) in Eqn. (7-13) was both constant with time and independent of internal humidity. Because the St. Anthony Falls Bridge had a large volume-to-surface ratio, and theoretically only the diffusion-based processes of drying creep and shrinkage are dependent on V/S, the measured time-dependent behavior was assumed to be dominated by basic creep. Therefore, the aggregate activation energy term for all time dependent effects was assumed to be equal to

$$\frac{Q}{R} = 110\left(w\right)^{-0.27}\left(\left(f_c\right)_{28}\right)^{0.54} \tag{7-26}$$

where w is the water content in pounds per cubic foot of concrete and $(f_c)_{28}$ is the mean concrete strength at 28 days. For the superstructure mix, this value was equal to 7,360 K. The time-dependent behavior of the piers and barrier rails was assumed to only minimally impact the strain and linear potentiometer results from the superstructure, and thus the pier and barrier rail concrete material parameters were not taken into account for purposes of data correction. The temperature dependence on the rate of hydration was ignored, as it was believed that this would only have a minor impact on the early age strains and deflections.

Prior to September 1, 2008, but after the closure pour was completed on July 25, 2008, no temperature data was available. To compute the temperature correction over this time period, an average bridge temperature was extrapolated back over this time period. The annual temperature fluctuations $T(t)$ were assumed to follow a sinusoidal pattern defined by

$$T(t) = A\sin\left(\frac{2\pi}{365.25}t + \theta\right) + C \tag{7-27}$$

where t is the time in days such that $t = 0$ is on July 25, 2008, and amplitude A, phase angle θ, and constant C were computed by minimizing the sum of squared errors between the temperature estimate and the measured temperatures from September 1, 2008, until February 19, 2013. Measured temperatures from the bridge were taken as the average temperature through Location 7 of the southbound bridge as computed by Eqn. (7-3). The best fit was provided by A = 31.0°F (17.2°C), θ = 1.712 radians, and C = 51.0°F (10.6°C). This fit is compared to the measured average bridge temperatures in Figure 7.3. Using the sinusoidal temperature approximation, the time adjustment procedure from Eqn. (7-25) was conducted from July 25, 2008, until September 1, 2008. Using the activation energy constant of Q/R = 7,360 K, the adjusted time at 11:00 AM CST on September 1, 2008, was equal to 62.1 days. From this point in time onwards, measured temperature data was always used for the time adjustment procedure.

Using the above described procedure, the linear potentiometer and strain gage readings presented in Figures 7.1 and 7.2 were plotted with respect to the adjusted time in Figures 7.4 and 7.5, respectively. For both the LP and VWSG data, using the adjusted time smoothed the measured data, such that the resulting plots resembled what would typically be seen for time-dependent behavior in a controlled environment. Of particular note, plotting the data in this fashion revealed that the time-dependent deflections and strains occasionally appeared to reverse in direction, particularly during the late winter and early spring months. A similar phenomena was observed by Sakata and Ayano (2000), where the shrinkage was found to reverse direction when the concrete was cooled. This behavior was believed to be due, at least in part, to the seasonal changes in ambient and internal relative humidity. During the winter, the ambient relative humidity is high. Conversely, when the concrete is cold, the internal relative humidity is low (Grasley and Lange, 2007) as discussed in Section 3.4.2.3. Thus, it is possible that the humidity differential reverses during the winter, such that water seeps into the concrete and causes swelling to occur. Also, changes in the concrete stress and post-tensioning caused by the seasonal temperature changes may have also played a role in the apparent reversal of the time-dependent behavior. The time-adjustment method could not directly account for either of these effects.

This time-adjustment procedure allowed for the comparison of the time-dependent predictions from constant-temperature finite element analysis with the readings from the in situ monitoring system. This rested on the assumption that the presence of temperature changes did not alter the time-dependent behavior of the concrete in any way other than by scaling the rate of creep and shrinkage. However, it is important to note that this time-adjustment procedure can, at best, be only approximately true for cases where the structure does not have uniform temperature at all times. Given the presence of thermal gradients, as was the case for the St. Anthony Falls Bridge, the adjusted age at any given point on the bridge could be different depending on the

temperature history of that point. For example, given a cyclic positive thermal gradient whereby the deck surface is heated relative to the webs and the bottom flange, the concrete in the deck would effectively have a higher adjusted age than the adjusted age computed using the average temperature throughout the cross section. Furthermore, this procedure did not account for any changes in stress, either due to seasonal temperature changes or thermal gradients.

Adoption of a single adjusted age for the entire structure was primarily driven by concerns over data analysis. Assigning individual adjusted times to each sensor based on the temperature at that sensor would make comparison of time-dependent trends at different locations in the bridge difficult. For the linear potentiometers which collected global behavior based on the total longitudinal elongation of the structure, assigning an adjusted time derived from average bridge temperature was only as good as the assumption that the temperature at a single cross section (i.e., location 7) was representative of the average temperature in the bridge. For the vibrating wire strain gages which collected local behavior, using average bridge temperatures may have introduced additional errors. These issues were explored using a time-dependent finite element model under changing thermal conditions presented in Chapter 10.

Chapter 8: FEM Results for Time-Dependent Behavior

Results from the time-dependent finite element model, as constructed and analyzed using the procedures in Chapter 6, were compared to the time-dependent behavior extracted from the linear potentiometer and vibrating wire strain gage field data. Also presented are relevant bridge behaviors that could not directly be compared to processed data from the bridge instrumentation presented in Chapter 2, including an investigation of long-term vertical deflections and the concrete stress state under service conditions both at the end of construction and the end of the expected bridge life. Simplified hand calculations and static short-term loading scenarios, documented in Appendix B, were conducted to ensure the validity of the St. Anthony Falls Bridge time-dependent finite element model. Due to the uncertain nature of predicting long-term time-dependent behavior of concrete, a brief investigation of how uncertainty manifests in the finite element estimations is also presented.

8.1 Comparison of Finite Element Model with Measured Data

Results from the time-dependent finite element model of the St. Anthony Falls Bridge computed according to the procedure documented in Chapter 6 were compared to measured data from the installed linear potentiometers and strain gages. Because the finite element results were computed assuming constant temperature equal to 68°F (20°C), whereas the measured data were obtained under varying environmental conditions, the measured data were adjusted to facilitate comparison. Two types of modifications were made to the measured data: (1) adjusted time scaling in accordance with the Arrhenius equation, and (2) extraction of time-dependent effects. First, the time scale of the measured data was converted to Arrhenius adjusted time according to the procedure documented in Section 7.3.2 such that the time-scale of the measured data represented the time-dependent response that would be anticipated had the data been obtained under constant temperature at 68°F (20°C). As discussed in Section 7.2, warm and cold

temperatures increase and decrease, respectively, the rates of time-dependent effects such as creep. Second, all measured data presented in this chapter represents only the time-dependent component as extracted from the total measured data using the linear regression procedure in Section 7.1. For the θ_5 term in the linear regression estimates of the time-dependent behavior, the form of the GL2000 curve using the unadjusted age as given in Eqn. (7-20) was selected. Other forms for θ_5 were examined in Section 7.3.1, though the choice of curve did not have a significant impact on the final extracted time-dependent values.

8.1.1 Longitudinal Deflections

To compare the finite element model results with the processed LP data, the calculated longitudinal deflections from the nodes located at the positions of the LP sensors were output. For results from the LPs attached to Span 1 – Abutment 1, changes in displacement predicted by the model were assumed to translate directly with displacements measured by the sensors. In other words, it was assumed that Abutment 1 did not move with time.

The FEM deflections from Span 3 could not be directly compared to the data from LP sensors attached to Span 3 – Pier 4. The modeled results captured only the time-dependent shortening of the continuous three-span structure. In contrast, the sensors attached to Span 3 measured the relative deflection between the top of Pier 4 and the Span 3 superstructure. Because Span 4 was pinned to the top of Pier 4 and integral with Abutment 5, time-dependent deflections of Span 4 caused corresponding movement in the attached boundaries. Given that Pier 4 was flexible compared to the integral Abutment 5, the total time-dependent shortening of Span 4 was assumed to translate as an equivalent horizontal deflection of Pier 4. Under these assumptions, the time-dependent effects extracted from the Span 3 LPs included the total shortening of Span 4 plus a portion of the shortening of the continuous Spans 1 through 3.

Span 4 was not explicitly modeled in the finite element model, and so as an alternative, the time-dependent axial deformation of Span 4 of the southbound bridge was estimated by hand

using each considered time-dependent model. Southbound Span 4 consisted of cast-in-place concrete poured between July 24, 2008 and August 2, 2008, and so an average cast date of July 28, 2008 was assumed for the entire span. An average jacking stress of 192 ksi (1,320 MPa) was applied to 212 in.^{2} (1,370 cm^2) of post-tensioning on August 5, 2008. Moist curing was assumed to take place up until post-tensioning was applied. Friction losses and seating losses were estimated assuming an average set length of 0.375 in. (9.5 mm) and a wobble coefficient of 0.0002/ft (0.00066/m) for the interior strands and zero for exterior strands, as specified in the as-built construction documents (Minnesota Department of Transportation, 2008). The friction coefficient was ignored, as all strands were assumed to be straight, which was only approximately true due to deviations near the ends of the strands to distribute the anchorage and jacking locations.

For analysis, Span 4 was divided into 16 segments along the length of the span. Each segment was 10 ft (3.0 m) long unless a sudden change in geometry, such as at the diaphragm above Pier 4, necessitated some shorter length segment. Cross-sectional properties, such as average concrete stress, *V*/*S* ratio, and cross-sectional area, were averaged over each segment individually. The time-dependent longitudinal deflection of each segment was summed together to compute the total shortening of Span 4. Total axial deformation was assumed to be due only to the average concrete stress throughout the cross section, and hence eccentricity of the strands and bending of Span 4 were not considered. The time-dependent deflections were computed by dividing the total time frame from August 5, 2008 until May 28, 2158 into 62 time steps of steadily increasing duration (beginning at 1 day and ending at 50 years). The principle of superposition was used to include the effects of post-tensioning losses due to creep, shrinkage, and relaxation. Relaxation was computed according to Magura et al. (1964), and creep and shrinkage followed the provisions documented in Chapter 4. Material properties for Span 4 were

assumed to be identical to those used for the superstructure concrete for each time-dependent model.

For comparison between the time-dependent models discussed in Chapter 4, the total time-dependent longitudinal deflections (zeroed at the beginning of the analysis on May 25, 2008) from the FEM results and Span 4 hand calculations are given in Figure 8.1. The estimated deflections at the Span 1 – Abutment 1 and Span 3 – Pier 4 expansion joints due to shortening of Spans 1 through 3 were computed by the FEM and are shown in Figures 8.1(a) and 8.1(b), respectively. The component of the Span 3 – Pier 4 expansion joint deflection due to the shortening of Span 4 was calculated by hand and is shown in Figure 8.1(c). The summation of the deflections from Figures 8.1(b) and 8.1(c) was representative of the deflections that were measured by the Span 3 – Pier 4 linear potentiometers. Adjusted age equal to zero corresponded to when the midspan closure pour was placed on July 25, 2008. Deflections before this time represented the elastic, creep and shrinkage strains prior to completion of the bridge, and were not of interest.

Prior to an adjusted age of 250 days (first year after bridge completion), the different time-dependent models can be divided into two clusters. The 1978 and 1990 CEB/FIP Model Codes and the B3 model all predicted similar early age deflections. The AASHTO, ACI-209, and GL2000 models constituted the second cluster of results prior to 100 adjusted age days. After this point, the models diverged. For long-term estimates, the B3 and GL2000 models predicted nearly identical deformations, despite differences in early-age behavior. Though the two CEB/FIP models had different time curves from 100 to 50,000 adjusted age days (137 adjusted age years), both approached similar asymptotic values. The AASHTO and ACI-209 provided similar predictions for what amounted to the smallest long-term deflections among all considered models. Long-term deflection predictions from the B3 and GL2000 models were nearly double those predicted by the AASHTO and ACI-209 models.

Comparison of the longitudinal deflections at Span 1 from the finite element results with the Span 1 sensor data from October 31, 2008 until June 5, 2013 (averaged between the LPs from both boxes of the southbound bridge) is presented in Figure 8.2. The computed longitudinal deflections summed from the finite element model at Span 3 and the hand calculations from Span 4 are compared to the Span 3 sensor data from September 8, 2009 until June 5, 2013 (again averaged between the LPs from both boxes of the southbound bridge) in Figure 8.3. The Arrhenius adjusted age for the LP data was computed according to the procedure in Section 7.3.2. The computed deflections were set equal to the measured results at 10:00 AM CST on May 16, 2010 (adjusted age equal to 400 days) for purposes of comparison. An earlier time was not chosen, as the LPs from southbound Span 3 did not collect any data until September 8, 2009 (refer to Section 2.3.2). Gaps in the data were due to either sensor or data acquisition system failures, documented in Section 2.3.2. For these plots, only relative deflections were meaningful, as the total movement at the expansion joints since bridge completion was unknown. For Figures 8.2 and 8.3, two subplots are presented. These subplots represent identical data, but part (a) presents the time frame for the FEM results out to an adjusted age of 150 years while part (b) zooms in to show the time frames with measured data. Given that 1 year of real time was approximately equal to 0.75 years in Arrhenius adjusted time for the measured temperature history of the St. Anthony Falls Bridge, the 150-year adjusted age analysis corresponded to nearly 200 years in real time.

The measured time-dependent longitudinal deflections were nearly linear with respect to log time. From inspection of the Span 1 LP data in Figure 8.2, the AASHTO and ACI-209 model results appeared to provide accurate relative deflections from 100 adjusted age days until approximately 400 adjusted age days after the closure pour (in terms of dates, October 31, 2008 until May 16, 2010, which approximately coincided with the first 1.5 years of bridge operation). After this point, however, the AASHTO and ACI-209 models began to systemically

underestimate the measured deflections, indicating that these models approached their asymptotic bounds more quickly than indicated by the data. As summarized in Section 4.9, these two models were unique in their treatment of specimen volume-to-surface ratio, insofar as they only scaled the ultimate creep and shrinkage values based on the *V*/*S* ratio and did not vary the rate at which the asymptote was approached. For analysis of a structure with as large a *V*/*S* ratio as the St. Anthony Falls Bridge, the evidence supports the conclusion that this approach to incorporating the *V*/*S* ratio is not valid.

All the other considered models overestimated the measured time-dependent deflections. Over the course of the 4.6 years of measurement, measured time-dependent deflections amounted to 0.85 in. (22 mm) at the Span 1 expansion joint. Over an equivalent time frame, the minimal prediction from the time dependent models was provided by the AASHTO LRFD provisions, which returned deflections of 0.60 in. (15 mm). The maximum prediction was given by the B3 model, which returned 2.2 in. (56 mm) of deflection over the same time period, nearly 3 times the measured deformation. The 1978 CEB/FIP Model Code and GL2000 also both overestimated the deflection over the 4.6-year time period, returning estimated deflections of 2.1 in. (53 mm) and 2.0 in. (51 mm), respectively. The 1990 CEB/FIP Model Code model provided better estimates than the B3, GL2000, and 1978 CEB/FIP Model Code, but still overestimated to the measured deflections, returning an estimate of 1.4 in. (35 mm) over 4.6 years. The closest prediction over the 4.6-year period was provided by the ACI-209 model, for which the Span 1 expansion joint longitudinal deflection was 0.78 in. (20 mm). Similar conclusions were drawn with regards to the Span 3 LP data in comparison with the Span 3 finite element results plus estimated Span 4 elongation.

The AASHTO and ACI-209 models provided accurate representations (in comparison to the other investigated models) of the time-dependent deflections extracted from the first 5 years of linear potentiometer data. However, if a longer time span was investigated (e.g., up to 30 years

after construction), the AASHTO and ACI-209 models would continue to underestimate the deflections by growing magnitudes. These models had reached their asymptotic limits within 3 to 5 years after construction, while the extracted time-dependent results for the first 5 years showed no sign of asymptotic behavior.

8.1.2 Concrete Strains

Time-dependent strains were extracted from longitudinal vibrating wire strain gages at Locations 3, 5, 7, 8, and 9 (shown in Figure 2.1) from the southbound bridge and compared to results from the finite element analysis for each considered time-dependent model, as shown in Figures 8.4 through 8.8. Processed time-dependent strains for each plot were taken as the average of all available gages of the designated description. For example "Top Flange (Centerline of Box)" results represent the average of all available longitudinal gages located in the top flange at the center of each box, while "Bottom Flange (Below Webs)" represents the average computed using all available gages located in the bottom flange below any of the four webs, and so on. Finite element results at the webs represented the average taken from all four webs, and results at the box centerlines were averaged between both boxes. Extracted time-dependent strains were available from September 1, 2008 until July 19, 2013, approximately 5 years after completion of the bridge. All results were plotted with respect to the Arrhenius adjusted age as computed in Section 7.3.2. Though the strain gages measured a local phenomena, the adjusted age was still computed using the average superstructure temperature as defined in Eqn. (7-3) to correct the time scale. This assumption was explored in detail in Chapter 9, and was found to be valid for the longitudinal time-dependent strains.

Investigation of measured results at Locations 3 and 9 in Figures 8.4 and 8.8 showed that both the top and bottom strains at 5 years after construction were best approximated by the AASHTO and ACI-209 provisions, and overestimated by all other examined time-dependent models. None of the models accurately captured the strains over the full timeframe of the

measured data from Locations 3 and 9. At Location 7 (Figure 8.6), the measured strains in the bottom flange were best captured by the 1990 CEB/FIP Model Code results over the full over investigated timeframe. However, the measured top flange strains were most closely predicted by the AASHTO and ACI-209 models, and overestimated by all other considered models.

Overall, measured time-dependent strains from Spans 1 and 3 (Locations 3 and 9) were more significantly overestimated by the finite element results than those from Span 2 (Locations 5, 7, and 8). These differences might be explained by differences in the cast-in-place (Spans 1 and 3) and precast (Span 2) concrete mixes not accounted for in the model, or randomness of the creep and shrinkage processes.

Depending on the location, the time-dependent strains extracted from the VWSG data were best approximated by the ACI-209 and 1990 CEB/FIP Model Code models. The ACI-209 model provided the closest predictions at Location 3, bottom flange of Location 5, top flange of Location 7, Location 8, and Location 9. The 190 CEB/FIP Model Code predictions were closest to the measured data in the top flange of Location 5 and bottom flange of Location 7.

Similar to the time-dependent longitudinal deflections extracted from the LP data, the measured time-dependent strains did not exhibit asymptotic behavior within the first 5 years, and instead followed a line in log time after 250 adjusted age days post construction (i.e., after the first year of data). From October 2008 until June 2009 (100 to 200 adjusted age days), the direction of the measured time-dependent strains appeared to reverse, particularly at Locations 3 and 9. None of the finite element results predicted this type of behavior. The cause for this reversal of strain was unclear, but was suspected to be related to the first application of large thermal gradients to the structure during the spring and summer of 2009. Effects of cyclic thermal gradients on time-dependent behavior are examined in Chapter 9.

The finite element model geometry did not include detailing such as anchorage blocks, exact reinforcement patterns, or diaphragms to deviate the draped tendons. Consequently the

model was not intended for investigation of local effects, but rather only the global behavior of the bridge. Despite these shortcomings, the concept of shear lag was explored by investigating the strain gages across the width of the deck and the bottom flange. Figures 8.9 and 8.10 show the measured time-dependent longitudinal strains in Locations 3 and 7, respectively, after 1, 2 and 3 years in Arrhenius adjusted age after the closure pour was placed. Other locations did not contain enough gages to permit this investigation. For comparison, these plots also include the longitudinal strains at Locations 3 and 7 computed at 3 adjusted age years after the closure pour and estimated using the ACI-209 provisions in the finite element model. The trends across the width of the section, though not the magnitudes of time-dependent strains, were similar for the finite element model results using the other investigated time-dependent models (not presented). Distances across the width of the cross section were measured relative to the breakpoint, defined as the path that the as-built profile grade line follows along the length of the bridge.

At Location 3, shown in Figure 8.9, the maximum measured time-dependent strains were seen at the east web of the exterior box and the centerline of the interior box. In the bottom flange of the exterior box of Location 3, the measured strains at the webs were notably higher than those at the centerline of the box. This was consistent with shear lag behavior, whereby time-dependent strains would be expected to be higher near the stiff webs where the strands were anchored than at the centerline of the box. An insufficient number of gages in the interior box meant that the large measured strains at the centerline of the interior box could not be compared to adjacent web gages. It was unclear why the interior box had larger measured time-dependent strains than the exterior box.

At Location 7, shown in Figure 8.10, the largest measured time-dependent strains occurred in the west webs of both the interior and exterior boxes. Minimum strains were found at the centerlines of the boxes. Measured strains in both boxes were similar. These findings were

consistent with the expectation that the stiffer components to which the post-tensioning was anchored would have larger time-dependent strains.

Measured results for time-dependent shear lag and strain distribution were not always consistent with finite element results. Time-dependent strains in the top flange from the finite element results were typically about 5% to 20% larger at the webs than at the centerlines of the boxes, which underestimated the variation in the measured time-dependent strains across the width of the bridge. FEM results of the time-dependent strains in the bottom flange were larger at the centerlines of the boxes than below the webs, which was inconsistent with the measured time-dependent strains.

In the worst cast, in the bottom flange at Location 3, the FEM strains at the centerlines were up to 35% higher than those computed at the webs. This was most likely a modeling problem associated with the anchorage of the post-tensioning to the concrete. In the physical structure, anchorage of the internal grouted tendons was done using blockouts at the corners of the box. On the other hand, the FEM tendons were simply terminated in the web and blockouts were not included, inducing local stresses at the point of anchorage. The elements at the webs of Location 3 were also the elements used to tie down the external draped tendons in Span 1, which caused further local stress concentrations. In the physical bridge, external tendons were held in place by deviator diaphragms which were not included in the model. Thus, the stress state at the intersection of the webs and the bottom flange of Location 3 was likely not accurately captured by the model. The FEM results for other instrumented locations were not affected locally by the presence of the draped strands, but were only marginally more reliable than results from Location 3. Thus, the lack of specific detailing such as anchor blocks and exact reinforcement patterns meant that investigating local effects with the finite element model was not advisable.

8.1.3 Vertical Deflections

Time-dependent vertical deflections at Locations 3, 7, and 9 were estimated from the finite element model, and are given in Figure 8.11. For each of the plots, zero deflection was associated with an elevation equal to the as-built profile grade line (PGL), with positive deflections above the PGL. The large jump in vertical deflection at an adjusted age of 2 days represented the tensioning of the bottom flange and draped tendons in Span 2 (adjusted age of zero being the placement of the closure pour).

Overall, the estimated time-dependent deflections were small. In the case of Location 7, all the models predicted a reversal in the direction of the deflection of the structure. This was expected to occur when the moments caused by the post-tensioning, constantly decreasing with time, were overtaken by the self weight moments. The total range of expected time-dependent motion beginning on September 1, 2008 until 150 adjusted age years (55,000 adjusted age days) was always less than 1.0 in. (25 mm) for Locations 3 and 9, and less than 4.5 in. (114 mm) for Location 7. The largest ranges for time-dependent deflection were predicted by the B3 and GL2000 models.

For comparison, surveys of the bridge to measure elevation changes were conducted on March 13, 2012, June 26, 2012, September 25, 2012, and March 21, 2013. For each survey, one set of elevations was shot at 8:00 AM CST to avoid the effects of thermal gradients on the bridge deflections. On June 26, 2012, additional elevations were taken hourly from 8:00 AM CST until 4:00 PM CST to capture the effects of thermal gradients. Elevation data at the end of construction was also available, but the exact time of the survey and the temperature of the structure were unknown.

Deflections due to temperature had similar magnitude to the expected time-dependent deflections of the bridge, and therefore elevations without associated temperature were not useful for analysis. For example, thermal gradients in the St. Anthony Falls Bridge were found to follow

the Priestley (1978) fifth-order curve with top surface temperature 46°F (25.6°C) higher than the web temperatures (Hedegaard et al., 2013). These gradients were expected to cause 1.2 in. (30 mm) of downward deflection at Location 7. On June 26, 2012 when hourly surveys were conducted, the maximum thermal gradient occurred at 3:00 PM CST, at which time the top surface temperature was about 32°F (18°C) higher than the webs. Over the course of this day, the measured range in Location 7 deflections due only to thermal behavior was 1.0 in. (25 mm).

Expected thermal displacements were subtracted from the survey measurements, and the time-dependent component of the measured vertical deflections was extracted. Expected deflections due to uniform temperature changes were estimated using the two-dimensional finite element model constructed for analysis of thermally induced stresses in the bridge (Hedegaard et al., 2013). These estimated deflections could not be validated against any survey measurements, as all available data contained a mixture of time-dependent and temperature-dependent deflections in unknown proportions. Deflections from the thermal gradients were estimated by linear regression on the data from the hourly surveys from June 26, 2012.

Over the course of the year from March 13, 2012 to March 21, 2013, the time-dependent deflections extracted from the surveys at Location 7 resulted in a net movement of 0.86 in. (22 mm) upward. The extracted time-dependent vertical deflections were computed as the total surveyed change in deflection minus the estimated temperature-dependent change in deflection. The surveyed Location 7 deflection was greater than deflections predicted by any of the FEM results over the same time period, for which the net movement was always less than 0.1 in. (2.5 mm) either upward or downward. Over the same time period at Locations 3 and 9, the net surveyed time-dependent deflections were less than 0.1 in. (2.5 mm) in either direction, which was consistent with the finite element model predictions.

This discrepancy was attributable to a number of causes. First, the net deflection for this structure was due to the competing moments caused by permanent gravity and post-tensioning

forces. These two sources were nearly balanced for this structure, so a small difference in loading might cause a large relative error (but small absolute error) in the expected deflections. Second, the interactions between time-dependent phenomena and temperature were ignored for the finite element analysis. The top surface of the bridge was, on average, warmer than the webs and bottom flange, and thus would be expected to creep and shrink more quickly. Furthermore, thermal gradients caused cyclic stresses which may have impacted the overall time-dependent behavior. As will be shown in Chapter 9, cyclic gradients cause the time-dependent behavior to shift in the opposite direction with regards to how the same gradients would impact the structure under elastic analysis. For example, because the elastic response of the bridge to a large thermal gradient was to deflect downwards at Location 7, the repeated application of such gradients would cause the time-dependent behavior to deflect upwards at Location 7. This was consistent with the comparisons between the FEM and survey results. The interactions between temperature and time-dependent behavior are explored in more detail in Chapter 9.

8.1.4 Longitudinal Concrete Stresses

Though no measured data were available for comparison, the long-term concrete stress estimates computed using the finite element model were of interest for purposes of planning for retrofit contingencies. The time-dependent finite element model was used to estimate the stress state due to dead and other permanent loads at the end of construction and end of service. Stress envelopes combining the computed dead-load stress state, vehicle live loading, and temperature effects were derived and subsequently compared to service stress limit states specified in the as-built construction documents (Minnesota Department of Transportation, 2008).

8.1.4.1 Permanent Loads and Post-Tensioning

Longitudinal concrete normal stresses in the top and bottom fibers of the superstructures were calculated at the end of construction (EoC) and the end of service (EoS). The end of construction stresses were extracted from the FEM after all permanent loads were applied to the

structure following the addition of the concrete barrier rail on August 5, 2008. End of service was assumed to be 150 years of Arrhenius adjusted time after completion of the bridge, which was expected to be approximately 200 years in total unadjusted time. To avoid local stress effects caused by the anchorage of the post-tensioning that were likely not indicative of the physical bridge conditions (per the discussion in Section 8.1.2), stresses were taken from the centerlines of the boxes.

Calculated top and bottom fiber longitudinal stresses due to gravity loading, permanent loads, and post-tensioning stresses at end of construction and end of service for each time-dependent model are shown in Figure 8.12. Station numbers along the x-axis (used for this and all subsequent stress state plots) can be referenced from Figures 2.2 through 2.5. All the considered models returned nearly identical stresses at the end of construction, meaning that the choice of time-dependent behavior was not critical for capturing the initial stresses even when considering the segmental construction and closure pour procedure. End of service stresses for each of the models were notably different, with the B3 and GL2000 models predicting the largest stress losses and AASHTO predicting the smallest losses. Over the course of the analysis, the top fiber lost compression along the entire length of the bridge, except near midspan of Span 2 which went further into compression. Losses in the bottom flange were largely concentrated in the region near midspan of Span 2, with only minor losses in the cast-in-place spans. The large loss of compression in the bottom fiber near midspan of Span 2 accompanied by the increase in compression in the top fiber at the same cross section indicated that post-tensioning losses were primarily concentrated in the bottom flange and draped strands crossing the Span 2 closure pour.

The as-built construction documents (Minnesota Department of Transportation, 2008) stated that the maximum compression stress limit due to permanent loads was 45% of f_c', in accordance with Table 5.9.4.2.1-1 of the AASHTO LRFD Specifications (2010). Conservatively assuming concrete strength equal to the nominal strength of 6,500 psi (44.8 MPa), this limit was

equal to 2,925 psi (20.2 MPa). Comparing the stresses in Figure 8.12 to this limit, all locations for all models satisfied this requirement except for the bottom fiber stresses at end of construction using the AASHTO LRFD time-dependent provisions. If instead a value of f_c' equal to 7,450 psi (51.4 MPa) was considered, as indicated by MnDOT measured strength results (Section 3.1.1), the compression limit would be increased to 3,350 psi (23.1 MPa) which was satisfied by all considered time-dependent models. None of the models predicted tension anywhere in the structure due to permanent loads either at end of construction or at end of service.

8.1.4.2 Service Limit States

The serviceability of the structure does not depend solely on the permanent loads, but also on transient loading such as live load and thermal effects. To check if the structure met service stress limits at end of construction and end of service, a number of load scenarios were considered. Limit states Service I and Service III from the AASHTO LRFD specifications (2010) were examined. The FEM models were not developed to consider strength limit states, as this would necessitate the addition of plastic behavior unrelated to time-dependent deformations, such as steel yielding and concrete damage. Service I represents normal operation of the bridge with all loads taken at nominal values. Service III is specifically used for longitudinal tensile stresses in prestressed structures, and is identical to Service I except that wind loading is ignored and only 80% of traffic loading is applied. Controlling stress envelopes for compression were generated using the Service I limit state, while the controlling envelopes for tension (or minimum compression) were generated using the Service III scenario.

For the calculations in this investigation, the only transient loads considered for service conditions were vehicular live loads (including light rail), thermal gradients, and uniform temperature changes. Wind loading was ignored.

The stresses due to vehicular live loading were derived from moment influence lines computed with the two-dimensional finite element model (French et al., 2012). Moment

envelopes and top and bottom concrete stresses were derived from the influence lines applying combinations of HL-93, permit vehicle, and light-rail live loads. The vehicle loads associated with each type of live load are presented in Figure 8.13. Each lane of HL-93 loading was accompanied by a lane load of 0.64 kips/ft (9.3 kN/m) positioned to maximize the moment at the location of interest. When permit vehicle loading was considered, one of the three types of permit vehicles (Standard C, MnDOT Standard P413, or the Special Permit Vehicle, as shown in Figure 8.13) was positioned in one of the lanes. When light-rail live loading was considered, one, two, or three light-rail cars were positioned to maximize the moment at the location of interest. The additional dead load associated with the addition of the light rail was not included, as it was unclear when this would be applied and how it might impact time-dependent behavior. An impact factor of 1.33 was applied to HL-93 truck and permit vehicle loading, while an impact factor of 1.2 was used for light-rail loading in accordance with the as-built drawings (Minnesota Department of Transportation, 2008).

The vehicular live load combinations and corresponding multiple presence factors considered in this analysis are summarized in Table 8.1. Multiple presence factors were taken from the as-built drawings (Minnesota Department of Transportation, 2008). For the HL-93 loading, these factors were dependent on the total number of loaded lanes, and not just the number of HL-93 lanes. Multiple presence factors for the permit vehicle and light-rail loading did not depend on the total number of loaded lanes, but rather on the particular load combination as shown in Table 8.1. Without light rail, a maximum of seven 12-ft (3.7-m) lanes were applied. When considering load cases with light rail, a maximum of six lanes (i.e., five lanes plus the light-rail lane), were placed on the bridge. Only one lane of the permit vehicle was applied at any given time, though the position of the lane across the width of the bridge could vary. Light-rail loading, if present, was limited to a single lane and always located on the outermost lane of the

eastern box (i.e., the lane closest to the northbound bridge). Any number of HL-93 lanes were allowed.

When computing moments to find the critical load case, load distribution was assumed such that the loaded box carried 70% of the total moment, while the remaining 30% of the load was carried by the other box. This assumption was supported by investigation of the truck test data (French et al., 2012) and recommendations from Podolny and Muller (1982).

The two-dimensional FEM presented in French et al. (2012) was utilized to compute the stresses due to thermal gradients. The thermal gradient was assumed to have the shape of the Priestley (1978) gradient with top surface temperature 46°F (25.6°C) higher than the web temperature. This thermal gradient, though not equivalent to the AASHTO LRFD (2010) gradient used for the design, was chosen because it was found to best match the maximum measured gradients from the St. Anthony Falls Bridge (Hedegaard et al., 2013). Though the Priestley (1978) recommendations do not prescribe a negative gradient (i.e., deck colder than the webs), stresses from negative gradients were considered by scaling the results from the positive gradient by −0.3, as per recommendations from the AASHTO LRFD (2010). The shapes of the measured negative gradients were not consistent and had considerable variation due to complex thermal and weather effects, but the expected strains induced by the scaled positive design gradient were similar to measured strain values during negative gradients (Hedegaard et al., 2013).

The two-dimensional FEM (French et al., 2012) was also used to compute the stresses due to uniform temperature changes in the structure. The temperature range applied to the model was ±75°F (±41.7°C), corresponding to a temperature range of −30 to 120°F (−34 to 49°C) as prescribed in the as-built documents (Minnesota Department of Transportation, 2008). This temperature range was nearly 35% greater than the range of −8.6 to 90°F (−22 to 32°C) measured from September 1, 2008 until July 19, 2013 by thermistor TSEWB002 located in the web at Location 7 (assumed to approximate uniform temperatures as it was isolated from thermal

gradient effects). Thus, the applied uniform temperature range was conservative. Even so, stresses caused by uniform thermal changes were typically much less than those from vehicle loading and thermal gradients.

The maximum compressive and tensile stress envelopes for the entire length of the bridge were computed using the worst-case combinations of the vehicle loads, thermal gradient, and uniform temperatures. When combining vehicle live loads and thermal gradients, the response due to the gradient was reduced by 50% according to the load factors in the as-built documents (Minnesota Department of Transportation, 2008). The full thermal gradient was only considered when no vehicular loading was applied. For checking compression using the Service I limit state, vehicle live load, when considered, was always applied in full (load factor equal to 1.0). For analyzing tension using Service III limit state, the vehicle live load was reduced using a load factor of 0.8 as per the AASHTO LRFD specifications (2010). The full stresses due to the uniform temperatures changes (either positive or negative to maximize the stresses) were applied in all cases.

The chosen load factors were not validated specifically for the St. Anthony Falls Bridge. The application of only half the thermal gradient when considering the full live load, and similarly the application of no live load when the full gradient is used, has been called into question (Hedegaard et al., 2013). However, no statistical analysis has yet been performed for the computation of more suitable load factors. Furthermore, no effort was made to match thermal effects together such that, as would be typical for the physical structure, high positive gradients would be correlated with high uniform temperatures. Thermal gradient and uniform temperature effects were superimposed in the analysis, but not correlation was assumed.

The top and bottom fiber stress envelopes for the combined live loading and thermal effects (with no permanent loads) are presented in Figure 8.14. Top fiber compressive stresses were controlled by the load case with full thermal gradient and no vehicle loading. Top fiber

tensile stresses in Span 2 were also controlled by the full thermal gradient case, while tensile stresses in Spans 1 and 3 were controlled by the full live load case with only 50% of the thermal gradient. Compressive and tensile stresses in the bottom flange for the entire bridge were controlled by the full vehicle load plus half the thermal gradient.

The top and bottom fiber longitudinal stress envelopes combining the end of construction stresses due to permanent loading with the Service I and Service III live loading stress envelopes are given in Figure 8.15. Stress limits were taken from the as-built documents (Minnesota Department of Transportation, 2008). The compressive limit was equal to $0.6\varphi_w f_c'$, where f_c' was conservatively assumed to be equal to the nominal strength value of 6,500 psi (44.8 MPa) and φ_w was a factor defined in Section 5.7.4.7 of the AASHTO LRFD specifications (2010). The φ_w factor was dependent on the slenderness of the flange of the box, and was approximately equal to 0.85 for the bottom flange and 1.0 for the top flange. No tension was allowed in the top slab, and instead a minimum compression limit of 250 psi (1.7 MPa) was required. For the bottom slab, the stress limit in the cast-in-place spans was $3.0\sqrt{f_c'}$ in units of psi, equal to 240 psi (1.7 MPa) of tension assuming nominal strength of 6,500 psi (44.8 MPa). For the precast segmental span, no tension was allowed in the bottom flange.

Except for the bottom flange stresses at the midspan closure pour using the AASHTO LRFD (2010) time-dependent model, compressive limits at end of construction were met by all considered time-dependent models. By assuming a concrete strength equal to 7,450 psi (51.4 MPa) equal to the average MnDOT measured 28-day strength, the compressive limits were always satisfied. The minimum compression limit in the top flange at the end of construction was violated just above Abutment 1 for all the time-dependent models, and also at the closure pour for models B3, 1990 CEB/FIP Model Code, and GL2000. In no case was tension developed, and at the closure pour, the limit was only exceeded by at most 50 psi (0.3 MPa), which was likely beyond the accuracy of the model. Low compressive stresses at Abutment 1 were likely related to

the moment restraint modeled into the bearing pad assemblies, and any damage at this location would only cause the structure to behave as though it rested on a perfect roller boundary, as was assumed for design.

Top and bottom fiber longitudinal stress envelopes for each of the models at end of service conditions are shown in Figure 8.16. The stress limits (Minnesota Department of Transportation, 2008) were identical to those used at the end of construction. Under no circumstances were the compressive limits exceeded. The tensile stress limit of the top fiber was exceeded near Abutment 1, though this was again likely related to the modeled moment restraint of the bearing pad assemblies. The top fiber stresses at the closure pour met the tensile stress requirements due to a gain in top fiber compression from the time-dependent effects. In the bottom fiber, tensile stresses were developed near the closure pour only for the B3 and GL2000 models. Maximum tensile stresses were equal to 370 psi (2.6 MPa) and 320 psi (2.2 MPa) for the B3 and GL2000 models, respectively. These were both less than the average UMN measured tensile strengths as recorded in Table 3.4. Also, the B3 and GL2000 models, which predicted the largest time-dependent strains among all the considered models, greatly overestimated the measured strains as shown in Section 8.1.2. If the current trends in time-dependent behavior continue, the physical bridge will likely remain in compression.

8.2 Uncertainty in Estimating Time-Dependent Behavior

8.2.1 Discussion of Creep and Shrinkage Uncertainty

As evinced by the comparison of the time-dependent model predictions with the creep and shrinkage laboratory data in Chapter 5 and the measured data from the St. Anthony Falls Bridge in the previous sections, the prediction of long-term behavior of even simple concrete structures is subject to multiple sources of uncertainty.

All the considered time-dependent models were expected to have large epistemic (i.e., systematic) uncertainty. Most models were designed for design office computations, and as such

were not intended to capture the physical processes driving time-dependent behavior, but rather just the trends in sets of measured data. All examined time-dependent models ignore or simplify many factors involved in creep and shrinkage, including the diffusion problem for drying creep and shrinkage, the increased hardening of the cement due to applied load, and other phenomena. Despite their distinct derivations, all the models are ultimately defined by fitting measured data using empirical coefficients. None of the models explicitly account for the inclusion of admixtures or the substitution of cementitious materials in the concrete. Also, none of the models directly include provisions for different aggregate stiffness or gradation. In short, all the models are empirical by nature and cannot capture all the complex interactions involved with the viscoelastic behavior of concrete.

This epistemic uncertainty is combined with aleatoric (i.e., statistical) uncertainty in material properties, construction techniques, loading and environmental conditions, measurement errors, and so on. The combined result of these factors is that the prediction of time-dependent behavior is subject to large overall uncertainty. According to Gardner and Lockman (2001), a model that could consistently predict shrinkage strains within 20% would be adequate. Creep experiments involve the subtraction of an uncertain shrinkage strain from the total measured time-dependent strain, and thus have larger aleatoric uncertainty than shrinkage experiments. Consequently, creep models calibrated using experimental creep data will likely have greater epistemic uncertainty than shrinkage models calibrated to laboratory data.

Several studies have examined the variation of creep and shrinkage models with respect to measured data. Bažant and Li (2008b) compared the B3 (Bažant and Baweja, 1995a), ACI-209 (1992), 1990 CEB/FIP Model Code, GL2000 (Gardner and Lockman, 2001), and GZ (Gardner and Zhao, 1993) time-dependent models to data from the NU-ITI database (Bažant and Li, 2008a), which contained 621 creep tests and 490 shrinkage tests and represents an expansion of the RILEM creep and shrinkage database. The authors argued that using the complete database

without weighting would introduce bias into the statistical study due to the lack of consistency in the distributions of load durations, concrete ages, and environmental factors among the samples. This was taken into account by dividing the datasets into parameter bins of equal weight. Multiple parameter bins were tested, including divisions of the data into bins based on the logarithm of the loading/drying duration, the logarithm of the loading/curing age, humidity, and the square root of the volume-to-surface ratio. Multi-dimensional bins involving variations on two or more of the aforementioned parameters were also tested. In addition, unmodified use of the full database would weight older and typically weaker (i.e., lower f_c') concrete mixes no longer in use more highly than modern mixes with higher f_c', particularly for long-duration tests. This was roughly accounted for by scaling the creep compliance and shrinkage strains in the database by the square root of the 28-day concrete strength of the sample. Regardless of the bin definition or whether or not scaling was performed based on sample strength, the B3 model was consistently the best predictor for both creep compliance and shrinkage, while the GL2000 model was consistently a close second. This was not a surprising result because, as discussed in Chapter 4, the B3 was calibrated using the entire RILEM database and the GL2000 model was calibrated using a selected subset of the database, while the other models used different datasets for calibration. None of the considered models had coefficients of variation less than 25% for either creep or shrinkage, regardless of bin definitions or data scaling.

A similar study was conducted by Gardner (2004) comparing the ACI-209 (1992), B3 (Bažant and Baweja, 1995a), 1990 CEB/FIP Model Code, and GL2000 (Gardner and Lockman, 2001) time-dependent models to the RILEM database. Only a subset of the database was used for comparison, limited only to samples with loading duration longer than 500 days, 28-day strengths between 2,300 and 12,000 psi (16 and 82 MPa), loading age and curing durations greater than 1 day, and volume-to-surface ratio greater than 0.75 in. (19 mm). This reduced the number of creep tests from 518 to 166, and the number of shrinkage tests from 426 to 107. To reduce the bias

introduced by the relatively numerous readings at early ages, the data was filtered such that each successive observation in any given dataset was twice the previous age. The coefficient of variation of the prediction methods was computed for each half logarithmic decade of loading, and an average coefficient of variation was also computed for the entire duration of loading. Model predictions were computed by two separate methods: first, by considering all available material parameters for the datasets; second by considering only the concrete strength and parameters that could be known by the designer prior to construction (specifically, only geometrical factors such as *V*/*S* and environmental factors such as relative humidity were included, while mix properties, measured elastic modulus, etc., where excluded). Regardless of which method was chosen, the GL2000 model was the best at predicting creep and shrinkage, followed by the B3 model, the 1990 CEB/FIP Model Code, and finally the ACI-209. This, again, was not surprising as the data used to calibrate the GL2000 model was filtered from the RILEM database in a similar fashion as was performed for this study (Lockman, 2000). Typical coefficients of variation on creep and shrinkage from the Bažant and Li (2008b) and Gardner (2004) studies are given in Table 8.2.

A study by Keitel and Dimmig-Osburg (2010) analyzed the uncertainty of the B3, GL2000, 1990 CEB/FIP Model Code, and ACI-209 creep models. This study combined uncertainty from the following sources: the epistemic model prognosis uncertainty (taken from the Gardner (2004) study discussed above), uncertainty in the measurements from the RILEM database, random scatter in the process of concrete creep of identical samples, and input parameter uncertainty including correlation among material properties. Though the uncertainty for any individual material parameter (for instance, concrete strength) was consistent among all considered creep models, the correlations between parameters depended strongly on the selected model, as not all models used similar parameters. For example, the parameters for the B3 model were entirely different from all the other models, and did not include the typical elastic modulus

but did use a variety of mix parameters. The B3 model was consistently found to have the lowest variation due to input parameters uncertainty. Most models were found to be most strongly influenced by changes in elastic modulus, a parameter excluded from the B3 model. Combining all the sources of uncertainty, the B3 and GL2000 models were found to have similar overall coefficients of variation around 25%, while the ACI-209 and 1990 CEB/FIP Model Code methods had variations around 33%. Overall uncertainty was largely dominated by the model prediction uncertainties, with other factors being secondary.

8.2.2 Investigating Time-Dependent Uncertainty using FEM

To investigate the uncertainty in time-dependent predictions, upper and lower bounds for the St. Anthony Falls Bridge time-dependent behavior were computed in the FEM using the GL2000 model. The GL2000 model was chosen as a conservative estimate of the time-dependent deformations of the St. Anthony Falls Bridge, as evinced by the FEM results from Section 8.1, to maximize the range of uncertainty. The bounds were computed for a 95% confidence interval assuming a coefficient of variation of the time-dependent strains equal to 25% per the study by Keitel and Dimmig-Osburg (2010). The mean prediction was equivalent to the results presented in this chapter for the GL2000 time-dependent model documented in Section 4.7. Thus, the upper bound estimate was computed by applying a multiplicative factor of 1.5 (equivalent to the mean plus two times the coefficient of variation) to the GL2000 creep and shrinkage provisions, while the lower bound used a factor of 0.5 (equivalent to the mean minus two times the coefficient of variation). The instantaneous elastic behavior was assumed to be deterministic, and thus was not modified for the upper or lower bounds.

The upper bound, lower bound, and mean longitudinal time-dependent deflections at the expansion joints, estimated from the FEM results, are compared with the processed linear potentiometer data in Figures 8.17 and 8.18 for Southbound Span 1 and Span 3, respectively. The FEM results were set equal to the measured data at 10:00 AM CST on May 16, 2010. The total

time-dependent deflections for the upper-bound estimate were not 50% greater than the mean estimate because the larger time-dependent strains caused larger post-tensioning losses. By similar logic, the lower bound estimate of the time-dependent deflections was greater than 50% of the mean estimate. The lower bound estimate trended closely with the measured data.

The mean and bounding estimates of the vertical deflections computed using the GL2000 time-dependent model are plotted in Figure 8.19. Compared to the LP estimates, the vertical deflections at Location 7 were more sensitive to the uncertainty in the time-dependent predictions. The reversal in the direction of the deflections occurred earlier in the bridge life for the upper bound estimate, and later in the bridge life for the lower bound estimate, as compared to the mean. This resulted in a much larger range of downward deflections for the upper bound estimate as compared to the mean.

Estimates of the mean and bounding longitudinal concrete stress due to dead loads and post-tensioning at the end of construction and end of service are shown in Figure 8.20. The uncertainty in the time-dependent models did not have a significant impact on the end of construction stresses, as expected from comparisons between the different time-dependent models in Section 8.1.4.1. In the bottom flange at midspan of the Span 2, the location of the largest post-tensioning losses, the upper bound estimate returned only approximately 30% greater losses at end of service than the mean estimate.

The top and bottom fiber longitudinal stress envelopes combining the end of service stresses due to permanent loading with the Service I and Service III live loading stress envelopes are given in Figure 8.21. Live load stress envelopes are presented in Figure 8.14. Loading and stress limits are discussed in Section 8.1.4.2. Stress envelopes at the end of construction were similar to those shown in Figure 8.15, and are consequently not provided in the case of time-dependent model uncertainty. The end of service tensile limit (Service III) in the bottom fiber was exceeded at midspan of Span 2 by 318 psi (2.2 MPa) and 717 psi (4.9 MPa) by the mean and

upper bound estimates, respectively. The average UMN measured split cylinder tensile strength of the southbound superstructure concrete (see Section 3.2) was 395 psi (2.7 MPa), and so the upper limit tensile stresses might be expected to cause cracking in the bottom flange at midspan of Span 2. However, damage was believed to be unlikely for the physical structure as the mean estimate returned nearly double the measured deflections and strains, which trended closely to lower bound estimates.

8.2.3 Accounting for Uncertainty of Time-Dependent Behavior in Design

The large uncertainty in creep and shrinkage model predictions has implications for designing concrete structures for time-dependent effects. For design, it cannot be expected that any currently available time-dependent model will accurately capture the behavior of the structure after completion. However, accounting for the large uncertainty can be nearly untenable for most structures, as long as economy is a concern.

Examining the end of construction stress envelope in Figure 8.15 and end of service stress envelope in Figure 8.16, the controlling location in compression at end of construction and the controlling location for tension (or minimum compression) at end of service were, for the I-35W St. Anthony Falls Bridge, both in the bottom flange at the midspan of Span 2. If the design of this bridge was conducted using the upper bound time-dependent estimate with the GL2000 model as described in Section 8.2.2, the stress limits could only be met by changing the bridge geometry, the mix design, the construction sequence, or the amount of mild reinforcement.

Altering the geometry would likely result in an uneconomical structure, and is the least desirable alternative. Many time-dependent prediction models, including the GL2000 and the 1990 CEB/FIP Model Code, allow for a reduction in creep and shrinkage by increasing concrete strength. According to the B3 model, the creep can be reduced by increasing the aggregate-to-cement ratio or decreasing the water-cement ratio. A reduction in time-dependent strains could also be achieved by loading the concrete at a later age. Delaying loading is only an economical

solution for concrete loaded at early ages (e.g., less than one week after casting), for which postponing the application of post-tensioning by a few days would have a significant reduction in ultimate creep deformations. Concrete sections loaded at older ages (for example, the segmental sections which were typically not loaded until at least one month after casting) would need to be delayed for a comparatively longer time to achieve significant reductions in creep strain, and thus would negatively impact the construction schedule. As discussed in Section 6.3.1, increasing the amount of mild steel reinforcement has a proportionally larger impact on the time-dependent strains than the elastic strains. Thus, increasing the amount of compressive mild steel can help control excessive time-dependent deformations.

8.3 Summary and Conclusions

The behavior of the time-dependent models incorporating the full construction sequence could be divided into three categories: the AASHTO and ACI-209 models which quickly approached low asymptotic values; the CEB/FIP 1978 and 1990 Model Code models which asymptotically approached moderate ultimate values; and the B3 and GL2000 models which followed a logarithmic form and returned the highest deformations.

In comparison with the measured linear potentiometer and vibrating wire strain gage data, none of the models consistently predicted the deformation of the as-built I-35W St. Anthony Falls Bridge. Among all the considered models, the ACI-209 and CEB/FIP 1990 Model Code results were often the closest to the measured results. The early age behavior (first 1.5 years after construction) was best predicted by the AASHTO and ACI-209 models. However, both these time-dependent models approached their asymptotic limits prior to 5 years after bridge completion. This was inconsistent with the time-dependent deformations extracted from the LP and VWSG data, which followed a line in the logarithm of adjusted time and showed no sign of asymptotic behavior over the total 5 years of collected data. This trend in the AASHTO and ACI-209 models was primarily due to the method by which these models account for the *V*/*S* ratio, as

discussed in detail in Section 4.9.3. Both the B3 and GL2000 models vastly overestimated the magnitude of measured deformations. The 1978 CEB/FIP Model Code model also greatly overestimated the measured time-dependent behavior but, at the end of service, converged to similar results as those computed using the 1990 CEB/FIP Model Code provisions. Not enough data has yet been collected to definitively state whether the long-term structural behavior will follow an asymptotic or logarithmic curve, though after five years of measurement, the deformations continue to increase in a logarithmic fashion.

Results from the finite element models showed that, for all time-dependent models, the direction of vertical deflections would reverse direction sometime after completion of the bridge. At midspan of Span 2, initial time-dependent vertical deflections proceeded upwards, then reversed direction and continued downwards until the end of the service life of the structure. Regardless of the chosen time-dependent model, the magnitudes of the time-dependent vertical deflections after completion of the structure were always less than 4 in. (100 mm). Thus, unlike the Koror-Babeldaob Bridge and other post-tensioned structures investigated by Bažant et al. (2010), the I-35W St. Anthony Falls Bridge does not appear to be susceptible to problems of excessive deflections.

The most likely contributor to the resistance of this structure to excessive deflections as compared to previous bridges was the manner by which continuity of the St. Anthony Falls Bridge was achieved. The Koror-Babeldaob Bridge was connected at midspan by a sliding hinge (Bažant et al., 2010). In contrast, the I-35W St. Anthony Falls Bridge was constructed with a midspan closure pour and draped and bottom flange post-tensioning along the entire length of the river span, thus achieving continuity for the three span structure. The particular balance of forces achieved in the St. Anthony Falls Bridge allowed for the Span 2 bottom post-tensioning to force the bridge upwards during the early life of the structure. After sufficient losses, gravity loading

was expected to overtake the post-tensioning forces, at which point the bridge would begin to deflect back to its original shape.

Concrete stresses and the associated Service I and III limit states were investigated using the finite element model at end of construction and end of service conditions. At end of service, the tensile limit was exceeded at midspan of Span 2 when using the B3 and GL2000 time-dependent models. Because these two models greatly overestimated the measured time-dependent data from the bridge, it was believed to be unlikely (barring any degradation of the structure or unexpected loss of post-tensioning) that this tensile limit would be exceeded in the physical structure due to time-dependent effects. No other time-dependent models exceeded the tensile limit state, and thus the I-35W St. Anthony Falls Bridge will likely remain within allowable stress bounds as the structure undergoes continued time-dependent deformations.

Predictions of time-dependent behavior are subject to large uncertainty, as evinced by comparisons of the finite element results with the measured data and also by comparisons of the RILEM (now NU-ITI) creep and shrinkage database values to predictions (Bažant and Li, 2008b; Gardner, 2004). According to results from Keitel and Dimmig-Osburg (2010) when accounting for epistemic uncertainty in the prediction models along with correlated input parameter uncertainty, all time-dependent model predictions have coefficients of variation equal to 25% or greater. If an appropriate bounding interval is considered in design, the resulting structure may need to be overdesigned to such a degree as to be untenable due to economic considerations. Some cost-effective alternatives exist to mitigate the impacts of time-dependent behavior, such as designing a concrete mix that minimizes creep and shrinkage, delaying the stressing of early-age concrete until it has gained a higher strength, or incorporating more mild steel to reduce the time-dependent deformation of the concrete.

Chapter 9: FEM Investigation of Thermal Effects on Time-Dependent Behavior

Most basic research on the time-dependent behavior of concrete, specifically creep and shrinkage, has taken place under controlled uniform thermal conditions. However, civil structures rarely experience constant temperatures, and instead are often subject to average temperature changes (either daily or seasonal) and thermal gradients. This chapter aims to discuss and analyze the impacts that changing thermal conditions can have on the time-dependent behavior of concrete structures, with a particular focus on post-tensioned concrete bridges.

The technique for extracting the time-dependent behavior from the measured data taken from the instrumentation in the St. Anthony Falls Bridge and correcting for temperature changes (documented in Sections 7.1 and 7.3.2) was based on the assumption that an adjusted age using the Arrhenius equation could be computed for the aggregate time-dependent behavior of the total structure using the spatially averaged structure temperature at one location. Thus, the average concrete temperature measured at Location 7 was used to correct the time scale for the processed LP and VWSG data. The processed data was then compared to results from a finite element model for which the temperature was held constant. To validate this methodology, a time-dependent finite element model of a box girder structure with a simplified geometry was constructed, and a variety of temperature histories were tested. The response of the modeled structure was observed for the impacts of spatially nonuniform temperatures and the temperature history on the overall time-dependent behavior.

The updated methodology for considering the interactions of temperature and time-dependent behavior using the finite element method is presented in Section 9.1. The methodology is validated in Section 9.2, and then a thorough examination of how cyclic seasonal temperature changes and daily thermal gradients impact the long-term time-dependent response of a post-tensioned box girder structure is presented in Section 9.3.

9.1 Methodology

To investigate the effects that thermal changes have on the time-dependent behavior of concrete, the finite element method presented in Chapter 6 was modified to account for temperature. The model for the I-35W St. Anthony Falls Bridge was too complicated and large to be efficiently analyzed for the interaction between temperature and time, and so simplified models were used instead. Consequently, the results from this study are not quantitatively relatable to the behavior of the St. Anthony Falls Bridge, but are meant instead to provide qualitative test cases. Construction of and results from the simplified model are presented in Section 9.3.

Analysis of the time-dependent behavior of the concrete and mild steel composite was conducted in accordance with the Kelvin Chain model procedure for steel-concrete composite materials documented in Section 6.3. All temperatures in the model were input in units of Kelvin because the time-adjustment procedure for correcting the rates of aging, creep, and shrinkage required the use of an absolute temperature scale.

The concrete coefficient of thermal expansion was found to increase linearly with temperature in Section 3.4.2.3. Therefore, the CTE of the concrete was specified as

$$\alpha(T) = -13.71 + 0.0845 \cdot T \tag{9-1}$$

where α is the coefficient of thermal expansion as a function of temperature specified in microstrain per Kelvin, and the temperature T is in Kelvin. This equation was only valid for typical operating temperatures from approximately 0°F to 120°F (255 K to 322 K), and thus would never be negative for this study. The CTE of the mild and post-tensioning steel was assumed to be constant with temperature, and was specified as a typical value of 12.2 με/K (6.78 με/°F). Thermal strains were incorporated in the *umat* subroutine in a manner identical to that used for the shrinkage strains, as summarized in Section 6.3.3.

The temperature dependence of the hydration rate, discussed in Section 7.2.1, was used to adjust the age of loading t_0. The adjusted concrete age was saved as an internal variable at each integration point, such that the hydration rate could vary across the model. During each time step, the following expression was called to determine how much the concrete had hydrated over the current step:

$$\Delta t_{hyd} = \int_{t_b}^{t_e} e^{\left[\frac{U_h}{R}\left(\frac{1}{T_0}-\frac{1}{T(t')}\right)\right]} dt' \tag{9-2}$$

where t_b and t_e are the unadjusted time at the beginning at the end of the step, respectively, U_h/R is the hydration activation energy constant equal to 4,000 K, $T(t')$ is the temperature in Kelvin and is assumed to vary linearly over the time step, T_0 is a constant equal to 293 K, and t' is the (unadjusted) time integration variable. At the end of each time step, Δt_{hyd} was added to the adjusted concrete age from the beginning of the time step and saved to the internal variable for use in the next time step. The adjusted concrete age was used whenever the concrete age at loading t_0 was required, such as in the expressions for strength gain with time or for loading age constants in the time-dependent models.

Temperature dependence of the creep rate, discussed in Section 7.2.2 for basic creep and Section 7.2.3 for drying creep, was used to adjust the duration of the current time step. Because the creep formulation was derived as a Kelvin Chain rate type formulation, it was not necessary to save any additional internal variables when accounting for temperature. Instead, the duration of the step was elongated or contracted for each integration point depending on the temperature at that integration point. The adjusted step duration Δt_{adj} was computed using a modification of Eqn. (7-12):

$$\Delta t_{adj} = \int_{t_b}^{t_e} e^{\left[\frac{U_c}{R}\left(\frac{1}{T_0}-\frac{1}{T(t')}\right)\right]} dt' \tag{9-3}$$

where t_b and t_e are the unadjusted time at the beginning at the end of the step, respectively, U_c/R is the creep activation energy constant assumed to be given by Eqn. (7-13) and equal to 7,360 K for the superstructure concrete mix, $T(t')$ is the temperature in Kelvin and is assumed to vary linearly over the time step, T_0 is a constant equal to 293 K, and t' is the time integration variable. The adjusted Δt_{adj} replaced the variable Δt in the Kelvin Chain model procedure, and was only used in determining the amount of creep strain over the time increment. Due to the lack of information in the literature regarding the dependence of drying creep on temperature, no distinction was made between basic creep and drying creep, meaning the adjusted Δt_{adj} was used for the total creep. Transitional thermal creep (Bažant, Cusatis, and Cedolin, 2004) was not considered in this investigation.

To incorporate the temperature dependence of the shrinkage strains, discussed in Section 7.2.3, the equivalent total duration of shrinkage was defined. This procedure was similar to that used for adjusting the hydration time. An additional internal variable was saved for each integration point to store the total amount of adjusted shrinkage time. During a time step, the change to the total shrinkage time was calculated by

$$\Delta t_{sh} = \int_{t_b}^{t_e} e^{\left[\frac{U_s}{R}\left(\frac{1}{T_0}-\frac{1}{T(t')}\right)\right]} dt' \tag{9-4}$$

where t_b and t_e are the unadjusted time at the beginning at the end of the step, respectively, U_s/R is activation energy constant for shrinkage, $T(t')$ is the temperature in Kelvin and is assumed to vary linearly over the time step, T_0 is a constant equal to 293 K, and t' is the time integration variable. To remain consistent with the procedure used to investigate the temperature dependence of the time-dependent strains in the measured data as shown in Section 7.3.2, the constant U_s/R was assumed to be the same as the creep activation energy constant U_c/R, which was equal to 7,360 K for the superstructure concrete. During each time step, the total adjusted shrinkage times at the beginning and end of the time step were input into the shrinkage curve to compute the shrinkage

strain during the time step. The internal variable was then updated to the final adjusted shrinkage time for use in the next time increment.

In contrast with the temperature dependence of the B3 model specifications given in Eqns. (7-14) and (7-15), the total creep and shrinkage strains were assumed to be independent of the temperature. Only the creep and shrinkage rates were adjusted for temperature.

Humidity was always assumed to be constant during all conducted finite element analyses. Ambient relative humidity is higher in the winter than during the summer, and consequently shrinkage and drying creep would be expected to accelerate during the summer. However, assuming that diffusion of water through the concrete is slow, transient changes in ambient relative humidity were not expected to significantly alter the expected deformations, and thus an average ambient humidity over time was adopted.

Because the temperature correction formulation was performed on each integration point individually, effects such as non-uniform hydration and differential shrinkage caused by thermal gradients through a cross section were captured by the described procedure. Stresses and strains due to geometric constraints were automatically included in the analysis due to the nature of finite element approximations. For example, if a thermal gradient was applied to a box beam such that the deck was heated relative to the web and bottom flange, compression and tension would be introduced in the top and bottom flanges, respectively, due to strain compatibility. The strain computed at each integration point would include creep at a rate dictated by the stress and temperature conditions at that point, so top flange points would creep much faster (due to increased compressive stress and temperature) than bottom flange points. This differential creep would in turn introduce additional stresses due to strain compatibility. To reiterate, no particular modifications needed to be made to the methodology to account for these complexities, as they were handled by the nature of the finite element method.

9.2 Validation of Temperature-Dependent FEM

To ensure the validity of the hydration, creep, and shrinkage rate-adjustment procedures implemented in the finite element method as described in Section 9.1, a simple model was tested. The model consisted of an 11-in. (280-mm) long by 4-in. (102-mm) diameter concrete cylinder under uniaxial compression along the cylinder axis. The volume-to-surface ratio of the cylinder was equal to 1.0 in. (25.4 mm), the 28-day concrete strength was equal to 7,450 psi (51.4 MPa), Type I cement was used, and the ambient humidity was 64.1%. The cylinder was moist cured for 1 day, and initially loaded at 5 days with a constant compressive stress of 1,900 psi (13.1 MPa). The stress was increased to 2,900 psi (20.0 MPa) at 30 days after casting, and this load was held constant until the end of the analysis. Stress was applied by a constant external traction, and therefore post-tensioning losses were not considered. The cylinders were unreinforced and gravity loads were neglected so that the external traction was the only stress applied to the cylinder. The GL2000 model (Gardner and Lockman, 2001) was used to model both shrinkage and creep. Parameters specific to the GL2000 time-dependent model, such as cement type factors, the aging curve, and the strength to modulus conversion, were identical to those discussed in Section 4.7.

The coefficient of thermal expansion of the concrete was assumed to vary with temperature according to Eqn. (9-1). Temperature effects on the hydration, creep, and shrinkage rates were introduced using the procedure discussed in Section 9.1. Temperature history was introduced to the model to test the validity of the finite element corrections from Section 9.1. For the 5 days prior to loading, the temperature was held at 293 K (68°F). When the load was applied at 5 days, the temperature was simultaneously changed to 273 K (32°F). The temperature was increased to 323 K (122°F) at a concrete age of 25 days. At 40 days, the temperature was reduced to 303 K (86°F), at which point onward the temperature was held constant. All temperature changes were assumed to occur instantaneously.

Strains from the finite element method were compared to hand calculations. The total strain in the concrete (excluding the initial thermal strains from the change from 293 K to 273 K at 5 days) from the finite element method and the hand calculations are shown in Figure 9.1 (compressive strain positive). Long-term strain differences between the two methods were within 1.5%, which was comparable to the accuracy of the Kelvin Chain approximation excluding temperature effects as discussed in Section 6.2.8.

The above analysis was repeated for the ACI Committee 209 (1992) time-dependent provisions as described in Section 4.3. The parameters were identical to those described above for the GL2000 model, except that the cement type was specified as Type III as determined by fit of the ACI-209 strength gain curve to the 7- and 28-day MnDOT measured strength data from the superstructure mix (see Section 3.1). Other parameters necessary for the definition of the ACI procedure that were excluded from the GL2000 model included slump, air content, total cement content, and fine aggregate ratio, which were set equal to the superstructure values presented in Section 4.3.4. The total strain in the concrete as computed by the ACI-209 procedure (excluding the initial thermal strains from the change from 293 K to 273 K at 5 days) from the finite element method and the hand calculations are shown in Figure 9.2 (compressive strains positive). Long-term strains from the finite element method were within 0.5% of the hand calculated results.

9.3 Effects of Cyclic Thermal Input on Time-Dependent Behavior

9.3.1 FEM Model Construction

The qualitative effects that seasonal temperature changes and daily thermal gradients have on time-dependent behavior were investigated using a simplified finite element model. The simplified model was constructed in Abaqus (Dassault Systèmes, 2010a) in a manner similar to the St. Anthony Falls Bridge model as presented in Chapter 6.

The simple model consisted of a single-celled three-span continuous concrete box beam. The box cross section, shown in Figure 9.3, was constant along the entire length of the bridge.

Span lengths were equal to 75 ft (22.9 m) for the outer spans and 83.3 ft (25.4 m) for the center span. All boundary conditions were approximated as rollers. Solid diaphragms were included at the piers and abutments. The diaphragms filled the entire interior of the box. At either end of the center span, the diaphragm was 40 in. (1.0 m) along the length of the bridge and centered above the roller. For the end rollers, the diaphragm was also 40 in. (1.0 m) long, but the roller was positioned at the end of the structure.

The box was post-tensioned with 40 in.^{2} (258 cm^2) of strands oriented longitudinally at each of the corners where the webs intersected with the bottom and top flanges, amounting to a total steel area in the entire cross section of 160 in.^{2} (1,030 cm^2). These strands were bonded to the concrete, and ran along the entire length of all three spans. Post-tensioning stresses at jacking were equal to 200 ksi (1,380 MPa) along the entire length of all the strands. Immediate friction and anchorage losses were not included. Elastic shortening losses were not considered, as though the strands were all jacked simultaneously. Consequently the initial stresses in the modeled steel were held constant over the first time step after initial activation.

Due to the symmetry of the bridge, only one quarter of the structure was modeled to reduce the computation time. All longitudinal deflections were constrained to be equal to zero at midspan of the center span, and transverse horizontal deflections were set equal to zero at all points along the centerline of the bridge, thus enforcing the symmetry of the structure while reducing the size of the model. A depiction of the box beam geometry used in the finite element model is shown in Figure 9.4.

The box section was composed of 20-node three-dimensional quadratic continuum elements with reduced integration (element type C3D20R). The characteristic element size was equal to 24 in. (0.61 m). Two elements were modeled through the thickness of the top flange to better capture thermal gradients. Thus, the model was discretized into 7 elements through the depth of the section and 59 elements along the length. The total element count was 1,580 for the

entire quarter section of the concrete beam. Post-tensioning strands were modeled as two-node linear truss elements (element type T3D2) with characteristic element size of 24 in. (0.61 m). The strands were constrained to the concrete along their entire length to emulate bonded post-tensioning.

The GL2000 (Gardner and Lockman, 2001) model and the ACI-209 (1992) model were considered for the interaction between time-dependent behavior and thermal effects. These models were chosen to contrast between a logarithmic creep model (GL2000) and asymptotic creep model (ACI-209). The concrete was specified with material properties identical to those for the St. Anthony Falls Bridge superstructure given in Chapter 4 and Section 9.1. The strength to modulus relation, concrete aging curve, and other parameters based on the cement type and unique to the GL2000 and ACI-209 models are discussed in Sections 4.7 and 4.3, respectively. For computation of the time-dependent behavior, the volume-to-surface ratio of the concrete was assumed to be equal to 10.0 in. (0.25 m) over the entire model, the ambient humidity was equal to 64.1%, and the moist curing duration was assumed to be 1 day.

The concrete was assumed to have a mild reinforcement ratio in the longitudinal direction equal to 0.003, and no reinforcement in the transverse and vertical directions. The mild steel was assumed to have an elastic modulus of 29,000 ksi (200 GPa), and was taken into account using the composite material procedure discussed in Section 6.3.

The post-tensioning strands were assumed to be Grade 270 low-relaxation strands with modulus equal to 28,500 ksi (196.5 GPa) and yield strength of 243 ksi (1,680 MPa). Relaxation of the strands was calculated using the procedure from Magura et al. (1964) as presented in Section 6.2.5.

To include gravity loading, the densities for reinforced concrete and post-tensioning steel were equal to 150 lbs/ft^3 (2,400 kg/m^3) and 480 lbs/ft^3 (7,700 kg/m^3), respectively. The total analysis duration was set equal to 10,950 days (approximately 30 years) with individual time

steps equal to 0.5 days throughout the entire analysis. No construction sequence was modeled; post-tensioning and gravity loads were applied to the beam 28 days after casting. The temperature before any load was applied was assumed to be equal to a constant 293 K (68°F) so that the hydration rate and shrinkage rate did not need to be corrected for temperature until the analysis began when the load was first applied. Load included post-tensioning, self weight, and thermal variations as described below.

9.3.2 Investigated Thermal Variations

Eight temperature history scenarios were applied to the finite element model to investigate the impacts of cycled temperatures on time-dependent behavior. For specification into the finite element model, the temperature histories were split into a uniform temperature component $T(t)$ and a thermal gradient $T_{grad}(t,y)$. Thermal gradients were assumed to follow the shape of the Priestley (1978) curve, and therefore the nodal temperatures in the top 47 in. (1,200 mm) of the section were defined as the sum of $T(t)$ and $T_{grad}(t,y)$. Temperatures below the top 47 in. (1,200 mm) were not modified by the applied gradient, and were simply equal to $T(t)$. The investigated temperature histories are summarized in Table 9.1 and described in the following paragraphs.

The "Constant" scenario kept the temperature at all locations for the entire loading history equal to a constant $T(t)$ = 293 K (68°F). The thermal gradient $T_{grad}(t,y)$ was equal to zero.

For the "Seasonal" scenario, the entire bridge temperature was cycled according to the sinusoidal expression

$$T(t) = -17.22\cos\left(\frac{2\pi}{365}t\right) + 283.55 \tag{9-5}$$

where $T(t)$ is the temperature in Kelvin, and t is the analysis time in days. The analysis time t was defined such that t = 0 when the concrete was first loaded at 28 days. This equation mimicked the form of the sinusoidal fit for measured temperature data given in Section 7.3.2, except that the

phase angle was shifted so that the temperature was at a minimum at time t = 0 (i.e., the analysis began at the coldest time during winter). No thermal gradients were present during this scenario, such that $T_{grad}(t,y)$ was equal to zero.

The "Winter Gradient" scenario modeled daily thermal gradients applied to the bridge. For this scenario, the uniform temperature was kept constant at $T(t)$ = 293 K (68°F). Daily thermal gradient temperatures were applied to the top 47 in. (1.2 m) of the box section with the form of the Priestley (1978) curve:

$$T_{grad}(t,y) = T_0(t)\left(\frac{47-y}{47}\right)^5 \tag{9-6}$$

where y is the distance in inches defined as positive down from the top surface of the deck, and $T_0(t)$ is the gradient temperature at the top surface of the deck. The Priestley (1978) fifth-order curve was found to be a good approximation of the shape of the maximum positive gradients measured from the St. Anthony Falls Bridge (Hedegaard et al., 2013). Daily thermal gradients were applied by linearly increasing $T_0(t)$ from zero at the beginning of each day (i.e., at t = 0, 1, 2 days, and so on) to a maximum at midday (i.e., at t = 0.5, 1.5, 2.5 days, and so on), and then linearly decreasing back to zero from midday to the end of the day. The daily maximum T_0 (i.e., the value of T_0 at t = 0.5, 1.5, 2.5 days, and so on) varied throughout the year according to the expression

$$T_0(t) = 25.6\left[\sin\left(\frac{\pi}{365}t\right)\right]^2 \tag{9-7}$$

where $T_0(t)$ is defined in Kelvin, and t is the analysis time in days. The value for the maximum gradient equal to 25.6 K (46.0°F) was equivalent to the positive design thermal gradient magnitude for Zone 2 in the AASHTO LRFD specifications (2010). This formulation enforced that the minimum gradients would be applied at t = 0, 365, 730 days, and so on, as though the bridge was first loaded during winter (hence, the Winter Gradient scenario).

The "Winter Gradient Plus Seasonal" scenario combined the seasonal temperature $T(t)$ from Eqn. (9-5) with the daily gradients $T_{grad}(t,y)$ from the "Winter Gradient" scenario described by Eqns. (9-6) and (9-7). At time $t = 0$, the minimum uniform temperature $T(t)$ and minimum gradient $T_{grad}(t,y)$ coincided, as though the bridge were first loaded on the coldest day during the winter. Furthermore, this ensured that the maximum gradients occurred during the summer months when the annual temperature was also maximum.

For the "Summer Gradient" scenario, daily thermal gradients were applied to the bridge but the uniform temperature was constant at $T(t) = 293$ K (68°F). The gradients were applied in an identical manner as for the "Winter Gradient" scenario, except that the gradient magnitudes were shifted by 0.5 years (182.5 days):

$$T_0(t) = 25.6\left[\sin\left(\frac{\pi}{365}(t-182.5)\right)\right]^2 \tag{9-8}$$

where $T_0(t)$ is defined in Kelvin, and t is the analysis time in days. This daily maximum gradient magnitude was applied to the bridge geometry according to the Priestley (1978) fifth-order curve in Eqn. (9-6). Due to the time shift, the maximum gradient occurred at $t = 0.5$ days (gradient at $t = 0$ was equal to zero in accordance with the procedure for cycling daily gradients), and thus corresponded to a structure first loaded during the peak of summer.

The "Summer Gradient Plus Seasonal" scenario combined uniform temperatures changes with the gradients as specified for the "Summer Gradient" scenario in Eqn. (9-8). In this case, the uniform temperature history $T(t)$ was equal to

$$T(t) = -17.22\cos\left(\frac{2\pi}{365}(t-182.5)\right) + 283.55 \tag{9-9}$$

where $T(t)$ is the temperature is Kelvin, and t is the analysis time in days. This was identical to the "Winter" scenarios, except time shifted by 0.5 years (182.5 days), so that the bridge was first loaded during the peak of summer. The combination of gradients from Eqn. (9-8) and uniform

temperatures from Eqn. (9-9) ensured that the highest gradients were always correlated with the maximum uniform temperatures during the summer throughout the analysis.

For the "Year 1 Gradient" scenario, the uniform temperature was constant at $T(t)$ = 293 K (68°F) throughout the analysis, and thermal gradients were only applied to the first 365 days of the analysis. Instead of cycling gradients as an annual trend according to Eqns. (9-7) or (9-8), the maximum gradient of T_0 = 25.6 K (46.0°F) was applied at midday (i.e., at t = 0.5, 1.5, 2.5 days, etc.) of every day for the first year. The gradient was cycled each day, such that no gradient was applied at times t = 0, 1, 2 days, and so on. The shape of the applied gradient was the Priestley fifth-order curve as given in Eqn. (9-6). This scenario was designed to investigate if the application of temporary gradients would impact the long term results, or if the behavior would return to the deformations from the constant temperature scenario.

The "Year 2 Gradient" scenario was equivalent to the "Year 1 Gradient" scenario except that the daily gradients were cycled starting at t = 365 days and ending at t = 730 days. This scenario was designed to investigate if beginning the temporary gradients at a different time would differently impact the long-term behavior.

The "Year 1 Gradient" and "Year 2 Gradient" scenarios were not intended to investigate realistic temperature histories. However, even the temperature changes intended to emulate annual temperature cycles, the "Winter Gradient Plus Seasonal" and "Summer Gradient Plus Seasonal" scenarios, had several notable discrepancies with how temperature changes occur in field structures. First, the assumption that the daily temperature gradient ramps from zero to the maximum at midday, then back down to zero at the end of the day is not realistic. For physical structures, negative gradients can occur during the nights, and gradient magnitudes are unlikely to change linearly throughout the day. The shape of the thermal gradients in the investigated gradient scenarios were always assumed to follow the fifth-order curve even though they can take a variety of shapes in physical bridges when transitioning from low to high gradients.

Furthermore, the assumption that the gradient was maximized and cycled everyday was extremely unlikely. Changes in precipitation, cloud cover, and other weather phenomena make the magnitude of the daily thermal gradient unpredictable. For purposes of this exercise, however, the shortcomings in the specification of the thermal gradients were considered acceptable. Because the modeled gradients were never negative and were maximized daily, any effects that the thermal gradients had on the time-dependent behavior of the bridge were exacerbated, and therefore these assumptions were considered conservative. Also, because the analysis of this test problem could only be related to the behavior of the St. Anthony Falls Bridge qualitatively, it was not critical to exactly capture the details of the temperature history.

9.3.3 Results

Results for strains, concrete stresses, and deflections were computed using the GL2000 and ACI-209 time-dependent models for the finite element analysis described in Section 9.3.1. Results from the temperature histories described in Section 9.3.2 were compared to discern the impacts of seasonal temperature changes, thermal gradients, construction season, and temporary gradients on the long term behavior.

The time-dependent finite element models contained instantaneous deformations from elastic behavior and thermal expansion. However, only the time-dependent strains from creep and shrinkage of the concrete were of interest. For each of the investigated cases, the elastic behavior was computed by finite element analyses identical to the time-dependent scenarios but with no creep, shrinkage, or steel relaxation. Concrete aging in terms of strength and modulus gain were still included in the corresponding elastic analysis, and therefore the GL2000 and ACI-209 models had minor differences in the elastic response. The results from the elastic analysis were subtracted from the total deformations from the time-dependent analysis, thus leaving only time-dependent deformations. Consequently, all presented results are relative deformations and stresses.

The time-dependent deformations and stresses were plotted with respect to the Arrhenius adjusted time computed in the same manner as used for the physical bridge data, as described in Section 7.3.2. The analysis time was post-processed using Eqn. (7-25) and the Q/R factor equal to 7,360 K to compute the Arrhenius adjusted time. The start of analysis (t = 0 at concrete age of 28 days) was specified to have adjusted time equal to zero. Temperatures prior to the start of analysis were assumed to be a constant 293 K (20°C). The temperature input into Eqn. (7-25) for each temperature history was the average temperature through the cross section, equal to the temperature profile integrated over the cross section then divided by the cross-sectional area. Consequently, each temperature history had a different Arrhenius adjusted time history. As discussed in Section 7.3.2, no time correction was made for hydration age as this was assumed to have an impact only on concrete loaded at early ages. In this way, the data from the "Gradient" scenarios mimicked the sensor data from the physical bridge (as the measured data included some form of dependence on the thermal gradient history), while the "Constant" scenario represented the FEM analyses conducted on the St. Anthony Falls Bridge under constant temperature conditions.

For each model, the output results included: longitudinal deflection at the far end of the outer span (positive contraction), which captured the deflections that would be measured by the expansion joint linear potentiometers; vertical deflection at midspan of the center span (positive upward); top and bottom fiber strains at midspan of the center span (positive tension); and top and bottom fiber concrete stresses at midspan of the center span (positive tension).

9.3.3.1 Effects of Seasonal Temperature Changes

To investigate the effects of seasonal (uniform) temperature changes on time-dependent behavior, the results from the "Constant" and "Seasonal" scenarios discussed in Section 9.3.2 were compared. The time-dependent longitudinal deflections plotted with respect to the Arrhenius adjusted time for the GL2000 and ACI-209 time-dependent models for both temperature histories

are shown in Figure 9.5. At any given adjusted time, the relative differences in longitudinal deflection between the two temperature histories was always less than 1% regardless of time-dependent model. The vertical deflections, strains, and stresses (not plotted) were also unaffected by the uniform seasonal temperature changes compared to the uniform temperature case. Therefore, other than minor differences in the concrete hydration age, the adjusted age procedure captured all the effects of uniform temperature changes.

9.3.3.2 Effects of Thermal Gradients

To examine the effects of non-uniform temperatures, results from the "Constant," "Winter Gradients," and "Winter Gradients Plus Seasonal" temperature scenarios were compared. Figure 9.6 shows the time-dependent longitudinal deflections for the GL2000 and ACI-209 models for these three temperature histories. After correction for adjusted age, the presence of cyclic thermal gradients appeared to have no effect on the longitudinal behavior, with relative differences between any two temperature histories less than 1%.

Figure 9.7 shows the time-dependent vertical deflections at midspan of the center span plotted with respect to the adjusted time. The thermal gradients appeared to have a significant impact on the vertical deflections when the time-correction procedure was taken into account. Furthermore, although the "Winter Gradient" and "Winter Gradient Plus Seasonal" temperature histories specified identical thermal gradients, these two scenarios returned different vertical deflections.

For the ACI-209 model, regardless of the temperature history, the vertical deflections approached similar asymptotic values (within 2% of the "Constant" model) after 30 years. Only the deflections from 10 to 1,000 adjusted age days were altered by the presence of thermal gradients. For other asymptotic models, it can be surmised that the ultimate deflections are not dependent on the temperature history, though differences will be present until the model approaches the asymptotic limits.

The vertical deflections never converged for the GL2000 model. After 1,000 adjusted age days, results from each of the three temperature scenarios continued in parallel with respect to the adjusted age. After 9,000 adjusted age days (near the end of the analysis for each scenario), the deflections from the "Winter Gradient" and "Winter Gradient Plus Seasonal" scenarios were 7% and 10% less, respectively, than those from the Constant scenario. Thus for logarithmic models, the long-term vertical deflections after correcting for adjusted time are dependent on the total temperature history as long as non-uniform temperatures are present.

The Arrhenius equation could not account for all the differences in vertical deflections between the "Gradient" and "Constant" scenarios. When performing the time-correction procedure, only the average temperature over the section was used to describe the temperature dependence. However, for behaviors strongly related to bending in the cross section such as midspan deflection, the correction procedure should additionally account for the distribution of strain rates throughout the cross section. Specifically, the first moment of the strain rate about the centroid of the section must be used for time-dependent curvature.

The strain rate at any point in the cross section is dependent on the temperature and stress histories at that point. The application of non-uniform, nonlinear temperatures introduces compatibility stresses into the structure, and thus the stress history is dependent on the temperature history. Consequently, composing a single adjusted time to account for both uniform temperature changes (i.e., uniform scaling of the strain rate across the section) and thermal gradients (i.e., non-uniform scaling of strain rate) is an extremely complex process that can likely be performed only on a case-by-case basis, if at all. Deriving such a relation was beyond the scope of this investigation.

In the case of the GL2000 model, the time-dependent deflections after the first year from the "Gradient" scenarios were nearly proportional to the deflection from the "Constant" scenario. For the ACI-209 model, the thermal gradients changed the deflection only from 10 to 1,000

adjusted age days but left the long-term deflections unchanged. Consequently, when using an asymptotic time-dependent model, long-term predictions from the FEM analysis can ignore temperature changes, as the deflections and strains will converge to the same asymptote regardless of the application of cyclic thermal gradients. This conclusion is predicated on the assumption that temperature changes only affect the rates of time-dependent phenomena, and not the ultimate values.

For both the GL2000 and ACI-209 models, the direction of the time-dependent deflection differences caused by the applied gradients was always opposite of the direction that the applied gradient had on the instantaneous behavior. Application of the thermal gradient caused instantaneous downward (negative) deflection at midspan, while the time-dependent behavior from the "Gradient" scenarios had upward (positive) deflection relative to the "Constant" scenario.

The difference between the "Winter Gradient" and "Winter Gradient Plus Seasonal" scenarios was due to the fact that the rates of time-dependent behavior are not linearly dependent on temperature. For example, if the uniform temperature of the bridge was 273 K (32°F) and a gradient of 25.6 K (46°F) was applied to the top flange, then using the relationship from Eqn. (9-3) with U_c/R equal to 7,360 K would result in the top fiber creeping 10 times faster than the bottom fiber (assuming equal stress). However, if the uniform temperature of the bridge is changed to 293 K (68°F) with the same 25.6 K (46°F) gradient, then the top fiber only creeps 7.5 times faster than the bottom flange (again assuming equal stress). Therefore, the effects of uniform seasonal temperatures cannot be linearly superimposed with thermal gradients to arrive at the combination of seasonal and cyclic gradients.

The time-dependent strains at midspan of the center span from the "Constant," "Winter Gradients," and "Winter Gradients Plus Seasonal" temperature scenarios using the GL2000 and ACI-209 time dependent provisions are plotted with respect to adjusted time in Figures 9.8 and

9.9 for the top and bottom fibers, respectively. The adjusted time procedure appeared to correct the time-dependent strains of the "Gradient" scenarios with respect to the "Constant" scenario for both the ACI-209 and GL2000 model, with relative differences between any two considered scenarios less than 1%.

These time-dependent longitudinal strains were composed of axial and bending components. The correction on the top strains was superior to that for the bottom strains, primarily because the top fiber was closer to the neutral axis of the section than the bottom fiber and was thus less sensitive to the time-dependent curvatures discussed above for the vertical deflections. By extension, the longitudinal strains at the neutral axis of the section would be corrected by the time adjustment procedure equally as well as the longitudinal deflections presented in Figure 9.6, as these strains would contain only an axial component.

Time-dependent longitudinal concrete stresses at midspan are plotted with respect to adjusted time using the GL2000 and ACI-209 models in Figures 9.10 and 9.11 for the top and bottom fibers, respectively. The time-dependent stresses from the "Gradient" scenarios did not resemble the stresses predicted by the "Constant" scenario. Concrete stress losses in the top fiber were far greater in the "Gradient" scenarios compared to the "Constant" scenario. These larger losses translate to less compression in the top flange.

Over the course of the 30-year analysis, the top fiber concrete stress losses from the "Winter Gradient" scenario were at most 640 psi (4.4 MPa) and 460 psi (3.2 MPa), respectively for the GL2000 and ACI-209 models, more than those from the "Constant" scenario. For the "Winter Gradient Plus Seasonal" scenario, the stress losses in the top fiber were at most 840 psi (5.8 MPa) and 560 psi (3.8 MPa), respectively for the GL2000 and ACI-209 models, more than those from the "Constant" scenario. In the bottom fiber, the trend was opposite; the "Gradient" scenarios exhibited lower concrete stress losses (i.e., more compression) than the "Constant" scenario. For the "Winter Gradient" scenario, the stress losses in the bottom fiber were at most

170 psi (1.2 MPa) and 120 psi (0.8 MPa), respectively for the GL2000 and ACI-209 models, less than those from the "Constant" scenario. For the "Winter Gradient Plus Seasonal" scenario, the concrete stress losses in the bottom fiber were at most 220 psi (1.5 MPa) and 150 psi (1.0 MPa), respectively for the GL2000 and ACI-209 models, less than the "Constant" scenario. These maximum differences occurred 5.5 years (total unadjusted time) after loading for the GL2000 model and 0.5 years (total unadjusted time) after loading for the ACI-209 model.

During the winter season of each year the differences between the "Gradient" and "Constant" scenarios shrank. Following the mentioned peaks, the stress differences between the "Gradient" and "Constant" scenarios declined until the end of the analysis.

Similar to the results for the vertical deflections, the instantaneous stresses caused by the thermal gradients were opposite in direction to those of the time-dependent losses. Large positive thermal gradients cause compression in the top fiber and tension in the bottom fiber, while the difference in the stress losses between the Gradient scenarios and the Constant scenario were tensile (more losses) in the top fiber and compressive (less losses) in the bottom fiber.

9.3.3.3 Effects of Construction Season

The effects of the construction season (when the temperature was first applied) was investigated by comparing the results from the "Winter Gradient" scenario to the "Summer Gradient" scenario, and the "Winter Gradient Plus Seasonal" scenario to the "Summer Gradient Plus Seasonal" scenario. The time-dependent longitudinal deflections and strains were not affected by the presence of uniform temperature changes or thermal gradients, and thus only the vertical deflections and concrete stress losses were examined.

The time-dependent vertical deflections at midspan of the center span for the four "Gradient" scenarios are plotted in Figure 9.12. Despite the differences during the first year due to the different early age temperatures, the "Winter Gradient" and "Summer Gradient" scenarios

limited to equivalent (relative differences less than 1%) long-term deflections, as did the "Summer Gradient Plus Seasonal" and "Winter Gradient Plus Seasonal" scenarios.

Concrete stress losses in the top and bottom fibers for the four examined "Gradient" scenarios are given in Figures 9.13 and 9.14, respectively. The early age and annual cycles were significantly different between the corresponding temperature histories, but long-term trends only showed minor discrepancies. Comparing the stresses only at the minimum temperature with no gradient (i.e., middle of winter), the top flange losses were 50 psi (0.34 MPa) more for the GL2000 and 25 psi (0.17 MPa) more for the ACI-209 model for the "Winter Gradient" compared to the "Summer Gradient" scenario. Likewise, the top flange losses were 25 psi (0.17 MPa) more for the GL2000 and 15 psi (0.10 MPa) more for the ACI-209 for the "Winter Gradient Plus Seasonal" compared to the "Summer Gradient Plus Seasonal" scenario. Long-term bottom fiber stress losses, investigated only at the minimum temperature with no gradient, were always within 10 psi (0.07 MPa) for any two corresponding temperature histories regardless of time-dependent model.

Thus, the impacts of the construction season on long-term behavior were negligible compared to the effects that cyclic gradients have on the vertical deflections and concrete stresses.

9.3.3.4 Effects of Temporary Gradients

The effects of the application of temporary gradients on the long-term time-dependent behavior were investigated by comparing the "Year 1 Gradient" and "Year 2 Gradient" scenarios to the "Constant" scenario. As expected from previous results, the longitudinal deflections and total strains were not impacted by the presence of thermal gradients, and are not presented.

The time-dependent vertical deflections comparing the "Year 1 Gradient," "Year 2 Gradient," and "Constant" scenarios are given in Figure 9.15. For both the "Year 1 Gradient" and "Year 2 Gradient" cases, the deflections returned to the values predicted by the "Constant"

scenario. The ACI-209 model returned to the "Constant" scenario values more quickly than the GL2000 model, likely due to the particular shape of the ACI-209 creep and shrinkage curves and that, even if the gradients were applied continuously instead of temporarily for one year, the same ultimate value would still be approached as evinced by the previous investigations. At the end of the 30-year analysis, relative differences between the vertical deflections from any two of the three examined temperature histories were always less than 1% regardless of the time-dependent model.

The concrete stress losses at midspan of the center span in the top and bottom fibers are plotted in Figures 9.16 and 9.17, respectively. Although the long-term stress losses nearly returned to the "Constant" scenario results, the presence of the thermal gradients left a small residual stress difference. For the ACI-209 model, the stresses at the end of the "Year 1 Gradient" analysis were within 5 psi (0.03 MPa) of the "Constant" results, whereas the difference between the "Year 2 Gradient" analysis and the "Constant" analysis was within 15 psi (0.10 MPa). Using the GL2000 model, the end-of-analysis "Year 1 Gradient" stresses were within 75 psi (0.52 MPa) of the "Constant" scenario stresses, while the "Year 2 Gradient" difference was less than 5 psi (0.03 MPa). It was unclear why the trend switched for the two time-dependent models, with the "Year 1 Gradient" results being closer to the "Constant" scenario than the "Year 2 Gradient" for the ACI-209 model, and vice versa for GL2000 model.

With the exception of the GL2000 model under the "Year 1 Gradient" scenario, these stress differences were deemed insignificant. For thermal gradients applied at early ages, the particulars of the strength aging curve and loading age dependence of the creep model may impact the long-term stress losses. For gradients applied at least one year after casting, the time-dependent behavior after removal of the thermal gradients should eventually return to values as though no thermal gradients had been applied. With regard to the investigation of instrumented

post-tensioned bridges for which temporary gradients are unlikely, this conclusion is only of academic interest.

9.4 Summary and Conclusions

The effects of temperature changes on the long-term time-dependent behavior of post-tensioned concrete box girder structures was evaluated qualitatively using a finite element model with simplified geometry compared to the I-35W St. Anthony Falls Bridge. The rates of hydration, creep, and shrinkage were assumed to be dependent on temperature according to the Arrhenius equation. A series of temperature history scenarios were devised to investigate how uniform seasonal temperatures, thermal gradients, the season during first loading, and temporary thermal gradients would impact the time-dependent behavior.

The temperature correction procedure documented in Section 7.3.2, which applied the Arrhenius equation to compute an adjusted age based on the average superstructure temperature, was found to account for the uniform temperature changes in the finite element models. With the exception of the minor impacts of temperature on hydration age, this correction was otherwise exact.

After correcting for adjusted age, thermal gradients were found to have a negligible effect on the modeled time-dependent longitudinal deflections at the expansion joints. Furthermore, time-dependent longitudinal strains as would be measured by vibrating wire strain gages were minimally changed by the presence of thermal gradients. Extending this finding to the time-dependent behavior extracted from the linear potentiometers and vibrating wire strain gages in the St. Anthony Falls Bridge, it can be concluded that the Arrhenius adjusted age procedure documented in Section 7.3.2 accurately captures the time-dependent longitudinal deformations of the bridge in the presence of both uniform temperature changes and thermal gradients.

Time-dependent behaviors primarily related to the bending of the structure, including curvature and vertical deflection, had a notable dependence on thermal gradients. This was

because the time-dependent bending of the cross section had a rate dictated by the first moment of the strain rate through the section. The strain rate at any given point was a function of both the temperature and stress histories at that point, and the stress history was dependent on the temperature history due to compatibility strains induced by thermal gradients. For temperature histories as complex as thermal gradients in field structures, such behavior is extremely difficult to predict. Bending behavior was not considered in the time-adjustment procedure, which used only the average temperature in the cross section.

As a corollary to the discussion regarding time-dependent bending, strains far from the bending neutral axis were dependent on thermal gradients, while strains at the neutral axis were insensitive to gradients. The reason that the computed strains were apparently insensitive to thermal gradients was because these strains contained both uniform (axial contraction) and differential (bending) components, of which the axial strains were more significant. On the other hand, the curvature was dependent only on the strain differential in the cross section, and was consequently more sensitive than individual strain gage readings to the presence of thermal gradients.

When using logarithmic time-dependent models such as the GL2000, the time-dependent vertical deflections when including thermal gradients were approximately proportional to the constant temperature case, excluding data from the first year after loading. When using asymptotic laws such as the ACI-209, the long-term deflection and curvature appeared to converge to the same values whether or not thermal gradients were considered, but behavior prior to the asymptote was still dependent on the temperature history.

The effects of thermal gradients on the structural time-dependent behavior were always opposite of the effect that the thermal gradient had on the instantaneous response. For example, if thermal gradients caused upward deflection of the structure according to elastic analysis, the

time-dependent analysis applying cyclic gradients had downward deflection relative to time-dependent analysis ignoring thermal effects.

The longitudinal concrete stresses were significantly impacted by the application of thermal gradients. When a positive thermal gradient was applied to a section, the top flange deformed quickly due to the combined effects of increased compression and temperature. The bottom flange deformed more slowly due to reduced temperature and compression with respect to the top flange. Once the thermal gradient had passed, residual tensile and compressive stresses remained, respectively, in the top and bottom flanges. Even after only one year of applied gradients, this developed a stress profile in the structure significantly different from what might be expected if thermal gradients were ignored.

Because the rate dependencies of hydration, creep, and shrinkage were not linear, the time-dependent deformations and stresses considering uniform seasonal temperature changes alongside daily cyclic thermal gradients was not equivalent to the superposition of the two analyses considering the uniform temperatures and gradients independently. For accurate computation of time-dependent behavior of field structures, the entire temperature history must therefore be included even though uniform temperatures alone have predictable impacts on the behavior.

The season at which the structure was first loaded appeared to only have a minor impact on the long-term time-dependent behavior. Long-term vertical deflections were nearly unchanged when comparing results from equivalent temperature histories but starting in the summer or winter. Likewise, the stress loss differences between corresponding winter and summer analyses were always less than 50 psi (0.34 MPa), which was insignificant compared to the difference between the scenarios with and without thermal gradients.

After the application and removal of temporary thermal gradients, the time-dependent behavior of the structure returned to the case as though no thermal gradients were applied, within

a residual due to continued hydration and the loading age dependence of the specific creep model. This was expected, as the creep behavior was specified to follow linear viscoelasticity and the Boltzmann superposition principle, and therefore would completely recover after removal of load. For thermal gradients applied during the first year, the residual may be significant depending on the chosen time-dependent model as was witnessed for the GL2000 time-dependent provisions, but still small compared to the difference between analyses with and without thermal gradients. Temporary thermal gradients applied at least one year after casting do not appear to have a significant impact on long-term behavior.

The dependence of time-dependent stress losses on thermal gradients has interesting implications for the application of thermal gradients in bridge design. As an example, assume that the stresses are first computed both at the end of construction and at the end of service (i.e., after all time-dependent behavior has occurred) while ignoring all thermal effects. Then, the response of the bridge due to thermal effects is computed independently using ordinary elastic analysis. Typically, the stresses from these two analyses would be added, with the use of load factors, assuming superposition. However, the results in this section show that when estimating the total stress in the bridge, application of the full thermal gradient is only valid when combined with the stresses at the end of construction before any time-dependent behavior has occurred.

To properly estimate the bridge stresses at the end of service, only some percentage of the thermal gradient should be applied to the long-term estimates. Furthermore, some percentage of the thermal gradient stresses should be applied in the opposite direction than would be expected from elastic analysis to capture the residual stresses locked into the structure. Therefore, when estimating the total stresses at the end of service, the designer should first compute the end of service stresses using time-dependent analysis but ignoring thermal effects. Then the designer should consider the range of stresses from +X% to −Y% of the thermal stresses. Without a thorough investigation of this phenomenon employing a variety of structures, realistic

temperature histories, and time-dependent models, it is impossible to suggest general values for X and Y. For the specific test cases examined here, the bounds of ±50% would be reasonable for the GL2000 model, while the bounds for the ACI-209 model would be better approximated by +75% and −25%.

A conservative assumption would be to apply the full gradient in both positive and negative directions. The extreme cases are that (1) the thermal gradient does not impact the time-dependent behavior, thus leading to bounds of +100% and −0%; or (2) the full elastic stresses due to the thermal gradient are locked into the cross section as residual stress, implying bounds of +0% and −100%. For most design scenarios, this would be an undesirable condition to meet considering the potentially large magnitudes of stresses induced by thermal gradients.

The current provisions for the application of thermal gradients to bridges (AASHTO, 2010) recommend the application of, at the end of service, the full positive thermal gradient and a negative gradient equal to −30% of the positive gradient. As noted above, the application of the full positive thermal gradient is conservative. In the case of the negative gradient, the current scale factor may need to be increased above −30% (for example, to −50%) to account for the combination of (1) the applied negative gradient and (2) the residual stress state caused by the cyclic application of the positive thermal gradients. Because of the manner in which gradients were cycled in this investigation, the impacts of cyclic thermal gradients on the residual stress state were exacerbated compared to what might be predicted by the application of a more realistic temperature history. Absent more precise recommendations that might be derived by thorough analysis of multiple bridge geometries and realistic temperature histories, the current scale factor of −30% for negative thermal gradients is likely sufficient for design.

In conclusion, the current provisions for thermal gradients in bridges is likely to be adequate, and thus no modifications are recommended. By extension, this means that the stress envelopes presented in Chapter 8 for the St. Anthony Falls Bridge provide valid

recommendations with regard to the end of service limit states, despite the findings in this chapter.

Chapter 10: Protocol for Long-Term Monitoring System

The ultimate goal of structural health monitoring is to aid in maintenance of and decision making for structural systems by providing tools which identify problematic behavior. An ideal system would be able to locate damage within a structural system, identify the cause of the damage, and present a plan of action to counter the damage. This goal has thus far been elusive. Sohn (2007) indicated that the impacts of environmental and other non-damage related factors have on data from instrumented in situ structures can mask changes caused by damage, and thus pose a significant challenge to accurate diagnostics regarding the condition of the structure. The data collected from the I-35W St. Anthony Falls Bridge support this claim, as evinced by the temperature dependence (French et al., 2012), time dependence (Chapters 7 and 8), and time-temperature interactions (Chapters 7 and 9) observed in the measured deformations.

To advance towards the goal of an ideal structural health monitoring system, the most basic objective must first be overcome: identification of anomalous data. Anomalous data is defined by measured data that fall outside of expected bounds. This requires (1) extraction of features from the measured data which provide relevant information regarding the structural behavior and (2) prediction of the expected values of these extracted features so that useful bounds can be defined. Feature extraction, also known as data normalization, can be used to isolate the behavior of interest from other expected behavioral changes, and thus can increase the efficacy of the predicted bounds in identifying anomalies in a changing environment.

Detection of an anomaly is not necessarily indicative of damage, but only provides a first step in evaluating the performance of the structure. Anomalies can be categorized into two types: true positives and false positives. For this investigation, a true positive was assumed to be the indication of an anomaly that would correctly require that further investigation or maintenance be taken. True positive results include anomalies caused by unexpected (possibly damage-related) changes in the structural behavior, as well as anomalies due to sensor or data acquisition

malfunction. A false positive was assumed to be an indication of an anomaly unrelated to the bridge behavior or monitoring system status, and thus should not warrant further investigation.

In practice, separating true and false positives can be difficult or even impossible if the presence of damage-related behavior in the data is not known a priori. An anomaly detection routine can only detect the presence of an anomaly, and cannot determine whether or not it represents a true positive or false positive. Therefore, anomaly detection routines must be tested on known data sets to determine the robustness of the identification methods. A robust anomaly detection routine is defined as one which minimizes false positives while maximizing the detection of true positives.

For continued monitoring of the I-35W St. Anthony Falls Bridge, a protocol for a long-term structural monitoring system was developed. Possible scenarios for this bridge that may be of interest for long-term maintenance include concrete cracking due to loss of post-tensioning, steel corrosion, changes in stiffness, excessive deflections, and bearing lockup. Of these scenarios, vertical deflections could not be directly monitored by any of the operational systems, and detecting cracks would be highly unlikely given the local nature of both the damage and strain gages. The effects of corrosion, such as an effective loss of post-tensioning stress, could be indirectly monitored using strain gages or linear potentiometers, but the process and rates of steel corrosion could not be directly analyzed. Changes in stiffness could, in theory, be captured using modal analysis on the accelerometer network, though such a task was beyond the scope of this investigation.

Consequently, efforts were focused on predicting trends and detecting anomalies in the longitudinal deflections at the expansion joints measured by the linear potentiometers. Data normalization was performed via the extraction of the time-dependent behavior from the measured LP data using the procedure discussed in Chapter 7. By removing the dependency of

the data on temperature, more narrow and consistent bounds could be developed for identifying bearing problems at the expansion joints.

The linear potentiometer system was chosen because the data was actionable, in that it provided direct information about scenarios of interest. These scenarios included bearing lockup, excessive longitudinal motion which might be indicative of structural degradation, and unexpected decreases in time-dependent deflection rates that could be caused by post-tensioning losses or corrosion. Furthermore, in the event of system or sensor failure, components could be replaced to ensure data continuity. Extension to other monitoring systems, such as vibrating wire strain gages or modal responses from accelerometers, was beyond the scope of this investigation, but could be a topic of future study.

To predict the expected time-dependent longitudinal deflections, and to provide a coherent method for defining bounds to use in anomaly detection, a Bayesian statistical framework was adopted. For background purposes, extrapolation using Bayesian methods is presented in Section 10.1. This is followed by application of Bayesian methods for detecting short-term anomalies in the measured time-dependent behavior provided in Section 10.2. Short-term anomalies were defined as changes in the data that evolved over the course of a month or less, and might be associated with bearing lockup or sensor failure. A separate method not based on Bayesian statistics was derived for the long-term check in Section 10.3. Long-term anomalies were defined as any change in behavior evolving for longer than one month, possibly up to several years. Examples of structural behavior that could cause a long-term anomaly are time-dependent deterioration, unexpected post-tensioning loss, or translation of the superstructure on the bearings. A long-term anomaly detection routine based on Bayesian regression using estimates of the time-dependent behavior computed via the finite element method was not expected to be robust due to the great uncertainty in time-dependent predictions over long durations.

10.1 Extrapolation of Time-Dependent Data

To identify anomalous data, a prediction of the expected behavior is first required. This prediction can be based on computational results, previously measured data, or a combination of both. For creep and shrinkage, computational results alone cannot predict long-term behavior. As discussed in Chapter 8, prediction of long-term time-dependent behavior of structures cannot be reliably accomplished by any of the available time-dependent models. Even when compared to laboratory results (Chapter 5) and databases of creep and shrinkage data (Section 8.2), time-dependent predictions have considerable uncertainty.

A Bayesian statistical framework was used to account for the uncertainty in time-dependent predictions. Bayesian statistical methods establish a paradigm for statistical inferences based on conditional probabilities (Bernardo, 2001). In effect, a Bayesian approach provides a framework for combining statistical information given a set of assumptions and present knowledge, and then updating the probabilities given some new information, typically measured data. Thus, the Bayesian framework can be used to integrate the uncertainty of the time-dependent models with the measured data to establish a comprehensive statistical prediction model. A discussion of Bayesian statistics follows.

10.1.1 Bayes' Theorem

The goal of implementing a Bayesian framework in the linear potentiometer anomaly detection system was to define credible bounds by which an anomaly could be flagged. Because the measured data contain aleatoric uncertainty and the time-dependent models contain large epistemic uncertainty, defined bounds must account for the total uncertainty in the predictions. Bayes' Theorem provided the means to rationally combine these sources of uncertainty.

All representations of probability in a Bayesian framework are formulated as conditional statements $p(E \mid S, K)$, meaning the probability of an event E given assumptions S and knowledge K. Typically, assumptions S and knowledge K are present only implicitly, and the above

statement is instead shown simply as $p(E)$, though this should still be understood as a statement of conditional probability. Given some measured data D, the probability of event E can be updated to $p(E \mid D)$. Likewise, the probability of measuring data D given the occurrence of event E can be listed as $p(D \mid E)$.

Bayes' Theorem forms the foundation of Bayesian statistics. Assume that data D is dependent on parameters w. Assuming known values for parameters w, the probability of measuring data D is given by the likelihood function $p(D \mid w)$. The parameters w may also be uncertain, and are defined by the prior distribution $p(w)$, where assumptions S and knowledge K are implicit in this definition. Bayes' Theorem states that the posterior distribution $p(w \mid D)$ is proportional to $p(D \mid w)p(w)$. This means that the posterior distribution, which represents an updated form of the statistical model for parameters w given new measured data D, is proportional to the prior (initial assumed) distribution of w multiplied by the likelihood of measuring data D.

In the context of the LP monitoring system, data D represents the time-dependent behavior extracted from the linear potentiometer data. Parameters w represent the time-dependent model. If the time-dependent model is deterministic and known, then data D will still have some aleatoric uncertainty $p(D \mid w)$ based on the scatter of the data. The time-dependent behavior, however, is not deterministically known and has a prior distribution $p(w)$. In anomaly detection, the prior distribution $p(w)$ alone could be used to define the bounds, but a narrower and more reliable bounding interval can be computed using the updated posterior distribution $p(w \mid D)$, which is proportional to $p(D \mid w)p(w)$. Thus, Bayes' Theorem allows for the large uncertainty in the time-dependent models to be combined with measurement uncertainty to formulate a coherent picture of the total uncertainty present in the monitoring of time-dependent behavior.

10.1.2 Bayesian Regression

The Bayesian framework can be applied to regression analysis of the time-dependent behavior. In the case of linear regression, fitting functions are assumed and linear coefficients are computed that minimize the error between the measured and predicted results. Unfortunately, linear regression does not capture any of the uncertainty present in either the data or the time-dependent prediction. Linear regression provides deterministic coefficients even though the presence of uncertainty in the data and the time-dependent model should translate to uncertainty in the regression coefficients.

Bayesian regression allows for the computation of probability models describing the coefficients of a regression analysis. The measured data can be assumed to follow the model

$$\mathbf{D} = \mathbf{A}\mathbf{w} + \boldsymbol{\varepsilon} \tag{10-1}$$

where **D** is a vector of length *n* of the measured data, **w** is the vector of length *k* of the fitting coefficients (i.e., the parameters), **A** is the *n* x *k* design matrix, and **ε** is the error term assumed to be Gaussian with mean of zero and variance of σ^2. To simplify the notation in future derivations, the variance of the data will instead be represented as the precision *a* equal to $1/\sigma^2$, the inverse of the variance. For the problem of regression of the measured time-dependent behavior, the design matrix can be specified as

$$\mathbf{A} = \begin{bmatrix} \boldsymbol{\xi} & \mathbf{U} \end{bmatrix} \tag{10-2}$$

where **ξ** is the vector of length *n* of the FEM longitudinal displacements at the expansion joints computed at times *t* corresponding to the times at which the measured data **D** was captured, and **U** is a vector with all entries equal to one to capture the constant offset term of the data. Thus, the first parameter w_1 is the scaling coefficient for the time-dependent outputs from the FEM, and the second parameter w_2 is the constant offset. The parameter w_1 can be thought of as a multiplicative factor to the creep and shrinkage predictions, but otherwise does not have any physical basis.

To compute the uncertainty of the parameters w_1 and w_2 given the measured data, Bayes' Theorem can be applied:

$$p(\mathbf{w}|\mathbf{D}) \propto p(\mathbf{D}|\mathbf{w})\,p(\mathbf{w}) \tag{10-3}$$

The likelihood of measuring data **D** given parameters **w** was derived from inspection of Eqn. (10-1). If parameters **w** are given, the uncertainty of **D** is captured entirely by the error term **ε**. Thus, the likelihood function was

$$p(\mathbf{D}|\mathbf{w}) \propto \exp\left[-\frac{a}{2}(\mathbf{D}-\mathbf{A}\mathbf{w})^T(\mathbf{D}-\mathbf{A}\mathbf{w})\right] \tag{10-4}$$

which represents the normal distribution with mean **Aw** and precision a.

The prior distribution $p(\mathbf{w})$ was assumed to be a normal distribution with mean **μ** and precision **B**. Because the finite element results were assumed to be the mean estimates of time-dependent behavior, the vector **μ** was equal to $[1\ \mu_2]^T$, where μ_2 was some arbitrary constant selected to approximately match the FEM results with the relative sensor readings. This definition of μ_2 was appropriate because only relative time-dependent deflections were possible to be measured (as LP data was not available until several months after completion of the bridge). The precision matrix **B** was computed as the inverse of the variance matrix:

$$\mathbf{B} = \begin{bmatrix} 1/C_{td}^2 & 0 \\ 0 & 1/v_2 \end{bmatrix} \tag{10-5}$$

where C_{td} is the coefficient of variation of the time-dependent models (typically in the range of 0.25 to 0.35 as discussed in Section 8.2), and v_2 is the assumed variance of the constant offset. No statistical information was known about the constant offset term, given that all sensors measured relative deformations. A low variance would mean that the μ_2-value specified in the **μ**-vector was strongly trusted, which was not the case as this value was selected arbitrarily. A high variance would mean that, when performing the regression, the measured data will be trusted more strongly than the prior information. Therefore, the variance v_2 should be chosen sufficiently high

such that the constant offset term is not strongly influenced by the selection of the prior mean μ_2. The prior distribution was thus equal to

$$p(\mathbf{w}) \propto \exp\left[-\frac{1}{2}(\mathbf{w}-\boldsymbol{\mu})^T \mathbf{B}(\mathbf{w}-\boldsymbol{\mu})\right] \tag{10-6}$$

which represents the normal distribution with mean $\boldsymbol{\mu}$ and precision matrix $\mathbf{B}$.

Substituting these expressions into Bayes' Theorem from Eqn. (10-3) gives

$$p(\mathbf{w}|\mathbf{D}) \propto \exp\left[-\frac{a}{2}(\mathbf{D}-\mathbf{A}\mathbf{w})^T(\mathbf{D}-\mathbf{A}\mathbf{w}) - \frac{1}{2}(\mathbf{w}-\boldsymbol{\mu})^T \mathbf{B}(\mathbf{w}-\boldsymbol{\mu})\right] \tag{10-7}$$

This equation can be rearranged into a quadratic form of $\mathbf{w}$:

$$p(\mathbf{w}|\mathbf{D}) \propto \exp\left[-\frac{1}{2}\mathbf{w}^T\left(a\mathbf{A}^T\mathbf{A}+\mathbf{B}\right)\mathbf{w} + \mathbf{w}^T\left(a\mathbf{A}^T\mathbf{D}+\mathbf{B}\boldsymbol{\mu}\right) - \frac{1}{2}\left(a\mathbf{D}^T\mathbf{D}+\boldsymbol{\mu}^T\mathbf{B}\boldsymbol{\mu}\right)\right] \tag{10-8}$$

When expanded out, the normal distribution $N(\mathbf{w}|\mathbf{m}, \boldsymbol{\Lambda})$ on independent variable $\mathbf{w}$ with mean $\mathbf{m}$ and precision matrix $\boldsymbol{\Lambda}$ takes the form

$$N(\mathbf{w}|\mathbf{m}, \boldsymbol{\Lambda}) \propto \exp\left[-\frac{1}{2}\mathbf{w}^T\boldsymbol{\Lambda}\mathbf{w} + \mathbf{w}^T\boldsymbol{\Lambda}\mathbf{m} - \frac{1}{2}\mathbf{m}^T\boldsymbol{\Lambda}\mathbf{m}\right] \tag{10-9}$$

Comparing Eqn. (10-9) to Eqn. (10-8) shows that the posterior distribution $p(\mathbf{w}|\mathbf{D})$ is normal with precision $\boldsymbol{\Lambda}_\mathbf{w}$ and mean $\mathbf{m}_\mathbf{w}$ given by

$$\boldsymbol{\Lambda}_\mathbf{w} = a\mathbf{A}^T\mathbf{A} + \mathbf{B} \tag{10-10}$$

$$\mathbf{m}_\mathbf{w} = \boldsymbol{\Lambda}_\mathbf{w}^{-1}\left(a\mathbf{A}^T\mathbf{D} + \mathbf{B}\boldsymbol{\mu}\right) \tag{10-11}$$

The variance matrix $\mathbf{V}_\mathbf{w}$ is the inverse of the precision matrix $\boldsymbol{\Lambda}_\mathbf{w}$, and will be symmetric but typically not diagonal. Diagonal terms of the variance matrix are the respective variances of each parameter in $\mathbf{w}$, while terms in the off-diagonal elements describe the covariance terms.

10.1.3 Bayesian Prediction

Using the process of Bayesian regression described in Section 10.1.2, the probability functions of the regression coefficients were derived. Bayesian prediction involves using the

uncertain regression coefficients and extrapolating the probability distributions of future data points. This combines the uncertainty in the measured data with the uncertainty in the regression coefficients to arrive at a probabilistic estimation of the future time-dependent behavior.

Predictions were computed using the same form of regression equation presented in Eqn. (10-1) with some changes in variables:

$$\widehat{\mathbf{D}} = \widehat{\mathbf{A}}\mathbf{w} + \boldsymbol{\varepsilon} \tag{10-12}$$

where $\widehat{\mathbf{D}}$ and $\widehat{\mathbf{A}}$ are the estimated data and design matrix values, respectively. The goal of Bayesian prediction is to compute the probability function $p(\widehat{\mathbf{D}} \mid \mathbf{D})$, or in other words, the probability of measuring some new set of data $\widehat{\mathbf{D}}$ given existing data **D**, implicit assumptions *S*, and knowledge *K*. The design matrix values were assumed to be deterministic, and so uncertainty was present only in the parameters **w** and the error **ε**. The posterior distribution $p(\mathbf{w} \mid \mathbf{D})$ was Gaussian with mean and precision derived in Section 10.1.2. The uncertainty of the data $p(\boldsymbol{\varepsilon} \mid \mathbf{D})$ was identical to $p(\boldsymbol{\varepsilon})$ because the noise of the measurements was assumed to be independent of the values of the measured data. Thus, $p(\boldsymbol{\varepsilon} \mid \mathbf{D})$ was Gaussian with mean zero and precision *a*. Because the constituent uncertainties were all Gaussian, distribution $p(\widehat{\mathbf{D}} \mid \mathbf{D})$ was also Gaussian.

To aid in the derivation of $p(\widehat{\mathbf{D}} \mid \mathbf{D})$, the expectation operator can be introduced. The expectation operator of function $g(x)$ is defined as

$$E\left[g(x)\right] = \int_{\forall x} g(x)\, p(x)\, dx \tag{10-13}$$

where $p(x)$ is the probability distribution of x. The mean m_x and the variance V_x of variable x can be given in terms of the expectation:

$$m_x = E\left[x\right] \tag{10-14}$$

$$V_x = E\left[\left(x - m_x\right)^2\right] \tag{10-15}$$

Because the distribution for $\hat{\mathbf{D}}$ was normal, the mean and variance completely defined the uncertainty. Applying Eqns. (10-14) and (10-15) to $\hat{\mathbf{D}}$ as given in Eqn. (10-12) returns

$$\mathbf{m_D} = E\left[\hat{\mathbf{A}}\mathbf{w} + \boldsymbol{\varepsilon}\right] = E\left[\hat{\mathbf{A}}\mathbf{w}\right] + E\left[\boldsymbol{\varepsilon}\right] = \hat{\mathbf{A}}\mathbf{m_w} \tag{10-16}$$

$$\mathbf{V_D} = E\left[\left(\hat{\mathbf{A}}\mathbf{w} + \boldsymbol{\varepsilon} - \mathbf{m_D}\right)\left(\hat{\mathbf{A}}\mathbf{w} + \boldsymbol{\varepsilon} - \mathbf{m_D}\right)^T\right] = \hat{\mathbf{A}}\mathbf{V_w}\hat{\mathbf{A}}^T + \frac{1}{a}\mathbf{U} \tag{10-17}$$

where $\mathbf{m_w}$ and $\mathbf{V_w}$ are mean and variance, respectively, of the parameters **w** as defined in Eqns. (10-10) and (10-11), a is the precision of the error term **ε**, and **U** is the q x q matrix with all entries equal to one where q is the length of the estimated data vector $\hat{\mathbf{D}}$.

Of particular interest is the credible region of the predicted data values. An r-credible region is defined as the region R such that

$$\int_R p\left(\hat{\mathbf{D}} \mid \mathbf{D}\right) d\hat{\mathbf{D}} = r \tag{10-18}$$

where r can be specified as any value between 0 and 1. For example, a 95%-credible region on $p(\hat{\mathbf{D}} \mid \mathbf{D})$ defines the region R within which, for given data **D**, assumptions S, and knowledge K, the true (unknown) value of $\hat{\mathbf{D}}$ will land 95% of the time (Bernardo, 2001).

The r-credible region was computed on a point-by-point basis, such that the bounds R_i were defined by the probability that the true value of a single point $\hat{D}_i$ would lie within the bounds with probability r, independent of all other predicted values in vector $\hat{\mathbf{D}}$. This simplified the analysis in that the covariance (off diagonal) terms in the variance matrix $\mathbf{V_D}$ were ignored and only the variance (diagonal) terms were used. The bounds R_i of the r-credible interval for point $\hat{D}_i$ with mean $(m_D)_i$ and variance $(V_D)_{ii}$ were defined as

$$R_i = \left(m_D\right)_i \pm c\sqrt{\left(V_D\right)_{ii}} \tag{10-19}$$

where *c* was chosen such that the probability contained within the bounds was equal to *r*. For a Gaussian distribution, a typical value of *c* is 2, which approximately defines a 95%-credible interval.

10.1.4 Long-Term Bayesian Predictions on Linear Potentiometer Data

Bayesian prediction was performed on the time-dependent behavior extracted from measured linear potentiometer data using the procedure defined in Section 7.1. For the fitting matrix **A** from Eqn. (10-2), the time-dependent behavior ξ was taken from the longitudinal deflection results from the FEM, as given in Section 8.1.1. Each of the models was considered independently, and for each regression analysis the shape of the time-dependent fitting equation was assumed to be deterministic. The process of Bayesian regression in Section 10.1.2 was based on the assumption that the FEM results could be scaled and translated to predict the time-dependent behavior of the instrumented structure. Theoretically, it should be feasible to consider the uncertainty of the shape of the time-dependent curve in addition to the uncertainty of the measured data and regression coefficients. However, this topic was beyond the scope of this report. In terms of Bayes' Theorem, the probabilities and predictions given in this section are only valid under the assumption that the shape of the time-dependent curve is deterministically known.

The prior distribution of the time-dependent predictions was assumed to be Gaussian with mean results equal to the FEM results. The coefficient of variation of the prior distribution was assumed to be equal to 25% for the B3 and GL2000 models and 33% for the ACI-209 and 1990 CEB/FIP Model Code models in accordance with results from Keitel and Dimmig-Osburg (2010), discussed in more detail in Section 8.2. For the AASHTO and 1978 CEB/FIP Model Code models, the coefficient of variation, though not presented by Keitel and Dimmig-Osburg (2010), was assumed to be 33% due to their similarity to the ACI-209 and 1990 Model Code models. As discussed in Section 8.2.2, the effective coefficient of variation of the predicted

longitudinal deflections should be less than that of the time-dependent models because increased creep and shrinkage are correlated with increased post-tensioning losses. However, for purposes of this regression analysis, the coefficients of variation for the predicted time-dependent longitudinal deflections were assumed to be equal to those from the time-dependent models.

The Gaussian error term $\boldsymbol{\varepsilon}$ from Eqn. (10-1) associated with the measured data scatter was chosen based on inspection of the linear regression fits presented in Section 7.3 and Tables 7.1 through 7.4. Bayesian statistical analysis can incorporate uncertainty in the standard deviation of the noise, but in this particular case the noise was assumed to be deterministically known. It was expected that the standard deviation of the residual for the best fits, ranging from 0.045 to 0.064 in. (1.1 to 1.6 mm) for the four LP locations, was due to scatter of the data and imperfections in the extraction of the time-dependent behavior by linear regression. Thus, the Gaussian error term $\boldsymbol{\varepsilon}$ was assumed to have a standard deviation σ equal to 0.05 in. (1.3 mm) and corresponding precision of 400 in.$^{-2}$ (0.62 mm^{-2}).

To investigate the validity of the Bayesian regression method, the measured linear potentiometer data was divided into a training set, used to compute the regression, and a test set, used only for validation of the method. Various durations for the training set were chosen to characterize the reliability of the regression. Training sets included the first nine months of data, the first year of data, the first two years of data, and the first three years of data. In terms of Arrhenius-adjusted age, the 9-month, 1-year, 2-year, and 3-year training sets had durations of approximately 100, 250, 530, and 800 adjusted age days, respectively. The test set for each case consisted of all data collected after the training set until June 5, 2013 (equivalently, 1,267 adjusted age days). Because data collection for the Southbound Span 3 linear potentiometers did not begin until September 28, 2009 (339 adjusted age days), the three-year training set was excluded, though the three shorter training sets were examined.

Training set durations shorter than nine months were not selected because data collection started during the winter when time-dependent behavior progressed slowly. To illustrate, the first six months of linear potentiometer data from October 31, 2008 to April 30, 2009 accounted for only approximately 30 adjusted age days, while the first nine months of data from October 31, 2008 to June 30, 2009 were equivalent to over 100 adjusted age days. Attempts to extrapolate regression results computed on fewer than 100 adjusted age days were unreliable, and are not presented here.

The results from Bayesian regression on the time-dependent linear potentiometer data are presented in Figures 10.1 through 10.4 for Span 1 of the southbound bridge, Span 3 of the southbound bridge, Span 1 of the northbound bridge, and Span 3 of the northbound bridge, respectively. The plots show the mean estimates using each of the time-dependent models for the training set durations specified above.

The consistency of the curve fit was judged by how strongly the long-term estimates were dependent on the duration of the training set. For example, the asymptotic limit of the AASHTO and ACI-209 models consistently increased as the training set expanded, implying that the predictions likely underestimated the long-term displacements. For the B3 and GL2000 models, the long-term estimates trended downwards as more data was added to the training set, so these estimates likely overestimated the long-term deflection. Both CEB/FIP Model Code estimates were consistent as the training set expanded, implying that the early age behavior could be fit well by both models. This, however, did not guarantee that the long-term estimates given by the CEB/FIP models were accurate, but only that the fit was consistent for the first 3 years of collected LP data.

For most of the datasets, the training set with only 9 months (100 adjusted age days) of data provided long-term estimates that, though often inferior to the estimates relying on more data in terms of predicting the test set behavior, did not significantly differ from the more complete

training sets. The data from Span 3 of the northbound bridge as shown in Figure 10.4, and to a lesser degree the data from Span 1 of the northbound bridge shown in Figure 10.3, were the exceptions to this trend. In general, these results support the assertion that at least one year of data (corresponding to 250 adjusted age days in this case) should be used for long-term monitoring.

The mean and 95%-credible regions for the Bayesian predictions using each of the time-dependent models with the 3-year training set on the southbound bridge Span 1 linear potentiometer data are shown in Figure 10.5. For all but the AASHTO and ACI-209 models, the predictions of the test set lay within the 95%-credible region. Furthermore, the distance between the bounds defining the credible region was nearly equivalent among all the considered models, despite the lower coefficients of variation assumed for the B3 and GL2000 models. As more data was added to the training set, the uncertainty of the posterior distribution was weighted more strongly towards the uncertainty of the data, and less influenced by the uncertainty of the prior distribution. For the training sets considered, so much data was available that the uncertainty of the prior distribution had negligible impact on the posterior distribution.

These results show that short-term predictions can be accurately made given a proper selection of the time-dependent model and a wealth of data. For purposes of monitoring, Bayesian regression can therefore be used to provide bounds for detecting anomalies that occur over a short period of time.

10.2 Short-Term Anomaly Detection

10.2.1 Criteria for Short-Term Anomaly Detection Algorithm

The developed short-term anomaly detection routine required input of the shape of the time-dependent curve, which was assumed to be deterministic, into the method for Bayesian regression presented in Section 10.1.3. Each of the time-dependent models given in Chapter 4 was analyzed independently in this section to derive recommendations for the most suitable model.

Anomaly detection requires that the available data be divided into a training set on which to perform the regression and a test set to compare to the extrapolated results. Any number of schemes may be adopted for data selection, each with advantages and disadvantages. For the training set, the full data record from beginning of collection to the beginning of the test set may be used. This maximizes the amount of data used for the regression. Another reliable alternative would be to use only some percentage of the previous data based on the adjusted age. For example, the training set might begin at an adjusted age equal to 50% of the beginning of the test set, so that 500 to 1,000 adjusted age days could be used for prediction of the test set beginning at 1,000 adjusted age days, and 600 to 1,200 adjusted age days could be used for the test set beginning at 1,200 adjusted age days. This is advantageous over the full record method if the dataset becomes very large thus making regression arduous. Selection of the training based on a static time block of past data (for example, past 1 year of data before the test set) is not recommended. As the bridge ages, 1 year of time-dependent data will likely have a slope of nearly zero and may be dominated by noise or other phenomena not accounted for in the extraction of the time-dependent behavior by linear regression. Considering the full dataset (100%) or some smaller fraction based on the adjusted age circumvents this issue. For the analysis conducted in this report, the full dataset prior to the test set was used as the training set, as the number of readings was still manageable.

Many alternatives also exist for selection of the test set. The test set should be selected to facilitate the anomaly detection routine in reliable detection of true positives while minimizing false positives. A static time window of the most recent data may be feasible. This could include the past 1 month of data, 1 year of data, or any other desirable interval. A large test set is undesirable because this would require the training set extrapolation to be reliable over a long time frame (i.e., greater than several months). On the other hand, short test sets also encounter problems when sensors fail. As documented in Section 2.3.2, the dynamic system and linear

potentiometers often ceased collecting data for several months at a time. If using a short static time window, sensor failure might result in very few or even no readings within the test set.

As a compromise instead of using a static time window, a static reading window was chosen, meaning that a specified number of readings was selected for the test set instead of a specified number of days. The window size was selected to be 1,000 hourly readings long. When the dynamic system was collecting as intended, this translated to approximately 42 days of data. If failures of the dynamic system occurred, the time duration of the window would expand so that small test sets could never be encountered.

The bounds provided by Bayesian regression provide a straightforward method for flagging an anomaly. For any given reading, assuming that the form of the time-dependent curve is deterministic and that all readings are independent of each other, the odds of that reading lying outside the 99%-credible interval is 1%. One method for detecting an anomaly is by counting the number of readings in the test set that lie outside the credible interval, and flagging that test set as anomalous if the probability of such an occurrence is sufficiently low.

Because the time-dependent curve was not deterministically known (contrary to the assumptions defining the Bayesian bounds), the limiting probabilities for flagging anomalies were set low to avoid false positives. A secondary concern for selecting the anomaly detection bounds was the responsiveness of the system. A detection routine that was overly responsive might diagnose too many false positives, while a slow responding system might delay the diagnosis of true positives for an unacceptable length of time. A warning (yellow) flag was assigned to the test set if over 72 of the 1,000 hourly readings were outside the 99%-credible interval defined by 3 standard deviations from the mean estimate. This was chosen so that sudden jumps in data could be detected after 3 days of out-of-bound readings, which was believed to be a suitably fast response time. Assuming a deterministic time-dependent curve, this event had a probability of occurrence less than 10^{-14}, and thus was believed to minimize false positives. An error (red) flag

was assigned if more than 144 of the 1,000 hourly readings were outside the 99%-credible interval. These bounds were chosen to correspond to a system response time of 6 days.

10.2.2 Summary of Short-Term Check Method

A flowchart summarizing the short-term check method from data collection to reporting is given in Figure 10.6. First, the time-dependent behavior was extracted from the measured linear potentiometer data using the linear regression procedure described in Section 7.1. Temperature readings were taken from the thermistors at Location 7 of the southbound bridge, as no other location was sufficiently instrumented to capture the full temperature profile. The time-dependent function θ_5 was estimated from the values of the time-dependent FEM output, given in Chapter 8. To keep computations manageable, the time-dependent FEM was not reanalyzed or updated for each test set case, and the results from Chapter 8 were reused for all calculations. To compute the adjusted age, the Arrhenius equation procedure as discussed in Section 7.3.2 was used assuming that the Q/R activation energy term was equal to 7,360 K according to Eqn. (7-26) and parameters from the superstructure mix design. The time-dependent behavior was plotted with respect to the adjusted age and divided into a test set, equal to the most recent 1,000 hourly readings, and a training set of all readings prior to the test set. Bayesian regression was conducted on the training set to predict the distribution of the test set. The test set was then flagged as green (normal), yellow (warning), or red (error), and the results were reported.

The form of the time-dependent curve (i.e., AASHTO, ACI-209, B3, etc.) was always the same for both the linear regression and Bayesian regression steps, and was assumed to be deterministically known. Because the FEM results were computed under constant temperature conditions, the FEM output was effectively presented in Arrhenius adjusted age. Therefore, in constructing the time-dependent function for both linear and Bayesian regression, the estimated time-dependent behavior for any given measured or estimated data point was computed by linear interpolation of the FEM output on the logarithm of adjusted age.

Linear regression for extracting time-dependent behavior was always conducted on the full data set (both the test and training set) so that extrapolation would only be required in the Bayesian regression for anomaly detection. This also allowed known jumps in the data (e.g., due to sensor replacement) to be removed from the test set using the Heaviside function as explained in Section 7.1.

For defining the prior distribution of the time-dependent behavior in the Bayesian regression, the mean value was assumed to be the FEM results, and the coefficient of variation was 25% for B3 and GL2000, and 33% for all other time-dependent models (Keitel and Dimmig-Osburg, 2010). The parameters of the Gaussian error term $\boldsymbol{\varepsilon}$ in Eqns. (10-1) and (10-12) were assumed to be deterministically known with zero mean and standard deviation equal to 0.05 in. (1.3 mm).

10.2.3 Validating Short-Term Check Methodology on Existing Data

The method for the short-term check was tested on the measured linear potentiometer data using each of the time-dependent models discussed in Chapter 4. Ideally, the short-term check should not return any warning flags for the existing data, and therefore any detected anomalies were assumed to be false positives. The method was checked on the existing time-dependent data using 1,000-point test sets beginning every 500 data points (50% overlap between adjacent test sets), with the final test set ending on October 24, 2013. The training set for each examined case contained all measured data prior to the beginning of the test set. Test sets with a corresponding training set duration less than 1 year were excluded from consideration.

The quantity of readings outside the 99%-credible interval for each of the generated test sets for linear potentiometer readings from the southbound bridge Span 1, southbound bridge Span 3, northbound bridge Span 1, and northbound bridge Span 3 are given in Figures 10.7 through 10.10. For each location, the method was checked assuming that the time-dependent

curve was deterministically known to be the AASHTO, ACI-209, B3, 1978 and 1990 CEB/FIP Model Codes, or the GL2000 model.

For the southbound bridge Span 1 data, all the time-dependent models appeared to provide a reliable check on the measured test set data, such that the quantity of readings outside the 99%-credible interval was always much less than the yellow warning bounds as shown in Figure 10.7. Similarly for the southbound bridge Span 3 data in Figure 10.8, all the time-dependent models appeared to capture the time-dependent behavior during all of the test sets. The AASHTO and ACI-209 models did not contain any out-of-bound measurements for the examined test sets. These predictions appeared to be reliable in spite of the breaks in measured linear potentiometer data as summarized in Section 2.3.2.

For the northbound bridge Span 1 data summarized in Figure 10.9, some of the models returned yellow or red flags (i.e., false positives) for a subset of the datasets. The AASHTO and ACI-209 models had two test sets beginning in June 7, 2010 and September 26, 2010 for which yellow or red flags were identified. From June 25, 2010 until September 21, 2010, no linear potentiometer data was collected for the northbound bridge Span 3. Consequently, the test set beginning on June 7, 2010 was approximately 140 days long, and the September 26, 2010 training set only contained a few days of data after the break. The AASHTO and ACI-209 models both failed to accurately predict the data across the break in the data, resulting in false positive warning flags. From May 2013 to August 2013, the B3 and GL2000 models occasionally returned yellow flags. These test sets did not correspond directly to a lapse in the measured data, though the extended break in data from May 27, 2012 until February 5, 2013 may have influenced the predictions. Both CEB/FIP Model Codes consistently returned only green flags.

Among all locations, the northbound bridge Span 3 data was predicted the worst by the Bayesian regression method, as shown in Figure 10.10. All the models except for the 1990 CEB/FIP Model Code triggered at least one yellow warning. The AASHTO model consistently

predicted red error flags starting at the test set beginning on April 29, 2012 and continued to the end of the examined test sets. Similarly for the ACI-209 model, yellow or red flags were assigned to all data sets beginning on April 29, 2012 until the set starting on July 21, 2013. For both the AASHTO and ACI-209 models, the number of out-of-bound readings decreased from May 13, 2013 until the end of the test sets. The 1978 CEB/FIP Model Code returned similar flags, though with markedly fewer out-of-bound readings, compared to the AASHTO and ACI-209 results during the same time-period. The B3, 1990 CEB/FIP Model Code, and GL2000 models all returned similar test set predictions, with jumps in out-of-bound readings typically occurring after breaks in the measured data. That more out-of-bound readings were found after breaks in the measured data was not surprising. The presence of breaks in the test set extended the 1,000-reading test set to a duration longer than 42 days, and thus made extrapolation of time-dependent behavior more uncertain. Breaks at the end of the training set, even if no breaks occurred during the test set, had a similar impact.

The time-dependent models that most rapidly approach their asymptotic values are, in order of fastest to slowest, the AASHTO, ACI-209, and 1978 CEB/FIP Model Code models. The 1990 CEB/FIP Model Code approaches its asymptote more slowly, and the GL2000 never reaches its asymptote within realistic structural lifetimes. The B3 model never reaches a limiting value. From examination of the northbound bridge Span 3 data in Figure 10.10, ranking the models in terms of incidence of false positives placed the AASHTO, ACI-209, and 1978 CEB/FIP Model Code models as the worst in the same order as how quickly the asymptotic values were approached. Among all the considered models, the 1990 CEB/FIP Model Code predictions were the most consistent regarding the ability to predict the short-term test set readings and minimize false positives.

10.2.4 Validating Short-Term Check with Artificially Induced Perturbations

To validate the ability of the short-term check to detect anomalies which might be indicative of structural or sensor-related problems (i.e., true positives), several perturbations were introduced to the measured data and analyzed with the discussed procedure. These perturbations were assumed to be indicative of probable scenarios that could be detected by the LP monitoring system, such as instantaneous jumps caused by sensor or acquisition system malfunction, bearing lockup, and long-term drift due to unexpected accelerations or decelerations in time-dependent deformations.

The ability to detect instantaneous jumps in the data was investigated using the measured southbound bridge Span 1 linear potentiometer data. As discussed in Section 2.3.2, replacement of the linear potentiometers at this location caused instantaneous jumps in the data at April 8, 2013, July 25, 2013, and August 6, 2013 (at 1,232, 1,356, and 1,371 adjusted age days, respectively). The magnitude of the jumps varied from less than 0.25 in. (6 mm) on April 8, 2013 up to several inches on July 25, 2013. The precise magnitude of the jumps was not known, as sensor replacement typically took place after an extended time when no data was collected, and thus changes in readings caused by sensor replacement and time-dependent behavior were inextricably connected. To test the ability of the short-term routine in detecting the perturbations associated with data jumps, the Heaviside functions used to correct for the data jumps were removed from the linear regression extraction of time-dependent behavior. Thus, the raw data with reading jumps induced by sensor replacement was used to examine the short-term routine. The linear potentiometer data from the southbound bridge Span 1 prior to extraction of the time-dependent behavior is plotted from January 1, 2012 until October 24, 2013 in Figure 10.11.

The jump occurring on April 8, 2013 (1,232 adjusted age days) was checked using the 1,000-reading window of data from May 7, 2012 to May 2, 2013. Based on the Heaviside function fits, the magnitude of this jump was estimated to be less than 0.25 in. (6 mm). Of the

1,000 readings in the test set, 468 were taken before the sensor replacement and 532 were taken after replacement. The test set duration, nearly a full year, was the longest of any investigated test sets, and consequently contained a mixture of unknown time-dependent deflections and sensor replacement errors. Using the AASHTO and ACI-209 time-dependent models, the short-term check flagged the test set as green with zero out-of-bound readings (i.e., no anomaly found). The 1978 CEB/FIP Model Code model flagged the test set as yellow with 93 out-of-bound readings. The B3, 1990 CEB/FIP Model Code, and GL2000 models all assigned the test set a red error flag, representative of a true positive given the a priori knowledge of the perturbation, each with over 400 out-of-bound readings. The measured time-dependent behavior (not corrected using the Heaviside functions for data jumps) and the 1990 CEB/FIP Model Code Bayesian prediction are shown in Figure 10.12 to illustrate the error caused by sensor replacement. Visual inspection of the time-dependent behavior showed a clear drop of approximately 0.25 in. (6 mm) immediately following the training set. An accurate prediction of time-dependent predictions is therefore critical for diagnosis of jumps with magnitudes on the order of the 99%-credible interval bounds of approximately ±0.15 in. (4 mm). The large jumps occurring on July 25, 2013 and August 6, 2013 (1,356 and 1,371 adjusted age days, respectively) were flagged as anomalies by all the time-dependent models, correctly identifying the artificially induced perturbations, though the jump magnitude introduced by replacement was over 1.0 in. (25 mm) in both cases and thus easily detectable from inspection of the raw data in Figure 10.11.

Bearing lockup was investigated in the southbound bridge Span 1 linear potentiometer data (now accounting for the known data jumps with the Heaviside function) by introducing a perturbation whereby the readings from one of the linear potentiometers were held constant plus a Gaussian error term with zero mean and standard deviation of 0.1 in. (2.5 mm), which was twice the expected standard deviation of the time-dependent deflections extracted from the (healthy) LP data. The exterior box LP was held constant for 276 readings starting on October 13, 2013 until

the end of the measured readings October 24, 2013. The interior box LP was assumed to be unaffected by the bearing lockup, and though unrealistic, was chosen to pull the southbound bridge Span 1 average readings closer to the measured results and theoretically making the lockup more difficult to detect. The 1,000-reading test set started on September 6, 2013, contained only the average data between the two LPs, and is plotted in Figure 10.13. The training set contained all previously collected average data.

The perturbation associated with bearing lockup was correctly identified as an anomaly regardless of the choice of time-dependent model. The quantity of out-of-bound readings varied from 142 to 153 readings depending on the choice of model, meaning all investigated models were similarly successful with regard to this check. The time-dependent behavior for the test set and a portion of the training set along with the Bayesian prediction using the 1990 CEB/FIP Model Code are plotted in Figure 10.14. The effects of the lockup are clearly visible by visual inspection of the sudden change in the time-dependent trend.

The short-term check was not expected to flag perturbations evolving over the course of several months or years as anomalies, but one such case was tested to estimate the efficacy of the method. A long-term perturbation was introduced to the Span 1 linear potentiometers in both the southbound and northbound bridges. The perturbation took the form of a linear drift in the measured readings of 0.5 in. (13 mm) over six months from April 24, 2013 until October 24, 2013. This perturbation was assumed to approximate some unexplained increase in the time-dependent movement of the structure, which might be caused by all the time-dependent deformation being transferred to a single expansion joint instead of both joints, or by degradation of the superstructure. The total time series of the northbound bridge Span 1 average LP readings including the six-month drift is plotted in Figure 10.15. The data plus the linear drift was nearly indistinguishable from the normal data when examining the total LP readings.

The short-term procedure was conducted for all the test sets as examined in Section 10.2.3. The known data jumps at April 8, 2013, July 25, 2013, and August 6, 2013 were removed from the southbound bridge Span 1 data using linear regression with the Heaviside function. Each of these jumps occurred either immediately prior or during the imposed six-month drift. The northbound bridge Span 1 data had no such jumps to remove. The quantity of readings outside the 99%-credible interval for each of the generated test sets from the southbound bridge Span 1 and northbound bridge Span 1 are given in Figures 10.16 and 10.17, respectively. Regardless of the choice of time-dependent model, the long-term perturbation was not flagged as an anomaly in the southbound bridge Span 1 data. However, an anomaly was detected for all time-dependent models in the northbound bridge Span 1 data. This indicated that if a Heaviside function was introduced to account for sensor replacement during the same time which long-term drift was occurring, then the drift could not be detected by the short-term check. Effectively, the measured time-dependent behavior was forced back to follow the expected time-dependent curve at each time when a Heaviside function was introduced. When the Heaviside function was not introduced in the case of the northbound bridge, the resultant measured time-dependent behavior including the perturbation drifted away from the expected behavior. Given enough time, the Bayesian regression would likely return to following the measured data regardless of the introduction of the drift.

In the general case, this short-term check should not be relied upon to detect changes in bridge behavior evolving over long periods of time. Though the six-month drift was flagged as an anomaly by all available time-dependent models in the case of the northbound bridge Span 1 data, the methodology cannot distinguish (without prior knowledge) between a true positive due to structural deterioration and a false positive triggered by imprecise estimation of the time-dependent behavior. Thus, this check cannot reliably provide recommendations for a course of action concerning anomalies that develop over a time period longer than the test set duration.

However, for short-term jumps in data or bearing lockup problems, the proposed methodology reliably flagged anomalies regardless of choice of time-dependent model. Ultimately, the choice of time-dependent model to be used in the Bayesian regression is driven primarily by the need to minimize false positives. Of the examined models, the 1990 CEB/FIP Model Code minimized false positives, followed by the B3 and GL2000 models, and then the 1978 CEB/FIP Model Code. The AASHTO and ACI-209 models were found to be unsuitable, and returned excessive false positives for some of the sensor locations.

10.3 Long-Term Anomaly Detection

10.3.1 Criteria for Long-Term Anomaly Detection Algorithm

Because the form of the time-dependent curve was not deterministically known, using Bayesian regression in the presented form to maximize detection of true positives and minimize false positives over durations of months or years was not reliable. Developing a suitable method that could integrate the uncertainty of the form of the time-dependent curve into a long-term prediction framework was beyond the scope of this report. For the present monitoring system, a directly actionable system without the need for reliable long-term predictions was desired.

Assuming constant or decreasing stress, the rate of time-dependent deformations of concrete should always decrease as time passes. For the longitudinal deflections measured by the linear potentiometers, this means that the time-dependent readings should always progress in the same direction and should slow down year after year. Regardless of the shape of the creep and shrinkage curves, all long-term rates will be small and positive given enough time. Therefore, bounds for long-term anomaly detection can be ascertained from previously measured rates of time-dependent behavior without knowledge of the specific form of the time-dependent curve.

The rate of the time-dependent behavior can be computed by measuring the slope of the time-dependent curves plotted with respect to the Arrhenius adjusted age. The method for computing the slope can impact the ability of the algorithm to flag anomalies. For example,

performing a least squares linear fit over a window of the data returns an average slope over the window. However, this method introduces an error in the case of non-uniformly sized windows. Shorter windows will tend to have a higher average slope, while a longer window will tend towards a lower slope. Given the breaks in the measured data, enforcing that all windows be exactly the same length in terms of adjusted age days was impossible.

Instead of fitting the measured data with a line, a window of time-dependent data was fit using linear regression employing the log-power equation:

$$TD = \alpha_1 \ln\left[1 + \left(t - t_0\right)_{adj}^{0.1}\right] + \alpha_2 + \delta \tag{10-20}$$

where *TD* is the measured time-dependent data extracted from the raw data according to the linear regression procedure discussed in Section 7.1, $(t - t_0)_{adj}$ is the Arrhenius adjusted age computed using the procedure in Section 7.3.2, α_1 and α_2 are fitting parameters, and δ is an error term assumed to be Gaussian with zero mean. Judging from the fitting parameters for the linear potentiometer data summarized in Tables 7.1 through 7.4, the log-power equation was approximately as accurate as the GL2000 and 1990 CEB/FIP Model Code equations in fitting the measured time-dependent curves. The log-power curve was chosen for simplicity, and preliminary analysis with other curves provided similar results.

The slope of the time-dependent behavior was taken as the first derivative of the fit with respect to the Arrhenius adjusted age:

$$\frac{\partial\left(TD\right)}{\partial\left(t - t_0\right)_{adj}} = \alpha_1\left[0.1\left(t - t_0\right)_{adj}^{-0.9}\right]\left[1 + \left(t - t_0\right)_{adj}^{0.1}\right]^{-1} \tag{10-21}$$

This slope corresponds to a tangent slope, as opposed to an averaged secant slope computed using the best fit line. Therefore, as long as the log-power equation provides a good approximation of the time-dependent behavior in the data window, then the slope at any given point is not dependent on the window duration.

If the Arrhenius age correction perfectly captured all interactions between temperature and time-dependent behavior, then the size of the window over which the slope was computed would be irrelevant as long as enough data points were incorporated so that creep and shrinkage could be separated from random scatter in the data. However, as discussed in Section 7.3.2, the Arrhenius age procedure did not distinguish between creep and shrinkage, nor did it account for aging or transient thermal creep. Furthermore, the temperatures used to compute the adjusted age were taken from only one location in the southbound bridge. Thus, it was expected that some seasonal effects still remained in the measured time-dependent behavior.

Because the time-dependent data plotted with respect to adjusted age did not remove all seasonal effects, the window for computing the slope was chosen to be equal to 500 adjusted age days, or approximately two full years. This minimized the impact of any seasonal effects, and also provided a large enough window for consistent regression using the log-power equation. Windows with duration equal to 250 adjusted age days (approximately one full year) were tested, but did not always contain enough data for reliable fitting due to the presence of data breaks up to nine months long.

Because the adjusted age procedure contracted time when it was cold and stretched time when it was warm, each year's worth of data contained a cluster of winter data points which all had similar adjusted ages and time-dependent deformations. This introduced bias into the regression, and therefore weighting was necessary. The two-year windows for computing slope were divided into 20 bins of equal adjusted age, and each bin was given equal weight in the regression. This was performed by weighting each reading by the inverse of the number of readings in that particular bin.

To investigate how the rates of time-dependent behavior changed as the bridge aged, the two-year windows used to compute the slope were moved reading-by-reading through the time-dependent behavior extracted from the linear potentiometer data. The 1990 CEB/FIP Model Code

model was used to approximate θ_5 for the linear regression procedure to extract the time-dependent behavior from the LP data as discussed in Section 7.1. Due to the specific form of the curve fitting over the two-year windows, the slopes computed at the beginning and end of any given window were not independent of each other. As shown in Eqn. (10-21), a single parameter α_1 characterized the slope over the entire window, and therefore only the slopes computed at the beginning of the windows were analyzed.

The measured rates at each instrumented location (averaged between the two sensors at each location), given at the beginning of the two-year windows, are shown in Figure 10.18. As expected, the rate of time-dependent behavior generally trended downwards with time, with occasional small increases or decreases.

Visual inspection of the rates of time-dependent behavior in the northbound bridge showed that, in the windows beginning at 700 to 1,000 adjusted age days (and ending at 1,200 to 1,500 adjusted age days, respectively), the Span 1 deflection rate decreased while the Span 3 rate increased. The total rate of contraction of the northbound appeared to consistently decrease, but more of the contraction was transferred to the north end of the bridge than to the south end. The reason for this behavior was unclear. However, this phenomena was determined to be unrelated to the slope computation methodology. Slopes were computed for the same data using different shapes for the θ_5 regression function (1990 CEB/FIP Model Code and GL2000), and also for the data with all gaps filled in with fictitious hourly readings (interpolated on log-time with a small Gaussian error term introduced), with each trial returning similar behavior as plotted in Figure 10.18.

When plotted in log-log space as shown in Figure 10.19, the rates followed a straight line, and thus could be approximated by a power function:

$$\frac{\partial(TD)}{\partial(t-t_0)_{adj}} = A(t-t_0)_{adj}^{B} \tag{10-22}$$

where *A* and *B* are fitting coefficients. For the measured LP data, *A* took values from 0.2 to 0.3 in. per adjusted age day, and the exponent *B* was approximately equal to −0.9.

Unlike the regression on the time-dependent behavior for the short-term check, a Bayesian framework did not offer significant advantages in the case of long-term slopes, as the prior distribution was unknown. Uninformative priors (for example, uniform prior distributions containing no meaningful information about the expected values) could be used, or performing Bayesian analysis on the computation of the slopes might also be able to quantify the prior uncertainty. However, because so many data points were available, linear regression with suitably chosen bounds to minimize false positive signals was believed to be functionally similar to, if statistically less rigorous than, a Bayesian approach in predictive capabilities.

The form of the equation for linear regression on the computed slopes with respect to adjusted age was chosen to be

$$SL = \alpha_3 \left(t - t_0\right)_{adj}^{-0.9} + \delta \tag{10-23}$$

where *SL* is the computed slope of the time-dependent behavior with respect to the Arrhenius adjusted age, α_3 is the regression coefficient, and δ is an error term assumed to be Gaussian with zero mean. No constant term was used in the regression, as the slope was expected to limit to zero given infinite time. Regardless of the precise form of the creep and shrinkage curves, the expected rate of time-dependent behavior after sufficient time was small and believed to be reasonably approximated by the power curve. The exponent was assumed to be a constant equal to −0.9 per the investigation of the slopes in Figure 10.19. If varied as a parameter in the regression, the exponent was found to be highly sensitive to changes in the data and occasionally was computed to have magnitude larger than −1.0 (i.e., value less than −1.0). Such a value implied that the power curve describing the time-dependent behavior had an exponent less than zero, which was unrealistic. Therefore, the exponent was held constant for consistency.

The training set for performing regression on the computed slopes was chosen to be all the windows for slope computation that contained the first year of measured data. Because the window size for computing the slope was approximately two years, the training set effectively contained information from the first three years of time-dependent behavior. Weighting was applied to the training set of the computed slopes, similar to the weighting procedure adopted in the computation of the slopes. The training set was divided into 20 bins of equal adjusted age (i.e., the adjusted ages at the beginning of the two-year windows), and the computed slopes in each bin were weighted by the inverse of the number of readings in the bin. The regression training set was never updated for future test sets, as it was believed that such updating might impact the efficacy of the method for long-term predictions.

The test set for flagging long-term anomalies was chosen to be the slopes computed from the most recent 1,000 two-year windows. Because only the most recent windows were used in the test set, the anomaly detection routine could return to predicting green flags after previously diagnosing yellow or red flags if the time-dependent rates returned to expected values.

Similar to the short-term check, upper and lower bounds were computed based on the regression results on the training set extrapolated to the test set data. However, because a Bayesian framework was not adopted, no holistic statistical method was available for determining the bounds. Therefore, upper and lower bounds were chosen to minimize false positives on the measured data. Bounds were selected to be the mean plus or minus the summation of 10% of the mean estimate and 3 times the standard deviation of the residual of the regression with respect to the training set data. Three standard deviations were chosen to approximate a 99%-confidence interval, and the additional ±10% of the mean estimate was added to enlarge the bounds when the time-dependent rates were higher and decrease the bounds at late ages when the rates were slow. Similar to the short-term check, yellow or red anomalies were flagged if more than 72 or 144 readings were out of bounds, respectively.

10.3.2 Summary of Long-Term Check Method

A flowchart summarizing the long-term check method from data collection to reporting is given in Figure 10.20. For extraction of the time-dependent behavior from the linear potentiometer data, only the first 750 adjusted age days (nearly three years) of data were used in computing the regression coefficients, which were then extrapolated to the entire data set. The choice of 750 adjusted age days corresponded to the length of the training set used for regression on the computed slopes using a power function (250 adjusted age days, or the first year of computed slopes), plus the length of the window over which the slopes were computed (500 adjusted age days, or approximately two years).

After extracting the time-dependent deflections in the above manner, a second linear regression was performed to remove any data jumps at known times from the entire data set. This was done by performing linear regression on the entire extracted time-dependent data series (not just the first 750 adjusted age days), using only the time-dependent function θ_5 and the necessary Heaviside functions to remove any data jumps due to sensor replacement.

The estimated regression function θ_5 for extracting the time-dependent behavior from the measured data was always assumed to take the form of the FEM results using the 1990 CEB/FIP Model Code time-dependent model. Validation of the short-term check on the measured data affirmed that this model could capture the measured expansion joint behavior at all locations. Ultimately, the choice of time-dependent model in this circumstance made little difference in the extracted time-dependent results as discussed in Section 7.3.1.

Slopes from the time-dependent behavior were computed with respect to adjusted age for all two-year windows of data (500 adjusted age days), moving reading-by-reading through the entire data set. Weighted linear regression using the log-power curve given in Eqn. (10-20) was performed over each window, and the slope was computed according to Eqn. (10-21). The two-year data window was divided into 20 equally sized bins in adjusted age, with each bin having

equal weight in the overall regression. Only the slope at the beginning of each window was examined, as the slopes at all other times during the same window were dependent on the single fitting parameter.

The extracted time-dependent slopes at the beginning of each window were plotted with respect to the adjusted age at the beginning of each window. Weighted linear regression using the power function in Eqn. (10-23) was performed on the first 250 adjusted age days (first year) of windows and extrapolated out to the rest of the computed slopes. The training set containing the first year of slopes was divided into 20 bins of equal adjusted age each with equivalent weighting to minimize fitting bias. Because a Bayesian approach was not adopted for this regression, no prior statistical information was used to define credible bounds. Instead, bounds on the extrapolation were defined to minimize false positive signals as discussed in Section 10.3.1.

10.3.3 Validating Long-Term Check on Existing Data

The validity of the long-term slope check was investigated using the measured linear potentiometer data from both the northbound and southbound bridges. The training set for each location contained the first year worth of slope calculations, with windows starting at October 31, 2008 (106 adjusted age days) until October 31, 2009 (350 adjusted age days) for data from Span 1 of the southbound bridge and Spans 1 and 3 for the northbound bridge, and windows starting at September 28, 2009 (339 adjusted age days) until September 28, 2010 (614 adjusted age days) for data from Span 3 of the southbound bridge (for which no data was collected during the first year after bridge completion as discussed in Section 2.3.2). All data from the end of the training sets until October 24, 2013 (1,467 adjusted age days) composed the test set and was checked against the computed predictions, as plotted in Figure 10.21.

For Span 1 of the southbound bridge, the extrapolated prediction nearly matched the measured slopes, and no computed slopes in the test set fell outside the defined bounds. A total of 59 computed slopes were outside the defined bounds for the data from Span 3 of the southbound

bridge. Because yellow flags were triggered only if 72 readings exceeded the bounds, no warning flags were recorded at this location. Despite the reduction in the measured slope starting near 700 adjusted age days, no readings from Span 1 of the northbound bridge exceeded the bounds. Compared to the other instrumented locations, the width of the acceptable bounds at Span 1 of the northbound bridge were large. This was due to the relative poorness of fit of the power curve to the training set for this location.

Anomalies were detected for Span 3 of the northbound bridge. Yellow flags were assigned starting at October 4, 2012 (slope computation window starting at 699 adjusted age days, June 7, 2011), and then transitioned to red flags beginning on October 27, 2012 (window starting at 708 adjusted age days, June 13, 2011). Red flags remained in place for nearly a year, when they transitioned back to yellow flags on August 29, 2013 (window starting at 914 adjusted age days, January 5, 2012). The yellow flags ended the next day on August 30, 2013 (window starting at 915 adjusted age days, January 8, 2012). Another period of yellow flags began on September 8, 2013 and ended on October 1, 2013 (windows beginning at 931 until 954 adjusted age days, equivalently March 22, 2012 until May 3, 2012). The cause of this anomalous behavior was unknown, and thus categorization as a true or false positive could not be made. Though the rate of time-dependent deflections returned to normal levels, future monitoring should focus on this location to ensure that normal behavior continues.

10.3.4 Validating Long-Term Check for Artificially Induced Perturbations

Slowly developing perturbations were introduced to the time-dependent behavior extracted from the LP data to test the efficacy of the long-term check. First, the three perturbations investigated for the short-term check were tested in the long-term routine.

To verify the efficacy of the long-term check in detecting instantaneous jumps in the data, the LP data from Span 1 of the southbound bridge was tested without removing the known jumps, as shown in Figure 10.11. The results from the long-term routine are shown in Figure

10.22. Red flags were triggered on April 8, 2013 (584 adjusted age days in Figure 10.22), the same day as the first jump of approximately 0.25 in. (6 mm), and persisted until the end of collection at October 24, 2013 (968 adjusted age days in Figure 10.22).

A perturbation emulating short-term bearing lockup starting on October 13, 2013 (two-year slope window starting at 964 adjusted age days) until the end of collection at October 24, 2013 (two-year slope window starting at 968 adjusted age days), shown in Figure 10.13, was tested using the long-term check. As shown in Figure 10.23, no computed slopes fell outside the bounds, and therefore the introduced perturbation was not identified as an anomaly by the long-term check. If the bearing lockup persisted for an extended period of time, it would be expected that eventually the long-term check would flag an anomaly. Because the short-term check proved effective at detecting this type of perturbation, the lack of ability to determine bearing lockup with the long-term check was not cause for concern.

The six-month linear drift from April 24, 2013 (two-year slope window starting at 736 adjusted age days) until October 24, 2013 (968 adjusted age days) of 0.5 in. (13 mm) in Span 1 of the southbound bridge and Span 1 of the northbound bridge, as plotted in Figure 10.15, was examined using the long-term check. As discussed in Section 10.2.4, the short-term check did not detect any anomalies in the southbound bridge but correctly flagged an anomaly in the northbound bridge, primarily due to the Heaviside function applied to the southbound bridge data to account for the sensor replacement and corresponding data jumps. Results of the long-term check applied to data from the southbound and northbound bridges are given in Figure 10.24. Again, the perturbation introduced into the data from the southbound bridge could not be detected by the long-term check. The introduction of the Heaviside functions will always correct the time-dependent behavior back to the expected curve, thus making it challenging to detect slowly developing perturbations that occur during sensor replacement. On the other hand, the drift was correctly flagged as an anomaly in the northbound bridge data, which did not have any jumps due

to sensor replacement. Red flags were triggered starting at August 22, 2013 (896 adjusted age days), nearly four months after the drift began, and persisted until the end of collection. The responsiveness of the long-term check regarding this perturbation would likely be faster for other instrumented locations, each of which had tighter bounds than Span 1 of the northbound bridge, or if the slope computation window were less than 500 adjusted age days. However, response times of several months were deemed acceptable for the long-term check based upon the nature of the perturbations that this routine was intended to detect.

To check the efficacy of the long-term check for slower developing perturbations, a linear drift of 0.5 in. (13 mm) applied over two years starting at October 24, 2011 (two-year slope window starting at 401 adjusted age days) until October 24, 2013 (968 adjusted age days) was introduced to the linear potentiometer data from Span 1 of the northbound bridge. The results of the long-term check are given in Figure 10.25. The method correctly identified the anomaly, with red flags first appearing on February 5, 2013 (609 adjusted age days) and persisting until the end of collection on October 24, 2013 (968 adjusted age days). The perturbation would likely have been flagged as an anomaly earlier, but no data was collected from May 27, 2012 until February 5, 2013 (two-year slope windows starting at 463 to 609 adjusted age days). Though not plotted, a perturbation in the opposite direction, represented by a linear drift of −0.5 in. (−13 mm) over two years, was also correctly identified as an anomaly.

To investigate how the method would behave given a slowly developing but temporary perturbation, a drift of 0.25 in. (6 mm) over one year starting October 24, 2011 (two-year slope windows starting at 401 adjusted age days) until October 24, 2012 (during the data break from May 27, 2012 until February 5, 2013 (463 until 609 adjusted age days)) was introduced to the linear potentiometer data from Span 1 of the northbound bridge. After the drift, the data continued as measured until the end of collection, albeit with an offset of 0.25 in. (6 mm) from the original measured results. This type of perturbation was meant to represent increased

movement in the bridge at one expansion joint, possibly due to translation of the structure, followed by a corrective procedure to halt (but not necessarily reverse) the motion. The results from the long-term check given this perturbation are shown in Figure 10.26. Red flags were identified on February 5, 2013 (609 adjusted age days) and persisted until August 6, 2013 (871 adjusted age days). The perturbation would have likely been flagged as an anomaly earlier if not for the 9-month break in data from May 27, 2012 until February 5, 2013. After the drift stopped propagating, the measured slopes returned to the expected range.

The evolution of the computed slopes from Span 1 of the northbound bridge with the introduced transient drift perturbation, shown in Figure 10.26, resembled the measured slopes from Span 3 of the northbound bridge given in Figure 10.21(d). Thus, the long-term anomaly detected in the time-dependent behavior at Span 3 of the northbound bridge was hypothesized to be caused by a transient change in the time-dependent behavior, possibly from translation of the superstructure, that was no longer progressing in the structure.

10.4 Summary and Conclusions

A prototype monitoring framework was developed to detect short-term and long-term anomalies in the linear potentiometer data. The short-term check was intended to detect anomalies related to immediate deviations from expected time-dependent behavior, or anomalies developing over a time frame less than one month. Such anomalies might be caused by bearing lockup or monitoring system failure. The long-term check was constructed to characterize trends over several years to ensure that the structure was behaving as expected. The developed methodology was intended only as a baseline level of structural monitoring, in that the framework could identify the presence of anomalies but not determine the causes.

The short-term check was based on Bayesian regression, which was used to combine the uncertainty in the time-dependent models with the uncertain measurements to arrive at rational bounds for defining anomalous results. Credible bounds were derived assuming that the form of

the time-dependent curve (as taken from finite element results documented in Chapter 8) was deterministic. Because the form of the creep and shrinkage curves was in fact uncertain, this had a tendency to underestimate the total uncertainty in the predicted values. As such, thresholds for flagging anomalies were set sufficiently high to minimize false positives from the measured data while aiming to maximize the system responsiveness to true positives.

The short-term check was examined assuming that the shape of the time-dependent curve deterministically followed FEM results from the AASHTO, ACI-209, B3, 1978 and 1990 CEB/FIP Model Codes, and GL2000 time-dependent models. When performing the short-term check on the measured LP data, the 1990 CEB/FIP Model Code results consistently minimized false positive flags. The AASHTO and ACI-209 models had many false positives, primarily related to the rate at which these two models approached their asymptotic values, which was much faster than observed in the measured data. The 1978 CEB/FIP Model Code, B3, and GL2000 models flagged occasional false positives, but overall performed better than the AASHTO and ACI-209.

To determine the effectiveness of the short-term check in flagging anomalies that might be associated with structural or instrumentation issues, perturbations were introduced to the measured data. The AASHTO, ACI-209, and 1978 CEB/FIP Model Code all failed to detect small and instantaneous data jumps of less than 0.25 in. (6 mm), but all models were equally capable at detecting larger instantaneous jumps and perturbations mimicking bearing lockup. Perturbations developing over the course of six months were successfully flagged as anomalies in data from Span 1 of the northbound bridge, but no anomalies were flagged in Span 1 of the southbound bridge. This was because sensor replacement occurred during the six-month drift in the case of the southbound bridge. Sensor replacement made detection of slowly developing perturbations difficult, as the introduction of the Heaviside function forced the extracted time-dependent behavior to follow the time-dependent predictions. Overall, the 1990 CEB/FIP Model

Code was found to be the most consistent model in terms of minimizing false positives while still correctly identifying perturbations as anomalies.

Because of the uncertainty in predicting long-term time-dependent behavior, the long-term check was not based on Bayesian analysis, nor did it focus on the total time-dependent deflections. Instead, the long-term check tracked the rate of time-dependent deflections with respect to the Arrhenius adjusted age. In the case of the linear potentiometer data, this rate was expected to continually decrease but never become negative. Thus, regardless of the form of the time-dependent curve, reasonable bounds could be placed on the diminishing creep and shrinkage rates. Bayesian analysis was not adopted because no prior statistical information was available for the uncertainty of the time-dependent rates. Though an uninformative prior could have been used in a Bayesian framework, a simpler scheme using weighted linear regression was adopted instead.

Time-dependent rates were computed by fitting the log-power curve to windows with duration equal to 500 adjusted age days (approximately two years), and then computing the derivative of the fit. Examination of the slopes over the course of the measured data revealed that the slopes followed the shape of a power curve when plotted with respect to the Arrhenius adjusted age. Therefore, weighted linear regression using the power curve was used to extrapolate the expected rates of time-dependent behavior, with bounds chosen to minimize false positive flags.

The long-term check was tested on the measured data from each of the instrumented locations. The methodology did not trigger any false positives for the southbound bridge data. For the northbound bridge, anomalous readings were identified in data from Span 3 starting at October 2012 until August 2013. During this time, the slopes at Span 3 increased while the slopes from Span 1 decreased (though no anomaly was flagged in Span 1 of the northbound bridge). Because of the opposite direction of deviations in Span 1 compared to Span 3, the time-dependent behavior of the total structure appeared to be continuing at the expected rate, but that more

deflection was concentrated in Span 3. The cause of these deviations was unknown, but were likely due to real changes in structural behavior (that is, not false positives). Both locations returned to the expected time-dependent rates in August 2013.

Perturbations developing over the course of months or years were introduced to the measured data to test the effectiveness of the long-term check. Again, perturbations developing at the same time at which a sensor was replaced in Span 1 of the southbound bridge were difficult to identify as anomalies due to how the linear regression method handled the corresponding data jumps. However, the method flagged perturbations as subtle as 0.25 in. (6 mm) of drift over two years in Span 1 of the northbound bridge as anomalies. Therefore, barring sensor replacement, this method was found to be effective in determining the presence of perturbations in long-term trends in time-dependent behavior, and thus was believed to minimize false positive while maximizing true positives.

The anomaly detection routine had several limitations which must be considered when extending the presented methodology to other instrumentation systems or structures. For example, in examining the longitudinal deflections at the expansion joints, the effects of cyclic thermal gradients as discussed in Chapter 9 were minimized. Systems which measure behavior related to beam bending, such as vertical deflections or curvatures, will be more strongly affected by the presence of thermal gradients. Consequently, using constant temperature finite element results for the prior mean in Bayesian regression might not accurately capture the shape of the measured time-dependent results. Furthermore, as shown in Figure 8.11, the rates of vertical deflections do not necessarily continually decrease, but instead may change directions. This invalidates the choice of the power curve in predicting the long-term rates of time-dependent behavior. Different measured behaviors, such as modal frequencies, might require a different expression for linear regression when removing the temperature dependence of the data. These issues would likely need to be tackled on a structure-by-structure basis. However, though each

individual implementation might vary, the methodology presented here should provide a general framework for any form of measured data dominated by temperature and time-dependent phenomena.

Chapter 11: Summary and Conclusions

This chapter summarizes the approach adopted for the investigation of time-dependent behavior in post-tensioned concrete box girder bridges, and the main conclusions from the study.

The conducted investigation consisted of four facets. The first was a laboratory investigation of time-dependent concrete behavior, whereby the aging strength and modulus, creep, and shrinkage were measured on concrete samples collected from the St. Anthony Falls Bridge. The second aspect was a study of the in situ behavior of the St. Anthony Falls Bridge, specifically the longitudinal deflections at the expansion joints of the bridge and the longitudinal strains throughout the superstructure. A methodology was developed to extract the time-dependent deformation, which involved removal of the temperature-driven response from the measurements, and also to adjust the time scale by using the Arrhenius equation to compute an adjusted age which normalized the temperature-dependent rates of the extracted creep and shrinkage of the concrete to an effective constant temperature.

The third facet of the investigation was the prediction of the time-dependent behavior of the St. Anthony Falls Bridge using the finite element method. The time-dependent behavior extracted from the bridge instrumentation and plotted with respect to the Arrhenius adjusted age was compared to the FEM predictions assuming constant temperature. Furthermore, finite element models with a simplified geometry were tested with different temperature history scenarios to observe the impacts that uniform temperature changes and thermal gradients might have on the long-term structural behavior, and to verify that the temperature dependence could accurately be separated from the time-dependent behavior in the measured LP and VWSG data.

The final feature of this investigation was the development of a prototype anomaly detection system using data measured from the linear potentiometers installed in the St. Anthony Falls Bridge. This monitoring system incorporated the findings from the in situ and numerical studies to form a routine that could identify anomalous time-dependent data that were rapidly

evolving (up to one month) and slowly evolving (up to two years). Rapidly evolving anomalies might be associated with an abnormal action such as a frozen bearing. The protocol for detection slowly evolving anomalies was developed to identify whether or not the structure might be undergoing gradual deterioration.

The primary outcomes from the described investigation include: insight into how temperature and time-dependent behaviors interact, and how these interactions affect structural performance and monitoring system data, summarized in Section 11.1; recommendations regarding the long-term time-dependent behavior of the St. Anthony Falls Bridge, and whether or not any precautionary measures need to be taken to overcome possible issues, presented in Section 11.2; description of the adopted anomaly detection routine that overcomes some of the challenges associated with long-term monitoring of in situ structures, presented in Section 11.3; and commentary on the usability and efficacy of the investigated time-dependent models to predict the behavior of large post-tensioned concrete bridges such as the St. Anthony Falls Bridge, discussed in Section 11.4.

11.1 Interactions between Temperature and Time-Dependent Behavior

11.1.1 Method for Separating Time- and Temperature-Dependent Behavior

A methodology based on linear regression was devised to extract the time-dependent behavior from measured strain and deflection readings. These readings were driven primarily by temperature and time-related phenomena, and so knowledge of the live traffic loading was not necessary for analysis.

Linear regression was conducted using five fitting functions: two functions described uniform temperature changes, one function described thermal gradients, one function defined time-dependent behavior, and one function was a constant term. Additional Heaviside step functions were added to fit any discontinuities in the data caused by known sources, for example, if a sensor was replaced.

The two fitting functions for uniform temperature included the integral of the temperature over the cross-sectional area at instrumented Location 7 at the midspan of the river span, and the integral of the same temperature squared. The first term was intended to approximate the average temperature over the full structure, but was confined to investigation of a single cross section because the necessary instrumentation was not located elsewhere in the bridge. The temperature-squared term was intended to capture the variation of the coefficient of thermal expansion with temperature. Measured data showed that the coefficient of thermal expansion of the bridge superstructure increased linearly as the temperature increased, by as much as 2.0 με/°F (3.6 με/°C) over the full measured temperature scale (0°F to 100°F (−18°C to 38°C)). The combination of the linear temperature and squared temperature terms thus captured the elongation of the structure due to uniform temperature changes.

Thermal gradients were approximated by a single function equal to the first moment of the temperature profile at instrumented Location 7 with respect to the section neutral axis. This function was intended to capture the bending behavior of the bridge under nonuniform temperatures.

A single function was required to approximate the time-dependent behavior so that the linear regression would not be adversely affected. As long as the chosen form of the time-dependent function approximately matched the measured behavior, the procedure could correctly identify the fitting coefficients for the temperature related phenomena.

The procedure for extracting the time-dependent readings was as follows. First, the measured data was fit using the five described functions, plus any necessary step functions to remove known jumps from the data. Then, using the coefficients from the two uniform temperature functions, one gradient function, the constant function, and all step functions, the temperature dependent behavior was subtracted from the original measured data. The fitting

coefficient for the assumed time-dependent function was ignored. The resulting data was the measured time-dependent behavior plus an error term assumed to be Gaussian with zero mean.

11.1.2 Temperature-Dependent Rates of Time-Dependent Phenomena

The interaction between temperature and time-dependent behavior was clearly seen in the time-dependent deformations extracted from the linear potentiometer and strain gage data from the St. Anthony Falls Bridge. Time-dependent trends followed a step-like pattern, accelerating during the summer and then nearly stopping during the winter.

The time-dependent phenomena of concrete aging, creep, and shrinkage all appear to follow the empirical relationship of the Arrhenius equation. This gives rise to an adjusted age, which is defined as the equivalent amount of time that would have to pass at standard temperature conditions to return equivalent strength gain or strain at the varying temperature conditions.

Because aging, creep, and shrinkage all depend on temperature differently, each phenomena is associated with a different activation energy coefficient in the Arrhenius equation, and thus each phenomena could have different adjusted ages. It was impossible to separate the individual types of time-dependent phenomena (i.e., aging, creep and shrinkage) in the measured data, so an aggregate coefficient needed to be defined for the total time-dependent behavior. This coefficient would likely vary by concrete composition. Typical activation energy coefficients for aging, creep, and shrinkage (using the material properties of the St. Anthony Falls Bridge superstructure) given in the literature vary from 4,000 K to 9,000 K. The aggregate coefficient for the St. Anthony Falls Bridge was taken as 7,360 K, as computed by the equation proposed for basic creep by Bažant and Baweja (1995a). A range of typical activation energy coefficients for other concrete compositions and structures requires further investigation.

The rates of the extracted time-dependent behavior were corrected using the average superstructure temperature, estimated from the thermistors installed at midspan of the southbound bridge. When adjusting the time scale using the Arrhenius equation, the average structural

temperature, and the chosen activation energy coefficient, the extracted time-dependent behavior from the bridge instrumentation followed a smooth curve similar to those from design equations.

11.1.3 Impact of Cyclic Temperatures on Time-Dependent Behavior

The effects of cyclic thermal gradients and seasonal temperature variations on time-dependent behavior were explored using the time-dependent finite element method and a post-tensioned beam approximating a greatly simplified geometry for the St. Anthony Falls Bridge. The computational methodology included temperature-dependent rates for creep, shrinkage, and hydration of the concrete, and was conducted using the ACI-209 and GL2000 models, considered to be representative of asymptotic and logarithmic time-dependent models, respectively.

Under seasonal temperature variations without daily thermal gradients, the behavior of the structure was changed exactly in the manner expected by the Arrhenius equation. Specifically, when the time-dependent data (excluding thermal expansion strains) containing seasonal temperature variations was compared to the constant temperature case, adjusting the time-scale with Arrhenius adjusted time resulted in equivalent results for longitudinal deflection, vertical deflection, strains, and stresses.

Introducing daily thermal gradients resulted in notable changes to the time-dependent behavior. Thermal gradients were cycled each day from zero up to the daily maximum gradient which varied by season. This temperature history, though not realistic, was expected to exacerbate any effects caused by the interactions between thermal gradients and time-dependent behavior, and thus make the impacts of cycled gradients more clear. Although the temperature state in the model was not uniform over the entire bridge, an average bridge temperature was still used to correct the modeled behavior according to the Arrhenius equation, as was done for the measured data. This correction resulted in nearly identical results for longitudinal deflection, regardless of the application of thermal gradients. However, vertical deflections were altered by the inclusion of the gradients. For the GL2000 model, this resulted in an end of service time-

dependent vertical deflection nearly 10% less than the constant temperature case. For the ACI-209 model, the end of service vertical deflections appeared to converge to the same values, regardless of the temperature history, though the deflection history from 10 to 1,000 adjusted age days was altered by the gradient.

Time-dependent stresses (after removal of the instantaneous stresses associated with the temperature changes) were very different with the inclusion of the thermal gradients. Compared to the constant temperature case, time-dependent stress losses were greater in the top fiber (less compression) and less in the bottom fiber (greater compression) when subject to cyclic gradients. Stress differences induced by 30 years of applied gradients ranged from −200 psi (−1.4 MPa) in the bottom flange up to +700 psi (+4.8 MPa) in the top flange using the GL2000 model, and −100 psi (−0.7 MPa) in the bottom flange to +360 psi (+2.5 MPa) in the top flange using the ACI-209 provisions. Furthermore, because the correction for creep and shrinkage rates is nonlinear with temperature and based on the Arrhenius equation, temperature histories including both seasonal (uniform) temperature changes and daily thermal gradients exhibit different time-dependent stress losses than the superposition of the losses assuming seasonal trends and daily gradients independently.

The reason for the large changes in time-dependent stresses is related to strain compatibility through the cross section. When the top surface is heated relative to the rest of the structure, compatibility will induce compression in the top surface and tension in the bottom surface. This causes the top surface to creep faster than the rest of the structure. In addition, the increased temperature of the top surface further accelerates the creep in the deck. Once the temperature gradient is removed, compatibility is once again applied, this time resulting in tension in the top surface and compression in the bottom. According to this process, the differences in the time-dependent behavior due to the application of thermal gradients were always in the opposite direction of the instantaneous elastic response.

When considering the effects of cyclic gradients, the season at which the structure was first loaded has no impact on long-term deflections and only minimal effect on time-dependent stress losses. Temporary thermal gradients when applied in the first year of the bridge life may impact the long-term stresses after the gradients are removed, but temporary gradients after the first year have negligible consequence for the long-term behavior. Regardless, the impacts of loading season and temporary gradients were much less than the differences between analyses accounting for thermal gradients and analyses assuming constant temperature.

Longitudinal deflections at the expansion joints and, to a lesser extent, longitudinal strains were affected by both uniform temperature changes and thermal gradients in a manner that could be predicted entirely by the Arrhenius equation using an average superstructure temperature. This is convenient for structural monitoring purposes, whereby the temperature corrections for expansion joint measurements or individual strain gages can be achieved by adopting the Arrhenius adjusted age. For vertical deflections, curvatures, and concrete stresses, the Arrhenius adjusted age does not capture the full impacts of cyclic thermal gradients.

Conducting cyclic thermal analysis while simultaneously computing time-dependent behavior is time consuming and challenging, so simplified methods are desirable for design. For longitudinal deflections, designers do not need to correct for cyclic temperature or gradients, as the impact is minimal. However, the conducted analyses showed that vertical deflections and stresses will be altered by the presence of thermal gradients. As noted, the changes in the time-dependent behavior are always opposite the direction of the instantaneous elastic response of the structure. Consequently, if thermal gradients deflect the structure upwards, then the net effect on the time-dependent displacement will be downward, and similarly for concrete stresses. Furthermore, the magnitude of the difference in the time-dependent behavior will always be less than the magnitude of the instantaneous response. For the specific case tested in this study, the

residual time-dependent response from the GL2000 model was approximately 50% of the instantaneous response, while the residual for the ACI-209 model was approximately 25%.

Though cyclic gradients impact the time-dependent vertical deflections and stress losses, no changes to the present design procedure for thermal gradients are recommended. At the end of construction, minimal time-dependent deformations have occurred, and therefore the findings in this study do not alter design procedures for investigating end of construction conditions. At end of service conditions, results from this investigation could be used to propose a methodology whereby the stresses from a positive thermal gradient are applied to the bridge as +X% and −Y% of the total instantaneous response, where X and Y sum to 100%. For example, the ACI-209 model was found to be bounded by +75% and −25% of the instantaneous response, while the GL2000 was bounded by ±50% of the elastic response. This provides benefits in terms of reducing the stresses due to large thermal gradients at the end of service, meaning that designing for the full positive thermal gradient as performed in current practice is conservative. However, the negative limit may be found to control for certain cases (for example, tension in the deck at end of service), meaning that the current provisions which require −30% of the positive gradient to be applied as a negative gradient (AASHTO, 2010) may be unconservative. However, this is unlikely, because the cyclic application of the thermal effects in this investigation was intended to exacerbate the impacts of thermal gradients on the time-dependent behavior, as explained above.

The numerical values given in the paragraph above for the GL2000 and ACI-209 models may depend on the temperature history and structural geometry. Without a thorough investigation of a variety of time-dependent models, structural shapes, and temperature histories, a more exact specification of the bounding factors is not possible. Because following the current thermal gradient design procedures for both positive and negative gradients is expected to be conservative, no changes to design are recommended.

11.2 Long-Term Behavior of St. Anthony Falls Bridge

The long-term performance of the St. Anthony Falls Bridge was evaluated by first extracting the time-dependent behavior from the in situ monitoring system and adjusting the time scale using the Arrhenius equation to derive the measured time-dependent response of the bridge assuming it was subject to a constant temperature. The derived data was then compared to finite element model predictions for each of the considered time-dependent models, which included the ACI-209 (1992), B3 (Bažant and Baweja, 1995a), the 1978 and 1990 CEB/FIP Model Codes, GL2000 (Gardner and Lockman, 2001), and AASHTO LRFD (2010) (which had to be combined with strength gain provisions from ACI-209 (1992) to provide a complete time-dependent model).

None of the models were able to accurately reproduce the measured behavior of the structure over the first five years following bridge completion. Of all the models, the ACI-209 and 1990 CEB/FIP Model Code provisions provided the closest fits to the bridge data. The ACI-209 and AASHTO models accurately predicted the first two years of time-dependent deflections, and only diverged from the measured results approximately 3 years after bridge completion. The 1990 CEB/FIP Model Code consistently, throughout the entire investigated 5-year time frame, overestimated the measured deformations by approximately 30%. The 1978 CEB/FIP Model Code, which was used by Figg Bridge Engineering for design of the St. Anthony Falls Bridge, overestimated the measured deformations by a factor of 2 for the first 5 years, but converged to similar predictions as the 1990 CEB/FIP Model Code after 150 years. The B3 and GL2000 models both greatly overestimated the time-dependent deformations by a factor greater than 2 over the first five years.

With respect to longitudinal time-dependent deflections that would need to be taken into account to prevent problems such as bearing runoff, no issues were identified for the St. Anthony Falls Bridge. The design of the bridge, using the 1978 CEB/FIP Model Code, accounted for

sufficiently larger deformations than the observed time-dependent motion over the first 5 years of bridge operation.

No instrumentation was provided to estimate the vertical deflections of the St. Anthony Falls Bridge. However, predictions from the finite element models showed that excessive deflections, such as those observed in the Koror-Babeldaob Bridge (Bažant et al., 2009, 2010), should not be a concern for the St. Anthony Falls Bridge. Regardless of the assumed time-dependent model, the direction of the predicted vertical deflections reversed. This reversal of deflections was due to the continuity of the St. Anthony Falls Bridge superstructure, which was achieved by jacking apart the two segmental cantilevers, placing a midspan closure pour, releasing the jacks, and then subsequently applying draped and bottom flange post-tensioning across the central region of Span 2. The balance of gravity and post-tensioning forces in the continuous superstructure enforced that the bridge would deflect upwards at midspan of the river span immediately following construction. After sufficient losses, the balance of forces would reverse, and thus the bridge would begin to deflect downwards. This greatly reduced the total range of expected time-dependent vertical deflections.

Stress envelopes combining gravity dead loads, post-tensioning, traffic live loads, uniform temperature changes, and thermal gradients were computed for each time-dependent model at the end of construction and end of service. In the top fiber at the end of service, the minimum compression limit was exceeded by all models near Abutment 1. This was due to the moment restraint induced by the bearings in the time-dependent model. Any damage at this location would cause the bridge to behave as though it had a perfect roller support at Abutment 1. As the design of the St. Anthony Falls Bridge assumed no moment restraint at this location, exceeding this minimum compression limit was not cause for concern.

In the bottom fiber at end of construction, tension was developed only for the B3 and GL2000 time-dependent models. This tension was less than the expected nominal tensile strength

of the concrete. These two models also greatly overestimated the measured time-dependent deformations, and consequently exhibited higher post-tensioning losses than were expected in the field structure. The models which better matched the measured time-dependent behavior, specifically the 1990 CEB/FIP Model Code provisions, did not predict tension at this location. Consequently, tension and cracking of the concrete due to excessive post-tensioning losses were not identified as a potential concern for the St. Anthony Falls Bridge.

In conclusion, the possibilities of excessive time-dependent deformations or development of tension due to post-tensioning losses in the St. Anthony Falls Bridge were considered remote, and consequently no actions are recommended for now or in the near future regarding the time-dependent behavior of this structure. To verify this, linear potentiometers can continue to be monitored for time-dependent behavior. If the longitudinal deflections continue to trend at values less than predicted by the 1990 CEB/FIP Model Code model, then the time-dependent behavior of the bridge can be assumed to be safe within a conservative factor of safety.

11.3 Anomaly Detection Routine for Structural Monitoring

At the most basic level, a structural monitoring system must be able to define whether or not a set of data is anomalous. Though anomalous data does not necessarily translate to structural damage or deterioration, anomaly detection is an important first step in accounting for the complex behaviors present during normal operation of an in situ structure. The developed anomaly detection routine consisted of two components, a short-term check and long-term check, which were both founded upon predicting the time-dependent behavior extracted from the linear potentiometer data.

Time-dependent behavior provides a useful metric for tracking the long-term performance of the structure. Total change in strain and deflection readings have very wide bounds due to daily and seasonal thermal effects, making traditional outlier analysis ineffective. Because creep and shrinkage progress slowly with time, the time-dependent measurements

provide a much more reliable baseline behavior for identifying short-term anomalous readings than the total change in strain or deflection values. Accounting for the interactions between temperature and time-dependent behavior further narrows the bounds for identifying anomalous data. Therefore, the short-term and long-term checks discussed below both used the time-dependent behavior extracted from the linear potentiometer data (Section 11.1.1), and plotted with respect to the Arrhenius adjusted age (Section 11.1.2) using the average bridge temperature.

11.3.1 Detecting Short-Term Anomalies

A method for detecting short-term anomalies in the measured longitudinal deflection (LP) data was developed. A short-term anomaly was assumed to develop instantaneously (which might be associated with sensor or data acquisition system failure) or, at most, over the course of approximately one month (which could be associated with bearing problems such as lockup). The methodology began with extracting the time-dependent behavior from the measured LP data and adjusting the time using the procedure summarized in Sections 11.1.1 and 11.1.2. The measured data was divided into a test set of the most recent readings and a training set of all previous data. Bayesian regression was conducted on the training set, and then extrapolated to the test set.

The primary benefit of adopting a Bayesian framework was that the epistemic uncertainty of time-dependent predictions could be combined with the aleatoric uncertainty in the measured data, thereby forming coherent statistical bounds with which to identify anomalies. For the short-term check, the computed deflections from the time-dependent finite element model of the St. Anthony Falls Bridge along with a coefficient of variation derived from the literature formed a prior distribution (i.e., a first-approximation statistical model describing the measured data). The prior distribution was then updated using the data in the training set. The resulting posterior distribution, with significantly narrowed bounds compared to the original prior distribution, was extrapolated to the test set and used to flag anomalous readings.

This method was tested on the measured linear potentiometer data using each of the considered time-dependent models for the prior distribution. In this check, each of the models was expected to return no warning flags, meaning that any flagged anomalies were presumed to be false positives. The AASHTO and ACI-209 models had many false positives, primarily due to the rate at which these two models approached their asymptotic values. The 1978 CEB/FIP Model Code, B3, and GL2000 models flagged occasional false positives, but performed better than the AASHTO and ACI-209 models. The 1990 CEB/FIP Model Code results consistently minimized false positive flags.

The short-term anomaly detection routine was then conducted for the measured LP data with added perturbations, including instantaneous jumps in the data (possibly related to sensor error), readings mimicking bearing lockup, and long-term drift (related to translation of the superstructure, or a change in the rate of time-dependent behavior due to unintended prestress changes or degradation). The method, regardless of the choice of time-dependent model, was successful at identifying data associated with instantaneous jumps in excess of 0.25 in. (6 mm) and bearing lockup as anomalies. The AASHTO, ACI-209, and 1978 CEB/FIP Model Code models were not capable of detecting jumps less than 0.25 in. (6 mm). Though not specifically designed to do so, the method was also capable of flagging some slower developing perturbations as anomalies, such as a linear ramp of 0.5 in. (13 mm) over six months (possibly associated with degradation or translation of the superstructure), but only if the sensors were not replaced during the time at which the drift was occurring.

11.3.2 Detecting Long-Term Anomalies

Because the methodology for the short-term anomaly check was not well suited for slower developing perturbations, a long-term anomaly detection routine was created to identify anomalous trends in the time-dependent behavior that develop over one month or for up to several years. Such anomalies could be associated with degradation of the bridge, an unexpected

change in the rate of time-dependent behavior due to strand loss, or translation of the superstructure.

Due to the uncertainty in the shape of the time-dependent behavior, as evinced by the vast differences among the considered time-dependent models, the total time-dependent deflections were not directly investigated. Instead, the rate of the time-dependent deflections with respect to the adjusted age were analyzed, as these rates should always decrease as the bridge ages and eventually approach zero. The adjusted age rates of time-dependent behavior were computed by fitting, by means of weighted linear regression, two-year long segments of the measured time-dependent behavior with a log-power function, and then computing the derivative of that function with respect to the adjusted age.

When plotted against adjusted age, the time-dependent rates (with respect to adjusted age) were found to decrease according to a power function. This function was used as the basis for prediction of the time-dependent rates. This method did not rely on finite element data computed for any of the investigated time-dependent models, as it could not be certain which model would best predict long-term rates.

The computed rates for the entire available history of LP data were divided into a training set, containing only the first year of rates, and the test set, containing all rates afterwards. Because no information was available to determine an informative prior distribution, Bayesian regression was not used as part of the long-term anomaly detection routine. Instead, weighted linear regression was applied to the training set, and then extrapolated to predict the mean rates of the test set. To minimize false positive signals, bounds were defined as 3 times the standard deviation of the residual on the training set plus 10% of the mean so that that the bounds narrowed as the rates decreased.

The adopted method was tested on the measured time-dependent rates extracted from each of the instrumented expansion joints. Results from the southbound bridge showed that no

warning flags would be assigned to the existing data, as expected. However, investigation of the northbound bridge data showed that, for the last year of collected rates, the slopes at Span 1 decreased while the slopes at Span 3 increased. No anomalies were flagged for Northbound Span 1, but anomaly flags were signaled for Northbound Span 3 for nearly one year. The cause of this behavior was unknown. It appeared that the total time-dependent rates for the northbound structure from Spans 1 through 3 were consistent with expectations, but more of the time-dependent bridge shortening was shifted to the Span 3 expansion joint than to the Span 1 expansion joint. The northbound bridge time-dependent rates returned to expected values after the year of anomalous behavior.

Long-term perturbations were introduced to the measured LP data and investigated using the long-term anomaly detection routine. If the sensor was replaced during the introduced drift, then the method had difficulty in flagging the anomaly. However, if the sensor was not replaced, then the method was capable of detecting drifts as slow as 0.25 in. (6 mm) over two years, even if data contained gaps as long as several months.

11.3.3 Present Drawbacks and Topics for Future Study

The primary drawback of the developed short-term anomaly detection routine was that the form of the time-dependent behavior must be specified as a deterministic property prior to analysis. Because the form of the long-term time-dependent curve is in fact not known, the Bayesian regression procedure underestimates the total uncertainty. In the proposed methodology, this was roughly accounted for by setting the warning flag thresholds sufficiently high to minimize false positives. However, the reliability of the system in accurate diagnosis of true positives (while simultaneously minimizing false positives) is dependent on the chosen time-dependent model and, in general, the efficacy of any given model cannot be known until testing is performed on existing data.

A more thorough procedure would need to account for uncertainty in the shape of the time-dependent curves. To achieve this, multi-model Bayesian analysis could be conducted with each model given a particular "trust" level, though it is unclear what values of trust should be placed with each particular model. Other methods that do not rely on extrapolation of a specific curve might be available, but uncovering such methods in the literature (if they exist) or developing suitable techniques was beyond the scope of this study.

The primary drawback of the long-term monitoring check is the specificity with regards to this particular application. For the LP data, the deflections increased monotonically, while the rates decreased monotonically with adjusted time. This allowed for predictions using linear regression and a power function, which in general would not be applicable for more complex time-dependent behavior. For example, vertical deflection was predicted to reverse direction at some point during the bridge service life, and thus could not rely on the use of the power function. For these other behaviors of interest, it may be feasible to derive some other appropriate predictor function, but only on a case-by-case basis.

More general limitations of the method are related to incomplete knowledge about how the structure will behave in the long-term. For example, the methodology does not account for how cyclic thermal gradients impact the time-dependent readings. This is not a concern for the investigated LP monitoring system, but adoption of similar methodology for vertical deflections may be difficult. Furthermore, if the temperature dependence of creep and shrinkage cannot be explained solely by the Arrhenius equation, then the extrapolation of expected time-dependent trends may result in false positives.

11.4 Efficacy of Investigated Time-Dependent Models

For the design of post-tensioned bridges, the investigation of these time-dependent models can provide guidance and advice with regards to long-term predictions of stresses and deformations. No existing time-dependent models are specifically calibrated for long-term

predictions of large structures. The data to which these models have been calibrated contain only a few samples with large *V*/*S*, with the maximum value for any sample being 6 in. (150 mm), and the vast majority of samples with ratios less than 1.5 in. (38 mm). Because structures such as the St. Anthony Falls Bridge have an average *V*/*S* around 8 in. (200 mm) and diaphragm regions with *V*/*S* up to 20 in. (510 mm), predictions of large structures inherently rely on extrapolation outside the calibrated range of time-dependent models.

Different models handle the effect of *V*/*S* differently. Intuitively, *V*/*S* should impact the rates of the drying creep and shrinkage which are dependent on diffusion of water in the concrete, but not impact the ultimate values of creep or shrinkage. The B3 model provides a method for scaling only the diffusion-driven deformations of drying creep and shrinkage based on *V*/*S*, though comparisons to measured results indicated that this model greatly overestimated the deformation of the St. Anthony Falls Bridge. The 1990 CEB/FIP Model Code method for scaling to structures with large *V*/*S*, though empirical in nature, appeared to provide good approximations for the St. Anthony Falls Bridge. The GL2000 model is similar to the B3 model in scaling, but also includes a predrying factor (i.e., a factor which reduces the amount of total creep dependent on the loss of water prior to loading) which is ignored by all other models. Though the predrying factor will be nearly equal to one for structures with large *V*/*S*, estimates for large structures may be impacted because the GL2000 model was calibrated to only small specimens often with a predrying factor less than one. The shape of the 1978 CEB/FIP Model Code did not appear to capture the early age behavior of the St. Anthony Falls Bridge. The AASHTO and ACI-209 models only incorporate *V*/*S*, as a change to the ultimate creep and shrinkage strains, rather than as an adjustment to the rate of time-dependent behavior that would be expected by diffusion theory. Thus, these models are not expected to provide reliable estimates of long-term deformations for large structures. Though these two models captured the early age (up to 3 years after bridge completion) time-dependent behavior of the St. Anthony Falls Bridge, they diverged

from measured deformations 4 years after construction. That the ACI-209 should be adjusted for analyzing large structures has been recognized by the ACI Committee 209 (1992) in Sections 2.4 and 2.8 of the ACI 209R-92, but the particular recommendations listed in these sections were not investigated in this study.

Shrinkage strains of concrete are commonly accepted to limit to an asymptotic value, but whether or not creep approaches an ultimate value is still not settled. Results from this study do not provide any specific guidance towards resolving this debate. The rate at which the AASHTO and ACI-209 models reached their asymptote, as explained above, was clearly at odds with the measured results. However, the rate of asymptotic behavior of the 1978 and 1990 CEB/FIP Model Code provisions appeared to provide reasonable estimates. Whether or not the long-term behavior is better captured by a logarithmic or asymptotic curve (with proper scaling for large structures) is left as a topic for future research.

Based on this investigation, the 1990 CEB/FIP Model Code and GL2000 time-dependent are recommended for use in design of large post tensioned segmental bridges. These recommendations are based on model usability and a shape that can scale to large structures. The 1990 CEB/FIP Model Code was found to provide a good, though conservative estimate of the time-dependent behavior from the St. Anthony Falls Bridge. The GL2000 model provided very conservative estimates of the time-dependent behavior of the bridge, but was convenient from a usability standpoint. The B3 model, having a complex form and many inputs that will typically be unknown to designers, and the 1978 CEB/FIP Model Code, being a graphical method and thus difficult to program into computational analysis, are acceptable but may be challenging to implement. The long-term time-dependent shape of the AASHTO and ACI-209 provisions do not appear to scale well to large structures. Though these models closely matched the early age time-dependent behavior of the St. Anthony Falls Bridge, they were found to be unconservative for the long-term, end of service conditions.

Tables

Table 1.1: Casting dates of CIP spans

Element	Casting date	Bottom flange tendons stressed	Age	Draped tendons stressed	Age
Segment 1 – Bed 1	1/31/2008				
Span 1 NB Super Structure Exterior (1/3)	4/2/2008				
Span 1 NB Super Structure Interior (1/3)	4/3/2008				
Span 1 SB Super Structure (1/3) Interior	4/4/2008				
Span 1 SB Super Structure (1/3) Exterior (1/3)	4/7/2008				
Span 1 NB Superstructure (2/4) Interior Barrel	4/12/2008				
Span 1 SB Superstructure (2/4)	4/15/2008				
Span 1 NB Superstructure (3/4) Exterior Barrel	4/18/2008				
Span 1 SB Superstructure (3/4) Interior Barrel	4/21/2008				
Span 1 SB Superstructure (3/4) Exterior Barrel	4/22/2008				
Span 1 NB Superstructure (4/4)	4/24/2008	5/22/2008	28	5/25/2008	31
Span 3 NB Exterior Barrel	4/29/2008				
Span 3 NB Interior Barrel	4/30/2008				
Span 1 NB Exterior Barrel	4/30/2008				
Span 1 SB Superstructure (4/4)	5/1/2008	5/25/2008	24	5/28/2008	27
Span 3 NB Int. and Ext. Soffit and Stems (To 2nd CJ)	5/3/2008				
Pier 2 NB Diaphragm 3rd Lift	5/7/2008				
Span 1 NB Top Deck (To 1st CJ)	5/7/2008				
Pier 2 SB Diaphragm 1st Lift	5/8/2008				
Span 1 SB Top Slab (1st CJ)	5/11 and 5/12/2008				
Span 1 NB Top Slab (2nd CJ)	5/12/2008				
Span 3 NB Soffit through Pier Diaphragm	5/13/2008	6/1/2008	19	6/7/2008	25
Span 1 NB Top Slab (Final Pour)	5/16/2008	5/22/2008	6	5/25/2008	9
Pier 3 NB Diaphragm 1st Lift	5/17/2008				
Span 1 SB Deck 2nd Pour	5/18/2008				
Span 3 SB Interior Soffit and Stems (1st CJ)	5/18/2008				
Span 1 SB Top Slab Final Pour	5/19/2008	5/25/2008	6	5/28/2008	9
Span 3 SB Exterior Soffit and Stems (1st CJ)	5/20/2008				
Pier 3 NB Diaphragm 2nd Lift	5/20/2008				
Pier 3 NB Diaphragm 3rd Lift	5/21/2008				
Span 3 SB Interior Stem and Soffit (2nd CJ)	5/23/2008				
Span 3 NB Top Deck to 1st CJ	5/27 and 5/28/2008				
Span 3 SB Exterior Soffit and Stems (2nd CJ)	5/29/2008				
Span 3 NB Top Deck to 2nd CJ	5/30/2008	6/1/2008	2	6/7/2008	8
Span 3 SB Interior Soffit (through diaphragm)	5/30/2008				
Span 3 SB Exterior Soffit (through diaphragm)	5/30/2008			6/19/2008	20
Pier 3 SB Diaphragm 2nd Lift	6/1/2008				
Span 3 SB Diaphragm	6/4/2008				
Span 3 SB Top Deck	6/8 and 6/9/2008				
Span 3 SB Top Deck (Final Pour)	6/12/2008			6/19/2008	7
Span 4 NB Stems and Soffit	7/17/2008				
Span 4 SB Soffit and Stems	7/24/2008				
Span 4 NB Deck	7/29/2008				
Pier 4 NB Diaphragm	7/29/2008				
Span 4 SB Top Deck	8/2/2008				
Pier 4 SB Diaphragm	8/5/2008				

Table 1.2: Casting and erection dates of the precast segments

NB Bridge West Box Segment	Concrete Cast Date	Segment Erected	Age at Erection (days)	Segment Weight (kips)
1'-6" CLOSURE	6/10/2008			
3NB-1	3/27/2008	6/5/2008	70	378.6
3NB-2	4/5/2008	6/16/2008	72	357.2
3NB-3	4/16/2008	6/18/2008	63	336.4
3NB-4	4/21/2008	6/21/2008	61	316.5
3NB-5	4/26/2008	6/22/2008	57	361.5
3NB-6	4/30/2008	6/25/2008	56	336.2
3NB-7	5/5/2008	6/26/2008	52	314.2
3NB-8	5/8/2008	6/28/2008	51	296.3
3NB-9	5/12/2008	6/29/2008	48	283.6
3NB-10	5/15/2008	6/30/2008	46	286.3
3NB-11	5/20/2008	7/1/2008	42	281.8
3NB-12	5/24/2008	7/2/2008	39	292.8
3NB-13	5/30/2008	7/3/2008	34	269.9
3NB-14	6/3/2008	7/4/2008	31	267.6
3NB-15	6/5/2008	7/5/2008	30	213.8
CLOSURE	7/16/2008			
2NB-15	5/3/2008	7/3/2008	61	378.6
2NB-14	4/30/2008	7/2/2008	63	357.2
2NB-13	4/25/2008	6/28/2008	64	336.4
2NB-12	4/19/2008	6/27/2008	69	316.5
2NB-11	4/14/2008	6/26/2008	73	361.5
2NB-10	4/10/2008	6/19/2008	70	336.2
2NB-9	4/7/2008	6/17/2008	71	314.2
2NB-8	4/1/2008	6/15/2008	75	296.3
2NB-7	3/27/2008	6/14/2008	79	283.6
2NB-6	3/24/2008	6/12/2008	80	286.3
2NB-5	3/19/2008	6/9/2008	82	281.8
2NB-4	3/17/2008	6/7/2008	82	292.8
2NB-3	3/10/2008	6/4/2008	86	269.9
2NB-2	3/1/2008	6/1/2008	92	267.6
2NB-1	2/19/2008	5/26/2008	97	213.8
1'-6" CLOSURE	5/30/2008			

NB Bridge East Box Segment	Concrete Cast Date	Segment Erected	Age at Erection (days)	Segment Weight (kips)
1'-6" CLOSURE	6/10/2008			
3NB-1	4/2/2008	6/5/2008	64	378.6
3NB-2	4/10/2008	6/16/2008	67	357.2
3NB-3	4/17/2008	6/18/2008	62	336.4
3NB-4	4/23/2008	6/21/2008	59	316.5
3NB-5	4/29/2008	6/22/2008	54	361.5
3NB-6	5/2/2008	6/25/2008	54	336.2
3NB-7	5/6/2008	6/26/2008	51	314.2
3NB-8	5/9/2008	6/28/2008	50	296.3
3NB-9	5/14/2008	6/29/2008	46	283.6
3NB-10	5/17/2008	6/30/2008	44	286.3
3NB-11	5/21/2008	7/1/2008	41	281.8
3NB-12	5/28/2008	7/2/2008	35	292.8
3NB-13	5/31/2008	7/3/2008	33	269.9
3NB-14	6/4/2008	7/4/2008	30	267.6
3NB-15	6/6/2008	7/5/2008	29	213.8
CLOSURE	7/16/2008			
2NB-15	5/2/2008	7/3/2008	62	378.6
2NB-14	4/29/2008	7/2/2008	64	357.2
2NB-13	4/25/2008	6/28/2008	64	336.4
2NB-12	4/17/2008	6/27/2008	71	316.5
2NB-11	4/12/2008	6/26/2008	75	361.5
2NB-10	4/8/2008	6/19/2008	72	336.2
2NB-9	4/5/2008	6/17/2008	73	314.2
2NB-8	3/29/2008	6/15/2008	78	296.3
2NB-7	3/26/2008	6/14/2008	80	283.6
2NB-6	3/21/2008	6/12/2008	83	286.3
2NB-5	3/18/2008	6/9/2008	83	281.8
2NB-4	3/12/2008	6/7/2008	87	292.8
2NB-3	3/6/2008	6/4/2008	90	269.9
2NB-2	2/26/2008	6/1/2008	96	267.6
2NB-1	2/14/2008	5/25/2008	101	213.8
1'-6" CLOSURE	5/30/2008			

SB Bridge West Box Segment	Concrete Cast Date	Segment Erected	Age at Erection (days)	Segment Weight (kips)
1'-6" CLOSURE	6/18/2008			
3SB-1	3/26/2008	6/16/2008	82	378.6
3SB-2	4/4/2008	6/21/2008	78	357.2
3SB-3	4/18/2008	6/22/2008	65	336.4
3SB-4	4/18/2008	6/23/2008	66	316.5
3SB-5	4/23/2008	6/24/2008	62	361.5
3SB-6	4/29/2008	6/25/2008	57	336.2
3SB-7	5/5/2008	6/29/2008	55	314.2
3SB-8	5/7/2008	7/1/2008	55	296.3
3SB-9	5/10/2008	7/4/2008	55	283.6
3SB-10	5/14/2008	7/5/2008	52	286.3
3SB-11	5/19/2008	7/6/2008	48	281.8
3SB-12	5/23/2008	7/7/2008	45	292.8
3SB-13	5/30/2008	7/8/2008	39	269.9
3SB-14	6/1/2008	7/9/2008	38	267.6
3SB-15	6/4/2008	7/10/2008	36	261.3
CLOSURE	7/24/2008			
2SB-15	5/3/2008	7/9/2008	67	378.6
2SB-14	4/30/2008	7/8/2008	69	357.2
2SB-13	4/25/2008	7/7/2008	73	336.4
2SB-12	4/21/2008	7/6/2008	76	316.5
2SB-11	4/15/2008	6/28/2008	74	361.5
2SB-10	4/11/2008	6/19/2008	69	336.2
2SB-9	4/7/2008	6/17/2008	71	314.2
2SB-8	4/2/2008	6/16/2008	75	296.3
2SB-7	3/28/2008	6/14/2008	78	283.6
2SB-6	3/25/2008	6/13/2008	80	286.3
2SB-5	3/20/2008	6/11/2008	83	281.8
2SB-4	3/15/2008	6/9/2008	86	292.8
2SB-3	3/11/2008	6/7/2008	88	269.9
2SB-2	3/5/2008	6/3/2008	90	267.6
2SB-1	2/21/2008	5/29/2008	98	261.3
1'-6" CLOSURE	6/1/2008			

SB Bridge East Box Segment	Concrete Cast Date	Segment Erected	Age at Erection (days)	Segment Weight (kips)
1'-6" CLOSURE	6/18/2008			
3SB-1	3/29/2008	6/16/2008	79	378.6
3SB-2	4/9/2008	6/21/2008	73	357.2
3SB-3	4/16/2008	6/22/2008	67	336.4
3SB-4	4/21/2008	6/23/2008	63	316.5
3SB-5	4/28/2008	6/24/2008	57	361.5
3SB-6	5/1/2008	6/25/2008	55	336.2
3SB-7	5/6/2008	6/29/2008	54	314.2
3SB-8	5/9/2008	7/1/2008	53	296.3
3SB-9	5/13/2008	7/4/2008	52	283.6
3SB-10	5/16/2008	7/5/2008	50	286.3
3SB-11	5/20/2008	7/6/2008	47	281.8
3SB-12	5/27/2008	7/7/2008	41	292.8
3SB-13	5/31/2008	7/8/2008	38	269.9
3SB-14	6/3/2008	7/9/2008	36	267.6
3SB-15	6/5/2008	7/10/2008	35	261.3
CLOSURE	7/24/2008			
2SB-15	5/1/2008	7/9/2008	69	378.6
2SB-14	4/28/2008	7/8/2008	71	357.2
2SB-13	4/25/2008	7/7/2008	73	336.4
2SB-12	4/18/2008	7/6/2008	79	316.5
2SB-11	4/14/2008	6/28/2008	75	361.5
2SB-10	4/9/2008	6/19/2008	71	336.2
2SB-9	4/5/2008	6/17/2008	73	314.2
2SB-8	3/31/2008	6/16/2008	77	296.3
2SB-7	3/27/2008	6/14/2008	79	283.6
2SB-6	3/24/2008	6/13/2008	81	286.3
2SB-5	3/18/2008	6/11/2008	85	281.8
2SB-4	3/13/2008	6/9/2008	88	292.8
2SB-3	3/7/2008	6/7/2008	92	269.9
2SB-2	2/29/2008	6/3/2008	95	267.6
2SB-1	2/16/2008	5/29/2008	103	261.3
1'-6" CLOSURE	6/1/2008			

Table 1.3: Load stages during construction

Date	Loading description
6/27/2008	Partial release of northbound Span 1 falsework bents 1–8, 1–7
6/28/2008	Partial release of northbound Span 1 falsework bents 1–6, 1–5
6/30/2008	Full release of northbound Span 1 falsework
7/4/2008	Partial release of northbound Span 3 falsework bents 3–1 to 3–5
7/5/2008	Full release of northbound Span 3 falsework - bent 3–6
7/4/2008	Hung Span 1 NB falsework deck (3M lbs)
7/7/2008	Lowered Span 1 NB falsework
7/8/2008	Lowered all Span 1 NB falsework
7/8/2008	Placed 60T crane and 24T alignment beams on 2NB cantilever tip
7/9/2008	Hung Span 3 NB falsework deck & poles
7/8/2008	Full release of southbound Span 1 falsework
7/9/2008	Hung Span 1 SB falsework deck (3M lbs)
7/9/2008	Full release of southbound Span 3 falsework
	Aligned NB cantilevers
	Aligned SB cantilevers
7/16/2008	Jacked NB midspan closure apart applying 1120 kips
7/24/2008	Jacked SB midspan closure apart applying 1120 kips

Table 2.1: Summary of gage types and locations

Gage Type	Gage Models	Total # of Sensors	Locations**
Vibrating wire strain gage (VWSG) and associated thermistor	Roctest EM-5 (superstructure)	139 (128*)	SB (Locs 3, 4, 5, 7, 8, 9, 14, 15); NB (Locs 3, 5, 7, 8, 9, 14, 15)
	Roctest SM-5A (superstructure)	8 (19*)	SB (Loc 6 and replacement gages)
	Geokon 4911A (pier, caisson)	40	SB (Pier 2 and Drilled Shafts 1 and 2)
	Geokon 4200 (pier)	10	SB (Pier 2)
Thermistor	Roctest Model TH-T	48	SB (Loc 7); NB (Loc 7)
Fiber optic (SOFO) sensors	SOFO Standard Deformation Sensor (13.12 ft (4 m))	12	Distributed along exterior box of Span 2, SB Bridge
Accelerometer	Kistler 8310B2	26	12 permanently installed near midspans of Spans 1, 2, and 3, both boxes of SB and NB Bridges 14 movable in exterior box of SB Bridge Span 2
Linear potentiometer (LP)	Unimeasure HX-P420	12	Span 1, Abutment 1; Span 3, Pier 4; Span 4, Pier 4; both boxes of SB and NB Bridges
Resistive strain gage	Geokon 3911A-4	24	SB (Pier 2 and Drilled Shafts 1 and 2)
Corrosion monitoring	Corsensys CS-040 corrosion current sensor	4	Near midspans of Spans 1 and 3, exterior box of SB and NB Bridges
	Corsensys CS-402 resistivity (moisture) sensor	4	Near midspans of Spans 1 and 3, exterior box of SB and NB Bridges

* Eleven (11) EM-5 gages replaced by externally mounted SM-5A on May 11, 2010 and June 18, 2010

** Refer to Figure 2.1 for Location numbers

Table 2.2: VWSG and thermistor labeling, locations, and connections

Gage Label	Gage Type	Bridge	Location	Station	Girder	X (in)	Y (in)
VN03EBL1	EM-5	NB	3	217+01.79	Exterior	−48.0	−141.8
VN03EWL1	EM-5	NB	3	217+01.79	Exterior	−137.9	−44.0
VN03ETL1	EM-5	NB	3	217+01.79	Exterior	48.0	−10.0
VN03ITL1	EM-5	NB	3	217+01.79	Interior	46.5	−8.6
VN03IBL1	EM-5	NB	3	217+01.79	Interior	48.0	−141.8
VS03IBL1	EM-5	SB	3	217+01.79	Interior	−48.0	−150.6
VS03ITL1	EM-5	SB	3	217+04.58	Interior	−140.0	−14.3
VS03ITT1	EM-5	SB	3	217+04.58	Interior	−140.0	−4.4
VS03ITT2	EM-5	SB	3	217+04.58	Interior	−140.0	−20.1
VS03ITL2	EM-5	SB	3	217+04.58	Interior	−48.0	−3.7
VS03ETL3	EM-5	SB	3	217+04.58	Exterior	48.0	−6.0
VS03ETT1	EM-5	SB	3	217+04.58	Exterior	121.0	−2.3
VS03ETL4	EM-5	SB	3	217+04.58	Exterior	131.0	−4.6
VS03ETT3	EM-5	SB	3	217+04.58	Exterior	141.0	−4.6
VS03ETL5	EM-5	SB	3	217+04.58	Exterior	220.0	−4.7
VS03ETT4	EM-5	SB	3	217+04.58	Exterior	141.0	−19.6
VS03ETT2	EM-5	SB	3	217+04.58	Exterior	121.0	−16.8
VS03EEV2	EM-5	SB	3	217+04.58	Exterior	131.4	−35.1
VS03EEV3	EM-5	SB	3	217+04.58	Exterior	141.4	−35.1
VS03EEV1	EM-5	SB	3	217+04.58	Exterior	130.5	−79.9
VS03EEA1	EM-5	SB	3	217+04.58	Exterior	130.5	−80.1
VS03EEL1	EM-5	SB	3	217+04.33	Exterior	131.4	−76.1
VS03EBL3	EM-5	SB	3	217+04.58	Exterior	112.4	−144.6
VS03EBT3	EM-5	SB	3	217+04.58	Exterior	97.5	−147.6
VS03EBT4	EM-5	SB	3	217+04.58	Exterior	98.5	−151.1
VS03EBL2	EM-5	SB	3	217+04.25	Exterior	48.0	−152.1
VS03EBT1	EM-5	SB	3	217+04.58	Exterior	−99.0	−148.1
VS03EBT2	EM-5	SB	3	217+04.58	Exterior	−98.5	−152.1
VS03EBL1	EM-5	SB	3	217+04.58	Exterior	−108.5	−144.1
VS03ETL1	EM-5	SB	3	217+04.58	Exterior	−218.0	−5.2
VS03ETL2	EM-5	SB	3	217+04.58	Exterior	−126.0	−3.6
VS04ETL1	EM-5	SB	4	218+61.9	Exterior	2.0	−6.5
VS04EEV1	EM-5	SB	4	218+61.9	Exterior	108.2	−138.3
VS04EEA1	EM-5	SB	4	218+61.9	Exterior	107.7	−140.4
VS04EEL1	EM-5**	SB	4	218+61.9	Exterior	108.5	−136.8
VS04EBL2	EM-5	SB	4	218+61.9	Exterior	79.9	−282.1
VS04EBL1	SM-5A*	SB	4	218+61.9	Exterior	48.0	−282.4
VS04EWV1	EM-5	SB	4	218+61.9	Exterior	−109.9	−130.8
VS04EWA1	EM-5	SB	4	218+61.9	Exterior	−109.2	−133.8
VS04EWL1	EM-5	SB	4	218+61.9	Exterior	−109.9	−130.8
VN05ETL1	EM-5	NB	5	219+09.1	Exterior	3.0	−6.0
VN05EBL1	EM-5	NB	5	219+10.1	Exterior	−3.5	−290.4
VN05EWL1	EM-5	NB	5	219+10.1	Exterior	−107.9	−141.1
VN05ITL1	EM-5	NB	5	219+09.1	Interior	−2.0	−5.8
VN05IBL1	SM-5A*	NB	5	219+10.1	Interior	2.0	−290.4
VS05ITL1	EM-5	SB	5	218+92.4	Interior	0.0	−6.5
VS05IBL1	EM-5	SB	5	218+92.4	Interior	0.0	−291.4
VS05ETL1	EM-5	SB	5	218+92.4	Exterior	2.5	−6.0
VS05EEL1	EM-5	SB	5	218+92.4	Exterior	108.9	−141.1
VS05EBL1	EM-5	SB	Closure 5	218+94.40	Exterior	0.0	−299.0
VS06ETL1	SM-5A†	SB	6	219+01.9	Exterior	−2.5	−11.5
VS06EEV1	SM-5A	SB	6	219+01.9	Exterior	108.1	−122.7
VS06EEA1	SM-5A	SB	6	219+01.9	Exterior	108.8	−119.7
VS06EEL1	SM-5A	SB	6	219+01.9	Exterior	107.4	−126.2
VS06EBL1	SM-5A	SB	6	219+01.9	Exterior	2.0	−231.2
VS06EWV1	SM-5A	SB	6	219+01.9	Exterior	−107.5	−125.7
VS06EWA1	SM-5A	SB	6	219+01.9	Exterior	−108.0	−123.2

* Gage replaced and collected data was satisfactory. New gage model shown.

** Thermistor does not provide readings. Strain measurements only. Never replaced.

† Gage replaced but newly collected data was not satisfactory. New gage model shown.

Table 2.2: VWSG and thermistor labeling, locations, and connections (cont'd.)

Gage Label	Gage Type	Bridge	Location	Station	Girder	X (in)	Y (in)
VS06EWL1	SM-5A	SB	6	219+01.9	Exterior	−106.9	−128.2
VN07ETL1	EM-5	NB	7	221+54.4	Exterior	0.0	−6.0
TNEEA003	THT	NB	7	221+54.4	Exterior	120.9	−80.2
TNEEA002	THT	NB	7	221+54.4	Exterior	126.0	−79.7
TNEEA001	THT	NB	7	221+54.4	Exterior	130.4	−79.2
TNEBA003	THT	NB	7	221+54.4	Exterior	−2.0	−128.2
TNEBA002	THT	NB	7	221+54.4	Exterior	−1.0	−130.7
TNEBA001	THT	NB	7	221+54.4	Exterior	−2.0	−133.2
VN07EBL1	EM-5	NB	7	221+54.4	Exterior	12.0	−133.2
VN07EWL1	SM-5A*	NB	7	221+54.4	Exterior	−130.2	−40.2
VN07ITL1	EM-5	NB	7	221+54.4	Interior	−12.0	−5.0
VN07IBL1	EM-5	NB	7	221+54.4	Interior	0.0	−131.7
VS07ITL4	EM-5	SB	7	221+39.4	Interior	0.0	−5.5
TSITB001	THT	SB	7	221+39.4	Interior	0.0	−2.0
TSITB002	THT‡	SB	7	221+39.4	Interior	0.0	−3.5
TSITB003	THT	SB	7	221+39.4	Interior	0.0	−5.0
TSITB004	THT	SB	7	221+39.4	Interior	0.0	−6.9
TSITB005	THT‡	SB	7	221+39.4	Interior	0.0	−7.8
TSITB006	THT‡	SB	7	221+39.4	Interior	0.0	−10.0
VS07ITL5	EM-5	SB	7	221+39.4	Interior	131.0	−5.5
TSITC001	THT	SB	7	221+39.4	Interior	149.0	−5.8 [@]
TSITC002	THT	SB	7	221+39.4	Interior	149.0	−5.3 [@]
TSITC003	THT	SB	7	221+39.4	Interior	149.0	−5.3 [@]
TSITC004	THT	SB	7	221+39.4	Interior	149.0	−4.8 [@]
TSITC005	THT	SB	7	221+39.4	Interior	149.0	−4.3 [@]
TSITC006	THT	SB	7	221+39.4	Interior	149.0	−2.8 [@]
VS07ITL6	EM-5	SB	7	221+39.4	Interior	220.0	−6.2
TSIEA001	THT	SB	7	221+39.4	Interior	137.0	−31.3
TSIEB001	THT	SB	7	221+39.4	Interior	131.3	−74.3
TSIEB002	THT	SB	7	221+39.4	Interior	127.6	−73.8
TSIEB003	THT	SB	7	221+39.4	Interior	122.2	−73.3
TSIEC001	THT	SB	7	221+39.4	Interior	117.0	−119.8
TSIBA002	THT	SB	7	221+39.4	Interior	0.0	−128.3
TSIBA001	THT	SB	7	221+39.4	Interior	0.0	−133.3
VS07IBL2	EM-5	SB	7	221+39.4	Interior	0.0	−132.8
VS07IBL1	EM-5	SB	7	221+39.4	Interior	−116.3	−128.3
VS07ITT2	EM-5	SB	7	221+39.4	Interior	−142.0	−12.3
TSITA001	THT	SB	7	221+39.4	Interior	−238.0	−6.75 [@]
TSITA002	THT	SB	7	221+39.4	Interior	−238.0	−8.25 [@]
TSITA003	THT	SB	7	221+39.4	Interior	−238.0	−9.75 [@]
VS07ITL1	EM-5	SB	7	221+39.4	Interior	−220.0	−4.7
VS07ITL2	EM-5	SB	7	221+39.4	Interior	−175.5	−4.9
VS07ITT1	EM-5	SB	7	221+39.4	Interior	−142.0	−7.3
VS07ITL3	EM-5	SB	7	221+39.4	Interior	−131.0	−6.0
VS07ETL4	EM-5	SB	7	221+39.4	Exterior	0.0	−5.5
VS07ETL5	EM-5	SB	7	221+39.4	Exterior	68.5	−5.8
VS07ETT1	EM-5	SB	7	221+39.4	Exterior	121.0	−5.8
VS07ETL6	EM-5	SB	7	221+39.4	Exterior	131.0	−5.5
VS07ETT3	EM-5	SB	7	221+39.4	Exterior	141.0	−6.0
VS07ETL7	EM-5	SB	7	221+39.4	Exterior	124.0	−8.2
VS07ETL8	EM-5	SB	7	221+39.4	Exterior	220.0	−5.7
VS07ETL9	EM-5	SB	7	221+39.4	Exterior	247.0	−5.8
VS07ETT4	EM-5**	SB	7	221+39.4	Exterior	141.0	−15.0
VS07ETT2	EM-5	SB	7	221+39.4	Exterior	121.0	−15.3
VS07EEV2	EM-5	SB	7	221+39.4	Exterior	130.7	−38.0
VS07EEV3	EM-5	SB	7	221+39.4	Exterior	140.0	−38.0
VS07EEV1	EM-5	SB	7	221+39.4	Exterior	129.2	−44.6
VS07EEA1	EM-5	SB	7	221+39.4	Exterior	129.2	−44.6

* Gage replaced and collected data was satisfactory. New gage model shown.
** Thermistor does not provide readings. Strain measurements only. Never replaced.
‡ Thermistor not operational. Never replaced.
[@] Gage locations not consistent. Thermistors excluded from thermal gradient analysis.

Table 2.2: VWSG and thermistor labeling, locations, and connections (cont'd.)

Gage Label	Gage Type	Bridge	Location	Station	Girder	X (in)	Y (in)
VS07EEL1	EM-5	SB	7	221+39.4	Exterior	129.2	−44.6
VS07EBL3	EM-5	SB	7	221+39.4	Exterior	115.3	−129.3
VS07EBT3	SM-5A†	SB	7	221+39.4	Exterior	104.4	−128.8
VS07EBT4	EM-5	SB	7	221+39.4	Exterior	99.2	−131.5
VS07EBL2	EM-5	SB	7	221+39.4	Exterior	0.0	−131.8
TSEBA003	THT‡	SB	7	221+39.4	Exterior	0.0	−128.3
TSEBA002	THT	SB	7	221+39.4	Exterior	0.0	−130.8
TSEBA001	THT	SB	7	221+39.4	Exterior	0.0	−133.5
VS07EBT1	EM-5	SB	7	221+39.4	Exterior	−105.1	−129.3
VS07EBT2	EM-5	SB	7	221+39.4	Exterior	−104.5	−131.8
VS07EBL1	EM-5	SB	7	221+39.4	Exterior	−110.9	−128.8
TSEWC001	THT	SB	7	221+39.4	Exterior	−115.7	−123.3
TSEWB001	THT	SB	7	221+39.4	Exterior	−130.7	−80.3
TSEWB002	THT	SB	7	221+39.4	Exterior	−125.5	−81.0
TSEWB003	THT	SB	7	221+39.4	Exterior	−120.8	−81.8
VS07EWV1	EM-5	SB	7	221+39.4	Exterior	−129.4	−43.9
VS07EWA1	EM-5	SB	7	221+39.4	Exterior	−129.4	−43.9
VS07EWL1	EM-5	SB	7	221+39.4	Exterior	−129.4	−43.9
TSEWA001	THT	SB	7	221+39.4	Exterior	−136.0	−36.9
VS07ETL1	EM-5	SB	7	221+39.4	Exterior	−220.0	−6.2
TSETA001	THT	SB	7	221+39.4	Exterior	−149.0	−2.5
TSETA002	THT	SB	7	221+39.4	Exterior	−149.0	−4.0
TSETA003	THT	SB	7	221+39.4	Exterior	−149.0	−6.0
TSETA004	THT	SB	7	221+39.4	Exterior	−149.0	−7.2
TSETA005	THT	SB	7	221+39.4	Exterior	−149.0	−8.5
TSETA006	THT	SB	7	221+39.4	Exterior	−149.0	−10.2
VS07ETL2	EM-5	SB	7	221+39.4	Exterior	−131.0	−19.3
VS07ETL3	EM-5	SB	7	221+39.4	Exterior	−68.5	−6.0
TSETB001	THT	SB	7	221+39.4	Exterior	−18.0	−1.7
TSETB002	THT	SB	7	221+39.4	Exterior	−18.0	−3.3
TSETB003	THT	SB	7	221+39.4	Exterior	−18.0	−4.9
TSETB004	THT	SB	7	221+39.4	Exterior	−18.0	−6.5
TSETB005	THT	SB	7	221+39.4	Exterior	−18.0	−8.1
TSETB006	THT	SB	7	221+39.4	Exterior	−18.0	−9.8
VN08ETL1	EM-5	NB	8	223+86.81	Exterior	0.0	−8.5
VN08EBL1	EM-5	NB	8	223+87.41	Exterior	0.0	−291.4
VN08EWL1	EM-5	NB	8	223+87.41	Exterior	−99.9	−141.3
VN08ITL1	EM-5	NB	8	223+86.61	Interior	−2.0	−8.8
VN08IBL1	SM-5A†	NB	8	223+87.41	Interior	0.0	−291.4
VS08ITL1	EM-5	SB	8	223+75.4	Interior	−3.0	−6.3
VS08IBL1	EM-5	SB	8	223+75.4	Interior	0.0	−291.6
VS08ETL1	SM-5A*	SB	8	223+75.4	Exterior	−1.0	−5.5
VS08EEV1	EM-5	SB	8	223+75.4	Exterior	106.1	−144.9
VS08EEA1	EM-5	SB	8	223+75.4	Exterior	106.4	−143.3
VS08EEL1	EM-5	SB	8	223+75.4	Exterior	105.4	−147.9
VS08EBL2	EM-5	SB	8	223+75.4	Exterior	83.3	−287.9
VS08EBL1	EM-5	SB	8	223+75.4	Exterior	0.0	−291.4
VS08EWV1	EM-5	SB	8	223+75.4	Exterior	−106.2	−142.3
VS08EWA1	EM-5	SB	8	223+75.4	Exterior	−106.4	−141.3
VS08EWL1	EM-5	SB	8	223+75.4	Exterior	−105.5	−145.3
VN09ETL1	EM-5	NB	9	225+53.17	Exterior	0.0	−6.0
VN09EBL1	EM-5	NB	9	225+53.17	Exterior	0.0	−165.6
VN09EWL1	EM-5	NB	9	225+53.17	Exterior	−123.1	−63.1
VN09ITL1	EM-5	NB	9	225+53.17	Interior	0.0	−6.0
VN09IBL1	EM-5	NB	9	225+53.17	Interior	0.0	−165.6
VS09ITL1	EM-5	SB	9	225+35.61	Interior	−1.0	−6.0
VS09IBL1	EM-5	SB	9	225+35.61	Interior	0.0	−170.3
VS09ETL1	EM-5	SB	9	225+35.61	Exterior	0.0	−6.0

* Gage replaced and collected data was satisfactory. New gage model shown.
† Gage replaced but newly collected data was not satisfactory. New gage model shown.
‡ Thermistor not operational. Never replaced.

Table 2.2: VWSG and thermistor labeling, locations, and connections (cont'd.)

Gage Label	Gage Type	Bridge	Location	Station	Girder	X (in)	Y (in)
VS09EEL1	SM-5A*	SB	9	225+35.61	Exterior	117.6	−61.8
VS09EBL1	EM-5	SB	9	225+35.61	Exterior	0.0	−169.8
VN14ETL1	EM-5	NB	14	227+11.75	Exterior	0.0	−5.8
VN14EBL1	EM-5	NB	14	227+11.75	Exterior	−2.5	−68.8
VN14EML1	EM-5	NB	14	227+11.75	Exterior	−50.0	−32.1
VN14ITL1	SM-5A*	NB	14	227+11.75	Interior	0.0	−5.8
VN14IBL1	SM-5A*	NB	14	227+11.75	Interior	0.0	−72.1
VS14ITL1	EM-5	SB	14	227+08.9	Interior	−8.0	−5.8
VS14IBL1	EM-5	SB	14	227+08.9	Interior	0.0	−69.1
VS14ETL1	EM-5	SB	14	227+08.9	Exterior	−8.0	−5.8
VS14EML1	EM-5	SB	14	227+08.9	Exterior	0.0	−30.6
VS14EBL1	EM-5	SB	14	227+08.9	Exterior	0.0	−68.1
VN15ETL1	EM-5	NB	15	227+69.82	Exterior	0.0	−5.8
VN15EBL1	SM-5A*	NB	15	227+69.82	Exterior	0.0	−102.7
VN15EML1	EM-5	NB	15	227+69.82	Exterior	−54.5	−37.3
VN15ITL1	EM-5	NB	15	227+69.82	Interior	0.0	−5.8
VN15IBL1	EM-5	NB	15	227+69.82	Interior	0.0	−103.7
VS15ITL1	EM-5	SB	15	227+69.82	Interior	−8.0	−5.8
VS15IBL1	EM-5	SB	15	227+69.82	Interior	0.0	−102.1
VS15ETL1	EM-5	SB	15	227+69.82	Exterior	−8.0	−5.8
VS15EML1	SM-5A*	SB	15	227+69.82	Exterior	0.0	−35.1
VS15EBL1	EM-5	SB	15	227+69.82	Exterior	0.0	−102.1

* Gage replaced and collected data was satisfactory. New gage model shown.

Table 2.3: Channel configuration for CR10 data collection during construction

Location	Dates	CR 10 Channel	Gage Label
Midspan of Span 1 (Location 3)	6/20/2008 to 7/21/2008	1	VS03EBL2
		2	VS03EBT4
		3	VS03EBT3
		4	VS03EBL3
		5	VS03EEL1
		6	VS03EEV1
		7	VS03EEA1
		8	VS03ETT1
		9	VS03ETT2
		10	VS03ETL4
		11	VS03ETL3
		12	VS03ETT3
		13	VS03ETT4
		14	VS03EEV3
		15	VS03EEV2
		16	VS03ETL5
Midspan of Span 2 (Location 7)	7/11/2008 to 7/21/2008	1	VS07EWV1
		2	VS07EWA1
		3	VS07EWL1
		4	VS07EBL1
		5	VS07EBT1
		6	VS07EBT2
		7	TSEWA001
		8	TSEWB001
		9	TSEWB002
		10	TSEWB003
		11	TSEWC001
Midspan of Span 2 (Location 7)	7/22/2008 to 8/4/2008	1	VS07EBL2
		2	VS07EBT3
		3	VS07EBT4
		4	VS07EBL3
		5	VS07ETT1
		6	VS07ETL7
		7	VS07ETL6
		8	VS07ETT3
		9	VS07ETL8
		10	VS07ETL9
		11	VS07EEV1
		12	VS07EEA1
		13	VS07EEL1
		14	VS07EEV2
		15	VS07ETL5
		16	VS07EEV3
Near Pier 2, Span 1 (Location 4)	7/25/2008 to 8/4/2008	1	Unknown
		2	Unknown
		3	Unknown

Table 2.4: Linear potentiometer labeling and locations

Acquisition Node	Acquisition Channel	Serial Number	Sensor Name (Location)	Before Feb. 1, 2010*		After Feb. 1, 2010*	
				Recording Node	Recording Channel	Recording Node	Recording Channel
1	1	38060484	NB SP 4 Ext	1	1	1	1 / 3 **
1	2	38060489	NB SP 4 Int	1	2	1	2 / 4 **
1	3	38060486	NB SP 3 Ext	1	3	1	3 / 5 **
1	4	38060491	NB SP 3 Int	1	4	1	4 / 6 **
3	1	38060487	NB SP 1 Ext	3	1	3	1
3	2	38060490	NB SP 1 Int	3	2	3	2
4	1	38060482	SB SP 1 Ext	4	1	4	1
4	2	38060482	SB SP 1 Int	4	2	4	2
8	1	38060485	SB SP 4 Ext	8	1	8	1
8	2	38060488	SB SP 4 Int	8	2	8	2
8	3	38060481	SB SP 3 Ext	8	3	8	3
8	4	38060492	SB SP 3 Int	8	4	8	4

* Recording node and channel refer to the channel the data was assigned to upon preprocessing. On February 1, 2010, "virtual nodes" were added to separate the accelerometers from the strain gage and LP measurements on the same channels to better facilitate preprocessing.
** On February 5, 2013, recording channels for these sensors were changed from channels 1 through 4 to channels 3 through 6 as noted.

Table 3.1: MnDOT test results for superstructure concrete compressive strength

Age (days)	Bridge	Number of samples tested	Average f_c' (ksi)	Coefficient of variation
7	SB	30	5.75	7.4%
	NB	34	5.55	4.1%
	Average	**64**	**5.64**	**6.2%**
28	SB	33	7.57	8.0%
	NB	38	7.35	5.5%
	Average	**71**	**7.45**	**6.9%**
56	SB	4	7.19	5.3%
	NB	3	7.60	7.4%
	Average	**7**	**7.37**	**6.5%**

Table 3.2: UMN test results for superstructure concrete compressive strength and modulus of elasticity

Test Date	Age (days)	Sample	f_c' (ksi)	Modulus (ksi)	Average f_c' (ksi)	Coefficient of Variation f_c'	Average Modulus (ksi)
10/4/2008	56	1	7.07	N/A	7.12	5.8%	4450
		2	7.55	4710			
		3	6.74	4190			
11/10/2008	93	1	7.08	N/A	6.70	5.0%	4730
		2	6.59	5000			
		3	6.43	4450			
12/17/2008	130	1	6.41	N/A	6.24	3.0%	4190
		2	6.04	4450			
		3	6.28	3930			
6/5/2014	2116	1	7.92	N/A	8.00	10.4%	5450
		2	8.17	4870			
		3	8.34	5570			
		4	6.80	5890			
		5	9.23	5630			
		6	8.56	5640			
		7	6.81	5590			
		8	8.17	5210			

Table 3.3: Cemstone test results for superstructure concrete compressive strength and modulus of elasticity

Age (days)	Strength			Modulus of Elasticity		
	Number of samples tested	Average f_c' (ksi)	Coefficient of variation	Number of samples tested	Average Modulus (ksi)	Coefficient of variation
1	3	1.83	6.8%	0	N/A	N/A
3	5	4.13	3.8%	6	4060	6.9%
7	6	5.28	5.1%	6	4280	3.7%
20	2	6.62	2.5%	3	5010	7.0%
28	6	7.44	4.1%	6	5100	2.0%
56	4	8.41	4.3%	0	N/A	N/A
90	6	8.47	6.4%	5	5190	6.0%

Table 3.4: Superstructure concrete tensile strength measured by UMN

Sample	Sample Origin	Age (days)	Tensile Strength (psi)
1	SB Span 4	58	386
2	SB Span 4	58	328
3	SB Span 4	58	469
4	NB Span 4	59	474
5	NB Span 4	59	347
SB average tensile strength:			395 psi
NB average tensile strength:			410 psi

Table 3.5: Creep sample loading and unloading

Date	Frame	Samples	Age	Load Applied	Stress Applied	Notes
10/4/2008	1	C4SB1 C4SB2	56	24.0 kips	1.90 ksi	Only two of three DEMEC sides measured due to frame difficulties.
10/5/2008	2*	C4SB3 S4SB3	57	36.8 kips	2.92 ksi	Shrinkage cylinder S4SB3 replacing failed cylinder in Frame #2. Only two of three DEMEC sides measured due to frame difficulties.
10/31/2008	1	C4SB1 C4SB2	83	Unloaded	Unloaded	Frame #1 unloaded because of significant bending of cylinders.
11/10/2008	4*	C4SB5 C4SB6	93	24.0 kips	1.90 ksi	All three DEMEC sides measured.
12/17/2008	1*	C4SB1 C4SB2	130	24.0 kips	1.90 ksi	Frame #1 reloaded at 130 days. All three DEMEC sides now measured.
12/17/2008	3*	C4SB7 C4SB8	130	24.0 kips	1.90 ksi	All three DEMEC sides measured.
1/19/2010	2	C4SB3 S4SB3	528	Unloaded	Unloaded	Specimen cracked and spalled during loading, subsequently unloaded.

* Measured data presented from these load applications.

Table 3.6: Summary of coefficient of thermal expansion using UMN laboratory specimens

Mix	Average CTE (με/°F)	Coefficient of Variation (%)
Superstructure (nominal strength = 6500 psi)	5.73	6.28%
Pier (nominal strength = 4000 psi)	4.85	3.51%

Table 3.7: Averaged coefficient of thermal expansion by location using VWSG data

Location	Average CTE (με/°F)
SB Loc 3, Midspan of Span 1	5.42
SB Loc 7, Midspan of Span 2	5.40
SB Loc 9, Midspan of Span 3	5.51
NB Loc 3, Midspan of Span 1	5.50
NB Loc 7, Midspan of Span 2	5.54
NB Loc 9, Midspan of Span 3	5.45

Table 3.8: Average superstructure coefficient of thermal expansion using LP data

Structure	Average CTE (με/°F)
Southbound	5.19
Northbound	5.29

Table 3.9: Summary of concrete coefficient of thermal expansion

Mix	Average CTE (με/°F)
Superstructure (nominal strength = 6500 psi)	**5.48**
- Laboratory VW strain gage	5.72
- In situ VW strain gage	5.47*
- In situ linear potentiometer	5.25*
Pier (nominal strength = 4000 psi)	**4.85**

* Results revised from French et al. (2012), for which the CTE measured by the in situ VWSG data and in situ LP data were equal to 5.46 με/°F and 5.60 με/°F, respectively.

Table 4.1: Mix design for superstructure and pier concrete

	Superstructure Concrete	Pier Concrete
Mix Number	ITF 6136	ITF 4136
Water*	260	245
Cement*	570	82
Fly Ash*	145	98
Silica Fume*	28	0
Slag*	0	365
Fine Aggregate*	1207	1372
Coarse Aggregate*	1650	1730

* All values in pounds per cubic yard.

Table 4.2: Volume-to-surface and reinforcement ratios for concrete elements in Span 1

Part*	Elements	V/S (in)	ρ_x (Transverse)	ρ_y (Vertical)	ρ_z (Longitudinal)
Abutment 1 Diaphragm, Section A to B	Top	20.36	0.0032	0.0100	0.0030
	Bottom	20.92	0.0100	0.0100	0.0030
Span 1, Section B to L	Deck	8.87	0.0032	0.0002	0.0025
	Web	8.00	N/A	0.0138	0.0043
	Bottom	5.13	0.0121	0.0015	0.0072
Span 1, Section L to M	Deck	8.87	0.0032	0.0002	0.0025
	Web	8.00	N/A	0.0138	0.0043
	Bottom	5.76	0.0067	0.0015	0.0059
Span 1, Section M to N	Deck	8.87	0.0032	0.0002	0.0025
	Web	8.00	N/A	0.0138	0.0043
	Bottom	7.44	0.0051	0.0015	0.0046
Span 1, Section N to P	Deck	8.87	0.0032	0.0002	0.0025
	Web	8.00	N/A	0.0138	0.0043
	Bottom	9.50	0.0039	0.0015	0.0035
Span 1, Section P to Q	Deck	8.87	0.0032	0.0002	0.0025
	Web	8.00	N/A	0.0138	0.0043
	Bottom	11.59	0.0030	0.0015	0.0027
Span 1, Section Q to R	Deck	8.87	0.0032	0.0002	0.0025
	Web	8.00	N/A	0.0138	0.0043
	Bottom	13.66	0.0024	0.0015	0.0021
Span 1, Section R to S	Deck	8.87	0.0032	0.0002	0.0025
	Web	8.00	N/A	0.0138	0.0043
	Bottom	15.65	0.0020	0.0015	0.0018
Span 1, Section S to T	Deck	8.87	0.0032	0.0002	0.0025
	Web	8.00	N/A	0.0138	0.0043
	Bottom	17.70	0.0017	0.0015	0.0015
Span 1, Section T to U	Deck	8.87	0.0032	0.0002	0.0025
	Web	8.00	N/A	0.0138	0.0043
	Bottom	19.75	0.0014	0.0015	0.0013
Span 1, Section U to V	Deck	8.87	0.0032	0.0002	0.0025
	Web	8.00	N/A	0.0138	0.0043
	Bottom	20.88	0.0013	0.0015	0.0011
Pier 2 Diaphragm, Section V to X	All	35.94	0.0030	0.0030	0.0030
Span 1, Section X to Y	Deck	8.87	0.0032	0.0002	0.0025
	Web	8.00	N/A	0.0138	0.0043
	Bottom	20.88	0.0013	0.0015	0.0011

* Section letters correspond to section designations in as-built construction documents (Minnesota Department of Transportation, 2008)

Table 4.3: Volume-to-surface and reinforcement ratios for concrete elements in Span 2

Part*	Elements	V/S (in)	ρ_x (Transverse)	ρ_y (Vertical)	ρ_z (Longitudinal)
Span 2, Segment 1	Deck	8.87	0.0032	0.0002	0.0025
	Web	8.00	N/A	0.0138	0.0043
	Bottom	19.75	0.0014	0.0015	0.0013
Span 2, Segment 2	Deck	8.87	0.0032	0.0002	0.0025
	Web	8.00	N/A	0.0138	0.0043
	Bottom	17.71	0.0017	0.0015	0.0015
Span 2, Segment 3	Deck	8.87	0.0032	0.0002	0.0025
	Web	8.00	N/A	0.0138	0.0043
	Bottom	15.66	0.0020	0.0015	0.0018
Span 2, Segment 4	Deck	8.87	0.0032	0.0002	0.0025
	Web	8.00	N/A	0.0138	0.0043
	Bottom	13.66	0.0024	0.0015	0.0021
Span 2, Segment 5	Deck	8.87	0.0032	0.0002	0.0025
	Web	8.00	N/A	0.0138	0.0043
	Bottom	11.58	0.0030	0.0015	0.0026
Span 2, Segment 6	Deck	8.87	0.0032	0.0002	0.0025
	Web	8.00	N/A	0.0138	0.0043
	Bottom	9.48	0.0058	0.0015	0.0034
Span 2, Segment 7	Deck	8.87	0.0032	0.0002	0.0025
	Web	8.00	N/A	0.0138	0.0043
	Bottom	7.69	0.0076	0.0015	0.0045
Span 2, Segment 8	Deck	8.87	0.0032	0.0002	0.0025
	Web	8.00	N/A	0.0138	0.0043
	Bottom	6.34	0.0098	0.0015	0.0058
Span 2, Segment 9	Deck	8.87	0.0032	0.0002	0.0025
	Web	8.00	N/A	0.0138	0.0043
	Bottom	5.70	0.0120	0.0015	0.0071
Span 2, Segment 10	Deck	8.87	0.0032	0.0002	0.0025
	Web	8.00	N/A	0.0138	0.0043
	Bottom	5.63	0.0128	0.0015	0.0076
Span 2, Segment 11	Deck	8.87	0.0032	0.0002	0.0025
	Web	8.00	N/A	0.0138	0.0043
	Bottom	5.63	0.0128	0.0015	0.0076
Span 2, Segment 12	Deck	8.87	0.0032	0.0002	0.0025
	Web	8.00	N/A	0.0138	0.0043
	Bottom	5.63	0.0128	0.0015	0.0076
Span 2, Segment 13	Deck	8.87	0.0032	0.0002	0.0025
	Web	8.00	N/A	0.0138	0.0043
	Bottom	5.63	0.0128	0.0015	0.0076
Span 2, Segment 14	Deck	8.87	0.0032	0.0002	0.0025
	Web	8.00	N/A	0.0138	0.0043
	Bottom	5.63	0.0128	0.0015	0.0076
Span 2, Segment 15	Deck	8.87	0.0032	0.0002	0.0025
	Web	8.00	N/A	0.0138	0.0043
	Bottom	5.63	0.0128	0.0015	0.0076
Span 2, Closure	Deck	8.87	0.0032	0.0002	0.0025
	Web	8.00	N/A	0.0138	0.0043
	Bottom	5.63	0.0128	0.0015	0.0076

* Segment numbers correspond to segment designations in as-built construction documents (Minnesota Department of Transportation, 2008). Segment 1 always nearest piers, while Segment 15 adjacent to closure pour.

Table 4.4: Volume-to-surface and reinforcement ratios for concrete elements in Span 3

Part*	Elements	V/S (in)	ρ_x (Transverse)	ρ_y (Vertical)	ρ_z (Longitudinal)
Span 3, Section A to B	Deck	8.87	0.0032	0.0002	0.0025
	Web	8.00	N/A	0.0138	0.0043
	Bottom	20.88	0.0013	0.0015	0.0011
Pier 3 Diaphragm, Section B to D	All	35.94	0.0030	0.0030	0.0030
Span 3, Section D to E	Deck	8.87	0.0032	0.0002	0.0025
	Web	12.00	N/A	0.0073	0.0028
	Bottom	22.87	0.0013	0.0015	0.0011
Span 3, Section E to F	Deck	8.87	0.0032	0.0002	0.0025
	Web	12.00	N/A	0.0073	0.0028
	Bottom	21.63	0.0014	0.0015	0.0012
Span 3, Section F to G	Deck	8.87	0.0032	0.0002	0.0025
	Web	12.00	N/A	0.0073	0.0028
	Bottom	20.01	0.0015	0.0015	0.0014
Span 3, Section G to H	Deck	8.87	0.0032	0.0002	0.0025
	Web	12.00	N/A	0.0073	0.0028
	Bottom	18.34	0.0018	0.0015	0.0016
Span 3, Section H to J	Deck	8.87	0.0032	0.0002	0.0025
	Web	12.00	N/A	0.0073	0.0028
	Bottom	16.64	0.0020	0.0015	0.0018
Span 3, Section J to K	Deck	8.87	0.0032	0.0002	0.0025
	Web	12.00	N/A	0.0073	0.0028
	Bottom	14.76	0.0024	0.0015	0.0021
Span 3, Section K to L	Deck	8.87	0.0032	0.0002	0.0025
	Web	12.00	N/A	0.0073	0.0028
	Bottom	12.74	0.0029	0.0015	0.0026
Span 3, Section L to M	Deck	8.87	0.0032	0.0002	0.0025
	Web	12.00	N/A	0.0073	0.0028
	Bottom	10.40	0.0055	0.0015	0.0033
Span 3, Section M to N	Deck	8.87	0.0032	0.0002	0.0025
	Web	12.00	N/A	0.0073	0.0028
	Bottom	8.69	0.0070	0.0015	0.0042
Span 3, Section N to P	Deck	8.87	0.0032	0.0002	0.0025
	Web	12.00	N/A	0.0073	0.0028
	Bottom	8.16	0.0087	0.0015	0.0052
Span 3, Section P to V	Deck	8.87	0.0032	0.0002	0.0025
	Web	12.00	N/A	0.0073	0.0028
	Bottom	8.00	0.0096	0.0015	0.0057
Span 3, Pier 4 Diaphragm, Section V to W	Top	20.36	0.0032	0.0100	0.0030
	Bottom	20.92	0.0100	0.0100	0.0030

* Section letters correspond to section designations in as-built construction documents (Minnesota Department of Transportation, 2008)

Table 4.5: Volume-to-surface and reinforcement ratios for concrete elements in piers and barrier rails

Part	Elements	V/S (in)	ρ_x (Transverse)	ρ_y (Vertical)	ρ_z (Longitudinal)
Piers	All	50.00	0.0075	0.0075	0.0075
Rail	All	5.27	0.0050	0.0050	0.0050

Table 4.6: Coefficients for increase in concrete strength with time (ACI 209R-92, Table 2.2.1)

Type of Curing	Cement Type	*a*	β
Moist cured	I	4.0	0.85
	III	2.3	0.92
Steam cured	I	1.0	0.95
	III	0.7	0.98

Table 4.7: Ultimate shrinkage correction for duration of curing (ACI 209R-92, Table 2.5.3)

Cure Duration (days)	Shrinkage Factor γ_{cp}
1	1.2
3	1.1
7	1.0
14	0.93
28	0.86
90	0.75

Table 4.8: Summary of model inputs required for time-dependent behavior of superstructure concrete

Parameter	Description	ACI-209	B3	CEB 1978	CEB 1990	GL2000	AASHTO
$(f_c)_{28}$	28-day mean strength	7.45 ksi	7.45 ksi	7.45 ksi	7.45 ksi	7.45 ksi	7.45 ksi
$(f_c)_\infty$	Maximum concrete strength	--	--	9.26 ksi	--	--	--
$(E_c)_{28}$	28-day modulus	4860 ksi	4920 ksi	5120 ksi	5380 ksi	4980 ksi	4890 ksi
Cement type	Type of cement	Type III	Type III	--	--	Type I	Type III
Curing	Type of curing	Moist cured	Moist cured	--	--	--	Moist-cured
t_c	Curing duration	4 days (precast) 7 days (CIP)	4 days (precast) 7 days (CIP)	4 days (precast) 7 days (CIP)	4 days (precast) 7 days (CIP)	4 days (precast) 7 days (CIP)	4 days (precast) 7 days (CIP)
H	Relative humidity	0.641	0.641	0.641	0.641	0.641	0.641
s	Slump	7.3 in.	--	--	--	--	--
κ	Fine aggregate ratio	0.423	--	--	--	--	--
c	Total cement content	743 lbs/yd^3	743 lbs/yd^3	--	--	--	--
α	Air content	0.069	--	--	--	--	--
w	Total water content	--	260 lbs/yd^3	--	--	--	--
w/c	Water-cement ratio	--	0.35	--	--	--	--
a/c	Aggregate-cement ratio	--	3.85	--	--	--	--
q	Rate of hardening factor (CEB 1978)	--	--	2.4	--	--	--
p	Rate of hardening factor (CEB 1990)	--	--	--	0.25	--	--
τ	Age adjustment factor for cement type	--	--	--	0	--	--
β_{sc}	Shrinkage cement type factor (CEB1990)	--	--	--	5	--	--
K	Shrinkage cement type factor (GL2000)	--	--	--	--	1	--

Table 4.9: Summary of model inputs required for time-dependent behavior of pier and barrier rail concrete

Parameters	Description	ACI-209	B3	CEB 1978	CEB 1990	GL2000	AASHTO
$(f_c)_{28}$	28-day mean strength	4.94 ksi	4.94 ksi	4.94 ksi	4.94 ksi	4.94 ksi	4.94 ksi
$(f_c)_\infty$	Maximum concrete strength	--	--	7.18 ksi	--	--	--
$(E_c)_{28}$	28-day modulus	3980 ksi	4020 ksi	4460 ksi	4690 ksi	4150 ksi	3980 ksi
Cement type	Type of cement	Type I	Type I	--	--	Type I	Type I
Curing	Type of curing	Moist cured	Moist cured	--	--	--	Moist-cured
t_c	Curing duration	7 days	7 days	7 days	7 days	7 days	7 days
H	Relative humidity	0.641	0.641	0.641	0.641	0.641	0.641
s	Slump	1.8 in.	--	--	--	--	--
κ	Fine aggregate ratio	0.442	--	--	--	--	--
c	Total cement content	545 lbs/yd^3	545 lbs/yd^3	--	--	--	--
α	Air content	0.064	--	--	--	--	--
w	Total water content	--	245 lbs/yd^3	--	--	--	--
w/c	Water-cement ratio	--	0.45	--	--	--	--
a/c	Aggregate-cement ratio	--	5.7	--	--	--	--
q	Rate of hardening factor (CEB 1978)	--	--	1	--	--	--
p	Rate of hardening factor (CEB 1990)	--	--	--	0.25	--	--
τ	Age adjustment factor for cement type	--	--	--	0	--	--
β_{sc}	Shrinkage cement type factor (CEB1990)	--	--	--	5	--	--
K	Shrinkage cement type factor (GL2000)	--	--	--	--	1	--

Table 4.10: Humidity dependent coefficients φ_{f1}, λ, and ε_{s1} from 1978 CEB/FIP Model Code

Environment	Relative Humidity	φ_{f1}	λ	ε_{s1}
Water	--	0.8	30	+0.00010
Very damp atmosphere	90%	1	5	−0.00013
Outside in general	70%	2	1.5	−0.00032
Very dry atmosphere	40%	3	1	−0.00052

Table 6.1: Analysis Steps for Erection Procedure

Step	Step Name	Step Start Date	Step End Date	Step Duration	Step Start Time	Step End Time	Notes
0	Prep	N/A	N/A	N/A	N/A	N/A	"Model Change - Remove" all necessary items, set initial conditions
1	Span1	5/25/2008	5/25/2008	0.001	0.000	0.001	Span 1 only, shored - Apply bottom tendon stresses in Span 1
2	C1	5/25/2008	5/28/2008	2.999	0.001	3.000	Creep time, no new loads
3	Span1D	5/28/2008	5/28/2008	0.001	3.000	3.001	Apply draped post-tensioning in Span 1
4	C2	5/28/2008	5/29/2008	0.999	3.001	4.000	Creep time, no new loads
5	SB21	5/29/2008	5/29/2008	0.001	4.000	4.001	Add segment SB2-1, tendons 2-C1 and 2-C2
6	C3	5/29/2008	6/3/2008	4.999	4.001	9.000	Creep time, no new loads
7	SB22	6/3/2008	6/3/2008	0.001	9.000	9.001	Add segment SB2-2, tendon 2-C3
8	C4	6/3/2008	6/7/2008	3.999	9.001	13.000	Creep time, no new loads
9	SB23	6/7/2008	6/7/2008	0.001	13.000	13.001	Add segment SB2-3, tendons 2-C4 and 2-C5
10	C5	6/7/2008	6/9/2008	1.999	13.001	15.000	Creep time, no new loads
11	SB24	6/9/2008	6/9/2008	0.001	15.000	15.001	Add segment SB2-4, tendons 2-C6 and 2-C7
12	C6	6/9/2008	6/11/2008	1.999	15.001	17.000	Creep time, no new loads
13	SB25	6/11/2008	6/11/2008	0.001	17.000	17.001	Add segment SB2-5, tendons 2-C8 and 2-C9
14	C7	6/11/2008	6/13/2008	1.999	17.001	19.000	Creep time, no new loads
15	SB26	6/13/2008	6/13/2008	0.001	19.000	19.001	Add segment SB2-6, tendons 2-C10 and 2-C11; add Span 3 and Pier 3
16	C8	6/13/2008	6/14/2008	0.999	19.001	20.000	Creep time, no new loads
17	SB27	6/14/2008	6/14/2008	0.001	20.000	20.001	Add segment SB2-7, tendons 2-C12 and 2-C13
18	C9	6/14/2008	6/16/2008	1.999	20.001	22.000	Creep time, no new loads
14	SB28-31	6/16/2008	6/16/2008	0.001	22.000	22.001	Add segments SB2-8 and SB3-1, tendons 2-C14, 2-C15, 3-C1 and 3-C2
20	C10	6/16/2008	6/17/2008	0.999	22.001	23.000	Creep time, no new loads
21	SB29	6/17/2008	6/17/2008	0.001	23.000	23.001	Add segment SB2-9, tendons 2-C16 and 2-C17
22	C11	6/17/2008	6/19/2008	1.999	23.001	25.000	Creep time, no new loads
23	SB210	6/19/2008	6/19/2008	0.001	25.000	25.001	Add segment SB2-10, tendons 2-C18 and 2-C19 - Apply post-tensioning in Span 3
24	C12	6/19/2008	6/21/2008	1.999	25.001	27.000	Creep time, no new loads
25	SB32	6/21/2008	6/21/2008	0.001	27.000	27.001	Add segment SB3-2, tendon 3-C3
26	C13	6/21/2008	6/22/2008	0.999	27.001	28.000	Creep time, no new loads
27	SB33	6/22/2008	6/22/2008	0.001	28.000	28.001	Add segment SB3-3, tendon 3-C4
28	C14	6/22/2008	6/23/2008	0.999	28.001	29.000	Creep time, no new loads
29	SB34	6/23/2008	6/23/2008	0.001	29.000	29.001	Add segment SB3-4, tendons 3-C5 and 3-C6
30	C15	6/23/2008	6/24/2008	0.999	29.001	30.000	Creep time, no new loads
31	SB35	6/24/2008	6/24/2008	0.001	30.000	30.001	Add segment SB3-5, tendons 3-C7 and 3-C8
32	C16	6/24/2008	6/25/2008	0.999	30.001	31.000	Creep time, no new loads
33	SB36	6/25/2008	6/25/2008	0.001	31.000	31.001	Add segment SB3-6, tendons 3-C9 and 3-C10
34	C17	6/25/2008	6/28/2008	2.999	31.001	34.000	Creep time, no new loads
35	SB211	6/28/2008	6/28/2008	0.001	34.000	34.001	Add segment SB2-11, tendons 2-C20 and 2-C21
36	C18	6/28/2008	6/29/2008	0.999	34.001	35.000	Creep time, no new loads
37	SB37	6/29/2008	6/29/2008	0.001	35.000	35.001	Add segment SB3-7, tendons 3-C11 and 3-C12
38	C19	6/29/2008	7/1/2008	1.999	35.001	37.000	Creep time, no new loads
39	SB38	7/1/2008	7/1/2008	0.001	37.000	37.001	Add segment SB3-8, tendons 3-C13 and 3-C14
40	C20	7/1/2008	7/4/2008	2.999	37.001	40.000	Creep time, no new loads
41	SB39	7/4/2008	7/4/2008	0.001	40.000	40.001	Add segment SB3-9, tendons 3-C15 and 3-C16
42	C21	7/4/2008	7/5/2008	0.999	40.001	41.000	Creep time, no new loads
43	SB310	7/5/2008	7/5/2008	0.001	41.000	41.001	Add segment SB3-10, tendons 3-C17 and 3-C18
44	C22	7/5/2008	7/6/2008	0.999	41.001	42.000	Creep time, no new loads
45	SB212-311	7/6/2008	7/6/2008	0.001	42.000	42.001	Add segments SB2-12 and SB3-11, tendons 2-C22, 2-C23, 3-C19, 3-C20
46	C23	7/6/2008	7/7/2008	0.999	42.001	43.000	Creep time, no new loads
47	SB213-312	7/7/2008	7/7/2008	0.001	43.000	43.001	Add segments SB2-13 and SB3-12, tendons 2-C24, 3-C21, 3-C22
48	C24	7/7/2008	7/8/2008	0.999	43.001	44.000	Creep time, no new loads
49	SB214-313	7/8/2008	7/8/2008	0.001	44.000	44.001	Add segments SB2-14 and SB3-13, tendons 2-C25, 3-C23; remove Span 1 shoring
50	C25	7/8/2008	7/9/2008	0.999	44.001	45.000	Creep time, no new loads
51	SB215-314	7/9/2008	7/9/2008	0.001	45.000	45.001	Add segments SB2-15 and SB3-14, tendons 2-C26, 3-C24; remove Span 3 shoring
52	C26	7/9/2008	7/10/2008	0.999	45.001	46.000	Creep time, no new loads
53	SB315	7/10/2008	7/10/2008	0.001	46.000	46.001	Add segment SB3-15, tendon 3-C25; aligned cantilevers
54	C27	7/10/2008	7/24/2008	13.999	46.001	60.000	Creep time, no new loads
55	Jack	7/24/2008	7/24/2008	0.001	60.000	60.001	Jack apart midspan with 1120 kips
56	C28	7/24/2008	7/25/2008	0.999	60.001	61.000	Creep time, no new loads
57	Closure	7/25/2008	7/25/2008	0.001	61.000	61.001	Place closure pour
58	Release	7/25/2008	7/25/2008	0.001	61.001	61.002	Release Jacks
59	C29	7/25/2008	7/27/2008	1.998	61.002	63.000	Creep time, no new loads
60	Strands	7/27/2008	7/27/2008	0.001	63.000	63.001	Apply Span 2 bottom and draped post-tensioning, remove alignment beams
61	C30	7/27/2008	8/5/2008	8.999	63.001	72.000	Creep time, no new loads
62	Barriers	8/5/2008	8/5/2008	0.001	72.000	72.001	Add barrier rails
63	TD	8/5/2008	…	…	72.001	…	Continued time-dependent analysis for completed structure

Table 6.2: Summary of post-tensioning stresses

Tendons	Average Specified Jacking Stress (ksi)	Modeled Stress after Anchorage* (ksi)
Top "cantilever" tendons	208	199
Span 1 bottom tendons	210	200
Span 2 bottom tendons	210	199
Span 3 bottom tendons	210	197
Span 1 draped tendons	190	188
Span 2 draped tendons	190	190
Span 3 draped tendons	190	188
Transverse tendons	187	180
Post-tensioning bars	127	121

* Includes friction and seating losses

Table 6.3: Approximation coefficients for creep terms $\beta_d(t-t_0)$ and $\beta_f(t)$ of 1978 CEB/FIP Model Code

Term	h (mm)	C_1	C_2	C_3	m
$\beta_d(t-t_0)$	N/A	0.3136	0.1856	0.5008	7.9369
$\beta_f(t)$	50	0.0684	0.6946	0.2370	25.01779
	100	0.1253	0.6582	0.2166	36.56954
	200	0.1811	0.5802	0.2387	53.1346
	400	0.2243	0.4869	0.2888	76.7857
	800	0.2521	0.3868	0.3612	110.3807
	1600	0.2388	0.2755	0.4857	120.1683

Table 6.4: Approximation coefficients for shrinkage term $\beta_s(t)$ of 1978 CEB/FIP Model Code

Term	h (mm)	m	n
$\beta_s(t)$	50	75.2786	0.4735
	100	116.5800	0.5935
	200	279.3839	0.6583
	400	505.1819	0.8058
	800	784.1180	1.1669
	1600	1161.4477	1.7198

Table 7.1: Fit parameters for Northbound Span 1 LP data using unadjusted time

Model	GL2000	CEB1990	AASHTO	ACI	Log Power
Sum of squared residuals (in.^{2})	91.9	93.0	250.5	118.0	87.5
Standard deviation of residual (in.)	0.066	0.066	0.109	0.075	0.064
α_1 – Temperature	−7.09E−02	−7.10E−02	−7.02E−02	−7.08E−02	−7.10E−02
α_2 – Temperature squared	−2.44E−04	−2.66E−04	−3.18E−04	−2.75E−04	−2.51E−04
α_3 – Gradient	1.41E+00	1.57E+00	1.75E+00	1.60E+00	1.46E+00

Table 7.2: Fit parameters for Northbound Span 3 LP data using unadjusted time

Model	GL2000	CEB1990	AASHTO	ACI	Log Power
Sum of squared residuals (in.^{2})	83.0	174.4	528.2	230.1	107.9
Standard deviation of residual (in.)	0.056	0.081	0.140	0.093	0.063
α_1 – Temperature	−7.02E−02	−7.06E−02	−7.07E−02	−7.07E−02	−7.04E−02
α_2 – Temperature squared	−2.62E−04	−2.81E−04	−3.16E−04	−2.86E−04	−2.67E−04
α_3 – Gradient	3.02E+00	3.12E+00	3.29E+00	3.15E+00	3.05E+00

Table 7.3: Fit parameters for Southbound Span 1 LP data using unadjusted time

Model	GL2000	CEB1990	AASHTO	ACI	Log Power
Sum of squared residuals (in.^{2})	39.9	57.2	166.8	77.2	45.2
Standard deviation of residual (in.)	0.045	0.054	0.092	0.063	0.048
α_1 – Temperature	−6.64E−02	−6.63E−02	−6.58E−02	−6.62E−02	−6.64E−02
α_2 – Temperature squared	−2.84E−04	−2.89E−04	−2.97E−04	−2.90E−04	−2.85E−04
α_3 – Gradient	1.62E+00	1.65E+00	1.64E+00	1.65E+00	1.63E+00

Table 7.4: Fit parameters for Southbound Span 3 LP data using unadjusted time

Model	GL2000	CEB1990	AASHTO	ACI	Log Power
Sum of squared residuals (in.^{2})	40.3	42.4	65.0	44.6	39.5
Standard deviation of residual (in.)	0.050	0.051	0.063	0.052	0.049
α_1 – Temperature	−7.19E−02	−7.12E−02	−7.06E−02	−7.11E−02	−7.17E−02
α_2 – Temperature squared	−2.64E−04	−3.09E−04	−3.64E−04	−3.16E−04	−2.78E−04
α_3 – Gradient	3.23E+00	3.30E+00	3.39E+00	3.31E+00	3.24E+00

Table 8.1: Load cases and corresponding multiple presence factors used for investigation of critical Service I and Service III vehicular live loading

Loading	Permit	LRT	HL-93 (by total loaded lanes)			
			1	2	3	4 or more
Permit + HL-93	1.20	N/A	1.20	1.00	0.85	0.75
Permit + HL-93 + LRT	1.00	1.00	1.20	1.00	0.85	0.75
Permit + LRT	1.20	1.00	N/A	N/A	N/A	N/A
Permit	1.20	N/A	N/A	N/A	N/A	N/A
HL-93	N/A	N/A	1.20	1.00	0.85	0.75
HL-93 + LRT	N/A	1.00	1.20	1.00	0.85	0.75

Table 8.2: Coefficients of variation of time-dependent prediction models

Coefficient of Variation (%) for Compliance					
Study	Time-Dependent Model				
	ACI-209	B3	1990 CEB/FIP MC	GL2000	GZ
Bažant and Li (2008)	43	27	31	30	42
Gardner (2004) - All parameters	30	27	29	22	N/A
Gardner (2004) - Design parameters	30	29	37	26	N/A

Coefficient of Variation (%) for Shrinkage					
Study	Time-Dependent Model				
	ACI-209	B3	1990 CEB/FIP MC	GL2000	GZ
Bažant and Li (2008)	42	29	47	31	44
Gardner (2004) - All parameters	41	20	25	19	N/A
Gardner (2004) - Design parameters	34	31	32	25	N/A

Table 9.1: Investigated temperature histories in finite element analysis

Temperature History Scenario	Uniform $T(t)$	Gradient $T_{grad}(t,y)$	Start Season (t = 0)
Constant	Constant: 293 K	None	N/A
Seasonal	Sinusoidal	None	Winter (min temp)
Winter Gradient	Constant: 293 K	Daily Gradients	Winter (min temp)
Winter Gradient Plus Seasonal	Sinusoidal	Daily Gradients	Winter (min temp)
Summer Gradient	Constant: 293 K	Daily Gradients	Summer (max temp)
Summer Gradient Plus Seasonal	Sinusoidal	Daily Gradients	Summer (max temp)
Year 1 Gradient	Constant: 293 K	During Year 1 Only	N/A
Year 2 Gradient	Constant: 293 K	During Year 2 Only	N/A

Figures

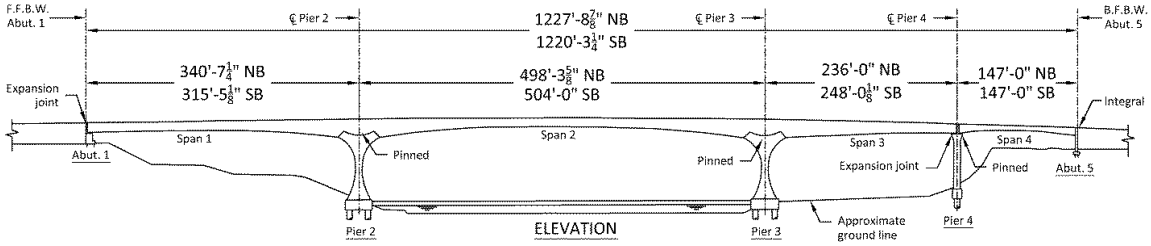

Figure 1.1: Elevation view of the St. Anthony Falls Bridge

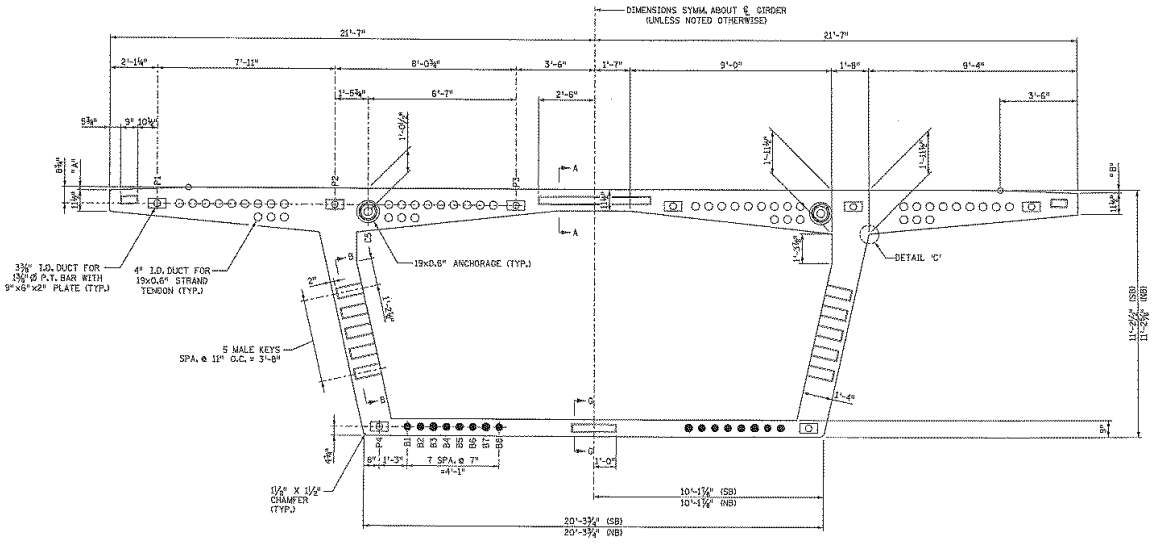

Figure 1.2: Cross section of the southbound bridge exterior box at midspan of Span 2 (other boxes similar)

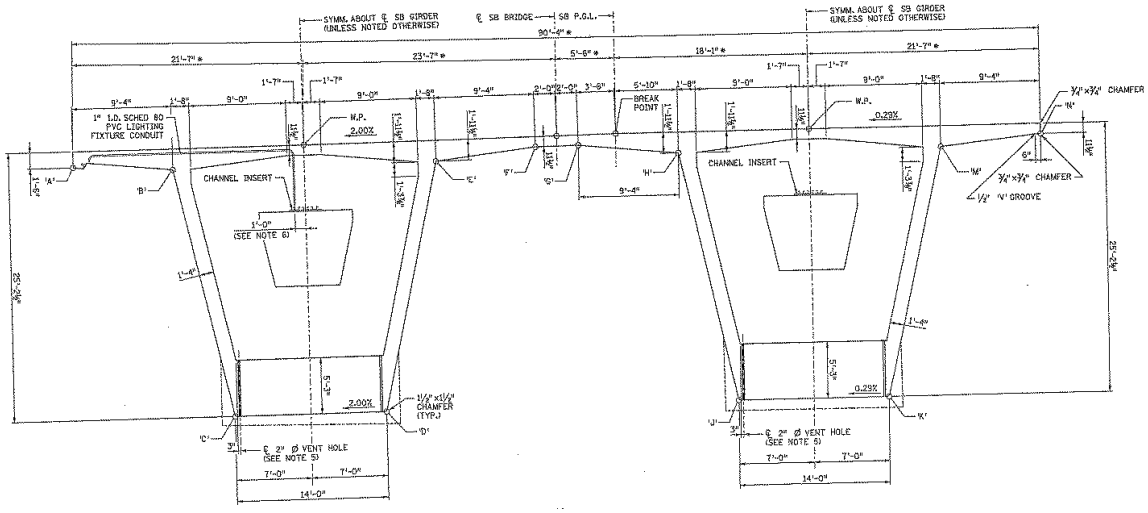

Figure 1.3: Cross section of Span 2 of the southbound bridge near Pier 2 (cross section near Pier 3 similar)

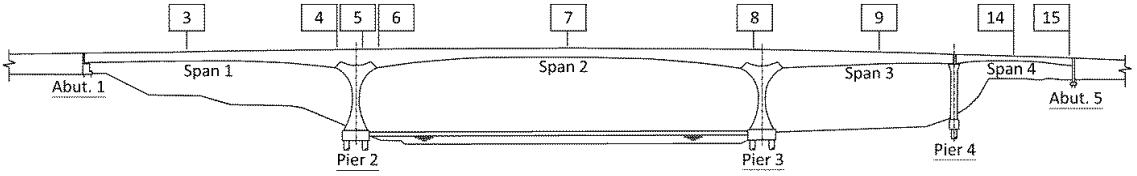

Figure 2.1: Elevation view of the St. Anthony Falls Bridge showing VWSG Locations 3, 4, 5, 6, 7, 8, 9, 14, and 15

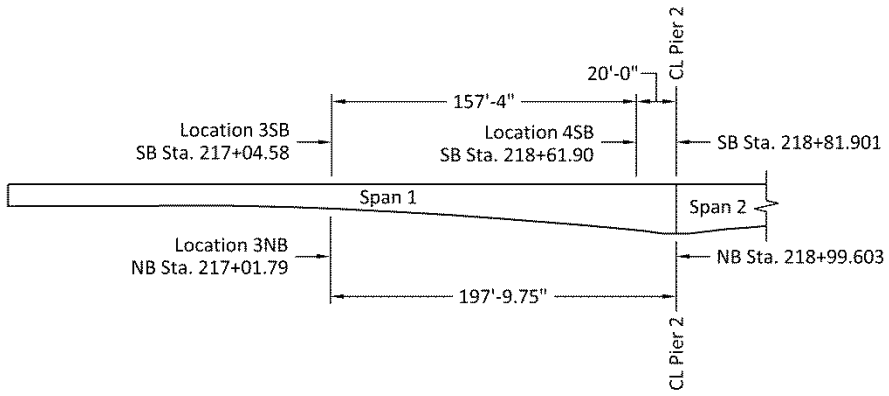

Figure 2.2: Elevation view of Span 1 of the adjacent bridges showing VWSG Locations 3 and 4

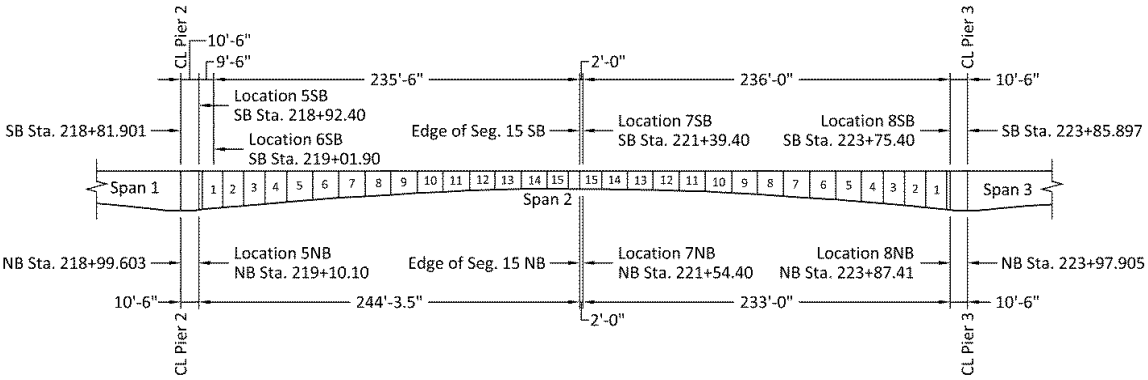

Figure 2.3: Elevation view of Span 2 of the adjacent bridges showing VWSG Locations 5, 6, 7, and 8

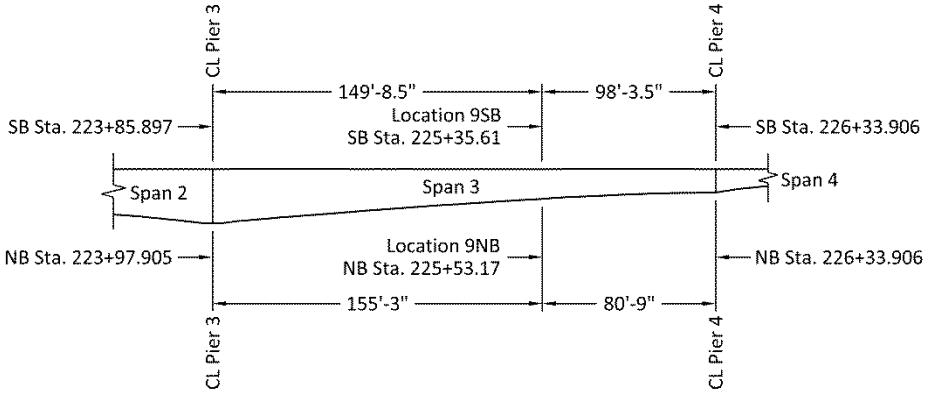

Figure 2.4: Elevation view of Span 3 of the adjacent bridges showing VWSG Location 9

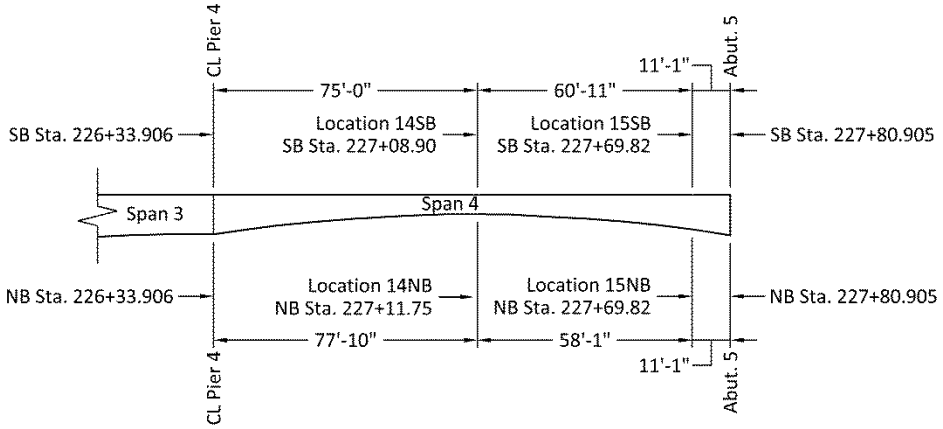

Figure 2.5: Elevation view of Span 4 of the adjacent bridges showing VWSG Locations 14 and 15

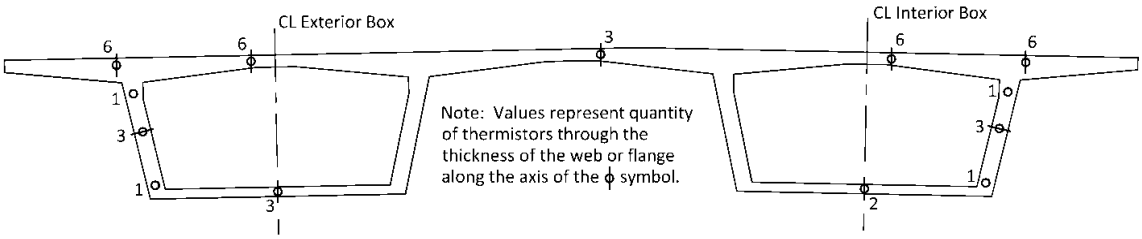

Figure 2.6: Thermistor layout near midspan of Span 2 (Location 7) on the southbound bridge looking upstation (i.e., north)

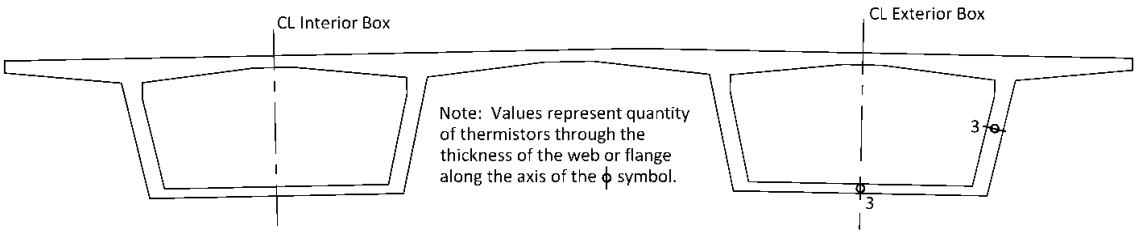

Figure 2.7: Thermistor layout near midspan of Span 2 (Location 7) on the northbound bridge looking upstation (i.e., north)

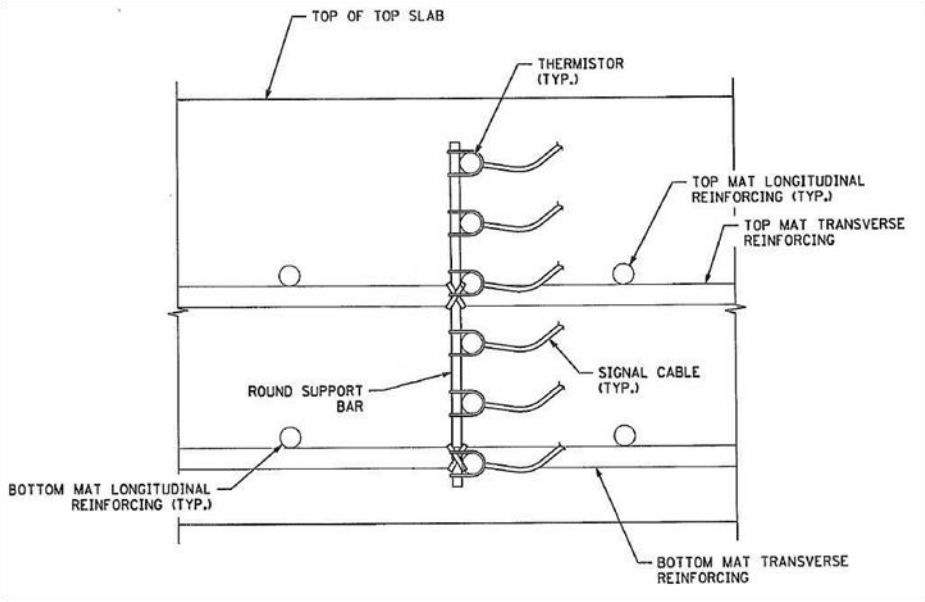

Figure 2.8: Typical thermistor installation for six thermistors in the top flange

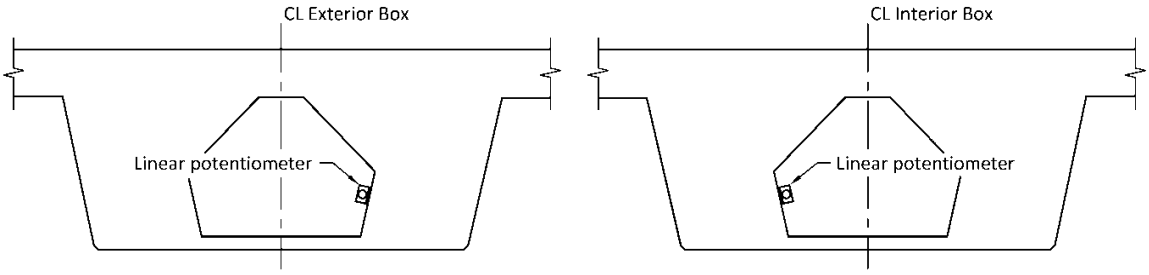

Figure 2.9: Linear potentiometer layout at the south end of Span 1 and the north end of Span 3 for the southbound bridge looking upstation (i.e., north). Span 1 and Span 3 of northbound bridge are similar, but exterior and interior box are switched.

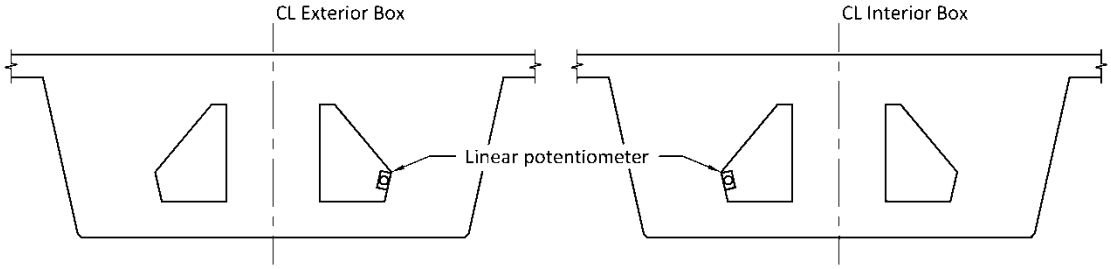

Figure 2.10: Linear potentiometer layout at the south end of Span 4 for the southbound bridge looking upstation (i.e., north)

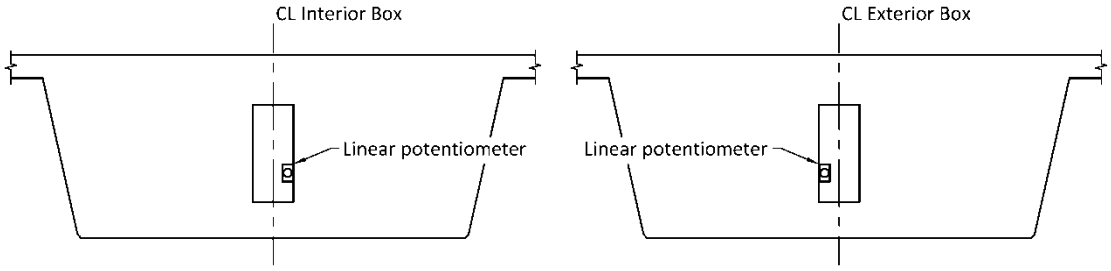

Figure 2.11: Linear potentiometer layout at the south end of Span 4 for the northbound bridge looking upstation (i.e., north)

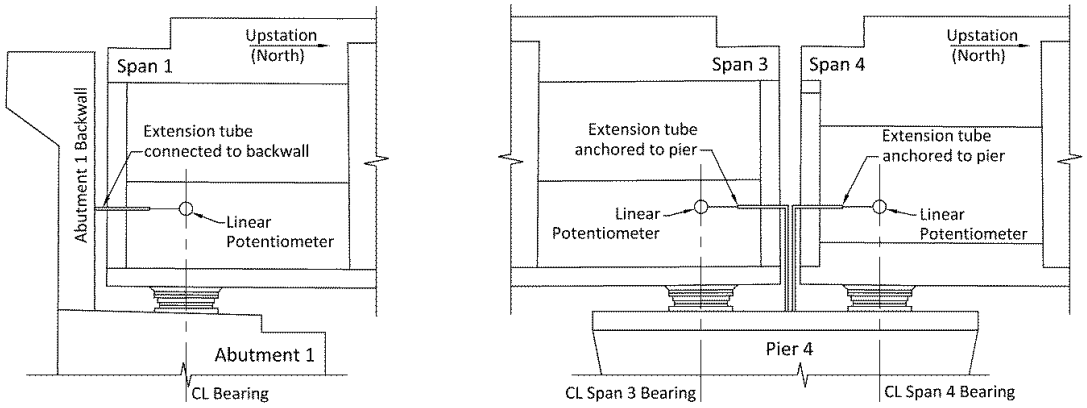

Figure 2.12: Typical linear potentiometer installations at Abutment 1 and Pier 4

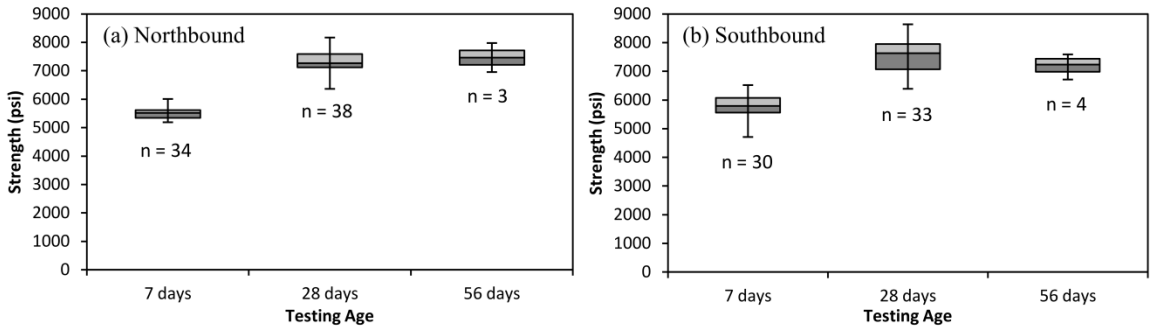

Figure 3.1: Box plots showing the minimum, maximum, first quartile, median, and third quartile of the MnDOT test results for superstructure concrete compressive strength

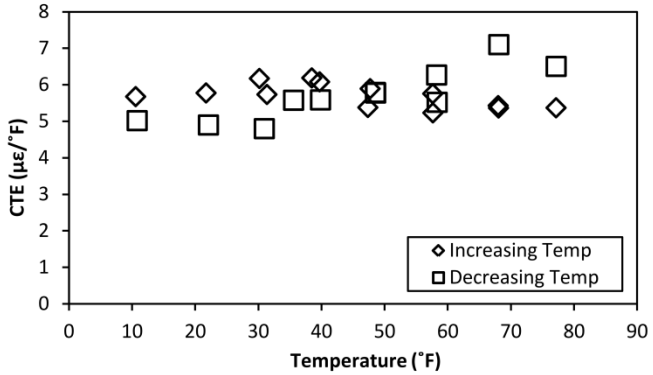

Figure 3.2: Incremental coefficient of thermal expansion for superstructure laboratory specimens plotted with respect to temperature

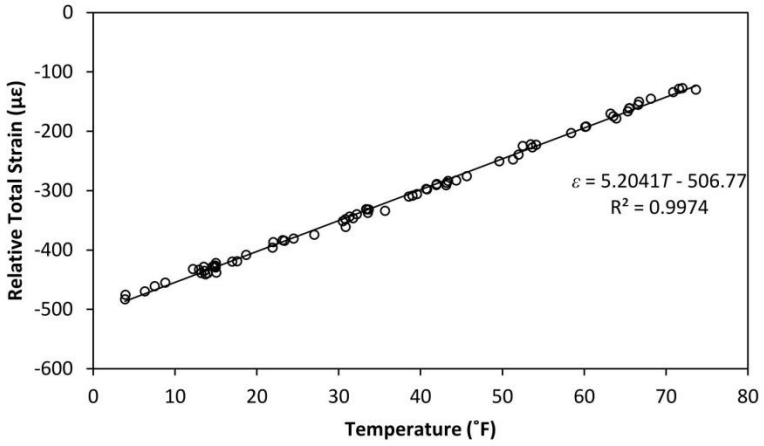

Figure 3.3: Gage VS03TEL2 change in total strain data plotted with respect to temperature from January 1, 2011 to June 30, 2011. Change in total strain was assumed zero at 6:00 AM on September 2, 2008.

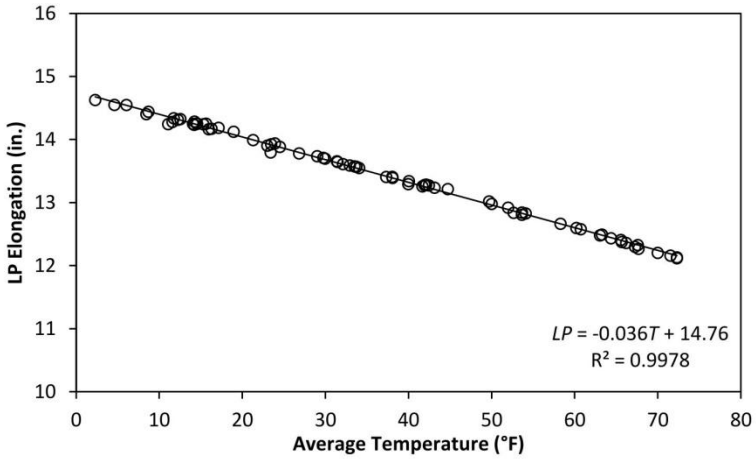

Figure 3.4: Linear potentiometer elongation from the exterior box of the southbound structure at Abutment 1 plotted with respect to temperature from January 1, 2011 until June 30, 2011

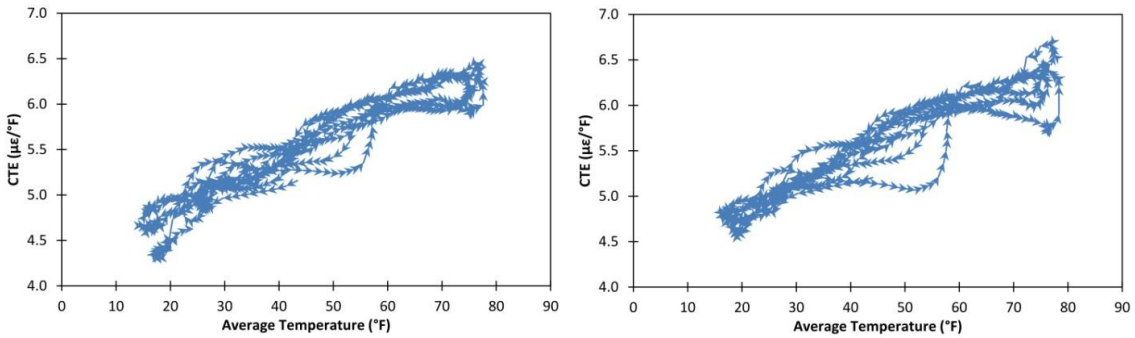

(a) SB Location 3 Vertical Gages (b) SB Location 7 Vertical Gages

Figure 3.5: Coefficient of thermal expansion values with respect to temperature computed from linear regression of VWSG data from September 1, 2008 until February 19, 2013

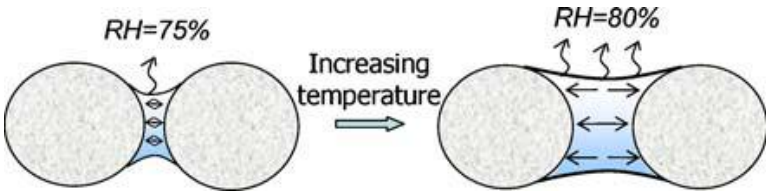

Figure 3.6: Expansion of concrete with temperature and associated changes on the adsorbed water and internal relative humidity (Grasley and Lange, 2007)

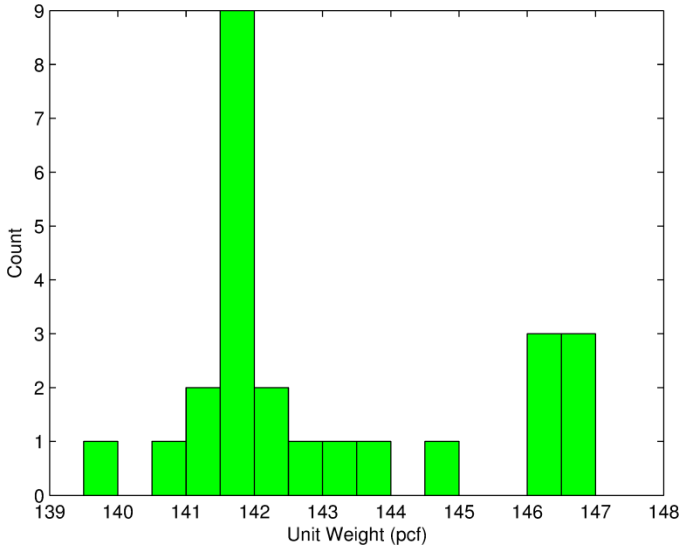

Figure 3.7: Histogram of concrete unit weights (n=25)

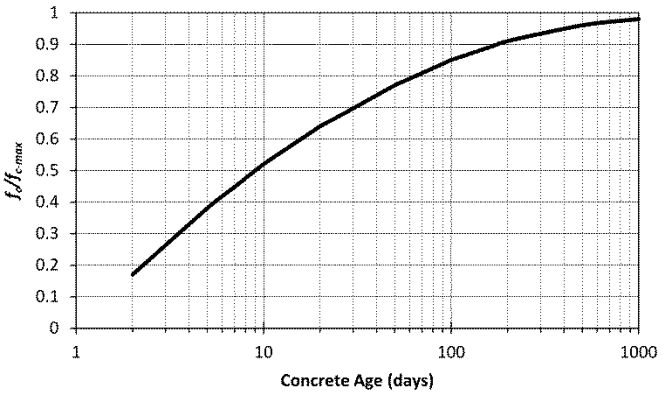

Figure 4.1: Time-dependent strength relation from 1978 CEB/FIP Model Code

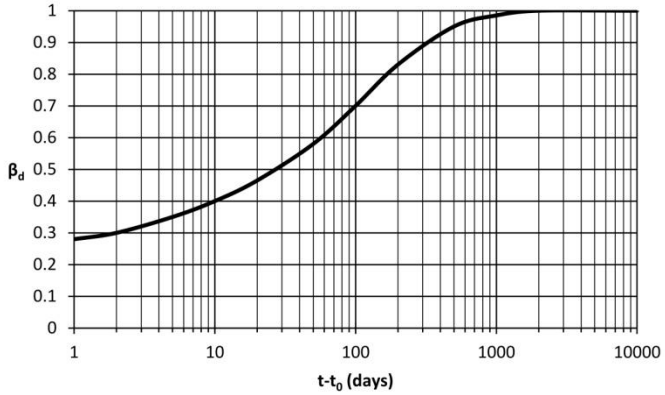

Figure 4.2: Recoverable deformation coefficient $\beta_d(t - t_0)$ from 1978 CEB/FIP Model Code

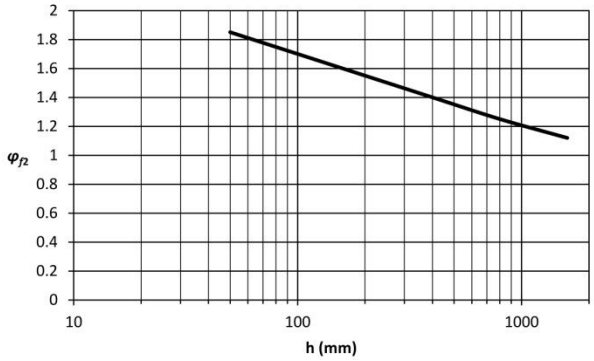

Figure 4.3: Shape-dependent creep flow coefficient φ_{f2} from 1978 CEB/FIP Model Code

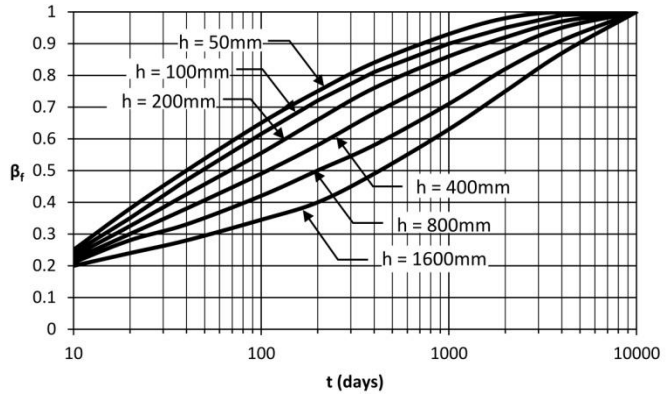

Figure 4.4: Unrecoverable deformation coefficient $\beta_f(t)$ from 1978 CEB/FIP Model Code

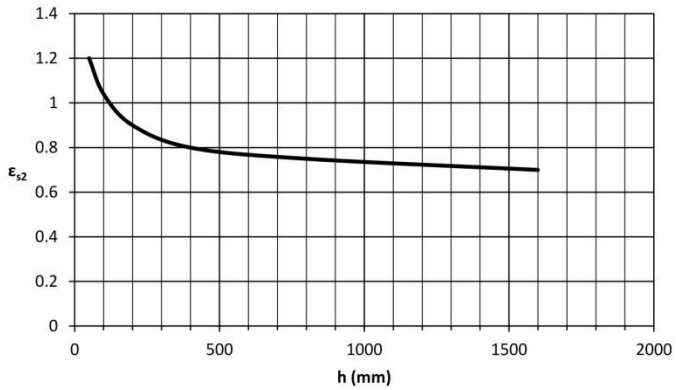

Figure 4.5: Shrinkage constant ε_{s2} from 1978 CEB/FIP Model Code

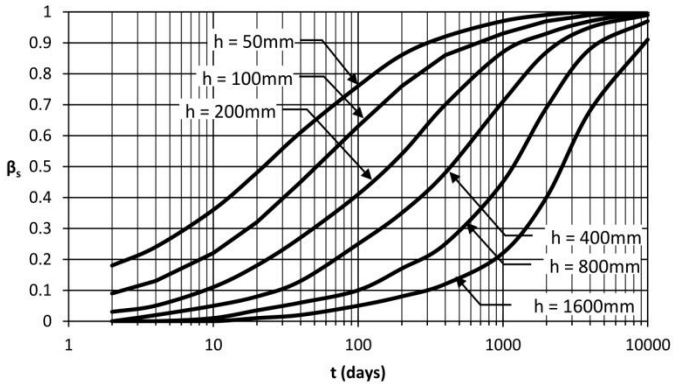

Figure 4.6: Shrinkage function $\beta_s(t)$ from 1978 CEB/FIP Model Code

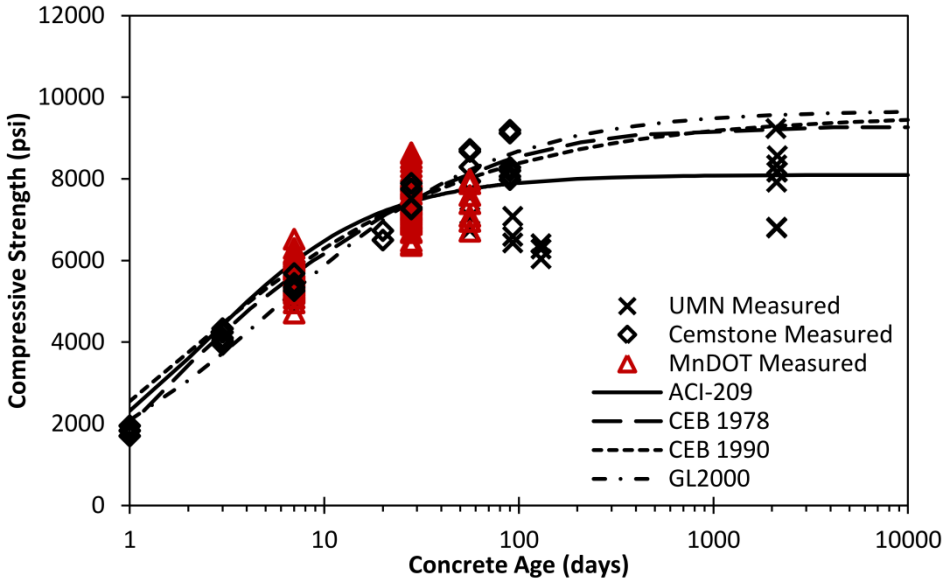

Figure 5.1: Modeled strength curves with time validated with respect to measured strength values for superstructure concrete

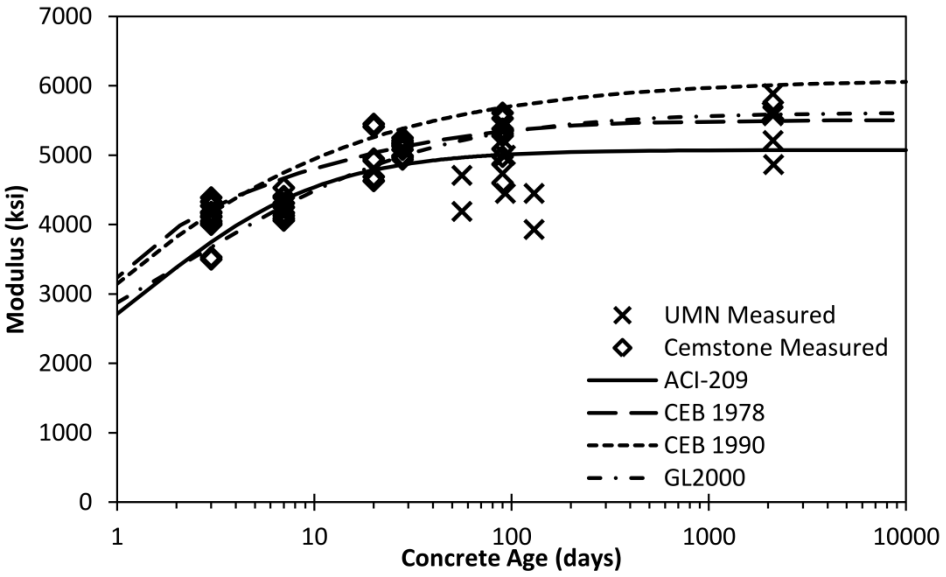

Figure 5.2: Modeled modulus with time validated with respect to measured modulus values for superstructure concrete

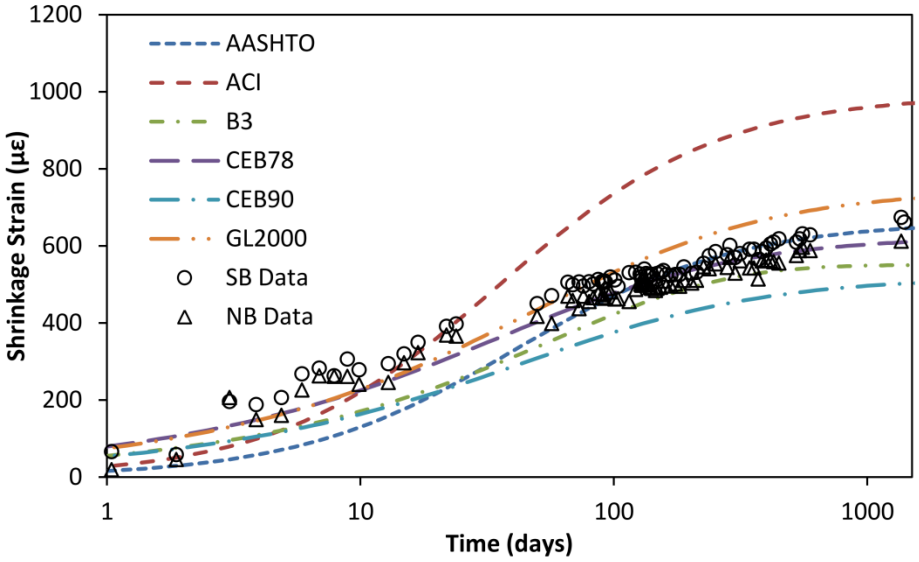

Figure 5.3: Southbound and northbound bridge average sample shrinkage strains compared to literature shrinkage models

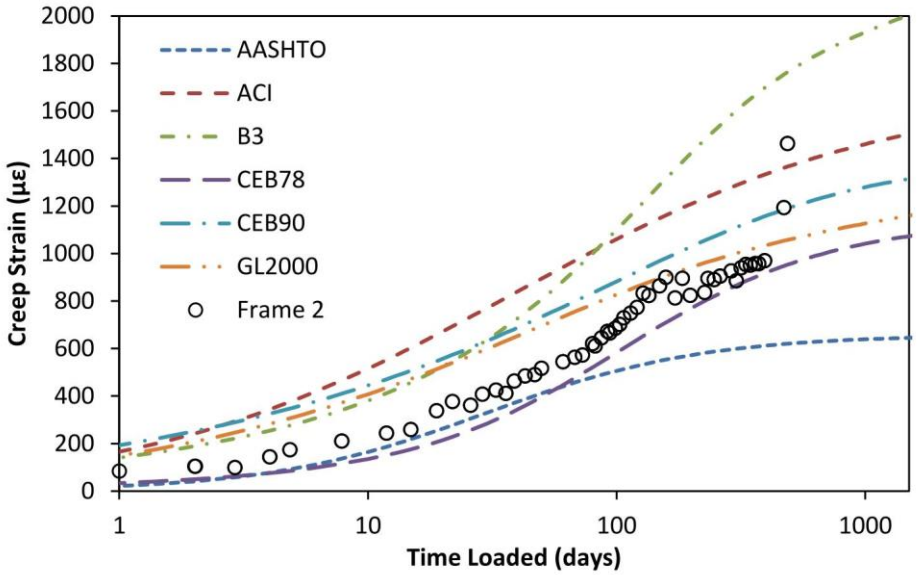

Figure 5.4: Creep strains for Frame 2 loaded with 2.92 ksi (45% of 28-day design strength of 6.5 ksi) at 57 days compared to creep predictions from literature. Only two of the three DEMEC point sides were used for computing strain in both Frame 2 samples.

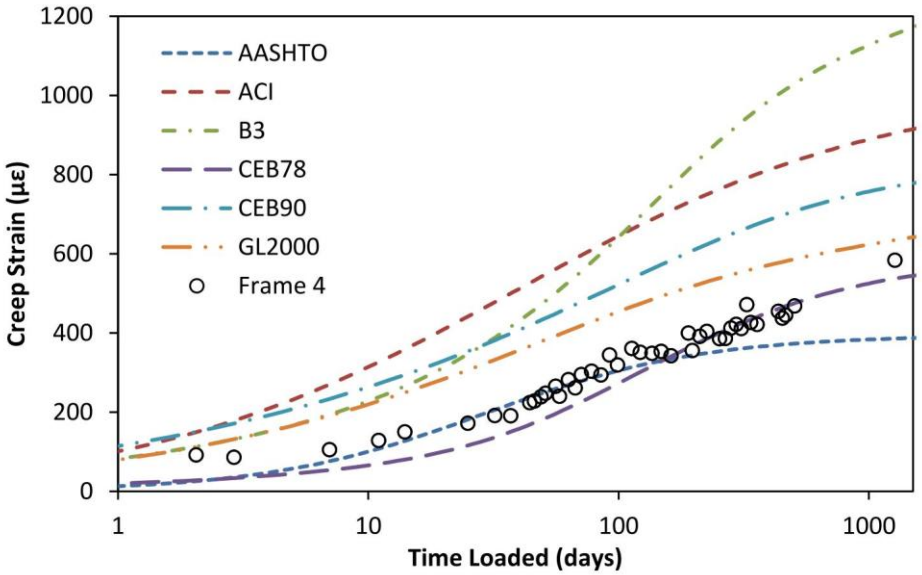

Figure 5.5: Creep strains for Frame 4 loaded with 1.90 ksi (29% of 28-day design strength of 6.5 ksi) at 93 days compared to creep predictions from literature

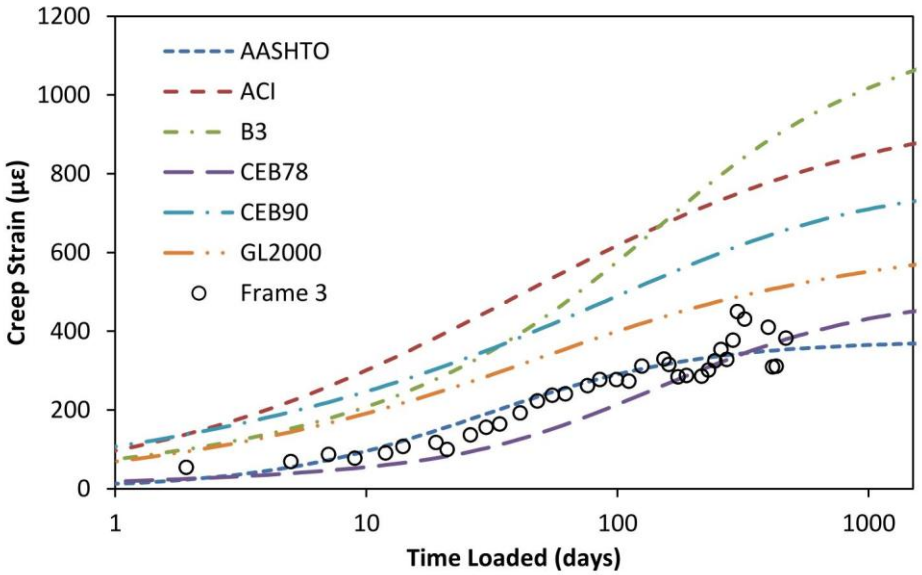

Figure 5.6: Creep strains for Frame 3 loaded with 1.90 ksi (29% of 28-day design strength of 6.5 ksi) at 130 days compared to creep predictions from literature

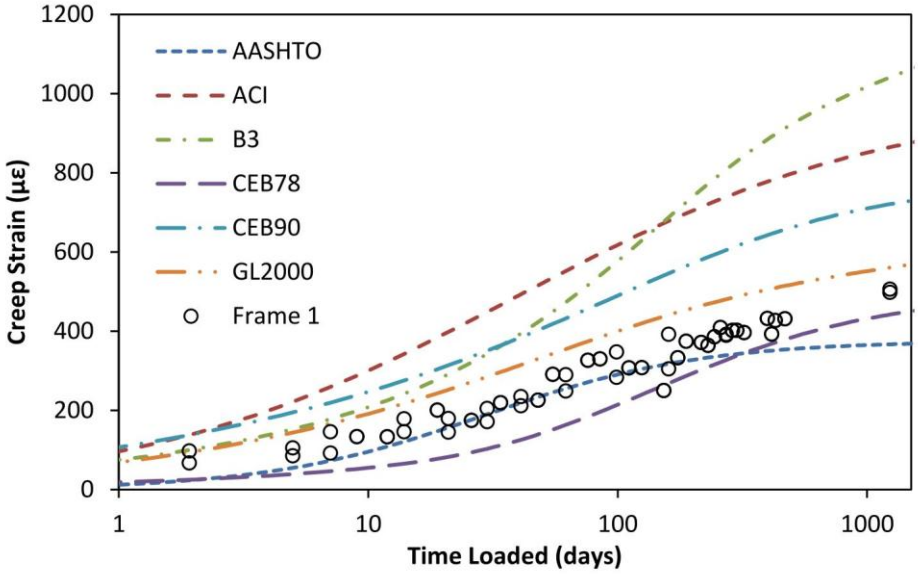

Figure 5.7: Creep strains for Frame 1 loaded with 1.90 ksi (29% of 28-day design strength of 6.5 ksi) at 130 days compared to creep predictions from literature

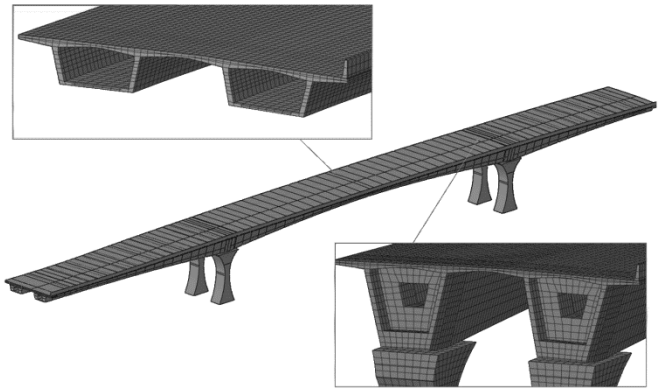

Figure 6.1: Three-dimensional finite element model of southbound bridge

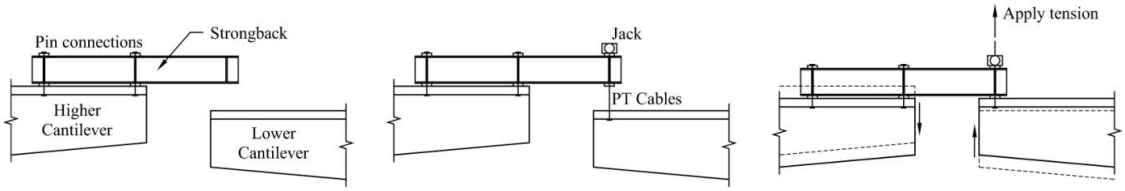

Figure 6.2: Alignment procedure for cantilever ends of as-built physical bridge

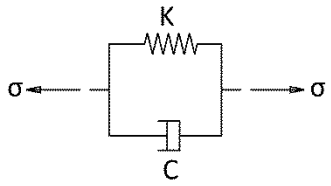

Figure 6.3: Kelvin model for viscoelastic behavior

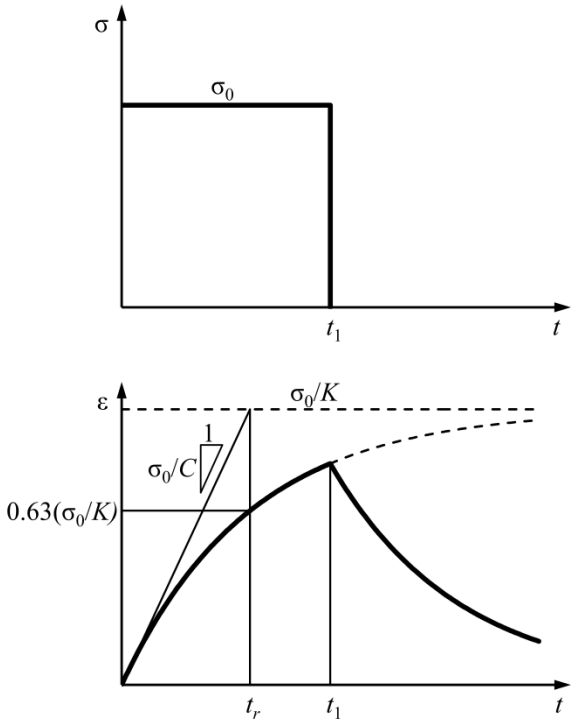

Figure 6.4: Kelvin model creep and recovery curves under step loading

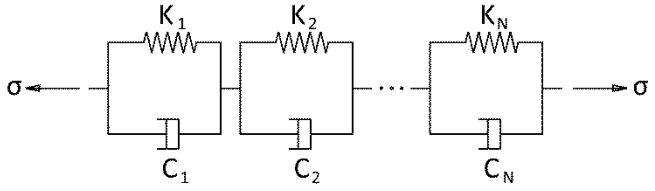

Figure 6.5: Kelvin Chain model for viscoelastic behavior

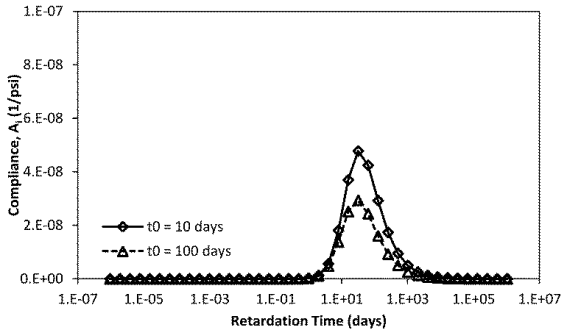

Figure 6.6: Spectrum of Kelvin Chain compliance values for approximation of AASHTO LRFD creep provisions

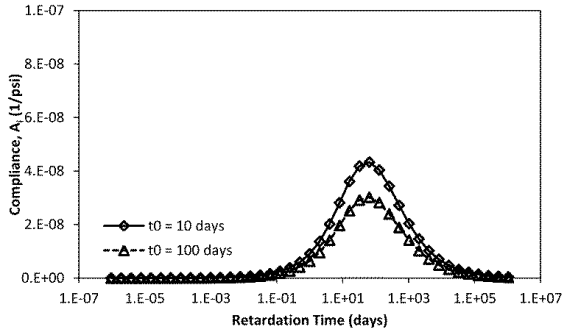

Figure 6.7: Spectrum of Kelvin Chain compliance values for approximation of ACI-209 creep model

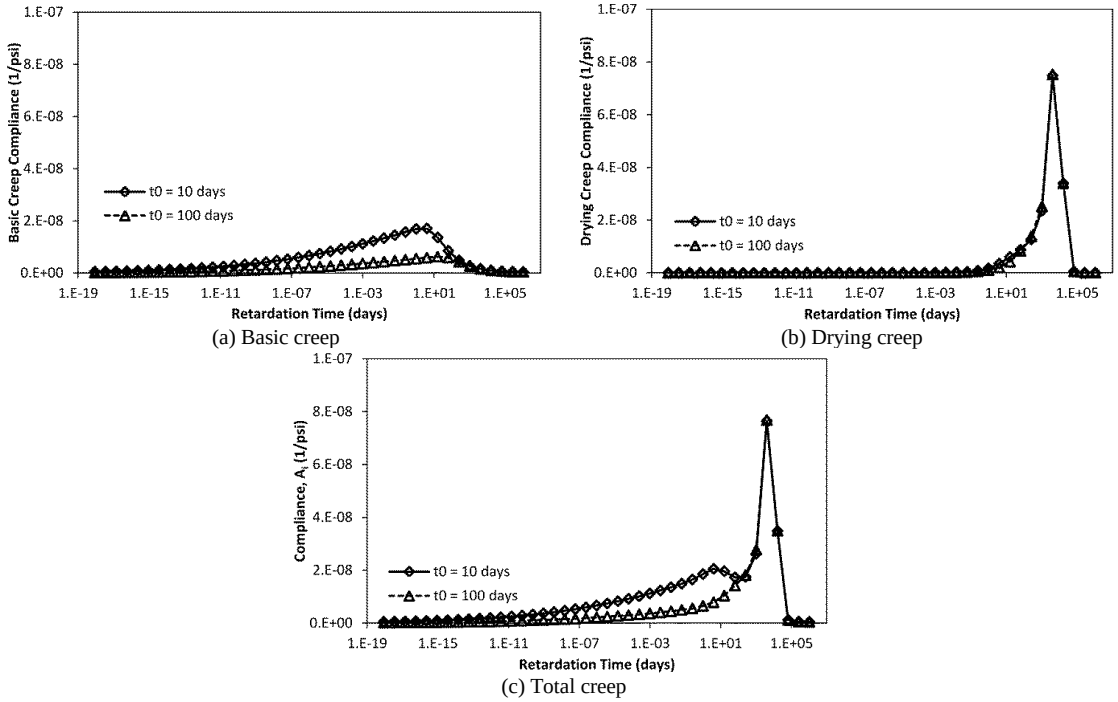

(a) Basic creep (b) Drying creep

(c) Total creep

Figure 6.8: Spectrum of Kelvin Chain compliance values for approximation of B3 creep model, divided into discretization for (a) basic creep (q_2 and q_3 terms), (b) drying creep (q_5 term), and (c) total creep excluding viscous flow

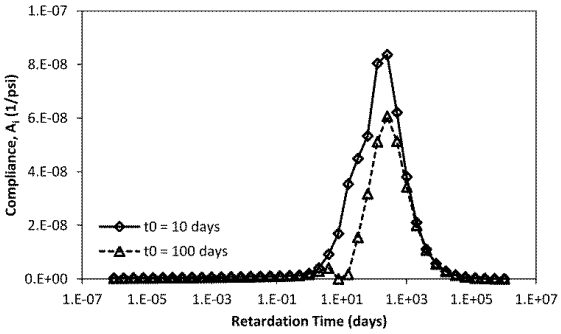

Figure 6.9: Spectrum of Kelvin Chain compliance values for approximation of the 1978 CEB/FIP Model Code creep model

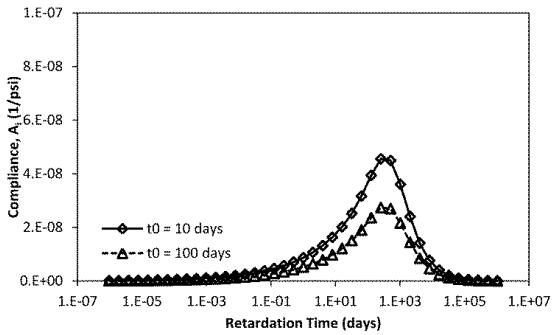

Figure 6.10: Spectrum of Kelvin Chain compliance values for approximation of the 1990 CEB/FIP Model Code creep model

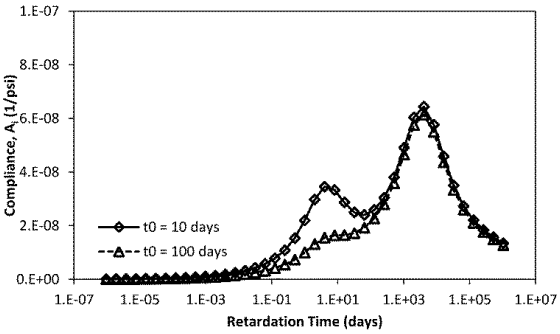

Figure 6.11: Spectrum of Kelvin Chain compliance values for approximation of the GL2000 creep model

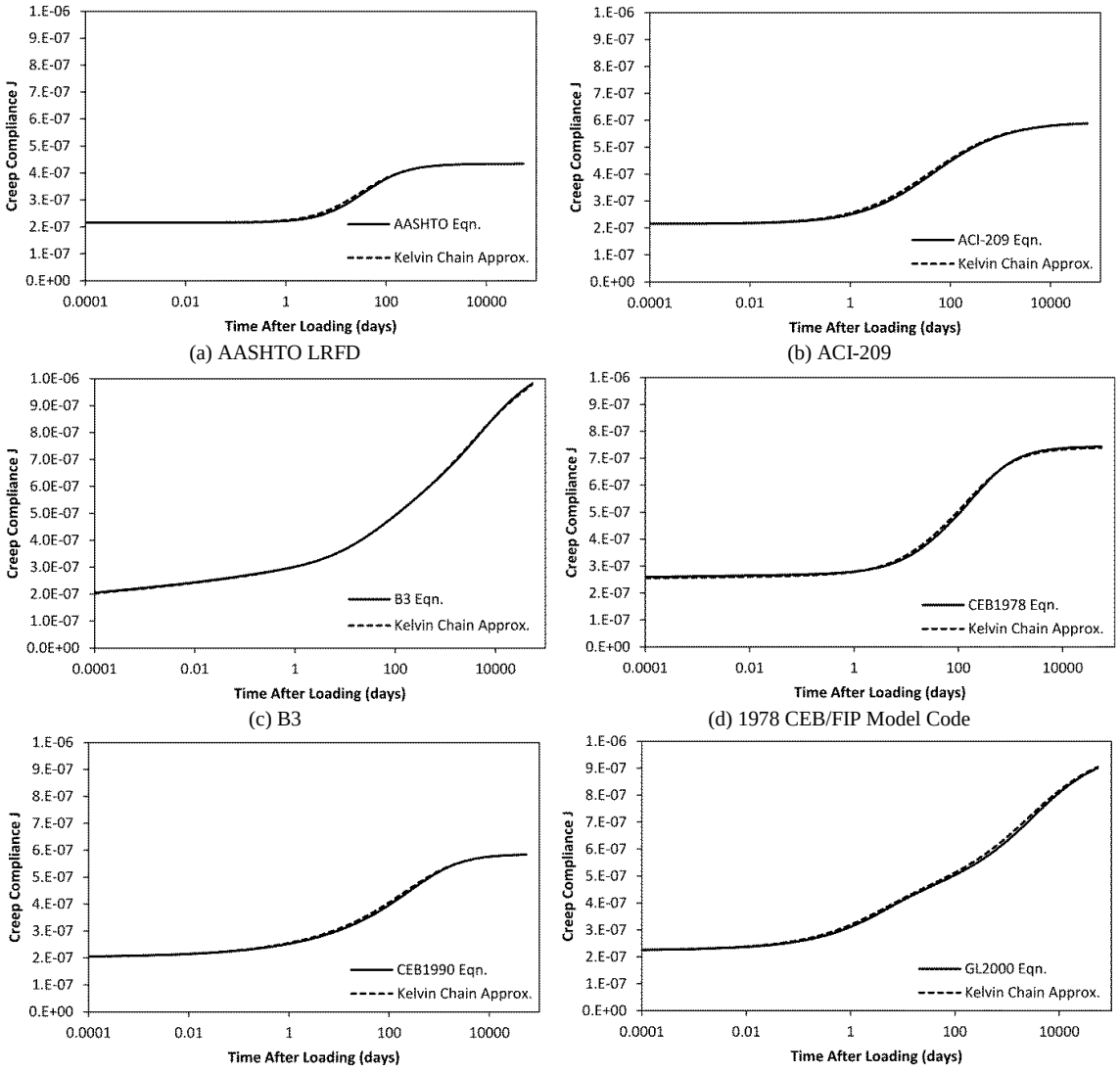

(a) AASHTO LRFD (b) ACI-209

(c) B3 (d) 1978 CEB/FIP Model Code

(e) 1990 CEB/FIP Model Code (f) GL2000

Figure 6.12: Comparison of creep compliance functions from literature with their respective Kelvin Chain approximation for superstructure concrete loaded at 10 days

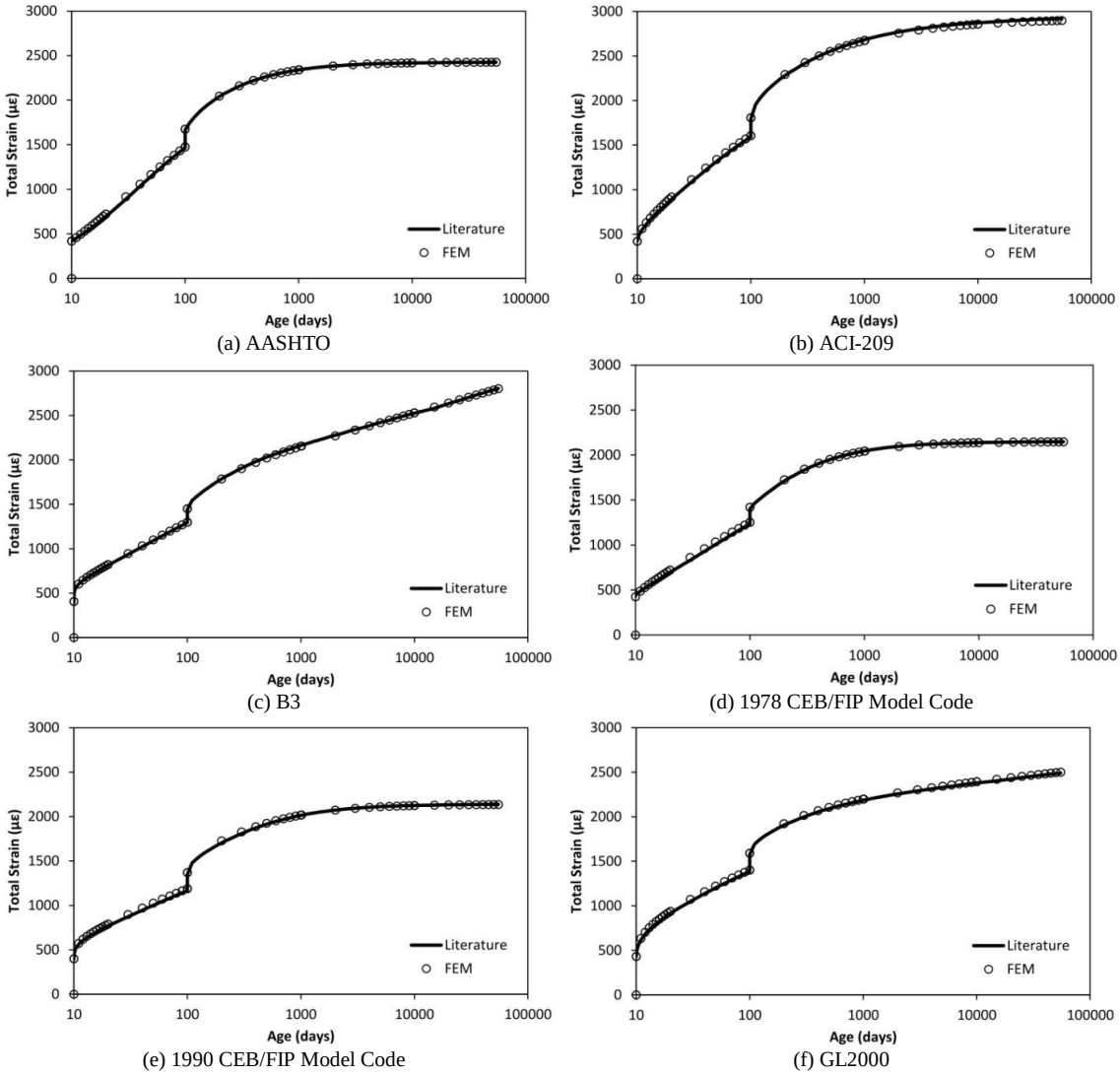

Figure 6.13: Total strains for plain concrete cylinder loaded at 10 and 100 days computed using time-dependent models presented in literature (hand calculations) compared to strains from Kelvin Chain approximation implemented in finite element model

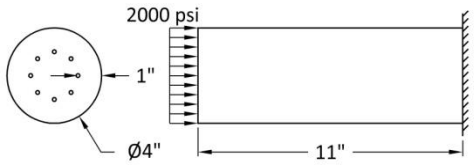

Figure 6.14: Reinforced concrete cylinder for investigation of composite uniaxial behavior

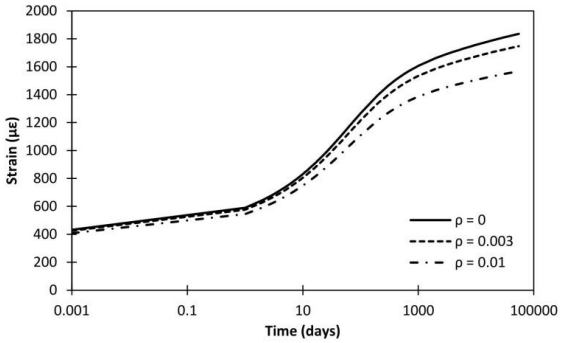

Figure 6.15: Strain with respect to time for differently reinforced cylinders assuming GL2000 creep and shrinkage behavior.

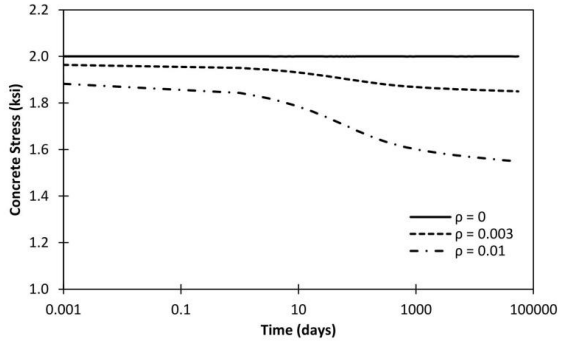

Figure 6.16: Concrete stress with respect to time for differently reinforced cylinders assuming GL2000 creep and shrinkage behavior.

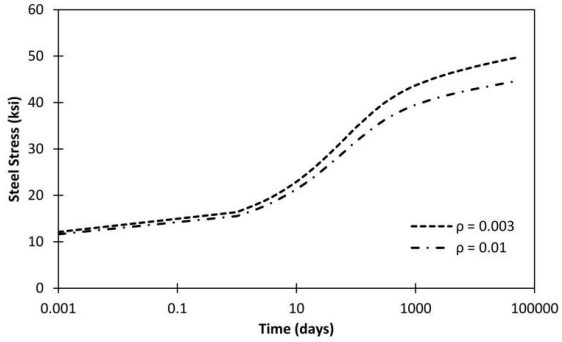

Figure 6.17: Mild steel stress with respect to time for differently reinforced cylinders assuming GL2000 creep and shrinkage behavior.

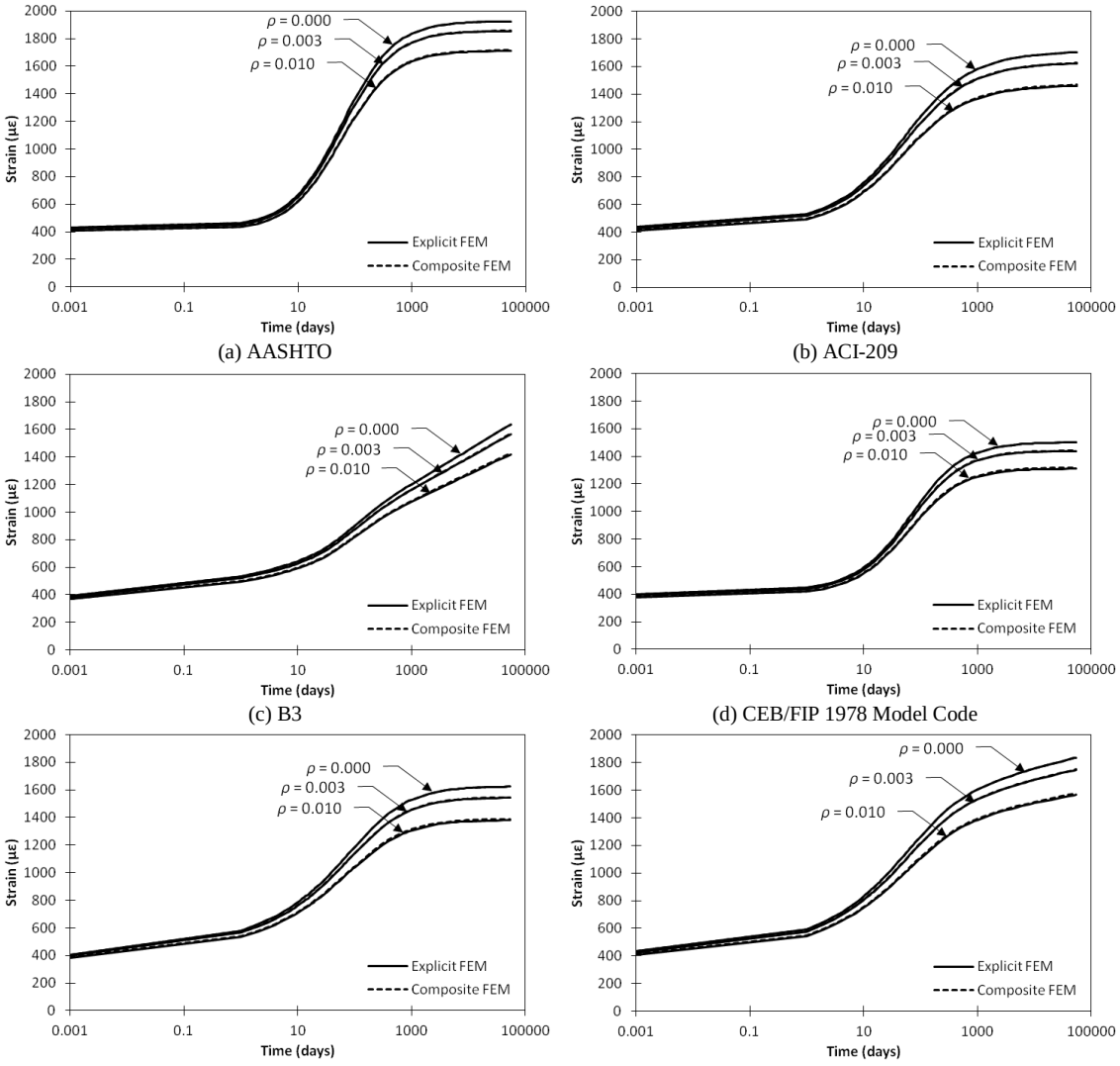

(a) AASHTO (b) ACI-209

(c) B3 (d) CEB/FIP 1978 Model Code

(e) CEB/FIP 1990 Model Code (f) GL2000

Figure 6.18: Comparison of total strains between explicitly modeled reinforcement and composite FEM methodologies for creep and shrinkage models

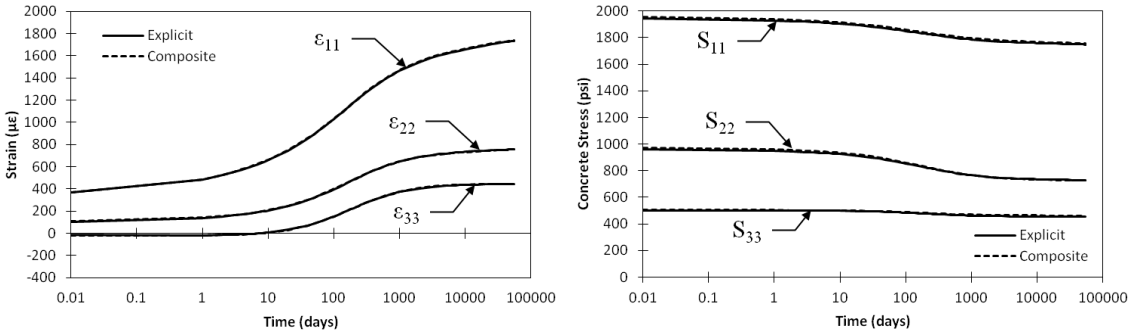

(a) Total Strain (b) Concrete Stress

Figure 6.19: Comparison of (a) total strains and (b) concrete stresses between explicitly modeled reinforcement and composite FEM methodologies for multiaxial loading on cube with reinforcement ratios of 0.005, 0.013, and 0.003 in the 1-, 2-, and 3-directions, respectively

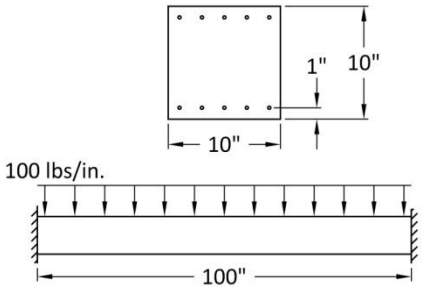

Figure 6.20: Reinforced concrete beam for validation of composite Kelvin Chain model

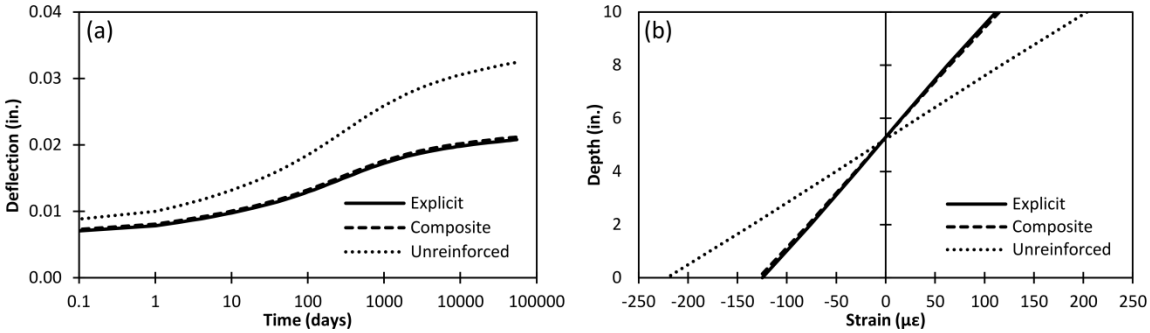

(a) Midspan deflection (b) Midspan strain profile (t = 150 years)

Figure 6.21: Comparison of (a) midspan deflections and (b) midspan strain profile among beam with explicitly modeled reinforcement, beam in the composite FEM, and an unreinforced beam

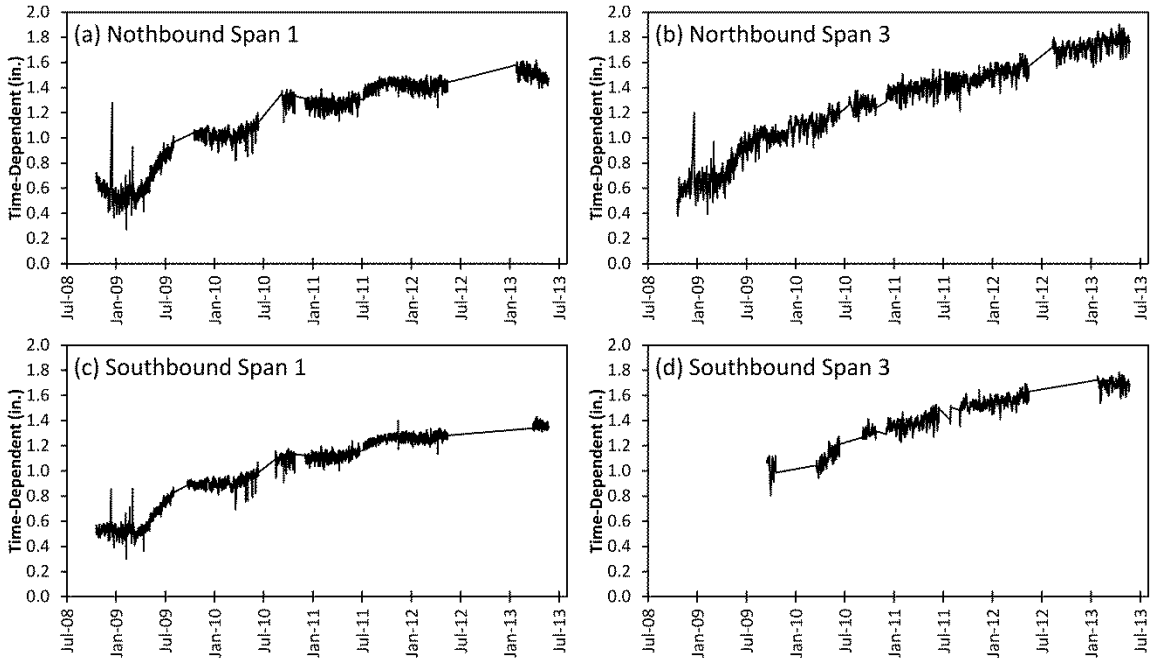

Figure 7.1: Time-dependent deflection extracted from linear potentiometer data by linear regression and plotted with respect to unadjusted time

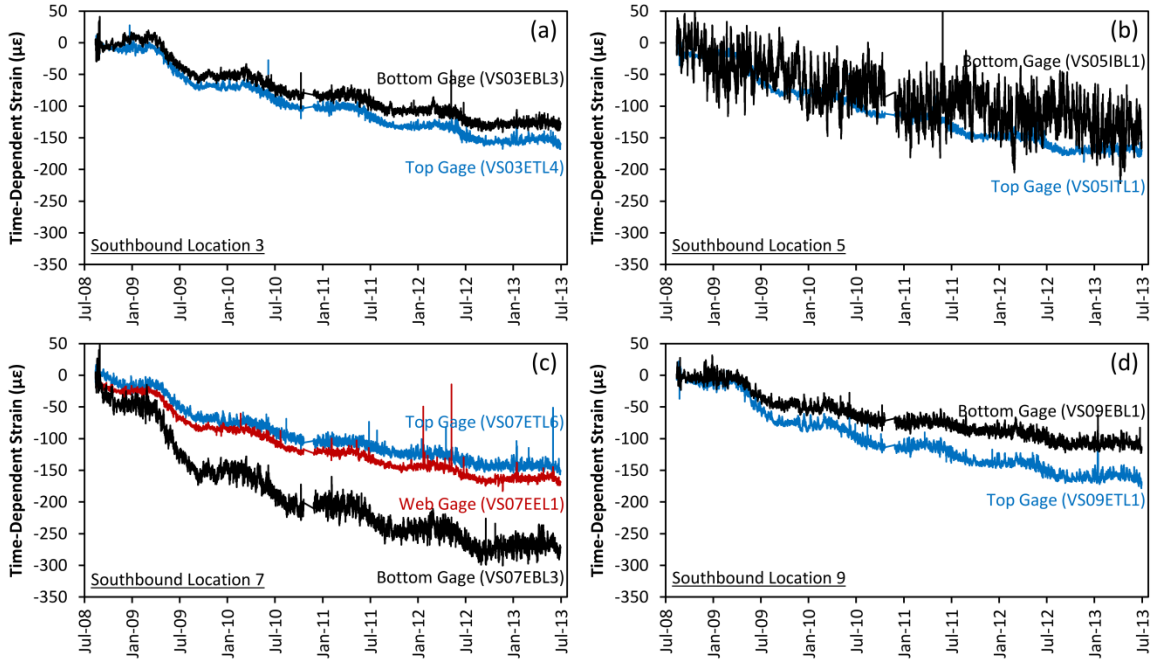

Figure 7.2: Time-dependent strains extracted from vibrating wire strain gage data by linear regression and plotted with respect to unadjusted time

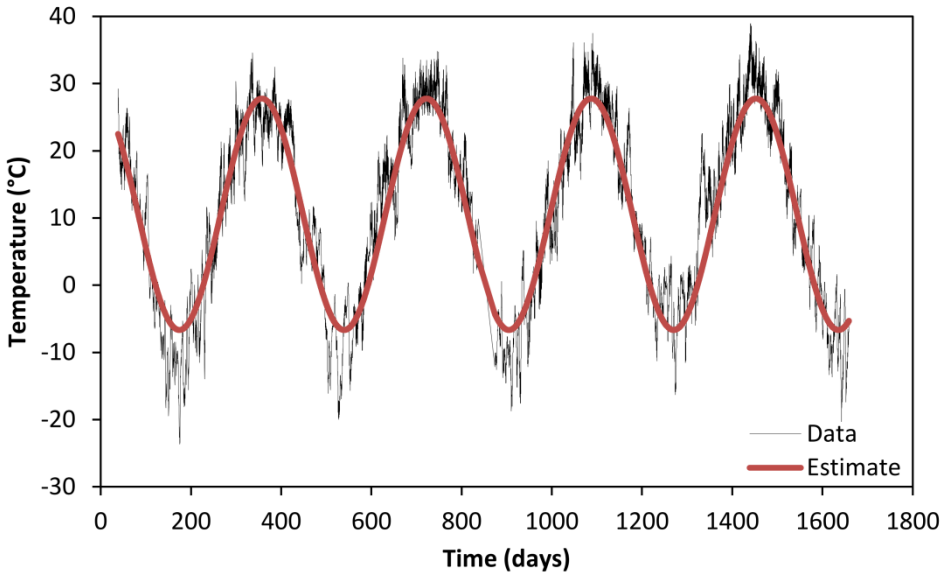

Figure 7.3: Average measured temperatures at southbound Location 7 compared to best-fit sinusoidal approximation

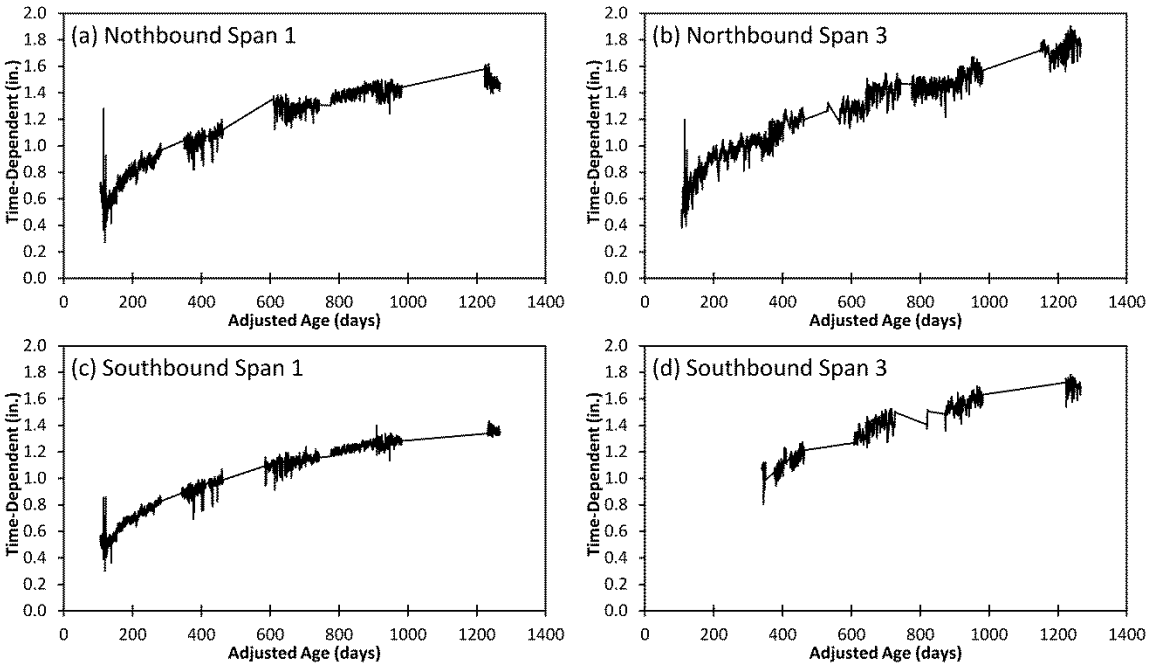

Figure 7.4: Time-dependent deflection extracted from linear potentiometer data by linear regression and plotted with respect to Arrhenius adjusted time

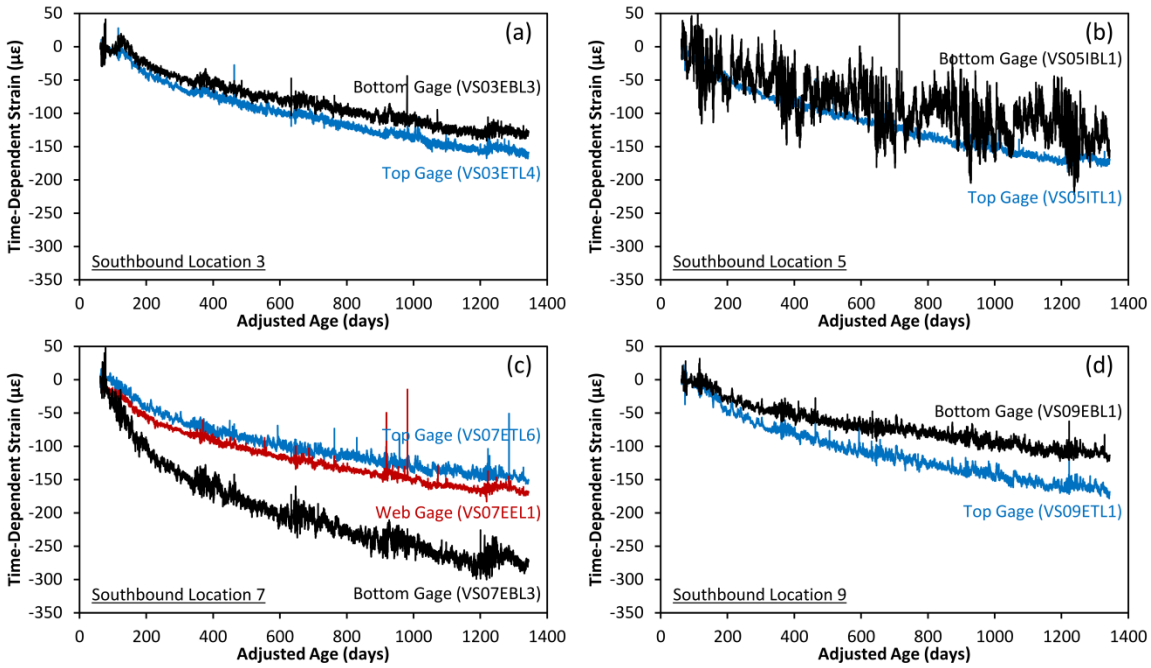

Figure 7.5: Time-dependent strains extracted from vibrating wire strain gage data by linear regression and plotted with respect to Arrhenius adjusted time

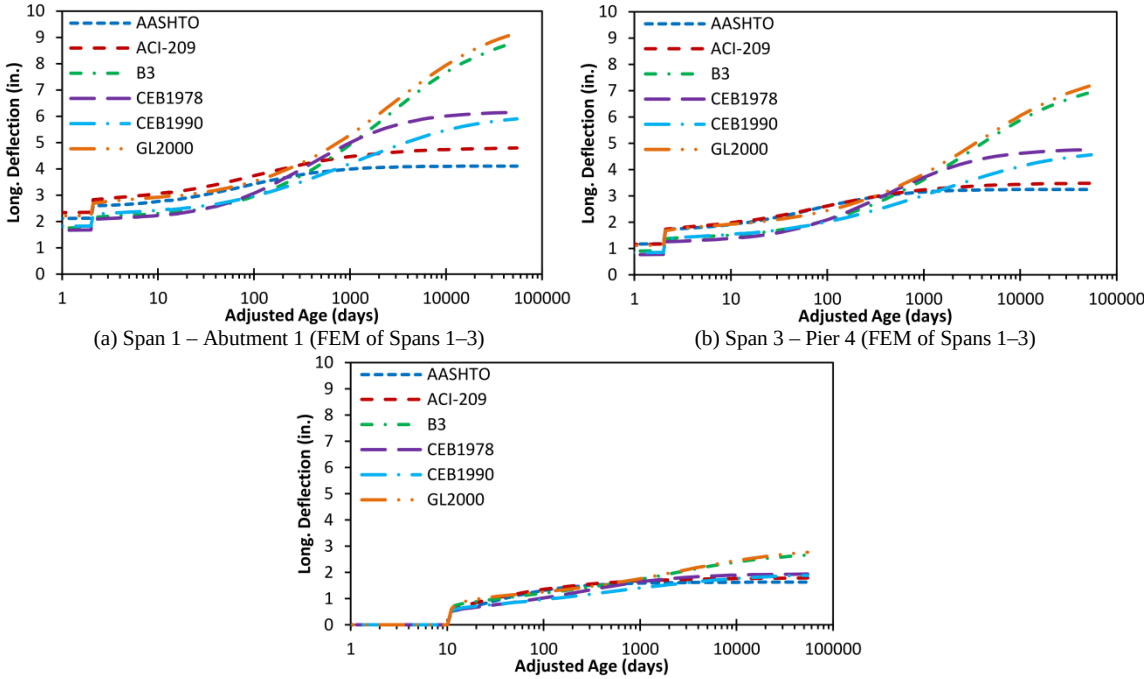

(a) Span 1 – Abutment 1 (FEM of Spans 1–3)

(b) Span 3 – Pier 4 (FEM of Spans 1–3)

(c) Span 3 – Pier 4 (Hand calculations for Span 4)

Figure 8.1: Comparison of estimated longitudinal deflections using all considered time-dependent models at (a) Span 1 – Abutment 1 expansion joint, due to shortening of Spans 1 through 3; (b) Span 3 – Pier 4 expansion joint, due to shortening of Spans 1 through 3; and (c) Span 3 – Pier 4 expansion joint, due to shortening of Span 4.

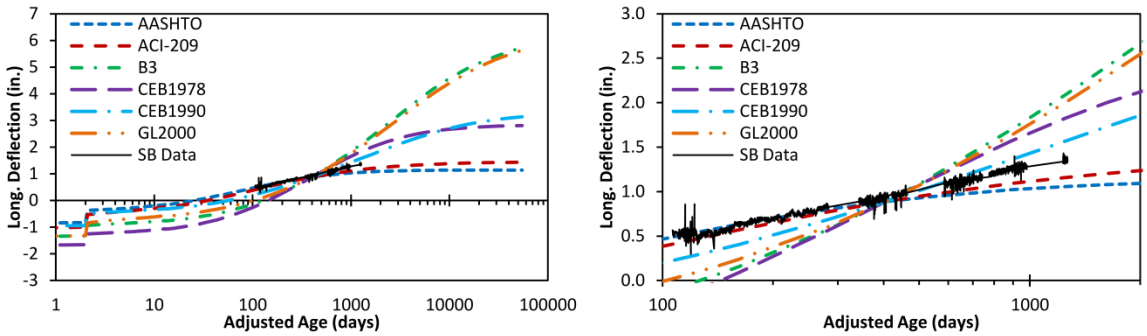

(a) Closure pour to 150-years adjusted age

(b) Zoomed to measured data

Figure 8.2: Comparison of estimated time-dependent longitudinal deflections with linear potentiometer data from southbound bridge Span 1

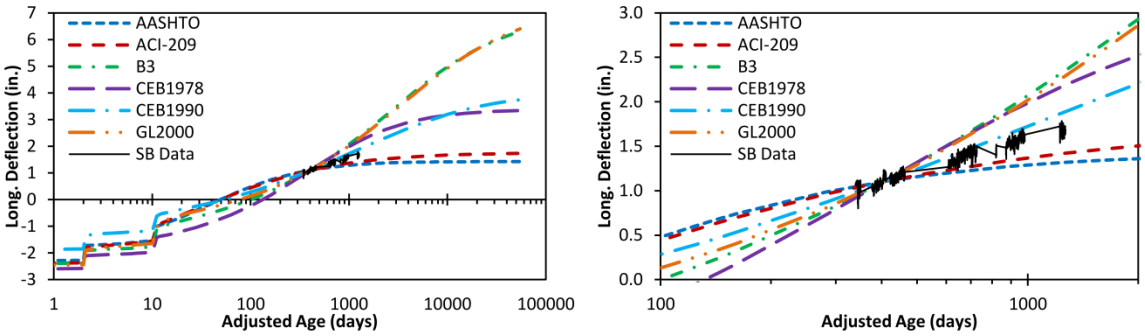

(a) Closure pour to 150-years adjusted age

(b) Zoomed to measured data

Figure 8.3: Comparison of estimated time-dependent longitudinal deflections with linear potentiometer data from southbound bridge Span 3

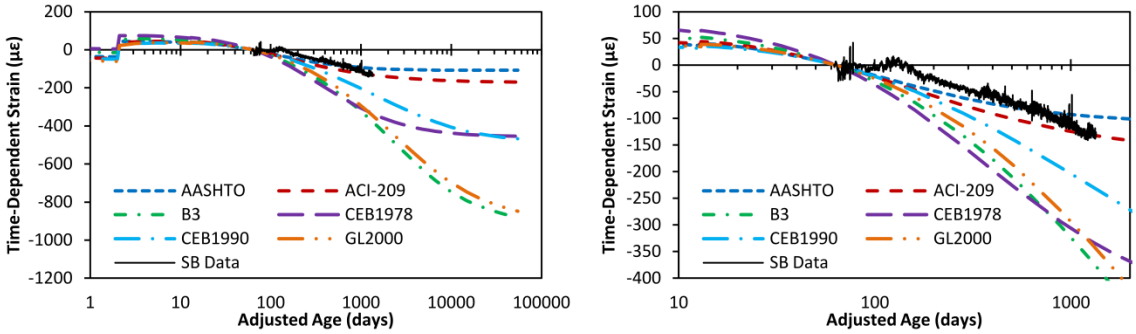

(a) Location 3 Bottom Flange (Below Webs) – 1. Closure to 150-years – 2. Zoomed to measured data

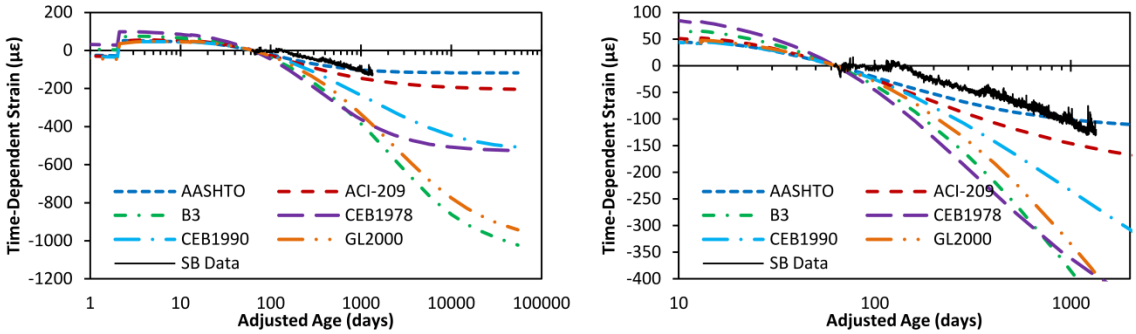

(b) Location 3 Bottom Flange (Centerline of Box) – 1. Closure to 150-years – 2. Zoomed to measured data

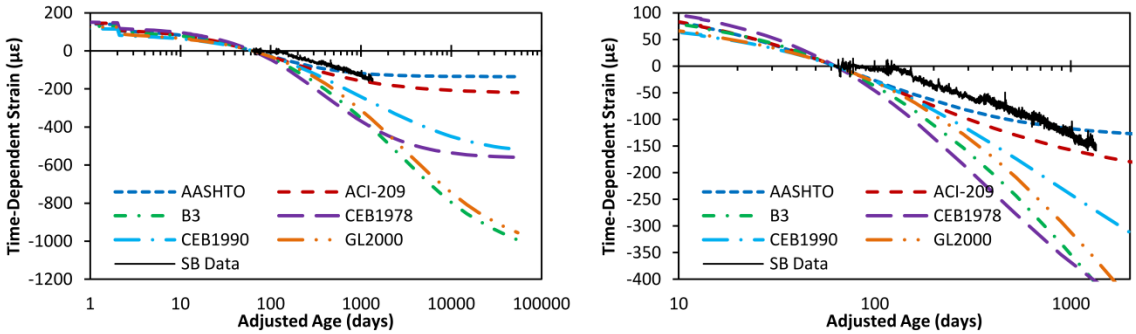

(c) Location 3 Top Flange (Above Webs) – 1. Closure to 150-years – 2. Zoomed to measured data

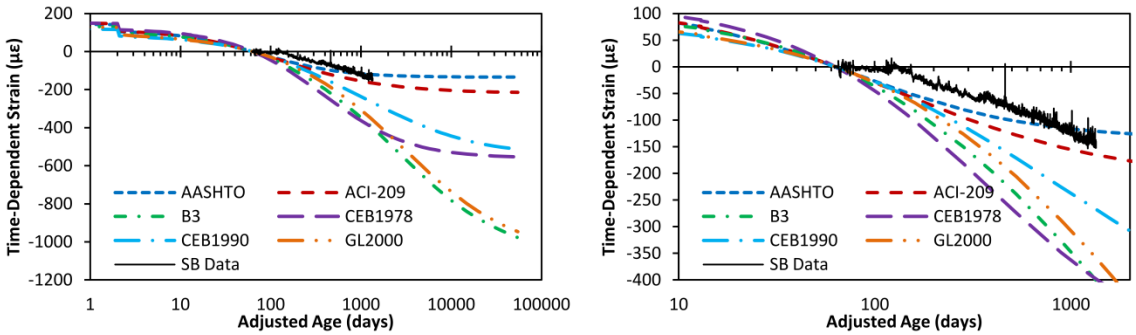

(d) Location 3 Top Flange (Centerline of Box) – 1. Closure to 150-years – 2. Zoomed to measured data

Figure 8.4: Comparison of measured longitudinal time-dependent strains to those computed with FEM using all considered time-dependent models at Location 3 of southbound bridge

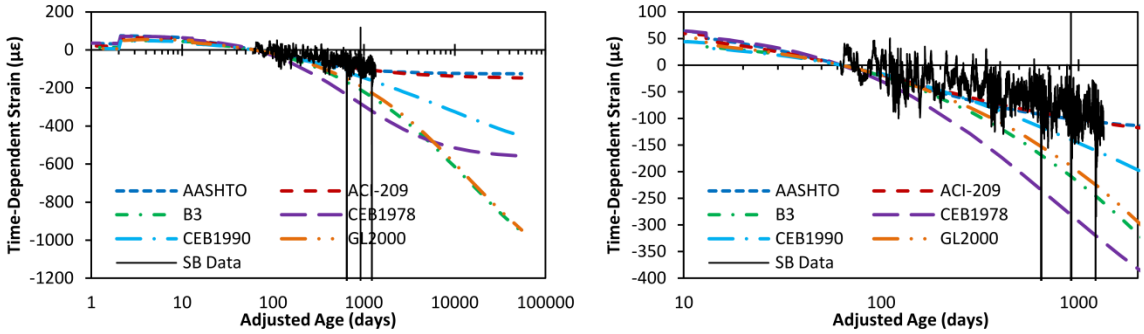

(a) Location 5 Bottom Flange (Centerline of Box) – 1. Closure to 150-years – 2. Zoomed to measured data

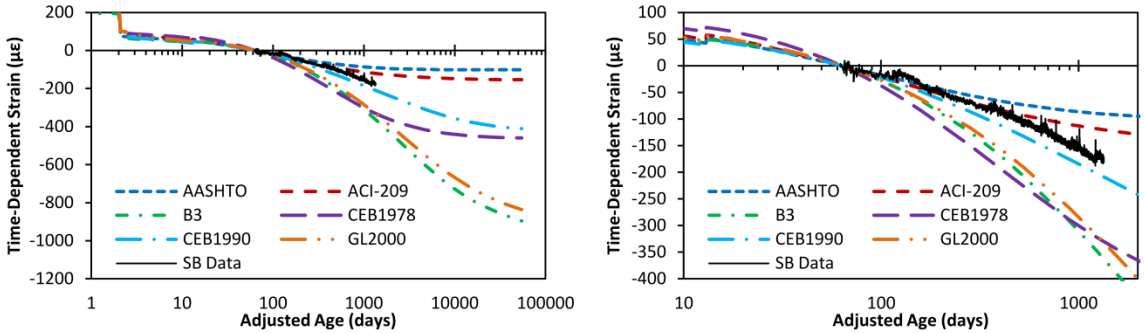

(b) Location 5 Top Flange (Centerline of Box) – 1. Closure to 150-years – 2. Zoomed to measured data

Figure 8.5: Comparison of measured longitudinal time-dependent strains to those computed with FEM using all considered time-dependent models at Location 5 of southbound bridge

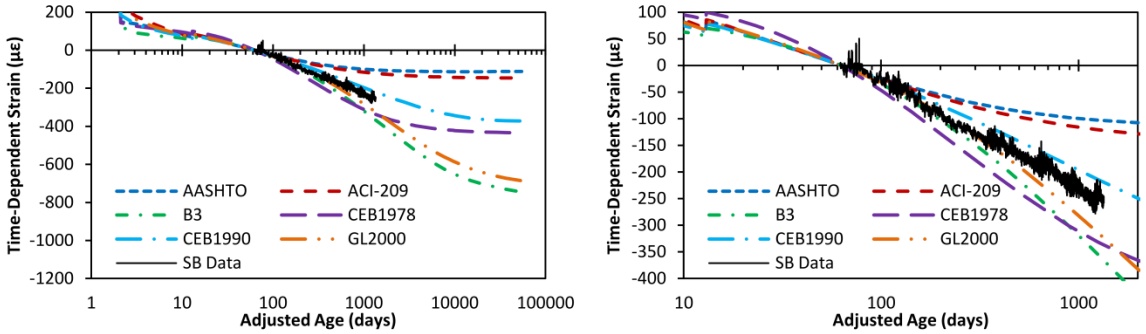

(a) Location 7 Bottom Flange (Below Webs) – 1. Closure to 150-years – 2. Zoomed to measured data

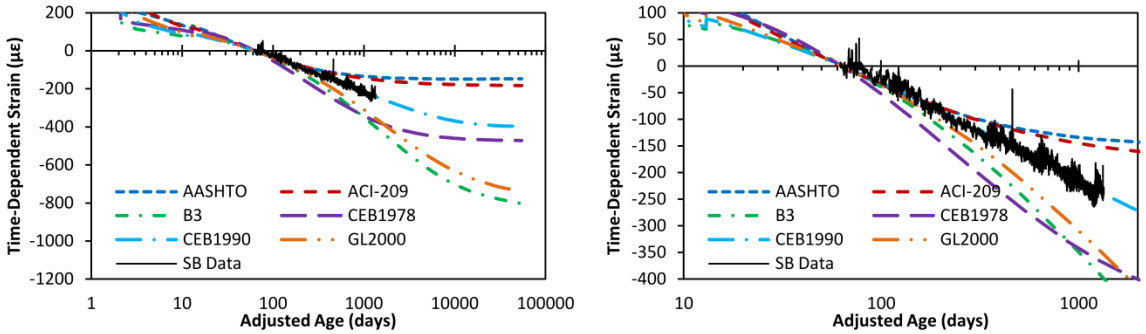

(b) Location 7 Bottom Flange (Centerline of Box) – 1. Closure to 150-years – 2. Zoomed to measured data

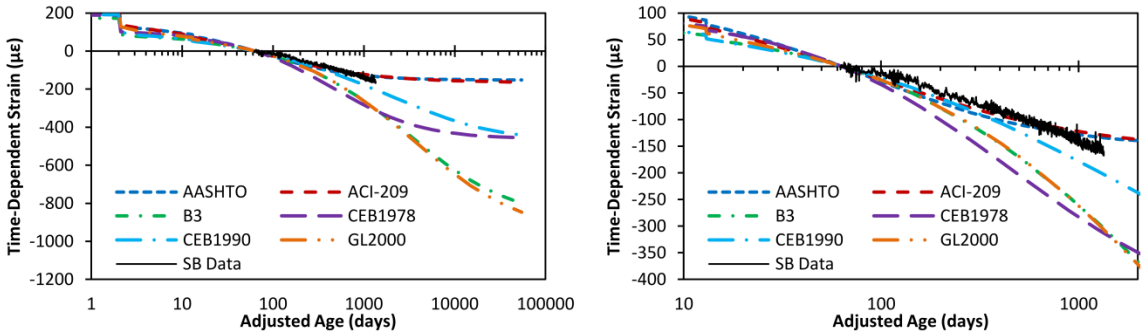

(c) Location 7 Top Flange (Above Webs) – 1. Closure to 150-years – 2. Zoomed to measured data

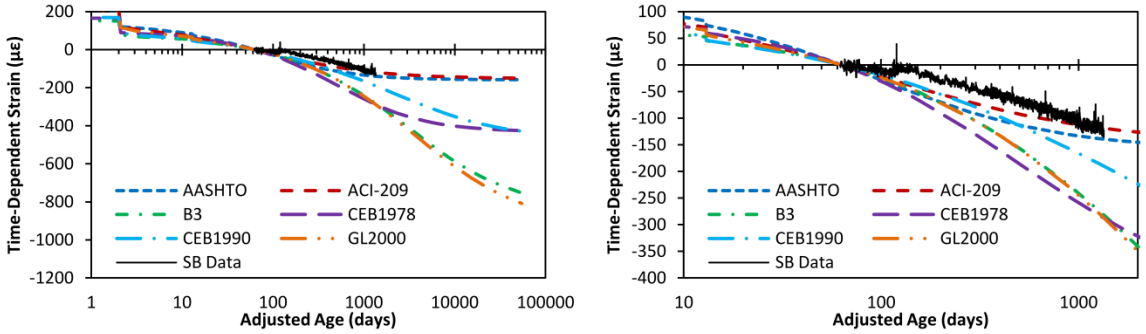

(d) Location 7 Top Flange (Centerline of Box) – 1. Closure to 150-years – 2. Zoomed to measured data

Figure 8.6: Comparison of measured longitudinal time-dependent strains to those computed with FEM using all considered time-dependent models at Location 7 of southbound bridge

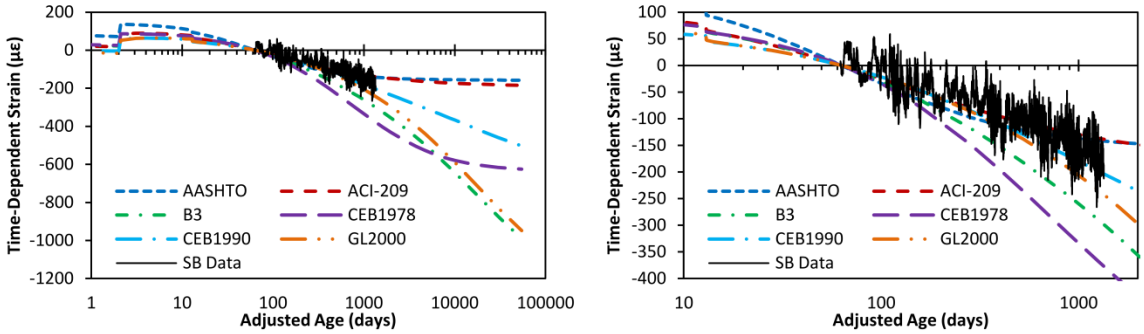

(a) Location 8 Bottom Flange (Centerline of Box) – 1. Closure to 150-years – 2. Zoomed to measured data

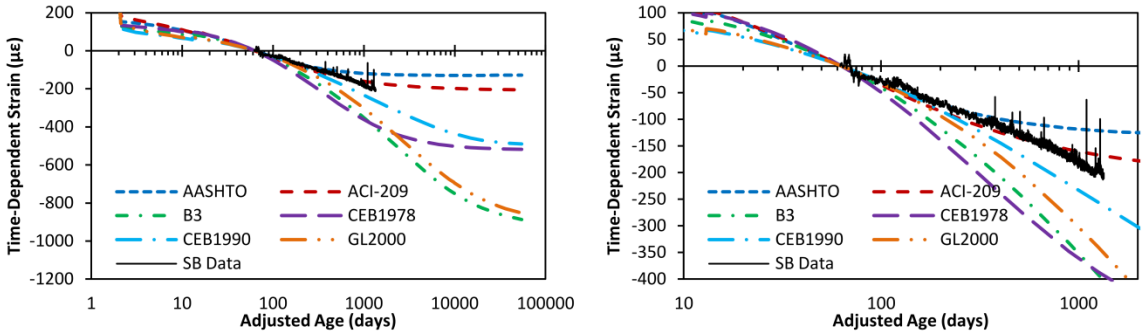

(b) Location 8 Top Flange (Centerline of Box) – 1. Closure to 150-years – 2. Zoomed to measured data

Figure 8.7: Comparison of measured longitudinal time-dependent strains to those computed with FEM using all considered time-dependent models at Location 8 of southbound bridge

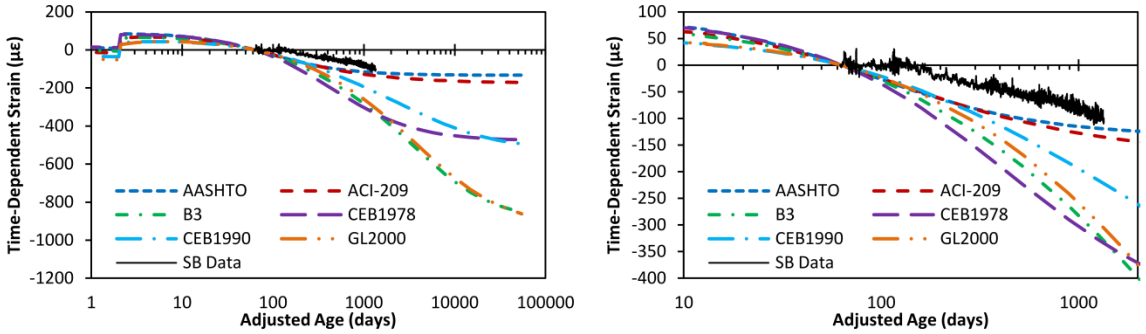

(a) Location 9 Bottom Flange (Centerline of Box) – 1. Closure to 150-years – 2. Zoomed to measured data

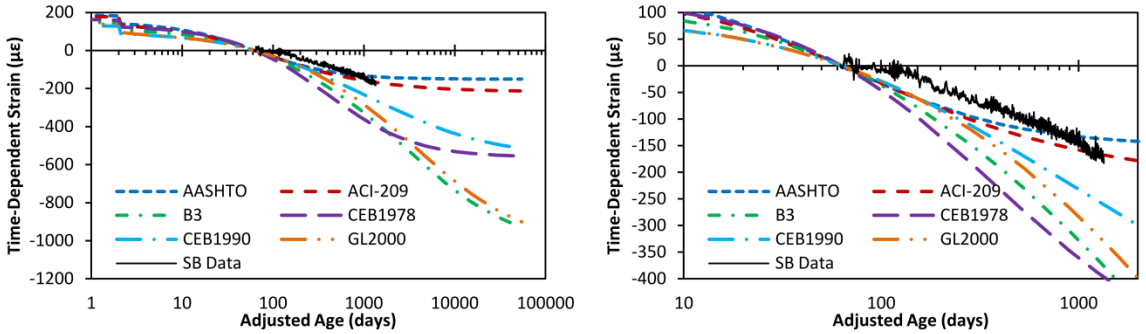

(b) Location 9 Top Flange (Centerline of Box) – 1. Closure to 150-years – 2. Zoomed to measured data

Figure 8.8: Comparison of measured longitudinal time-dependent strains to those computed with FEM using all considered time-dependent models at Location 9 of southbound bridge

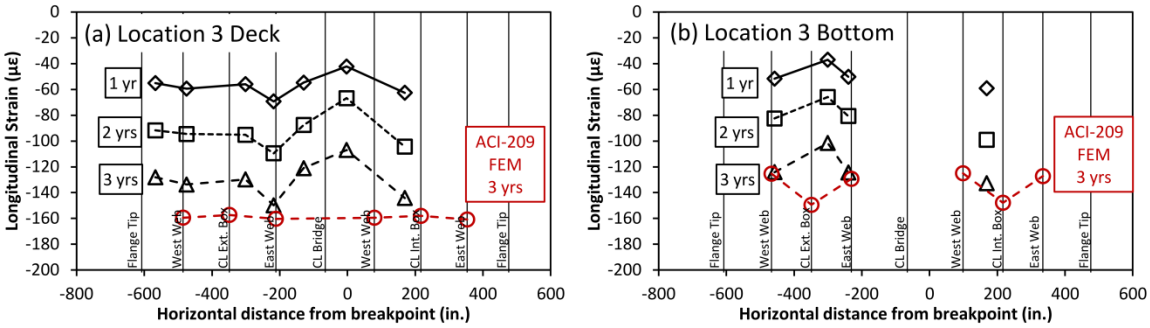

Figure 8.9: Longitudinal time-dependent strains across width of (a) deck and (b) bottom flange of Location 3 of the southbound bridge

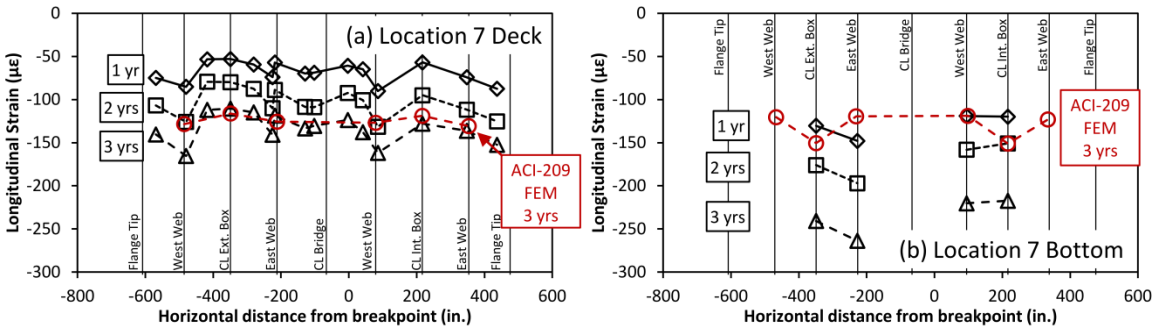

Figure 8.10: Longitudinal time-dependent strains across width of (a) deck and (b) bottom flange of Location 7 of the southbound bridge

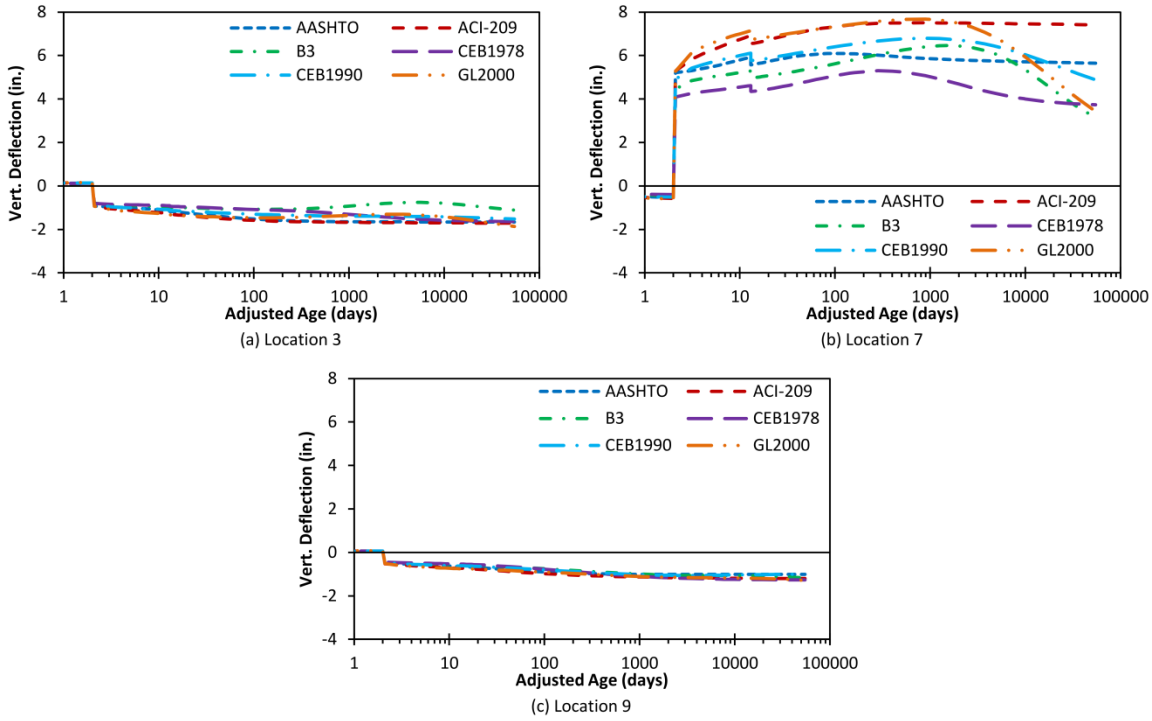

Figure 8.11: Vertical time-dependent deflections at (a) Location 3 – midspan of Span 1, (b) Location 7 – midspan of Span 2, and (c) Location 9 – midspan of Span 3 of the southbound bridge computed using FEM

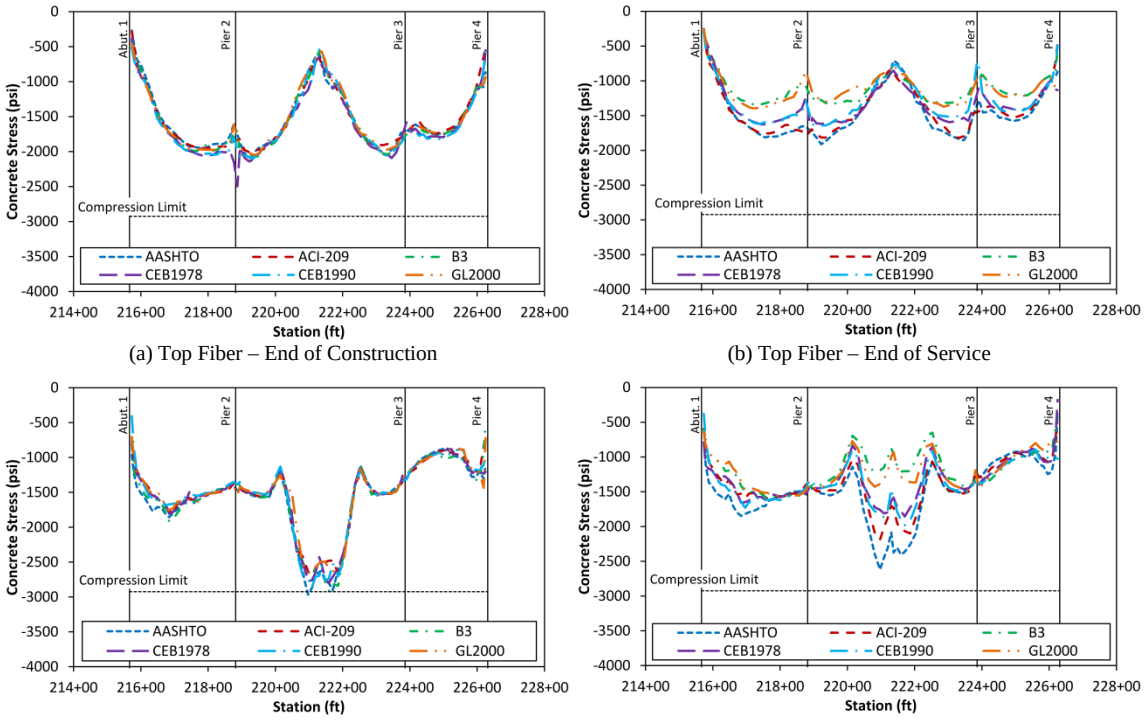

(a) Top Fiber – End of Construction

(b) Top Fiber – End of Service

(c) Bottom Fiber – End of Construction

(d) Bottom Fiber – End of Service

Figure 8.12: Longitudinal concrete stresses in top and bottom flanges due to permanent loads at end of construction and end of service

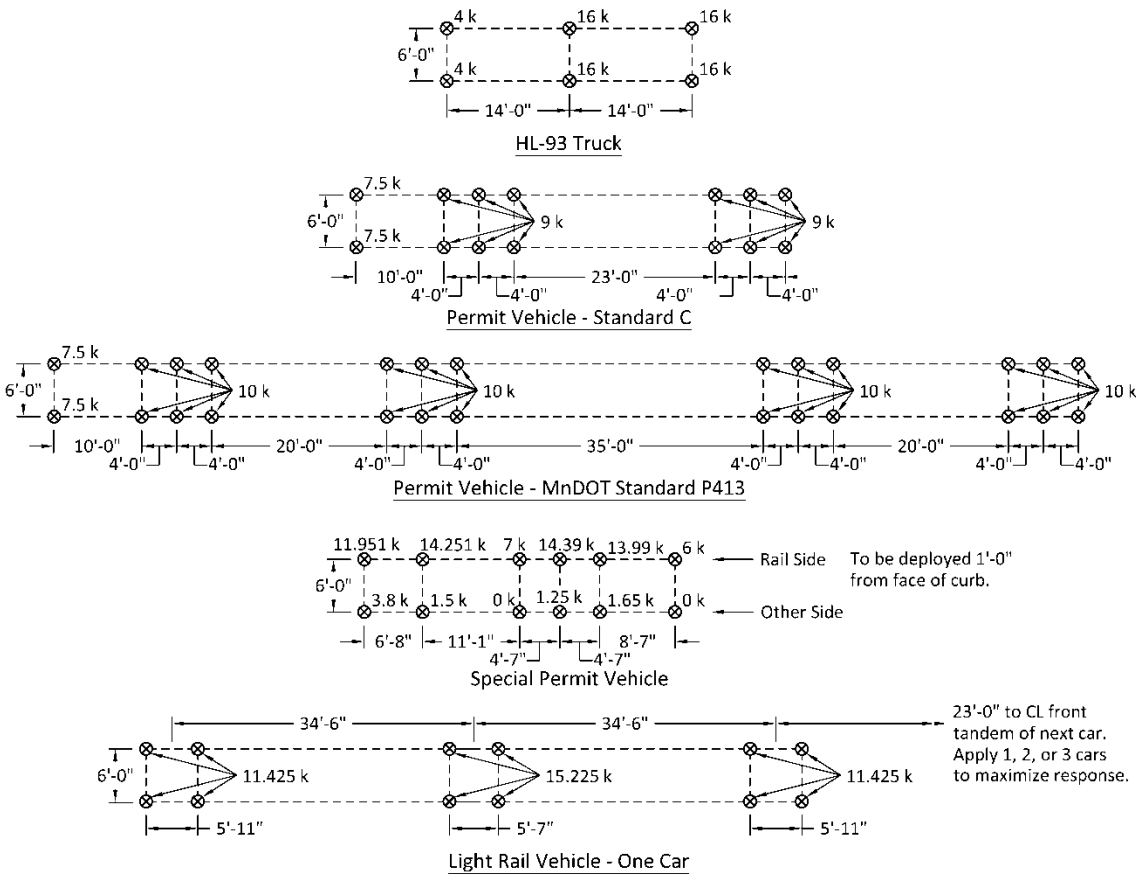

Figure 8.13: HL-93, permit, and light-rail vehicle live loads

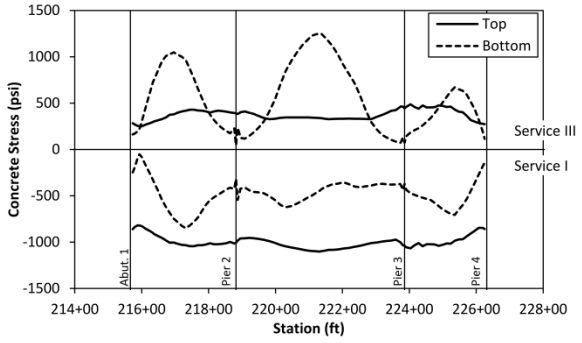

Figure 8.14: Top and bottom fiber longitudinal concrete stress envelopes considering combinations of vehicle live loading, thermal gradients, and uniform temperature changes (no permanent loading or time-dependent effects)

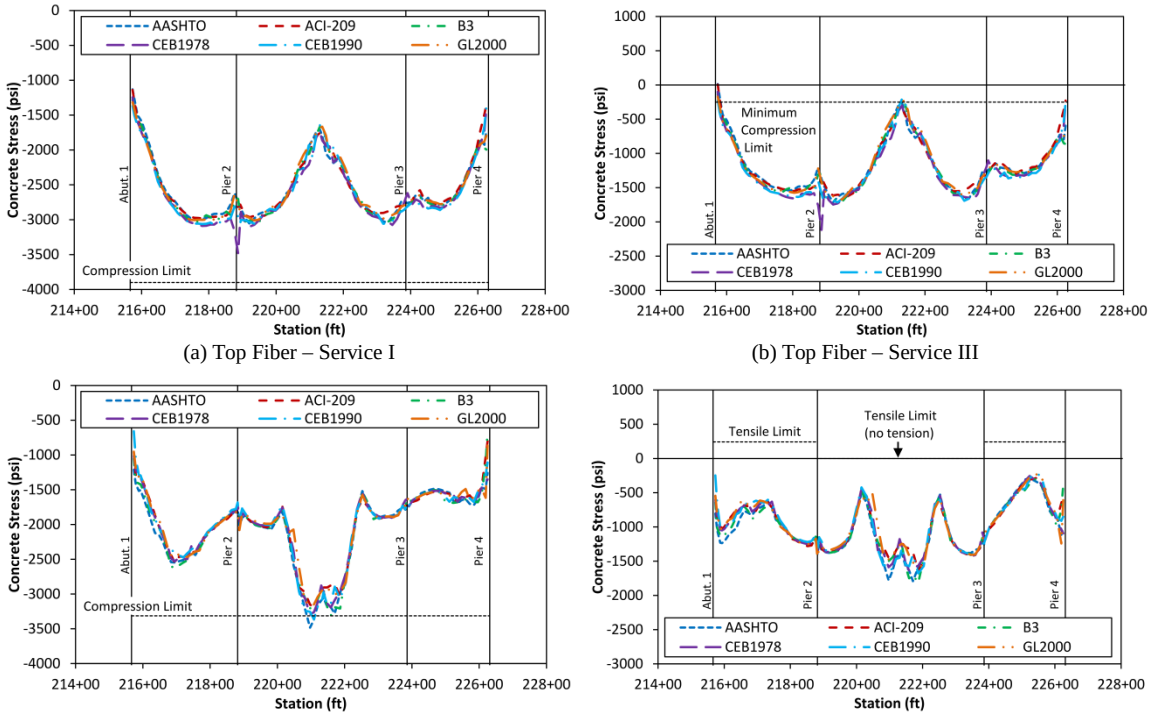

(a) Top Fiber – Service I

(b) Top Fiber – Service III

(c) Bottom Fiber – Service I

(d) Bottom Fiber – Service III

Figure 8.15: End of construction stress envelopes for permanent loading (including time-dependent effects) plus live loading, thermal gradients, and uniform temperature changes

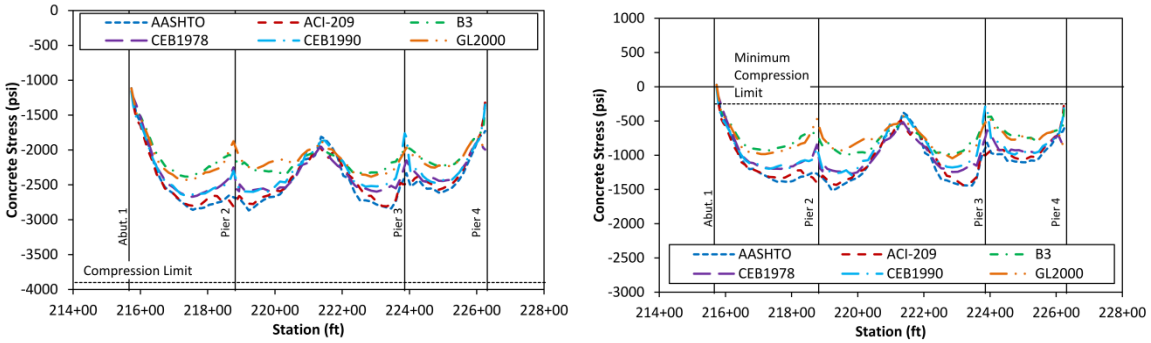

(a) Top Fiber – Service I

(b) Top Fiber – Service III

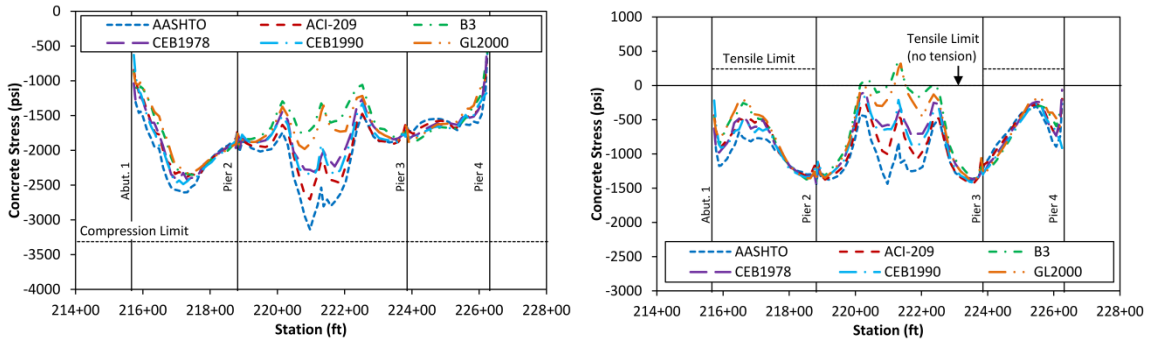

(c) Bottom Fiber – Service I

(d) Bottom Fiber – Service III

Figure 8.16: End of service stress envelopes for permanent loading (including time-dependent effects) plus live loading, thermal gradients, and uniform temperature changes

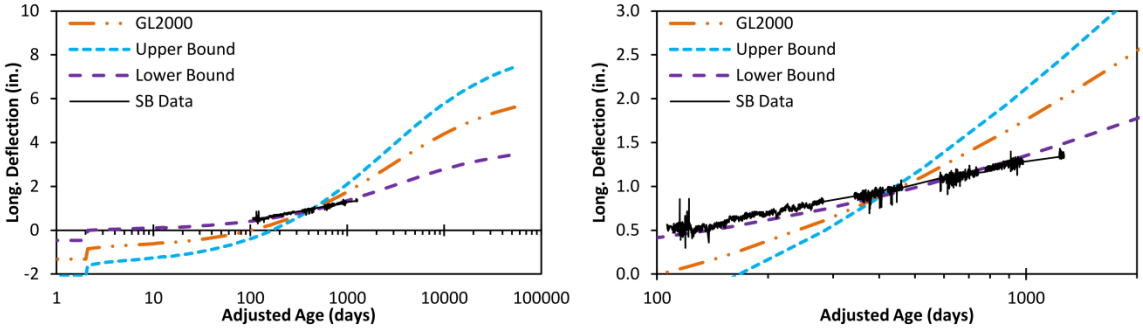

(a) Closure pour to 150-years adjusted age

(b) Zoomed to measured data

Figure 8.17: Comparison of longitudinal deflections from mean and bounding estimates using GL2000 model with linear potentiometer data from southbound bridge Span 1

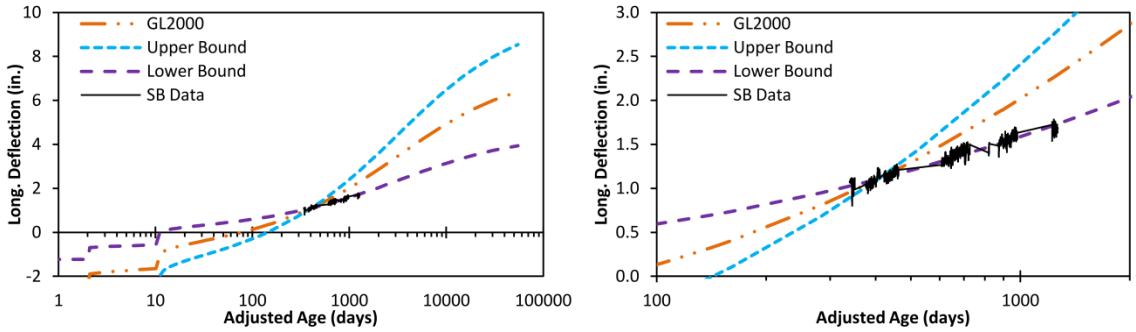

(a) Closure pour to 150-years adjusted age (b) Zoomed to measured data

Figure 8.18: Comparison of longitudinal deflections from mean and bounding estimates using GL2000 model with linear potentiometer data from southbound bridge Span 3

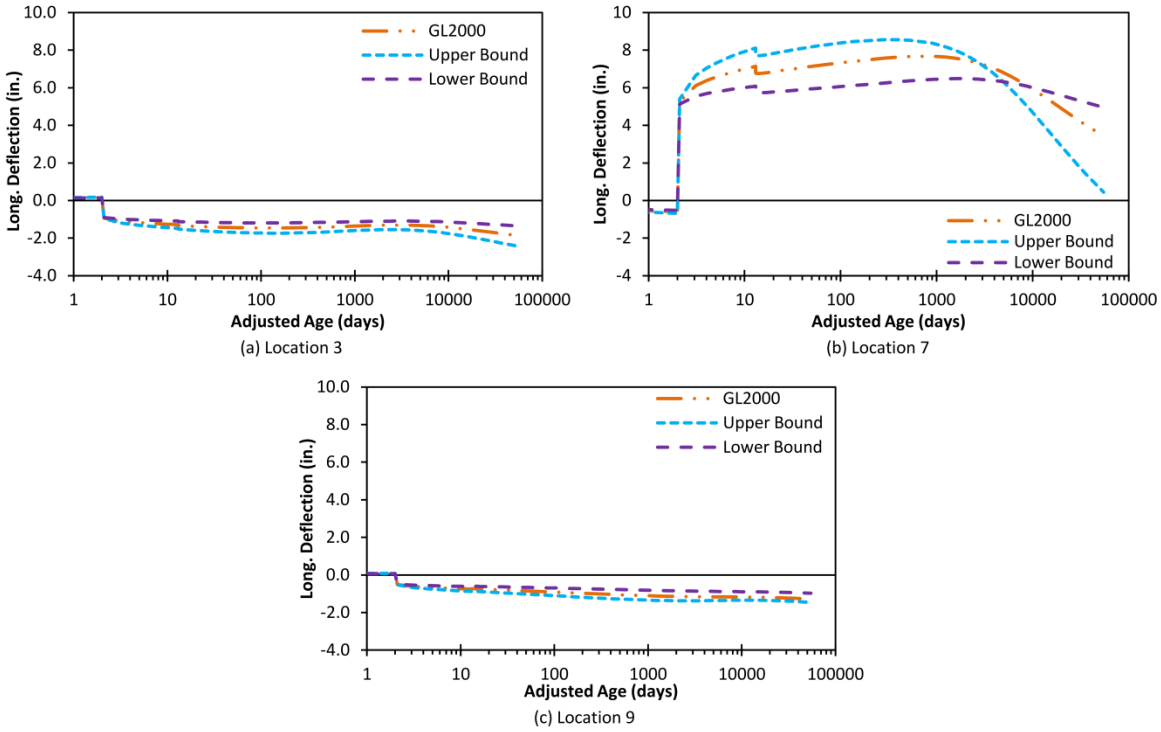

(a) Location 3 (b) Location 7

(c) Location 9

Figure 8.19: Mean and bounding estimates of vertical time-dependent deflections at (a) Location 3, (b) Location 7, and (c) Location 9 of the southbound bridge computed using FEM and GL2000 time-dependent model

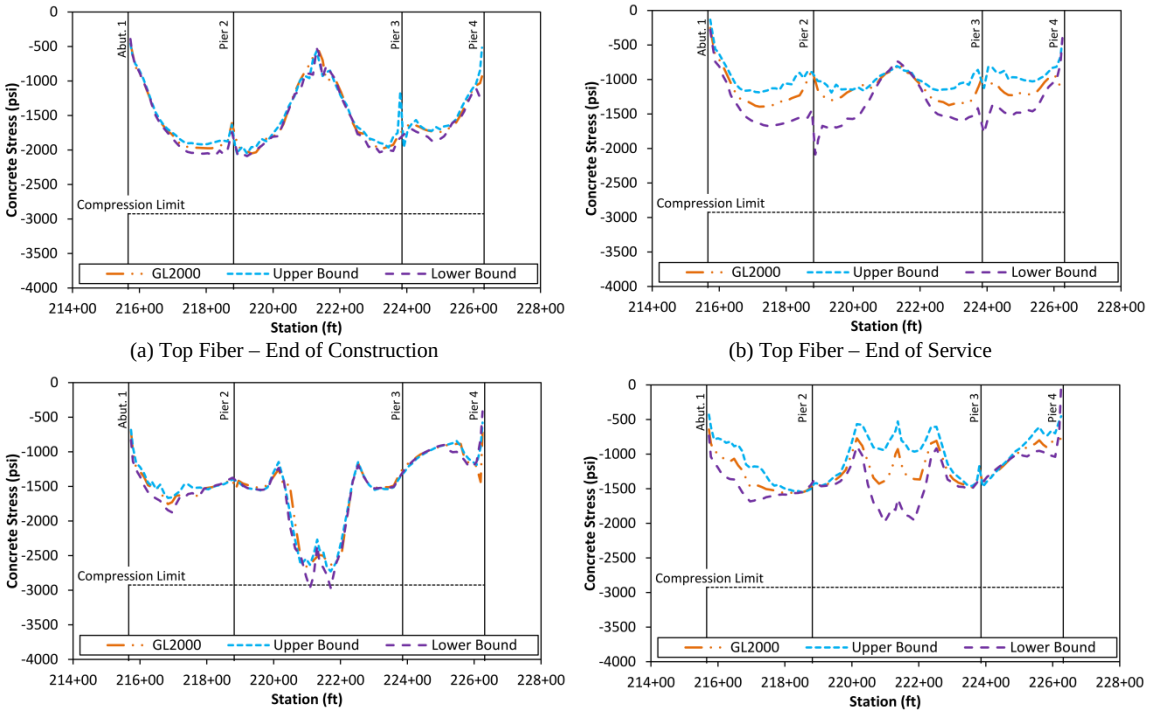

(a) Top Fiber – End of Construction

(b) Top Fiber – End of Service

(c) Bottom Fiber – End of Construction

(d) Bottom Fiber – End of Service

Figure 8.20: Mean and bounding estimates of longitudinal concrete stresses in top and bottom flanges due to permanent loads (including time-dependent effects) at end of construction and end of service assuming GL2000 time-dependent model

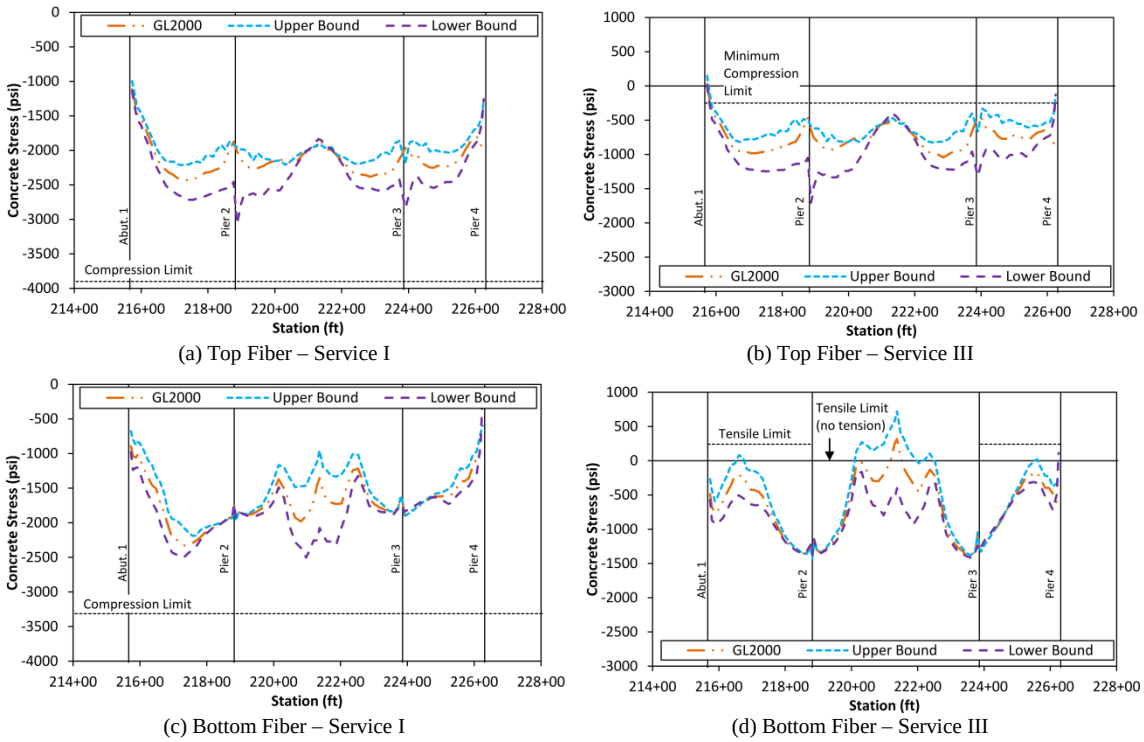

(a) Top Fiber – Service I

(b) Top Fiber – Service III

(c) Bottom Fiber – Service I

(d) Bottom Fiber – Service III

Figure 8.21: Mean and bounding estimates of end of service stress envelopes for permanent loading (including time-dependent effects) plus live loading, thermal gradients, and uniform temperature changes assuming GL2000 time-dependent model

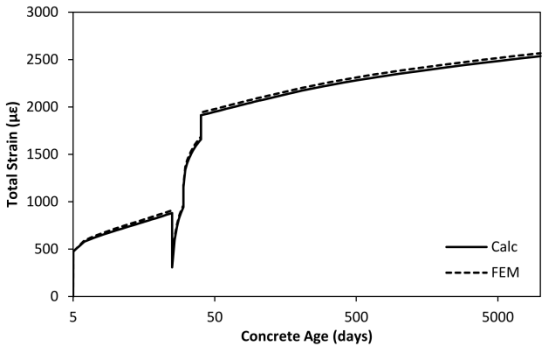

Figure 9.1: Comparison between total strains for hand calculation and finite element method accounting for temperature changes using GL2000 time-dependent model

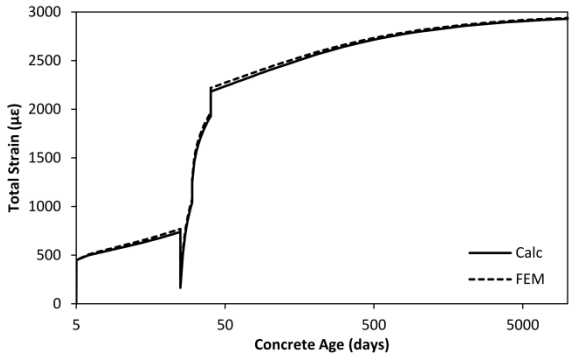

Figure 9.2: Comparison between total strains for hand calculation and finite element method accounting for temperature changes using ACI-209 time-dependent model

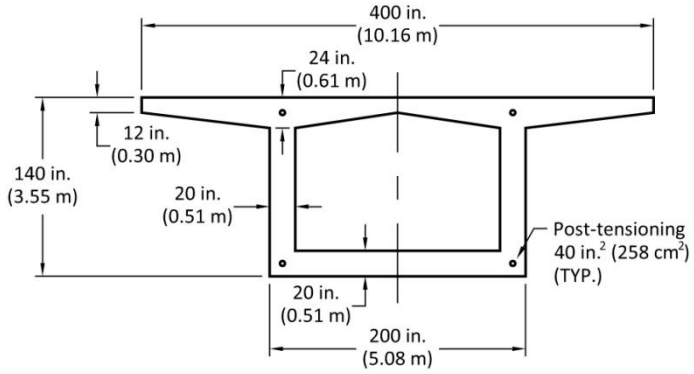

Figure 9.3: Cross section of test case box beam for investigating thermal effects

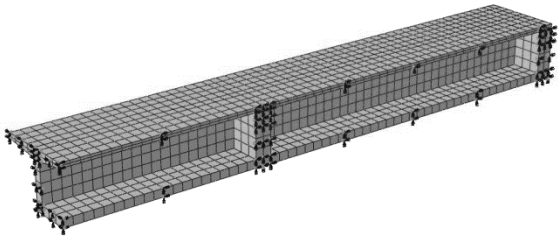

Figure 9.4: Finite element model of test case box beam for investigating interaction between temperature and time-dependent behavior

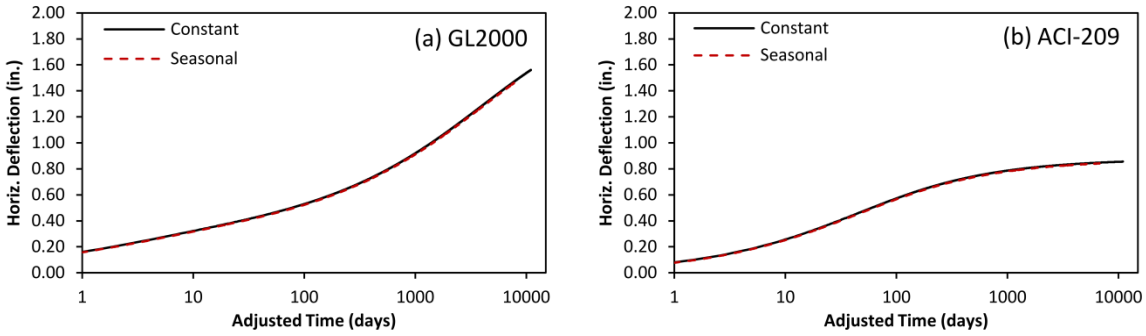

Figure 9.5: Time-dependent longitudinal deflections for investigation of impacts of uniform seasonal temperature changes using Constant and Seasonal temperature histories

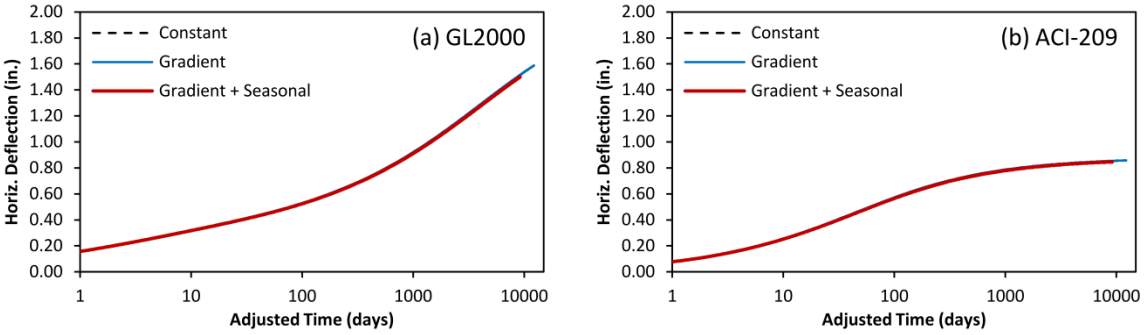

Figure 9.6: Time-dependent longitudinal deflections for investigation of impacts of cyclic thermal gradients using Constant, Winter Gradient, and Winter Gradient Plus Seasonal temperature histories

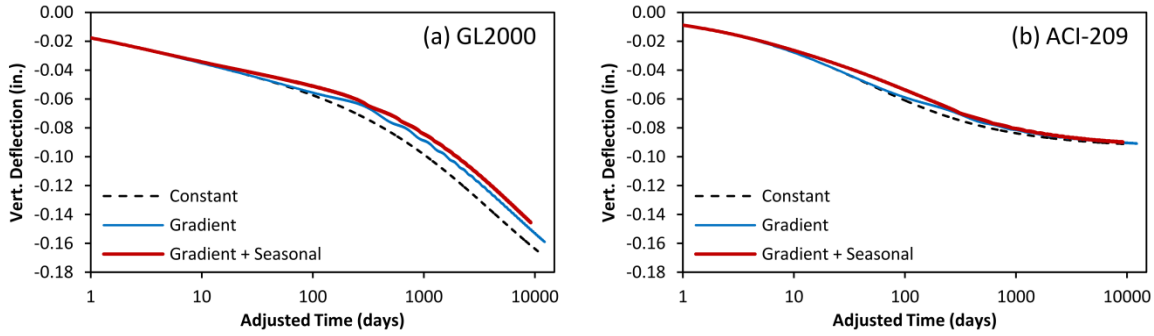

Figure 9.7: Time-dependent vertical deflections for investigation of impacts of cyclic thermal gradients using Constant, Winter Gradient, and Winter Gradient Plus Seasonal temperature histories

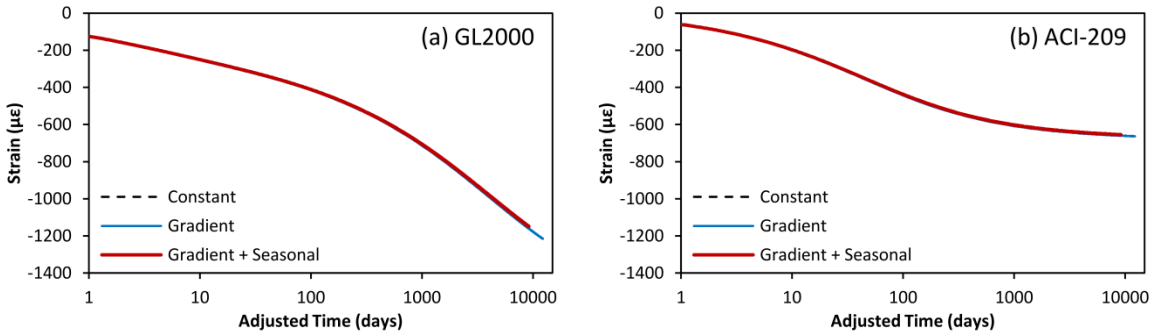

Figure 9.8: Time-dependent top fiber strains for investigation of impacts of cyclic thermal gradients using Constant, Winter Gradient, and Winter Gradient Plus Seasonal temperature histories

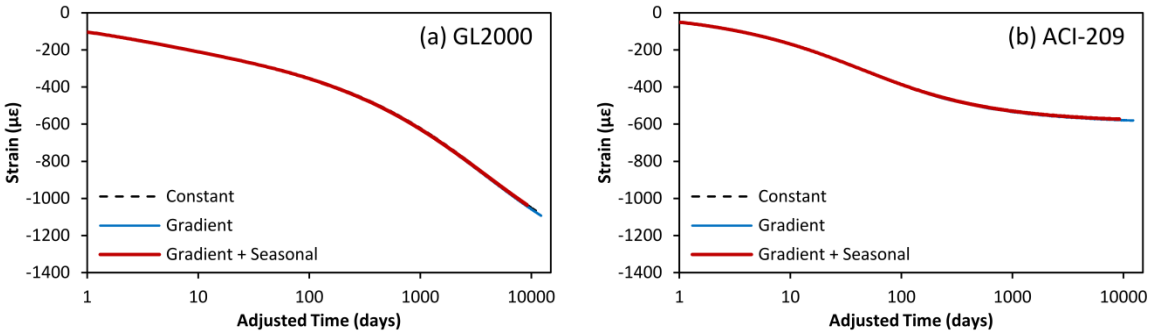

Figure 9.9: Time-dependent bottom fiber strains for investigation of impacts of cyclic thermal gradients using Constant, Winter Gradient, and Winter Gradient Plus Seasonal temperature histories

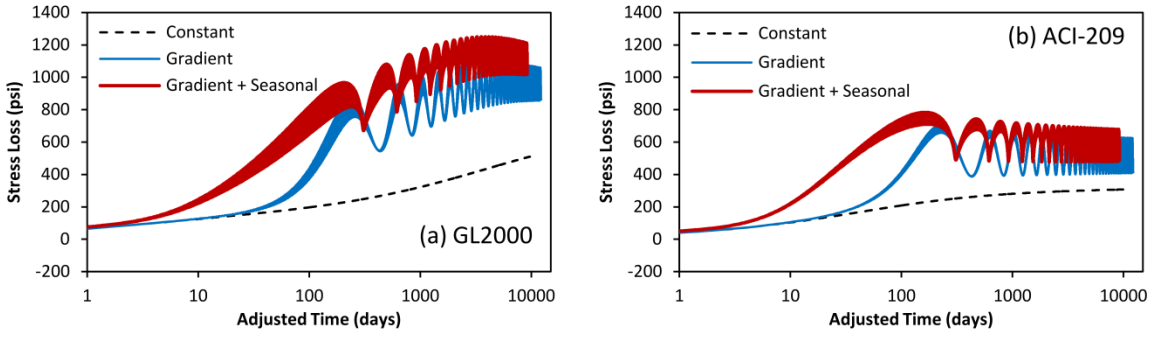

Figure 9.10: Time-dependent top fiber stress losses for investigation of impacts of cyclic thermal gradients using Constant, Winter Gradient, and Winter Gradient Plus Seasonal temperature histories

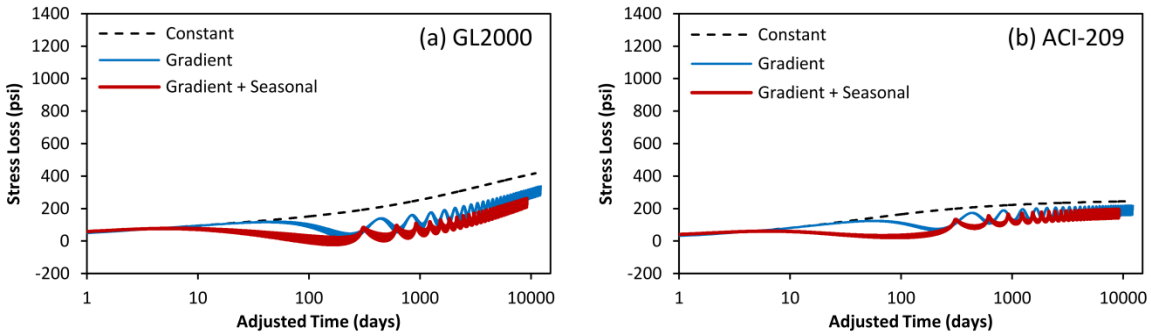

Figure 9.11: Time-dependent bottom fiber stress losses for investigation of impacts of cyclic thermal gradients using Constant, Winter Gradient, and Winter Gradient Plus Seasonal temperature histories

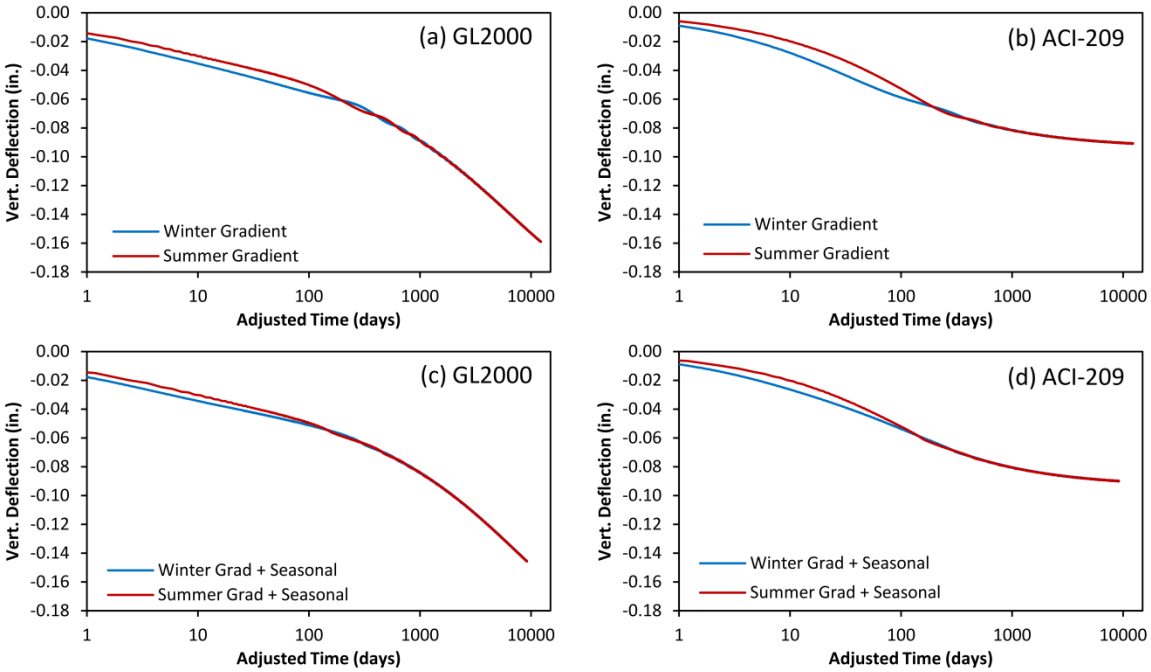

Figure 9.12: Time-dependent vertical deflections for investigation of impacts of construction season using Winter Gradient, Summer Gradient, Winter Gradient Plus Seasonal, and Summer Gradient Plus Seasonal temperature histories

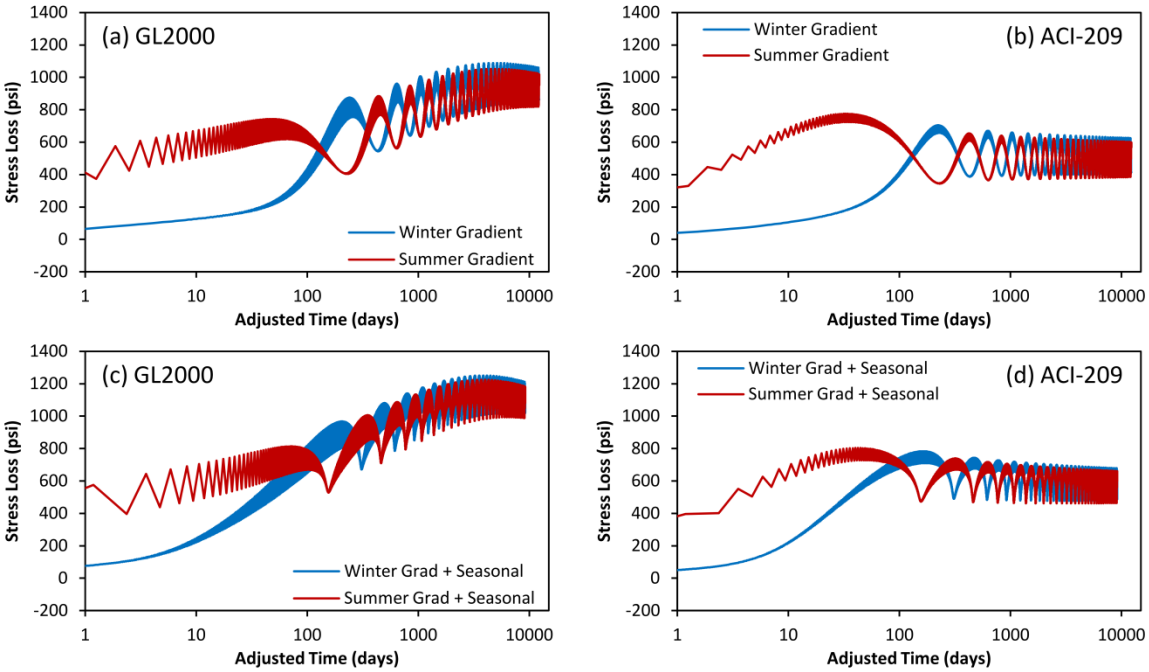

Figure 9.13: Time-dependent top fiber stress losses for investigation of impacts of construction season using Winter Gradient, Summer Gradient, Winter Gradient Plus Seasonal, and Summer Gradient Plus Seasonal temperature histories

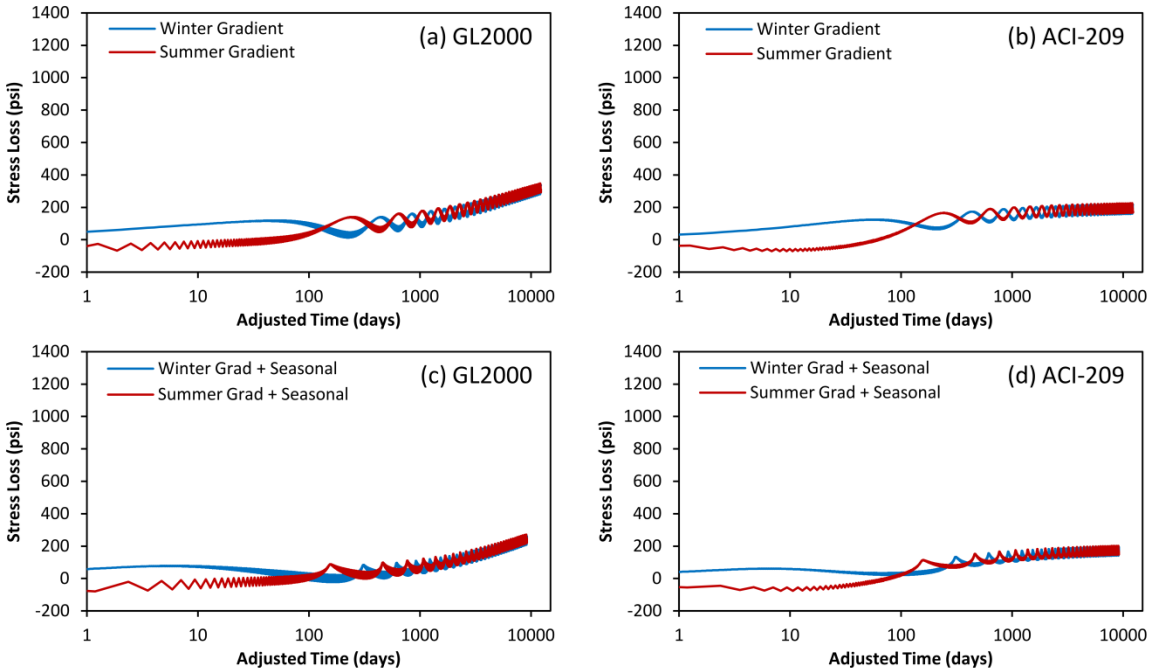

Figure 9.14: Time-dependent bottom fiber stress losses for investigation of impacts of construction season using Winter Gradient, Summer Gradient, Winter Gradient Plus Seasonal, and Summer Gradient Plus Seasonal temperature histories

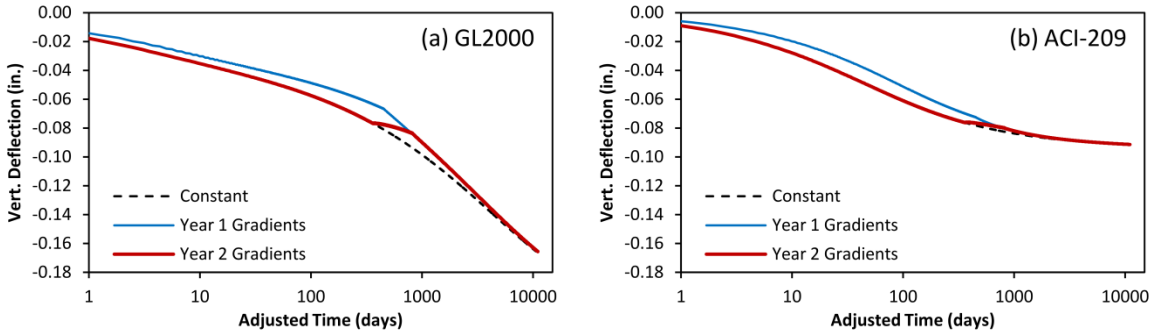

Figure 9.15: Time-dependent vertical deflections for investigation of temporary cyclic gradients on long-term behavior using Year 1 Gradient and Year 2 Gradient temperature histories

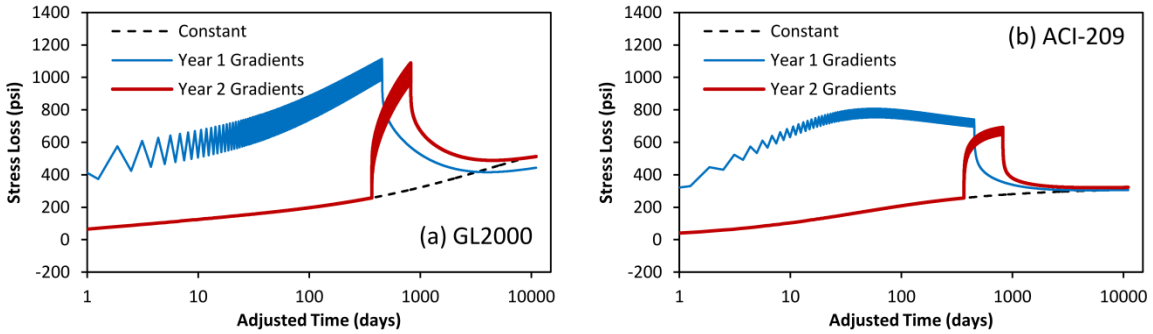

Figure 9.16: Time-dependent top fiber stress losses for investigation of temporary cyclic gradients on long-term behavior using Year 1 Gradient and Year 2 Gradient temperature histories

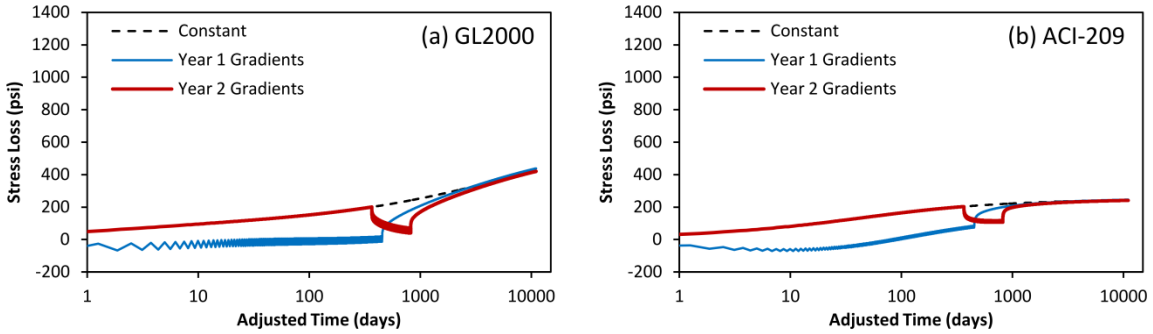

Figure 9.17: Time-dependent bottom fiber stress losses for investigation of temporary cyclic gradients on long-term behavior using Year 1 Gradient and Year 2 Gradient temperature histories

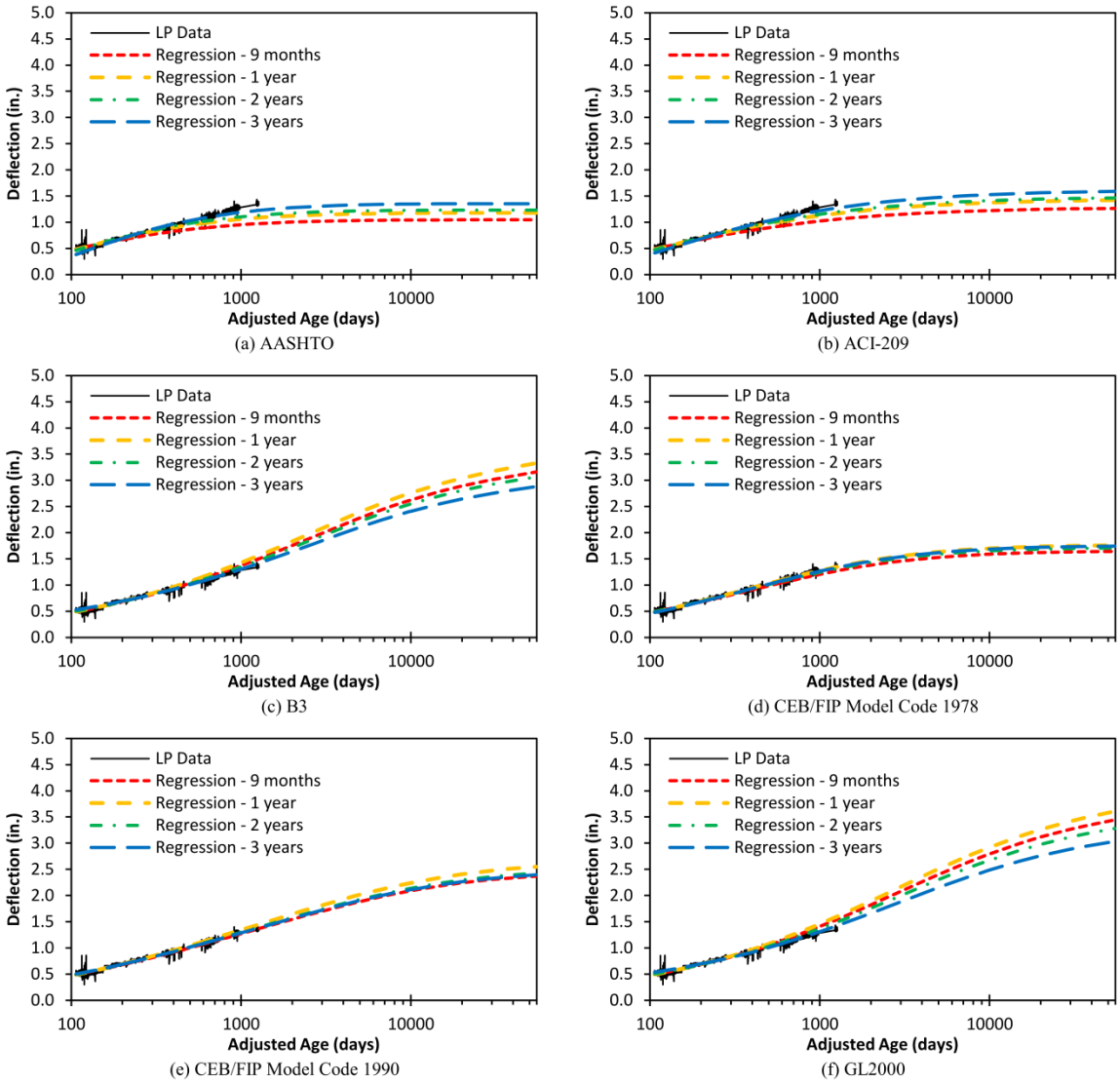

Figure 10.1: Bayesian regression of time-dependent linear potentiometer data from southbound bridge Span 1

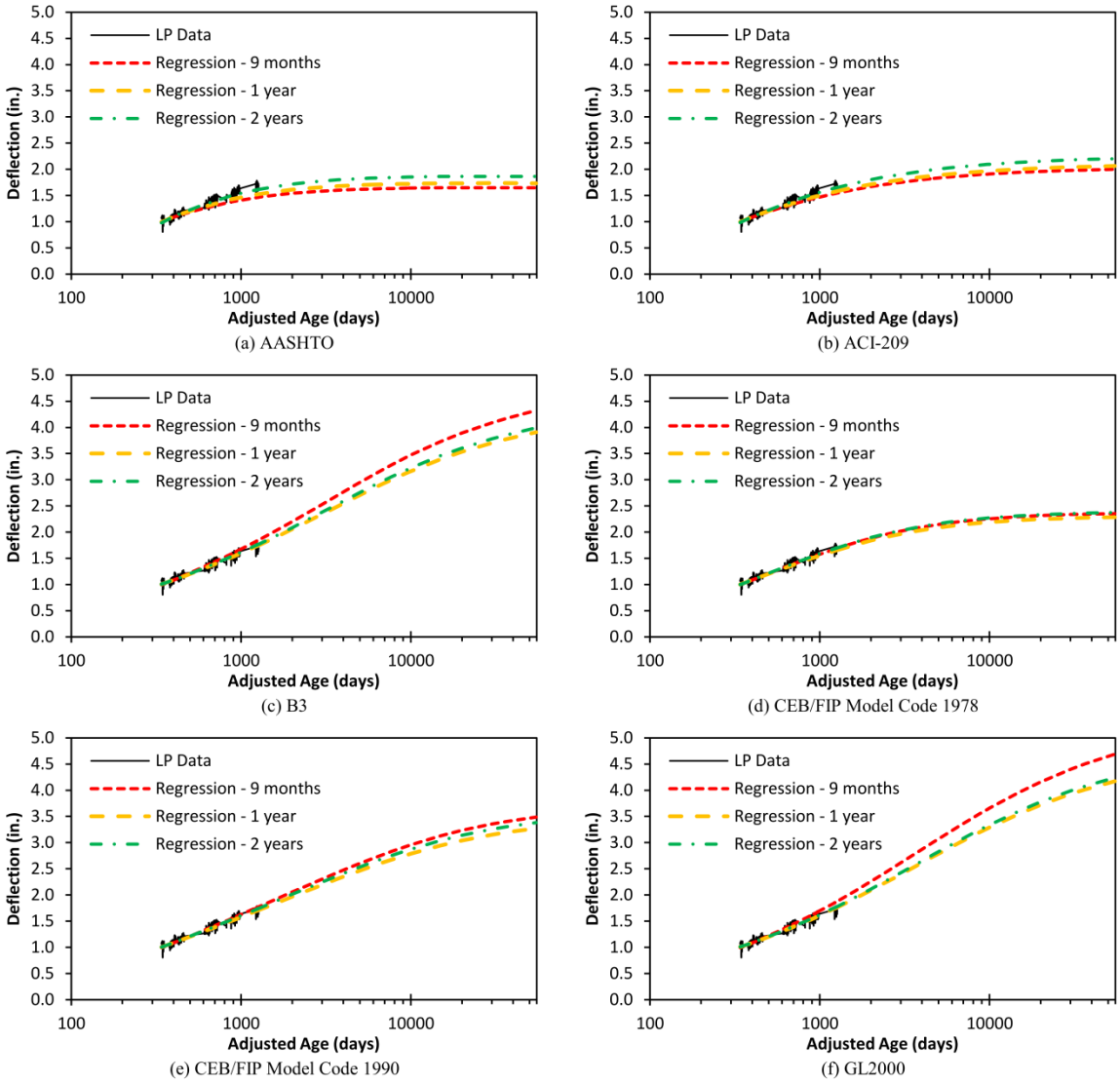

Figure 10.2: Bayesian regression of time-dependent linear potentiometer data from southbound bridge Span 3

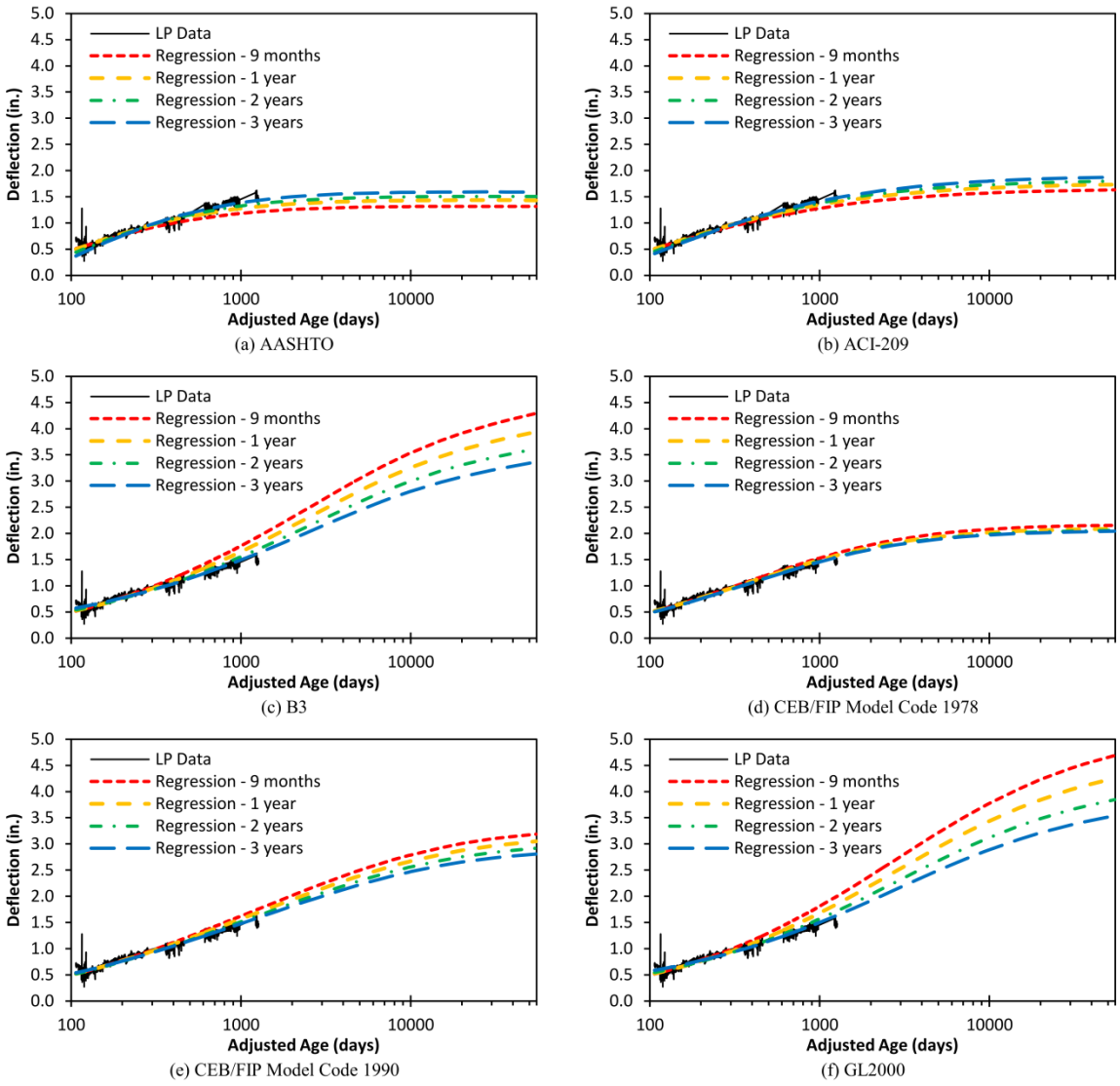

Figure 10.3: Bayesian regression of time-dependent linear potentiometer data from northbound bridge Span 1

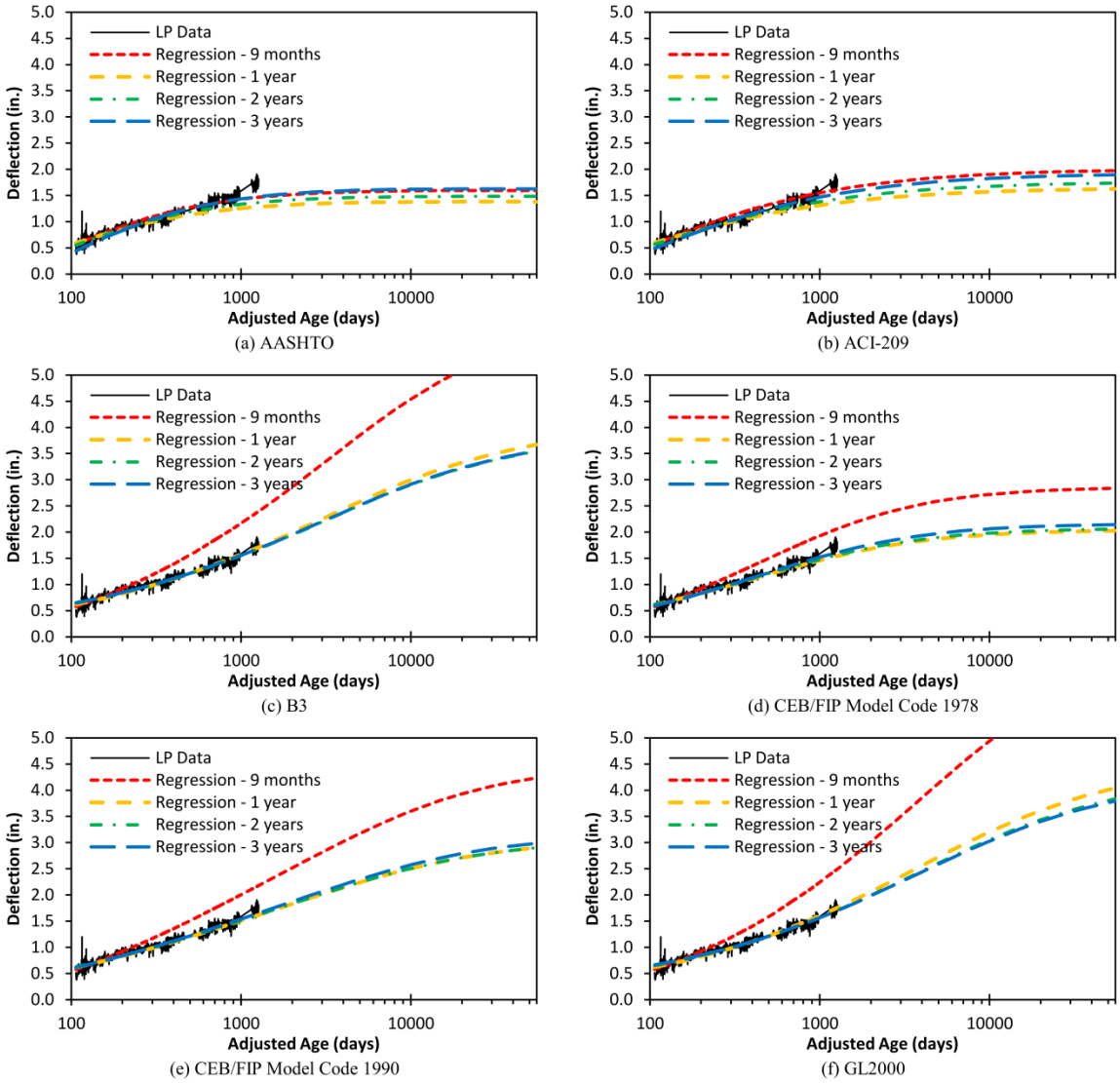

Figure 10.4: Bayesian regression of time-dependent linear potentiometer data from northbound bridge Span 3

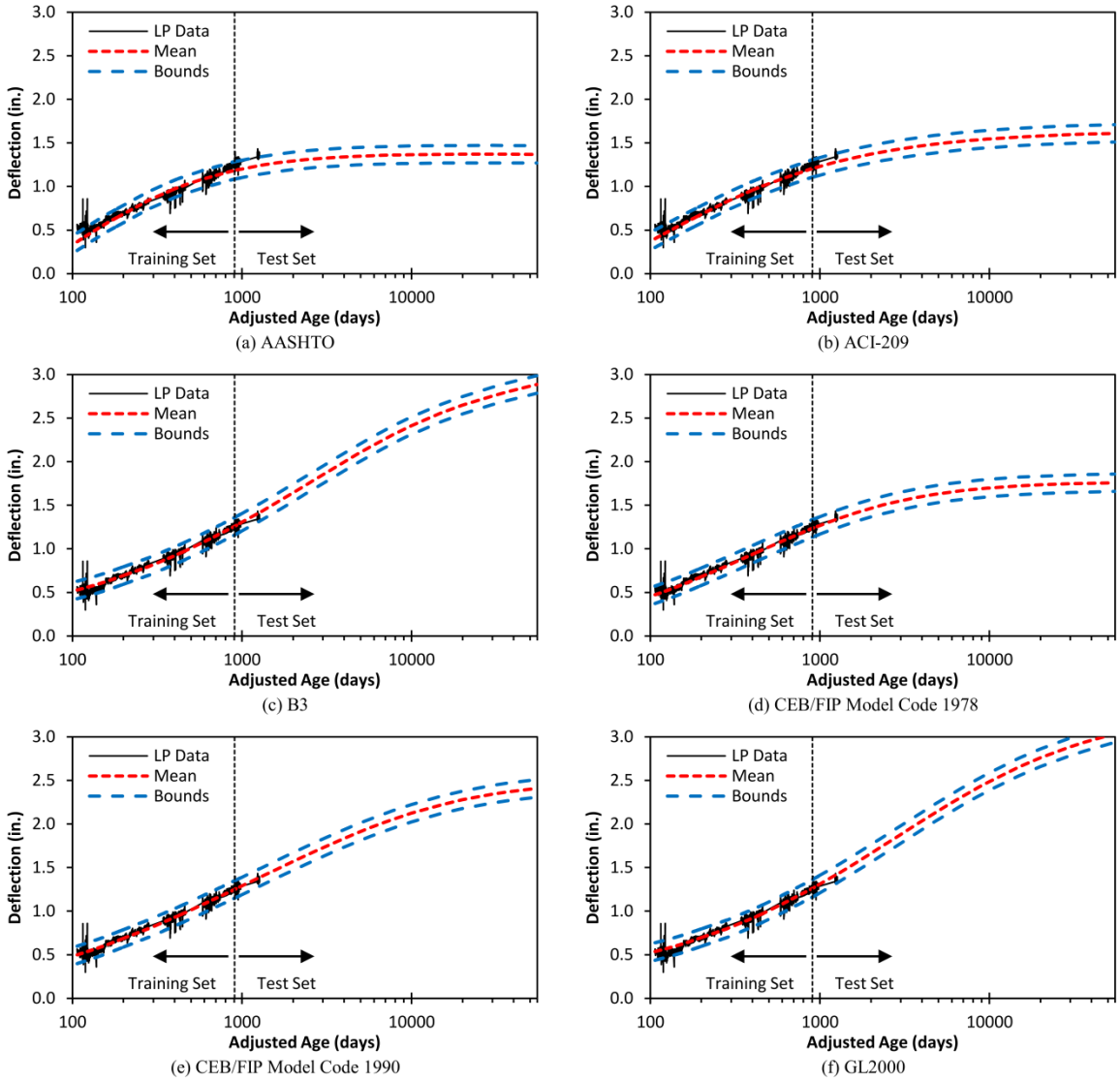

Figure 10.5: Mean estimates and 95%-credible intervals using Bayesian regression of time-dependent linear potentiometer data from southbound bridge Span 1

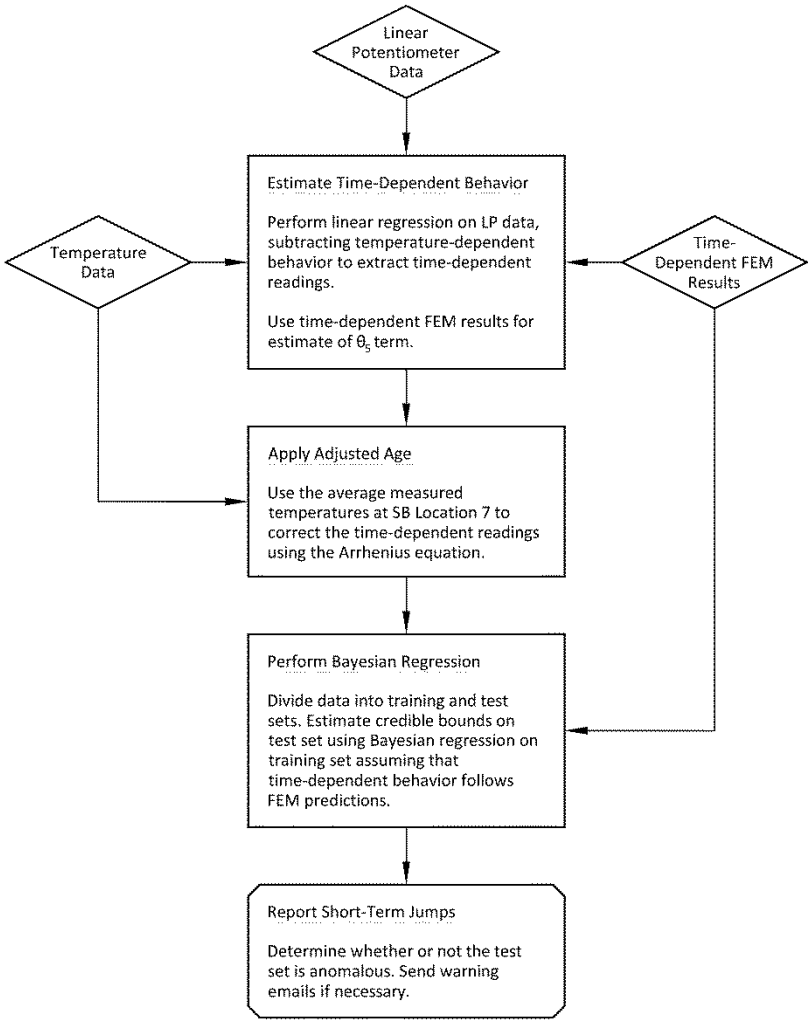

Figure 10.6: Summary of short-term anomaly detection routine for linear potentiometer data

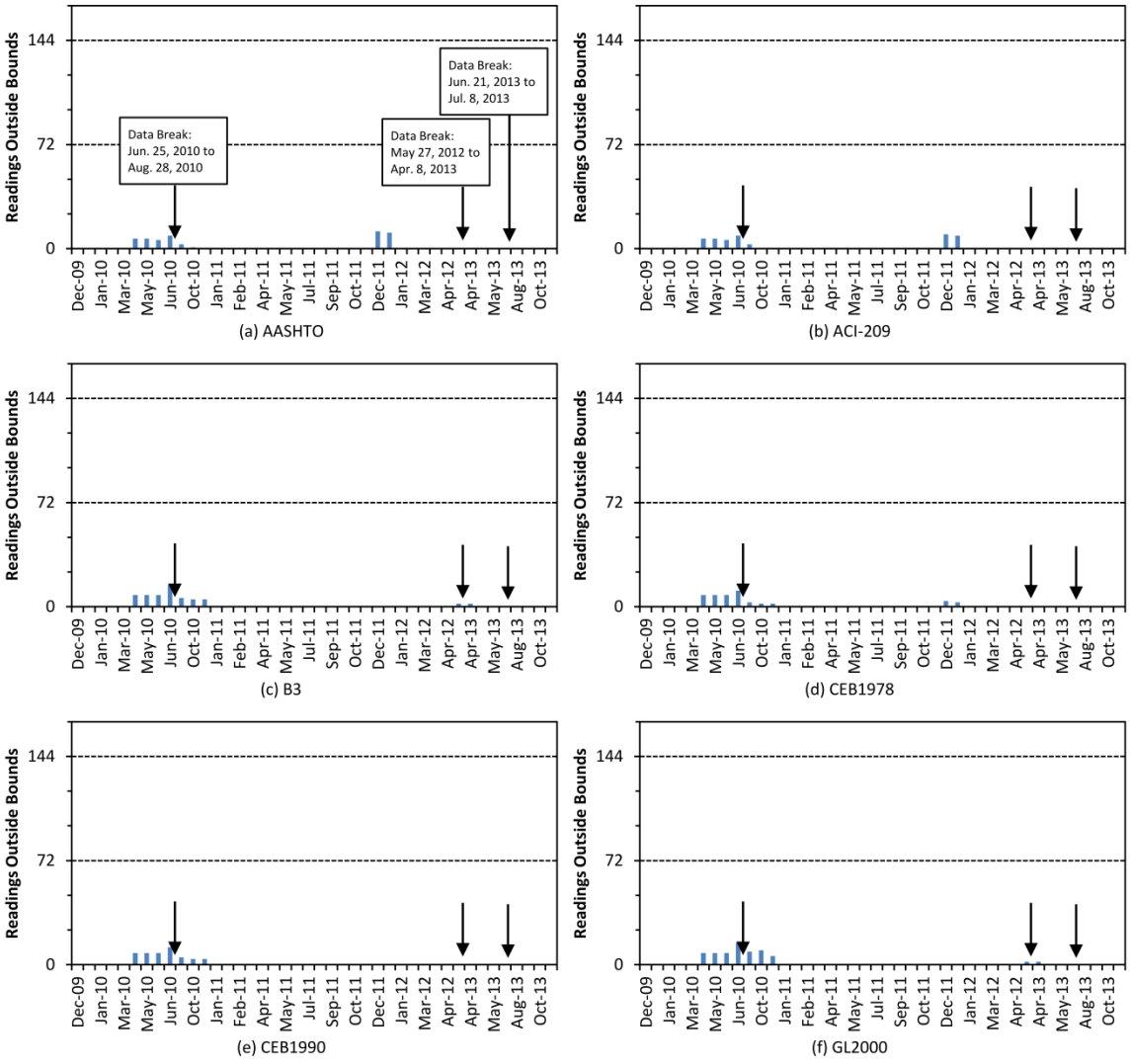

Figure 10.7: Quantity of readings outside 99%-credible interval for test sets extracted from southbound bridge Span 1 linear potentiometer data checked using Bayesian regression

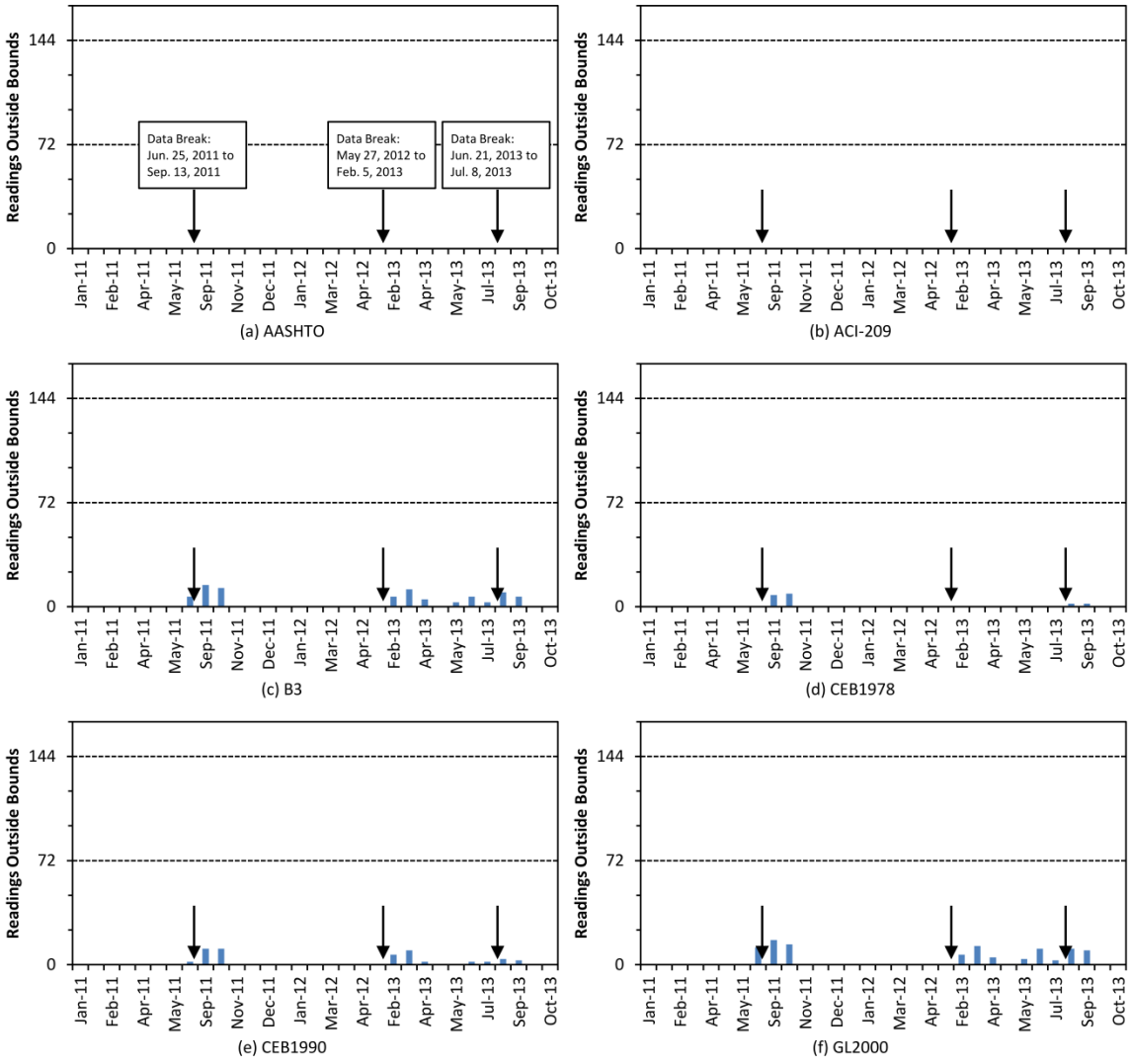

Figure 10.8: Quantity of readings outside 99%-credible interval for test sets extracted from southbound bridge Span 3 linear potentiometer data checked using Bayesian regression

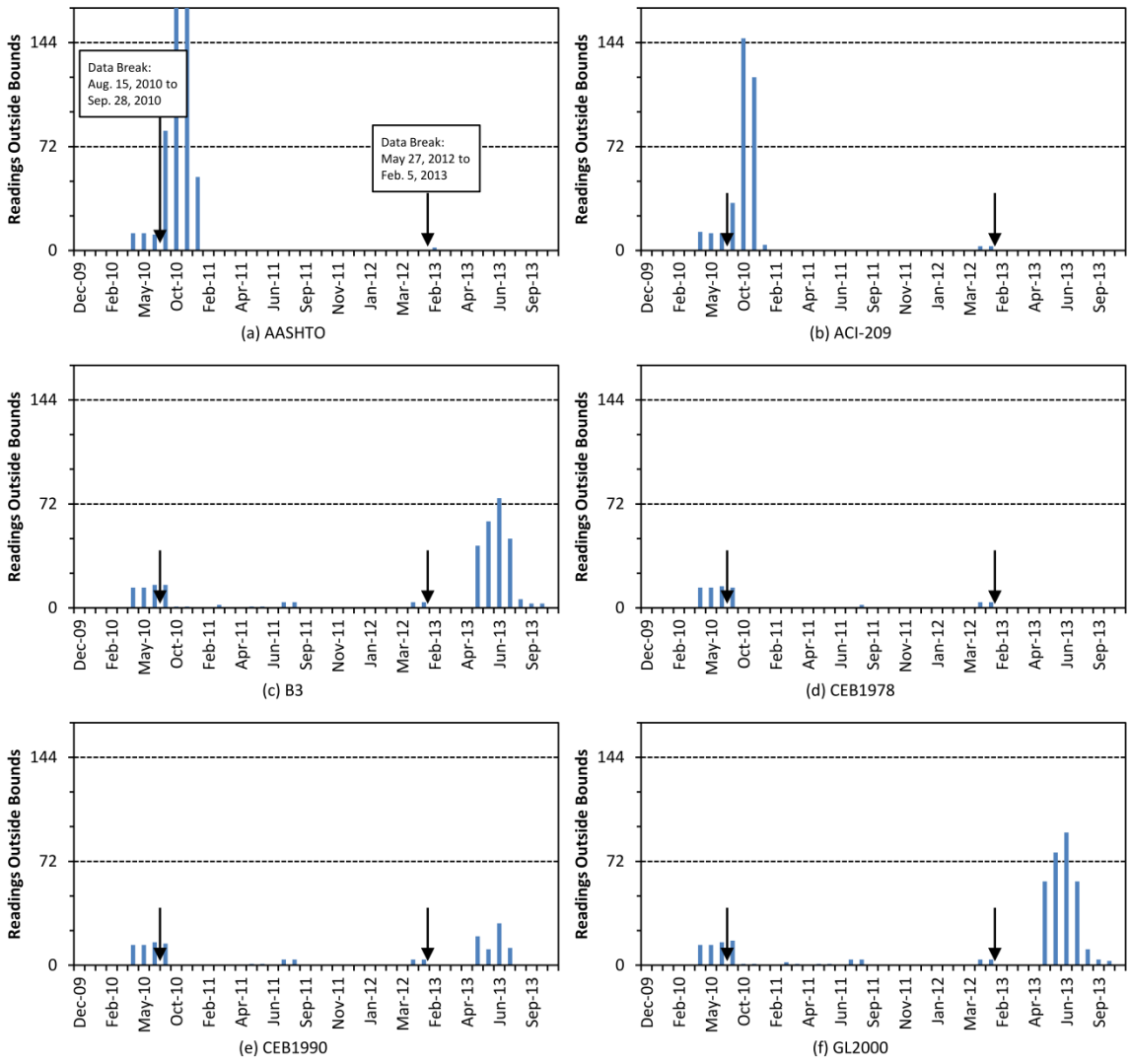

Figure 10.9: Quantity of readings outside 99%-credible interval for test sets extracted from northbound bridge Span 1 linear potentiometer data checked using Bayesian regression

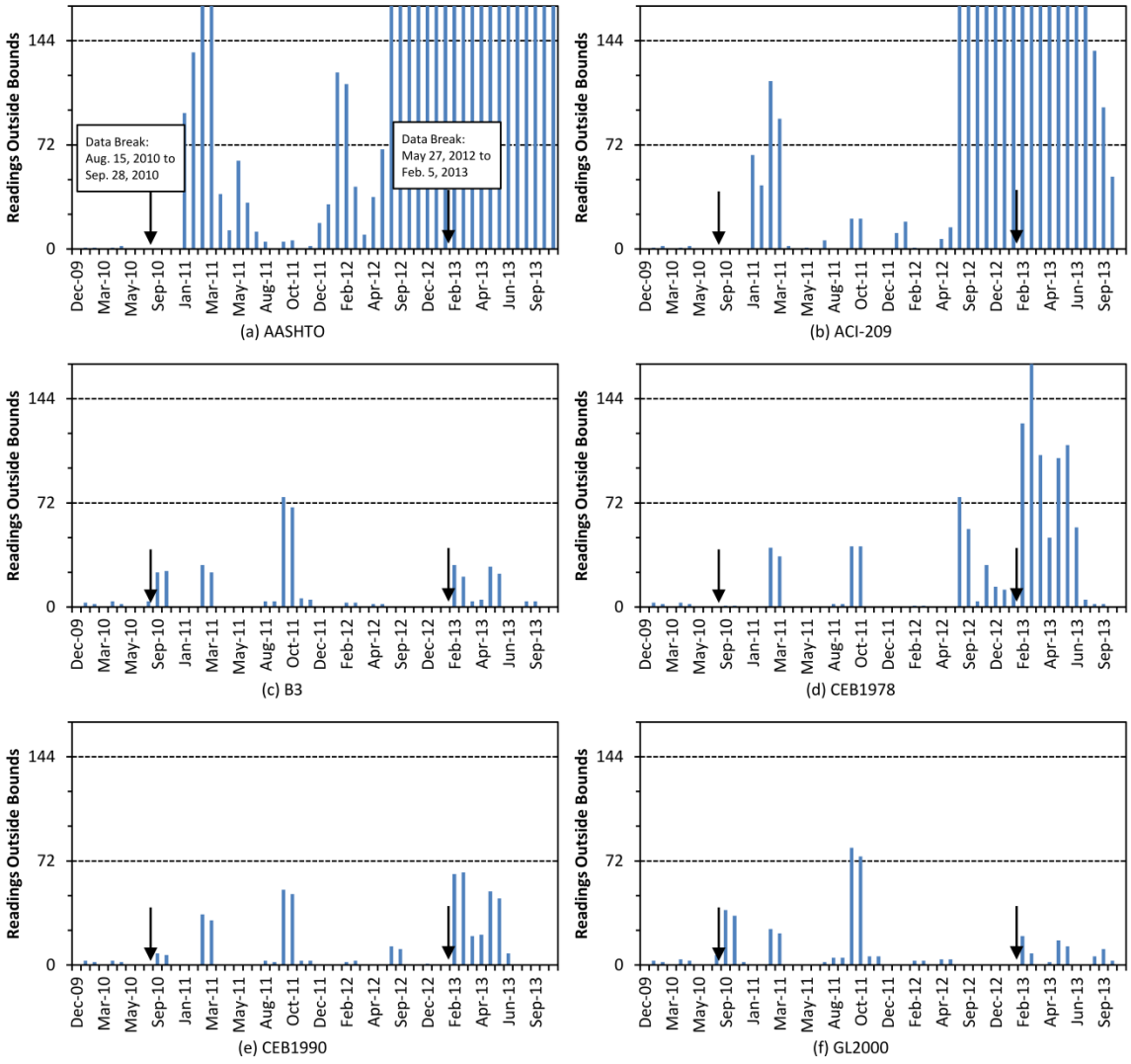

Figure 10.10: Quantity of readings outside 99%-credible interval for test sets extracted from northbound bridge Span 3 linear potentiometer data checked using Bayesian regression

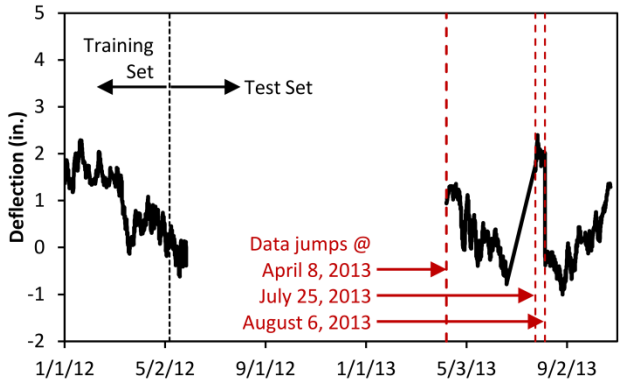

Figure 10.11: Southbound bridge Span 1 linear potentiometer data from January 1, 2012 to October 24, 2013 showing times of data jumps caused by sensor replacement

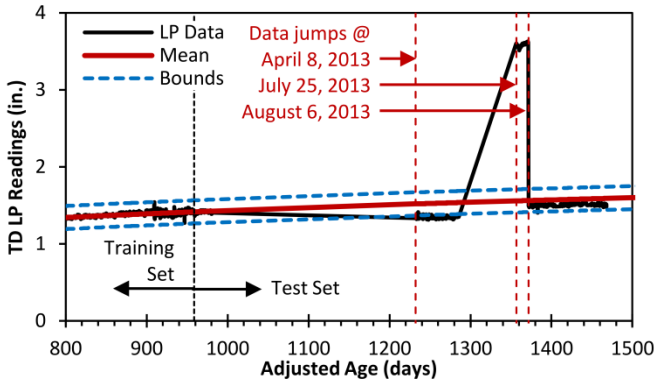

Figure 10.12: Time-dependent southbound bridge Span 1 linear potentiometer data with sensor replacement data jumps at April 8, 2013, July 25, 2013, and August 6, 2013 (1,232, 1,356, and 1,371 adjusted age days, respectively) left uncorrected. Mean and bounds computed using Bayesian regression with 1990 CEB/FIP Model Code model.

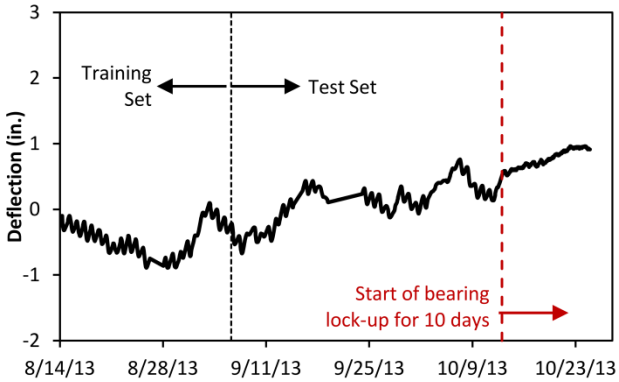

Figure 10.13: Tests set for southbound bridge Span 1 linear potentiometer data including perturbation emulating bearing lockup on exterior box sensor

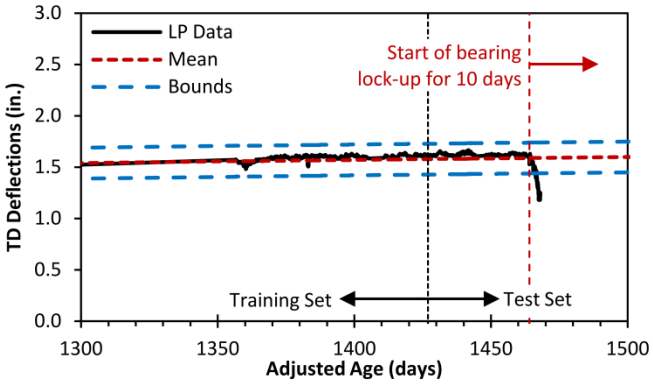

Figure 10.14: Time-dependent southbound bridge Span 1 linear potentiometer data with perturbation emulating bearing lockup on exterior box sensor. Mean and bounds computed using Bayesian regression with 1990 CEB/FIP Model Code model.

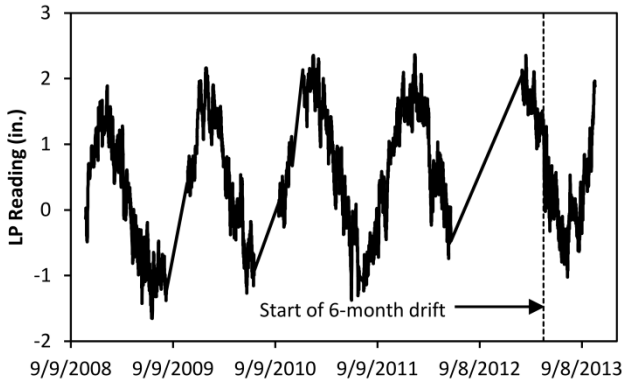

Figure 10.15: Northbound bridge Span 1 linear potentiometer readings including six-month drift of 0.5 in. (13 mm) beginning at April 24, 2013

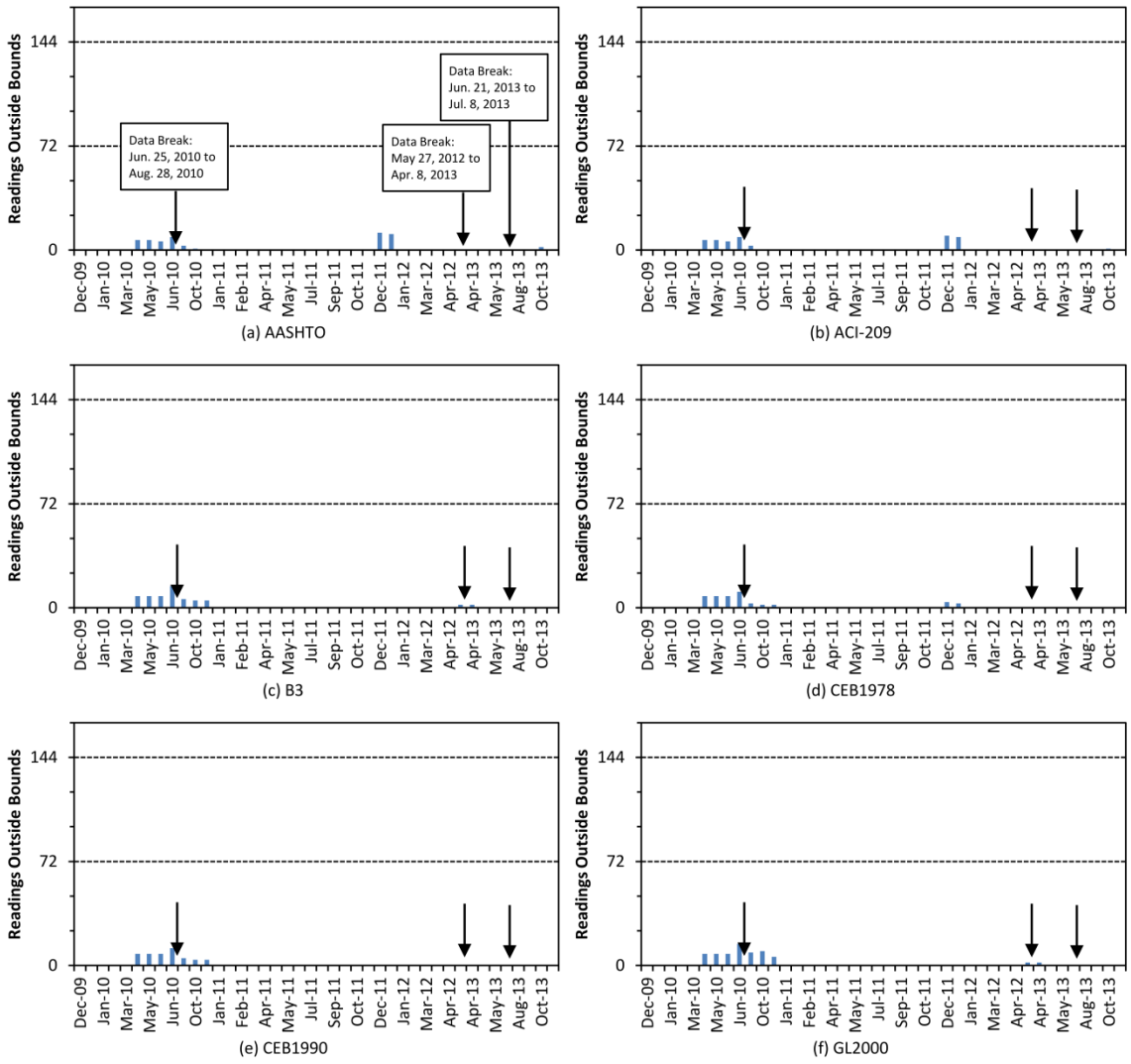

Figure 10.16: Quantity of readings outside 99%-credible interval for test sets extracted from southbound bridge Span 1 linear potentiometer data with six-month drift of 0.5 in. (13 mm) beginning at April 24, 2013 checked using Bayesian regression

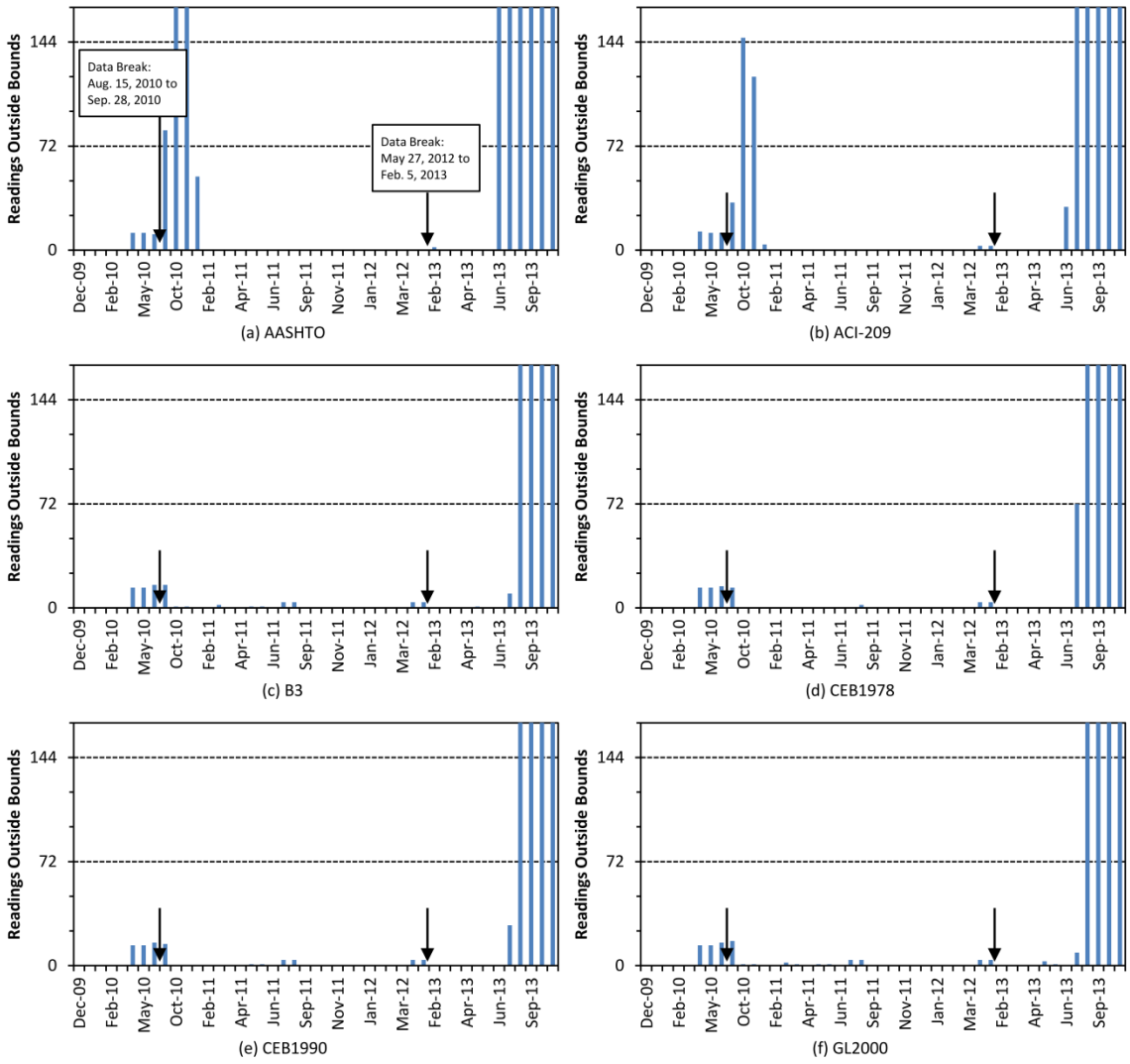

Figure 10.17: Quantity of readings outside 99%-credible interval for test sets extracted from northbound bridge Span 1 linear potentiometer data with six-month drift of 0.5 in. (13 mm) beginning at April 24, 2013 checked using Bayesian regression

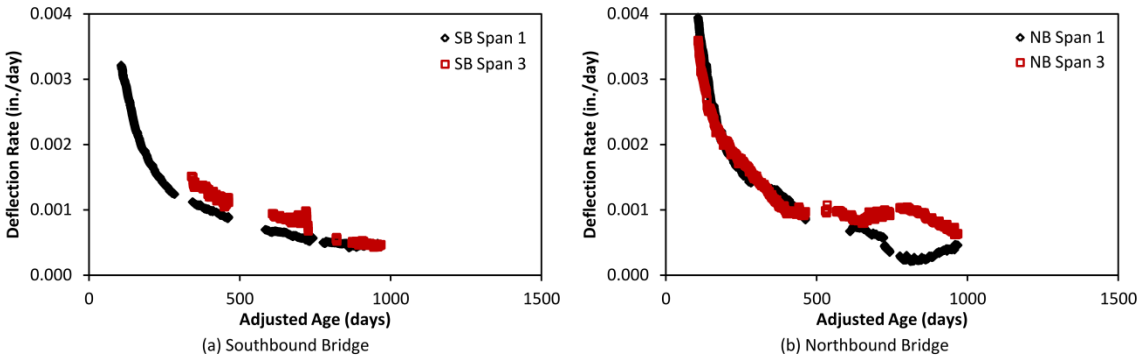

Figure 10.18: Adjusted-age rate of time-dependent deflections at expansion joints plotted with respect to adjusted age

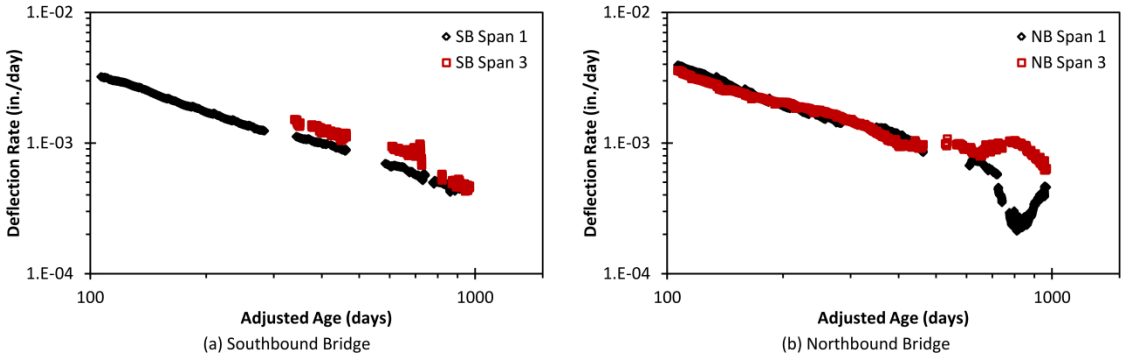

Figure 10.19: Adjusted-age rate of time-dependent deflections at expansion joints plotted with respect to adjusted age in log-log space

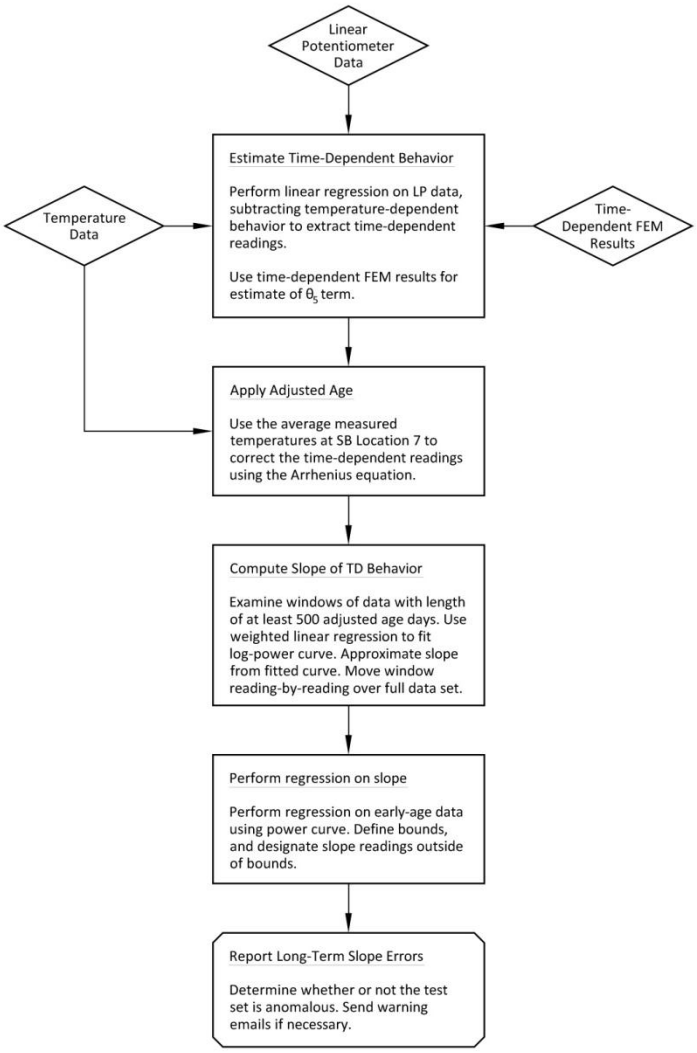

Figure 10.20: Summary of long-term anomaly detection routine for linear potentiometer data

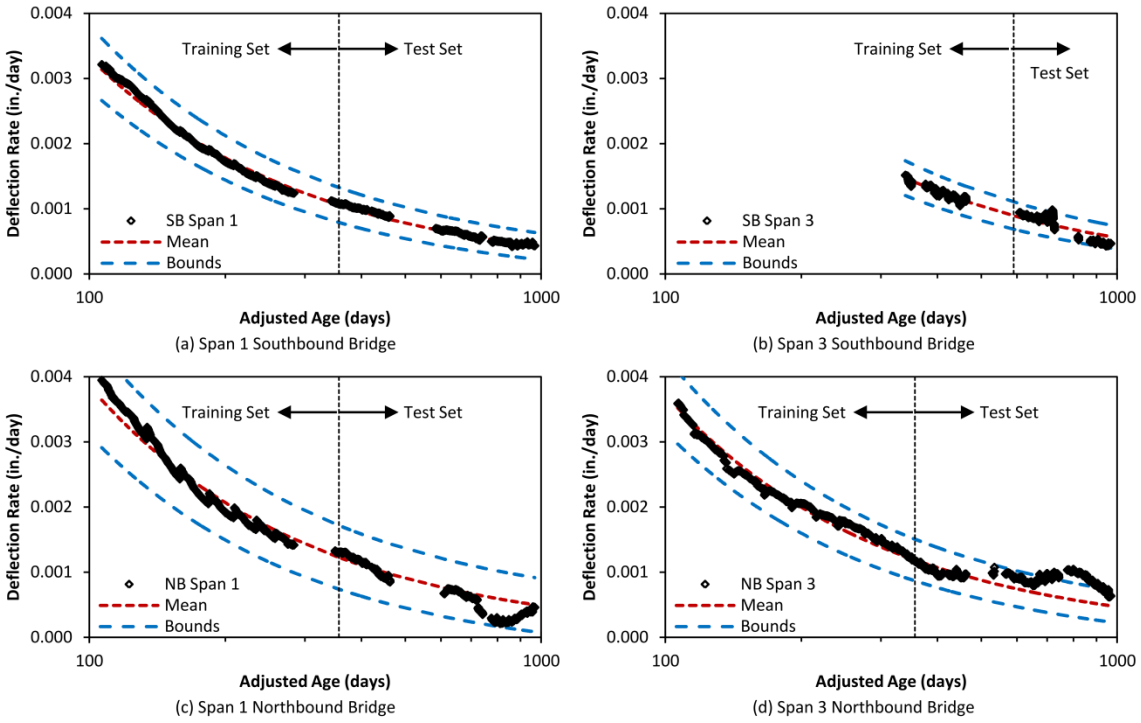

Figure 10.21: Long-term anomaly detection routine validated using measured linear potentiometer data

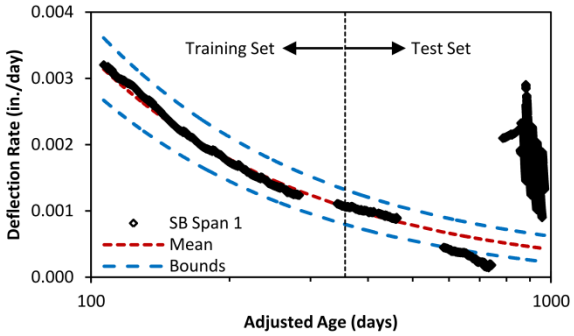

Figure 10.22: Long-term anomaly detection routine applied to southbound bridge Span 1 linear potentiometer data with sensor replacement data jumps left uncorrected

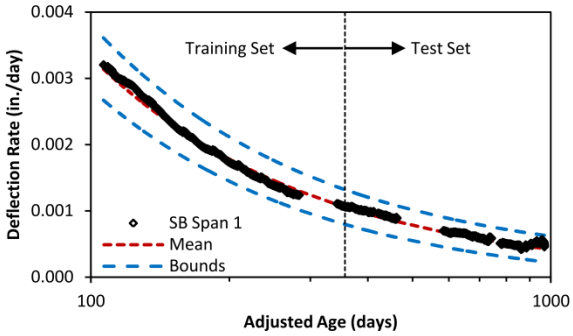

Figure 10.23: Long-term anomaly detection routine applied to southbound bridge Span 1 linear potentiometer data with added perturbation associated with bearing lockup introduced at October 13, 2013 until the end of collection at October 24, 2013

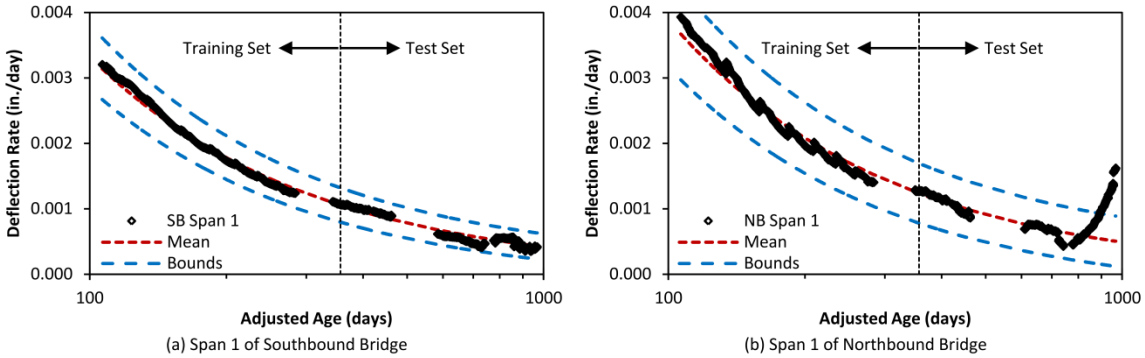

Figure 10.24: Long-term anomaly detection routine applied to (a) southbound bridge Span 1 and (b) northbound bridge Span 1 linear potentiometer data with six-month linear drift of 0.5 in. (13 mm) introduced at April 24, 2013 until the end of collection at October 24, 2013

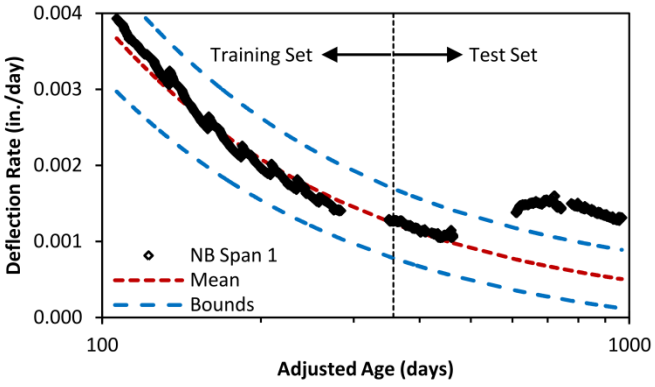

Figure 10.25: Long-term anomaly detection routine applied to northbound bridge Span 1 linear potentiometer data with two-year linear drift of 0.5 in. (13 mm) introduced at October 24, 2011 until the end of collection at October 24, 2013

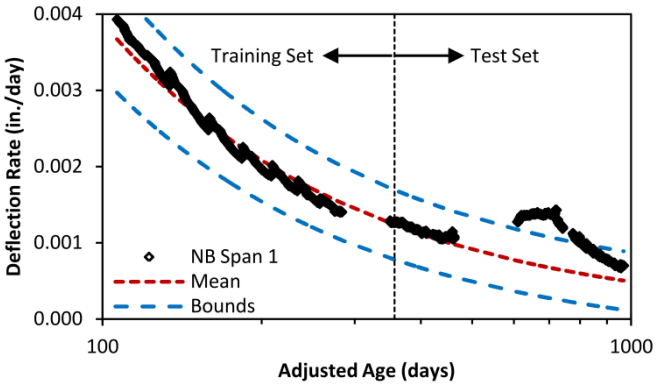

Figure 10.26: Long-term anomaly detection routine applied to northbound bridge Span 1 linear potentiometer data with one-year linear drift of 0.25 in. (6 mm) introduced at October 24, 2011 until October 24, 2012

References

1. ACI Committee 209 (1982). *ACI 209R-82 Prediction of Creep, Shrinkage, and Temperature Effects in Concrete Structures*, American Concrete Institute, Detroit, MI.
2. ACI Committee 209 (1992). *ACI 209R-92 Prediction of Creep, Shrinkage, and Temperature Effects in Concrete Structures*, American Concrete Institute, Detroit, MI.
3. American Association of State Highway and Transportation Officials (1998). *AASHTO LRFD Bridge Design Specifications*, Second Edition, Washington, DC.
4. American Association of State Highway and Transportation Officials (2010). *AASHTO LRFD Bridge Design Specifications*, Fifth Edition, Washington, DC.
5. American Concrete Institute (2008). *Building Code Requirements for Structural Concrete (ACI 318-08) and Commentary*, Second Printing, Farmington Hills, MI.
6. Bažant, Z.P. (1982). "Mathematical Models for Creep and Shrinkage of Concrete," *Creep and Shrinkage in Concrete Structures*, Z.P. Bažant and F.H. Wittmann, eds., John Wiley and Sons, New York, NY, pp. 163-258.
7. Bažant, Z.P., and Baweja, S. (1995a). "Creep and Shrinkage Prediction Model for Analysis and Design of Concrete Structures – Model B3," *Materials and Structures*, Vol. 28, pp. 357-365.
8. Bažant, Z.P., and Baweja, S. (1995b). "Justification and refinements of model B3 for concrete creep and shrinkage: 1. Statistics and sensitivity," *Materials and Structures*, Vol. 28, pp. 415-430.
9. Bažant, Z.P., and Baweja, S. (1996). "Short form of creep and shrinkage prediction model B3 for structures of medium sensitivity," *Materials and Structures*, Vol. 29, No. 194, pp. 587-593.

10. Bažant, Z.P., and Kim, J.-K. (1992). "Improved prediction model for time-dependent deformations of concrete: Part 4 – temperature effects," *Materials and Structures*, Vol. 25, pp. 84-94.
11. Bažant, Z.P., Kim, J.-K., and Panula, L. (1991). "Improved prediction model for time-dependent deformations of concrete: part 1 – shrinkage," *Materials and Structures*, Vol. 24, pp. 327-345.
12. Bažant, Z.P., and Li, G.-H. (2008a). "Comprehensive database on concrete creep and shrinkage," *Structural Engineering Report No. 08-3/A210c*, Infrastructure Technology Institute, Northwestern University, Evanston, IL.
13. Bažant, Z.P., and Li, G.-H. (2008b). "Unbiased statistical comparison of creep and shrinkage prediction models," *ACI Materials Journal*, Vol. 105, No. 6., pp. 610-621.
14. Bažant, Z.P., and Prasannan, S. (1989a). "Solidification Theory for Concrete Creep. I: Formulation," *Journal of Engineering Mechanics*, Vol. 115, No. 8, pp. 1691-1703.
15. Bažant, Z.P., and Prasannan, S. (1989b). "Solidification Theory for Concrete Creep. II: Verification and Application," *Journal of Engineering Mechanics*, Vol. 115, No. 8, pp. 1704-1725.
16. Bažant, Z.P., and Xi, Y. (1995). "Continuous Retardation Spectrum for Solidification Theory of Concrete Creep," *Journal of Engineering Mechanics*, Vol. 121, No. 2, pp. 281-288.
17. Bažant, Z.P., Cusatis, G., and Cedolin, L. (2004). "Temperature effect on concrete creep modeled by microprestress-solidification theory," *Journal of Engineering Mechanics*, Vol. 130, No. 6, pp. 691-699.
18. Bažant, Z.P., Yu, Q., and Li, G.-H., (2009). "Excessive Long-Time Deflections of Prestressed Box Girders," *Structural Engineering Report No. 09-12/ITI*, Infrastructure Technology Institute, Northwestern University. Revised July 26, 2010.

19. Bažant, Z.P., Yu, Q., Li, G.-H., Klein, G.J., and Křístek, V. (2010), "Excessive deflections of record-span prestressed box girder: Lessons learned from the collapse of the Koror-Babeldaob Bridge in Palau," *ACI Concrete International*, Vol. 32, No. 6, pp. 44-52.
20. Bernardo, J.M. (2001). "Bayesian Statistics." *Encyclopedia of Life Support Systems*, UNESCO.
21. Branson, D.E., and Christiason, M.L. (1971). "Time-dependent concrete properties related to design – Strength and elastic properties, creep and shrinkage," *ACI Special Publication 27-13*, pp. 257-277.
22. Cohen, A.M. (2007). "The Post-Widder Inversion Formula." *Numerical Methods for Laplace Transform Inversion*, C. Brezinski, ed., Springer Science+Business Media, LLC, New York, NY, pp. 37-39.
23. Comité Euro-International du Béton (CEB) and the Fédération International de la Précontrainte (FIP) (1978). *1978 CEB/FIP model code*.
24. Comité Euro-International du Béton (CEB) and the Fédération International de la Précontrainte (FIP) (1990). *1990 CEB/FIP model code*.
25. Dassault Systèmes (2010a). "Abaqus," *SIMULIA*. Providence, RI.
26. Dassault Systèmes (2010b). "Element and contact pair removal and reactivation," *Abaqus Analysis User's Manual*, version 6.10.
27. Dassault Systèmes (2010c). "Nonlinear solution methods in Abaqus/Standard," *Abaqus Theory Manual*, version 6.10.
28. Day, R.L., and Gamble, B.R. (1983). "The effect of changes in structure on the activation energy for the creep of concrete," *Cement and Concrete Research*, Vol. 13, pp. 529-540.
29. Emanuel, J.H., and Hulsey, J.L. (1977). "Prediction of the thermal coefficient of expansion of concrete," *ACI Journal*, Vol. 74, No. 4, pp. 149-155.

30. Figg Bridge Engineers (2008). *St. Anthony Falls (I-35W) Bridge Erection Manual*, Figg Project Number 1665.
31. French, C.E.W., Shield, C.K., Stolarski, H.K., Hedegaard, B.D., and Jilk, B.J. (2012). "Instrumentation, Monitoring, and Modeling of the I-35W Bridge," *Report MN/RC 2012-24*, Minnesota Dept. of Transportation, St. Paul.
32. Gardner, N.J. (2000). "Design Provisions for Shrinkage and Creep of Concrete," *ACI Special Publication 194-3, The Adam Neville Symposium: Creep and Shrinkage – Structural Design Effects*, pp. 101-134.
33. Gardner, N.J. (2004). "Comparison of prediction provisions for drying shrinkage and creep of normal-strength concretes," *Canadian Journal of Civil Engineering*, Vol. 31, No. 5, pp. 767-775.
34. Gardner, N.J., and Lockman, M.J. (2001). "Design Provisions for Drying Shrinkage and Creep of Normal-Strength Concrete," *ACI Materials Journal*, Vol. 98, No. 2, pp. 159-167.
35. Gardner, N.J., and Zhao, J.W. (1993). "Creep and shrinkage revisited," *ACI Materials Journal*, Vol. 90, No. 3, pp. 236-246.
36. Goel, R., Kumar, R., and Paul, D.K. (2007). "Comparative study of various creep and shrinkage prediction models for concrete," *Journal of Materials in Civil Engineering*, Vol. 19, No. 3, pp. 249-260.
37. Grasley, Z.C., and Lange, D.A. (2007). "Thermal dilation and internal relative humidity of hardened cement paste," *Materials and Structures*, Vol. 40, No. 3, pp. 311-317.
38. Grasley, Z.C., Lange, D.A., D'Ambrosia, M.D., and Villalobos-Chapa, S. (2006). "Relative humidity in concrete," *Concrete International*, Vol. 28, pp. 51-57.
39. Hansen, T.C., and Mattock, A.H. (1966). "Influence of size and shape of member on the shrinkage and creep of concrete," *ACI Journal*, Vol. 63, No. 2, pp. 267-290.

40. Hashin, Z. (1970). “Complex moduli of viscoelastic composites – II. Fiber reinforced materials.” *International Journal of Solids and Structures*, Vol. 6, No. 6, pp. 797-807.
41. Hashin, Z. (1983). “Analysis of composite materials,” *J. Applied Mechanics*, Vol. 50, No. 2, pp. 481-505.
42. Hashin, Z., and Rosen, B.W. (1964). “The elastic moduli of fiber-reinforced materials,” *J. Applied Mechanics*, Vol. 31, No. 2, pp. 223-232.
43. Hauggaard, A.B., Damkilde, L., and Hansen, P.F. (1999). “Transitional thermal creep on early age concrete,” *Journal of Engineering Mechanics*, Vol. 125, No. 4, pp. 458-465.
44. Hedegaard, B.D., French, C.E.W., and Shield, C.K. (2013). “Investigation of thermal gradient effects in the I-35W St. Anthony Falls Bridge” *Journal of Bridge Engineering*, Vol. 18, No. 9, pp. 890-900.
45. Hill, R. (1964). "Theory of mechanical properties of fibre-strengthened materials: I. Elastic behaviour." *Journal of the Mechanics and Physics of Solids*, Vol. 12, No. 4, pp. 199-212.
46. Hilsdorf, H.K. (1967). “A method to estimate the water content of concrete shields,” *Nuclear Engineering and Design*, Vol. 6, No. 3, pp. 251-263.
47. Hilsdorf, H.K., and Müller, H.S. (1999). “Materials: Concrete,” *Structural Concrete – Textbook on Behaviour, Design and Performance*, Bulletin 1, International Federation for Structural Concrete, Laussane, Switzerland, pp. 21-84.
48. Hilsdorf, H.K., Müller, H.S., and Oppermann, D. (1983). “Optimization of shrinkage and creep prediction as given in the CEB/FIP Model Code 1978,” *Summary Report on the work of General Task Group 9: Appendix C*, Karlsruhe, Germany.
49. Keeton, J.R. (1965). "Study of creep in concrete," *Technical Reports R333-I, II, and III*, U.S. Naval Civil Engineering Laboratory, Port Hueneme, CA.

50. Keitel, H., and Dimmig-Osburg, A. (2010). "Uncertainty and sensitivity analysis of creep models for uncorrelated and correlated input parameters," *Engineering Structures*, Vol. 32, No. 11, pp. 3758-3767.
51. Lockman, M.J. (2000). *Compliance, Relaxation, and Creep Recovery of Normal Strength Concrete*, M.S. Thesis, University of Ottawa, Ontario, Canada.
52. Magura, D.D., Sozen, M.A., and Siess, C.P. (1964). "A study of stress relaxation in prestressing reinforcement," *PCI Journal*, Vol. 9, No. 2, pp. 13-57.
53. Maréchal, J.C. (1969). "Le fluage du béton en fonction de la température," *Materials and Structures*, Vol. 2, No. 2, pp 111-115.
54. Minnesota Department of Transportation (2008). "As-built construction plan for bridge nos. 27409 and 27410," *State Proj. 2783-120, Fed. Proj. E.R.MN07(300)*, St. Paul, MN.
55. Mola, F., and Pellegrini, L.M. (2012). "The new model for creep of concrete in FIP Model Code 2010," *Proceedings from 37th Conference on Our World in Concrete and Structures*, Singapore Concrete Institute, Singapore.
56. Müller, H.S., and Hilsdorf, H.K. (1990). *Evaluation of the time dependent behavior of concrete: summary report on the work of General Task Group 9*, Comité Euro-Internationale du Béton, Lausanne, Switzerland.
57. Müller, H.S., Küttner, C.H., and Kvitsel, V. (1999). "Creep and shrinkage models of normal and high-performance concrete: concept for a unified code-type approach," *Revue française de génie civil*, Vol. 3, Nos. 3-4, pp. 113-132.
58. Neville, A.M. (1996). *Properties of Concrete, 4th Ed.* John Wiley and Sons, New York, NY.
59. Nowak, A.S., and Szerszen, M.M. (2003). "Calibration of Design Code for Buildings (ACI 318): Part 1 – Statistical Models for Resistance," *ACI Structural Journal*, Vol. 100, No. 3, pp. 377-382.

60. Pang, X., Meyer, C., Darbe, R., and Funkhouser, G.P. (2013). "Modeling the effect of curing temperature and pressure on cement hydration kinetics," *ACI Materials Journal*, Vol. 110, No. 2, pp. 137-147.
61. Podolny, W., and Muller, J.M. (1982). *Construction and Design of Prestressed Concrete Segmental Bridges*, John Wiley and Sons, New York.
62. Precast/Prestressed Concrete Institute (2004). *PCI Design Handbook*, 6th edition, Chicago, IL.
63. Priestley, M. J. N. (1978). " Design of concrete bridges for temperature gradients," *ACI Journal*, Vol. 75, No. 5, pp. 209-217.
64. R.J. Watson, Inc. (2008). *St. Anthony Falls (I-35W) Bridge Replacement Project No. S.P.2783-120, E.R.MN07(300)*. Amherst, NY.
65. Robertson, I.N. (2005). "Prediction of vertical deflections for a long-span prestressed concrete bridge structure," *Engineering Structures*, Vol. 27, No. 12, pp. 1820-1827.
66. Roctest (2006). *Instruction Manual: Embedded Strain Gage Model EM-5*, Saint-Lambert, Quebec, Canada.
67. Ross, A.D. (1937). "Concrete creep data," *Structural Engineer*, Vol. 15, No. 8, pp. 314-326.
68. Rüsch, H., Jungwirth, D., and Hilsdorf, H.K. (1983). *Creep and Shrinkage: Their Effects on the Behavior of Concrete Structures*, Springer-Verlag, New York, NY.
69. Russell, H.G., and Larson, S.C. (1989). "Thirteen years of deformations in Water Tower Place." *ACI Structures Journal*, Vol. 86, No. 2, pp. 182–191.
70. Sakata, K., and Ayano, T. (2000). "Effect of ambient temperature and humidity on creep and shrinkage of concrete." *ACI Special Publication 194-7, The Adam Neville Symposium: Creep and Shrinkage – Structural Design Effects*, pp. 115-235.
71. Schapery, R.A. (1967). "Stress analysis of viscoelastic composite materials," *J. Composite Materials*, Vol. 1, No. 3, pp. 228-267.

72. Sohn, H. (2007). "Effects of environmental and operational variability on structural health monitoring," *Philosophical Transactions of the Royal Society A*, Vol. 365, pp. 539-560.
73. Tadros, M.K., Al-Omaishi, N., Seguirant, S.P., and Gallt, J.G. (2003). "Prestress losses in pretensioned high-strength concrete bridge girders." *NCHRP Report 496*, Transportation Research Board, National Research Council, Washington, DC.
74. Thomas, J.J., and Jennings, H.M. (2006). "A colloidal interpretation of chemical aging of the C-S-H gel and its effects on the properties of cement paste," *Cement and Concrete Research*, Vol. 36, pp. 30-38.
75. Troxell, G.E., Raphael, J.M., and Davis, R.R. (1958). "Long-Term Creep and Shrinkage Tests of Plain and Reinforced Concrete," *ASTM Proceedings*, Vol.58, pp. 1101-1120.
76. Wang, C.-K., Salmon, C.G., and Pincheira, J.A. (2007). *Reinforced Concrete Design*, 7th edition, John Wiley & Sons Inc., New Jersey, USA.
77. Wittman, F.H. (1982). "Creep and shrinkage mechanisms," *Creep and Shrinkage in Concrete Structures*, Z.P. Bažant and F.H. Wittmann, eds., John Wiley and Sons, New York, NY, pp. 129-161.

Appendix A: Proof of Rate-Type Creep Methodology

This appendix provides a mathematical proof of the rate-type creep methodology from Bažant and Prasannan (1989a, 1989b), presented in Section 6.2.3. Knowledge of the Kelvin Chain model as presented in Section 6.2.1 is prerequisite to this proof.

The following development assumes a one-dimensional stress-strain relationship. The proof is similar for three-dimensional problems, with the addition of the isotropic material matrix **D**. The generalization to three-dimensional analysis will take place at the end of this proof.

The creep function is assumed to follow the Kelvin Chain model, such that

$$J(\xi) = \frac{1}{E_0} + \sum_{i=1}^{N} A_i \left(1 - e^{-\xi/t_{ri}}\right) \tag{A-1}$$

where E_0 is instantaneous modulus, A_i and t_{ri} are the compliance and retardation time, respectively, of the i-th element in the Kelvin Chain series, and $\xi = t - t_0$ is the time since loading. The change in strain $\Delta\varepsilon$ over a time step Δt must be computed for an increment of stress $\Delta\sigma$. The strain is both a function of time and stress, and thus can be computed using a total derivative:

$$d\varepsilon = \frac{\partial\varepsilon}{\partial t} dt + \frac{\partial\varepsilon}{\partial\sigma} d\sigma \tag{A-2}$$

$$\Delta\varepsilon = \Delta\varepsilon_{time} + \Delta\varepsilon_{stress} = \int_{t_b}^{t_e} \frac{\partial\varepsilon}{\partial t} dt + \int_{\sigma_0}^{\Delta\sigma+\sigma_0} \frac{\partial\varepsilon}{\partial\sigma} d\sigma \tag{A-3}$$

Hence the total change in strain can be computed by summing the change in strain with time assuming constant stress and the change in strain with stress.

Starting with the change in strain due to stress, the second term from Eqn. (A-3) is the hereditary integral from the superposition principle:

$$\Delta\varepsilon_{stress} = \int_{t_b}^{t_e} \frac{\partial\varepsilon}{\partial\sigma} \frac{d\sigma}{dt_0} dt_0 = \int_{0}^{\Delta t} J(\xi) \frac{d\sigma}{d\xi} d\xi \tag{A-4}$$

where the change of variables from time t_0 to $\xi = t - t_0$ has been made. Computing this change in strain:

$$\Delta\varepsilon_{stress} = \int_0^{\Delta t}\left(\frac{1}{E_0} + \sum_{i=1}^{N} A_i\left(1 - e^{-\xi/t_{ri}}\right)\right)\frac{d\sigma}{d\xi}d\xi \tag{A-5}$$

$$\Delta\varepsilon_{stress} = \int_{\sigma_0}^{\Delta\sigma+\sigma_0}\left(\frac{1}{E_0}\right)d\sigma + \int_0^{\Delta t}\left(\sum_{i=1}^{N} A_i\left(1 - e^{-\xi/t_{ri}}\right)\right)\frac{d\sigma}{d\xi}d\xi \tag{A-6}$$

For considerations of implementation in the finite element model, it is convenient to assume that the stress changes linearly over the time step. This assumption is valid for sufficiently small time steps. Therefore, letting

$$\frac{d\sigma}{d\xi} = \frac{\Delta\sigma}{\Delta t} = \text{constant} \tag{A-7}$$

Eqn. (A-6) can be simplified as follows:

$$\Delta\varepsilon_{stress} = \frac{\Delta\sigma}{E_0} + \int_0^{\Delta t}\left(\sum_{i=1}^{N} A_i\left(1 - e^{-\xi/t_{ri}}\right)\right)\frac{\Delta\sigma}{\Delta t}d\xi \tag{A-8}$$

$$\Delta\varepsilon_{stress} = \frac{\Delta\sigma}{E_0} + \frac{\Delta\sigma}{\Delta t}\left[\sum_{i=1}^{N} A_i\left(\xi + t_{ri}e^{-\xi/t_{ri}}\right)\right]_{\xi=0}^{\xi=\Delta t} \tag{A-9}$$

$$\Delta\varepsilon_{stress} = \Delta\sigma\left[\frac{1}{E_0} + \sum_{i=1}^{N} A_i\left(1 - \frac{t_{ri}}{\Delta t} + \frac{t_{ri}}{\Delta t}e^{-\Delta t/t_{ri}}\right)\right] \tag{A-10}$$

The first term from Eqn. (A-3), $\Delta\varepsilon_{time}$, is the creep of the material under a constant stress. To aid in the computation of this quantity, the remaining creep $\gamma_{ci}^{(n)}$ can be introduced. This quantity signifies the remaining total creep in the *i*-th Kelvin element of the Kelvin Chain model at the end of the *n*-th time step.

For a stress σ_0 applied instantaneously at time $\xi = 0$, each Kelvin Chain will asymptotically approach a strain equal to $A_i\sigma_0$. Therefore, assuming constant stress, the remaining creep strain γ_{ci} in the *i*-th Kelvin Chain is equal to

$$\gamma_{ci}(\xi) = A_i\sigma_0 - \sigma_0 J(\xi) = A_i\sigma_0 e^{-\xi/t_{ri}} \tag{A-11}$$

Much like the total strain in Eqn. (A-2), the remaining creep strain in each Kelvin Chain is a function of time and stress, and therefore can be computed using a total derivative:

$$d\gamma_{ci} = \frac{\partial\gamma_{ci}}{\partial t}dt + \frac{\partial\gamma_{ci}}{\partial\sigma}d\sigma \tag{A-12}$$

$$\Delta\gamma_{ci} = \Delta\gamma_{ci-time} + \Delta\gamma_{ci-stress} = \int_{t_b}^{t_e}\frac{\partial\gamma_{ci}}{\partial t}dt + \int_{t_b}^{t_e}\frac{\partial\gamma_{ci}}{\partial\sigma}\frac{d\sigma}{dt_0}dt_0 \tag{A-13}$$

The second term from Eqn. (A-13) is again the hereditary integral from the superposition principle:

$$\Delta\gamma_{ci-stress} = \int_{t_b}^{t_e}\frac{\partial\gamma_{ci}}{\partial\sigma}\frac{d\sigma}{dt_0}dt_0 = \int_0^{\Delta t} A_i e^{-\xi/t_{ri}}\frac{d\sigma}{d\xi}d\xi \tag{A-14}$$

where the change of variables from time t_0 to $\xi = t - t_0$ has been made. Using the assumption that the change in stress is linear, Eqn. (A-14) becomes

$$\Delta\gamma_{ci-stress} = -\frac{\Delta\sigma}{\Delta t}\left[A_i t_{ri} e^{-\xi/t_{ri}}\right]_{\xi=0}^{\xi=\Delta t} \tag{A-15}$$

$$\Delta\gamma_{ci-stress} = \frac{A_i\Delta\sigma}{\Delta t}\left(t_{ri} - t_{ri}e^{-\Delta t/t_{ri}}\right) \tag{A-16}$$

The first term of Eqn. (A-13), the change in remaining creep due to time under constant stress, can be conveniently written in an iterative form. At the beginning of the *n*-th time step, the remaining creep in the *i*-th Kelvin element is equal to

$$\gamma_{ci}^{(n-1)} = Be^{-t'/t_{ri}} \tag{A-17}$$

where *B* is a constant based on the stress history and Kelvin element properties. Assuming no change in stress over the time step Δt, an assumption consistent with the partial derivative of the first term in Eqn. (A-12) with respect to time, at the end of that same time step the remaining creep in the *i*-th Kelvin element is equal to $\gamma_{ci}^{(n)}$:

$$\gamma_{ci}^{(n)}\Big|_{\Delta\sigma=0} = Be^{-(t'+\Delta t)/t_{ri}} = \gamma_{ci}^{(n-1)} e^{-\Delta t/t_{ri}} \tag{A-18}$$

Therefore, the change in remaining creep due to time under constant stress is equal to

$$\Delta\gamma_{ci-time} = \gamma_{ci}^{(n-1)} e^{-\Delta t/t_{ri}} - \gamma_{ci}^{(n-1)} \tag{A-19}$$

Updating the total remaining creep for the end of the time step produces:

$$\gamma_{ci}^{(n)} = \gamma_{ci}^{(n-1)} + \Delta\gamma_{ci-time} + \Delta\gamma_{ci-stress} \tag{A-20}$$

$$\gamma_{ci}^{(n)} = \gamma_{ci}^{(n-1)} e^{-\Delta t/t_{ri}} + \frac{A_i \Delta\sigma}{\Delta t}\left(t_{ri} - t_{ri} e^{-\Delta t/t_{ri}}\right) \tag{A-21}$$

Eqn. (A-19) is directly related to the $\Delta\varepsilon_{time}$ term from Eqn. (A-3). If under constant stress, the remaining creep in the *i*-th element decreases by the value given in Eqn. (A-19), then the creep (plus other stress-independent strains, such as shrinkage $\Delta\varepsilon_{sh}$ and thermal expansion $\Delta\varepsilon_T$) experienced by the Kelvin Chain model under the same conditions must be

$$\Delta\varepsilon_{time} = -\sum_{i=1}^{N} \Delta\gamma_{ci-time} + \Delta\varepsilon_{sh} + \Delta\varepsilon_T = \sum_{i=1}^{N} \gamma_{ci}^{(n-1)}\left(1 - e^{-\Delta t/t_{ri}}\right) + \Delta\varepsilon_{sh} + \Delta\varepsilon_T \tag{A-22}$$

Therefore, the total strain change over time step with duration Δt and linearly changing stress $\Delta\sigma$ is equal to

$$\Delta\varepsilon = \Delta\sigma\left[\frac{1}{E_0} + \sum_{i=1}^{N} A_i\left(1 - \frac{t_{ri}}{\Delta t} + \frac{t_{ri}}{\Delta t} e^{-\Delta t/t_{ri}}\right)\right] + \sum_{i=1}^{N} \gamma_{ci}^{(n-1)}\left(1 - e^{-\Delta t/t_{ri}}\right) + \Delta\varepsilon_{sh} + \Delta\varepsilon_T \tag{A-23}$$

For convenience, the incremental modulus E'' is defined as

$$E'' = \left[\frac{1}{E_0} + \sum_{i=1}^{N} A_i\left(1 - \frac{t_{ri}}{\Delta t} + \frac{t_{ri}}{\Delta t} e^{-\Delta t/t_{ri}}\right)\right]^{-1} \tag{A-24}$$

and the inelastic strain unrelated to changes in stress $\Delta\varepsilon''$ is defined as

$$\Delta\varepsilon'' = \Delta\varepsilon_{time} = \sum_{i=1}^{N} \gamma_{ci}^{(n-1)}\left(1 - e^{-\Delta t/t_{ri}}\right) + \Delta\varepsilon_{sh} + \Delta\varepsilon_T \tag{A-25}$$

so that Eqn. (A-23) can be rewritten as

$$\Delta\sigma = E''\left(\Delta\varepsilon - \Delta\varepsilon''\right) \tag{A-26}$$

To extend the proof to three dimensions, the isotropic material matrix **D** is added where appropriate. Specifically, Eqn. (A-21) and Eqn. (A-26) become, respectively,

$$\boldsymbol{\gamma}_{\mathbf{ci}}^{(n)} = \boldsymbol{\gamma}_{\mathbf{ci}}^{(n-1)} e^{-\Delta t/t_{ri}} + \frac{A_i \mathbf{D}^{-1} \Delta \boldsymbol{\sigma}}{\Delta t}\left(t_{ri} - t_{ri} e^{-\Delta t/t_{ri}}\right) \tag{A-27}$$

$$\Delta \boldsymbol{\sigma} = E'' \mathbf{D}\left(\Delta \boldsymbol{\varepsilon} - \Delta \boldsymbol{\varepsilon}''\right) \tag{A-28}$$

where the definition of E'' from Eqn. (A-24) remains unchanged, and $\Delta\boldsymbol{\varepsilon}''$ from Eqn. (A-25) becomes the vector equation

$$\Delta \boldsymbol{\varepsilon}'' = \sum_{i=1}^{N} \boldsymbol{\gamma}_{\mathbf{ci}}^{(n-1)}\left(1 - e^{-\Delta t/t_{ri}}\right) + \Delta \boldsymbol{\varepsilon}_{\mathbf{sh}} + \Delta \boldsymbol{\varepsilon}_{\mathbf{T}} \tag{A-29}$$

In the implementation of the routine, Eqns. (A-24), (A-27), (A-28), and (A-29) are necessary, and are provided as Eqns. (6-24), (6-21), (6-25), and (6-26), respectively, in Section 6.2.3. The values of $\underline{\boldsymbol{\gamma}}_{\mathbf{ci}}^{(n-1)}$ must be saved as a state variable in order to update the values of $\underline{\boldsymbol{\gamma}}_{\mathbf{ci}}^{(n)}$ using Eqn. (A-27).

Appendix B: Validation of Time-Dependent FEM of St. Anthony Falls Bridge

B.1 Longitudinal Behavior

As a check on the validity of the finite element analysis, the total axial contraction of the bridge (starting at the beginning of the construction sequence and ending 150 years after completion) was estimated using a simple hand calculation and compared to the total axial deformation from the finite element model results over the same time period. The purpose of this check was to ensure that the time-dependent models were properly input and that the applied stresses in the FEM were valid in terms of the average longitudinal deformation. This check was neither intended to investigate bending behavior, nor to thoroughly validate the applied stresses at each cross section.

For the hand-calculated contraction, the creep, shrinkage, and elastic strains were computed using the time-dependent models as described in Chapter 4. The following assumptions were made for the hand calculation to simplify the procedure:

1. The geometry of the bridge was assumed to be constant along the entire length, such that the volume-to-surface ratio was equal to 8.0 in. (200 mm).
2. Design calculations by Figg Bridge Engineering indicated that the mean longitudinal stress throughout the entire superstructure over time was approximately equal to 1,400 psi (9.7 MPa). For purposes of the hand calculation, this applied stress was assumed to be uniform compression and constant with time.
3. All stress was applied simultaneously at a concrete age of 50 days, which was near the average age at which any given concrete in the bridge (precast or cast-in-place) was first stressed. The moist curing duration was set equal to 4 days as was assumed for the precast segments in the finite element analysis. The construction staging sequence was ignored.

4. Concrete material properties were identical to those assigned to the superstructure in the finite element analysis, as discussed in Chapter 4.
5. Temperature was assumed to be constant at 69°F (20°C). Ambient humidity was set equal to 64.1%, identical to that used for the finite element analysis.

The hand-calculated change in axial strain was equal to the full creep and shrinkage strains plus half the instantaneous elastic strains due to the applied stress. The rationale for using only half the elastic strains was that during the construction staging sequence in the FEM results, application of longitudinal post-tensioning would cause deflection at both the expansion joint and the free end of the cantilever. Considering the total axial contraction as the change in distance between the locations of the LPs installed at the ends of Spans 1 and 3, any deflection at the free end of the cantilever would not affect the total contraction. As an approximation, it was assumed that half the elastic deformation went to the cantilever ends and thus had no effect on the total contraction. Shrinkage strains were computed as the relative shrinkage strains since loading, similar to how the finite element model excluded shrinkage strains prior to the erection of each individual segment. The estimated total longitudinal deflection from the beginning of the construction sequence to 150 years after completion was equal to the strain change multiplied by the length of Spans 1 through 3, equal to 12,780 in. (324.6 m).

The longitudinal deflection from the FEM was computed as the total change in length of the superstructure as recorded at the locations of the linear potentiometers at the ends of Spans 1 and 3. In this way, the total axial contraction according to finite element results was compatible with the assumptions in the hand-calculated estimate.

Figure B.1 compares for each time-dependent model the approximate hand calculated contraction with the contraction computed using the finite element method. The hand-calculated approximation overestimated the total contraction from the FEM in all cases, though due to the nature of the approximation, this was not surprising. The GL2000 hand calculation was the most

inaccurate with a relative error of 17% at 55,000 days after loading, followed by the B3 estimate with a relative error of 12%. Estimates for all other models exhibited relative errors of less than 10%. From 50 to 200 days, the shapes of the AASHTO and ACI-209 hand-estimated deflections differed from the FEM results of the same models, but for the other time-dependent models the shapes of the long-term time-dependent deflections were similar between the hand-calculated results and the FEM output. It was likely that the primary difference between the hand-calculated estimate and the FEM results was in the modeling of the construction staging sequence. Similar to the justification for using only half the total elastic strains in the hand calculation, only some percentage of the creep and shrinkage strains should have been applied. This percentage would be related to (1) the amount of creep and shrinkage strains that occurred during the construction staging sequence and (2) the portion of these strains that caused deflection at the expansion joint as compared to the free cantilever end. Because no simple reason existed for how to divide up the estimated creep and shrinkage strains, 100% of these strains were applied as total elongation, and thus the hand calculation overestimated the FEM results.

Due to the closeness of fit provided by the rough hand-calculated estimate as compared to the FEM predictions, and due to the similarity in the shapes between the hand-calculated deflection and FEM results, the longitudinal behavior of the finite element model was believed to valid.

B.2 Bending Behavior

Accurately estimating the total time-dependent vertical deflections of the bridge using hand-calculation methods was believed to be too involved for validation of the finite element model. The simplifying assumptions used for estimating the axial contraction would not be valid for estimating the vertical deflection. The final vertical deflection is the difference between two components of roughly similar magnitude: downward deflection due to dead weight and upward deflection due to post-tensioning. Consequently, inaccurate assumptions in the estimation of

either of these components would cause large relative errors in the total vertical deflection, which would make validation of the vertical deflections using a simplified model particularly challenging.

Instead of estimating the long-term time-dependent deflections using a simplified method, the truck load test data was used to validate the behavior of the bridge in longitudinal bending. The procedures and results for the truck tests conducted on the I-35W St. Anthony Falls Bridge are documented in French et al. (2012). The rationale for using the truck test data for validation was as follows:

1. Assume that longitudinal behavior is valid (Section B.1).
2. Because longitudinal behavior is valid, then it is assumed that the time-dependent strains predicted by any application of stress and the given compliance and shrinkage curves are accurate.
3. Assume that vertical deflection and bending behavior are caused by moments induced by gravity and post-tensioning loads.
4. Assume that the model is defined with proper initial stress conditions and bridge geometry, and that the post-tensioning was properly applied.
5. If the moments caused by some known applied load are found to be valid, then the moments applied by gravity and post-tensioning are valid.
6. If the moments caused by gravity and post-tensioning are valid, then the time-dependent vertical deflection and bending behavior of the model are accurate.

Using this logic, showing that the model behaves properly under the truck load tests implies that the vertical deflection and longitudinal bending behavior of the bridge will be accurately computed by the model. These assumptions were justified because models with identical geometry, but no construction sequence, were used to estimate the static behavior of the structure under truck test loading and thermal effects (French et al., 2012). To ensure that the

modeled construction staging sequence was valid, the complete sequence was modeled before applying the truck loads during the validation of the time-dependent finite element model.

The vertical deflection and longitudinal bending were validated by using the full time-dependent finite element model and the complete construction staging sequence up until September 4, 2008 (the time at which the first truck tests were conducted). At this time, loads from the truck tests were applied to the model, and the change in strain due to the loading was compared to measured results. Truck loads were ramped from zero to the total load over a time step of 0.01 days (14.4 minutes), and the truck test strains were computed using the time-dependent constitutive laws as discussed in Chapter 4. The duration of the truck load ramp specified in the finite element analysis was chosen to coincide with the approximate duration that the trucks were in position for the conducted truck tests.

If the construction staging sequence was improperly input into the model, it would be expected that the FEM results from the truck tests would not correspond to the measured results. If on the other hand the construction staging sequence was correct and the FEM results were found to be accurate with respect to measured data, then it would be concluded that the time-dependent model was valid for longitudinal bending behavior.

Figure B.2 shows the longitudinal curvatures predicted by the time-dependent FEM using the AASHTO LRFD (2010) provisions (Section 4.8) compared to the measured truck test results from tests STI3SB (eight trucks facing south and positioned across the width of the bridge with rear tandem centered on Location 3) and STI7SB (identical to STI3SB but at Location 7). The maximum error at any location between the FEM results and the measured data from either of the truck tests was less than 0.045 με/in. (1.7 με/m). With the exception of the B3 model, results from the other time-dependent models were similar.

Figure B.3 shows the longitudinal curvatures predicted by the time-dependent FEM using the B3 model (Section 4.4) compared to the measured data from truck tests STI3SB and STI7SB.

The FEM using the B3 model predicted much lower curvatures than the other models. This was likely due to the considerable amount of short-term creep included in the B3 model. As discussed in Section 4.4.1, the instantaneous elastic modulus of the B3 model is constant with time and higher than the elastic modulus assumed in all other models, while short-term creep strains account for the additional strains observed during typical concrete modulus tests. Thus, the specific application of the load in the FEM had a great impact on the total output strains when using the B3 model. According to Bažant and Baweja (1995a), the traditional definition of the ACI-209 (1992) elastic modulus corresponds to the total B3 compliance for a step load held for 0.01 days, which was conveniently the same duration as chosen for the truck load ramp duration. If the load were applied as a step load and held for 0.01 days, the change in curvature due to time-dependent behavior would be approximately double that for a load ramp from zero to the full load over the course of 0.01 days, as was performed in this analysis.

Considering truck test STI7SB, the instantaneous curvature at Location 7 using the B3 model was equal to 0.34 με/in. (13 με/m), and the time-dependent curvature over the 0.01-day ramp loading was equal to 0.11 με/in. (4.3 με/m). Doubling this time-dependent curvature to emulate a step load held for 0.01 days resulted in a total curvature at Location 7 equal to 0.56 με/in. (22 με/m), which was within 0.05 με/in. (2.0 με/m) of the measured truck test results. Had a step load been applied instead of a ramp load for the B3 model, the computed curvatures at all locations for both truck tests would be approximately 25% larger than shown in Figure B.3,

Therefore, after accounting for the discrepancies in the B3 definition of elastic modulus, all examined time-dependent models were found to closely match the measured truck test data. The longitudinal bending behavior of the time-dependent FEM was consequently believed to be valid.

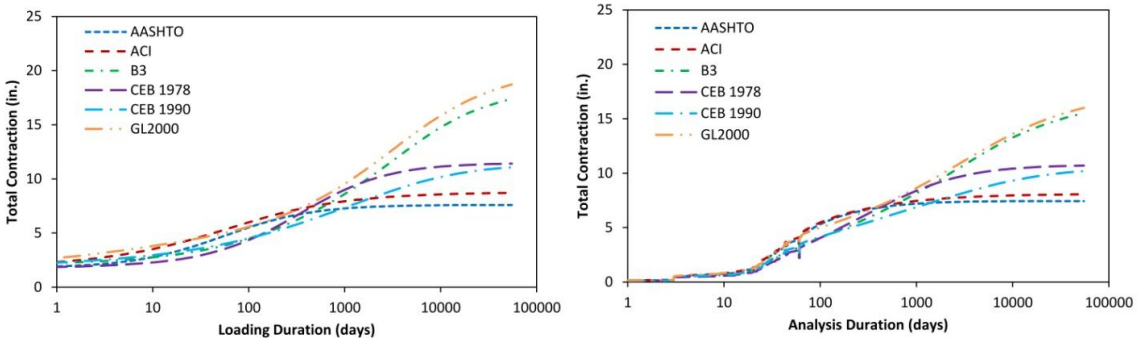

(a) Hand calculation (b) FEM

Figure B.1: Total contraction of the southbound bridge Spans 1 through 3 estimated using (a) simplified hand-calculation and (b) finite element model results

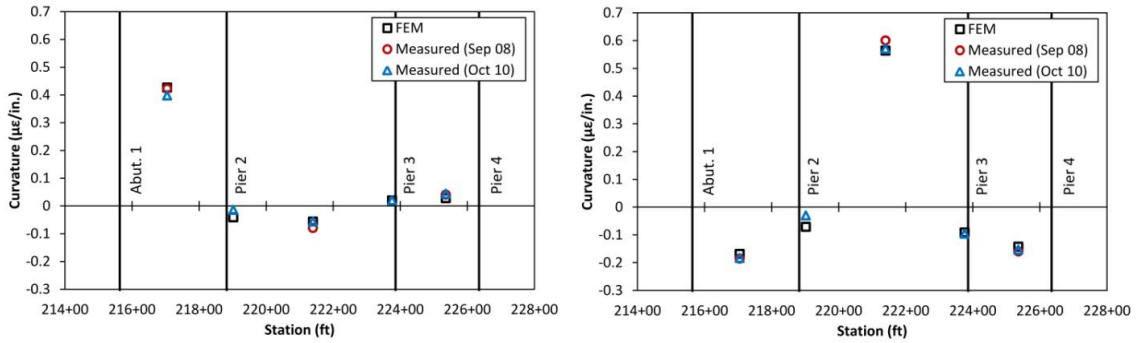

(a) STI3SB (b) STI7SB

Figure B.2: Comparison of measured longitudinal curvature from truck tests (a) STI3SB and (b) STI7SB with estimates from time-dependent FEM using AASHTO LRFD provisions

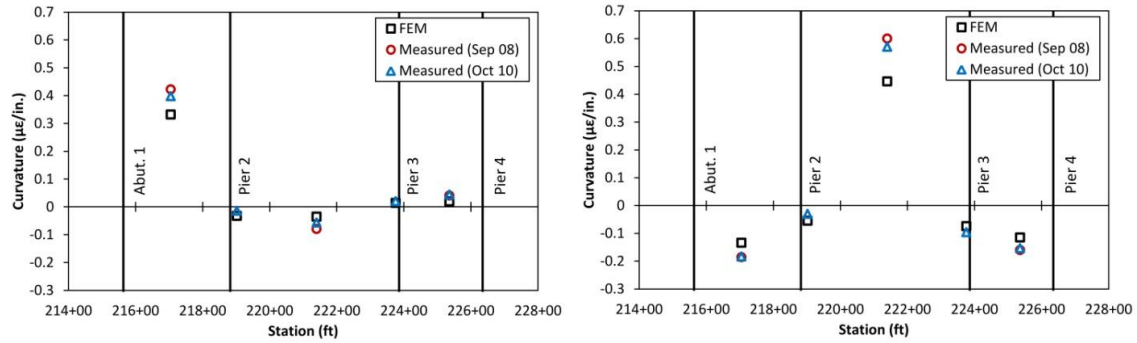

(a) STI3SB (b) STI7SB

Figure B.3: Comparison of measured longitudinal curvature from truck tests (a) STI3SB and (b) STI7SB with estimates from time-dependent FEM using B3 provisions

Appendix C: Investigation of Simplified Construction Staging Procedure

The results from the time-dependent analyses presented in Sections 8.1 and 8.2 mimicked the full (as-built) construction staging sequence as described in Section 6.1.3. To investigate whether or not this level of detail was required for accurate predictions of time-dependent deformations and service stress states over the life of the structure, time-dependent finite element analysis was conducted for the St. Anthony Falls Bridge using a simplified construction sequence. This study was performed to (1) evaluate how sensitive design predictions for the stress states at end of construction and end of service were to the details of the assumed construction sequence, and in particular on the proper modeling of the closure pour, and (2) if the FEM predictions used in the monitoring system (Chapter 10) would be negatively impacted if the modeled construction sequence differed significantly from the as-built construction sequence.

Although the construction sequence could have been simplified in many ways, for this study, all the post-tensioning was applied within a day of the closure pour procedure, rather than over the course of the segmental erection procedure. The erection procedure and closure pour were not modeled. The simplified model did account for the different concrete ages throughout the superstructure, though because of the change in the stressing schedule, the ages at first loading were not comparable between the full and simplified procedures.

C.1 Simplified Finite Element Model Construction Sequence

For simplicity, the finite element model utilizing the full construction sequence (described in Section 6.1.3) was modified to the simplified case so that all construction steps prior to the placement of the midspan closure pour were removed. Some facets of the construction sequence were still included in the simplified case, such as the original casting dates of each segment and the sequence of loading after the closure pour was placed.

Following the analysis steps listed in Table 6.1, the simplified procedure began at Step 59, C29, on July 25, 2008. The list of analysis steps for the simplified construction procedure are given in Table C.1. The start of the simplified analysis was directly after the midspan closure pour had been placed, and so all concrete was in place at the start of the simplified analysis except for the barrier rail. The midspan jacks, the shoring for Spans 1 and 3, and the strongback alignment beams across the closure pour were not included in the simplified procedure.

All post-tensioning except for the Span 2 bottom flange tendons and Span 2 draped strands was applied simultaneously at the start of the analysis. The Span 2 bottom and draped tendons were added 2 analysis days later in Step 2 (Strands), just as had been performed for the model with the complete construction staging sequence.

In the complete construction procedure, strands were added sequentially as the segments were added, and thus strands stressed earlier in the sequence were subject to elastic shortening losses from the strands stressed later. To approximate these elastic shortening losses in the simplified construction procedure, half the computed elastic shortening losses were simulated to occur in all applied post-tensioning. This was done by specifying an initial stress state but halving the modulus of elasticity of the tendons during the first step when the initial stress in the steel was equilibrated by inducing compression in the concrete. The reduction in steel modulus reduced the elastic shortening stress losses by a factor of two. The steel modulus was increased to the full value after equilibrium had been obtained so that the proper stiffness would be used for all subsequent time steps. The rationale for incorporating half the elastic shortening losses was that the first stressed tendons would undergo the full elastic shortening losses of all future tendons, while the final stressed tendons would not exhibit any elastic shortening. Thus, on average the stress state in any given tendon would have halve the elastic shortening caused by the total post-tensioning application.

Permanent loads such as gravity, the exterior barrier rail, and the utility allowance as specified in Section 6.1.4 were identical between the simplified procedure and full construction procedure. The transient loads on the cantilever tips that were applied before the closure pour and then removed after tensioning the Span 2 bottom and draped tendons, as discussed in Section 6.1.4, were not included in the simplified model.

By ignoring the full construction staging sequence, it was impossible to precisely consider the concrete ages at which any given segment was loaded. Other than the midspan closure pour, most segments were at least one month old when first loaded. Because the aging process for older concrete is greatly slowed compared to early age concrete, the response due to a sustained load applied at, for example, two months was likely within 10% of the response to a load applied several months later. Because casting dates were already incorporated into the full-construction model, the ages of the concrete segments in the simplified model were kept the same as the ages from the full construction sequence. This meant that for all post-tensioning forces except for those from Span 2 bottom and draped tendons, the load was applied up to two months later in the simplified model as compared to the full construction model. Also by keeping the same concrete ages, the relative shrinkage strains after the placement of the closure pour would be equivalent between the two models.

Only the ACI-209 (1992) and GL2000 (Gardner and Lockman, 2001) time-dependent models were examined when investigating the construction procedure. The ACI-209 model was assumed to be qualitatively similar to the other investigated asymptotic time-dependent models, while the GL2000 was believed to be representative for the logarithmic B3 model.

C.2 Comparison of Results using Simplified and Full Construction Sequences

For all comparisons, the closure pour on July 25, 2008 was assumed to occur at adjusted age time equal to zero, meaning that the application of the Span 2 bottom and draped tendons

occurred at an adjusted age of 2 days. In general, the results prior to an adjusted age of 2 days were incomparable between the two modeling methods due to inherent differences in the loading procedures.

C.2.1 Longitudinal Deflections

The computed longitudinal deflections, zeroed just after the Span 2 bottom and draped tendons were stressed at an adjusted age of 2 days, are plotted in Figures C.1 and C.2 for the Span 1 and the Span 3 expansion joints, respectively. The computed deflection at Span 3 represents the FEM calculated deflections at the north end of Span 3 plus the expected deflection at the top of Pier 4 due to the time-dependent behavior. Pier 4 deflections were computed in the same manner as documented in Section 8.1.1, and were assumed to be equal for the simplified and full construction sequence models.

The longitudinal deflections at the expansion joints calculated using the simplified construction sequence were larger than those computed using the full construction sequence. By the end of service, approximately 150 adjusted age years (55,000 adjusted age days) after completion, differences between the longitudinal deflections computed from the simplified and full construction models were always less than 0.5 in. (13 mm) regardless of the adopted time-dependent model. The relative differences between the simplified and full construction modeling methods were greater for the ACI-209 time-dependent model than for the GL2000 provisions.

The increase in deflections for the simplified procedure was primarily because the results from the full construction procedure included creep and shrinkage prior to an adjusted age of zero (i.e., the time at which the closure pour was cast). The simplified procedure delayed these deformations until after the closure pour, so the plotted deformations for the simplified sequence appeared larger than those for the full sequence. A secondary, though related factor was that, for the full construction procedure, creep and shrinkage prior to the placement of the midspan closure pour resulted in deflections at both the free cantilever end and the expansion joint. For the

simplified procedure, all creep and shrinkage strains were realized as displacement at the expansion joint, thus further increasing the estimates from the simplified procedure. The increase in apparent creep and shrinkage for the simplified procedure was countered by an expected decrease in creep strains due to the older concrete ages at loading in the simplified procedure as compared to the full procedure, though this effect was expected to be minor.

For both the ACI-209 and GL2000 time-dependent models, including the full construction sequence had no effect on the relative deflections after approximately 100 adjusted age days. To illustrate this, the finite element results from the simplified and complete construction sequence models, set equal to the measured linear potentiometer data at 10:00 AM CST on May 16, 2010 as was done in Section 8.1.1, are plotted for Span 1 and Span 3 in Figures C.3 and C.4, respectively. Only the behavior prior to 100 adjusted age days was meaningfully changed.

C.2.2 Concrete Strains

The computed longitudinal strains at Location 3, zeroed to the beginning of the measured vibrating wire strain data, are plotted in Figures C.5. Similar to the longitudinal deflections, the behavior during the first 100 adjusted age days after completion of the bridge differed between the two procedures for modeling the construction sequence, while the behavior after this point in time was only slightly affected. Strains at other instrumented locations showed similar trends to those presented for Location 3, and are thus not reproduced here.

C.2.3 Vertical Deflections

Computed vertical deflections for the simplified and complete construction methods are compared in Figures C.6, C.7, and C.8 for southbound bridge Locations 3, 7, and 9, respectively. Plotted deflections were zeroed just after application of the Span 2 bottom and draped post-tensioning at an adjusted age of 2 days. Unlike the longitudinal deflections measured by the linear

potentiometers, the computed vertical deflection rates over the course of the bridge service life were affected strongly by the inclusion of the construction staging sequence.

Vertical deflections are caused by bending of the structure induced by the difference between two large forces (gravity dead load and post-tensioning). On the contrary, time-dependent longitudinal deflections are largely driven only by the post-tensioning forces and axial deformation. Following this argument, the construction staging sequence, which involves an incremental addition of gravity loading and an evolving bending profile, should have a significant impact on the long-term bending behavior and vertical deflections. The axial forces imparted by the post-tensioning will be nearly equivalent regardless on the order in which they are added, excepting the midspan closure pour and the small additional losses caused during the segmental erection procedure. Thus, the inclusion of the construction sequence will more strongly affect the time-dependent vertical movement and bending behavior of the structure as compared to the longitudinal movement.

C.2.4 End of Construction and Service Stress States

For comparison of stress conditions, the estimated total stresses after the barrier rail was added (August 5, 2008) were considered to be the end of construction conditions, while the end of service conditions were 150 adjusted age years (55,000 adjusted age days) after the end of construction. The computed top and bottom fiber stresses along the lengths of Spans 1 through 3 of the southbound bridge due to permanent loads and post-tensioning are plotted at the end of construction and end of service states in Figure C.9.

At the end of construction, the top fiber stresses were only minimally affected by modeling the construction sequence. Maximum differences were found at the midspan of Span 2, where the simplified procedure returned approximately 200 psi (1.4 MPa) more compression than the complete construction sequence. However, end of construction stresses in the bottom fiber were substantially changed along the entire length of the bridge, though primarily at the midspan

of Span 2, by the simplification of the construction procedure. At most, the simplified construction model returned 800 psi (5.5 MPa) less compression than the complete construction model. These differences in stress were likely because all post-tensioning in the simplified model was applied after continuity of the three-span structure was established. This distributed the applied compression in a different manner than had the stresses been added during cantilever construction and followed by the addition of a stress-free closure pour. As expected, the choice of time-dependent model had negligible effect on the end of construction stresses regardless of the modeling procedure.

At the end of service, the top fiber stresses were unexpectedly similar between the simplified and complete construction models. The bottom stresses between the two methods were different at the end of service, but the magnitude of the differences observed at the end of service were less than the differences at the end of construction. In the bottom fiber for both the ACI-209 and GL2000 time-dependent models, the simplified procedure experienced lower losses than the complete construction procedure, though likely because the initial compression was lower for the simplified procedure. The predicted end of service stresses using the GL2000 model appeared to be less sensitive to the details of the construction procedure than those predicted by the ACI-209 model.

C.3 Conclusions on Construction Staging Sequence Modeling

The method for incorporating the construction staging sequence into numerical modeling of the I-35W St. Anthony Falls Bridge was found to have a significant impact on some aspects of behavior of the structure. For longitudinal (axial) behavior, early age deformations (before 100 adjusted age days following the closure pour) were increased by adopting a simplified construction sequence. Though the rates of the long-term axial behavior coincided between the two methods, differences in early age behavior would mean that the models using the simplified and complete construction sequences would predict different total deflections. In the case of the

expansion joint movement measured by the linear potentiometers, this amounted to a difference of approximately 0.5 in. (13 mm). Similarly for longitudinal strains measured by vibrating wire strain gages, differences during the first 100 adjusted age days after completion of the bridge returned up to 200 με differences in the expected time-dependent strains.

With regard to vertical deflections associated with time-dependent bending of the structure, rates throughout the entire service life of the bridge will be impacted by the details of the erection procedure. Differences in vertical deflections between the simplified and full modeled construction sequences were often of similar magnitude, up to 2 in. (50 mm), as the total time-dependent deflections over the life of the bridge.

Both end of construction and end of service stresses cannot be accurately captured unless the construction sequence is modeled. For this particular application, the stress state given the simplified construction procedure had lower concrete compression (up to 500 psi (3.4 MPa) lower in the worst case) than that from the full construction model, meaning the simplified procedure happened to be conservative in this respect. Whether or not this is true for other structures, or for other simplifying assumptions regarding the construction procedure, is not evident from this study. Therefore, reliable design predictions of end of construction and end of service stress states should account for the full construction.

For the monitoring system using the longitudinal deflections measured by the linear potentiometer as documented in Chapter 10, the FEM results showed that relative longitudinal deflections after the first year were not significantly impacted by the manner of the construction sequence. Thus, using the first year of data to predict trends to future years may be unreliable if the construction sequence is not properly assumed in the FEM approximations. However, using data from the second or future years to predict trends should be reliable. For this specific application, linear potentiometer data was not available immediately at the placement of the closure pour (defined as an adjusted age of zero). As evinced by the time-dependent deflections

plotted in Figures C.3 and C.4, the FEM results from either the simplified construction model or the full construction model would have produced nearly identical extrapolations.

Table C.1: Analysis Steps for Simplified Erection Procedure

Step	Step Name	Step Start Date	Step End Date	Step Duration	Step Start Time	Step End Time	Notes
0	Initial	N/A	N/A	N/A	N/A	N/A	Remove barrier rail, Apply PT to all strands except Span 2 bottom and draped strands.
1	C29	7/25/2008	7/27/2008	1.998	61.002	63.000	Creep time, no new loads
2	Strands	7/27/2008	7/27/2008	0.001	63.000	63.001	Apply Span 2 bottom and draped PT
3	C30	7/27/2008	8/5/2008	8.999	63.001	72.000	Creep time, no new loads
4	Barriers	8/5/2008	8/5/2008	0.001	72.000	72.001	Add barrier rails
5	TD	8/5/2008	…	…	72.001	…	Continued time-dependent analysis for completed structure

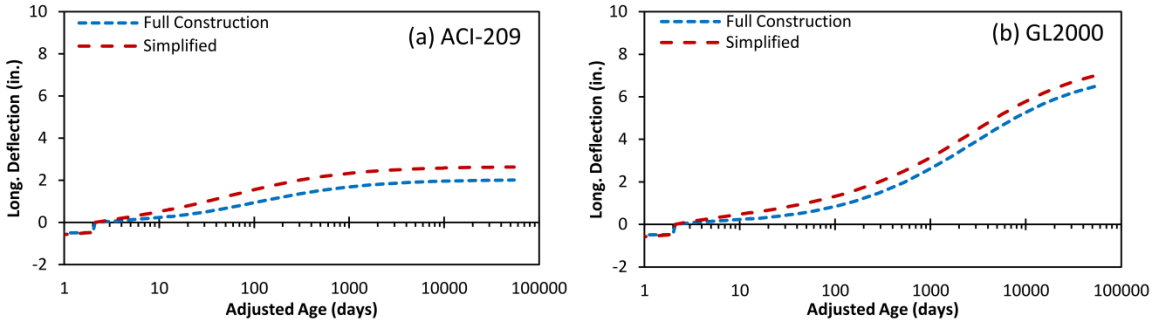

Figure C.1: Predicted longitudinal deflections at Span 1 expansion joint using (a) ACI-209 and (b) GL2000 time-dependent models with the full construction sequence and the simplified construction sequence

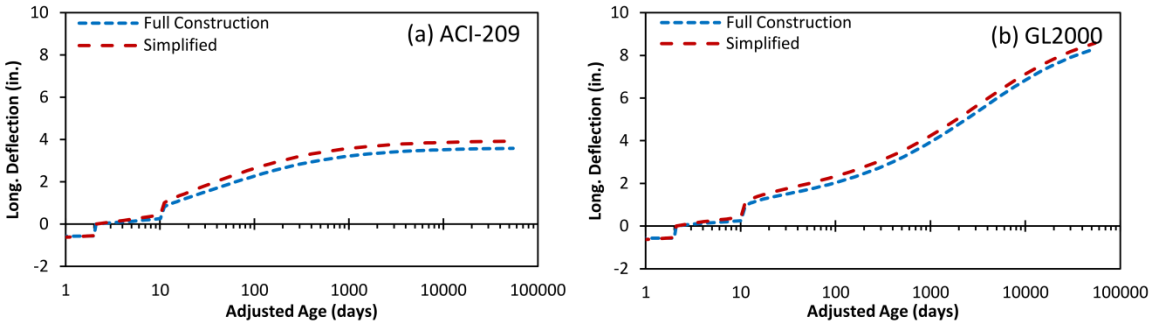

Figure C.2: Predicted longitudinal deflections at Span 3 expansion joint using (a) ACI-209 and (b) GL2000 time-dependent models with the full construction sequence and the simplified construction sequence

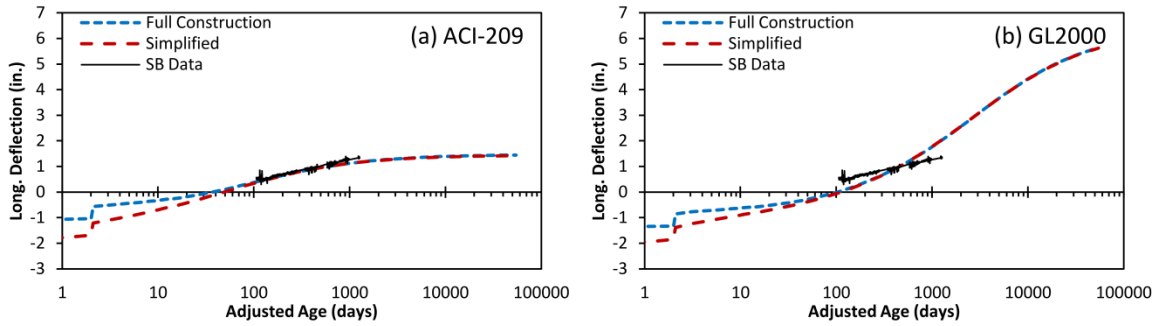

Figure C.3: Predicted longitudinal deflections at Span 1 expansion joint using complete and simplified construction procedures compared to measured southbound bridge Span 1 time-dependent linear potentiometer data

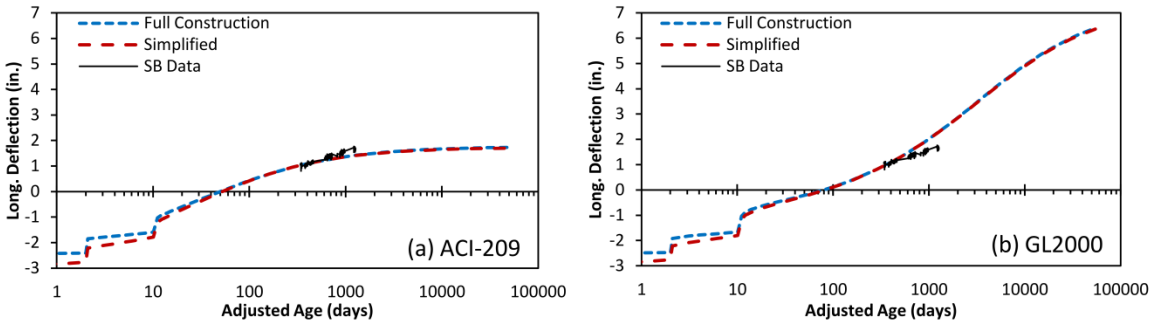

Figure C.4: Predicted longitudinal deflections at Span 3 expansion joint using complete and simplified construction procedures compared to measured southbound bridge Span 3 time-dependent linear potentiometer data

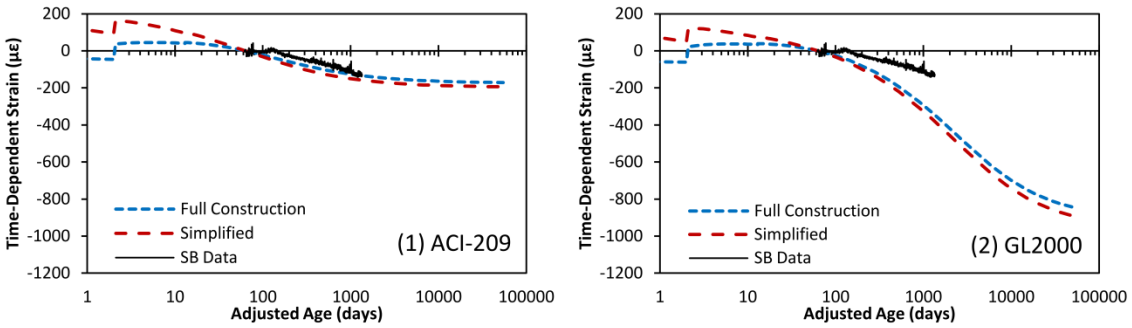

(a) Location 3 Bottom Flange (Below Webs) – 1. ACI-209 Model – 2. GL2000 Model

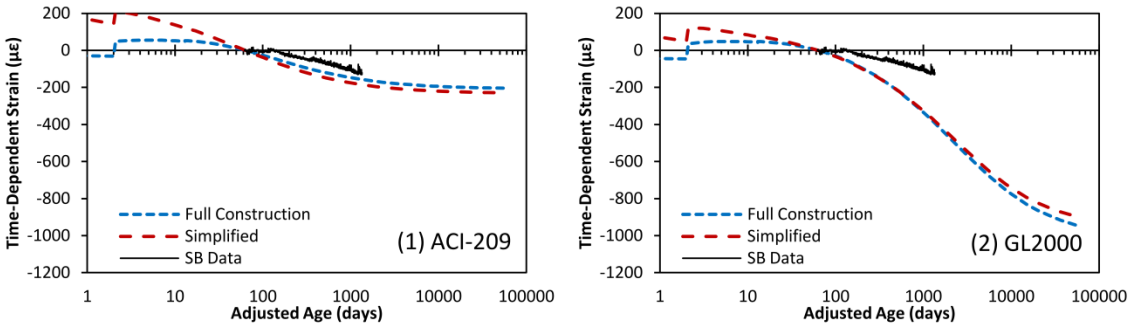

(b) Location 3 Bottom Flange (Centerline of Box) – 1. ACI-209 Model – 2. GL2000 Model

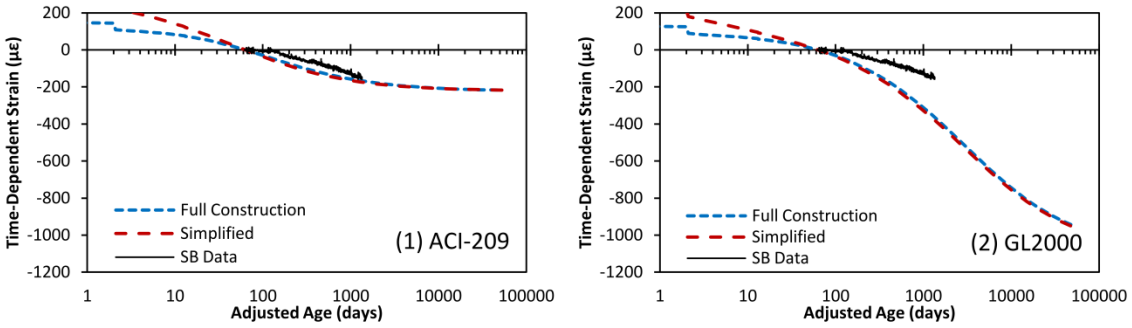

(c) Location 3 Top Flange (Above Webs) – 1. ACI-209 Model – 2. GL2000 Model

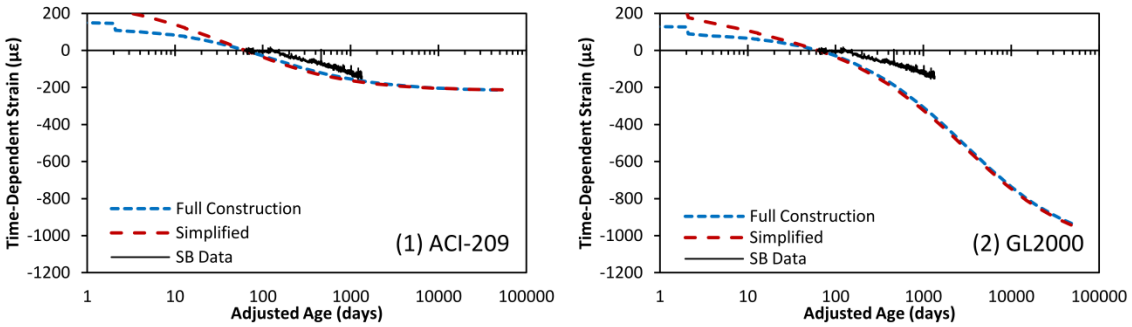

(d) Location 3 Top Flange (Centerline of Box) – 1. ACI-209 Model – 2. GL2000 Model

Figure C.5: Predicted longitudinal strains at Location 3 using complete and simplified construction procedures compared to measured time-dependent vibrating wire strain gage data

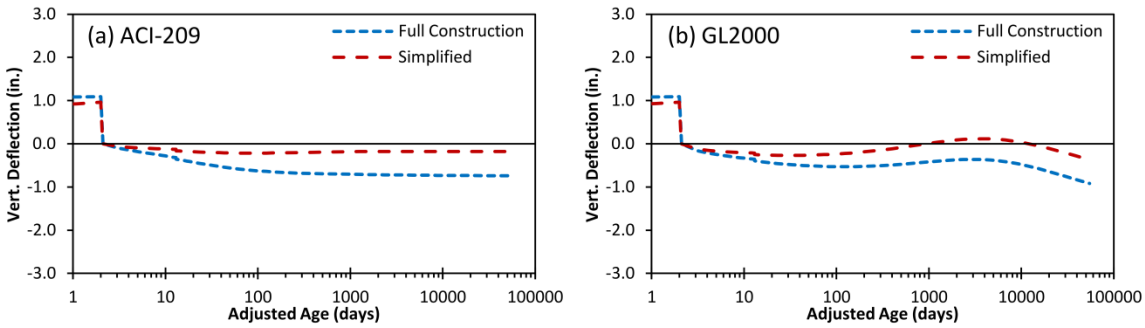

Figure C.6: Predicted vertical deflections strains at southbound bridge Location 3 using complete and simplified construction procedures

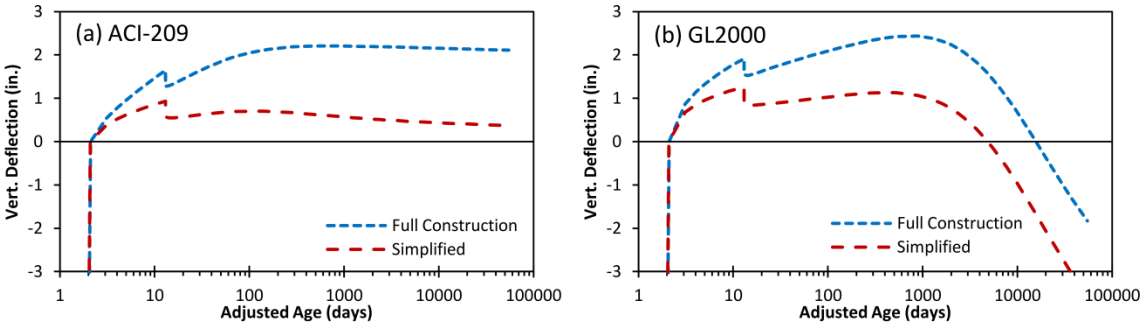

Figure C.7: Predicted vertical deflections strains at southbound bridge Location 7 using complete and simplified construction procedures

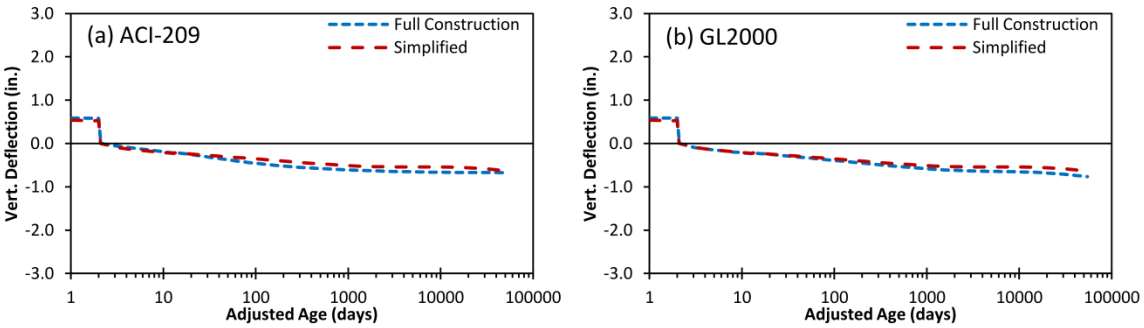

Figure C.8: Predicted vertical deflections strains at southbound bridge Location 9 using complete and simplified construction procedures

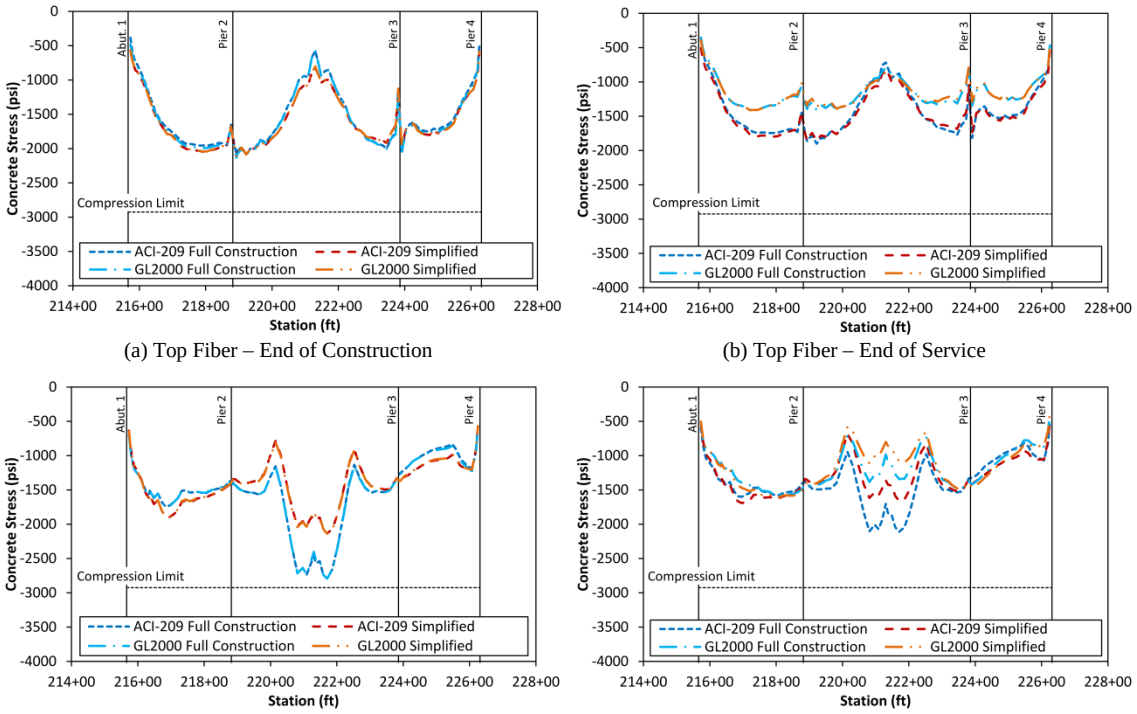

(a) Top Fiber – End of Construction

(b) Top Fiber – End of Service

(c) Bottom Fiber – End of Construction

(d) Bottom Fiber – End of Service

Figure C.9: Predictions of longitudinal concrete stresses in top and bottom flanges due to permanent loads at end of construction and end of service using complete and simplified construction procedures